eman ta zabal zazu
Universidad del País Vasco
Euskal Herriko Unibertsitatea
FACULTY OF SCIENCE AND TECHNOLOGY
UNIVERSITY OF THE BASQUE COUNTRY

Laser spectroscopic characterization of molecular aggregates

Doctoral Thesis

Ander Camiruaga Leza

Supervisors:

Dr. José Andrés Fernández González

Dr. Imanol Usabiaga Gutierrez

Department of Chemical Physics

Leioa, 2021

Ander Camiruaga was recipient of a predoctoral fellowship from the Basque Government. This research was supported by the Ministry of Economy and Competitiveness (CTQ2015-68148-C2-1-P and PGC2018-098561-B-C21) and the Basque Government (IT1162-19). Thanks also to the SGIker (UPV/EHU) Laser and Computational resources.

En primer lugar, querría agradecer a mis directores de tesis José Andrés e Imanol por la confianza depositada en mí y por facilitarme el camino durante éste complicado proyecto de tesis. Mi desarrollo como científico no habría sido posible sin los conocimientos y consejos aportados durante los últimos años.

Muchas gracias a todos los miembros del Grupo de Espectroscopía, pasados y presentes, por vuestra amistad y apoyo durante esta larga etapa.

Por otro lado, he de agradecer al Dr. Pierre Çarçabal, y al resto de miembros del "Institut des sciences moléculaires d'Orsay", por su hospitalidad y por convertir mi estancia en una experiencia muy enriquecedora.

Por supuesto, me gustaría dedicar todo este trabajo a mi familia. Llegar aquí no habría sido posible sin todo vuestro apoyo.

Finalmente, a Idoia, por haber compartido conmigo todo este camino, por su amor y maravillosa compañía en los buenos momentos, pero, sobre todo, por su paciencia y apoyo incondicional en los malos momentos.

Eskerrik asko

Index

The appendix in this thesis is available in electronic format. The reader can access it online as a pdf file in the following website link:

https://drive.google.com/file/d/1acMd16fyx4YlehX6Op6tQWatLANTkL0x/view?usp=sharing

Chapter 1

Introduction

1.1. Introduction

One of the most fascinating subjects in chemistry is the study of the intermolecular interactions and the structure of supramolecular systems. Non-covalent interactions (NCIs) are ubiquitous in Nature and govern a plethora of chemical, industrial and biological processes, ranging from formation of small molecular aggregates to large-scale supramolecular physical phenomena, such as aerosol formation, protein folding, ligand docking or signal recognition.[1] These intra- and intermolecular forces are purely quantum in nature, as they arise from the interaction between the electronic clouds of neighbor molecules, in a process called electron dynamic correlation.[2–4] They are often classified into van der Waals interactions (electrostatic, dispersion and exchange-repulsion) and hydrogen bond interactions. In comparison with covalent bonds, the great diversity of possible combinations of different atomic groups and the wide structural and energetic limits allows NCI to generate a specialized language that governs molecular aggregations.[5] The ability to "sense" nearby molecules and to form weak bonds that can be dissociated in a short time scale are some of the properties that play a fundamental role in the aggregation of biological systems, for example.

Among the above-mentioned NCIs, hydrogen bonds (HBs) deserve special mention. Many are the studies about this type of bond, but all of them agree in that its essential for life because it strongly modulates the intermolecular interactions: it is the responsible of the liquid and solid structures of water, but at the same time, it controls the complex process of signal recognition in biochemistry. Therefore, it is of no surprise that characterization of HBs has attracted a lot of scientific interest, resulting in the developments of sophisticated experimental and computational procedures for their study.

Evidences from experimental and theoretical studies in the last decades regarding the formation of HB required a re-definition by the UIPAC of the classic concept of HB proposed by Pauling[6] and by Pimentel and McCleallan,[7] in order to include more diverse interactions with electronegative atoms different from O, N or S:[8]

"*The hydrogen bond is an attractive interaction between a hydrogen atom from a molecule or a molecular fragment X-H in which X is more electronegative than H, and an atom or a group of atoms in the same or a different molecule, in which there is evidence of bond formation.*"

The name of this interaction comes from the sharing of a hydrogen atom between the donor and acceptor groups. Traditionally, the HB is represented as X-H···Y, where X and Y are electronegative atoms. From a quantum point of view, part of the electron density of atom Y jumps into the anti-bonding orbitals of the X-H group. This orbital overlapping gives the HB some covalent character, and a particularly high strength.

Hydrogen bonds involving O and N atoms are of special interest (O-H···O, O-H···N, N-H···O or N-H···N) due to their essential activity in nature. Together with van der Waals forces, they are fundamental in the stabilization and solvation of biological macromolecules, such as DNA, RNA and proteins.

However, considering the nature of NCIs and their weak module compared to covalent bonds, it is of no surprise that their characterization is a complex task. Their study at room temperature is difficult, as they tend to dissociate, and only the strongest interactions are able to survive. Solvation can also mask these interactions, generating a dynamic and constantly changing environment.[9] Therefore, the study of NCIs is a challenging for both experimental and theoretical methodologies.[10–14]

Few experimental techniques are capable of providing a clear molecular description, unbiased by crystal or matrix effects. That is why there is an increasing interest in the development of experimental and theoretical methodologies that provide high-quality data for molecular systems bounded by NCIs. In the early stages, data provided by crystal structures measured using X-ray diffraction were used as a reference as the preferred source of experimental data. However, the perturbations introduced by the crystal matrix to the NCIs precluded a correct evaluation of the structures. With the introduction of new techniques, and the improved resolution of the radiation sources, spectroscopy techniques, especially those in gas phase, raised as a solid alternative to provide experimental data on the structure of molecular aggregates.[15] In particular, spectroscopic studies in jets were a total revolution since the development of the first experimental set ups in the early 80's.[14,16–23] Jets are usually formed using a pulsed valve, which injects a gas mixture through a small orifice (nozzle) into a high vacuum chamber. The high-pressure difference generates an adiabatic expansion, during which the internal ro-vibrational energy of the molecules is transferred into translational energy thanks to collisions with the buffer gas.[19,24,25] Thus, the expansion generates a high density, "cooled" molecular beam, where the molecules travel isolated (without any external perturbations). Additionally, the environment offered by supersonic jets also simplifies the spectroscopy of the target system, as due to the low populated ro-

vibrational levels, line-widths and spectral congestion are reduced. The outstanding conditions provided by jets enable their combination with multiple spectroscopic techniques, like electronic, vibrational or rotational spectroscopy.[20,21,23,26–28]

In this project, we combined supersonic jets with mass-resolved laser spectroscopy techniques in order to obtain electronic and vibrational information from the molecular aggregates formed in supersonic expansions. Moreover, the mass-resolved detection strongly facilitates the study of molecular aggregates of different sizes, avoiding undesired interferences. However, one of the main advances in the spectroscopic studies of isolated compounds was the introduction of laser desorption systems. This powerful tool enables the desorption of thermolabile molecules, which can be immediately picked up by the expanding gas.[29–34] In this thesis, complex experimental setups complemented with laser desorption systems (see detailed description in Chapter 2) were used in order to study molecules that suffer degradation at high temperatures, like carbohydrates; or biologically relevant compounds with low-vapor pressure, like DNA nucleobases.

The beam formed in the supersonic expansion containing the molecular aggregates enters the ionization chamber, where they are excited and ionized using resonance enhanced multiphoton ionization (REMPI). Then, they are sent, using electric fields, to the free-flight region of a time of flight (TOF) mass-spectrometer. The REMPI technique can be combined with IR lasers (IR/UV double resonance techniques) in order to obtain the mass-resolved IR spectrum of the desired molecules/aggregates. In this thesis, the spectral region covering 2800-4000 cm^{-1} was extensively explored, which provides valuable structural information due to the sensibility of the position of the NH/OH groups to the environment. As mentioned previously, these groups are prone to form HBs. The perturbations in the vibrational stretching modes introduced by the formation of such interactions appear as shifts in the position of the bands, providing information on the intra- or inter-molecular interactions formed and their strength.

Another advantage of using spectroscopic techniques on supersonic expansions is that the spectra can be directly compared to the data obtained from computational chemistry. Usually, the information obtained using REMPI and IR/UV laser spectroscopic techniques is not easy to interpret. Most of the time, the difficulty of the interpretation of experimental data is directly related with the flexibility of the molecule/molecular aggregate. In molecular systems with reduced size, or with low flexibility, the number of

stable conformational isomers is limited, and therefore, assignment of the bands can be readily done by simple comparison with the computational simulations.

However, as the size of the system grows, so it does the number of possible conformers. This complicates the interpretation of the experimental spectrum, which can contain the contribution from several conformational families, presenting a congested set of vibrational transitions. In those cases, the computational exploration of all possible low-energy conformers is mandatory in order to perform a correct interpretation of the experimental results.[35–41]

One of the strategies to characterize the intermolecular interactions is to study them in small (mass-selected) and simple clusters, containing only one or two selected chemical groups. For example, the study of aggregation of water allows one to finely characterize the biologically relevant O-H···O interaction in absence of any external perturbation, as exceptionally illustrated with the water decamer.[42,43] Further introduction of additional chemical groups provides modulation of the O-H···O hydrogen bonds. In this way, characterization of the O-H···O interaction has proceeded through systems of increasing complexity, mainly aliphatic[41,44–49] and aromatic alcohols[50–55]. The introduction of an aromatic ring in the aggregation of alcohols completely changes the landscape. The large electron density in the aromatic enables formation of new interactions, such as C-H···π, O-H···π and π···π, which may condition large scale or macromolecular aggregation. However, as the aromatic ring is a chromophore, it enables using electronic spectroscopy. As mentioned before, the advantage of the electronic spectroscopy is that it opens the possibility of using mass-resolved double resonance techniques, which gives a better control of the species studied. One must take into account that the spectra of all the aggregates appear in the same spectral region because, in the end, the spectrum of the aggregate is somehow the spectrum of the monomer, perturbed by its interaction with the rest of the molecules of the aggregate.

The goal of this thesis is to explore several supramolecular systems using a combination of mass-resolved excitation spectroscopy (MRES) and quantum chemical calculations, to increase the present knowledge on the mechanisms of molecular aggregation.

In order to explore the interplay between dispersive forces and OH···O HBs in the molecular aggregation this thesis dedicates Chapter 3 to study the aggregation preferences of model aromatic alcohols.

As aforementioned, NCIs are particularly crucial for living organism. After millions of years of evolution, each molecule went through a complex selection process in order to pick those species best fitted to play the specialized roles that take place in the metabolism of the living beings. Such is the case of saccharides. These molecules are mainly produced by photosynthetic organisms as a way to storage energy.[56] However, the role they play in the cellular metabolism goes far beyond.[57,58] They are structural blocks, such as in DNA, chitin or cellulose, but also form part of the immune system.[59–63] For example, glycans are polysaccharides attached to protein and lipids, which are located in the extracellular side of the cell membrane. Cells from the immune system have specialized receptors to interrogate those glycans. If the glycan does not contain a recognizable sequence of monosaccharides, an immune response is triggered.[60–63]

The high flexibility of the saccharides allows them to effectively adapt to the environment and to optimize their association with the target receptor, achieving a high selectivity in the recognition process. Moreover, glycan receptors are designed in such a way that they are able to detect not only modifications in the sequence or the saccharide unit, but also in their ramifications, and intermolecular bonds, as those between sugar units.[64] A very common example of the selectivity inside these glycan receptors can be found in the case of the blood groups, where a change in the orientation of a single hydroxyl group in one sugar unit of the glycan is enough to change the receptors affinity.[65]

Understanding such processes requires of a deep knowledge of the interaction mechanism at a molecular scale. The virtually infinite number of interactions in aqueous phase of these biomolecules turns characterization of the intrinsic properties of non-covalent interactions into a very difficult task. There is an extensive literature on the conformational preferences of sugars, especially of studies in gas-phase by rotational[30,66] and vibrational spectroscopy.[37,67–71] Studies reported with this latter technique produced an outstanding set of experimental data for the investigation of NCIs, as big size biomolecules or molecular complexes can be studied.[72,73] One of the objectives of this thesis involves the characterization of NCIs in sugar complexes, using MRES in combination with computational chemistry. We present in Chapter 4 a detailed exploration of the interactions between sugar derivatives and a number of molecules. The data collected demonstrate the ability of these molecules to establish multiple interactions and to adapt their flexible hydroxymethyl group to maximize them. These studies are continued in Chapter 5 with the characterization of two monosaccharides with their O3 esterified by a fatty acid, forming a model glycolipid.

NCIs are of extraordinary importance in the biological role played by the nucleobases. Cytosine (C), guanine (G), adenine (A) and thymine (T) are the four DNA bases. They are found forming pairs attached by two or three hydrogen bonds. Such pairs form strands by combination with a sugar-phosphate backbone. The four DNA bases constitute what has been called "the alphabet of life", as their combination in DNA is the mechanism used in most living being to pack the genetic code.[57] Furthermore, nucleotides play a variety of roles in cellular metabolism apart from the well-known genetic code, such as constituting part of the ATP/ADP energetic tokens ,[74] or GTP/GDP in the metabolism of G-protein coupled receptors (GPCR).[75] Thus, one of the most exciting questions in science is the origin of DNA and the reason for its chemical composition. Why nature selected CGAT as the "alphabet of life" is still an open question. There is a general agreement in that they are the result of the evolutionary pressure at several different stages.[76] However, many other metabolites with similar structures coexist in the cell, which, apparently, could perform the same roles as DNA bases.

The initial molecules from which CGAT have evolved may have been substantially different from the present nucleobases. Among other reasons, because the physico-chemical conditions in the primal broth were probably very different from those in present days. The oldest rocks found are 3.6 billion years old and already contain rests of cellular organisms. This means that life appeared in the first 400 million years of existence of our planet.[77–79] At those times, no free oxygen existed and very likely, the atmosphere was not strongly reducing.[80] Depending on the iron redox chemistry and on the speed at which iron sunk to the core, the atmosphere could have been from very rich to very poor in methane.[81] With time, atmosphere might evolve to contain mainly CO, CO_2, H_2O H_2 and N_2, but no ammonia.[76,82] Under such conditions, the rich chemistry of the condensation of HCN in presence of H_2CO may have contributed to the appearance of the first prebiotic molecules.[83] Among the results of such condensation not only CGAT, but also many other purines, pyrimidines as well as other heterocyclic compounds are formed.[84–86] Perhaps, chemical stability could contribute to produce an enrichment of the medium in some of those compounds. However, studies on half-life of purines and pyrimidines demonstrate that this was not the determinant (or at least the only determinant) factor for the selection of CGAT, as there are compounds, such as 2,6-diaminopurine or 2,4-diaminopyrimidine that are more stable or at least equally stable than the canonical nucleobases.[87–89]

An important selection factor could be light irradiation. Most authors agree in that the primal atmosphere was substantially more permeable to VUV[90] and therefore, it may

have helped to both, drive synthetic reactions and select the most stable products. The pioneering works by de Vries,[91] Crespo-Hernández,[92] and Hobza,[93,94] among others, have demonstrated that the canonical nucleobases present very short electronic excited state lifetimes. This fact has been taken as a protection against photodamage. However, other prebiotic compounds also present very short lifetimes, even shorter than the nucleobases. For example, hypoxanthine has an excited state lifetime of 0.13 ps,[95] compared to adenine (0.18 ps)[96] or guanine (0.16 ps).[97]

One of the problems to understand why nature selected the canonical nucleobases is that they were not selected in the first instants of life formation. Or that they continued evolving in parallel to the evolution of the first biopolymers. In a compelling review, Rios and Tor identify several stages at which such selection may have taken place.[76] According to these authors, the rich variety of compounds produced by the prebiotic chemistry was later refined during assembly of the first informational polymers, the emergence and early evolution of life and the formation of the last universal common ancestor (LUCA). Actually, some authors speculate with the idea of an initial set of nucleobases containing more than just four units (see Figure 1.1). In favor of such hypothesis is the existence of modified nucleobases in ancestral organisms, such as bacteriophages,[98] or the possibility of creating expanded alphabets using synthetic chemistry.[99]

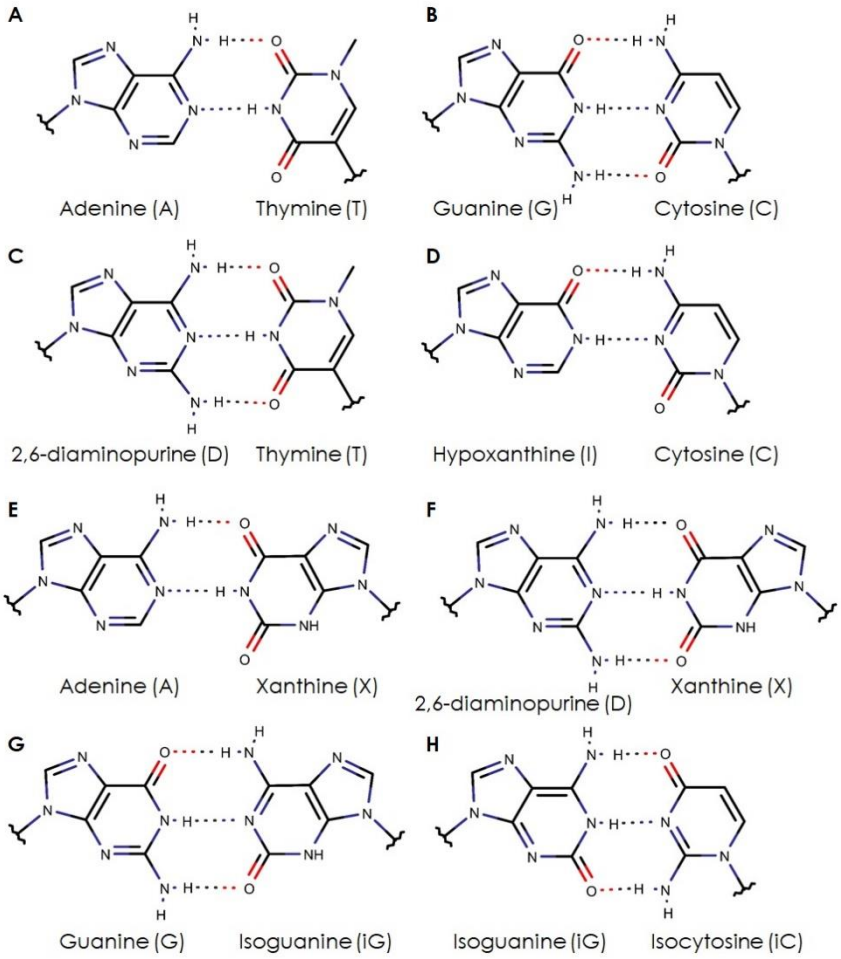

Figure 1.1: (A-B) Watson-Crick interactions between canonical nucleobases. (C-H) Watson-Crick like interactions between several non-canonical nucleobases.[82]

In an interesting essay, Siegel and Tor[86] formulated a hypothesis about a possible pre-RNA base (see Figure 1.2), which evolved to the todays known C and U by hydrolysis in aqueous environment. The difference in that prebiotic base (called D) is that it forms a N-glycosidic bond through the exocyclic amine of the base. That initial and successful first configuration could have been later refined by mutations to incorporate purine bases like A or G.

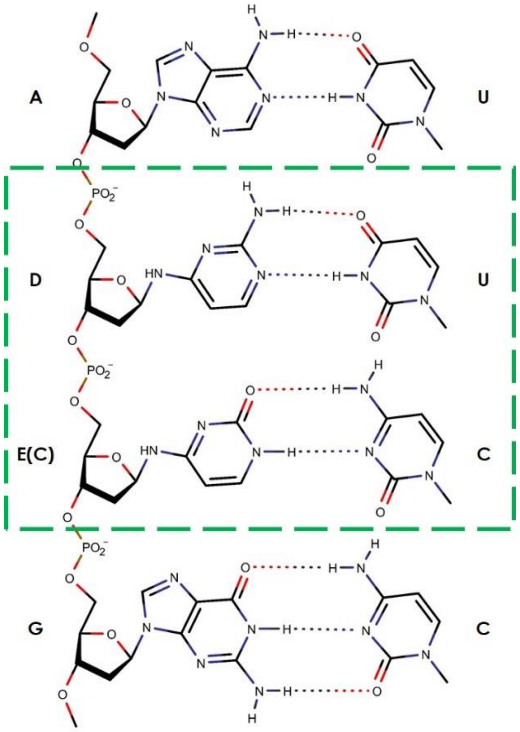

Figure 1.2: Alternative base pairing inside a proto-RNA double helix sequence proposed by Siegen and Tor.[86]

Regarding the stages of the evolutionary path depicted above, our hypothesis is that NCIs also played a decisive role in the selection of nucleobase candidates. The special combination of functional groups in DNA bases allows them to couple with their complementary base, but additionally, their functional groups might allow them to interact with other biomolecules, like proteins. In order to elaborate on this topic, this thesis presents a joined experimental and computational analysis over some possible nucleobase candidates from the xanthine family.

Xanthines are a very interesting family of compounds that can be found in nature, and in human body as part of the guanine metabolism.[100] Thanks to their purine backbone (similar to A or G), and their functional groups (same CONHCO motif as T or U), they play various roles in the metabolism. In fact, their similarities with DNA/RNA bases are those that give them the ability to interfere with the molecular recognition processes in which DNA/RNA bases are involved.[101] The methylated versions of xanthine are quite interesting from that point of view.[101–104] For example, some studies revealed that theophylline is specifically recognized by a RNA aptamer (see Figure 1.3).[104,105] In such structure, theophylline preferentially interacts with cytosine and uracil bases forming HBs, and additional π···π stacking interactions stabilize the complex.

Theobromine, on the other hand, presents the same binding motif as T or U, and thus, it could perform analogue interactions to those observed in DNA/RNA nucleobase pairs. Finally, the fully methylated xanthine, caffeine, is a commonly known stimulating substance which acts as a non-selective antagonist o the adenosine receptors (A_1, A_{2A}, A_{2B}, and A_3) in the human brain.[106,107] In order to understand what rules the selectivity and activity of xanthines in their biological functions, it is necessary to study what the variables that affect this process are and distinguish the importance of each one at a molecular scale.

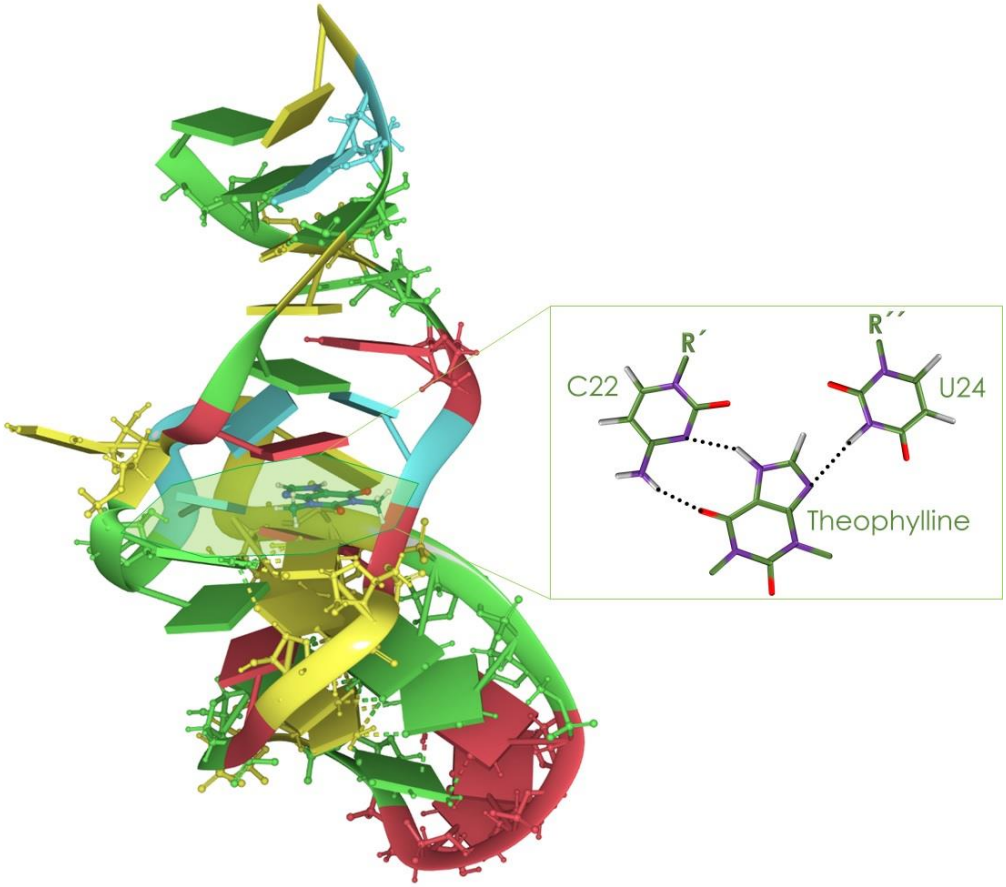

Figure 1.3: RNA aptamer in complex with theophylline (PDB: 1EHT).[104]

The main objective in chapters 6-8 of the thesis is to characterize the interaction preferences of xanthine derivatives, and to determine the structure the first complexes between DNA bases and xanthines in the gas-phase. On the one hand, the results presented in Chapter 4 and 6 highlight the stacking preferences of caffeine with sugar and phenol derivatives. Those are dimers formed by weak interactions and therefore, difficult to model. On the other hand, Chapters 7 and 8 are dedicated to the

characterization of methylxanthine monomers, and their combination with adenine, as they are capable of mimicking Watson-Crick interactions of DNA. Additionally, we paired theobromine with 4-aminopyrimidine. The latter exhibits similar interaction points than A, but with a pyrimidine base. The comparison of possible prebiotic W-C mimic interactions to those observed in the canonical nucleobases may help to understand if the interactions formed between bases was indeed a selection pressure for the evolution of the first informational polymers.

1.2. References

[1] H. Margenau and N. R. Kestner, *Theory of intermolecular forces*, Pergamon Press, Oxford, 2nd Editon., 1971.

[2] T. Steiner, The Hydrogen Bond in the Solid State, *Angew. Chemie Int. Ed.*, 2002, **41**, 48–76.

[3] J. Perlstein, The Weak Hydrogen Bond In Structural Chemistry and Biology (International Union of Crystallography, Monographs on Crystallography, 9) By Gautam R. Desiraju (University of Hyderabad) and Thomas Steiner (Freie Universität Berlin). Oxford University Press: , *J. Am. Chem. Soc.*, 2001, **123**, 191–192.

[4] P. Hobza and K. Müller-Dethlefs, *Non-covalent interactions: theory and experiment*, Royal Society of Chemistry, 2010, vol. 2.

[5] S. Scheiner, *Noncovalent forces*, Springer, 2015, vol. 19.

[6] L. Pauling and others, *The Nature of the Chemical Bond...*, Cornell university press Ithaca, NY, 1960, vol. 260.

[7] G. C. Pimentel and A. L. McClellan, *The hydrogen bond*, WH Freeman, 1960.

[8] E. Arunan, G. R. Desiraju, R. A. Klein, J. Sadlej, S. Scheiner, I. Alkorta, D. C. Clary, R. H. Crabtree, J. J. Dannenberg, P. Hobza, H. G. Kjaergaard, A. C. Legon, B. Mennucci and D. J. Nesbitt, Definition of the hydrogen bond (IUPAC Recommendations 2011), *Pure Appl. Chem.*, 2011, **83**, 1637–1641.

[9] A. S. Mahadevi and G. N. Sastry, Cooperativity in Noncovalent Interactions, *Chem. Rev.*, 2016, **116**, 2775–2825.

[10] I. Usabiaga, A. Camiruaga, C. Calabrese, A. Maris and J. A. Fernández, Exploring Caffeine–Phenol Interactions by the Inseparable Duet of Experimental and Theoretical Data, *Chem. - A Eur. J.*, 2019, **25**, 14230–14236.

[11] A. Poblotzki, H. C. Gottschalk and M. A. Suhm, Tipping the Scales: Spectroscopic Tools for Intermolecular Energy Balances, *J. Phys. Chem. Lett.*, 2017, **8**, 5656–5665.

[12] A. S. Christensen, T. Kubař, Q. Cui and M. Elstner, Semiempirical Quantum Mechanical Methods for Noncovalent Interactions for Chemical and Biochemical Applications, *Chem. Rev.*, 2016, **116**, 5301–5337.

[13] J. A. Frey, C. Holzer, W. Klopper and S. Leutwyler, Experimental and Theoretical Determination of Dissociation Energies of Dispersion-Dominated Aromatic Molecular Complexes, *Chem. Rev.*, 2016, **116**, 5614–5641.

[14] K. Müller-Dethlefs and P. Hobza, Noncovalent Interactions: A Challenge for Experiment and Theory, *Chem. Rev.*, 2000, **100**, 143–168.

[15] O. F. Hagena and W. Obert, Cluster Formation in Expanding Supersonic Jets: Effect of Pressure, Temperature, Nozzle Size, and Test Gas, *J. Chem. Phys.*, 1972, **56**, 1793–1802.

[16] F. Biedermann and H.-J. Schneider, Experimental Binding Energies in Supramolecular Complexes, *Chem. Rev.*, 2016, **116**, 5216–5300.

[17] M. Becucci and S. Melandri, High-Resolution Spectroscopic Studies of Complexes Formed by Medium-Size Organic Molecules, *Chem. Rev.*, 2016, **116**, 5014–5037.

[18] O. Dopfer and M. Fujii, Probing Solvation Dynamics around Aromatic and Biological Molecules at the Single-Molecular Level, *Chem. Rev.*, 2016, **116**, 5432–5463.

[19] D. H. Levy, Laser Spectroscopy of Cold Gas-Phase Molecules, *Annu. Rev. Phys. Chem.*, 1980, **31**, 197–225.

[20] T. J. Balle and W. H. Flygare, Fabry–Perot cavity pulsed Fourier transform microwave spectrometer with a pulsed nozzle particle source, *Rev. Sci. Instrum.*, 1981, **52**, 33–45.

[21] B. H. Pate and F. C. De Lucia, Broadband Molecular Rotational Spectroscopy Special Issue, *J. Mol. Spectrosc.*, 2012, **280**, 1–2.

[22] S. Oswald, M. Wallrabe and M. A. Suhm, Cooperativity in Alcohol–Nitrogen Complexes: Understanding Cryomatrices through Slit Jet Expansions, *J. Phys. Chem. A*, 2017, **121**, 3411–3422.

[23] T. S. Zwier, Laser Spectroscopy of Jet-Cooled Biomolecules and Their Water-Containing Clusters: Water Bridges and Molecular Conformation, *J. Phys. Chem. A*, 2001, **105**, 8827–8839.

[24] T. A. Miller, Chemistry and Chemical Intermediates in Supersonic Free Jet Expansions, *Science (80-.).*, 1984, **223**, 545 LP – 553.

[25] M. V Johnston, Supersonic jet expansions in analytical spectroscopy, *TrAC Trends Anal. Chem.*, 1984, **3**, 58–61.

[26] J.-P. Schermann, *Spectroscopy and modeling of biomolecular building blocks*, Elsevier, 2007.

[27] T. S. Zwier, THE SPECTROSCOPY OF SOLVATION IN HYDROGEN-BONDED AROMATIC CLUSTERS, *Annu. Rev. Phys. Chem.*, 1996, **47**, 205–241.

[28] G. Meijer, M. S. de Vries, H. E. Hunziker and H. R. Wendt, Laser desorption jet-cooling of organic molecules, *Appl. Phys. B*, 1990, **51**, 395–403.

[29] J. L. Alonso, C. Pérez, M. Eugenia Sanz, J. C. López and S. Blanco, Seven conformers of l-threonine in the gas phase: a LA-MB-FTMW study, *Phys. Chem. Chem. Phys.*, 2009, **11**, 617–627.

[30] E. J. Cocinero, A. Lesarri, P. Écija, F. J. Basterretxea, J.-U. Grabow, J. A. Fernández and F. Castaño, Ribose Found in the Gas Phase, *Angew. Chemie Int. Ed.*, 2012, **51**, 3119–3124.

[31] I. Peña, C. Cabezas and J. L. Alonso, The Nucleoside Uridine Isolated in the Gas Phase, *Angew. Chemie Int. Ed.*, 2015, **54**, 2991–2994.

[32] F. O. Talbot and J. P. Simons, Sugars in the gas phase: the spectroscopy and structure of jet-cooled phenyl β-D-glucopyranoside, *Phys. Chem. Chem. Phys.*, 2002, **4**, 3562–3565.

[33] E. J. Cocinero, P. Çarçabal, T. D. Vaden, J. P. Simons and B. G. Davis, Sensing the anomeric effect in a solvent-free environment., *Nature*, 2011, **469**, 76–79.

[34] S. De Camillis, J. Miles, G. Alexander, O. Ghafur, I. D. Williams, D. Townsend and J. B. Greenwood, Ultrafast non-radiative decay of gas-phase nucleosides, *Phys. Chem. Chem. Phys.*, 2015, **17**, 23643–23650.

[35] I. León, E. J. Cocinero, J. Millán, A. M. Rijs, I. Usabiaga, A. Lesarri, F. Castaño and J. A.

Fernández, A combined spectroscopic and theoretical study of propofol·(H2O)3, *J. Chem. Phys.*, 2012, **137**, 74303.

[36] J. González, I. Usabiaga, P. F. Arnaiz, I. León, R. Martínez, J. Millán and J. A. Fernández, Competition between stacked and hydrogen bonded structures of cytosine aggregates, *Phys. Chem. Chem. Phys.*, 2017, **19**, 8826–8834.

[37] I. Usabiaga, J. González, P. F. Arnáiz, I. León, E. J. Cocinero and J. A. Fernández, Modeling the tyrosine–sugar interactions in supersonic expansions: glucopyranose–phenol clusters, *Phys. Chem. Chem. Phys.*, 2016, **18**, 12457–12465.

[38] I. Usabiaga, J. González, I. León, P. F. Arnaiz, E. J. Cocinero and J. A. Fernández, Influence of the Anomeric Conformation in the Intermolecular Interactions of Glucose, *J. Phys. Chem. Lett.*, 2017, **8**, 1147–1151.

[39] I. Usabiaga, A. Camiruaga, C. Calabrese, A. Maris and J. A. Fernández, Exploring Caffeine–Phenol Interactions by the Inseparable Duet of Experimental and Theoretical Data, *Chem. – A Eur. J.*, 2019, **25**, 14230–14236.

[40] I. León, I. Usabiaga, P. F. Arnaiz, A. Lesarri and J. A. Fernández, Stepwise Nucleation of Aniline: Emergence of Spectroscopic Fingerprints of the Liquid Phase, *Chem. – A Eur. J.*, 2018, **24**, 10291–10295.

[41] M. Juanes, I. Usabiaga, I. León, L. Evangelisti, J. A. Fernández and A. Lesarri, The Six Isomers of the Cyclohexanol Dimer: A Delicate Test for Dispersion Models, *Angew. Chemie Int. Ed.*, 2020, **59**, 14081–14085.

[42] C. Pérez, S. Lobsiger, N. A. Seifert, D. P. Zaleski, B. Temelso, G. C. Shields, Z. Kisiel and B. H. Pate, Broadband Fourier transform rotational spectroscopy for structure determination: The water heptamer, *Chem. Phys. Lett.*, 2013, **571**, 1–15.

[43] C. Pérez, D. P. Zaleski, N. A. Seifert, B. Temelso, G. C. Shields, Z. Kisiel and B. H. Pate, Hydrogen Bond Cooperativity and the Three-Dimensional Structures of Water Nonamers and Decamers, *Angew. Chemie Int. Ed.*, 2014, **53**, 14368–14372.

[44] J. P. I. Hearn, R. V. Cobley and B. J. Howard, High-resolution spectroscopy of induced chiral dimers: A study of the dimers of ethanol by Fourier transform microwave spectroscopy, *J. Chem. Phys.*, 2005, **123**, 1–7.

[45] T. N. Wassermann and M. A. Suhm, Ethanol Monomers and Dimers Revisited: A Raman Study of Conformational Preferences and Argon Nanocoating Effects, *J. Phys. Chem. A*, 2010, **114**, 8223–8233.

[46] D. Loru, I. Peña and M. E. Sanz, Ethanol dimer: Observation of three new conformers by broadband rotational spectroscopy, *J. Mol. Spectrosc.*, 2017, **335**, 93–101.

[47] M. S. Snow, B. J. Howard, L. Evangelisti and W. Caminati, From Transient to Induced Permanent Chirality in 2-Propanol upon Dimerization: A Rotational Study, *J. Phys. Chem. A*, 2011, **115**, 47–51.

[48] A. K. King and B. J. Howard, A microwave study of the hetero-chiral dimer of butan-2-ol, *Chem. Phys. Lett.*, 2001, **348**, 343–349.

[49] A. Maris, B. M. Giuliano, D. Bonazzi and W. Caminati, Molecular recognition of chiral conformers: A rotational study of the dimers of glycidol, *J. Am. Chem. Soc.*, 2008, **130**, 13860–13861.

[50] N. A. Seifert, A. L. Steber, J. L. Neill, C. Pérez, D. P. Zaleski, B. H. Pate and A. Lesarri, The interplay of hydrogen bonding and dispersion in phenol dimer and trimer: structures from broadband rotational spectroscopy, *Phys. Chem. Chem. Phys.*, 2013, **15**, 11468–11477.

[51] J. Altnöder, S. Oswald and M. A. Suhm, Phenyl- vs cyclohexyl-substitution in methanol: Implications for the OH conformation and for dispersion-affected aggregation from vibrational spectra in supersonic jets, *J. Phys. Chem. A*, 2014, **118**, 3266–3279.

[52] R. Medel and M. A. Suhm, Understanding benzyl alcohol aggregation by chiral modification: the pairing step, *Phys. Chem. Chem. Phys.*, 2020, **22**, 25538–25551.

[53] I. Leon, E. J. Cocinero, J. Millán, S. Jaeqx, A. M. Rijs, A. Lesarri, F. Castaño and J. A. Fernández, Exploring microsolvation of the anesthetic propofol, *Phys. Chem. Chem. Phys.*, 2012, **14**, 4398.

[54] I. Leõn, J. Millán, E. J. Cocinero, A. Lesarri and J. A. Fernández, Shaping micelles: The interplay between hydrogen bonds and dispersive interactions, *Angew. Chemie - Int. Ed.*, 2013, **52**, 7772–7775.

[55] I. León, A. Lesarri and J. A. Fernández, in *Intra- and Intermolecular Interactions Between Non-covalently Bonded Species*, ed. E. R. B. T.-I. I. I. B. N. B. S. Bernstein, Elsevier, 2021, pp. 143–188.

[56] P. M. Collins and R. J. Ferrier, *Monosaccharides: their chemistry and their roles in natural products.*, 1996.

[57] D. L. Nelson, A. L. Lehninger and M. M. Cox, *Lehninger principles of biochemistry*, Macmillan, 2008.

[58] D. Solís, N. V Bovin, A. P. Davis, J. Jiménez-Barbero, A. Romero, R. Roy, K. Smetana and H.-J. Gabius, A guide into glycosciences: How chemistry, biochemistry and biology cooperate to crack the sugar code, *Biochim. Biophys. Acta - Gen. Subj.*, 2015, **1850**, 186–235.

[59] B. Fiege, C. Rademacher, J. Cartmell, P. I. Kitov, F. Parra and T. Peters, Molecular Details of the Recognition of Blood Group Antigens by a Human Norovirus as Determined by STD NMR Spectroscopy, *Angew. Chemie Int. Ed.*, 2012, **51**, 928–932.

[60] S. Hakomori and Y. Igarashi, Functional Role of Glycosphingolipids in Cell Recognition and Signaling, *J. Biochem.*, 1995, **118**, 1091–1103.

[61] H.-J. Gabius, S. André, J. Jiménez-Barbero, A. Romero and D. Solís, From lectin structure to functional glycomics: principles of the sugar code, *Trends Biochem. Sci.*, 2011, **36**, 298–313.

[62] E. C. Stanca-Kaposta, D. P. Gamblin, E. J. Cocinero, J. Frey, R. T. Kroemer, A. J. Fairbanks, B. G. Davis and J. P. Simons, Solvent Interactions and Conformational Choice in a Core N-Glycan Segment: Gas Phase Conformation of the Central, Branching Trimannose Unit and its Singly Hydrated Complex, *J. Am. Chem. Soc.*, 2008, **130**, 10691–10696.

[63] H. Ghazarian, B. Idoni and S. B. Oppenheimer, A glycobiology review: Carbohydrates, lectins and implications in cancer therapeutics, *Acta Histochem.*, 2011, **113**, 236–247.

[64] M. del C. Fernández-Alonso, F. J. Cañada, J. Jiménez-Barbero and G. Cuevas, Molecular Recognition of Saccharides by Proteins. Insights on the Origin of the Carbohydrate–Aromatic Interactions, *J. Am. Chem. Soc.*, 2005, **127**, 7379–7386.

[65] A. P. Davis and R. S. Wareham, Carbohydrate recognition through noncovalent interactions: a challenge for biomimetic and supramolecular chemistry, *Angew. Chemie Int. Ed.*, 1999, **38**, 2978–2996.

[66] I. Peña, E. J. Cocinero, C. Cabezas, A. Lesarri, S. Mata, P. Écija, A. M. Daly, Á. Cimas, C. Bermúdez, F. J. Basterretxea, S. Blanco, J. A. Fernández, J. C. López, F. Castaño and J. L. Alonso, Six Pyranoside Forms of Free 2-Deoxy-D-ribose, *Angew. Chemie Int. Ed.*, 2013, **52**, 11840–11845.

[67] A. Camiruaga, I. Usabiaga, A. Insausti, I. León and J. A. Fernández, Sugar–peptidic bond interactions: spectroscopic characterization of a model system, *Phys. Chem. Chem. Phys.*, 2017, **19**, 12013–12021.

[68] A. Camiruaga, I. Usabiaga, A. Insausti, E. J. Cocinero, I. León and J. A. Fernández, Understanding the role of tyrosine in glycogenin, *Mol. BioSyst.*, 2017, **13**, 1709–1712.

[69] I. Usabiaga, A. Camiruaga, A. Insausti, P. Çarçabal and M. D. Marshall, Phenyl- β -D-glucopyranoside and Dimers : Small Structural Differences but Very Different Interactions, 2018, **6**, 1–9.

[70] P. Çarçabal, E. J. Cocinero and J. P. Simons, Binding energies of micro-hydrated carbohydrates: measurements and interpretation, *Chem. Sci.*, 2013, **4**, 1830–1836.

[71] E. J. Cocinero and P. Çarçabal, in *Gas-Phase IR Spectroscopy and Structure of Biological Molecules*, eds. A. M. Rijs and J. Oomens, Springer International Publishing, Cham, 2015, pp. 299–333.

[72] R. A. Jockusch, R. T. Kroemer, F. O. Talbot, L. C. Snoek, P. Çarçabal, J. P. Simons, M. Havenith, J. M. Bakker, I. Compagnon, G. Meijer and G. von Helden, Probing the Glycosidic Linkage: UV and IR Ion-Dip Spectroscopy of a Lactoside, *J. Am. Chem. Soc.*, 2004, **126**, 5709–5714.

[73] I. A. Bermejo, I. Usabiaga, I. Compañón, J. Castro-López, A. Insausti, J. A. Fernández, A. Avenoza, J. H. Busto, J. Jiménez-Barbero, J. L. Asensio, J. M. Peregrina, G. Jiménez-Osés, R. Hurtado-Guerrero, E. J. Cocinero and F. Corzana, Water Sculpts the Distinctive Shapes and Dynamics of the Tumor-Associated Carbohydrate Tn Antigens: Implications for Their Molecular Recognition, *J. Am. Chem. Soc.*, 2018, **140**, 9952–9960.

[74] M. Klingenberg, The ADP and ATP transport in mitochondria and its carrier, *Biochim. Biophys. Acta - Biomembr.*, 2008, **1778**, 1978–2021.

[75] D. M. Rosenbaum, S. G. F. Rasmussen and B. K. Kobilka, The structure and function of G-protein-coupled receptors, *Nature*, 2009, **459**, 356–363.

[76] A. C. Rios and Y. Tor, On the Origin of the Canonical Nucleobases: An Assessment of Selection Pressures across Chemical and Early Biological Evolution, *Isr. J. Chem.*, 2013, **53**, 469–483.

[77] G. F. Joyce, RNA evolution and the origins of life, *Nature*, 1989, **338**, 217–224.

[78] R. Buick, J. S. R. Dunlop and D. I. Groves, Stromatolite recognition in ancient rocks: an appraisal of irregularly laminated structures in an Early Archaean chert-barite unit from North Pole, Western Australia, *Alcheringa An Australas. J. Palaeontol.*, 1981, **5**, 161–181.

[79] M. Schidlowski, P. W. U. Appel, R. Eichmann and C. E. Junge, Carbon isotope geochemistry of the 3.7 × 109-yr-old Isua sediments, West Greenland: implications for the Archaean carbon and oxygen cycles, *Geochim. Cosmochim. Acta*, 1979, **43**, 189–199.

[80] J. W. Schopf, *Earth's earliest biosphere: Its origin and evolution*, Princeton University Press, United States, 1983.

[81] S. Chang, D. J. Des Marais, R. Mack, S. L. Miller and G. Strathearn, *Earth's Earliest Biosphere: Its Origin and Early Evolution*, Princeton University Press, 1983.

[82] B. J. Cafferty and N. V Hud, Was a Pyrimidine-Pyrimidine Base Pair the Ancestor of Watson-Crick Base Pairs? Insights from a Systematic Approach to the Origin of RNA, *Isr. J. Chem.*, 2015, **55**, 891–905.

[83] Y. Nosenko, M. Kunitski, T. Stark, M. Göbel, P. Tarakeshwar and B. Brutschy, Vibrational signatures of Watson–Crick base pairing in adenine–thymine mimics, *Phys. Chem. Chem. Phys.*, 2013, **15**, 11520–11530.

[84] V. M. Kolb, J. P. Dworkin and S. L. Miller, Alternative bases in the RNA world: the prebiotic synthesis of urazole and its ribosides, *J. Mol. Evol.*, 1994, **38**, 549–557.

[85] R. Saladino, G. Botta, S. Pino, G. Costanzo and E. Di Mauro, Genetics first or metabolism first? The formamide clue, *Chem. Soc. Rev.*, 2012, **41**, 5526–5565.

[86] J. S. Siegel and Y. Tor, Genetic alphabetic order: what came before A?, *Org. Biomol. Chem.*, 2005, **3**, 1591–1592.

[87] M. Levy and S. L. Miller, The stability of the RNA bases: Implications for the origin of life, *Proc. Natl. Acad. Sci.*, 1998, **95**, 7933 LP – 7938.

[88] M. P. Robertson, M. Levy and S. L. Miller, Prebiotic synthesis of diaminopyrimidine and thiocytosine, *J. Mol. Evol.*, 1996, **43**, 543–550.

[89] C. H. House and S. L. Miller, Hydrolysis of Dihydrouridine and Related Compounds, *Biochemistry*, 1996, **35**, 315–320.

[90] C. Sagan, Ultraviolet selection pressure on the earliest organisms, *J. Theor. Biol.*, 1973, **39**, 195–200.

[91] S. Boldissar and M. S. de Vries, How nature covers its bases, *Phys. Chem. Chem. Phys.*, 2018, **20**, 9701–9716.

[92] C. T. Middleton, K. de La Harpe, C. Su, Y. K. Law, C. E. Crespo-Hernández and B. Kohler, DNA Excited-State Dynamics: From Single Bases to the Double Helix, *Annu. Rev. Phys. Chem.*, 2009, **60**, 217–239.

[93] H. Kang, K. T. Lee, B. Jung, Y. J. Ko and S. K. Kim, Intrinsic Lifetimes of the Excited State of DNA and RNA Bases, *J. Am. Chem. Soc.*, 2002, **124**, 12958–12959.

[94] M. M. Brister, T. Gustavsson and C. E. Crespo-Hernández, *Mol.*, 2020, 25.

[95] M. K. Shukla and J. Leszczynski, *Radiation Induced Molecular Phenomena in Nucleic Acids*, Springer Netherlands, 2008.

[96] B. Cohen, P. M. Hare and B. Kohler, Ultrafast Excited-State Dynamics of Adenine and Monomethylated Adenines in Solution: Implications for the Nonradiative Decay Mechanism, *J. Am. Chem. Soc.*, 2003, **125**, 13594–13601.

[97] J. P. Villabona-Monsalve, R. Noria, S. Matsika and J. Peón, On the Accessibility to Conical Intersections in Purines: Hypoxanthine and its Singly Protonated and Deprotonated Forms, *J. Am. Chem. Soc.*, 2012, **134**, 7820–7829.

[98] J. H.Gommers-Ampt and P. Borst, Hypermodified bases in DNA, *FASEB J.*, 1995, **9**, 1034–1042.

[99] H.-J. Kim, N. A. Leal and S. A. Benner, 2′-Deoxy-1-methylpseudocytidine, a stable analog of 2′-deoxy-5-methylisocytidine, *Bioorg. Med. Chem.*, 2009, **17**, 3728–3732.

[100] P. J. Marro, S. Baumgart, M. Delivoria-Papadopoulos, S. Zirin, L. Corcoran, S. P. McGaurn, L. E. Davis and R. R. Clancy, Purine Metabolism and Inhibition of Xanthine Oxidase in Severely Hypoxic Neonates Going onto Extracorporeal Membrane Oxygenation, *Pediatr. Res.*, 1997, **41**, 513–520.

[101] I. M. Johnson, S. G. B. Kumar and R. Malathi, RNA Binding Efficacy of Theophylline, Theobromine and Caffeine, *J. Biomol. Struct. Dyn.*, 2003, **20**, 687–692.

[102] R. D. Jenison, S. C. Gill, A. Pardi and B. Polisky, High-resolution molecular discrimination by RNA, *Science (80-.).*, 1994, **263**, 1425–1429.

[103] M. P. Latham, G. R. Zimmermann and A. Pardi, NMR chemical exchange as a probe for ligand-binding kinetics in a theophylline-binding RNA aptamer, *J. Am. Chem. Soc.*, 2009, **131**, 5052–5053.

[104] G. R. Zimmermann, R. D. Jenison, C. L. Wick, J.-P. Simorre and A. Pardi, Interlocking structural motifs mediate molecular discrimination by a theophylline-binding RNA, *Nat. Struct. Biol.*, 1997, **4**, 644–649.

[105] P. C. Anderson and S. Mecozzi, Unusually short RNA sequences: Design of a 13-mer RNA that selectively binds and recognizes theophylline, *J. Am. Chem. Soc.*, 2005, **127**, 5290–5291.

[106] R. K. Y. Cheng, E. Segala, N. Robertson, F. Deflorian, A. S. Doré, J. C. Errey, C. Fiez-Vandal, F.

H. Marshall and R. M. Cooke, Structures of Human A1 and A2A Adenosine Receptors with Xanthines Reveal Determinants of Selectivity, *Structure*, 2017, **25**, 1275-1285.e4.

[107] A. S. Doré, N. Robertson, J. C. Errey, I. Ng, K. Hollenstein, B. Tehan, E. Hurrell, K. Bennett, M. Congreve, F. Magnani, C. G. Tate, M. Weir and F. H. Marshall, Structure of the adenosine A 2A receptor in complex with ZM241385 and the xanthines XAC and caffeine, *Structure*, 2011, **19**, 1283–1293.

Chapter 2

Methodology

2.1. Experimental Setup

The molecular systems presented in this work were studied with different experimental setup, depending on the sample preparation method, but all of them are based on Mass Resolved Excitation Spectroscopy (MRES) techniques.[1–3] This tool allows extracting both electronic and vibrational data from the molecules or aggregates formed under supersonic expansions (see Figure 2.1).

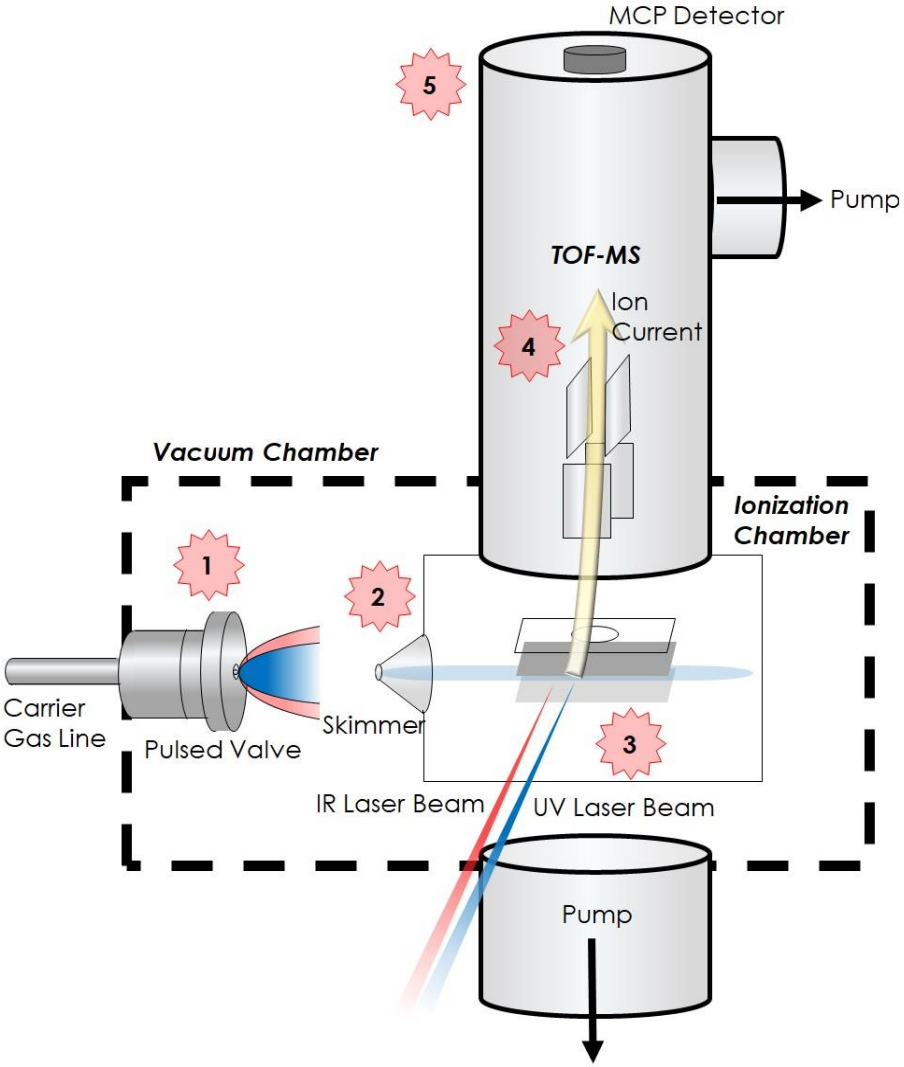

Figure 2.1: General scheme of a MRES experimental setup. A pulsed valve (1) coupled to a high vacuum chamber generates a supersonic expansion of a rare gas (normally He, Ne or Ar) seeded with the sample, through a nozzle (0.1 mm$^{\varnothing}$). The coolest part of the molecular beam is selected with a skimmer (2) before entering the ionization chamber. When the beam reaches the ionization region, the molecules and aggregates are probed using several laser sources. In a perfect synchronization with the molecular beam pulse, ionization laser excites and ionize**s** the molecules (3). The ions formed are accelerated by an electric field produced by two plates over which, a high-voltage is applied (extraction plate and acceleration plate). In this way, the ions are extracted accelerated towards a time of flight (ToF) mass spectrometer (4). During

the free-flight region, ions are separated according to their m/z ratio and finally reach a multichannel plate detector (MCP) producing an electric signal, which is monitored using an oscilloscope.

2.1.1. Laser sources

Depending on the spectral region and/or on the type of information to be extracted from the molecules, one or more laser resources were employed. Laser sources were used to transfer the molecules and aggregates into the electronic excited state, ionize them (tunable UV radiation), to depopulate molecular systems in double resonance techniques (both tunable UV and IR radiation), and for thermolabile compound desorption.

2.1.1.1. Tunable UV dye lasers

The optical distribution and configuration of each dye varies depending on its fabricant. However, in general terms, they all share the following optical layout (see Figure 2.2). The output laser beam is routed to the ionization chamber using a collection of prisms, lenses and iris. The laser models used in this work were:

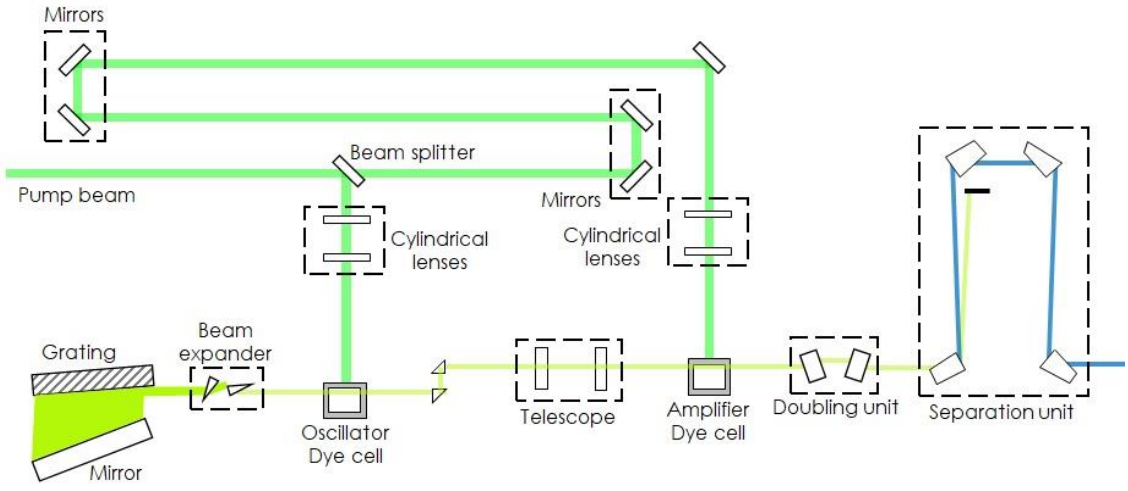

Figure 2.2: Scheme of the optical path through typical UV tunable dye laser.

Q-Scan Dye Laser (Quantel): Pumped by Nd:YAG laser (Q-Smart, Quantel, 220 mJ/pulse at 355 nm) used to scan in the range between 265-290 nm using Coumarin 540A dye.

Pulsare Pro-S Dye Laser (Fine Adjustment): Pumped by Nd:YAG laser (Brilliant-b, Quantel, ~180 mJ/pulse at 355 nm) used to scan in the range between 250-270 nm using Coumarin 540A and Coumarin 500 dyes.

TDL-90 Dye Laser (Quantel): Pumped by Nd_YAG laser (YG-980, Quantel, 500 mJ/pulse at 532 nm) used to scan in the range between 295-310 nm using Rhodamine 590, 600 and 610 dyes.

2.1.1.2. Tunable IR laser

An OPO/OPA (Optical Parametric Oscillator/Optical Parametric Amplifier) laser (LaserVision) was used as IR radiation source in the IDIR experiments. This type of laser is significantly different from the dye lasers, as it is based in solid state technology. The OPO/OPA incorporates a Nd:YAG laser (Continuum Surelite II; 500 mJ/pulse at 1064 nm) as pumping laser. Thanks to an optical layout composed by several frequency mixing crystals, the final laser output can be tuned from 2500 to 4000 cm^{-1} (~5-10 mJ/pulse, ~10 cm^{-1} bandwidth). A general scheme of the Laservision OPO/A showed in the Figure 2.3.

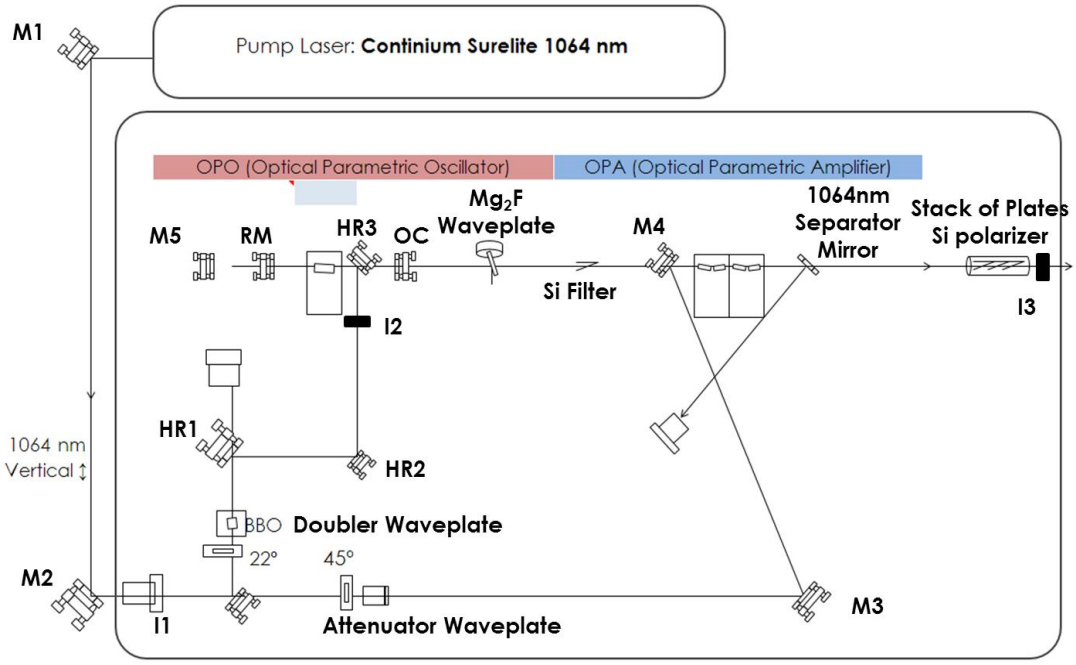

Figure 2.3: Scheme of the optical path through the LaserVision OPO/OPA laser.

2.1.1.3. Desorption lasers

In the studies of thermolabile samples, it was not possible to transfer the molecules to gas phase by simple warming. Conversely, a laser desorption (LD) system was required. During this thesis, several lasers were used for LD: a Quantel Ultra (Quantel, 30 mJ/pulse at 1064 nm, working at 10 Hz, pulse duration is about 8ns, with an output beam size of

3mm), a Minilite (Continuum, 30 mJ/pulse at 1064 nm, working at 10 Hz, pulsewidth ~5-7 ns, output beam size of 3mm), and a Brilliant-b (Quantel, 850 mJ/pulse at 1064 nm, working at 10 Hz, pulse duration is about 6 ns). Output power and beam size of the different lasers used were modified with iris plates and CaF_2 lenses to optimize the desorption process.

2.1.2. Electronic sources

One of the strictest requirements to run a successful MRES experiment is to have a perfect timing between all the components of the experiment. All the events (gas valve opening, desorption laser, ionization laser and detection) must be synchronized in a narrow time window. For that purpose, all the laser sources and electronics were externally triggered and controlled by multiple digital delay/pulse generators. Figure 2.4 shows a schematic of the delays and pulse sequence between the different elements of the experiment. Depending of the type of experiment, small adjustments may be done in the time windows.

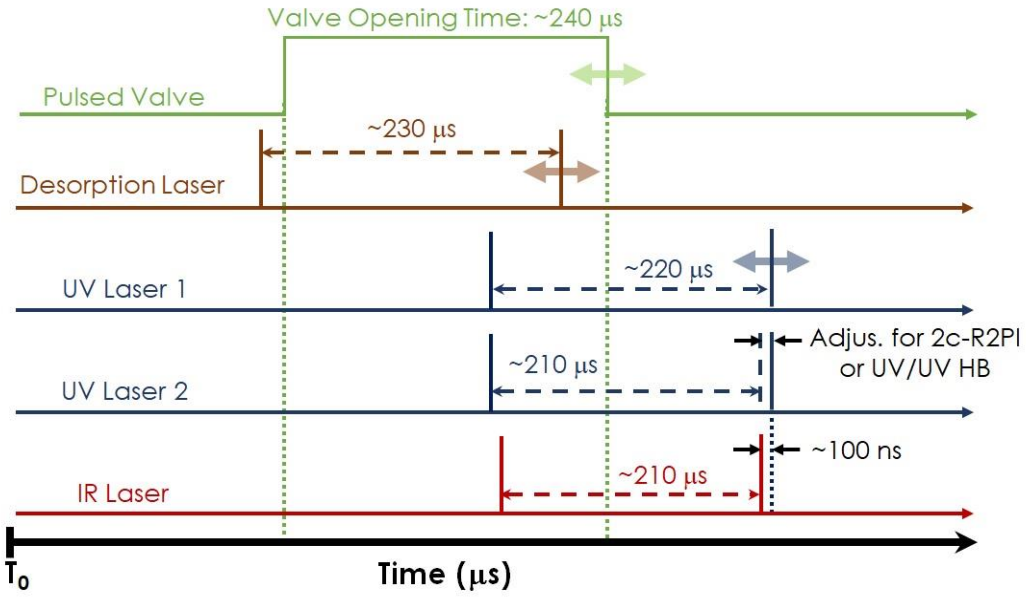

Figure 2.4: Time distribution of a single experimental event.

2.1.3. ToF Mass Spectrometer

Mass spectrometer are key devices in the MRES techniques. They enable the mass-selected detection of the species ionized in the expansion. Additionally, fragments and protonated species can be monitored during the experiments.[4,5]. The whole mass spectrometer works under high vacuum conditions, achieved with the aid of a pair of

turbomolecular/rotatory pumping systems (see detailed description below). The vacuum in the ionization chamber is usually maintained at $1 \cdot 10^{-7}$ mbar between experiments, and around $10^{-6} - 10^{-4}$ mbar during the gas valve operation (depending on the carried gas employed and the duration of the valve aperture). The ToF also incorporates a pair of Einzel lenses that focus the ion package into the detector, to maximize the signal and the spatial resolution.

Two different mass spectrometers were used in the UPV/EHU experiments: a smaller one with detectors for electrons and ions in which ZEKE experiments can be also carried out (Experimental set up 1), and a longer one, with improved mass resolution, equipped with a LD system (Experimental set up 2). In addition, a third experimental system was used during the short stay at Dr. Çarçabal research group

2.1.3.1. Experimental set up 1

In this setup[6–8], the molecules to study are placed in a small repository outside the pulsed valve. Repository and the gas line until the pulsed valve can be heated with a heating blanket to increase vapor concentration. Thus, a mixture of the evaporated sample and the carrier gas (He, Ne or Ar, with backing pressures between 0.5-3 bar) is expanded through the 0.5 mm nozzle of a pulsed valve (R.M. Jordan), into the time of flight mass spectrometer (TOF-MS, R.M. Jordan, in-house design). The molecular beam generated in the supersonic expansion is skimmed to select the coldest part. The vacuum system consists of three turbomolecular pumps (two Pfeiffer Vacuum TMU 071 of 200m^3/h and a Pfeiffer Vacuum TMU 521 of 1870 m^3/h), evacuated by a single rotatory pump (Varian DS402, 20 m^3/h). Generated ions are extracted by an electric field created by 1 cm separated plates connected to a high voltage power supply (PS350 High Voltage Power Supply, SRS Stanford Research Systems, IMC.). The field generated by the plates accelerate the ions towards the 18 mm multichannel plate (MCP) detector. The signal generated in the detector is recorded and monitored in a digital oscilloscope (Tektronics TDS 3032, 300 MHz). Tight control of the events was achieved with the aid of pulsed delay generators (Stanford DG535/645). A picture and scheme of the described setup is shown in Figure 2.5.

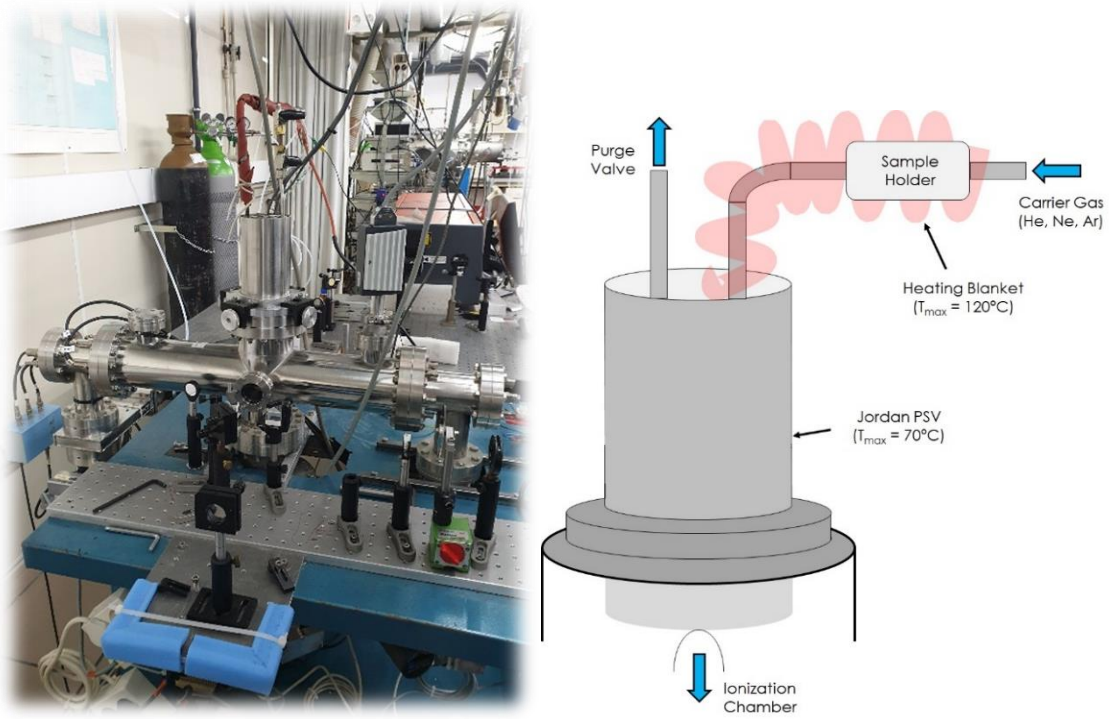

Figure 2.5: (Left) Experimental set up 1; (Right) Schematics of the heating system attached to the valve.

2.1.3.2. Experimental set up 2

This experimental setup is equipped with a linear time of flight mass spectrometer (MS-TOF, R.M. Jordan) with a longer flight tube, resulting in a better mass resolution. The ionization chamber is an original design from Simon's group (Oxford University) that was later modified in the UPV/EHU.[9,10] This chamber has multiple ports for the entrance of the desorption and probe lasers and the controls of the stepper motor, which allows the rotation and translation movements of the sample. The vacuum inside the chamber is maintained by two turbomolecular pumps (Leybold Turbovac 151 of 145 l/s, and Leybold TW 701 of 680 l/s) connected to a rotatory pump (Varian SD700, 27 m^3/h). The rest of the electronics (power supplies, oscilloscope and pulse generators) are similar to those in the Experimental set up 1.

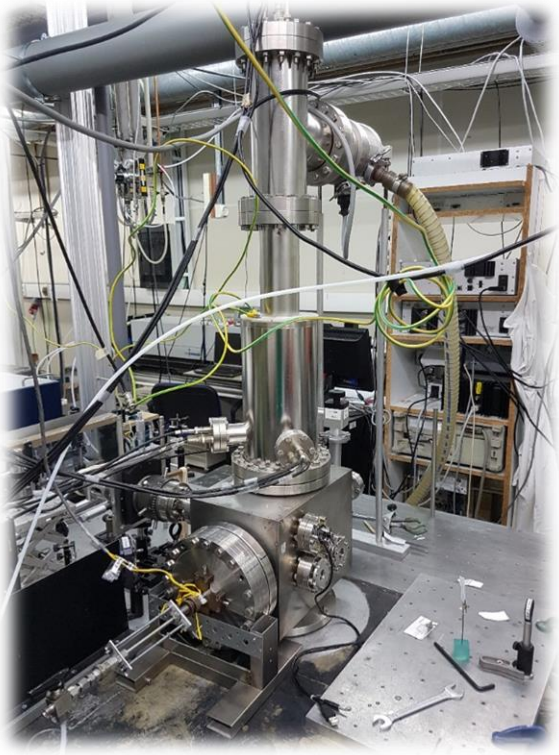

Figure 2.6: Picture of the mass spectrometer coupled to a laser ablation system, located at UPV/EHU lab.

The main characteristic of this experimental set up is that it is equipped with a LD source, which enables measuring sugars, peptides and other thermolabile molecules. The cylindrical sample holder is placed at the exit of a modified pulsed valve (General Valve, Series 9, 0.1 mm nozzle) and it is rotated thanks to a stepper motor (RS 440-442 stepping motor, 1.8°/step), see Figure 2.7. Laser desorption is synchronized with the valve aperture (typically Ar 6-12 bar) so the desorbed molecules are picked up by the supersonic jet. High Ar pressures are required, because the desorbed plume has to be picked and cooled by the still-expanding gas, and therefore, the cooling process is not as efficient as when the sample is seeded directly in the rare gas.

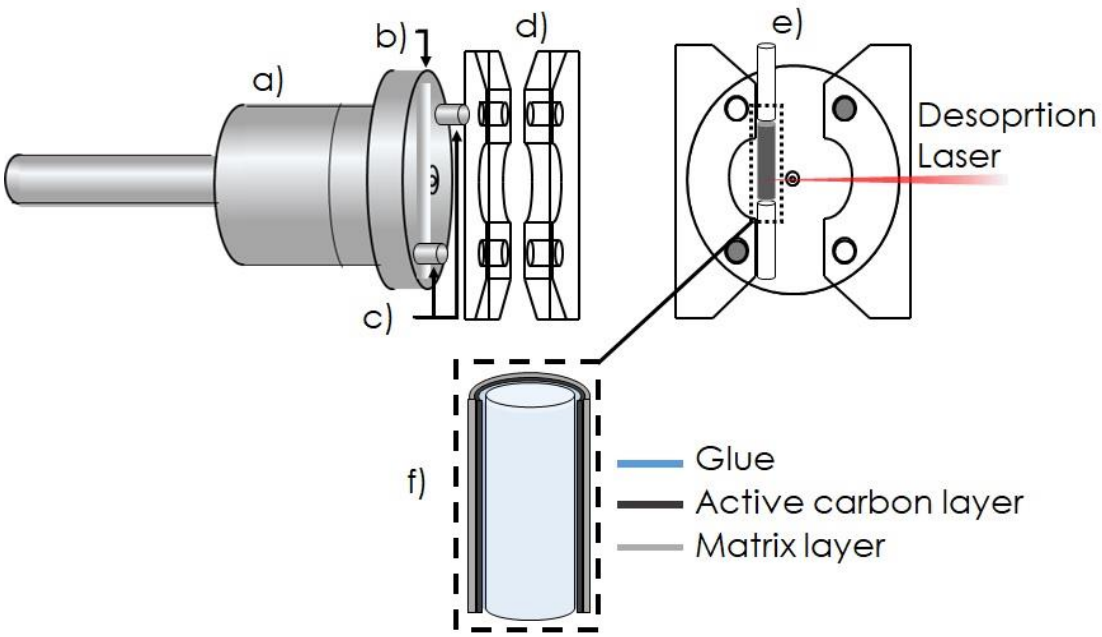

Figure 2.7: Scheme of the laser desorption system coupled to a pulsed valve. a) General Valve Series 9, 28V, Kel-F poppet. b) Groove to adapt the sample rod closer to the nozzle. c) Spikes for fixing the valve position. d) End flange. e) Sample rod, attached to a stepper motor. f) Sample holder covered with the mixture of the substance of interest and carbon nanotubes.

Sample preparation for this laser desorption system is a delicate step: it is necessary to deposit a homogeneous layer of a mixture of the sample plus a substance that helps the laser desorption process, on the surface of the cylindrical sample holder. An inhomogeneous sample will result in strong variations in the signal intensity which are difficult to correct for during the experiment. First, a homogeneous mixture of the substance of interest with carbon nanotubes (MWCNT, Cheaptubes Inc.) is produced. Then, the mixture is deposited on the surface of a graphite cylinder. Sample deposition may vary depending on the texture of the sample, but gluing a thin layer of active carbon to the cylinder before matrix deposition always improved the result.

Some samples present high viscosity that difficult their manipulation. Such is the case of the experiments with N-methylacetamide/β-phenyl-D-glucopyranoside (see Chapter4). N-methylacetamide is a viscous solid, whose melting point is close to room temperature (26ºC). The increase in entropy due to the mixture with the matrix is enough to melt the substance, hampering its deposition on the sample holder. The attempts to introduce the liquid directly in the expansion and heating it were unsuccessful: it was not possible to find the experimental conditions to cluster a molecule seeded in the rare gas and with the second molecule introduced using LD. Therefore, a new methodology for sample preparation was developed (see Figure 2.8).

First, a drop of liquid glue was deposited on the surface of the cylindrical sample holder, and it was extended until the whole surface was covered, and allowed to dry. Then, a previously prepared homogeneous mixture of carbon nanotubes and β-phenyl-D-glucopyranoside was deposited on the surface of the sample holder by pressing the holder against the powdered sugar/nanotubes mixture. Finally, some drops of liquid N-methylacetamide were applied to the holder and gently distributed over the whole sample.

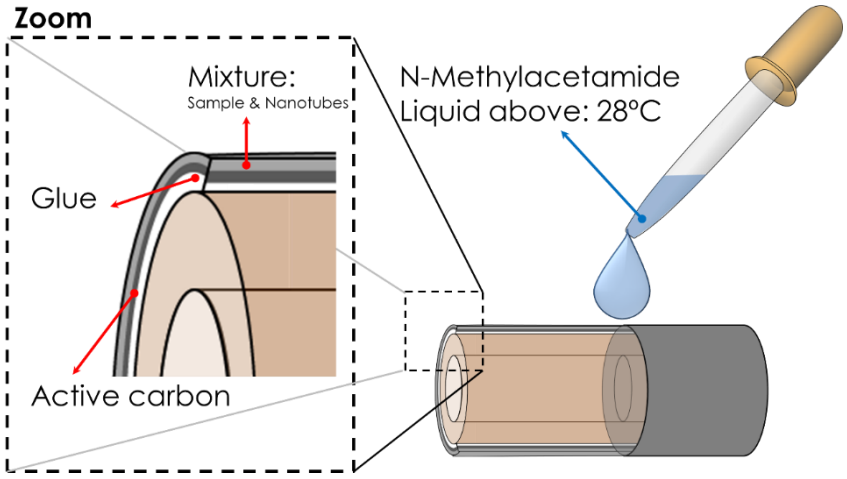

Figure 2.8: Scheme of the sample preparation followed for viscous solids.

2.1.3.3. Carlotta mass spectrometer (ISMO)

During the stay at the ISMO (Institut des Sciences Moléculaires d'Orsay) lab, under the supervision of Dr. Pierre Çarçabal, a third experimental set up was used. The design is similar to that of the experiments in the UPV/EHU, although sample preparation was somehow different.

The procedure starts with the sample as a powder, which is grounded with traces of graphite in order to form a homogeneous mixture. Then, the mixture is rubbed on to the surface of a solid graphite bar to form a thin layer. The graphite bar with the sample is affixed at the exit of a pulsed supersonic valve (R. M. Jordan, 500 μm diameter nozzle), operating at 10 Hz with backing pressures of 5 bar (Ne and Ar were used). The fundamental output of a Nd:YAG laser (Minilite, Continuum) synchronized with the opening of the pulsed valve and focused on the surface of the graphite bar was used as radiation source. The molecular beam crossed a 3 mm skimmer (Beam Dynamics) before entering a differentially pumped chamber and reaching the ionization region of a linear Time of Flight (TOF-MS, R. M. Jordan), where the molecules interact with the laser

radiation. Finally, the generated photo-ions were mass-selected in the mass-spectrometer and detected with a dual micro-channel plate (MCP) detector.

2.2. Experimental Methodology

Several techniques have been using during this thesis in order to extract relevant and accurate structural information from the isolated biomolecules and their aggregates. All of them were based in multiphoton ionization processes (MPI), where photons can come from one or two different laser sources. A more in depth explanation on the subject can be found in refs.[11,12]

2.2.1. Resonance Enhanced Multi-Photon Ionization spectroscopy (REMPI spectroscopy)

The REMPI technique[13,14] is based in the absorption of a minimum of two photons from the ground state (S_0) to the final ion state (I_0^+), exciting the molecule through an intermediate excited state (S_1). Therefore, this technique gives spectroscopic information about the electronic excited state, which in turn, increases the ionization efficiency, compared to a pure coherent absorption. However, there are some requisites that the system may fulfil for the REMPI process to take place: *(i)* the existence of a real electronic excited state so that the ionization process can be considered enhanced, *(ii)* to have a non-zero electronic transition moment and *(iii)* a sufficiently long lived excited state for the absorption of the second photon to take place. If these conditions are fulfilled, the spectroscopy of the electronic excited state may be explored, with vibrational or even rotational resolution, by scanning the excitation energy, while monitoring the ion current generated (see figures 2.9 and 2.10).

Depending on the energy difference between the states involved in the process, different REMPI configurations are accessible. If a unique laser source is used as photon generator, the process is usually called one-color REMPI spectroscopy (1c-REMPI). This process is usually described as 1+1 (one photon for excitation, one photon for ionization), but depending on the molecular system, multiphoton absorption can occur for both excitation or ionization processes, giving rise to 2+1 or 1+2 one-color REMPI schemes.

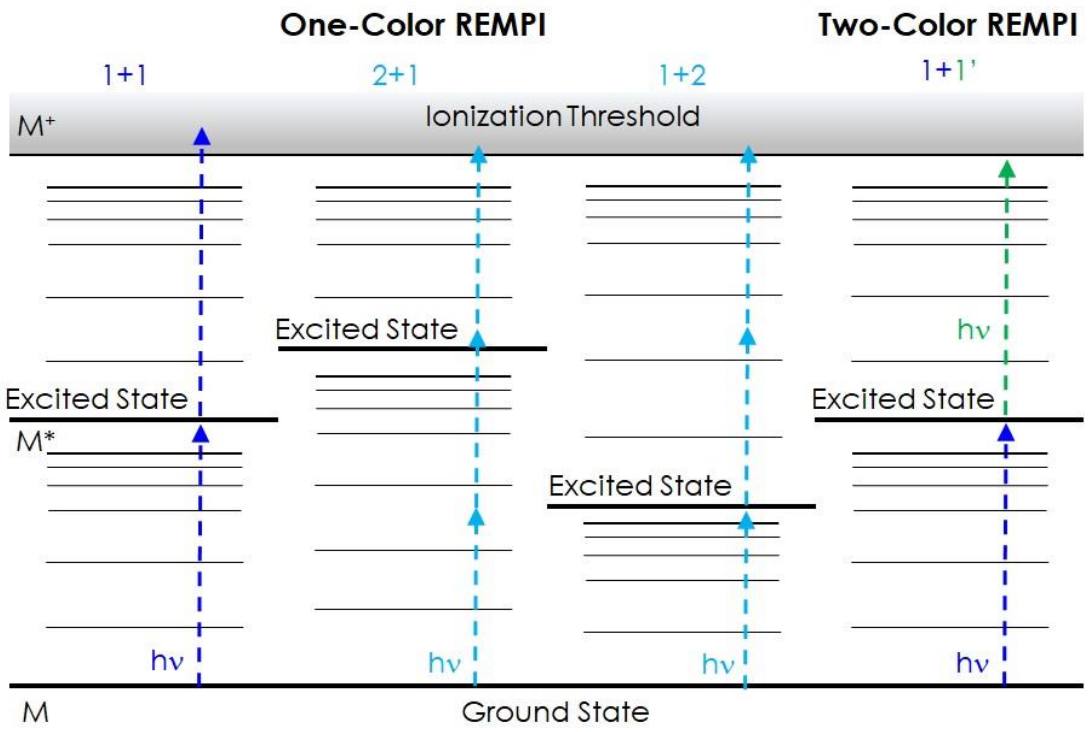

Figure 2.9: One and two-color REMPI spectroscopy schemes.

In the one-color REMPI spectroscopy, it is not possible to fine tune the energy of the photons to reach the ionization threshold, and therefore, the ion is usually produced with an excess of energy. This is because the energy of the $S_1 \leftarrow S_0$ transition does not match with that of $I_0^+ \leftarrow S_1$. Such extra energy may lead to fragmentation of the ions, which are therefore detected in the mass channel corresponding to smaller species, complicating their identification and their study. In order to avoid such processes, a second laser is used to deliver the photons for the $I_0^+ \leftarrow S_1$ transition. This technique is called two-color REMPI spectroscopy (2c-REMPI),[15,16] and requires of the usage of two-laser beams spatially and temporally overlapped. The vibronic spectra recorded with this technique usually present an improved s/n ratio, as the fine selection of the ionization energy also avoids the presence of bands due to power saturation or impurities, in addition to those bands due to fragmentation from larger clusters. Using two-color REMPI has the additional benefit of allowing one to determine the ionization threshold and the excited electronic state lifetime.

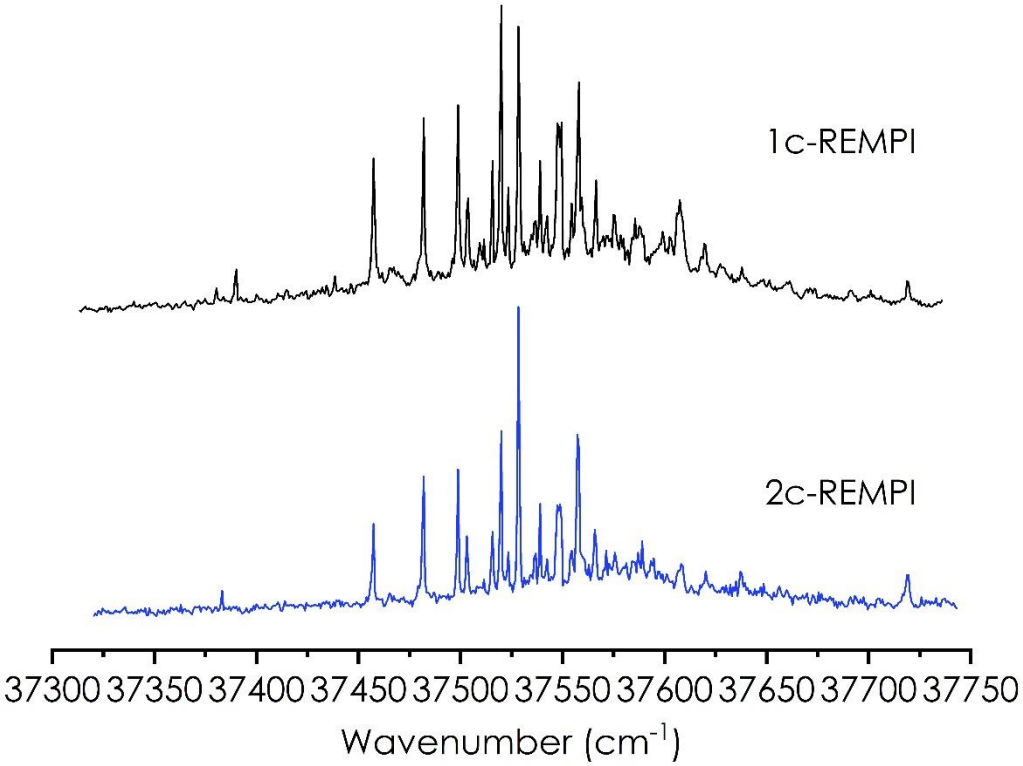

Figure 2.10: One-color and two-color REMPI spectra of benzyl alcohol dimer. As it can be observed, some bands disappeared in the 2c spectrum, and the overall background of the absorption was reduced.

REMPI spectroscopy is a very powerful technique, but it constitutes only the first step in the study of molecular aggregates. These complicated systems may present multiple conformational isomers whose contribution to the REMPI spectrum cannot be separated, unless double resonance techniques are used, such as UV/UV hole burning and IDIRS (Ion Dip InfraRed Spectroscopy).

2.2.2. Hole Burning Spectroscopy: UV/UV Hole Burning

This technique enables determining the number of conformational isomers that are contributing to a given REMPI spectrum, and it is based on the use of two tunable lasers. The first laser, the pump laser, is tuned to a transition of the REMPI spectrum. Usually the red-most transition is chosen as it usually is taken as the 0_0^0 transition. In some cases, such transition is weak, or the overall spectrum is noisy. In such cases, the strongest transition is usually chosen. Then, a second UV laser (probe) is scanned through the spectral interval containing the REMPI spectrum, while the ion current is monitored. The pump laser is fired 100-200 ns earlier than the probe. In this way, when the probe laser hits a transition belonging to the same isomer as the transition pumped, a depopulation

takes place and the probe laser finds less molecules to excite, and a drop in the signal intensity is produced.

A further refinement of the technique requires the probe laser to be fired at 5 Hz, while the pump laser is operated at 10 Hz. In that way, a real-time active subtraction can be performed, substantially increasing the s/n ratio (see Figure 2.11). This double resonance technique is a very powerful tool to easily identify different conformations in situation where the REMPI spectrum is very congested.

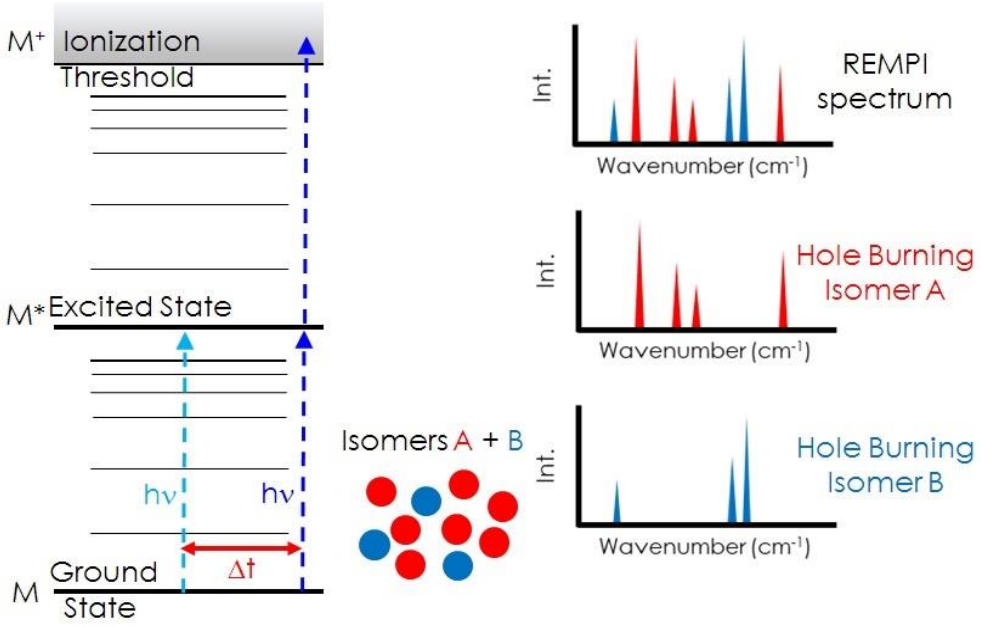

Figure 2.11: Scheme of an UV/UV Hole Burning double resonance experiment.

2.2.3. Ion Dip InfraRed Spectroscopy (IDIRS)

This technique, also called IR/UV double resonance, allows one to obtain the isomer specific IR spectrum. Combined with the mass resolved detection, IDIRS is the most powerful technique to obtain structural information from complexes in isolated phase.

IDIRS is based on the same configuration as Hole Burning spectroscopy. A tunable IR laser is used as a pump, working at 5Hz and 100-200 ns delayed before the UV probe laser. The probe UV laser is tuned to a specific transition of the isomer of interest. Active subtraction is employed to record both signal and reference at 5 Hz. Again, scanning the IR laser produces a dip in the ion signal, each time the laser is resonant with a vibrational transition of the isomer probed. By subtracting the depopulated spectra from the reference signal, the ground state IR spectrum of the isolated isomer is obtained.

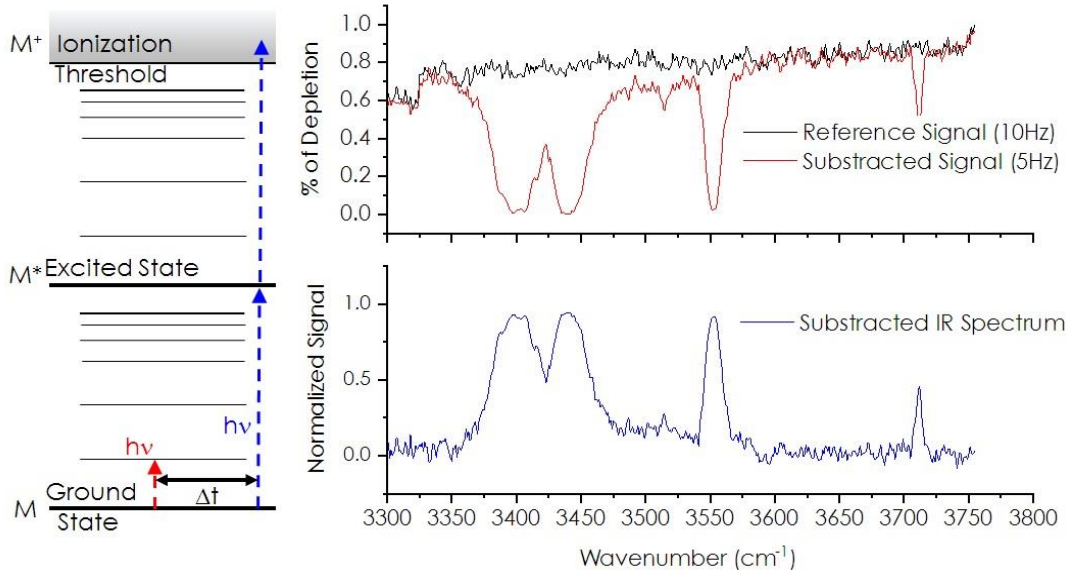

Figure 2.12: Scheme of the IDIRS technique with active subtraction.

2.2.4. IR/UV Hole Burning spectroscopy

The aim of this technique is the same as in the UV/UV Hole Burning, but changing the UV probe laser for an IR one. Fixing the IR wavelength to excite a known vibrational transition, a population of molecules that shares that transition will be depleted. Then, scanning the UV with the pump laser, we obtain the isomer specific REMPI spectrum. The configuration of the technique is the same used in IDIR, but the scanning laser is changed from the IR to the UV.

2.3. Theoretical Methodology

The main goal of the theoretical analysis is to fully explore the conformational landscape of the system under study, locating all the relevant minima and to provide reliable relative energy and binding energy values and accurate simulations of the IR spectra to help with the interpretation of the experimental data. In the last decades, advances in computing power and the development of new computational method allowed experimental scientists to go a step forward in their experimental researches.[17–19] In this work, such developments enabled the characterization of large aggregates with complex conformational landscapes.

The theoretical methodology followed is summarized in Figure 2.13. Briefly, a wide exploration of the conformational landscape with molecular mechanics is carried out. Then, the geometry of the structures found are optimized using quantum mechanics. The true nature of the minima is verified by the absence of negative frequencies in a normal mode analysis. In this step, reliable energetic values are also obtained. Finally, the simulated IR, and sometimes UV, spectra are built, to aid in the interpretation of the experimental data.

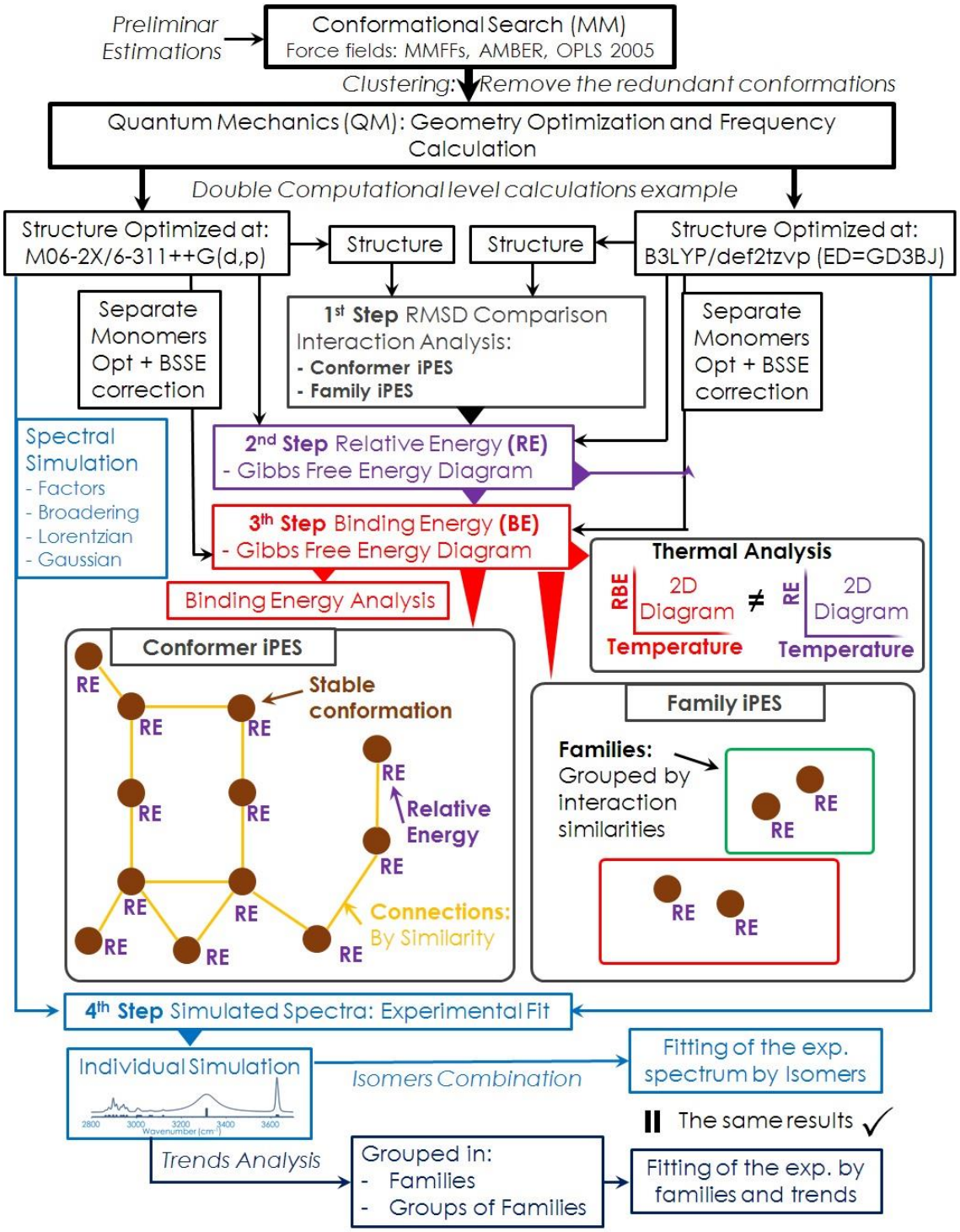

Figure 2.13: Scheme of the general computational protocol followed for the theoretical analysis of the systems under study.

2.3.1. Conformational Search

The conformational panorama and the diversity of non-covalent interactions are directly related to the flexibility of the molecules. Dihedral angle rotations, functional group torsions or even the tautomerism of functional groups would generate an

extended potential energy surface with various local minima. The flexibility and complexity of the systems studied in this thesis makes compulsory the development of an elaborated protocol to ensure that all the relevant structures are found during the conformational search. The exhaustive conformational search performed in this first step is carried out using molecular mechanics (MM). These methods scan all degrees of freedom without any restriction, defining a list of all the possible conformation that the molecule or the aggregate can adopt.[20] Maestro software with the MacroModel tool (Schrödinger Suite)[21] was employed in this search.

The structures were generated using Monte Carlo algorithms, which explore the potential energy surface of the molecules following a variation of their bond angles, distances and dihedrals. Then, the structures obtained are perturbed using a mixed-torsional large scale low mode sampling method to find new local minima. Finally, the perturbed structures are energy minimized before adding them to the final list of all possible conformations. Although this method is a very powerful tool to easily build a general conformational panorama, energetic minimizations are not very accurate, since they are based on classical physics. For this reason, previously mentioned chemical intuition and variables analysis has to be used in order to recognize all the possible conformational families.

Some tools can be used to simplify the large list of all possible conformers. Choosing an energy window will reduce significantly the number of structures, by rejecting all those isomers that are too high in energy. Then, the clustering methods in the Maestro software can be used to group geometries based on their similarities. This enables reducing the study to structural families instead to individual species. Representative structures of those families are afterwards submitted to full optimization using DFT methods. Using different force fields is recommendable to prevent missing relevant structures, since they are differently parametrized. OPLS3[22], MMFFs[23] and AMBER[24,25] force fields were employed during this thesis.

2.3.2. Quantum computations: Structure optimization and Frequency calculations

The Quantum Mechanics (QM) provides an accurate description of the molecular properties of the structures obtained in the conformational search (MM). Geometries are subjected to an exhaustive geometrical optimization method, which accuracy varies

depending on the computational level employed. In this work, density functional theory (DFT) was the method of choice. Among the functionals available, those chosen explicitly take into account dispersion interactions. The most used functionals in this thesis were: the M06-2X functional, developed by Truhlar,[26] and the B3LYP functional along with the Grimme's Dispersion (GD3-BJ) corrected factor.[27] For the M06-2X functional, Pople's double and triple ζ basis sets (6-31+G(d) and 6-311++G(d,p)) were used, whereas the def2tzvp basis set was employed in combination with the dispersion-corrected B3LYP. Both methods have extensively proven their ability to accurately predict the electronic properties of molecular aggregates.[10,28–30,31–36] In cases were the computational work needs to be extended, an updated version of the Truhlar's group functional, MN15;[37] and MP2 ab initio method were employed.

After geometry optimization, the structures are grouped into families depending on their type of interaction. Depending on the molecular system and the flexibility of it, a connexion diagram close to the one depicted in Figure 2.14 can be built. This diagram shows the interaction Potential Energy Surface (iPES), and summarizes all the isomerization pathways between the most stable/relevant families.

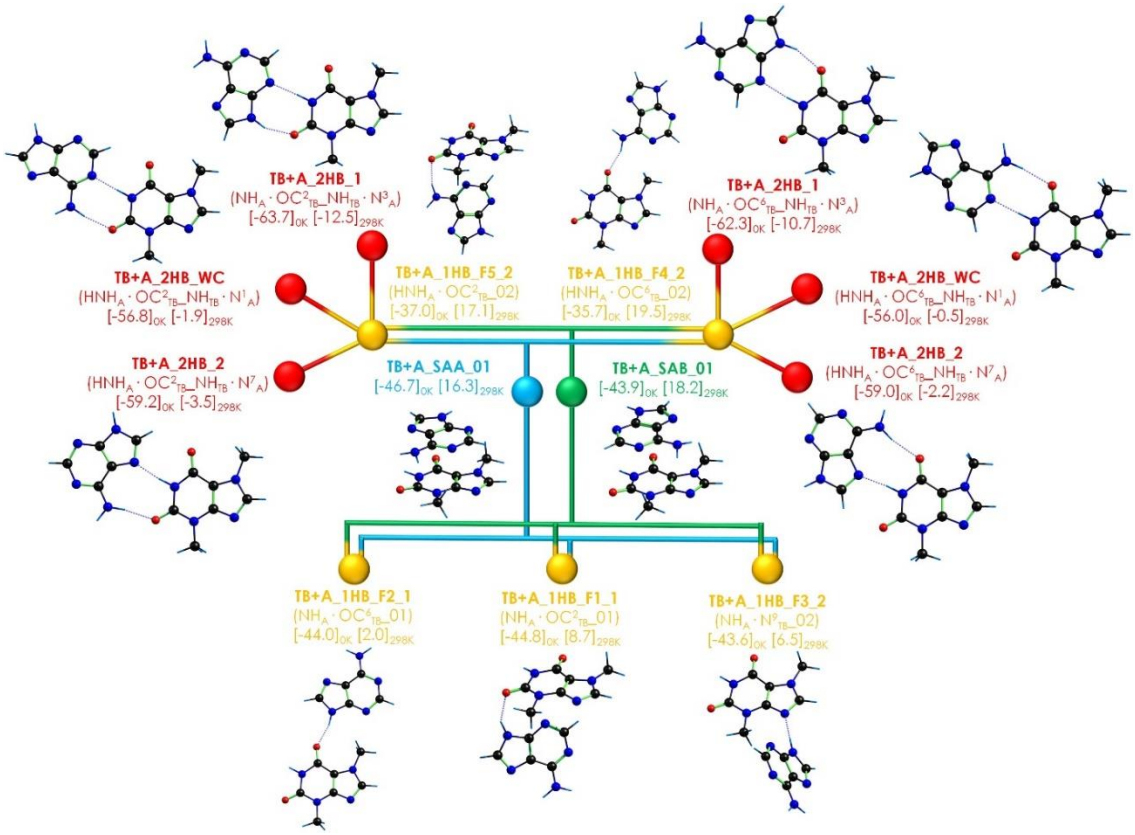

Figure 2.14: Example of an interaction Potential Energy Surface (iPES) diagram. Each type of interaction is assigned a color: double HB (red), single HB (yellow) and stacking (blue and green, depending on the face participating in the interaction). The same color is used during the next steps, to aid connecting all the data to the computed structures.

Minimum electronic energy values of the structures are not always a good indicative of the experimentally isolated conformers. In most of the complexes presented in this thesis, the binding energy (BE) values are also used, because as it will be shown, for some systems, strongly bonded species were detected instead of other more stable but less strongly bond ones. Additionally, comparison between the BE of different systems gives important insights into de nature of the interactions. Calculation of the relative stability and BE of a system is done using equations (1) - (5):

$$E_{mono,i} = E_{Elec.} + E_{ZPE} + \Delta G_{TC,i} \quad (1)$$

$$E_i = E_{Elec.} + E_{ZPE} + E_{BSSE} + \Delta G_{TC,i} \quad (2)$$

$$RE_i = E_i - E_{GM} \quad (3)$$

$$BE_i = E_i - (E_{mono1,i} + E_{mono2,i}) \quad (4)$$

$$RBE_i = BE_i - BE_{SB} \quad (5)$$

The energy of a single molecule (monomer) is defined as the sum of the electronic energy ($E_{elec.}$), the zero-point energy correction (ZPE) and the thermal correction for the Gibbs free energy (ΔG_{TC}) (see Equation 1). For the energy of a molecular aggregate (Equation 2), an additional basis set superposition error (BSSE), computed using the counterpoise method developed by Boys and Bernardi,[38] is needed. This correction takes into account the extra stabilization of the complex, due to the higher number of basis set used to computed it, compared to those used to calculate the energy of its individual components. The binding energy of a complex (BE_i) is obtained by the difference between the energy of the complex (E_i) and the sum of the energies of the monomers. Ej, for a dimer, $BE = E_{dimer} - (E_{mono1,I} + E_{mono2,\ I})$ (see Equation 4). It is worth noting that, in general, RE and BE values are proportional, except in those cases in which the monomers present several conformational isomers. Since the binding energy of the complex depends also in the conformation of the monomers, there can be cases where two complexes have similar RE but different BE. This phenomenon occurs when one of the monomers adopt a less stable arrangement that entangles a stronger bond in the complex (see Figure 2.15 for a schematic explanation). Finally, Equation 5 can be used to compare all the binding energies of a system, by subtracting the binding energy of the most strongly bonded complex (BE_{SB}) from that of the resto of isomer (BE_i).

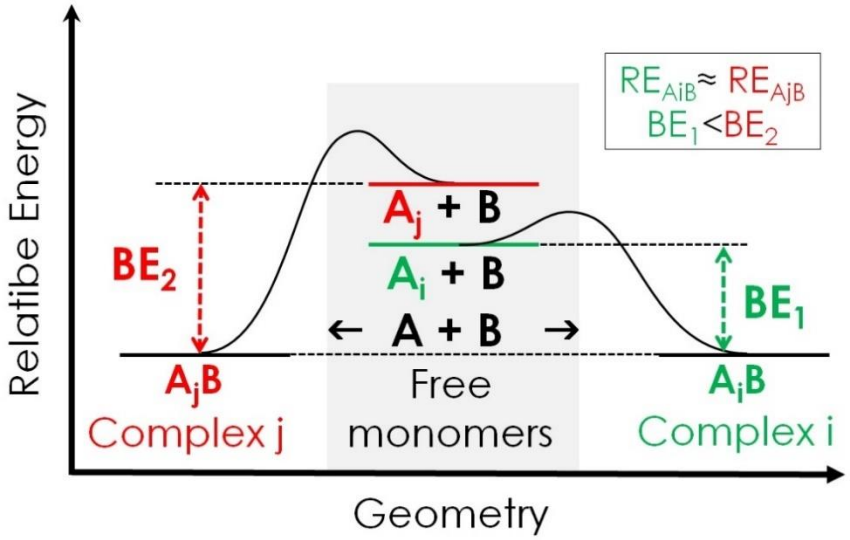

Figure 2.15: Energy diagram of the binding energy of different complexes. Despite A_jB and A_iB complexes having similar stability, they present different binding energies,

The stability of the molecules above 0 K has also been calculated for all the systems studied. The results presented along this work demonstrate that the LD procedure used to vaporize the molecules introduce high amounts of the energy. The collision cooling

process may trap part of the hot population into local minima, which are particularly stable at high temperatures and therefore, taking into account such species is compulsory to interpret the experimental results. For that reason, we also calculated the Gibbs Free Energy and the Binding Gibbs Free Energy of the complexes at different temperatures. This procedure is further explained in the next section.

2.3.3. Conformational cooling during supersonic expansions

One of the most remarkable properties of supersonic expansions is the high cooling efficiency. The expanded gas goes through a non-equilibrium state, transferring the rotational and vibrational energy components of the temperature to the translational one.[1] That non-equilibrium state is also achieved in the systems studied in this thesis, when they are mixed in the expansion with the carrier gas. As explained in the experimental methods, the sample was transferred into gas phase either by heating and seeded in the carrier gas; or desorbed with a laser at the exit of the nozzle, where the evaporated molecules are picked by the expanded gas. In the heating setup, conformers are in thermodynamic equilibrium in the nozzle. The population of the conformers follows a Boltzmann distribution. During the supersonic expansion, collisions with carrier gas cools the rotational and vibrational populations of the molecules, trapping different conformers.[39–41] However, the final number of isolated conformers depends on two aspects: *(i)* the population distribution before the expansion, and *(ii)* the height of the isomerization barriers thanks. Depending on the second factor, the barriers may isolate the conformers or they can be surmounted with the energy provided from an inelastic collision with the carrier gas. Figure 2.16 summarizes these situations in an energy diagram scheme.

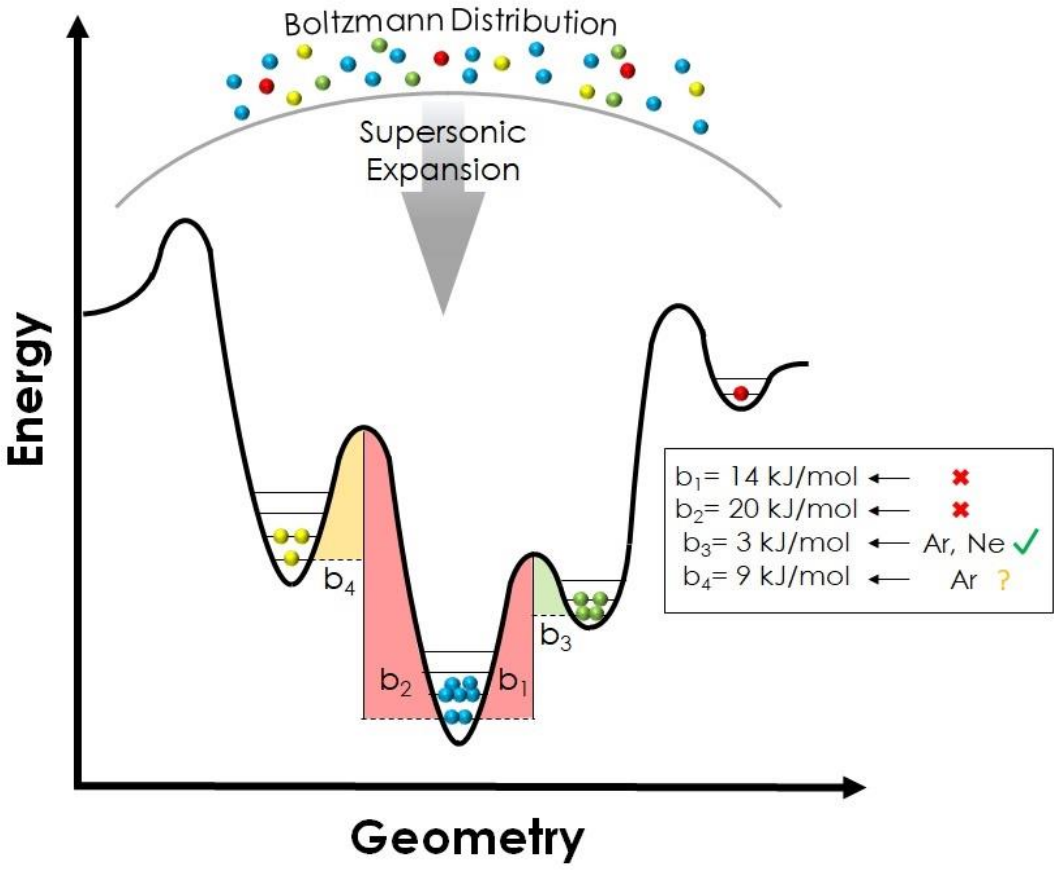

Figure 2.16: Energy diagram of the conformational cooling process during a supersonic expansion. Distribution of conformers before the expansion corresponds to a Boltzmann distribution as a function of the temperature. Colored balls represent different conformations of a molecule, being the blue balls the most stable and populated conformer. After the supersonic expansion, collisions with carrier gas cools the molecules, which are trapped in different conformations, separated by barriers. In some cases, those collisions may transfer enough energy to the molecule to overcome interconversion barriers. Considering that the speed reached in the supersonic expansion is ~Mach 2, the kinetic energy transferred during an inelastic collision with a single atom of carrier gas should allow b_3 and b_4 to be surpassed.

When the molecules are vaporized with the LD system, more uncertainties are added to the equation, because the molecules in the ablation plume present a wide range of high temperatures.[42] Those temperatures are high enough to allow the same isomerization processes as in the heating system before the expansion, although the initial temperature for the desorbed molecules is unknown.

In order to study the temperature effect in the final conformer population, we used the so-called Gibbs Free Energy diagrams from 0 K to 700 K, limit at which most organic molecules decompose. Such diagrams allow one to identify conformers that are particularly stable at higher temperatures and that, therefore, can be relevant to understand the experimental spectrum.

2.3.3.1. Binding Gibbs Free Energy

Equations (6) and (7) were used to calculate the Gibbs free energy of the monomers:

$$\Delta G_{Mono,i,T} = \Delta E_{Elec.,i} + \Delta E_{ZPE,i} + \Delta E_{ddH,i,T} - T \cdot \Delta S_{dS,i,T} \quad (6)$$

$$\Delta G_{Rel,Mono,i,T} = \Delta G_{Mono,i,T} - \Delta G_{GM,T} \quad (7)$$

With equation (6), we obtain the Gibbs free energy of the monomer adopting i-th conformer at the desired temperature (T). Enthalpic contribution at each temperature ($\Delta E_{ddH,i,T}$) and the corresponding entropic contribution ($T \cdot \Delta S_{dS,i,T}$) are added to the zero-point energy corrected electronic energy. Once the Gibbs free energy for all isomers of the monomer under study is calculated, the relative Gibbs free energy of the isomers is readily obtained by subtracting the global minimum energy ($\Delta G_{GM,T}$) from the energy value of each isomer ($\Delta G_{Mono,i,T}$). Plotting this relative Gibbs free energy value as a function of the temperature, a diagram like the one depicted in Figure 2.17 is obtained. The use of these equations is mandatory in order to obtain the Gibbs free energy of the complexes.[43–45]

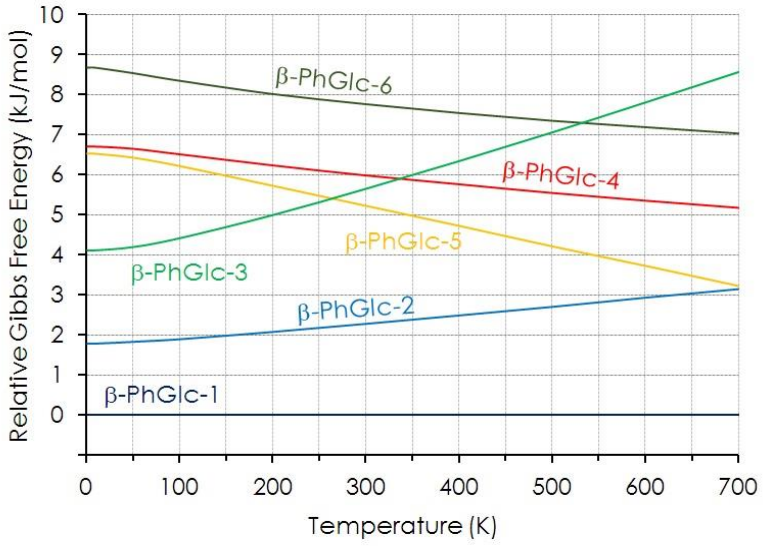

Figure 2.17: Example of a Relative Gibbs Free Energy diagram for a PhGlc monomer. Gibbs free energy of each conformation was calculated following equations (6) and (7), at different temperatures.

Regarding the calculation of the relative stability, as explained in section 2.3.2, there are two possible situations: the monomers have a single conformation or they can adopt multiple conformations. In the former case, the relative Gibbs free energy (ΔΔG) is computed by simple subtraction. But if the monomers can adopt multiple

conformations, and additional quantity can be defined: the relative binding Gibbs free energy ($\Delta\Delta G_B$). Equation (8) defines the Gibbs free energy for a given complex. As it can be seen, it includes the same terms as for the monomer, plus a new term to take into account the BSSE correction:

$$\Delta G_{AB,i,T} = \Delta E_{Elec.,i} + \Delta E_{ZPE,i} + \Delta E_{BSSE,i} + \Delta E_{ddH,i,T} - T \cdot \Delta S_{dS,i,T} \quad (8)$$

Then, the relative Gibbs free energy can be determined, using equation (9) in case the monomers present a single conformation, or equation (10) if the monomers can adopt several conformations:

$$\Delta\Delta G_{AB,i,T} = \Delta G_{AB,i,T} - (\Delta G_{A,T} + \Delta G_{B,T}) \quad (9)$$

$$\Delta\Delta G_{B\,AB,i,T} = \Delta G_{AB,i,T} - (\Delta G_{A,i,T} + \Delta G_{B,i,T}) \quad (10)$$

$$\Delta\Delta G_{Rel.,AB,i,T} = \Delta\Delta G_{AB,i,T} - \Delta\Delta G_{GM,AB,i,T} \quad (11)$$

The data obtained using equation 11 enable the comparison of stability of different complexes. Representing this Relative Binding Gibbs Free Energy as a function of the temperature, similar diagrams to those in Figure 2.18 are obtained. These diagrams permit a fast comparison between the relative stability of multiple conformers in a wide temperature window, allowing the identification of all the species with a high chance of being trapped during the expansion.

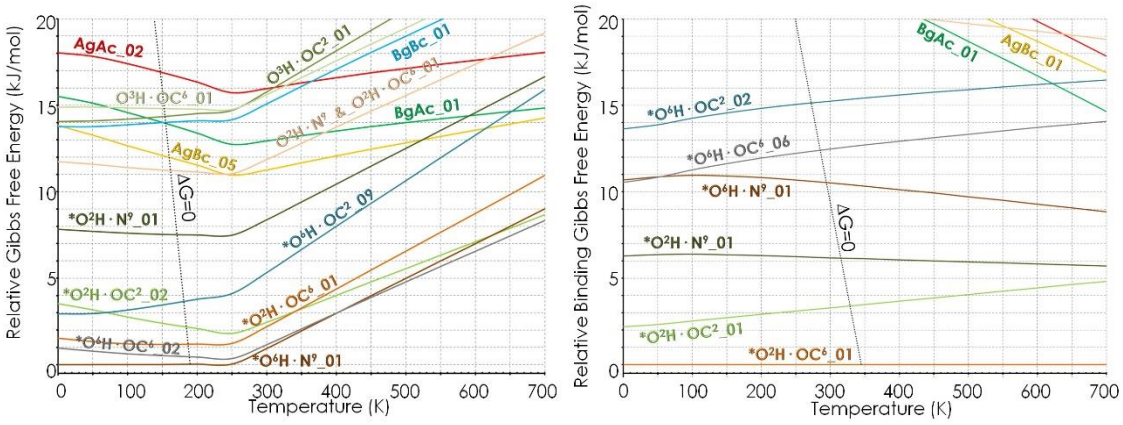

Figure 2.18: Left: Example of a Relative Gibbs Free Energy diagram for the Caf+PhGlc complex. For this case, equation 9 was applied. Right: Relative Binding Gibbs Free Energy diagram for the same Caf+PhGlc complex, but computed with equation 10. Note that despite being the same conformational isomers, significant changes in stability order can be appreciated.

2.3.4. Non-covalent interaction approach

The electron density (ρ) obtained from quantum mechanics calculations can be analyzed to characterize the intermolecular interactions ruling the aggregation process. The Non-Covalent Interaction (NCI) approach[46,47] evaluates the intermolecular interactions based on the electron density and the reduced density gradient (s), coming from the density and its first derivative:

$$s = \frac{1}{2(3\pi^2)^{1/3}} \frac{|\nabla\rho|}{\rho^{4/3}} \tag{12}$$

When inter- or intramolecular interaction of weak character are present, there is a substantial change in the reduced density gradient, producing density critical points, which appear as minima in the reduced density gradient. However, when representing s vs ρ, further analysis of the electron density in the troughs is required, as both attractive and repulsive interactions appear in the same region. The sign of the second eigenvalue of the Hessian matrix of the electron density (λ_2) indicates if the minimum corresponds to an attractive (-) or repulsive (+) interaction

Plotting s as a function of the electron density, ρ multiplied by the sign of λ_2, graphics as the one represented in Figure 2.19. The sign of the second eigenvalue of the Hessian matrix can be either positive or negative depending on the nature of the interaction: (*i*) bonding interactions, such as hydrogen bonds, appear when $\lambda_2 < 0$; (*ii*) non-bonding interactions, like steric repulsion, appear when $\lambda_2 > 0$; and (*iii*) weak delocalized interactions, like vdW interactions, appear at $\lambda_2 \leq 0$. Therefore, the analysis of the sign λ_2 at 2D NCI plots allows distinguishing different types of interactions, while the value at ρ provides information about the interaction strength.

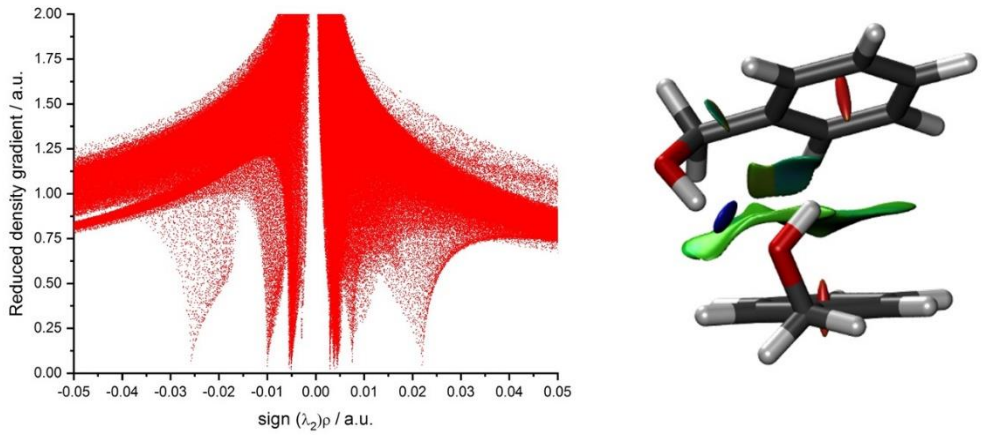

Figure 2.19: Left: 2D NCI plot of the reduced density gradient against λ_2/ρ. Signed λ_2 value allows one to identify the interaction type: bonding interactions appear on the left, repulsive interactions on the right and weak vdW interactions near zero. Right: Representation of the NCI as 3D isosurfaces. BGR scale is used to classify interactions. In this example, the OH···O interaction appears as an intense blue disk, while the stacking interaction between the two aromatic rings is represented by a green surface. Repulsive interactions inside each aromatic rings are appear as red dots. The isosurfaces were generated with value of s = 0.5 au, with a color scale of $-2.0 < \rho < 2.0$ au.

Additionally, a three dimensional representation of the non-covalent interactions as isosurfaces may be integrated with the ball&stick representation of the molecules. In these 3D plots, the interactions appear as isosurfaces of the reduced density gradient between nuclei, colored according to their strength, using a BGR color code: blue is used for bonding interactions, green for weak vdW interactions, and red for repulsive forces. Intensity of the color tone within this scale indicates the strength of the interaction. These isosurfaces are generated by the analysis of the local properties on a cubic grid constructed with the NCIPlot program.

2.3.5. Spectral Simulations

Direct comparison between the DFT predictions and the experimental spectra is of tremendous help for the assignment of the experimental IR spectra. But, at the same time, the comparison serves as a benchmark for the calculations, since both datasets are obtained in isolated conditions. QM computations also produce the normal mode frequencies from the optimized structures, and therefore, it is necessary to introduce a factor to account for anharmonicity. It is possible to adjust the correction factors using databases,[48] but in our case, we used our own factors, obtained by comparison with experimental data obtained from molecules with unequivocal assignment.[49] Table 2.1

collects the different scaling factors used for the OH, NH and CH stretches, at different computational levels.

Table 2.1: Correction factors employed to account for anharmonicity at different computational levels.

Computational Level (Method/Basis set)	**OH scaling factor**	**NH scaling factor**	**CH scaling factor**
M06-2X/6-311++G(d,p)	0.935	0.953	0.953
M06-2X/def2TZVP	0.945	0.951	0.951
B3LYP-ED=GD3BJ/6-311++G(d,p)	0.954	0.963	0.963
B3LYP-ED=GD3BJ/def2TZVP	0.963	0.963	0.963
B3LYP-ED=GD3/cc-pVTZ	0.96	0.96	0.96
MN15/6-311++G(d,p)	0.937	0.953	0.953
MN15/def2TZVP	0.945	0.953	0.953
MP2/6-311++G(d,p)	0.945	0.951	0.951

To simulate the experimental spectrum several steps were followed. First, each frequency was represented by a Lorentzian function with a FWMH of 5 cm^{-1}. Then, the experimental band broadening due to laser was taken into account. As our IR laser has a Gaussian profile of ~6 cm^{-1}, the whole theoretical spectrum was convoluted with a Gaussian function of 6 cm^{-1} of bandwidth. Finally, the band broadening due to strong anharmonic effects or inefficient cooling of the low vibrational energy modes must be also introduced. This experimental broadening is quite usual in molecular aggregates, and it commonly increases proportional to the red shift (which is related with the strength of the interaction). We corrected this effect by an experimental parametrized broadening factor, extracted from a quadratic function (see Figure 2.20).

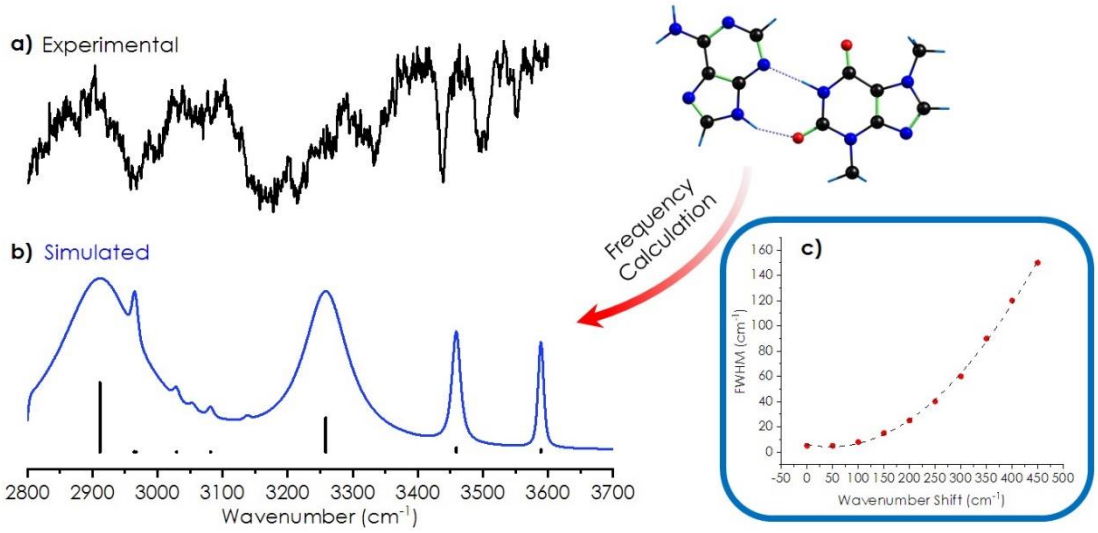

Figure 2.20: Example of the theoretical spectrum simulation of a single conformation. Frequency values from the computed vibrational modes are represented with a Lorentzian function (FWHM=5 cm^{-1}) and convoluted with a Gaussian function (FWHM=6 cm^{-1}). The bandwidth of the bounded vibrational modes is extracted from the quadratic function (c).

2.4. References

[1] D. H. Levy, The spectroscopy of very cold gases., *Science*, 1981, **214**, 263–9.

[2] M. S. de Vries and P. Hobza, Gas-Phase Spectroscopy of Biomolecular Building Blocks, *Annu. Rev. Phys. Chem.*, 2007, **58**, 585–612.

[3] T. Ebata, Y. Inokuchi and A. Nakajima, in *Physical Chemistry of Cold Gas-Phase Functional Molecules and Clusters*, eds. T. Ebata and M. Fujii, Springer Singapore, Singapore, 2019, pp. 3–32.

[4] T. R. Rizzo and O. V Boyarkin, in *Gas-Phase IR Spectroscopy and Structure of Biological Molecules*, eds. A. M. Rijs and J. Oomens, Springer International Publishing, Cham, 2015, pp. 43–97.

[5] A. L. Patrick and N. C. Polfer, in *Gas-Phase IR Spectroscopy and Structure of Biological Molecules*, eds. A. M. Rijs and J. Oomens, Springer International Publishing, Cham, 2015, pp. 153–181.

[6] I. León, J. Millán, F. Castaño and J. A. Fernández, A Spectroscopic and Computational Study of Propofol Dimers and Their Hydrated Clusters, *ChemPhysChem*, 2012, **13**, 3819–3826.

[7] I. León, E. J. Cocinero, J. Millán, A. M. Rijs, I. Usabiaga, A. Lesarri, F. Castaño and J. A. Fernández, A combined spectroscopic and theoretical study of propofol·(H2O)3, *J. Chem. Phys.*, 2012, **137**, 74303.

[8] I. Leon, University of the Basque Country, 2011.

[9] I. Usabiaga, University of the Basque Country, 2017.

[10] I. Usabiaga, J. González, P. F. Arnáiz, I. León, E. J. Cocinero and J. A. Fernández, Modeling the tyrosine-sugar interactions in supersonic expansions: glucopyranose-phenol clusters., *Phys. Chem. Chem. Phys.*, 2016, **18**, 12457–12465.

[11] W. Demtröder, *Laser Spectroscopy*, 2003.

[12] J. M. Hollas, *Modern Spectroscopy*, 2004.

[13] D. M. Lubman and M. N. Kronick, Mass spectrometry of aromatic molecules with resonance-enhanced multiphoton ionization, *Anal. Chem.*, 1982, **54**, 660–665.

[14] R. Tembreull and D. M. Lubman, Use of resonant two-photon ionization with supersonic beam mass spectrometry in the discrimination of cresol isomers, *Anal. Chem.*, 1984, **56**, 1962–1967.

[15] J. Yao, H. S. Im, M. Foltin and E. R. Bernstein, Spectroscopy of Neurotransmitters and Their Clusters: Phenethylamine and Amphetamine Solvation by Nonpolar, Polar, and Hydrogen-Bonding Solvents, *J. Phys. Chem. A*, 2000, **104**, 6197–6211.

[16] R. T. Kroemer, K. R. Liedl, J. A. Dickinson, E. G. Robertson, J. P. Simons, D. R. Borst and D. W. Pratt, Conformationally Induced Changes in the Electronic Structures of Some Flexible Benzenes. A Molecular Orbital Model, *J. Am. Chem. Soc.*, 1998, **120**, 12573–12582.

[17] J. Leszczynski, Handbook of computational chemistry, *Handb. Comput. Chem.*, 2012, 1–1430.

[18] V. Barone, R. Improta and N. Rega, Quantum Mechanical Computations and Spectroscopy: From Small Rigid Molecules in the Gas Phase to Large Flexible Molecules in Solution, *Acc. Chem. Res.*, 2008, **41**, 605–616.

[19] J. F. Dobson, G. Vignale and M. P. Das, *Electronic Density Functional Theory*, Springer US, Boston, MA, 1998.

[20] K. Vanommeslaeghe, O. Guvench and A. D. MacKerell, Molecular Mechanics, *Curr. Pharm. Des.*, 2014, **20**, 3281–3292.

[21] L. Schro dinger, 2020.

[22] E. Harder, W. Damm, J. Maple, C. Wu, M. Reboul, J. Y. Xiang, L. Wang, D. Lupyan, M. K. Dahlgren, J. L. Knight, J. W. Kaus, D. S. Cerutti, G. Krilov, W. L. Jorgensen, R. Abel and R. A. Friesner, OPLS3: A Force Field Providing Broad Coverage of Drug-like Small Molecules and Proteins, *J. Chem. Theory Comput.*, 2016, **12**, 281–296.

[23] T. A. Halgren, Merck molecular force field. I. Basis, form, scope, parameterization, and performance of MMFF94, *J. Comput. Chem.*, 1996, **17**, 490–519.

[24] D. A. Case, T. E. Cheatham III, T. Darden, H. Gohlke, R. Luo, K. M. Merz Jr., A. Onufriev, C. Simmerling, B. Wang and R. J. Woods, The Amber biomolecular simulation programs, *J. Comput. Chem.*, 2005, **26**, 1668–1688.

[25] K. N. Kirschner, A. B. Yongye, S. M. Tschampel, J. González-Outeiriño, C. R. Daniels, B. L. Foley and R. J. Woods, GLYCAM06: A generalizable biomolecular force field. Carbohydrates, *J. Comput. Chem.*, 2008, **29**, 622–655.

[26] Y. Zhao and D. G. Truhlar, The M06 suite of density functionals for main group thermochemistry, thermochemical kinetics, noncovalent interactions, excited states, and transition elements: Two new functionals and systematic testing of four M06-class functionals and 12 other function, *Theor. Chem. Acc.*, 2008, **120**, 215–241.

[27] S. Grimme, J. Antony, S. Ehrlich and H. Krieg, A consistent and accurate ab initio parametrization of density functional dispersion correction (DFT-D) for the 94 elements H-Pu, *J. Chem. Phys.*, 2010, **132**, 154104.

[28] A. Camiruaga, I. Usabiaga, A. Insausti, I. León and J. A. Fernández, Sugar–peptidic bond interactions: spectroscopic characterization of a model system, *Phys. Chem. Chem. Phys.*, 2017, **19**, 12013–12021.

[29] I. Usabiaga, J. González, I. León, P. F. Arnaiz, E. J. Cocinero and J. A. Fernández, Influence of

the Anomeric Conformation in the Intermolecular Interactions of Glucose, *J. Phys. Chem. Lett.*, 2017, **8**, 1147–1151.

[30] I. Usabiaga, A. Camiruaga, A. Insausti, P. Çarçabal, E. J. Cocinero, I. León and J. A. Fernández, Phenyl--D-glucopyranoside and Phenyl--D-galactopyranoside Dimers: Small Structural Differences but Very Different Interactions, *Front. Phys.*, 2018, **6**, 3.

[31] E. Caldeweyher, C. Bannwarth and S. Grimme, Extension of the D3 dispersion coefficient model, *J. Chem. Phys.*, 2017, **147**, 34112.

[32] S. Grimme, S. Ehrlich and L. Goerigk, Effect of the damping function in dispersion corrected density functional theory, *J. Comput. Chem.*, 2011, **32**, 1456–1465.

[33] I. Uriarte, A. Insausti, E. J. Cocinero, A. Jabri, I. Kleiner, H. Mouhib and I. Alkorta, Competing Dispersive Interactions: From Small Energy Differences to Large Structural Effects in Methyl Jasmonate and Zingerone, *J. Phys. Chem. Lett.*, 2018, **9**, 5906–5914.

[34] T. Forsting, H. C. Gottschalk, B. Hartwig, M. Mons and M. A. Suhm, Correcting the record: the dimers and trimers of trans-N-methylacetamide, *Phys. Chem. Chem. Phys.*, 2017, **19**, 10727–10737.

[35] B. Hartwig, M. Lange, A. Poblotzki, R. Medel, A. Zehnacker and M. A. Suhm, The reduced cohesion of homoconfigurational 1,2-diols, *Phys. Chem. Chem. Phys.*, 2020, **22**, 1122–1136.

[36] F. Kollipost, K. E. Otto and M. A. Suhm, A Symmetric Recognition Motif between Vicinal Diols: The Fourfold Grip in Ethylene Glycol Dimer, *Angew. Chemie*, 2016, **128**, 4667–4671.

[37] H. S. Yu, X. He and D. G. Truhlar, MN15-L: A New Local Exchange-Correlation Functional for Kohn–Sham Density Functional Theory with Broad Accuracy for Atoms, Molecules, and Solids, *J. Chem. Theory Comput.*, 2016, **12**, 1280–1293.

[38] S. F. Boys and F. Bernardi, The calculation of small molecular interactions by the differences of separate total energies. Some procedures with reduced errors, *Mol. Phys.*, 1970, **19**, 553–566.

[39] R. Campargue, Progress in overexpanded supersonic jets and skimmed molecular beams in free-jet zones of silence, *J. Phys. Chem.*, 1984, **88**, 4466–4474.

[40] R. E. Smalley, L. Wharton and D. H. Levy, Molecular optical spectroscopy with supersonic beams and jets, *Acc. Chem. Res.*, 1977, **10**, 139–145.

[41] D. Patterson and J. M. Doyle, Cooling molecules in a cell for FTMW spectroscopy, *Mol. Phys.*, 2012, **110**, 1757–1766.

[42] R. Srinivasan and B. Braren, Ultraviolet laser ablation of organic polymers, *Chem. Rev.*, 1989, **89**, 1303–1316.

[43] P. Çarçabal, E. J. Cocinero and J. P. Simons, Binding energies of micro-hydrated carbohydrates: measurements and interpretation, *Chem. Sci.*, 2013, **4**, 1830–1836.

[44] P. D. Godfrey and R. D. Brown, Proportions of Species Observed in Jet Spectroscopy–Vibrational Energy Effects: Histamine Tautomers and Conformers, *J. Am. Chem. Soc.*, 1998, **120**, 10724–10732.

[45] http://www.nist.gov/mml/csd/informatics_research.

[46] J. Contreras-García, E. R. Johnson, S. Keinan, R. Chaudret, J.-P. Piquemal, D. N. Beratan and W. Yang, NCIPLOT: A Program for Plotting Noncovalent Interaction Regions, *J. Chem. Theory Comput.*, 2011, **7**, 625–632.

[47] R. Chaudret, B. de Courcy, J. Contreras-García, E. Gloaguen, A. Zehnacker-Rentien, M. Mons and J.-P. Piquemal, Unraveling non-covalent interactions within flexible biomolecules: from electron density topology to gas phase spectroscopy, *Phys. Chem.*

Chem. Phys., 2014, **16**, 9876–9891.

[48] NIST Standard Reference Database, Computational Chemistry Comparison and Benchmark DataBase, https://cccbdb.nist.gov/vibscalejust.asp.

[49] I. Usabiaga, A. Camiruaga, C. Calabrese, A. Maris and J. A. Fernández, Exploring Caffeine–Phenol Interactions by the Inseparable Duet of Experimental and Theoretical Data, *Chem. - A Eur. J.*, 2019, **25**, 14230–14236.

Chapter 3

Aggregation of aromatic alcohols

Manuscript for publication in preparation

3.1. Introduction

One of the most relevant non-covalent interactions is the OH···O hydrogen bond, as the hydroxyl group is one of the fundamental and most frequently found chemical groups. Also, the OH···O hydrogen bond presents a relatively high strength, compared with similar interactions, such as NH···N or CH···O/N. Therefore, the characterization of this type of interactions is of paramount importance in order to understand the aggregation of complex biological systems (sugars, proteins, etc.). Here we characterize the aggregation process between aromatic alcohols, in which the OH···O interaction is one of the driving forces. Besides, the relative simplicity of the molecules allowed us to isolate the interaction and to better characterize its structural parameters, using the powerful combination of MRES in jets and quantum computations.

In this chapter, we present the characterization of the aggregation process of benzyl alcohol (BnzA) and 2-phenylethanol (PEAL). Both are aliphatic alcohols that incorporate an aromatic ring, and their study may be taken as the continuations of previous studies of alcohol aggregation in isolated phase.[1–5] Despite their simplicity, they present two key groups for non-covalent interaction: the terminal hydroxyl group, and the aromatic ring. On the one hand, one would expect these molecules to form relatively strong O-H···O hydrogen bonds, and even to form stable HB networks. Similar studies in the past demonstrated that these bond networks are responsible for the formation of unusually organized aggregates.[6,7] On the other hand, the electron density of the aromatic ring, is also an appealing interaction site, not only able to establish π-π stacking interactions, but also to form O-H···π interactions, which are usually taken as weaker than the OH···O but that have less demanding requirements regarding the angle of attack. The difference between both alcohols is the length of the spacer between the OH and the aromatic ring: a single CH_2 in BnzA and an CH_2CH_2 in the case of PEAL. Although small difference, a single carbon atom, it gives PEAL additional degrees of freedom and certain flexibility that results in a substantially more complex conformational landscape. As an additional difficulty, the stereoisomery of both molecules increases the number of possible combinations for a giving family of interactions. Our goal here is to characterize the stepwise aggregation of these aromatic alcohols, studying the OH/aromatic competition in the aggregates and the influence of the length of the alkyl chain in such process.

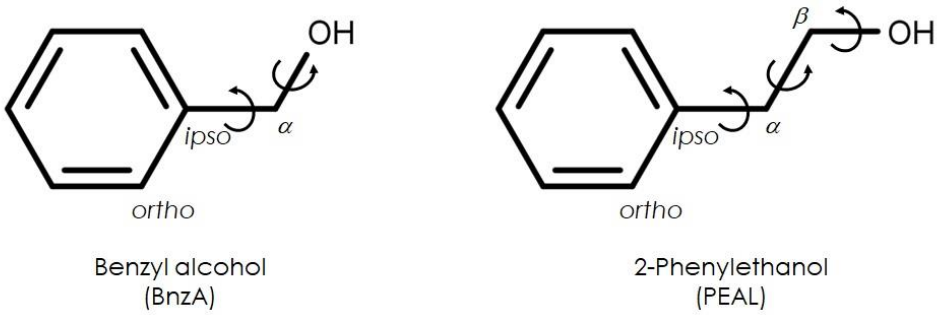

Figure 3.1: Scheme of benzyl alcohol and 2-phenylethanol, with the corresponding atom labelling.

3.2. Benzyl alcohol spectroscopy

The results presented in this section were obtained using the heating nozzle. A piece of absorbent paper moistened with some mL of benzyl alcohol (Sigma Aldrich, 98%) was placed in the sample compartment. To avoid condensation of the vapor and to maximize the sample evaporation, repository, gas line and pulsed valve were heated to 80°C. He was employed as a carrier gas, with a backing pressure of 1.5 bar.

3.2.1. Benzyl alcohol monomer

BnzA and its homodimer were previously studied using MRES by Bernstein et al.,[8] C.E.H. Dessent et al.[9] and M. Mons et al.[10] They concluded that the most stable arrangement for BnzA presents the hydroxyl group in gauche conformation (see Figure 3.2). The first step in the study was to reproduce those previous results to test the performance of our experimental system and to optimize the experimental conditions. The experimental data on the monomer were also used to test the DFT predictions.

BnzA has two dihedral angles: $C_{ortho}C_{ipso}C_{\alpha}O$ and $C_{ipso}C_{\alpha}OH$. Therefore, the conformations of BnzA are obtained by simple rotation of the $C_{ipso}C_{\alpha}$ and $C_{\alpha}O$ bonds. The calculations show only two stable conformations. In the global minimum, the -CH_2OH group presents a *gauche* arrangement (see BnzA_01 structure in Figure 3.2). Depending on the angle adopted with respect to the ring, this conformation has a mirror image. The extra stability of this conformation comes from the formation of a weak $C_{ortho}H\cdots O$ interaction.

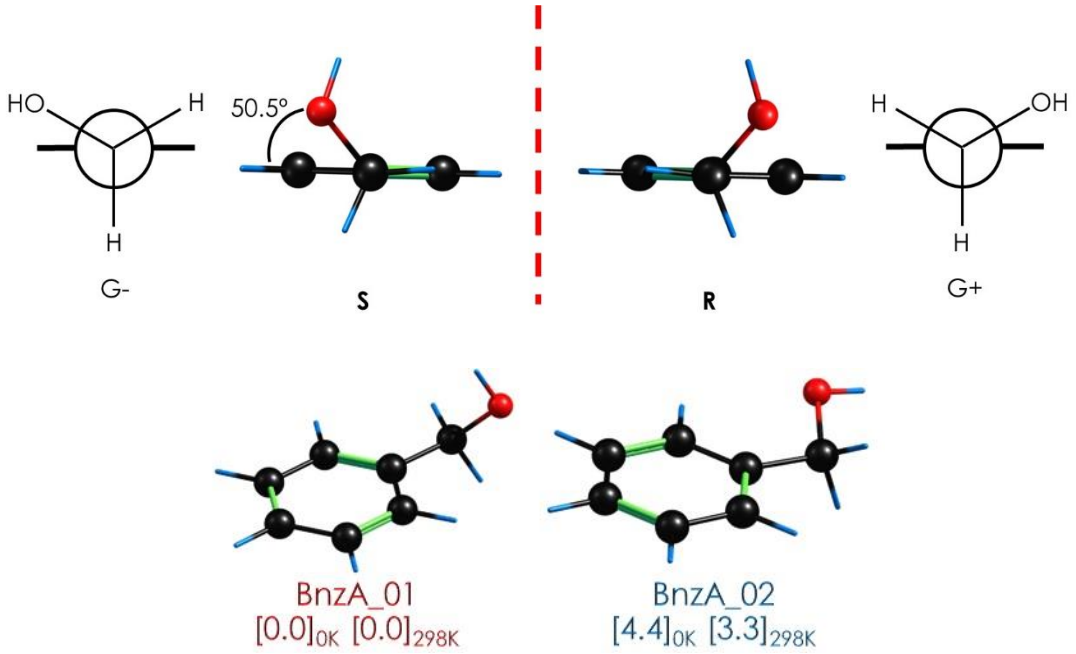

Figure 3.2: Most stable conformers of benzyl alcohol. Energy values in kJ/mol, computed at B3LYP(ED=GD3BJ)/6-311++G(d,p) level.

In *trans* conformation, the hydroxyl group is pointing away from the aromatic ring, in what is also known as extended conformation.

Exploration of the electronic spectroscopy of BnzA resulted in the spectra in Figure 3.3. The two-color REMPI spectrum of BnzA monomer presents the origin band (0_0^0) at 37528 cm^{-1}, in good agreement with previous studies.[8–10] It is accompanied by a clear progression of vibronic bands. The weaker features to the red of the origin band correspond to hot bands coming from non-relaxed vibrational modes and fragmentation from larger clusters.[10] The intensity of these hot bands increases with an 1+1 ionization process, or in warmer jet conditions.

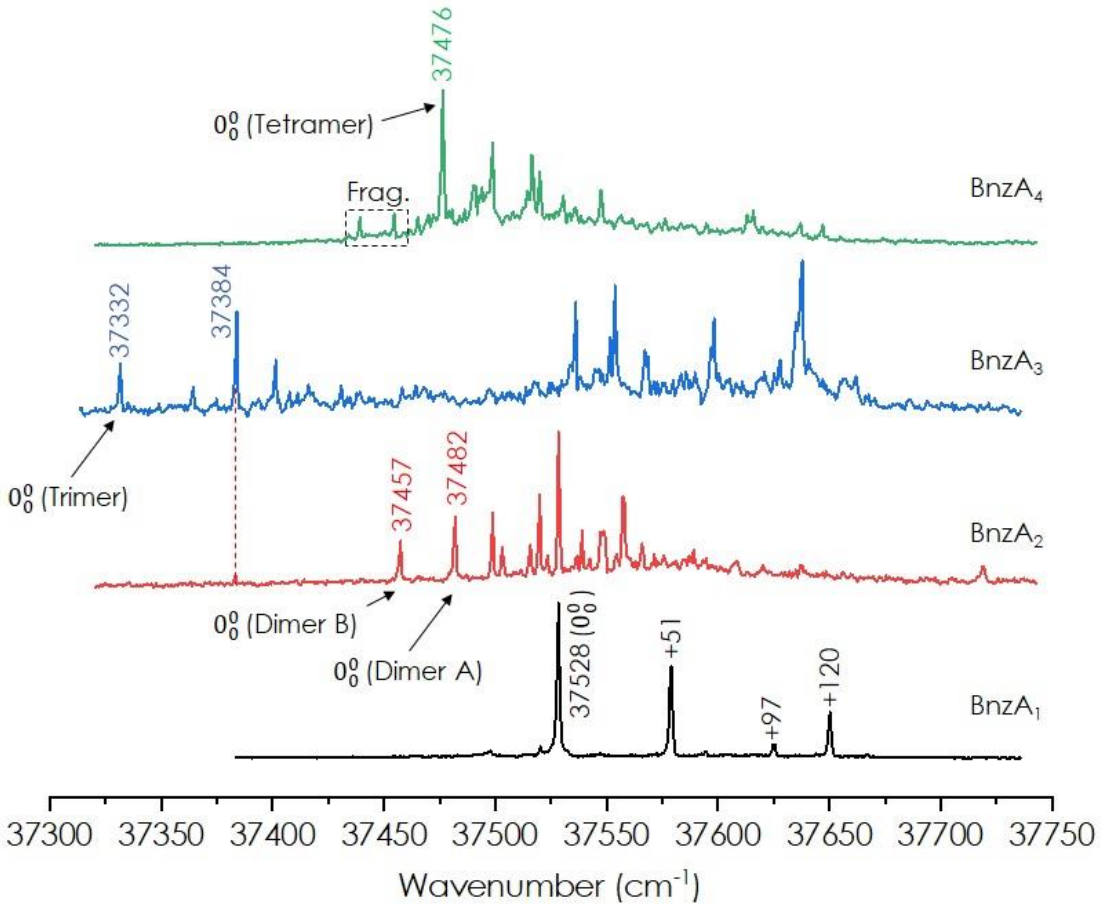

Figure 3.3: Two-color REMPI spectra of BnzA and its aggregates up to the tetramer, between 37300 and 37750 cm^{-1}. The ionization laser was tuned at 35714 cm^{-1}.

After recording the electronic spectrum, IR/UV double resonance was employed probing the origin band (37528 cm^{-1}) to record the mass-resolved IR spectrum. With this experimental data, it was possible to confirm the nature of the detected species, to calibrate the computational methods and to compare with those spectra from the aggregates. The shift in the OH transitions after formation of an intermolecular interaction is directly related to the strength of the interaction.

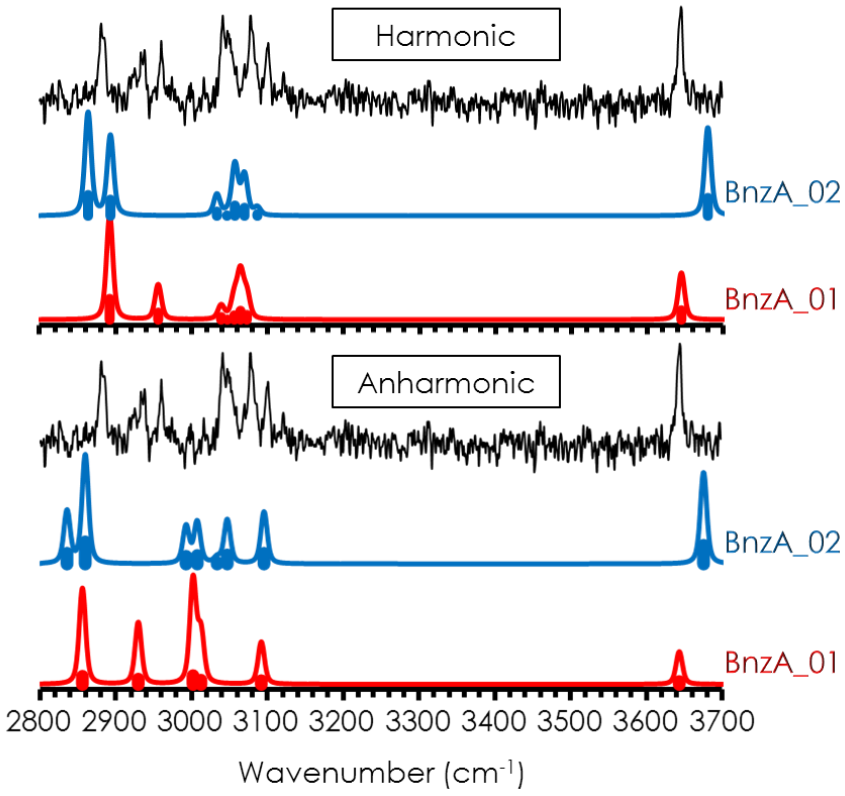

Figure 3.4: IDIR spectrum of benzyl alcohol compared to the harmonic and anharmonic frequency predictions. Spectra simulations were calculated at B3LYP(ED=GD3BJ)/6-311++G(d,p) level. For the harmonic approximation, a scaling factor of 0.954 was used for both OH and CH groups. No scaling factors were needed for the anharmonic frequency calculations.

As we can observe in Figure 3.4, CH and OH stretching regions of the spectrum were covered. A single band arises at 3645 cm^{-1} in the OH region. There is an excellent agreement between the experimental and the simulated IR spectrum for the BnzA_01 conformation. Thus, the band appearing at 3645 cm^{-1} is assigned to the stretch of the OH bond. This means a red shift of 25 cm^{-1} from the OH stretch of ethanol, which appears at 3670 cm^{-1},[11] also in good agreement with previous studies.[10] The shift in the OH stretch may be due to the mild CH···O interaction or to a hyperconjugation of the CO bond with the π aromatic cloud.

The small size of the molecule, allowed us to compute the anharmonic frequencies, using the algorithms implemented in Gaussian 16.[12,13] While the CH region is still not well reproduced in the simulation, the anharmonic frequency calculation of the OH band matches perfectly well the position of the OH stretch in the experimental spectrum. It is worth mentioning that the difference between the predicted OH···π and free OH bands is the same as the one in scaled harmonic simulation.

3.2.2. Benzyl alcohol dimer

Once the conformation of isolated BnzA was identified under our experimental conditions, and before analyzing the dimer, the chirality of the monomer must be taken into account. As already shown in Figure 3.2., depending on the angle of the CH_2OH, two mirror conformations arise (named G- and G+). These enantiomers are spectroscopically identical, but upon the formation of the dimer, this transient chirality will form homo- or hetero-chiral aggregates, which are no longer identical from a spectroscopic point of view. There are four possible combinations of *gauche*-BnzA: G-G+, G+G-, G+G+ and G-G-, which can be grouped in pairs of mirror images, as homo- and hetero-chiral dimers and which are diastereoisomers that can be spectroscopically identified (Figure 3.5).

The potential energy surface (PES) of the BnzA dimer was explored at the B3LYP/6-311++G(d,p) level and the optimized structures were classified depending on their interaction type. Figure 3.6 collects the most stable structure of each family. Special attention was put to the heterochiral aggregation of the first family (red box). True enantiomers (CH_2OH group angle and ring inversion) were not taken into account, as they are equivalent. The G-G+ structure (BnzA2_dias1) seemed to be unstable and its optimization ended in the most stable structure.

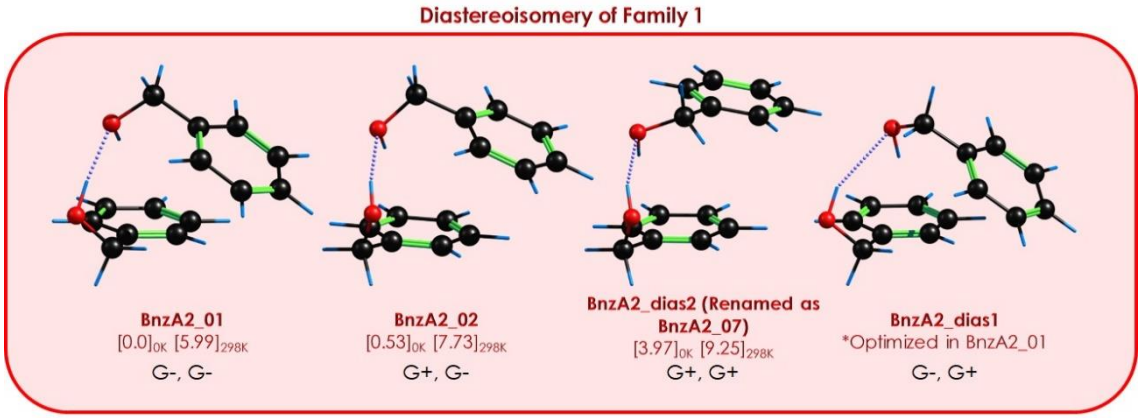

Figure 3.5: Diastereoisomeric structures for the $BnzA_2$ most stable family, computed at B3LYP(ED=GD3BJ)/6-311++G(d,p) level. Energy values are given in kJ/mol.

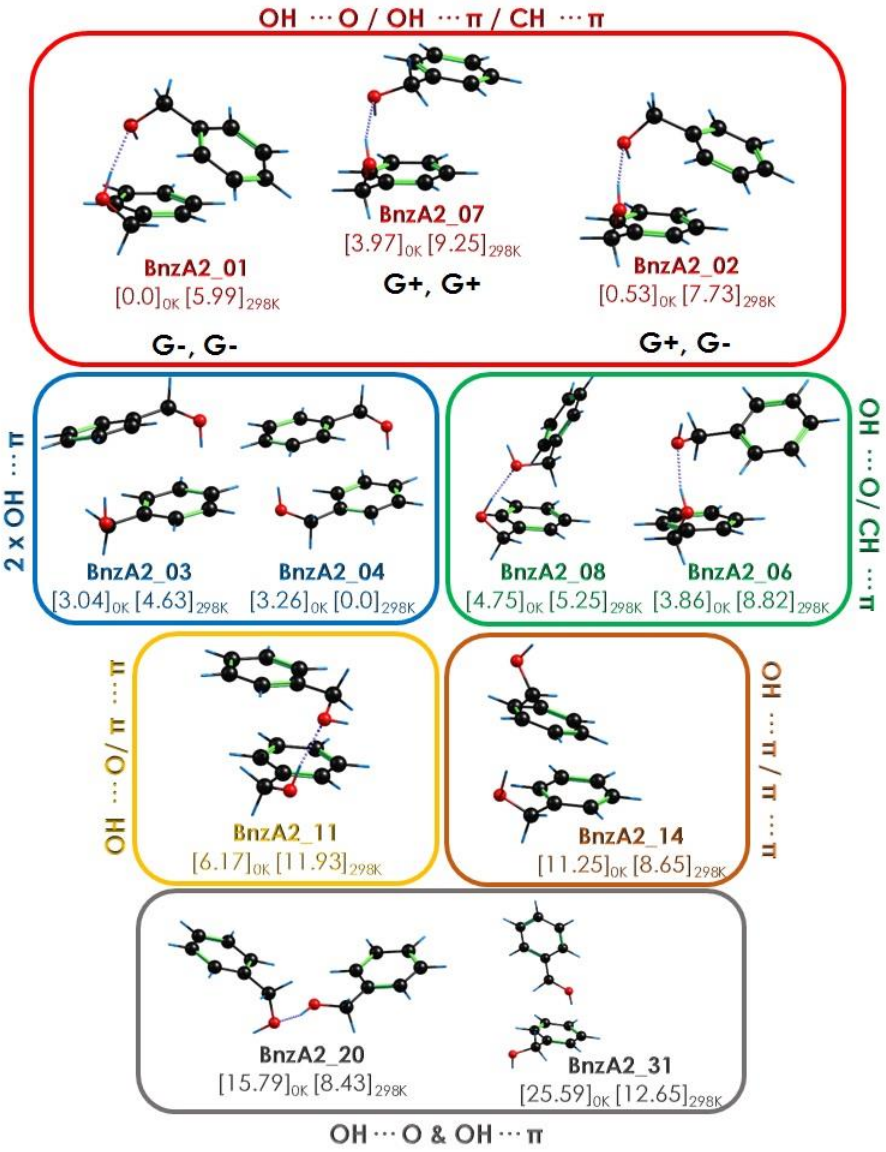

Figure 3.6: Representative structures of the families found for benzyl alcohol dimer. Structures and families are classified according to their interactions. All structures were optimized at B3YLP(ED=GD3BJ)/6-311++G(d,p) level. Energy values are given in kJ/mol.

As can be observed, the leading interaction is the O-H···O hydrogen bond, accompanied by an O-H···π interaction of the second hydroxyl group with the ring and a secondary C(sp^2)-H···π interaction between the rings. Perhaps due to the higher tolerance of the O-H···π towards the angle of the attack of the donor molecule, or to a strength not far away from that of the O-H···O, the isomers formed by two O-H···π interactions are not very high in energy, compared to the global minimum. Structures BnzA2_06 and BnzA2_08 are interesting due to their relevance during the cluster's growth (see section 3.2.3

below), where the OH···π interaction was replaced by a π···π interaction, in such a way that the OH···O HB is maximized.

Figure 3.7 presents the two-color REMPI spectrum of BnzA dimer. Compared to the monomer's absorption, it presents a larger abundance of vibronic transitions. Such a rich collection of bands may arise from the isolation of more than one stable conformers in the supersonic jet, or from fragmentation from larger species. To determine the number of isomers/species contributing to the spectrum, UV/UV hole burning was employed. As a result, two different REMPI spectra (red and blue traces) were obtained by proving at 37528 and 37457 cm^{-1}, marked as blue and red asterisks in the spectrum. The transitions at 37457 and 37482 cm^{-1} were taken as the origin bands of isomers 1 and 2, respectively. These origin bands are shifted to the red (-71 cm^{-1} for Isomer 1 and -46 cm^{-1} for Isomer 2) in comparison with the monomer's origin band (37528 cm^{-1}). This seems to indicates the existence of an interaction with the aromatic ring due to dispersive forces. The most red-shifted band, located at 37383 cm^{-1} corresponds to the fragmentation of the trimer, as can be appreciated in the comparison of all REMPI spectra of BnzA aggregates (see Figure 3.3)

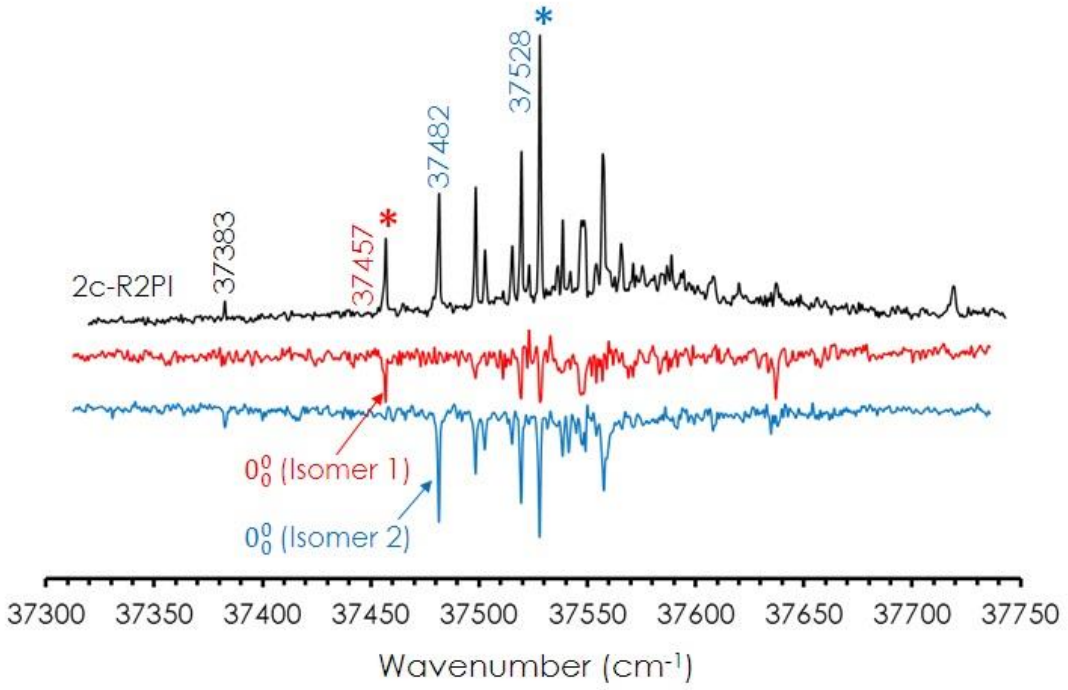

Figure 3.7: Two-color REMPI spectrum of the benzyl alcohol dimer, along with the isomer specific REMPI spectra obtained in UV/UV Hole Burning experiments. Ionization laser was set at 35714 cm^{-1}. Transitions at 37457 and 37528 cm^{-1} where probed in UV/UV hole burning experiments, obtaining red and blue traces, respectively.

In order to extract the maximum structural information, the IDIR spectrum of the two isolated dimers was recorded in the OH and CH stretching regions. The IR spectra obtained by fixing the UV laser at 37457 cm^{-1} (red asterisk) and at 37528 cm^{-1} (blue asterisk) are collected in Figure 3.8. Besides, the rest of the transitions were also probed, resulting in the same traces presented below.

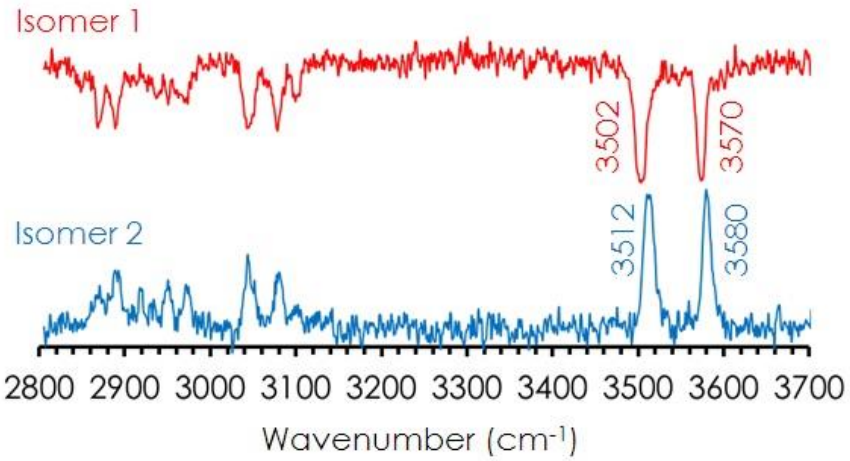

Figure 3.8: IDIR spectra of benzyl alcohol dimers. The blue spectrum was flipped to help the comparison between the position of the bands.

In these spectra, two bands appear in the OH region and some well-resolved CH bands are also observable. A closer look at longer wavelengths shows a little but noticeable shift in the position of the bands between the two IR spectra: the two OH bands of the red trace are shifted by 10 cm^{-1}.

Before any comparison with the theoretical data, experimental data can be used to speculate about the structure of the dimer. Two OH bands are clearly visible in the spectrum of isomer 1. Presumably, the one at ~3580 cm^{-1} presents weaker interactions than the one at ~3512 cm^{-1}, because the shift of the OH band depends on the strength of the interaction in which the hydroxyl group is involved. Therefore, it can be assumed that the band shifted more to the red, at ~3512 cm^{-1} is forming an OH···O bond type, whereas the band appearing at ~3580 cm^{-1} may correspond to a weaker OH···π interaction.

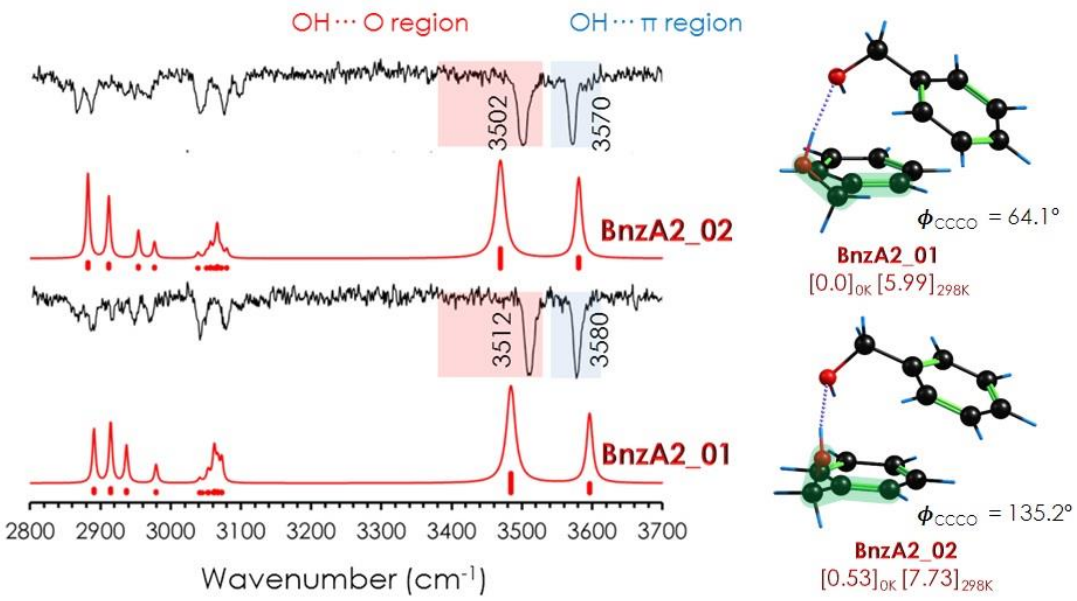

Figure 3.9: IDIR spectra of $BnzA_2$ compared to the simulations of the most stable structures. Frequency calculation was done at B3LYP(ED=GD3BJ)/6-311++G(d,p) level, and a scaling factor of 0.954 was used to correct anharmonicity of both OH and CH groups.

Figure 3.9 shows a comparison between the simulated spectra of the most stable structures of the dimer with the two experimental IR. The spectra predicted for BnzA2_01 and BnzA2_02 reproduce very well the experimental bands in the OH stretching region. Note that the previously mentioned shift in the OH bands of the two isolated isomers is also well reproduced by the theory. Observing the assigned structures, the difference between BnzA2_01 and BnzA2_02 is the orientation of the donor CH_2OH group, which also results in the interaction with a different lone pair of the acceptor oxygen atom. Thus, the small structural differences between the diastereoisomers (G-G-→BnzA2_01 and G+G-→BnzA2_02) introduce a subtle perturbation in the OH stretching frequencies that is detected in the experiment and captured by the calculations.

To further test the assignment, we computed the IR spectrum of the two structures assigned at two additional computational levels: B3LYP/def2tzvp and M06-2x/6-311++G(d,p) (see Figure 3.10). Interestingly, the computation using the Minnesota functional seems to better reproduce the bands position, although they lead to the same assignment.

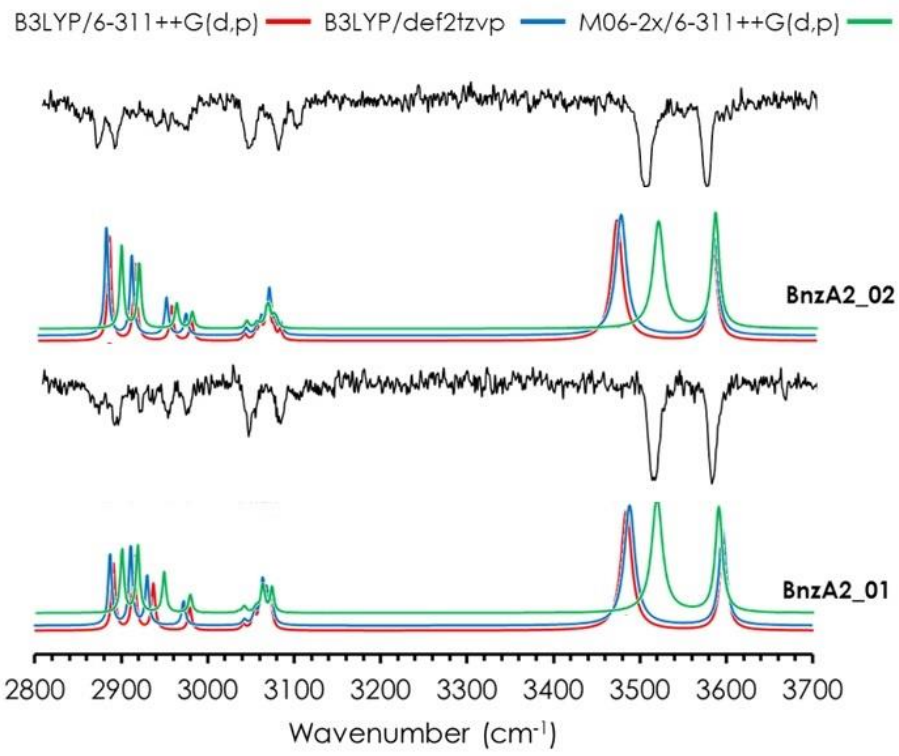

Figure 3.10: Comparison between the experimental IDIR spectra of the two isomers for $BnzA_2$ and the simulation for the most stable structures at different computational levels. OH scaling factor was set to 0.954 for B3LYP/6-311++G(d,p), 0.962 for B3LYP/def2TZVP and 0.937 for M06-2X/6-311++G(d,p). CH scaling factor was maintained at 0.962 for all computational levels.

The energetics of the most stable structures of each family was also analyzed at the computational levels used for the simulation. Despite the Minnesota functional reproduced better the experimental spectra, it did not identify BnzA2_01 and BnzA2_02 structures as the most stable ones. Instead, BnzA2_03 and BnzA2_04 (blue family) were predicted to be the two most stable structures at M06-2x.

Relative Binding Gibbs free energy diagrams were also built for this dimer at each computational level, in order to explore the temperature effect in the stability of the families. B3LYP methods described red family as the most stable at lower temperatures, but as it increases, stacked dimers seemed to be favored (see Figure A3.3). Interestingly, M06-2x level predicted the opposite trend with the red family being the most stable at high temperatures.

Comparisons with recent results reported by Medel and Suhm,[14] shows a general agreement: both works report the same species as the most stable ones and were detected experimentally. However, the authors also reported the presence of the

heterochiral dimer formed by double OH···π interactions (structure BnzA2_04). The absence of the third isomer in our spectra may be due to a reduced population under the conditions of our expansion. Therefore, REMPI spectrum of BnzA dimer was recorded using different buffer gases (see Figure 3.11), in an attempt to detect additional species.

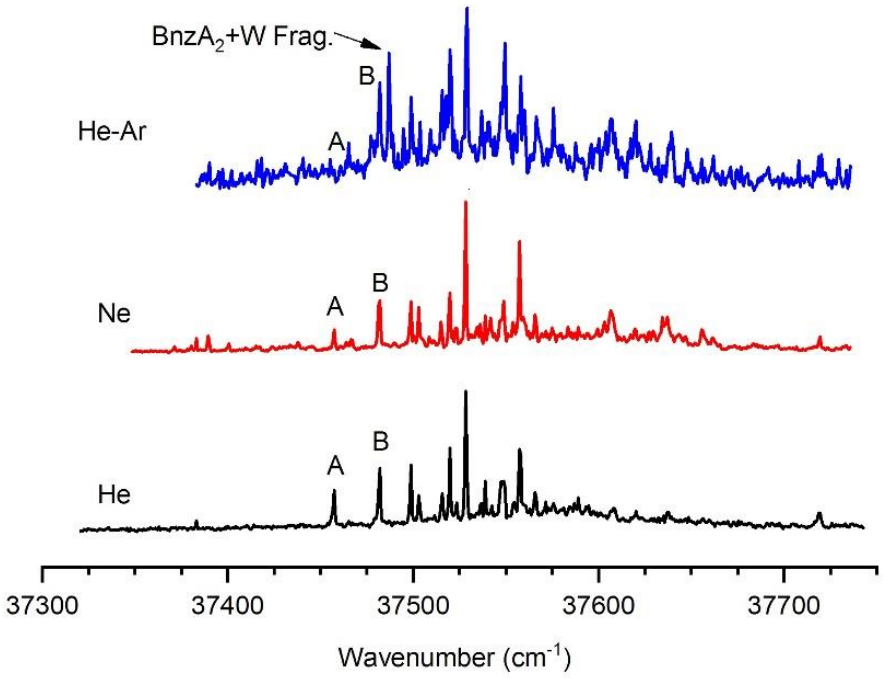

Figure 3.11: Comparison between REMPI spectrum of BnzA dimer recorded using He, Ne or 10% Ar/He as carrier gases.

A and B notations in Figure 3.11 correspond to the already assigned BnzA2_02 and BnzA2_01 structures, respectively. Replacing He by Ne improves cooling and may enable trapping population of less stable isomers. Using 10% Ar/He instead, a better cooling is achieved, but also the more energetic collisions with Ar are sometimes able to transfer population from local minima to more stable isomers.[15,16] In the present system, replacing He by Ne strongly favored formation of large clusters. The m/z peaks up to the nonamer were clearly visible in the mass spectrum. However, the spectrum of the dimer did not show relevant differences. There was a variation in the relative intensity of some secondary bands, which were due to fragmentation from the trimer or from the BnzA:water 2:1 cluster. Apparently, improving the cooling did not permit trapping new isomers. A slight reduction in the relative intensity of the 0-0 transition of the less stable isomer was observed, pointing to a lower final isomeric temperature in the beam.

The main impact caused by the use of the Ar/He mixture as buffer gas was the increase in fragmentation from BnzA:water clusters. Careful probe of all the bands in the spectrum showed that no new isomers were trapped. There was a noticeable reduction in the intensity of the 0-0 transition of the less stable isomer, which is now hardly visible over the background created by fragmentation.

Concluding with the dimer, its formation is primarily driven by an O-H···O-H···π cooperative hydrogen bond network, leaving the cluster in a semi-stacking position.

3.2.3. Benzyl alcohol trimer

Cluster growth usually follows an additive process, accumulating molecules sequentially over the previous structure, which acts as a kernel, although certain re-organization of the molecules may take place. Consequently, the natural growth of BnzA is expected to proceed preferentially by adding the new molecule to the structure of the most stable isomers of the dimer. In the present case, such extension can yield an OH···OH···OH···π linear hydrogen bond network or a cyclic hydrogen bond network. Most of the systems reported in the literature, have a general tendency towards the second possibility.[17–19]

The computations showed a rich conformational landscape for BnzA trimer, with a large number of structures grouped into two main families in the 20 kJ/mol energy window. Thorough exploration of the PES is beyond the scope of this work, and therefore, we limited the analysis to the families in Figure 3.12 and in Figure A3.4 of the appendix.

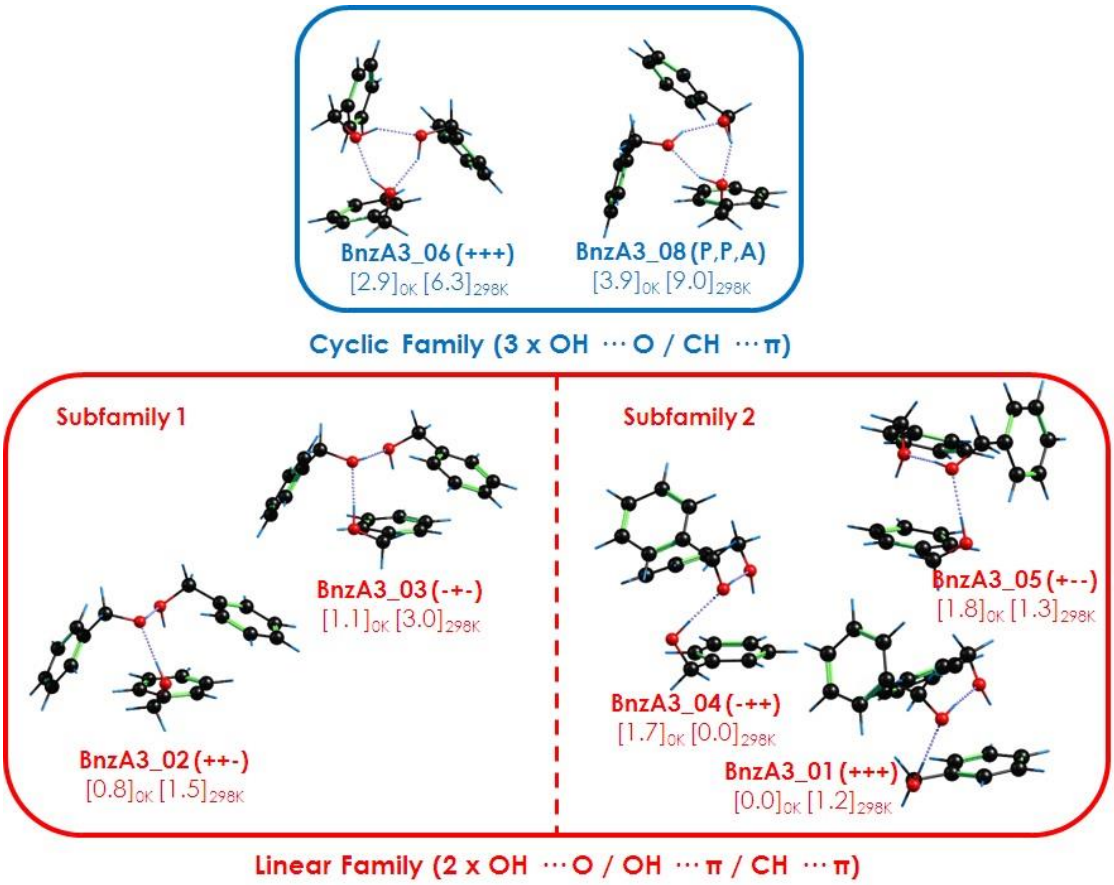

Figure 3.12: Most stable families of $BnzA_3$ computed at B3LYP(ED=GD3BJ)/6-311++G(d,p) level. Relative energy values below each structure are given in kJ/mol. Each structure name is followed by the dihedral angle disposition of the G conformation of each BnzA molecule. The dihedral angle analysis was done following the sequence of the HB network, so the first sign corresponds to the proton donor. In the case of BnzA3_08, P and A correspond to "planar" and "anti" conformations, respectively.

The main difference between the most stable families (red and blue) is the orientation of the aromatic rings: on opposite sides of the aggregate in subfamily 1 and adopting a more compact arrangement in subfamily 2. Nevertheless, such difference is due to the conformation adopted by the monomers and in the end, all the members of the family present an OH···OH···OH···π hydrogen bond network, following the same trend as in $BnzA_2$. Interestingly, the most stable structure is an G+G+G+ homochiral aggregate.

Regarding the blue family, which is also close in relative energy, presents a cyclic HB network. It is worthy to note the high symmetry of BnzA3_06, which presents a C3 symmetry axis, with all the monomers in G+ conformation. Therefore, this structure is also homochiral, as in the case of the global minimum.

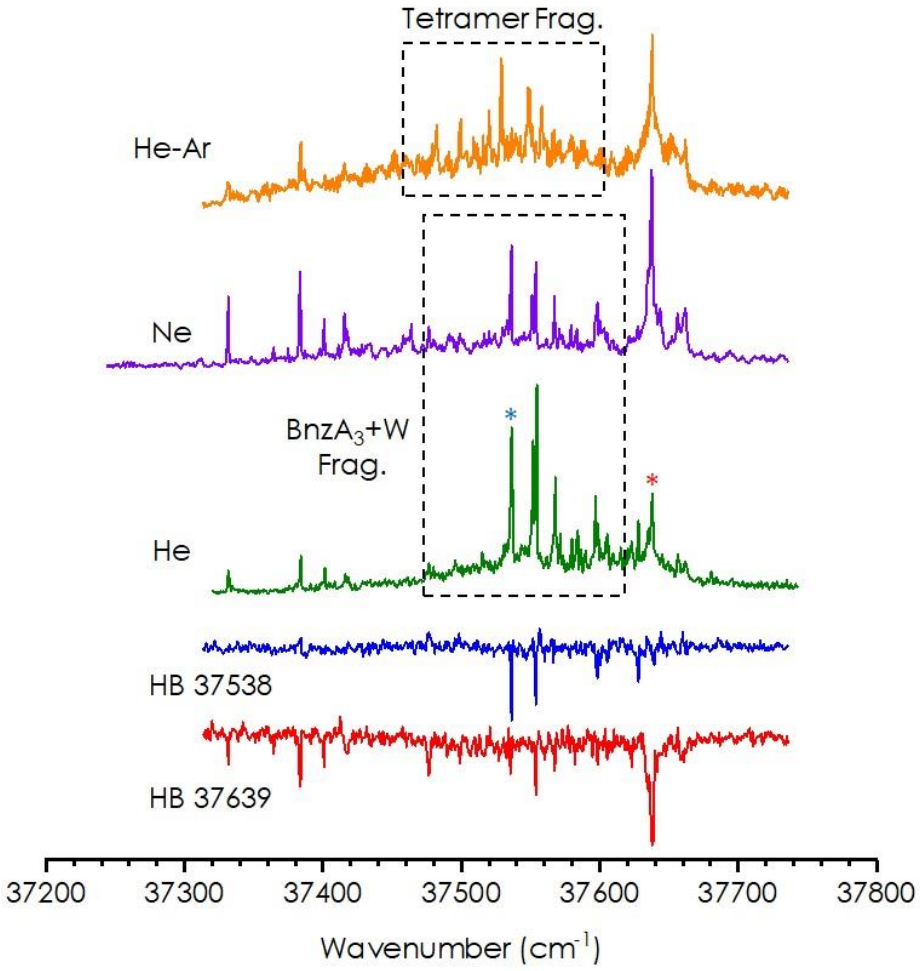

Figure 3.13: Two-color REMPI spectrum of benzyl alcohol trimer, along with the UV/UV Hole Burning spectra obtained probing the transitions at 37538 and 37639 cm^{-1} (blue and red asterisks respectively). The ionization laser was set to 35714 cm^{-1} for all the spectra.

Figure 3.13 collects the two-color REMPI spectrum of $BnzA_3$ with different carrier gases. The spectra are complex and gain intensity as they progress to the blue. Depending on the conditions of the expansion, formation of larger aggregates and/or clusters with water was maximized. However, even in the most favorable conditions fragmentation from BnzA:water 3:1 could not be avoided.

UV/UV hole burning experiments were done probing the bands at 37538 and 37639 cm^{-1}, marked with asterisks in Figure 3.13. The trace recorded tuning the UV laser at 37538 cm^{-1} shows the bands coming from the 3:1 cluster with water, while the UV spectrum recorded tuning the probe laser at 37639 cm^{-1} contains the bands due to the BnzA trimer. The position of the origin band of this isomer, which presents a red shift of 125 cm^{-1} with respect to the dimer, indicates that it presents a linear hydrogen bond network

as the one predicted for the global minimum. Exploration of the REMPI spectrum in search for other isomers with the 0-0 transition shifted to the blue gave negative results, indicating that cyclic isomers of the trimer were not formed.

Interestingly, probing the transitions at 37332 and 37384 cm^{-1}, two different IDIR spectra were obtained, which means that both isomers share transitions in the UV spectrum and therefore, their respective contributions cannot be separated using the UV/UV-double resonance technique.

Figure 3.14 shows a comparison between the experimental spectra probing 37325 (A) and 37378 cm^{-1} (B) and the spectra simulated for the most stable structures. The number of OH bands inside each spectrum is not consistent with the prediction of a single isomer. Thus, one can expect that more than one isomer is contributing to the spectra shown in Figure 3.14.

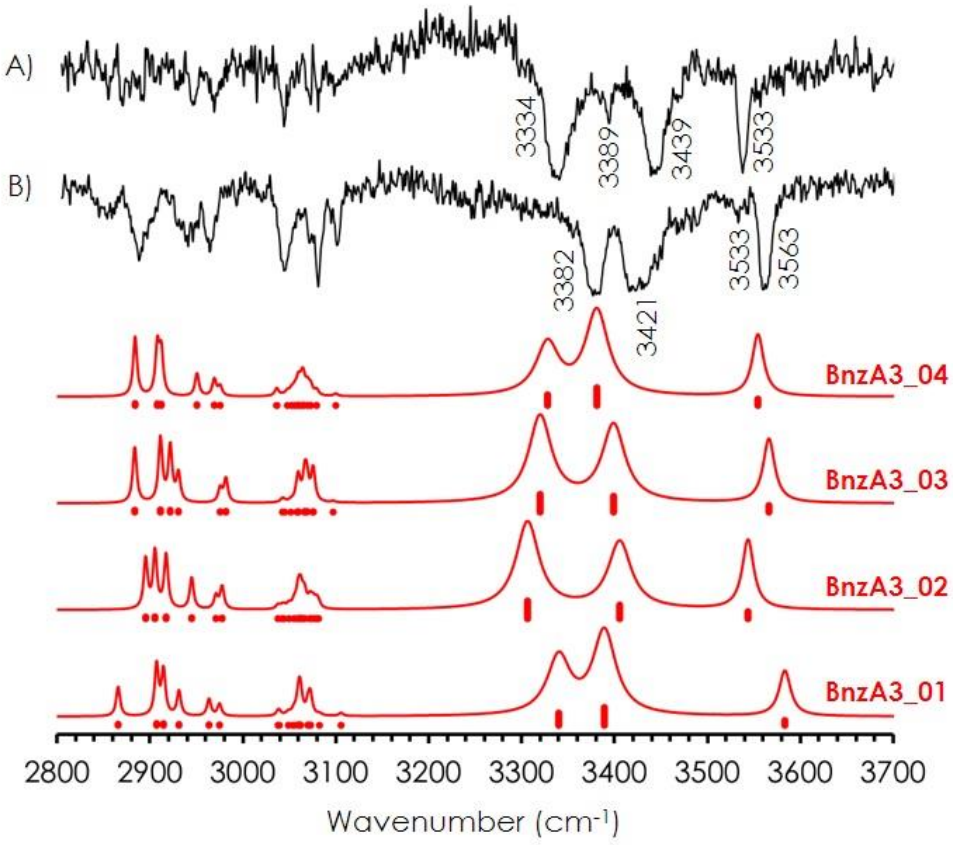

Figure 3.14: Comparison between the IDIR spectra of $BnzA_3$ and the simulations from the most stable structures of its linear family. Frequency calculation was done at B3LYP(ED=GD3BJ)/6-311++G(d,p) level, and a scaling factor of 0.954 was used to correct anharmonicity of both OH and CH groups. (A) and (B) traces were obtained by probing 37332 and 37384 cm^{-1} wavelengths, respectively.

The separation of the OH stretching bands in Figure 3.14 point to a different environment for each OH group. In good agreement, the isomers that can reproduce such behavior are those from Family 2 (see Figure 3.12) in which a linear HB chain ending in an OH···π interaction is formed. These structures lay very close in energy (less than 2 kJ/mol), so they can coexist in the jet. Structure BnzA3_01 is assigned to the lower trace, whereas BnzA3_02 and BnzA3_03 structures can be tentatively assigned to the upper trace. The difference between these two assignments lay in the arrangement of the aromatic rings due to heterochiral aggregation.

Probing all the transitions in the UV spectrum of Isomer 2 always resulted in the spectrum showed in Figure 3.15, in which, all the OH stretching modes are grouped together, indicating that all the OH groups are involved in hydrogen bonds of similar strength. Such observation is compatible with the isomers forming cyclic HB networks. However, there is an additional bands around 3700 cm^{-1}, a spectral region that typically corresponds to water free OH stretches. This indicates that the observed spectrum corresponds to fragmentation from a water cluster. Moreover, probing all the transitions in the REMPI spectrum of Isomer 2 (Figure 3.13) always resulted in the same IR trace. Thus, one can conclude that no isomers with cyclic hydrogen bond networks were detected.

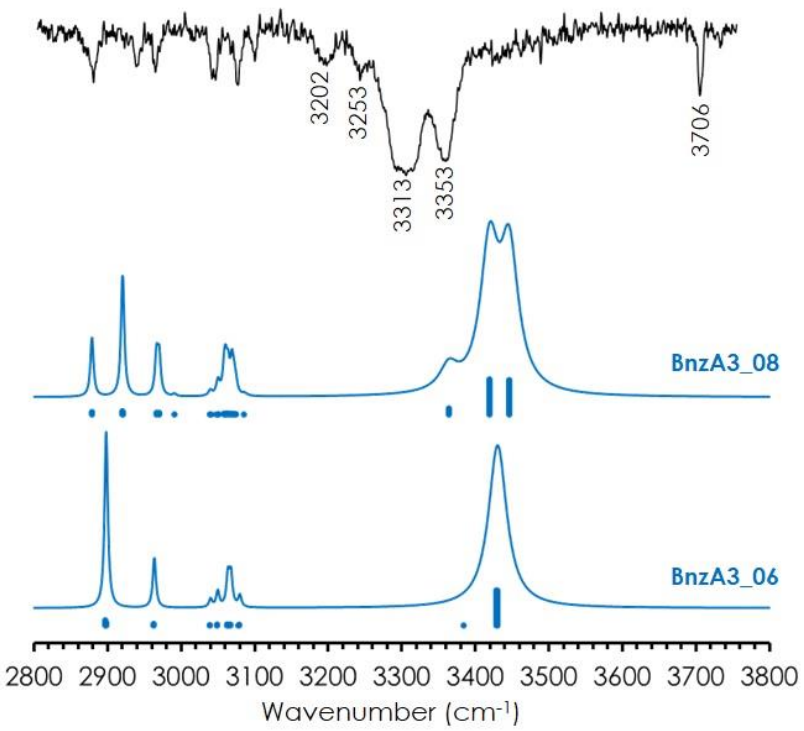

Figure 3.15: Comparison between the IDIR spectrum of $BnzA_3$ + W_1 and the simulations from the most stable structures of cyclic family of BnzA trimer. Frequency calculation was done at B3LYP(ED=GD3BJ)/6-

311++G(d,p) level, and a scaling factor of 0.954 was used to correct anharmonicity of both OH and CH groups. Spectrum was obtained by probing at 37536 cm^{-1}.

As performed in the dimer, a selection of the most representative structures from the trimer's PES was computed at B3LYP/def2tzvp and M06-2x/6-311++G(d,p) levels, to further test and confirm the experimental assignment. An energy diagram comparing the energy values from the three different computational levels can be found in the appendix (see Figures A3.6 and A3.7), along with the simulated spectra. In general terms, the assignment is well reproduced both at B3LYP/def2tzvp and M06-2x/6-311++G(d,p) computational levels.

3.2.4. Benzyl alcohol tetramer

Exploration of the tetramer is substantially more difficult due to the natural reduction in signal intensity that accompanies cluster growth and to the narrow set of experimental conditions that maximized its detection, reducing at the same time fragmentation from larger clusters. All those facts precluded also recording the UV/UV hole burning spectrum.

Figure 3.16 shows the REMPI spectrum of the tetramer. The spectrum covers a narrow region in which several transitions appear, built over a broad background. The 0-0 transition (37476 cm^{-1}) is shifted to the blue from that of the trimer, anticipating the formation of a cyclic HB networks. Weak transitions at the red of the origin band came from the fragmentation of larger clusters.

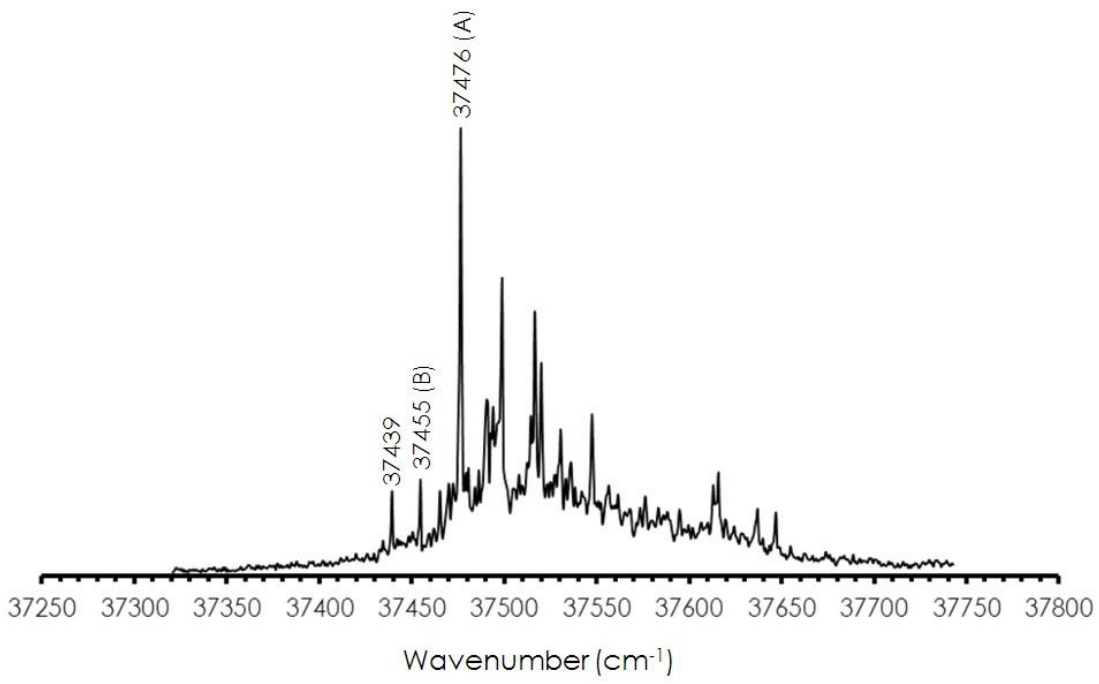

Figure 3.16: Two-color REMPI spectrum of benzyl alcohol tetramer. The ionization laser was set at 35714 cm^{-1}.

Without hole burning information, the only way to detect more than one conformer in the spectrum is by proving all the possible transitions using IDIRS. Probing the band at 37476 cm^{-1} the IR spectrum in Figure 3.17 was obtained. Using the rest of the transitions to the blue of this band also resulted in the same spectrum. It shows a central strong band at 3313 cm^{-1} containing the contribution from several OH stretches. That band is flanked by a shoulder at 3353 cm^{-1} and a satellite band at 3253 cm^{-1}. Further to the red, the CH stretches appear. This spectrum clearly is the signature of the formation of a cyclic hydrogen bond network, as all the OH stretches are grouped together, indicating that they are immersed in a similar environment.

Because of the high number of possible combinations of the monomers and spatial arrangements of four benzyl alcohol molecules, the tetramer presents a complex conformational landscape. After optimization of the most relevant structures found in the conformational search, only cyclic and linear families that contain at least three OH···O bonds were identified. Furthermore, the cyclic family seems to be the most stable one.

Within all the cyclic structures found in a wide energy window, BnzA4_01 (see Figure 3.17) is by far the most stable conformation. It is the homo-aggregation of all four BnzA molecules in *gauche* conformation. Furthermore, the aggregate presents a C_2 symmetry

axis, thanks to the HB network and the well-organized CH···π interactions between the aromatic rings. The rest of the structures contain at least one monomer in *anti* conformation, and therefore do not present any symmetry element. It is interesting how homo-aggregation of BnzA is by far the most stable species, as in the case of the trimer and the dimer.

Regarding the assignment of the experimental IR spectrum, Figure 3.17 shows a comparison between the predicted spectra for some selected structures and the experimental trace. As it can be seen, all the isomers present a maximum absorption in the correct position, with the most important difference between them being the symmetry of the band's contour. The experimental trace is clearly non-symmetric, although it could be due to contribution from several species. Frequency predictions for BnzA4_01 structure are in good agreement with the observed experimental bands position, which corresponds to a hydrogen bond network with similar bond strength However, the simulation for some of the species, such as Isomer 02 or 03, faithfully reproduces the experimental spectrum, indicating that the spectrum could contain contribution from several species.

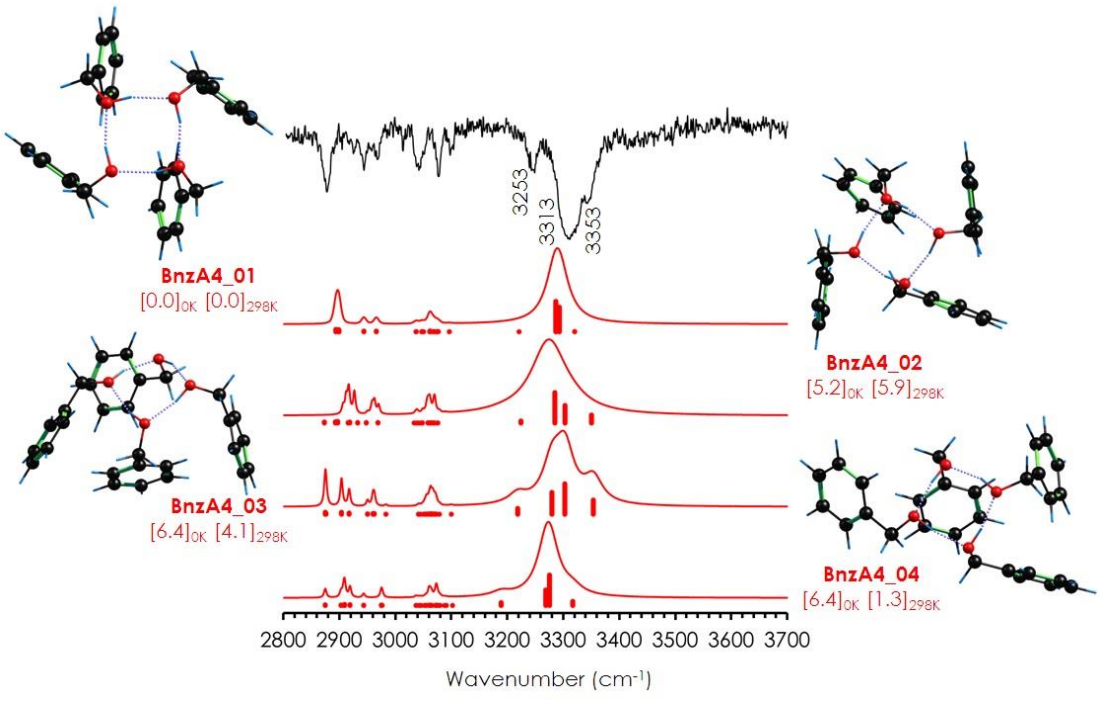

Figure 3.17: Comparison between the IDIR spectra of $BnzA_4$ with the simulated spectra of the most stable structures. Frequency calculation was done at B3LYP(ED=GD3BJ)/6-311++G(d,p) level, and a scaling factor of 0.954 was used to correct anharmonicity of both OH and CH groups. Spectrum obtained by probing at 37469 cm^{-1} (A). Energy values are given in kJ/mol.

Returning to the spectrum in Figure 3.16, probing the band labelled as B, a different IR spectrum was obtained (see Figure 3.18). It contains a saturated absorption similar to the spectrum in Figure 3.17, but red-shifted and with a band at 3700 cm^{-1}. This latter absorption indicates that the spectrum corresponds to fragmentation from the 4:1.[20] The broad nature of the spectrum precludes a detailed analysis of the cluster, but allowed us to anticipate the formation of a cyclic hydrogen bond network that also incorporates the water molecule, in the same way as already observed for propofol/water clusters.[21]

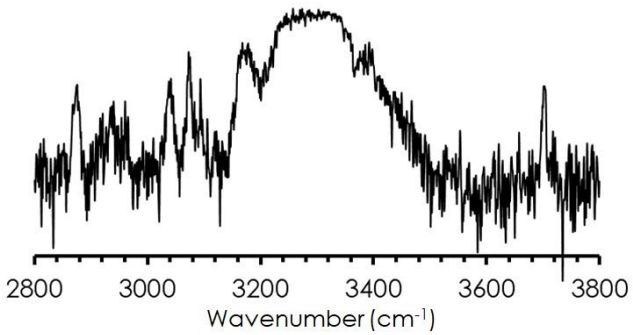

Figure 3.18: IDIR spectra of $BnzA_4$ obtained when probing at 37455 cm^{-1} (B).

3.3. 2-Phenylethanol spectroscopy

The same experimental setup employed for BnzA was used to characterize 2-phenylethanol (PEAL). A paper moistened with PEAL was kindly heated to 80ºC in the reservoir, and mixed with 1.5 bar of He to generate the expansion.

3.3.1. 2-Phenylethanol monomer

Compared to BnzA, the extra methyl group of PEAL gives the molecule an additional degree of freedom (see Figure 3.1). Thus, in addition to the orientation of the hydroxyl group, it was also necessary to explore the values that the $C_{ortho}C_{ipso}C_{\alpha}C_{\beta}$ and $C_{ipso}C_{\alpha}C_{\beta}O$ dihedral angles may adopt. The final optimization showed five stable conformations (see Figure 3.19a). Both *gauche*- and *anti* conformations are stable, with the Gg conformation being the global minimum. In this conformation, the OH group is pointing towards the aromatic ring. As revealed by the NCI plot analysis (Figure 3.19b), a weak OH···π interaction exists.

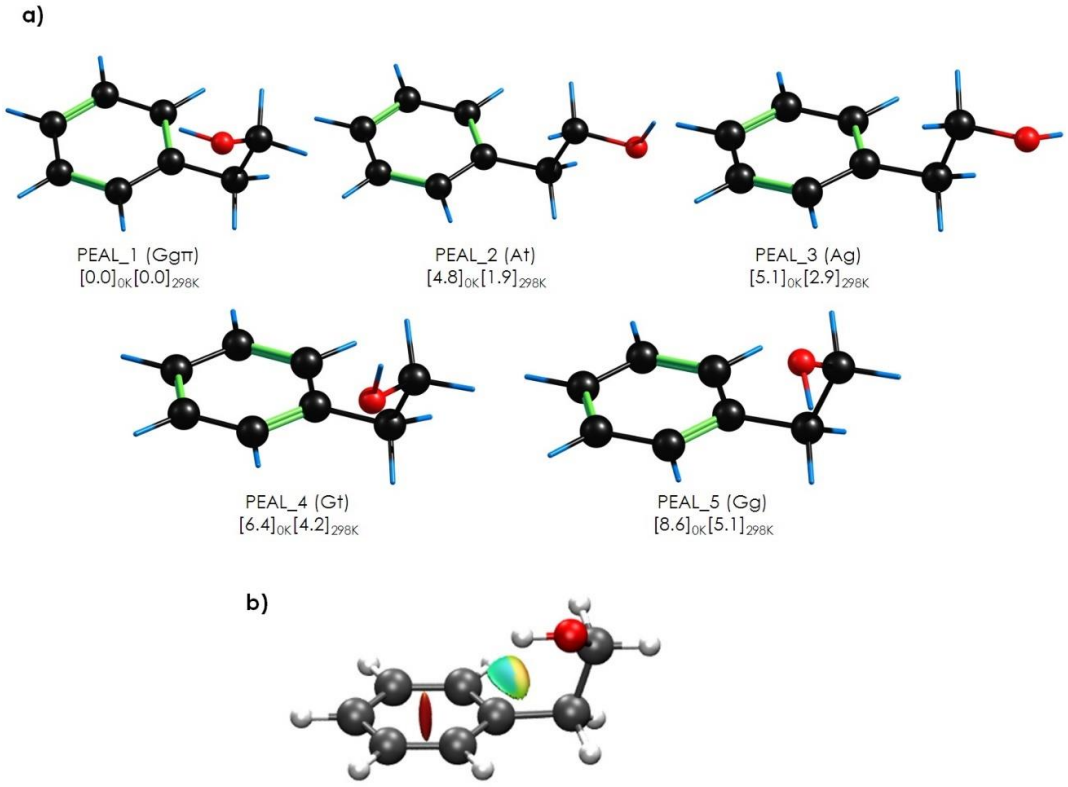

Figure 3.19: a) Most stable conformations for PEAL, computed at B3LYP-ED=GD3BJ/6-311++G(d,p) level. Energy values in kJ/mol. b) NCI plot for PEAL_1 conformation.

Exploration of the electronic spectroscopy of PEAL resulted in the spectrum depicted in Figure 3.20. The MRES spectroscopy of PEAL was already explored by Mons et al.[22] The origin band appears at 37627 cm^{-1} (red asterisk) and is followed by some weaker intensity transitions, in good agreement with previous studies. Overall, the spectrum is very clean and presents very little vibrational activity. According to previous studies, the band at 37627 cm^{-1} corresponds to the Ggπ isomer, while a weak transition at 37675 cm^{-1} is due to the At conformer. The weakness of this origin band is in agreement with the computed lower stability of this conformer (4.8 kj/mol at B3LYP-ED=GD3BJ/6-311++G(d,p) level). The UV/UV hole burning experiment, Figure 3.21, confirmed the existence of two isomers. Excitation wavelength marked by asterisks were used in IR/UV experiment, obtaining two different IR spectra (see Figure 3.22).

The strong vibrational activity of the dimer is in clear contrast with the spectrum of the monomer. Its red-most band appears at 37460 cm^{-1}, which means a red shift of 167 cm^{-1}. The other two traces presented in Figure 3.20. correspond to the trimer and the tetramer. Both of them start further to the red and contain less discrete vibronic transitions, built on top of a broad background.

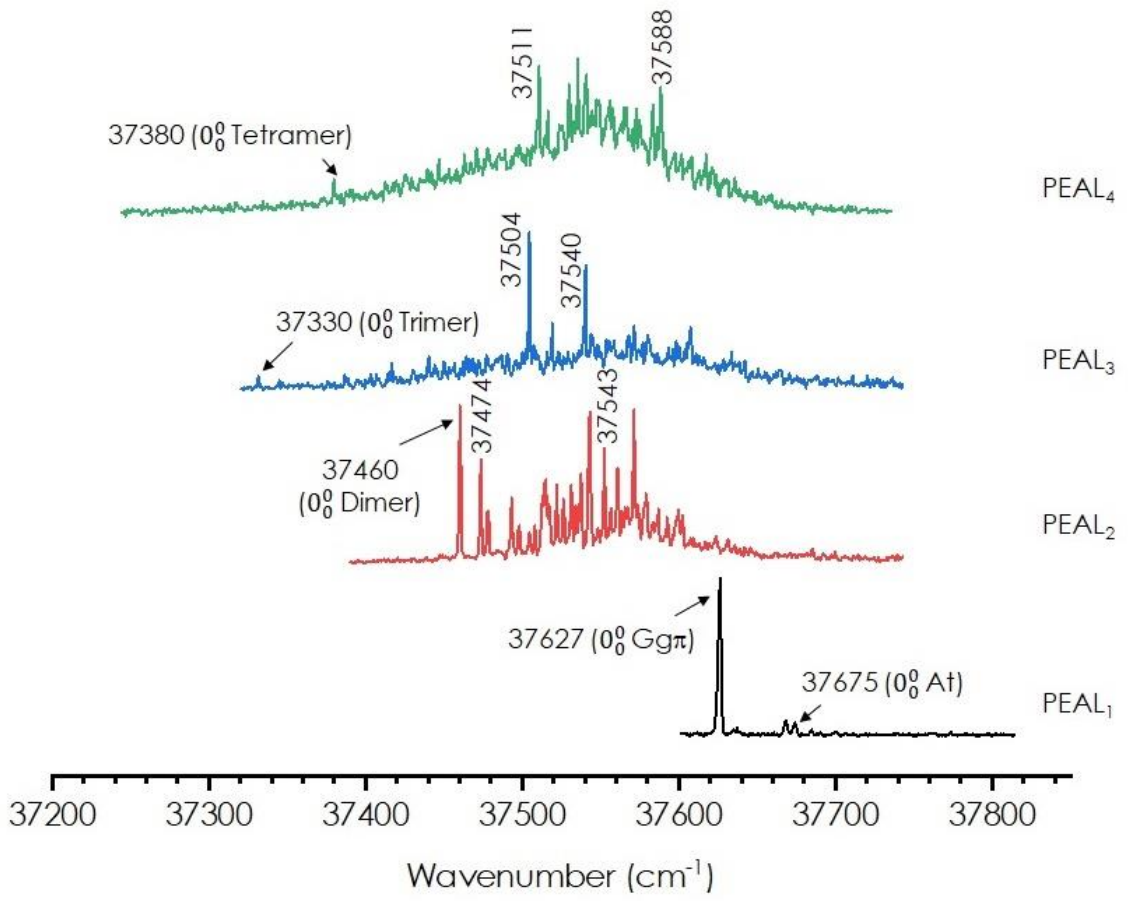

Figure 3.20: Two-color REMPI spectra of PEAL and its aggregates up to the tetramer. Ionization wavelength was set to 35714 cm^{-1}.

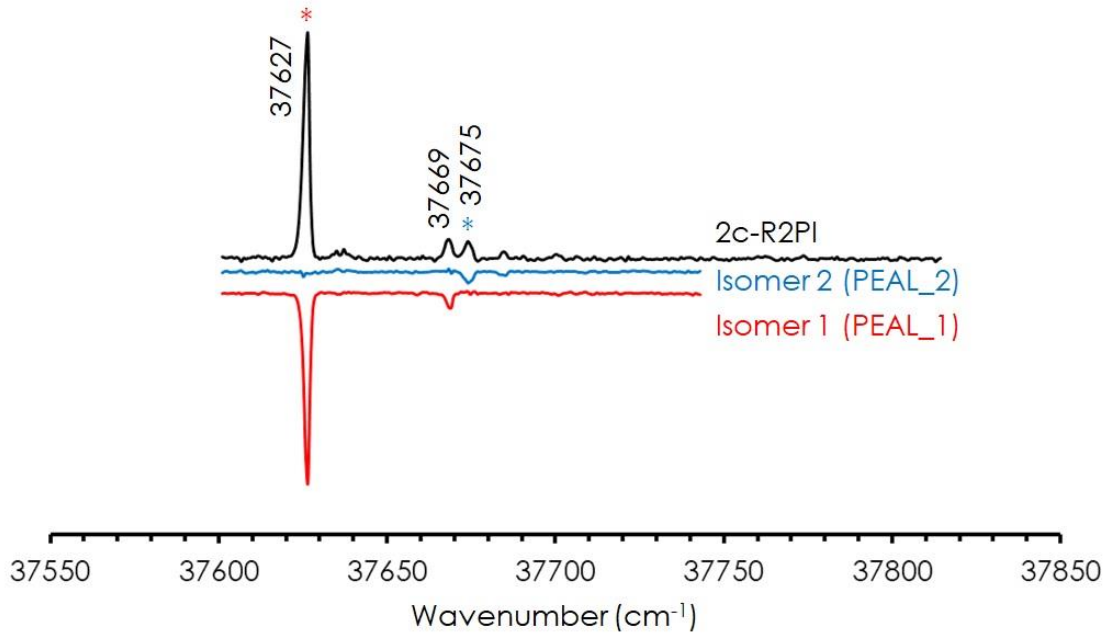

Figure 3.21: Two-color REMPI spectra of PEAL, along with the isomer specific REMPI spectra obtained from UV/UV Hole Burning experiments. Ionization wavelength was set to 35714 cm^{-1}. Electronic transitions marked by asterisks were probed with the second laser in hole burning experiments.

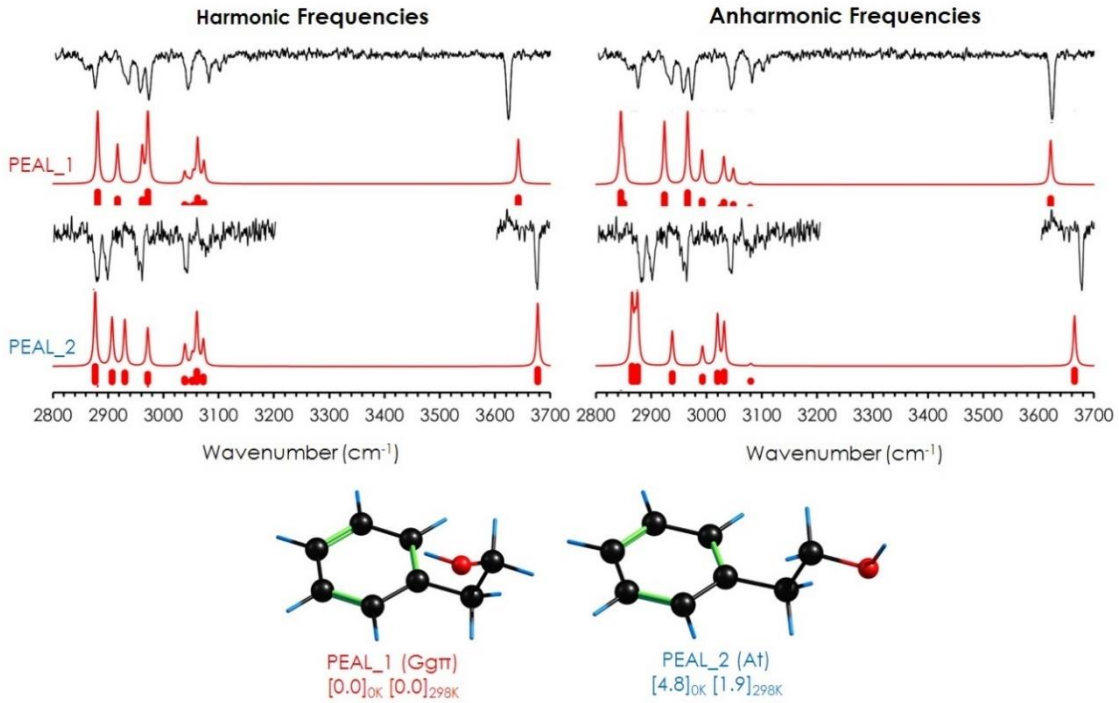

Figure 3.22: IDIR spectra of PEAL compared to the harmonic and anharmonic frequency predictions of the most stable structures. Spectra simulations were calculated at B3LYP(ED=GD3BJ)/6-311++G(d,p) level. For

harmonic approximation, a scaling factor of 0.9565 was used for OH stretching and 0.962 for CH stretching. No scaling factors were needed for anharmonic frequency calculations.

The spectroscopic characterization of the monomer continued with the recording of the IDIR spectra of the two detected isomers. Figure 3.22 shows the comparison of the two experimental IR spectra with the theoretical predictions for the most stable PEAL conformations, at B3LYP-ED=GD3BJ/6-311++G(d,p) level. Both spectra show well resolved CH and OH bands. There is a clear change of the free OH band position, indicating a different arrangement of the -CH_2CH_2OH motif of PEAL. This change can also be appreciated in the CH region. PEAL_01 and PEAL_02 structures are unequivocally assigned to the experimental data. As predicted, the observed red shift in the OH band is due to the intermolecular OH···π interaction formed in PEAL_01.. As in BnzA, anharmonic frequencies were also computed at the same level, which faithfully reproduce the position of the OH stretching mode, without artificially introducing a correction factor. However, the fine details of the CH stretches are not completely reproduced in the predicted traces. Probably, the existence of fermi resonances and other effects would require of a more complex Hamiltonian.

3.3.2. 2-Phenylethanol dimer

As in BnzA, dimer formation induces an asymmetry that requires of considering all the possible orientations of the CH_2CH_2OH motif respect to the aromatic ring. Two conformers of the monomer were already identified. Therefore, to reduce the complexity of the study, we will assume that only those dimers containing the two already detected monomers may be found. In the case of dimers formed by two units of the most stable conformation, Ggπ, four diasteroisomers may be formed. Thus, the combination of two monomers with their stereoisomery, results in an extraordinarily complex conformational landscape, already for the dimer.

Exploration of such conformational landscape at B3LYP=ED=GD3BJ/6-311++G(d,p) computational level, resulted in the situation presented in Figure 3.23. Interestingly, the structure of the members of the most stable (red) family, resemble those of the previously characterized BnzA dimer. In fact, the first four stable structures are diastereoisomers, as they present the same interaction, while the only difference is the orientation of the CH_2CH_2OH group. Interestingly, the increasing flexibility of the aliphatic separator enables the acceptor molecule to form OH···π interactions with its own aromatic ring, instead of with the interaction partner.

Surprisingly, the dimers containing at least one monomer in At conformation lie relatively high in energy (see structure PEAL2_08 and PEAL2_17), and therefore very small population of those isomers is expected in the beam.

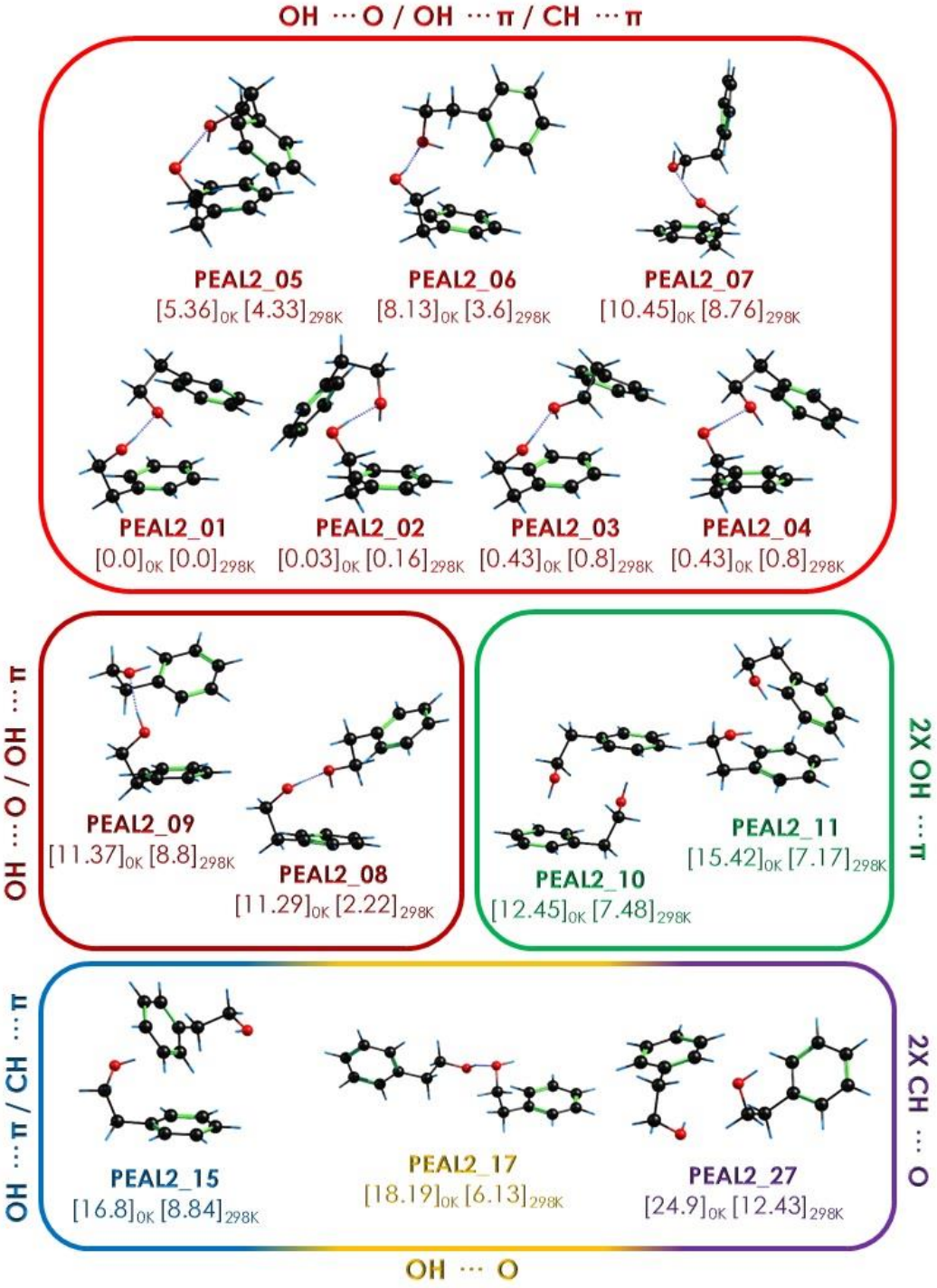

Figure 3.23: Summary of the most relevant conformers of PEAL dimer, optimized at B3YLP(ED=GD3BJ)/6-311++G(d,p) level. Energy values are given in kJ/mol.

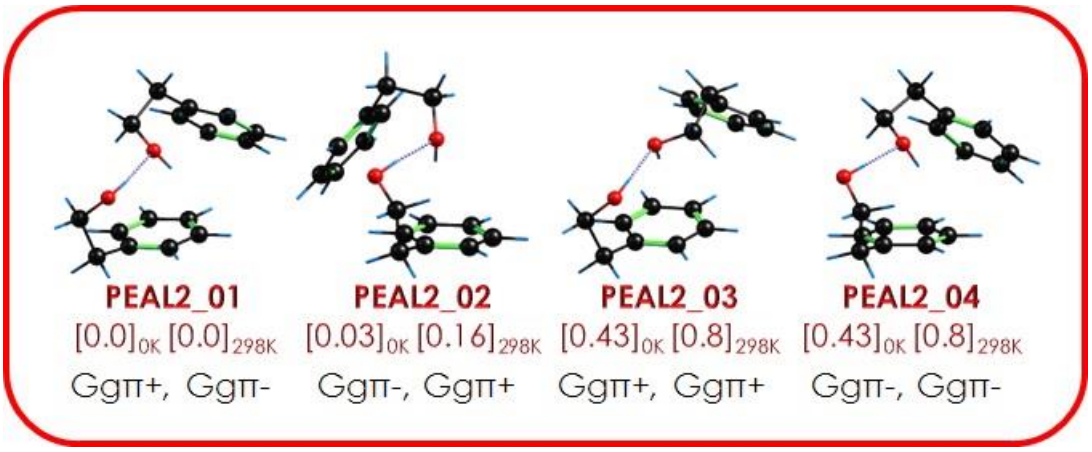

Figure 3.24: Most stable diastereoisomers of $PEAL_2$.

Figure 3.23 also shows some other possible interactions that result in isomers of very different stability. Clearly, the leading interaction is a combination of OH···O and OH···π hydrogen bonds, with the monomers always in gauche conformation. The +/- conformation introduces a subtle modulation on the final binding energy, smaller than in the case of BnzA, because the flexible ethyl separator has enough degrees of freedom to allow the molecules to accommodate and optimize the leading interactions. Actually. the most stable family contains all the possible combinations of the most stable monomer (Ggπ). These leading interactions are also accompanied by some CH···π/π···π interactions between the aromatic rings. Losing one of these interactions results in the structures grouped in less-stable families. Interestingly, the calculations predict the hetero-chiral aggregates to be more stable, in clear contrast with BnzA.

Relative binding Gibbs free energy diagrams also shows that structures from the red family are stable in a wide temperature window (see Figure A3.8). Additionally, there is no significant stabilization of other types of structures, discarding the possible presence of stable structures from other families in the jet.

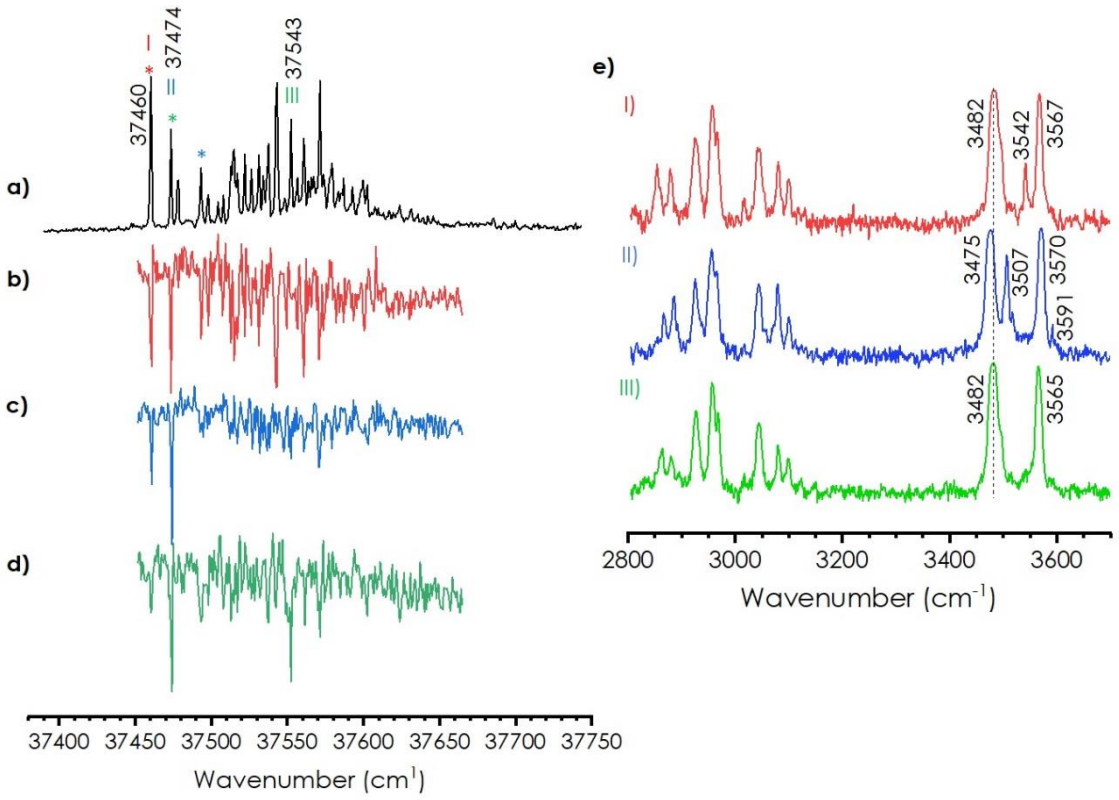

Figure 3.25: a) Two-color REMPI spectrum of $PEAL_2$, along with the UV/UV hole burning spectra probed at b) 37460 cm^{-1} (red asterisk), c) 37493 cm^{-1} (blue asterisk) and d) 37474 cm^{-1} (green asterisk). Ionization wavelength was set to 35714 cm^{-1}. e) IDIRS spectra of $PEAL_2$. Roman numbers mark the transitions probed to obtain each IR spectrum.

Exploration of the vibronic transitions in the REMPI spectrum using UV/UV hole burning unveiled a surprising complexity: contributions to the electronic spectrum from at least three different species were identified, as reported in Figure 3.25. However, hole burning experiments were not very conclusive because, as it happened in BnzA, some of the species present overlapping vibronic transitions and therefore, their relative contribution cannot be separated by conventional hole burning. Nevertheless, recording the IDIR spectra it was possible to demonstrate the existence of, at least, three different isomers of $PEAL_2$ (right panel in Figure 3.25).

In order to clarify which are the electronic transitions of each isomer, we performed IR/UV hole burning experiments by fixing the IR laser in the non-shared OH bands (see Figure 3.26).

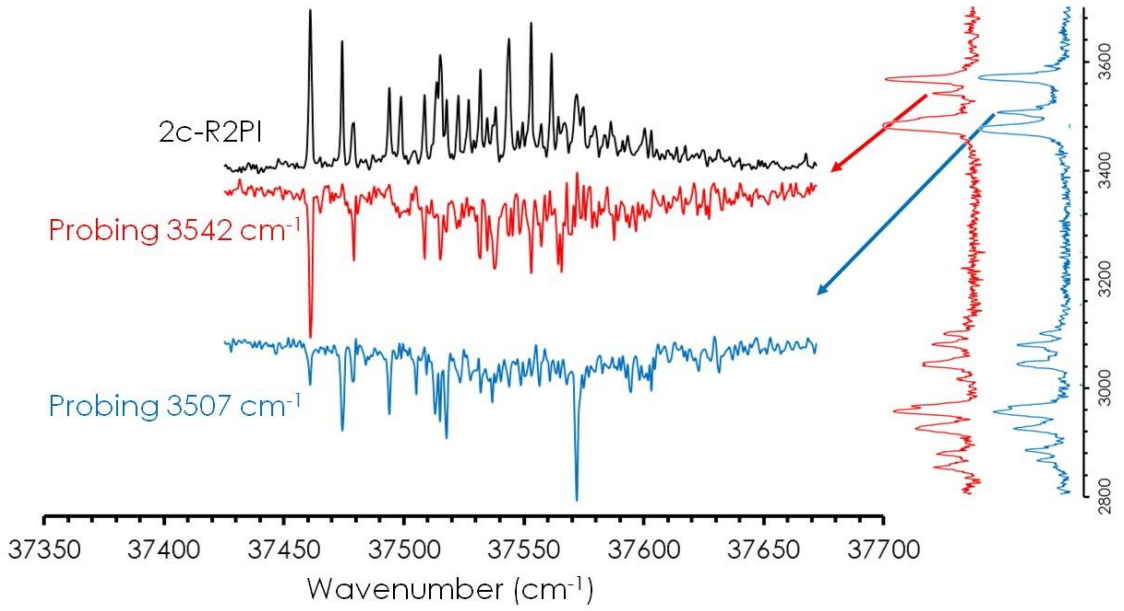

Figure 3.26: IR/UV Hole Burning spectra obtained for $PEAL_2$.

Probing the central band in the OH region, two different hole burning spectra were obtained, which contain most of the transitions, confirming the overlapping between them. All these experimental evidences a very complicated conformational landscape of PEAL dimer. Further comparison with theoretical predictions is needed in order to identify the isolated isomers. In summary, the following conclusions may be extracted from the data obtained by different spectroscopic techniques:

- Two-color REMPI spectrum presents a collection of electronic transitions and progressions that come from the contribution of at least three different isomers, which share a common origin band, but present different IR spectra.
- IR spectra of blue and red colored isomers have a number of OH bands that indicate the existence of at least two structures contributing to the spectrum (there are three OH bands instead of two, for a dimer). The green-colored IR spectrum seems to be the common contribution in red and blue traces (Figure 3.25).

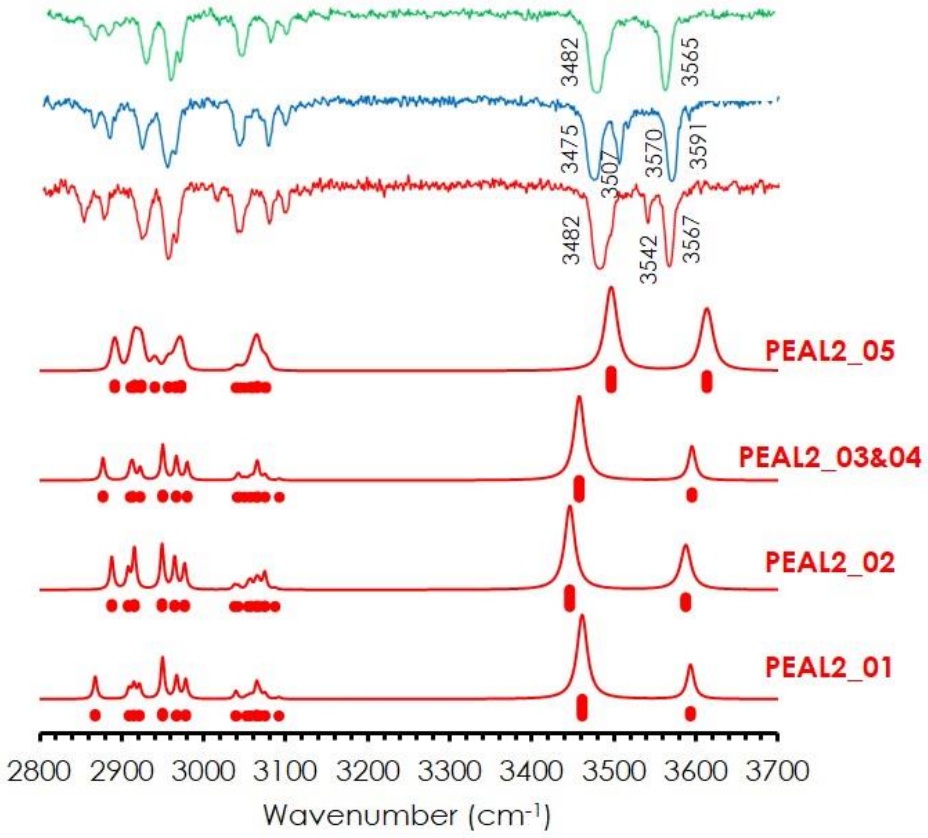

Figure 3.27: Comparison between the IDIR spectra of $PEAL_2$ and the simulations from the most stable structures. Frequency calculations were done at B3LYP(ED=GD3BJ)/6-311++G(d,p) level, and a scaling factor of 0.9565 was used to account for anharmonicity of both OH and CH groups.

Figure 3.27 shows the comparison between the experimental spectra and the predictions for the most stable isomers of $PEAL_2$. Special attention was put on the computed diastereoisomers, as they are very close in relative energy. Despite the interaction inside these dimers is very similar, computations seem to reveal some differences in the OH band positions. Those differences could explain the multiple OH bands observed in each experimentally isolated isomers. Higher energy structures in this family were also compared to the experiment (see Figure A3.9), but their predictions did not fit as well as the ones in Figure 3.27. The small difference in the position of the bands in the theoretical predictions is in agreement with the small differences also observed between the experimental spectra of the three isomers. Furthermore, taking into account the uncertainties in the computations, it is difficult to propose an unequivocal assignment. To test the accuracy of the calculations, the IR spectra of the most stable structures of $PEAL_2$ were also computed at M06-2x/6-311++G(d,p) and B3LYP-ED=GD3BJ/def2TZVP levels (see Figure 3.28).

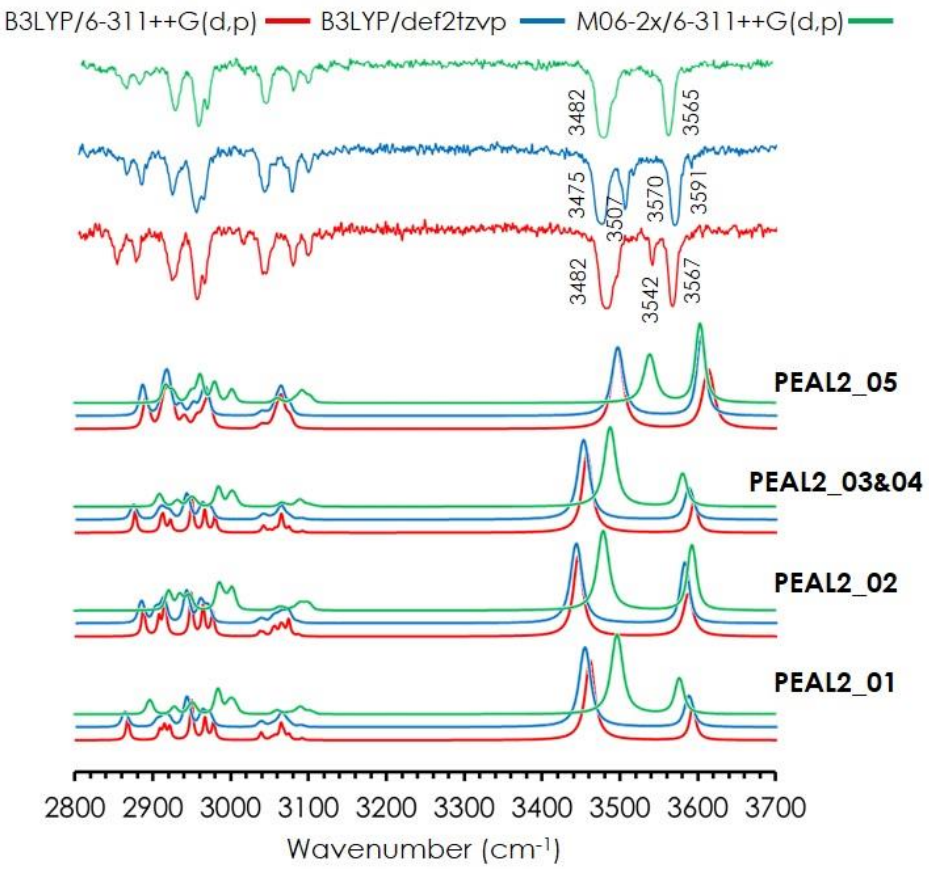

Figure 3.28: Simulation of $PEAL_2$ most stable structures IR spectra at different computational levels. OH scaling factor was set to 0.9565 for B3LYP/6-311++G(d,p), 0.962 for B3LYP/def2TZVP and 0.937 for M06-2X/6-311++G(d,p). CH scaling factor was maintained at 0.962 for all computational levels.

In general terms, all computational methods tested shows nearly the same differences in the frequency predictions between $PEAL_2$ structures. While using the def2TZVP basis set in the dispersion corrected B3LYP method shows no difference respect with the computed frequencies using Pople's triple-ς basis set, M06-2x/6-311++G(d,p) method makes a better prediction for position of the bands corresponding to the bounded OH groups. On the light of the comparison, one can conclude that three isomers, of the four most stable computed structures are present in the expansion.

A close look at the spectra in Figure 3.28 shows that there is a weak and narrower transition at 3542 cm^{-1} in the red trace and at 3507cm^{-1} in the blue trace. The origin of this band is not clear but most likely is a combination band, resulting from the coupling of the stretches with a libration motion of the hydroxyl group. Similar combination bands were already observed for other systems, such as water attached to carbonyl-containing organic molecules[23] or to protonated amines.[24] If such is the case, precise identification could greatly help with the identification of PEAL dimers and other related

systems. A similar weak transition was already observed in the spectra of BnzA trimer (Figure 3.14).

3.3.3. 2-Phenylethanol trimer

On the light of previous results for BnzA and those from the dimer, we can anticipate a complex landscape for $PEAL_3$. Previously reported BnzA trimer revealed linear conformations were formed in isolated phase, although the cyclic structures were predicted not to be very high in energy.

Potential energy surface of PEAL trimer resulted in a very extended and complex set of families, because of all the possible combinations that the CH_2CH_2OH group may adopt in the three PEAL molecules. In order to keep the system to a reasonable size, the energy window of the analysis was reduced and only the most stable conformations were taken into account. Figure 3.29 shows the structures corresponding to the two most stable families of $PEAL_3$. Similar to the observation in BnzA trimer, these families are composed by structures arranged either in a linear, or in a cyclic HB network.

A closer look at the most stable conformations of the linear family reveals that the trimers are formed by the addition of a third PEAL molecule to the previously formed stable dimers. Therefore, these aggregates are formed by two OH···O HBs, and an additional OH···π interaction. Finally, aromatic rings seem to arrange themselves by stacking interactions. Interestingly, the homochiral aggregation is not the most stable arrangement in the PEAL trimer. Nevertheless, all the presented structures are close in energy, and as the presence of more than one stable dimer was assigned in the expansion, different trimer structures could coexist. It is also worthy to note, that isomer PEAL3_07 has one monomer acting as a double proton acceptor. This structure is predicted to be the most stable arrangement at higher temperatures, indicating that when entropy comes into play there could be a re-arrangement of the HB network in the cluster.

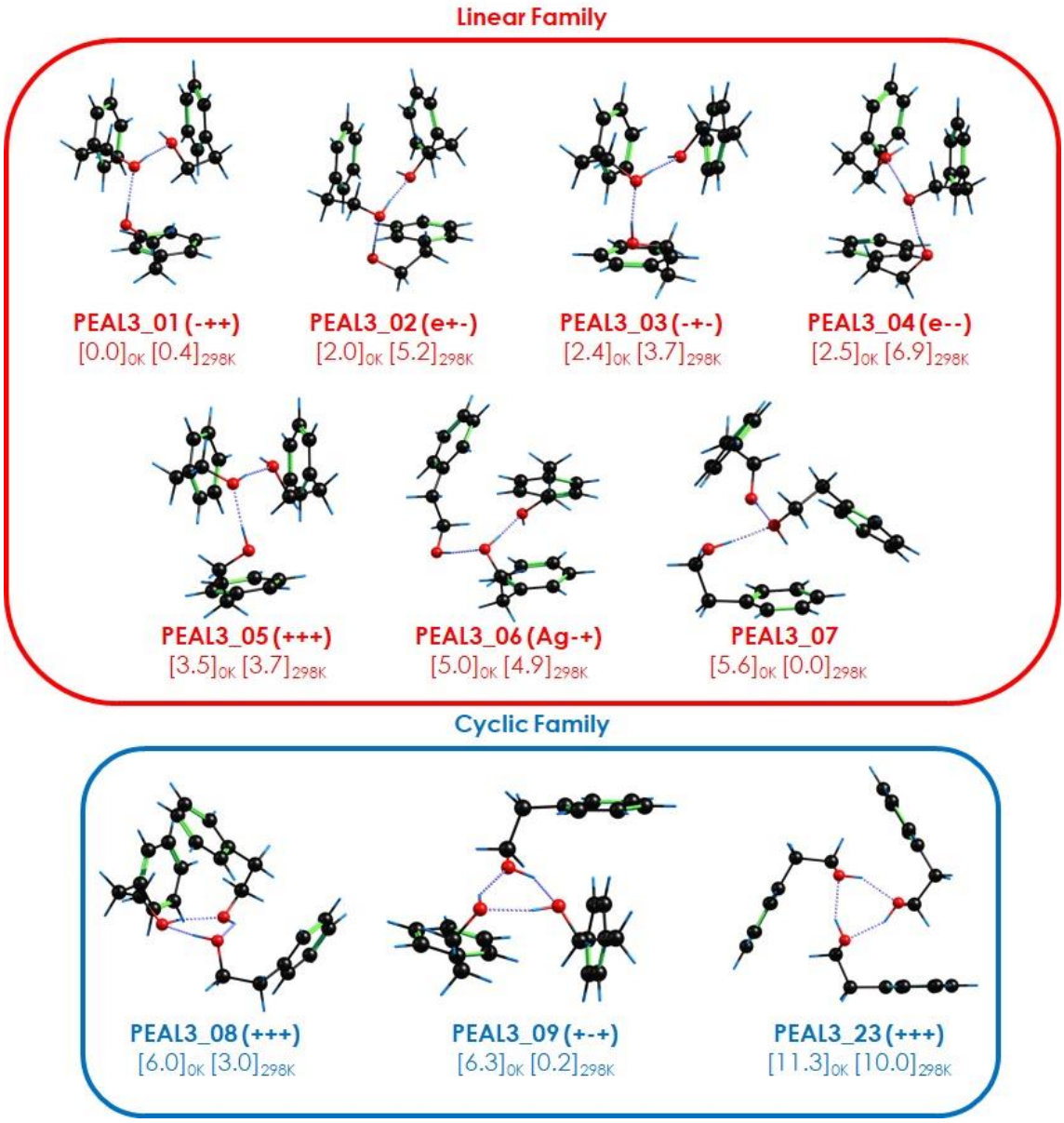

Figure 3.29: Most stable families of $PEAL_3$ computed at B3LYP(ED=GD3BJ)/6-311++G(d,p) level. Energy values bellow each structure are given in kJ/mol. Each structure name is followed by the dihedral angle disposition of the Ggπ conformation of each PEAL molecule. The dihedral angle analysis was done in the order of the HB network, so the first sign corresponds to the donor monomer. In the case of PEAL3_02, 04 and 06, the first PEAL is in a different conformation (e – eclipsed, Ag – *anti gauche*).

Cyclic HB network are not as stable as the linear ones. However, such structures do not lie very high in energy either and therefore, they could also be found in the expansion, especially at higher temperatures, as such structures are favored by entropy (Figure A3.12). Interestingly, the C_3 symmetric homo-cycle is not the most stable inside the cyclic family, against what was found for BnzA.

Figure 3.30 shows the recorded REMPI spectrum for PEAL trimer. As usual in clusters of this size, signal weakness precluded recording of the UV/UV hole burning experiments.

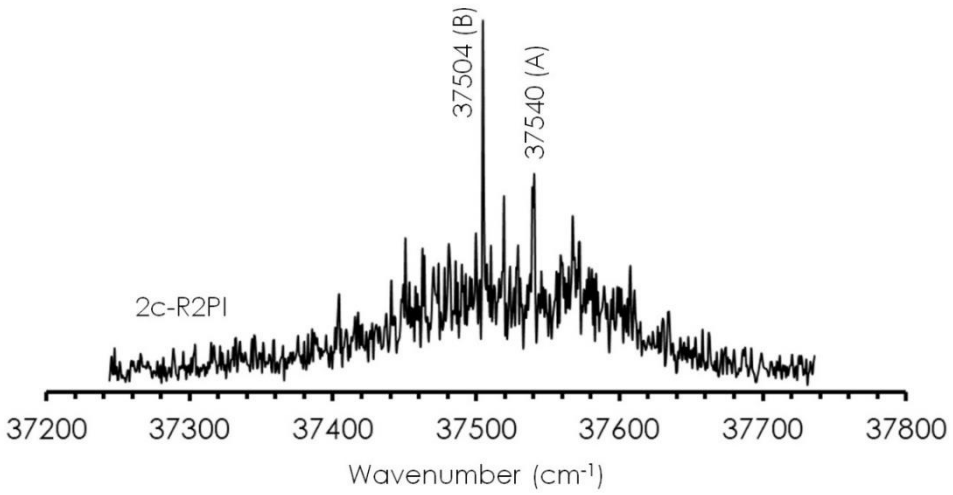

Figure 3.30: Two-color REMPI spectrum of $PEAL_3$. Ionization laser was set to 35714 cm^{-1}.

The absorption spectrum presents some discrete electronic transitions standing out from a noisy background. The small number of bands in the spectrum anticipate fewer conformations, compared to $BnzA_3$. several wavelengths were tested for IDIR experiments, revealing two different IR spectra when probing the transitions labelled as (A) and (B) in the REMPI spectrum. No additional IR spectra were obtained when probing the rest of the transitions.

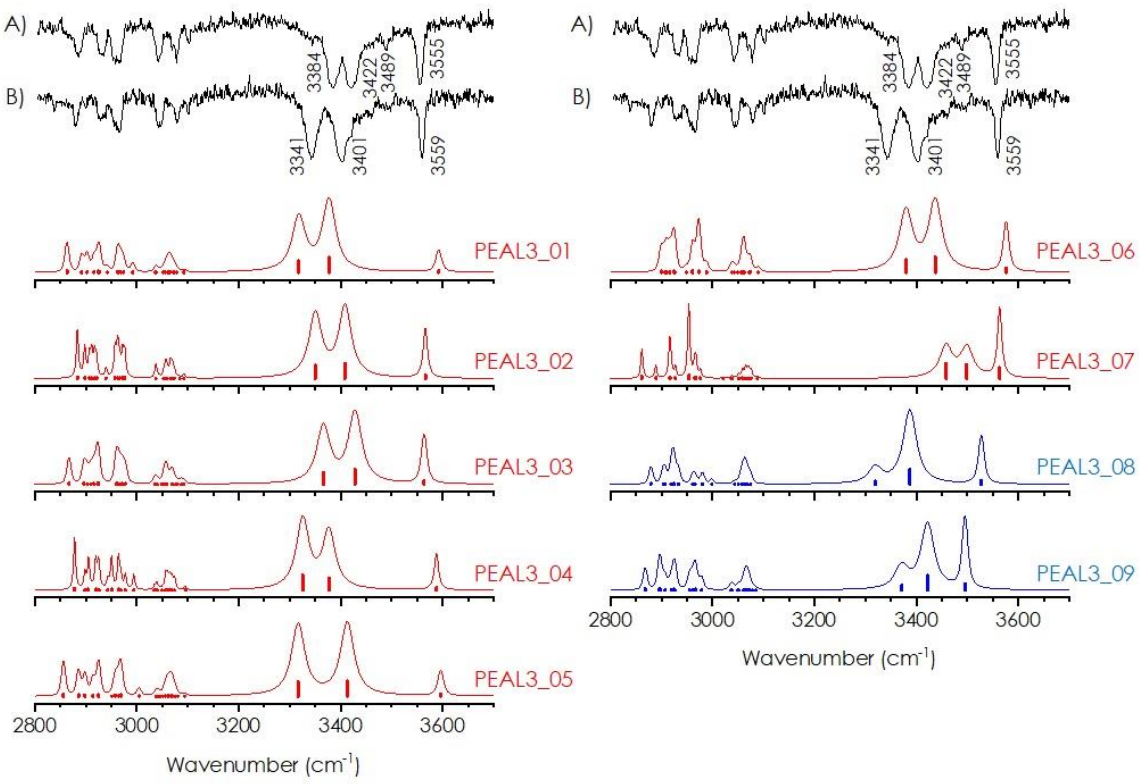

Figure 3.31: Comparison between the IDIR spectra of $PEAL_3$ and the simulations for the most stable structures. Frequency calculations were done at B3LYP(ED=GD3BJ)/6-311++G(d,p) level, and a scaling factor of 0.9565 was used to account for anharmonicity of both OH and CH groups. (A) and (B) traces were recorded fixing the UV laser at 37540 and 37504 cm^{-1}, respectively.

A comparison between the experimental IR spectra obtained for $PEAL_3$ and the computational predictions for the most stable conformations may be found in Figure 3.31. Both spectra present a pair of bonded OH stretching bands and a band due to the stretching of an OH involved in weak interactions. The similarity between the spectra suggests that both isomers have very similar structures. However, weaker features (3489 cm^{-1}) can be found between OH stretches, evidencing the presence of additional conformations or combination bands, as in the case of $BnzA_3$.

It is clear in Figure 3.31 that the predictions for the linear structures well reproduce the observed bands, but their predictions are, again, too similar to perform an unequivocal assignment. Since we detected several dimeric structures in the expansion, and computations showed that most stable trimer conformations are formed by the addition of a third PEAL to the most stable dimers, one could expect to have several at least two families of trimeric structures, each one based on one of the dimers already reported. Despite their similarities in the simulated spectra, slight changes in the OH···O interaction strength were captured by theory. Structures PEAL3_01 and _04 well

reproduce the overall spectrum in trace B, while structures PEAL3_02 and 03 better reproduce the position of the bands in trace A. Structure PEAL3_07, which presents a double proton acceptor, can be safely discarded due to its poor agreement with the experimental spectra.

Comparison with the predictions for PEAL3_08 and _09 cyclic structures is interesting, as they could explain the weaker features around 3489 cm^{-1}. Moreover, the rest of the bonded OH bands are also predicted between the 3330-3430 cm^{-1} interval. The relative lower stability of those isomers compared to the linear conformations, anticipate, at most, a low population in the expansion, which would explain the low intensity of their contribution to the IR spectrum. Nevertheless, such weak evidences are not enough to confirm their presence in the jet.

3.3.4. 2-Phenylethanol tetramer

Cluster growth in PEAL tetramer followed a similar aggregation pathway as BnzA, despite the increasing complexity of its conformational landscape. From the computational point of view, $PEAL_4$ presents a virtually infinite number of possible arrangements. Compared to the previous PEAL complexes, at tetramer size, computational exploration only revealed cyclic structures in a wide energy window. Figure 3.32 shows the most stable arrangement found for PEAL tetramer. As can be observed, homochirality and symmetry are missing in the most stable conformations. The most stable structure, PEAL4_01, is formed by a mixture of monomeric conformations. Similar configurations can be observed in the rest of the structures. Besides, the energetic difference between conformations is small, which in principle, permits the coexistence (or connections) of more than one species under experimental conditions, unless the topology of the PES enables relaxation during the cooling process.

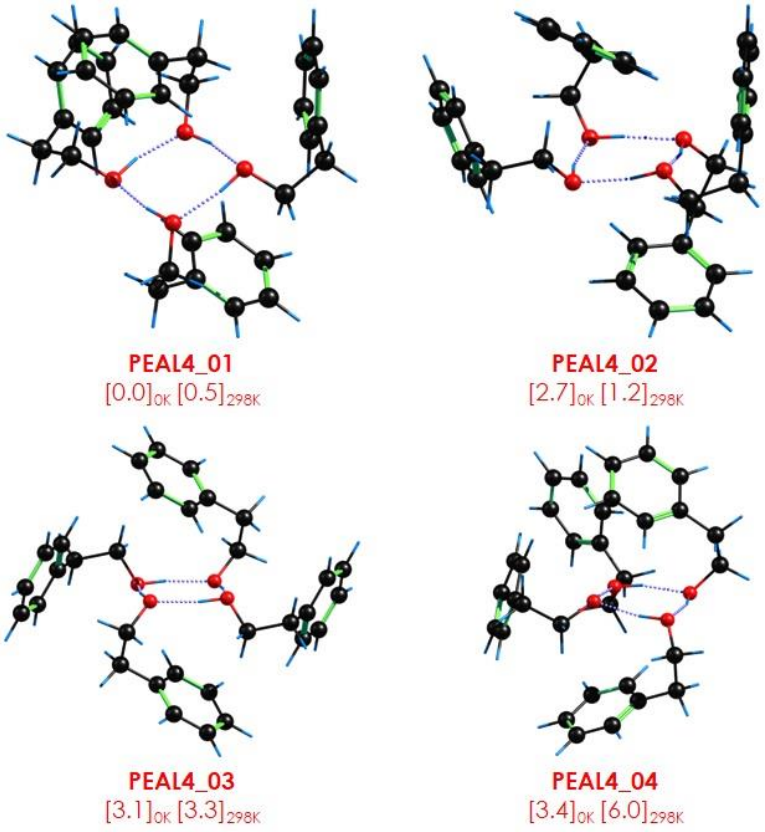

Figure 3.32: Most representative structures found for PEAL tetramer, computed at B3LYP-ED=GD3BJ/6-311++G(d,p) level. Energy values are given in kJ/mol inside brackets.

Despite the weak signal of this aggregate, it was still possible to record its two-color REMPI spectrum (Figure 3.33). As can be observed, it is a very congested spectrum that extends from 37300 to 37700 cm^{-1}. The first discrete vibronic transition appears at 37380 cm^{-1} and it is therefore taken as the 0_0^0.The spectrum gains intensity to the blue, were stronger transitions were observed. The bands at 37510 and 37588 cm^{-1} were used to record the IDIR spectra, shown in Figure 3.34.

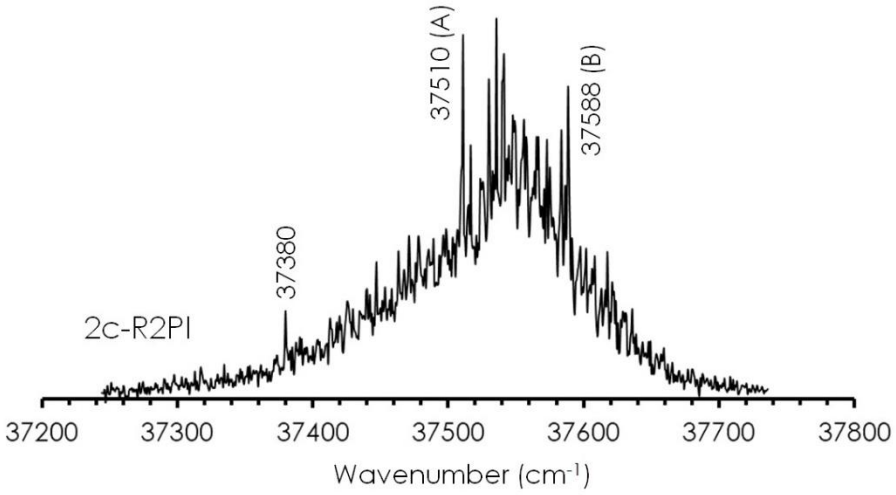

Figure 3.33: Two-color REMPI spectra of $PEAL_4$. Ionization laser was set to 35714 cm^{-1}.

As observed in $BnzA_4$, all the stretches of the OH groups of PEAL appear grouped around 3250-3300 cm^{-1} in both experimental traces, shifted to the red of the free OH stretching region. This is a clear indication of the formation of a cyclic hydrogen bond network. Moreover, the absence of bands corresponding to OH···π interactions allows us to discard linear arrangements of the HB network.

The differences between the experimental traces points to the presence of more than one conformation with a different cyclic configuration. Trace A contains two strong, broad absorptions at 3235 and 3287 cm^{-1}, with a weaker shoulder at 3340 cm^{-1}. However, trace B presents a broader absorption, on top of which, three features can be distinguished (3330, 3295 and 3274 cm^{-1}). Besides, a fourth band can be observed at 3151 cm^{-1}.

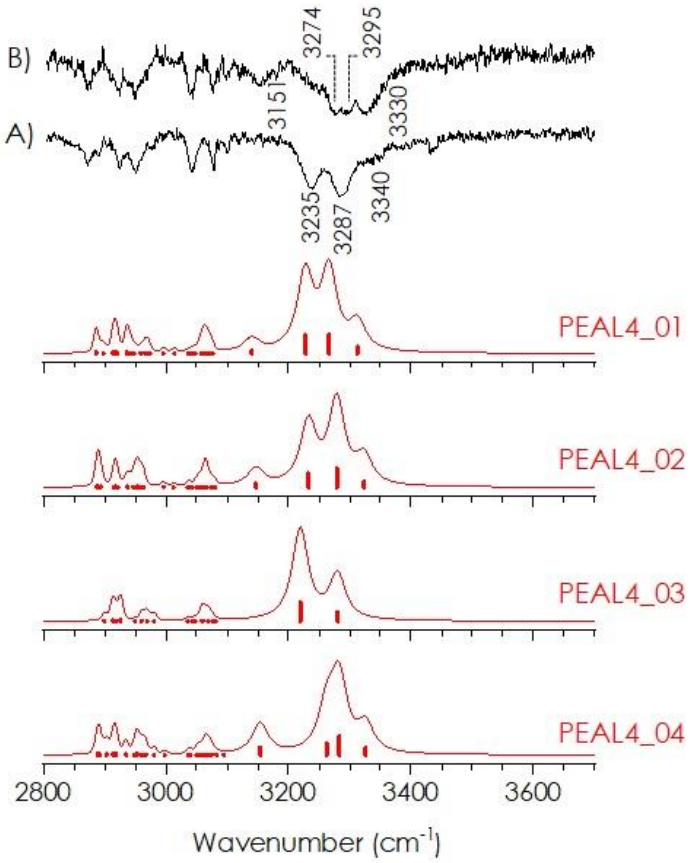

Figure 3.34: Comparison between the IDIR spectrum of $PEAL_4$ and the simulations from the most stable structures. Frequency calculations were done at B3LYP(ED=GD3BJ)/6-311++G(d,p) level, and a scaling factor of 0.9565 was used to correct anharmonicity of both OH and CH groups.

A comparison between the computational predictions for the most stable PEAL tetramers and the experimental traces may be found in Figure 3.34. Unequivocal assignment of such broad IR bands is not simple. However, the most stable conformations very well reproduce the observed features. In fact, structure PEAL4_01 and _02 well predict the appearance of the most red-shifted OH bands at 3151 cm^{-1}. The simulated spectrum of PEAL4_03 accurately reproduces the position of the bands in trace A.

The exact assignment of more than one conformation in this system is not straightforward. All the computed structures present cyclic arrangements, and therefore, all of them present similar spectra, which are in turn, in good agreement with the experimental spectrum. Additional experiments or combination with other spectroscopic techniques would be needed in order to give a more accurate assignment. However, applying an energetic criterion, we can tentatively assign the experimental traces to (at least) two of the three most stable conformations of $PEAL_4$.

3.4. Discussion

In previous sections we presented an exhaustive spectroscopic analysis of BnzA and PEAL complexes. In general terms, aggregation of each aromatic alcohol was governed by OH···O hydrogen bonds. This interaction dominates the association in water and small saturated alcohols.[25] The presence of other functional groups modifies the molecular interplay, acting as an additional or alternative acceptor for a HB, for example. In the above-studied aggregates, additional non-covalent interactions, especially those involving the aromatic rings, have shown to be responsible of the final shape of the conformations.

Both BnzA and PEAL molecules are interesting cases to study the aggregation preferences of aromatic alcohols, as their OH group is not directly attached to the aromatic ring. Therefore, it is isolated from the aromatic cloud, avoiding delocalization effects, but at the same time, the aromatic ring is an important source of secondary interactions. In addition, the flexibility sequence from BnzA to PEAL allows us to calibrate how the additional degrees of freedom influence the aggregation process, especially when the present results are compared to the aggregates of the prototypical phenol molecule. Due to the torsional rigidity of phenol, most of the interaction energy comes from the formation of a single, *classical* OH···O HB, but dispersion between the phenyl groups is already able to influence the geometry of the dimer.[17]

The extra elongation of the alkyl chain introduced a complication in the cluster analysis due to the creation of a chiral center. The dimer showed that the small difference in stability between the collection of stereoisomers is not negligible, as we observed a splitting in the dimers into homo- and hetero-chiral conformations. This splitting acquires more importance in larger complexes, producing a diversity in structures due to the possible combination of enantiomers inside each family.

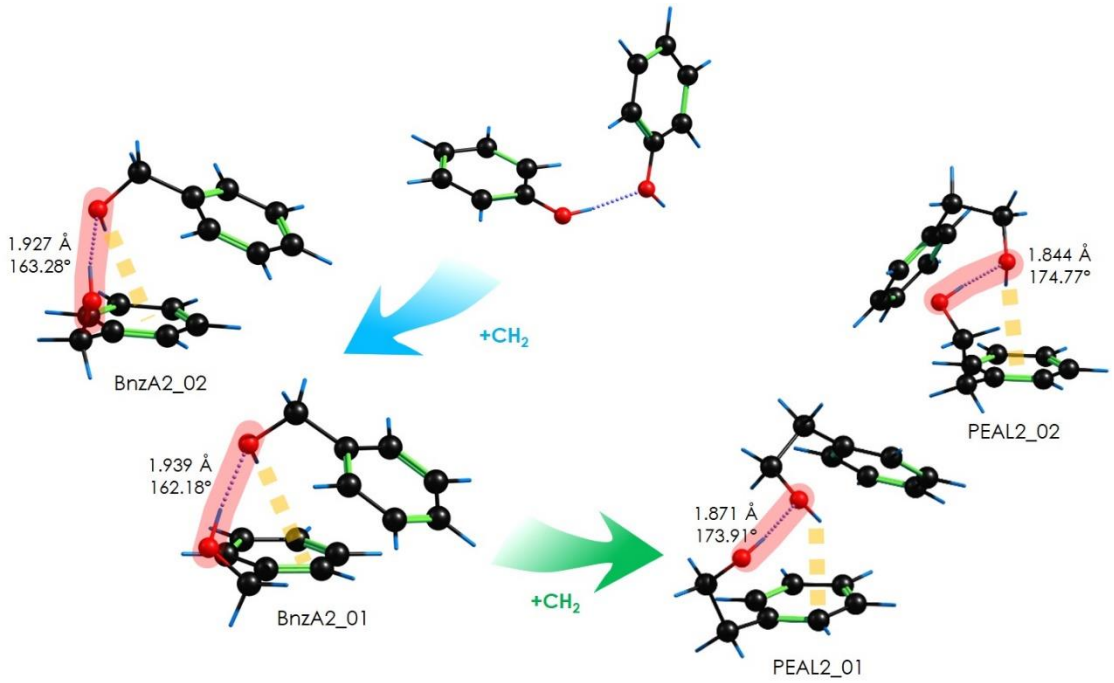

Figure 3.35: Comparison between the assigned structures of BnzA and PEAL dimers with phenol dimer reported from bibliography.[17] The structures were computed at B3LYP(ED=GD3BJ)/6-311++G(d,p) level. OH···O hydrogen bonds are marked in red, while secondary OH···π interactions are marked with a yellow dashed line.

Figure 3.35 presents the assigned structures of BnzA and PEAL dimers, compared to that of phenol. The flexibility introduced by the methylene linker between the hydroxyl and the phenol group in BnzA enables the additional formation of an OH···π HB. The addition of a second methylene in PEAL improves the flexibility of the system, enabling the formation of the OH···π interaction in the monomer. Regarding the dimer, the most stable conformation of PEAL presents stronger OH···O HB than those observed in $BnzA_2$, with shorter distances and wider angles. This was also observed in the experimental IR spectrum of the dimers, where the bands assigned to OH···O interactions are shifted further to the red in PEAL than in BnzA (~ 15-20 cm^{-1}). Additional topological analysis of the most stable dimers of each complex confirmed this difference in the interaction strength (see Figure 3.36), as in the numerical representation of the reduced density gradient the low-density, low-gradient plot through the OH···O interaction appears at more negative values in PEAL than in BnzA.

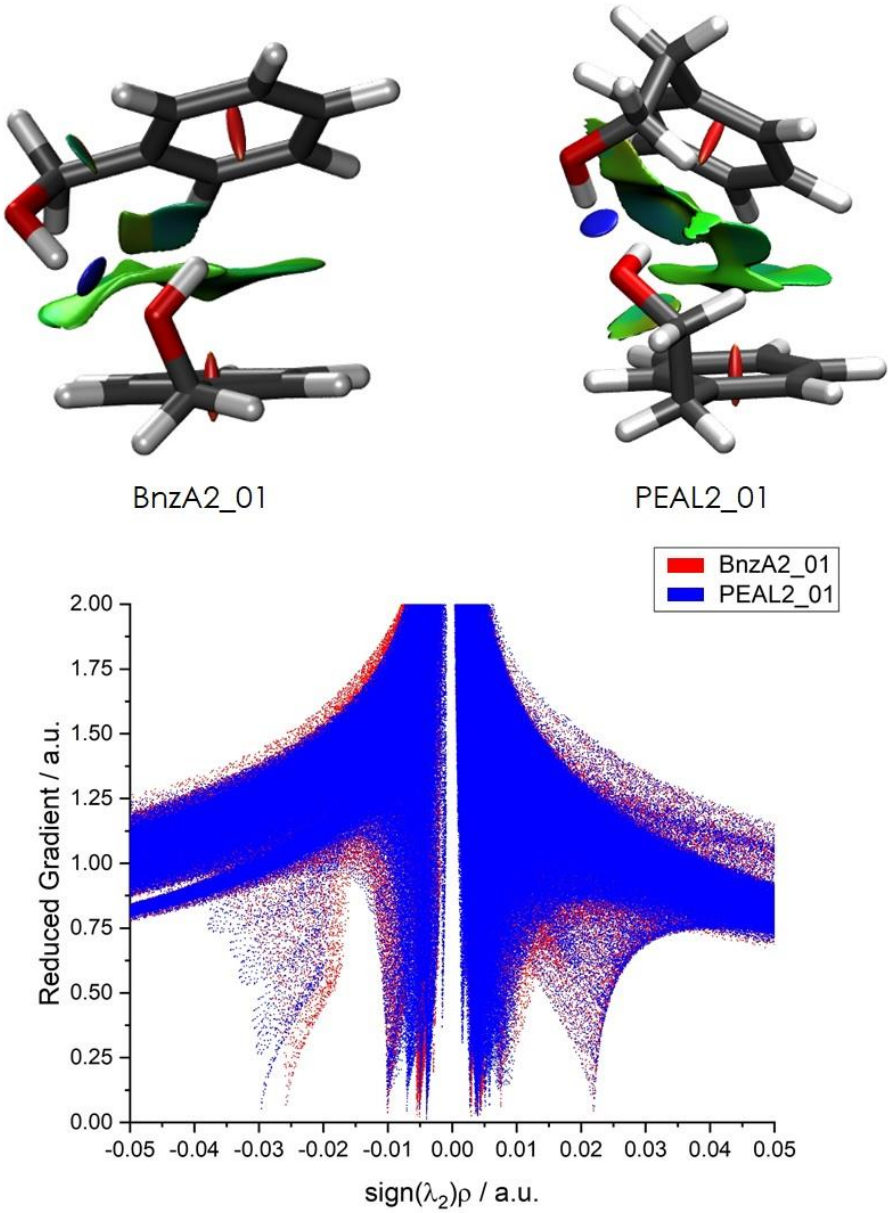

Figure 3.36: NCI plots for structures BnzA2_01 and PEAL2_01, together with the representation of RDG vs sign(λ_2)ρ diagram for both dimers.

Both BnzA and PEAL dimers showed a rich conformational landscape, where each conformational family is stabilized by multiple non-covalent interactions. The assigned structures present, as expected, strong OH···O interaction between alcohol groups, but the additional OH···π interaction in $BnzA_2$ and $PEAL_2$ give the final shape to the complex. This cooperative patter is also found in the most stable dimers for 1-phenylethanol,[14] 1-indanol,[26] and propargyl alcohol.[27,28]

In phenol dimer, the proton acceptor OH group points away from the partner molecule, whereas in BnzA and PEAL it forms an additional OH···π interactions, which also leave a

distinctive fingerprint in the IR spectra, appearing (the stretches) mid-way from those of tightly-bonded OH and the region of the free OH stretches. This additional interaction provides a relative stability of about 3-6 kJ/mol in $BznA_2$ and about 8-10 kJ/mol in $PEAL_2$, compared to the structures that presents a single OH···O. Hence, increasing the aliphatic chain between the hydroxyl group and the aromatic ring seems to have a direct influence in the interaction preference towards the aggregation.

The length of the linker also had the additional effect of increasing the degrees of freedom, and therefore, the complexity of the intermolecular PES, especially in the case of PEAL. The additional flexibility induced by the ethylene substitution between the OH group and the aromatic ring allowed the creation of a wider window for stable dimers containing OH···O and OH···π HBs. As we observed in section 3.3.2, the experimental IR spectra contained the contribution from several conformers, probably all possible diastereoisomers of $PEAL_2$. As the predictions for them are very similar, additional experiments would be required in order to identify the correct diastereoisomer contribution. An additional weaker band in the spectra may be due to a resonance or a combination band. Similar combination bands have been described for monohydrated dimers of molecules containing a carbonyl group.[23] If such is the case, it could be very helpful to propose a final assignment, as such combination bands are very sensible to the structure of the aggregates. Also, rotational spectroscopy could provide a more accurate assignment.

Addition of a third molecule complicated both the theoretical and experimental panorama. In the trimers of water,[18] saturated alcohols[19] and phenol,[17] a cyclic hydrogen bond network is formed between hydroxyl groups. BnzA3_06 structure present a C3 symmetry axis, similar to the one observed in phenols trimer. Computations predicts that cyclic structures are not as stable as linear ones for $BnzA_3$. This difference is even larger in $PEAL_3$. Cyclic arrangements are 10 kJ/mol above the most stable linear structure, and their presence was not detected in the jet. Even though the chain topology involves a loss in cooperativity, the replacement of an OH···O HB with a weaker OH···π HB is apparently favored due to a more suitable arrangement of aromatic rings. And the reduced stress, compared to the cyclic hydrogen bond network. This behavior was also observed in 1-indanol[26] and 2-fluoroethanol,[29] where the HB cooperativity produced by three OH···O bonds is replaced with a linear chain of weaker HBs.

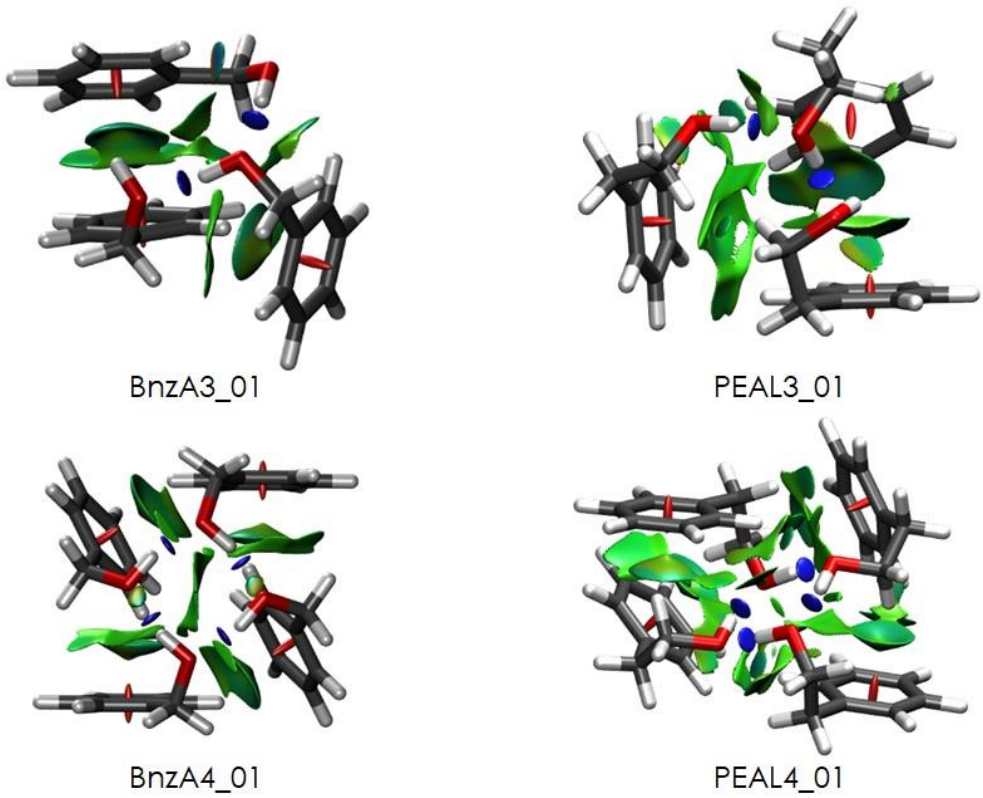

Figure 3.37: NCI plots of the most stable, assigned structures of BnzA and PEAL trimers and tetramers.

Figure 3.37 shows the NCI plots for the most stable trimer and tetramer of BnzA and PEAL. In general terms, both linear trimers are quite similar. The hydrogen bond network observed in the dimers is elongated with an additional OH···O interaction, but the hydrogen bond chain still ends with an OH···π termination. As observed for BnzA, aromatic rings can arrange in different ways, modelling different stable geometries. This tendency is also observed in PEAL structures. The most stable structure in $BnzA_3$ (BnzA3_01) is formed by the homo-aggregation of BnzA monomers. However, in the case of PEAL that preference is lost, perhaps due to the improved flexibility provided by the extra methylene group, allowing trimer arrangements with reduced ring strain at the cost of less stable monomer conformations.

The largest clusters studied for these systems was the tetramer. In both cases, the recorded infrared spectra correspond to a cyclic hydrogen bond organization, in good agreement with the computational predictions. Interestingly, the energetic gap between chain HB network and cyclic arrangements in the tetramer increases, pointing out that the reduced ring strain in the tetramer strongly encourages the cyclic hydrogen bond pattern. The most stable conformer for BnzA, BnzA4_01, presents a C_2-symmetric structure. Additionally, it is a homomolecular aggregate, as all BnzA molecules present

the same G+ conformation. This conformational preference is completely lost in PEAL tetramer. The most stable conformation did not even show all the PEAL monomers adopting the same conformation. Moreover, the increased flexibility results in the formation of structures with lower symmetry, with all rings located in the same plane. It is worth mentioning that the cyclic arrangement at tetramer size is the most stable structure in water,[29] small saturated alcohols[30,31], and in similar aromatic[7] and non-aromatic systems.[6]

3.5. Conclusions

In this chapter the first instants of the aggregation preferences of two aromatic alcohols were studied. Jet cooled spectroscopy, in combination with mass resolved laser spectroscopy techniques demonstrated, once more, to be an excellent tool for characterizing these type of complexes.

The results obtained suggest that OH groups and their interactions govern the molecular aggregation. Strong OH···O hydrogen bonds are the main forces of nucleation, whereas secondary OH···π and π···π interactions give the final shape to the conformations, especially for the trimers studied, where an OH···OH···OH···π HB network was found to be more stable than a more cooperative OH···O cyclic network. Linear structures where not detected at tetramer size, indicating that at this point, there is a change of tendency, with the cyclic structures becoming the most stable arrangements.

The extended characterization of the stepwise aggregation of BnzA and PEAL molecules helped us to better understand the forces that guide the initial nucleation processes in alcohols in isolated phase. The alkyl chain elongation completely changed the interaction preference in the observed molecules, since the normal cyclization of the HB network at trimer size was replaced by the formation of more stable, linear structures. Thus, dispersive forces located in the most hydrophobic parts of the aromatic alcohols seems to compete with the interactions in the hydrophilic parts at the first stages of aggregation. The subtle interplay between interactions and the small energy difference between aggregates with different chirality makes the systems studied in this chapter excellent bench works to test and refine the modern computational theories.

3.6. References

[1] I. León, J. Millán, F. Castaño and J. A. Fernández, A Spectroscopic and Computational Study of Propofol Dimers and Their Hydrated Clusters, *ChemPhysChem*, 2012, **13**, 3819–3826.

[2] I. León, I. Usabiaga, J. Millán, E. J. Cocinero, A. Lesarri and J. A. Fernández, Mimicking anesthetic--receptor interactions in jets: the propofol--isopropanol cluster, *Phys. Chem. Chem. Phys.*, 2014, **16**, 16968–16975.

[3] I. León, J. Millán, E. J. Cocinero, A. Lesarri, F. Castaño and J. A. Fernández, Mimicking anaesthetic–receptor interaction: a combined spectroscopic and computational study of propofolphenol, *Phys. Chem. Chem. Phys.*, 2012, **14**, 8956–8963.

[4] I. León, R. Montero, A. Longarte and J. A. Fernández, IR mass-resolved spectroscopy of complexes without chromophore: Cyclohexanol·(H2O)n, n = 1–3 and cyclohexanol dimer, *J. Chem. Phys.*, 2013, **139**, 174312.

[5] M. Juanes, I. Usabiaga, I. León, L. Evangelisti, J. A. Fernández and A. Lesarri, The Six Isomers of the Cyclohexanol Dimer: A Delicate Test for Dispersion Models, *Angew. Chemie Int. Ed.*, 2020, **59**, 14081–14085.

[6] I. León, R. Montero, A. Longarte and J. A. Fernández, Influence of dispersive forces on the final shape of a reverse micelle, *Phys. Chem. Chem. Phys.*, 2015, **17**, 2241–2245.

[7] I. León, J. Millán, E. J. Cocinero, A. Lesarri and J. A. Fernández, Shaping Micelles: The Interplay Between Hydrogen Bonds and Dispersive Interactions, *Angew. Chemie Int. Ed.*, 2013, **52**, 7772–7775.

[8] H. S. Im, E. R. Bernstein, H. V. Secor and J. I. Seeman, Supersonic jet studies of benzyl alcohols: Minimum energy conformations and torsional motion, *J. Am. Chem. Soc.*, 1991, **113**, 4422–4431.

[9] C. E. H. Dessent, W. D. Geppert, S. Ullrich and K. Müller-Dethlefs, Ionization-induced conformational changes: REMPI and ZEKE spectroscopy of salicyl and benzyl alcohol, *Chem. Phys. Lett.*, 2000, **319**, 375–384.

[10] M. Mons, E. G. Robertson and J. P. Simons, Intra- and Intermolecular π-Type Hydrogen Bonding in Aryl Alcohols: UV and IR-UV Ion Dip Spectroscopy, *J. Phys. Chem. A*, 2000, **104**, 1430–1437.

[11] H. L. Fang and R. L. Swofford, Molecular conformers in gas-phase ethanol: A temperature study of vibrational overtones, *Chem. Phys. Lett.*, 1984, **105**, 5–11.

[12] V. Barone, Anharmonic vibrational properties by a fully automated second-order perturbative approach, *J. Chem. Phys.*, 2004, **122**, 14108.

[13] J. Bloino, A VPT2 Route to Near-Infrared Spectroscopy: The Role of Mechanical and Electrical Anharmonicity, *J. Phys. Chem. A*, 2015, **119**, 5269–5287.

[14] R. Medel and M. A. Suhm, Understanding benzyl alcohol aggregation by chiral modification: the pairing step, *Phys. Chem. Chem. Phys.*, 2020, **22**, 25538–25551.

[15] R. S. Ruoff, T. D. Klots, T. Emilsson and H. S. Gutowsky, Relaxation of conformers and isomers in seeded supersonic jets of inert gases, *J. Chem. Phys.*, 1990, **93**, 3142–3150.

[16] P. Felder and H. H. Günthard, Conformational interconversions in supersonic jets: Matrix IR spectroscopy and model calculations, *Chem. Phys.*, 1982, **71**, 9–25.

[17] N. A. Seifert, A. L. Steber, J. L. Neill, C. Pérez, D. P. Zaleski, B. H. Pate and A. Lesarri, The interplay of hydrogen bonding and dispersion in phenol dimer and trimer: structures from broadband rotational spectroscopy, *Phys. Chem. Chem. Phys.*, 2013, **15**, 11468–11477.

[18] F. N. Keutsch, J. D. Cruzan and R. J. Saykally, The Water Trimer, *Chem. Rev.*, 2003, **103**,

2533–2578.

[19] R. W. Larsen, P. Zielke and M. A. Suhm, Hydrogen-bonded OH stretching modes of methanol clusters: A combined IR and Raman isotopomer study, *J. Chem. Phys.*, 2007, **126**, 194307.

[20] N. Guchhait, T. Ebata and N. Mikami, Structures of hydrogen-bonded clusters of benzyl alcohol with water investigated by infrared-ultraviolet double resonance spectroscopy in supersonic jet, *J. Chem. Phys.*, 1999, **111**, 8438–8447.

[21] I. León, J. Millán, E. J. Cocinero, A. Lesarri and J. A. Fernández, Water Encapsulation by Nanomicelles, *Angew. Chemie Int. Ed.*, 2014, **53**, 12480–12483.

[22] M. Mons, E. G. Robertson, L. C. Snoek and J. P. Simons, Conformations of 2-phenylethanol and its singly hydrated complexes: UV–UV and IR–UV ion-dip spectroscopy, *Chem. Phys. Lett.*, 1999, **310**, 423–432.

[23] T. L. Fischer, T. Wagner, H. C. Gottschalk, A. Nejad and M. A. Suhm, A Rather Universal Vibrational Resonance in 1:1 Hydrates of Carbonyl Compounds, *J. Phys. Chem. Lett.*, 2021, **12**, 138–144.

[24] C.-K. Lin, R. Shishido, Q.-R. Huang, A. Fujii and J.-L. Kuo, Vibrational spectroscopy of protonated amine–water clusters: tuning Fermi resonance and lighting up dark states, *Phys. Chem. Chem. Phys.*, 2020, **22**, 22035–22046.

[25] M. A. Suhm, *Adv. Chem. Phys.*, 2009, 1–57.

[26] J. Altnöder, A. Bouchet, J. J. Lee, K. E. Otto, M. A. Suhm and A. Zehnacker-Rentien, Chirality-dependent balance between hydrogen bonding and London dispersion in isolated (±)-1-indanol clusters, *Phys. Chem. Chem. Phys.*, 2013, **15**, 10167–10180.

[27] J. Saini and K. S. Viswanathan, Discerning Near-Isoergic Isomers. A Matrix Isolation Infrared and ab Initio Study of the Propargyl Alcohol Dimers, *J. Phys. Chem. A*, 2017, **121**, 1448–1459.

[28] D. Mani and E. Arunan, Rotational spectra of propargyl alcohol dimer: A dimer bound with three different types of hydrogen bonds, *J. Chem. Phys.*, 2014, **141**, 164311.

[29] J. Thomas, X. Liu, W. Jäger and Y. Xu, Unusual H-Bond Topology and Bifurcated H-bonds in the 2-Fluoroethanol Trimer, *Angew. Chemie Int. Ed.*, 2015, **54**, 11711–11715.

[30] N. A. Seifert, J. Thomas, W. Jäger and Y. Xu, Rotational spectra and theoretical study of tetramers and trimers of 2-fluoroethanol: dramatic intermolecular compensation for intramolecular instability, *Phys. Chem. Chem. Phys.*, 2018, **20**, 27630–27637.

[31] T. B. Adler, N. Borho, M. Reiher and M. A. Suhm, Chirality-Induced Switch in Hydrogen-Bond Topology: Tetrameric Methyl Lactate Clusters in the Gas Phase, *Angew. Chemie Int. Ed.*, 2006, **45**, 3440–3445.

Chapter 4

Non-covalent interactions in sugar derivatives

Adapted from:

A. Camiruaga, I. Usabiaga, A. Insausti, I. León and J. A. Fernández, *Phys. Chem. Chem. Phys.*, 2017, 19, 12013-12021.

A. Camiruaga, I. Usabiaga, A. Insausti, E. J. Cocinero, I. León and J. A. Fernández, *Mol. BioSyst.*, 2017, 13, 1709-1712.

I. Usabiaga, A. Camiruaga, A. Insausti, P. Çarçabal, E. J. Cocinero, I. León and J. A. Fernández, *Front. Phys.*, 6:3.

4.1. Introduction

The objective of this chapter is to carry out an exhaustive experimental exploration of the potential energy surface for the non-covalent interactions of biologically-relevant sugars, in order to seed light into the molecular recognition processes in which they take part. For that purpose, using a reductionist approach, we reduce the interactions inside the target receptor to pairs of molecules that serve as model systems. The small size of these systems, enable a thorough exploration using mass-resolved excitation spectroscopy, while comparison with DFT calculations leads us to understand the conformational preferences of these systems.

To be able to use laser spectroscopy in the study of carbohydrates, introduction of a chromophore is required, because the sugar units do not present an excited electronic state that can be used as step stone during the REMPI process. Many of the systems presented in this chapter contain such modification (PhGlc or PhGal based complexes) linked to the anomeric oxygen (O1). Although the presence of the chromophore can introduce some differences in the behavior of the molecules, compared to the true biological model, many sugar derivatives also present glyosidic linkages with functional groups not very different from the chromophore we have introduced.

We reported in the past a study on β-phenyl-D-glucopyranoside/phenol dimer, as a model system of the interaction of a glucose unit with tyrosine[1], were we demonstrated the preference of phenol to interact with the hydroxymethyl group and the role of stacking interactions in the stabilization of the complex. Here, we continue with the exploration of several sugar complexes with different molecular systems, to increase the knowledge on the intermolecular interactions of sugars. The monosaccharides studied were D-glucopyranoside and D-galactopyranoside. versions of these sugars with a chromophore attached, β-phenyl-D-glucopyranoside and β-phenyl-D-galactopyranoside, allowed us to use mass-resolved excitation spectroscopy.

4.2. Modelling the interaction between glucose and a peptidic bond: the β-phenyl-D-glucopyranoside/N-methylacetamide model system

In addition to the interaction with the amino acid lateral chains, sugars also present interactions with the peptidic bonds. Most of the previous studies on the interactions of

monosaccharides explored the former, but to the best of our knowledge, there are no previous reports on the interaction between sugars and the NHCO motif of the peptidic bond, at least using MRES. To model such interactions, we have selected N-methylacetamide (mAct) as a model peptidic bond and glucose, as it is one of the most abundant monosaccharides.

From the experimental point of view, formation of the dimers of PhGlc/mAct present an added difficulty: while β-phenyl-D-glucopyranoside is a solid at room temperature, N-methylacetamide is a viscous solid (melting point 26ºC). Therefore, incorporation of mAct to the ablation matrix was not easy, and a different approach was necessary. After the normal deposition of the sample mixture (β-phenyl-D-glucopyranoside, Sigma Aldrich 98%, and carbon nanotubes) on the surface of the sample holder, several drops of N-methylacetamide (Sigma Aldrich, 98%) were deposited on the surface (see Chapter 2, section 2.1.3.2).

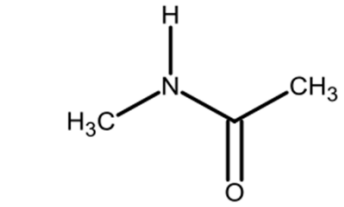

N-methylacetamide

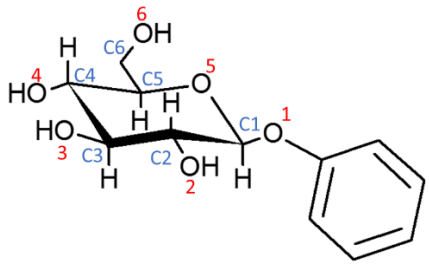

β-Phenyl-D-glucopyranoside

Figure 4.1: Structure of N-methylacetamide (mAct) and β-phenyl-D-glucopyranoside (PhGlc)

Figure 4.1. shows the structure of PhGlc and mAct monomers. Two potential HB interaction points can be identified in the amide group of mAct: the carbonyl group, which is a good proton acceptor, and the NH group, which can act as both proton donor and acceptor, although it predominantly plays the former role. In the case of glucose, the hydroxyl groups are involved in the formation of an intermolecular hydrogen bond network that extends through most part of the molecule.

The potential energy surface of PhGlc+mAct dimer was computationally explored. As explained above, the flexibility of the hydroxymethyl group of PhGlc and the abundance of docking sites in the sugar unit, resulted in a large number of possible structures for the dimer. On one hand, it is well known that three isomers of β-PhGlc have been detected in supersonic expansions, with different orientations of the O6H moiety[2]. On the other hand, mAct is a small molecule that contains both HB donor and acceptor groups, capable of interact in different binding sites of the glucose. Figure 4.2 shows the six most stable structures computed for the dimer, while the complete set of structures with their corresponding stability can be found in Figure A4.3 and Tables A4.1-A4.3.

The family that contains the largest number of conformations presents a strong O2H···O=C hydrogen bonds. Additionally, dispersive forces between NH group of mAct and the aromatic ring of PhGlc further stabilize the structures from this family (01, 02, 03 and 06, as depicted in Figure 4.2). Conformers 03 and 06 are very similar to 02, as they only differ in a small displacement in the relative position of both molecules. Thus, one can expect no significant isomerization barriers between these conformations and very likely, they will relax into the most stable structure during the cooling stage.

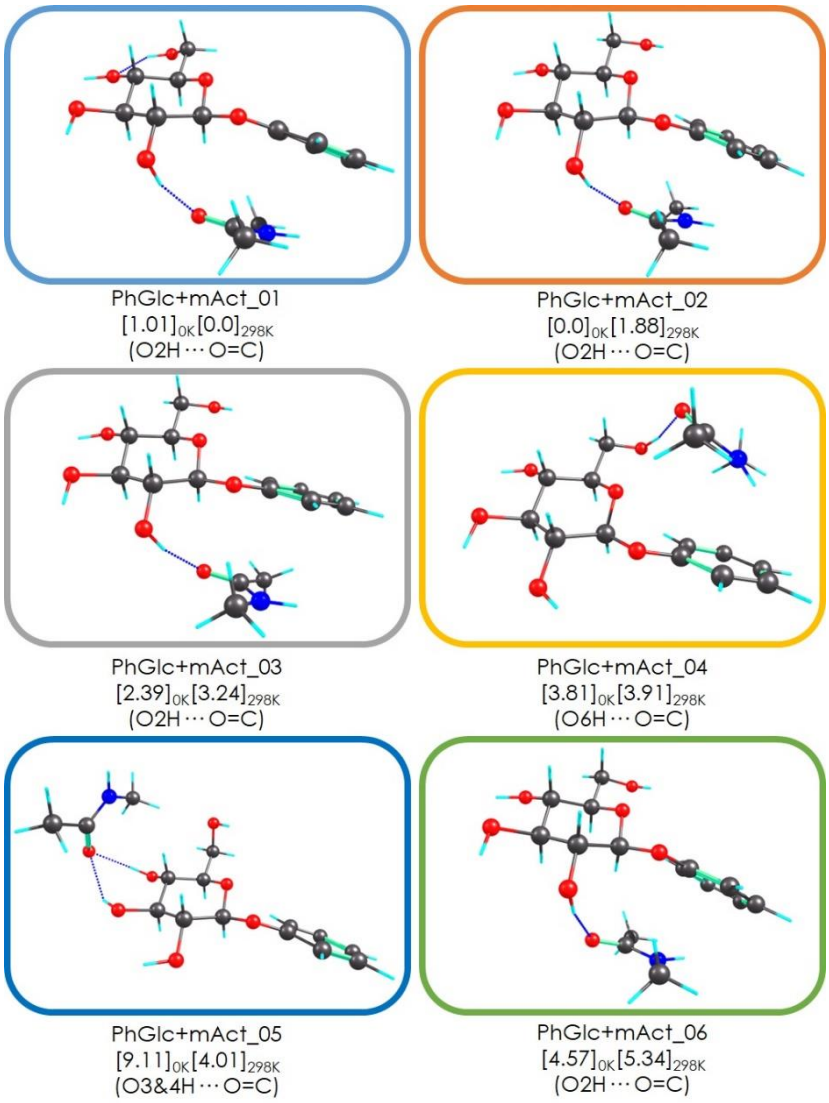

Figure 4.2: Most stable conformations found for PhGlc+mAct complex, computed at M06-2X/6-311++G(d,p) level. Relative energy values are given inside brackets in kJ/mol, at both 0 and 298 K. Energy values are ZPE and BSSE corrected.

Structures 01 and 02 are very close in energy and they present a change in the relative stability as the temperature of the system is increased. The main difference between these conformations is the position that the hydroxymethyl group (O6H) adopts. In other words, they are equivalent from an intermolecular point of view, and only differ in the conformation that the sugar unit adopts. It is already known that the isomerization barrier between the sugar conformations is high enough to isolate and detect both structures simultaneously[3]. As the thermal analysis of the cluster reveals (see appendix Figure A4.2), there is a clear change in the stability of conformers PhGlc+mAct_01 and PhGlc+mAct_02 at relatively low temperatures (~120K), evidencing that the extra

stabilization gained by the cooperative effect in sugar OH···O network is entropically favored. Those conformational temperatures are usually reached in supersonic expansions, pointing out that both conformers would be almost isoenergetic at experimental conditions. The rest of structures adopt different and less stable hydrogen bond configurations. For example, in structure PhGlc+mAct_04, the carbonyl group of mAct acts as proton acceptor from O6H instead of O2H; and in structure PhGlc+mAct_05, mAct inserts between oxygen atoms O3 and O4, strongly perturbing the cooperative hydrogen bond network of the monosaccharide. As a global observation, the peptide fragment presents always an interaction involving the carbonyl group (structures with NH group as proton donor are quite high in energy), making it the key interacting point.

Figure 4.3 shows a comparison between the REMPI spectra of PhGlc, PhGlc+mAct and phenol. PhGlc REMPI spectrum is in good agreement with previous publications by Talbot *et al.*[2] and Usabiaga *et al.*[1]. The molecule presents two flexible substituents: the hydroxymethyl group and the phenoxyl substituent, giving rise to different conformational isomers based on their relative orientation.

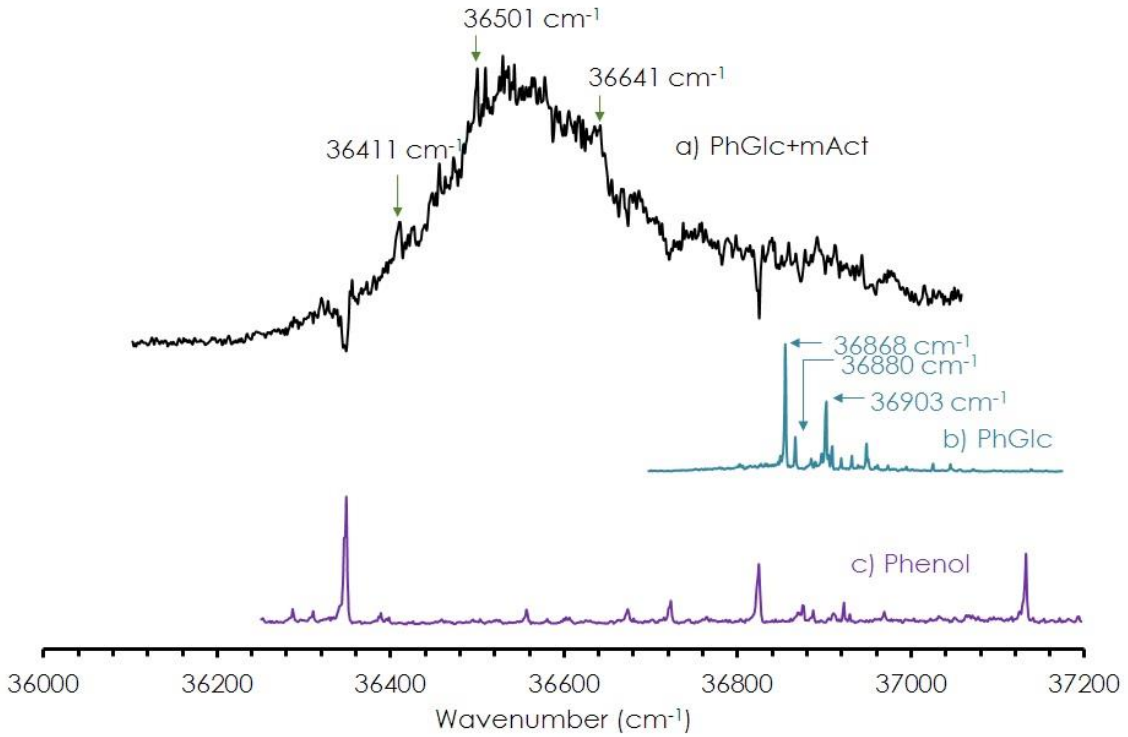

Figure 4.3: One-color REMPI spectra of a) PhGlc+mAct complex, b) PhGlc monomer and c) phenol.

The REMPI spectrum of the complex is significantly different from that of the monomer. It consists of a broad absorption, whose origin is red-shifted from the monomer by

about 500 cm^{-1}. The two dips in the spectrum correspond to the strong absorption of phenol molecule in the jet (36349 and 36824 cm^{-1}), which appears as a by-product of PhGlc photodissociation. As phenol arrives earlier to the detector and produces such a strong signal, it somehow "blinds" the detector, which shows a reduced sensibility towards the ions of PhGlc+mAct dimer. The peaks marked in the REMPI spectrum of PhGlc+mAct were used to record IDIRS double resonance experiments, as they could denote the presence of several isomers. However, the same IR spectrum was always obtained.

After the exploration of the conformational landscape, the spectra from the most stable structures were simulated and compared with the experimental IDIR spectrum (see Figure 4.4). Two bands appear at the blue-end of the spectrum, at 3612 and 3630 cm^{-1}, which come from the sugar's OH groups involved in the cooperative HB network. There is another narrow band at 3490 cm^{-1} built on top of a broad absorption that goes from 3250-3450 cm^{-1}. Finally, some discrete features arise at the CH region.

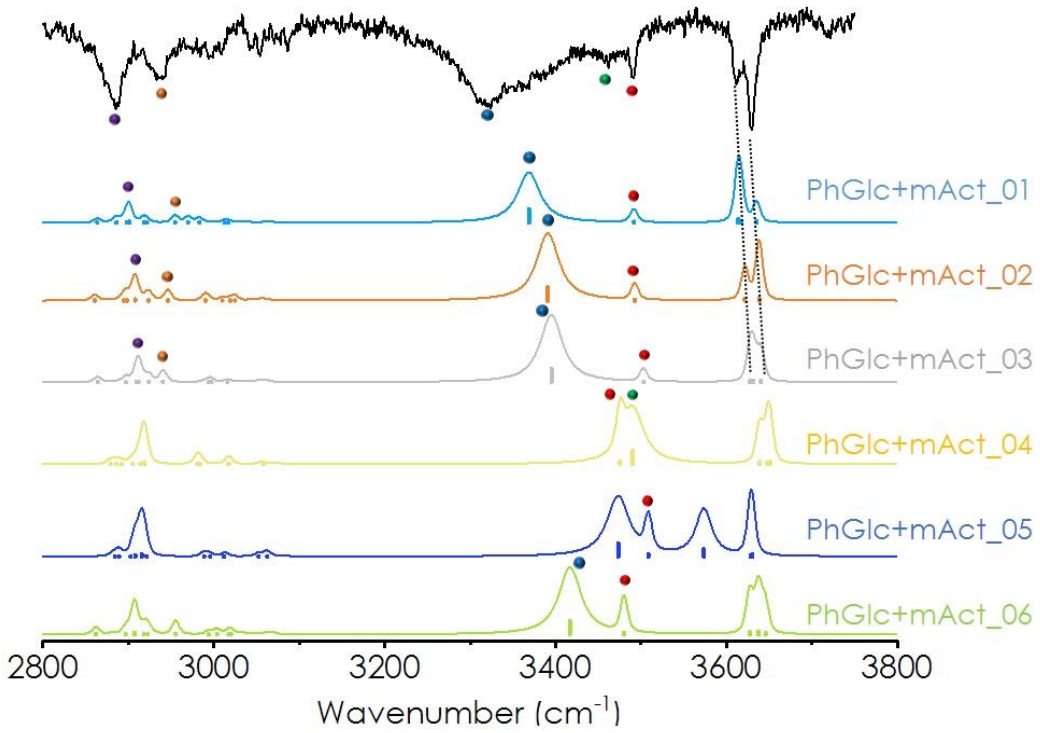

Figure 4.4: IDIR spectrum of PhGlc+mAct compared to the predicted spectra of the six most stable conformations of the cluster, calculated at M06-2X/6-311++G(d,p). The experimental spectrum was obtained probing the transition at 36480 cm^{-1}. To account for the anharmonicity a correction factor of 0.939 was employed for OH groups, and 0.953 for NH/CH groups. Colored balls are used to highlight possible assignments.

A first comparison between the simulated spectra and the experimental one advances that no single conformer explains all the observed bands. Conformers 01, 02, 03 (also 06) well reproduce the almost unperturbed OH stretching of the glucose and the weak NH···π interaction around 3490 cm^{-1}. Additionally, the broad absorption at 3350 cm^{-1}, which would correspond to the formation of the strong O2H···O=C hydrogen bond, is predicted to be to the red of the actual position, which means that it is stronger than predicted. The strong anharmonicity that transforms the vibronic transition into a broad absorption is connected to the strength of the hydrogen bond formed. None of the structures belonging to the O2H···O=C family explain the broad absorption close to the free NH band (green ball in the figure). However, the computed spectrum of structure PhGlc+mAct_04 presents a band that matches with that absorption, as the O6H···O=C hydrogen bond is weaker, and thus, it does not appear as red-shifted as the O2H···O=C one. Structure 05 can be discarded, as its predicted spectrum is very different from the experimental one.

Figure 4.5 summarizes the assigned structures for PhGlc+mAct complex. Conformers 01 and 02 are almost isoenergetic and are stabilized by an O2H···O=C hydrogen bond. They only differ in the orientation of the O6H group, whose isomerization barrier is high enough to allow both species to be present in the expansion. The rest of structures inside this family lie very close in energy, possibly connected by low interconversion barriers, as the only difference is the relative position of mAct stacked below the aromatic ring. The other observed conformer, 04, shows the peptide fragment interacting with the hydroxymethyl group, additionally stabilized by dispersive forces between the NH group and the phenolic ring. It is interesting how the peptide fragment shows a clear preference to interact either with the O2H or O6H hydroxyl groups and with the aromatic ring at the same time, leaving O3H and O4H unperturbed for future interactions. More details on this study can be found in the already published article[4].

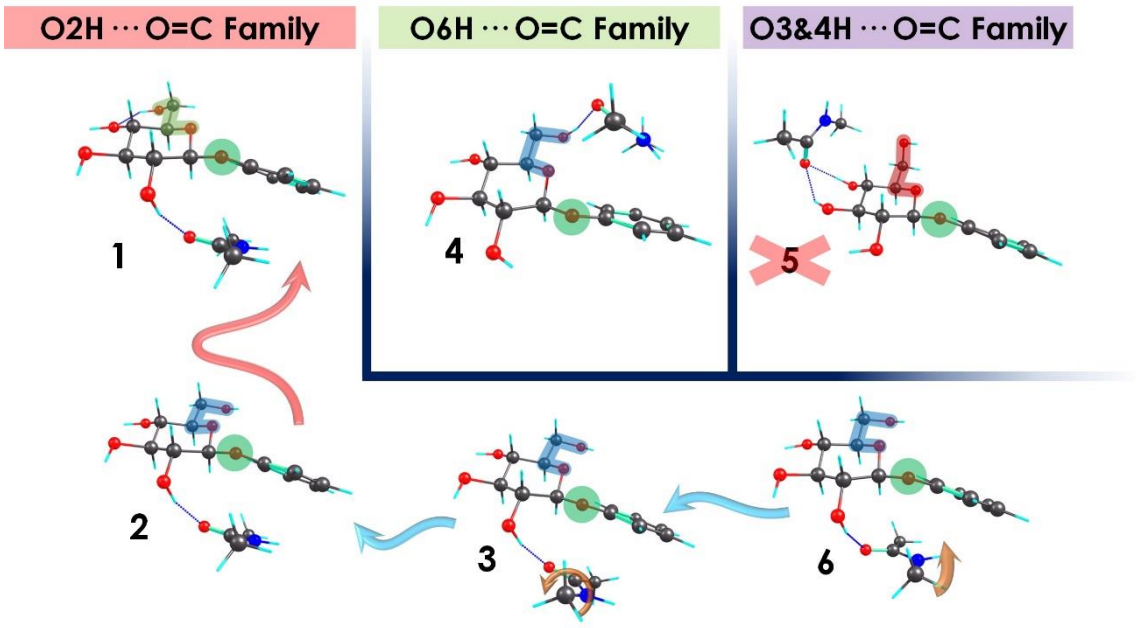

Figure 4.5: Assigned structures of PhGlc+mAct complex, classified by the interaction families. Possible interconversion barriers are depicted as blue arrows, whereas the red arrow represents the isomerization barrier between different PhGlc O6H group conformations.

4.3. Hydrogen bond competition in phenolic derivatives: glucose – paracetamol complexes

The above-described study of N-methylacetamide complexes showed a competition towards the formation of a stable hydrogen bond with a relatively small molecule. Moreover, an additional stabilization with dispersive forces was observed in the assigned structures, highlighting the importance of the aromatic ring in the anomeric carbon. In order to test the influence of the aromatic ring in more complex molecules containing several interaction points, the interaction between β-PhGlc and β-MeGlc with paracetamol (4'-hydroxyacetanilide) was explored. Furthermore, the results from these two system, along with those obtained in section 4.2, were compared with the previously published results from phenol-sugar complexes, to give a more general view of the interaction preferences in these systems.

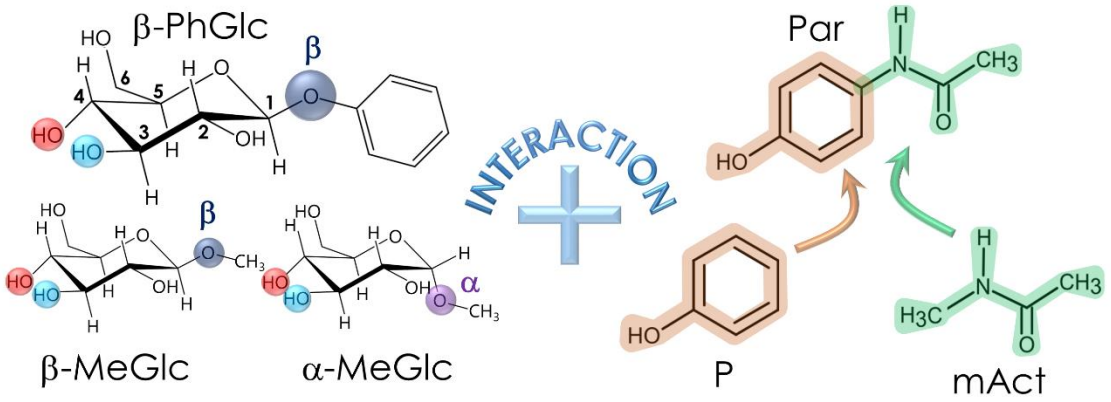

Figure 4.6: Scheme of the systems studied in this section: β-PhGlc, phenyl-β-D-glucopyranose; β-MeGlc, methyl-β-D-glucopyranose; α-MeGlc, methyl-α-D-glucopyranose; Par, paracetamol; P, phenol; and mAct, N-methylacetamide.

Figure 4.6 shows the molecules studied in this section. Paracetamol is a phenol derivative with an amide substituent in *para* position that resembles the previously studied mAct. This substituent gives phenol additional interaction sites and enlarges the molecule, giving a different perspective for this study.

To obtain an overall view of all the possible interactions inside these systems, a large number of calculations were carried out to locate all the relevant minima in the potential energy surface (PES). Figure 4.7 shows the six most stable structures of both PhGlc+Par and MeGlc+Par complexes. Due to relatively big size of Par and its aromatic ring, one would expect a close contact between the two molecules in a stacked position. In the most stable structures of PhGlc+Par (01 and 02), O6H and O2H hydroxyl groups interact with Par (O_{Par}H···O6H and O2H····O=C bonds). The dimer is further stabilized by CH···π interactions. Furthermore, the calculations show that these structures are also the entropically most stable ones in a wide temperature range (see Figure A4.5). the rest of the structures present different orientations of both molecules, but in most of them the O2H···O=C interaction is present.

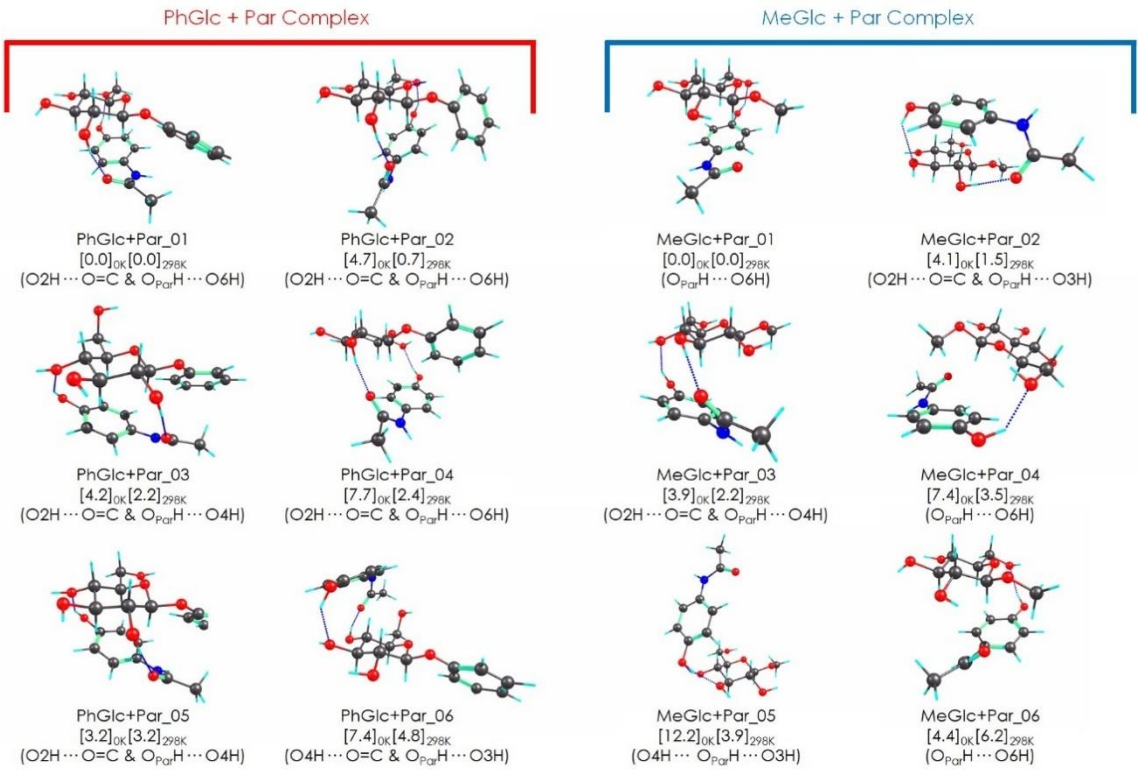

Figure 4.7: Six most stable conformations found for PhGlc+Par and MeGlc+Par, computed at M06-2X/6-311++G(d,p) level. Relative energy values are given inside brackets in kJ/mol, at both 0 and 298 K. Energy values are ZPE and BSSE corrected. Energy order of the structures was shorted according to their relative energy at 298 K.

The situation changed when PhGlc was replaced by MeGlc. In that case, an enhanced competition between different hydrogen bonds was revealed in the conformational landscape. On the one hand, MeGlc+Par_01 present a single hydrogen bond between the paracetamol's hydroxyl group and the O6H group of MeGlc ($O_{Par}H\cdots O6H$). The absence of the aromatic ring in O1 avoids establishing dispersive interactions between the π electronic clouds around the aromatic rings of both molecules. This pushed Par to arrange in a direct stacked position below the sugar, stabilizing the complex with CH···π interactions. This structural arrangement prevented O2H group of the sugar to from hydrogen bonds with the carbonyl group of Par in most of the presented structures.

On the other hand, in the family composed by structure MeGlc+Par_02 and MeGlc+Par_03, two new HB networks are formed. In structure 02, O2H interacts with the C=O group of paracetamol, and the paracetamol hydroxyl group interacts with the O3H. However, in structure 03, the hydrogen bonds involve O3H and O4H groups. Moreover, the cluster is further stabilized by CH···π interactions between the sugar and paracetamol's ring. The calculations show that, in fact, these structures become more stable at higher temperatures (~298 K) (see Figure A4.5), pointing out that the newly

formed intramolecular HB network is entropically favored. More information on the theoretical results can be found in Appendix 4, or in the already published article[5].

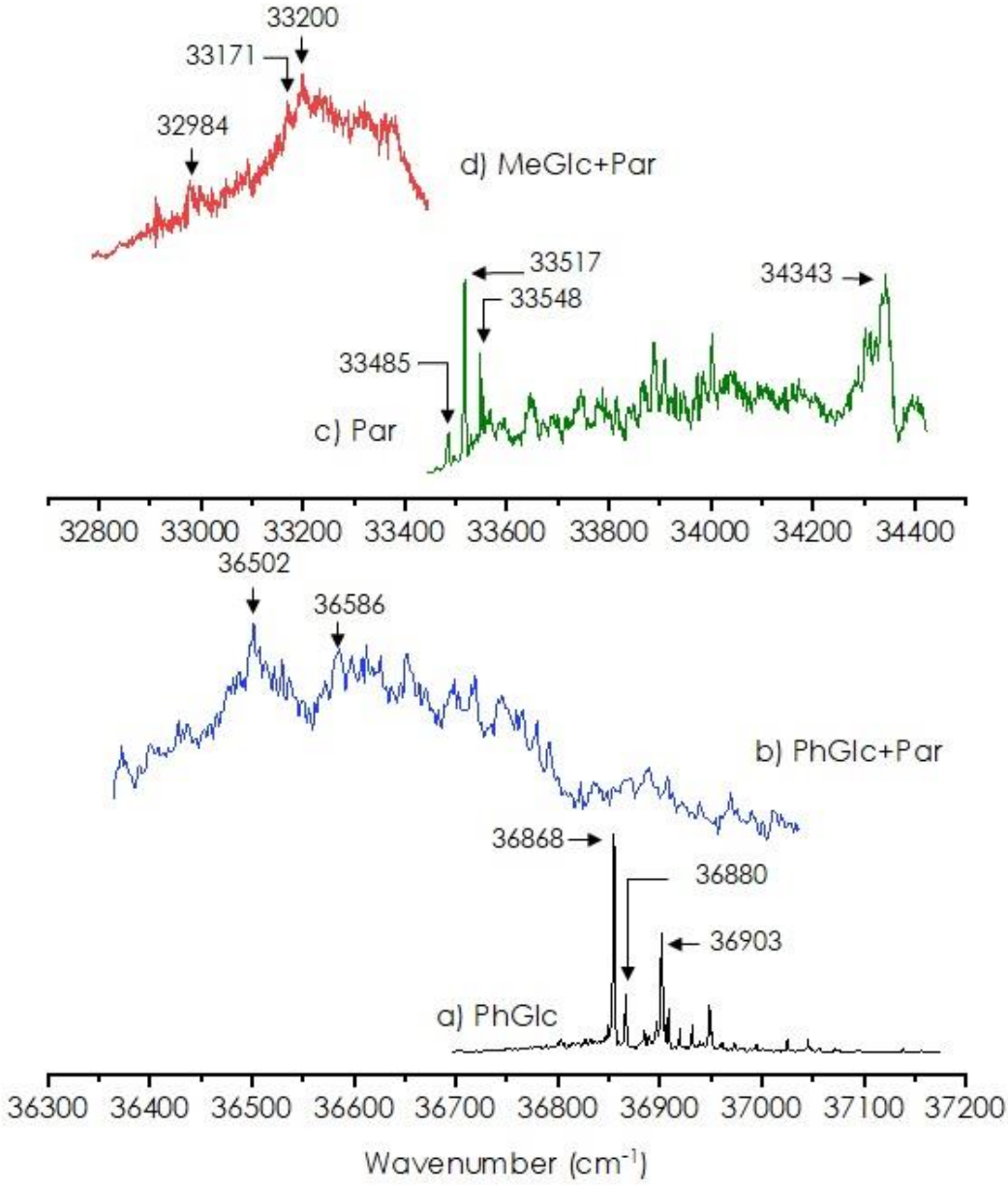

Figure 4.8: One-color REMPI spectra of a) β-phenyl-D-glucopyranoside, b) PhGlc+Par dimer, c) Paracetamol and d) MeGlc+Par dimer. The phenyl chromophore of β-phenyl-D-glucopyranoside was employed to excite PhGlc+Par complex, and paracetamol in the case of MeGlc+Par complex.

Figure 4.8 shows the REMPI spectra of PhGlc+Par and MeGlc+Par complexes, compared to those of PhGlc and Par monomers. As observed for most of the sugar complexes studied with mass-resolved laser spectroscopy, both spectra are structureless absorptions, in contrast with the electronic absorption spectrum of the monomers.

Electronic transitions observed in Par REMPI spectrum are in good agreement with previous studies:[6,7] but the reproduced spectrum present a broad background (which intensity is increased as it goes to the blue), probably coming from fragmentation of larger cluster or from an excess in the ionization energy.

Both PhGlc and Par molecules can act as chromophores for the REMPI process. In the case of MeGlc+Par, the chromophore used was the paracetamol ring, and therefore, it required of photons with a longer wavelength. In the case of PhGlc+Par, the REMPI spectrum was recorded using the Ph chromophore attached to the sugar, as it produced a stronger signal, and because, in this way, a direct comparison with the spectrum of PhGlc+mAct (see Figure 4.1.) can be carried out. Nevertheless, in both cases, the spectra presented an unresolved vibronic structure. Several wavelengths were proved over the broad absorptions, but in both PhGlc+Par and MeGlc+Par cases no different isomers were detected.

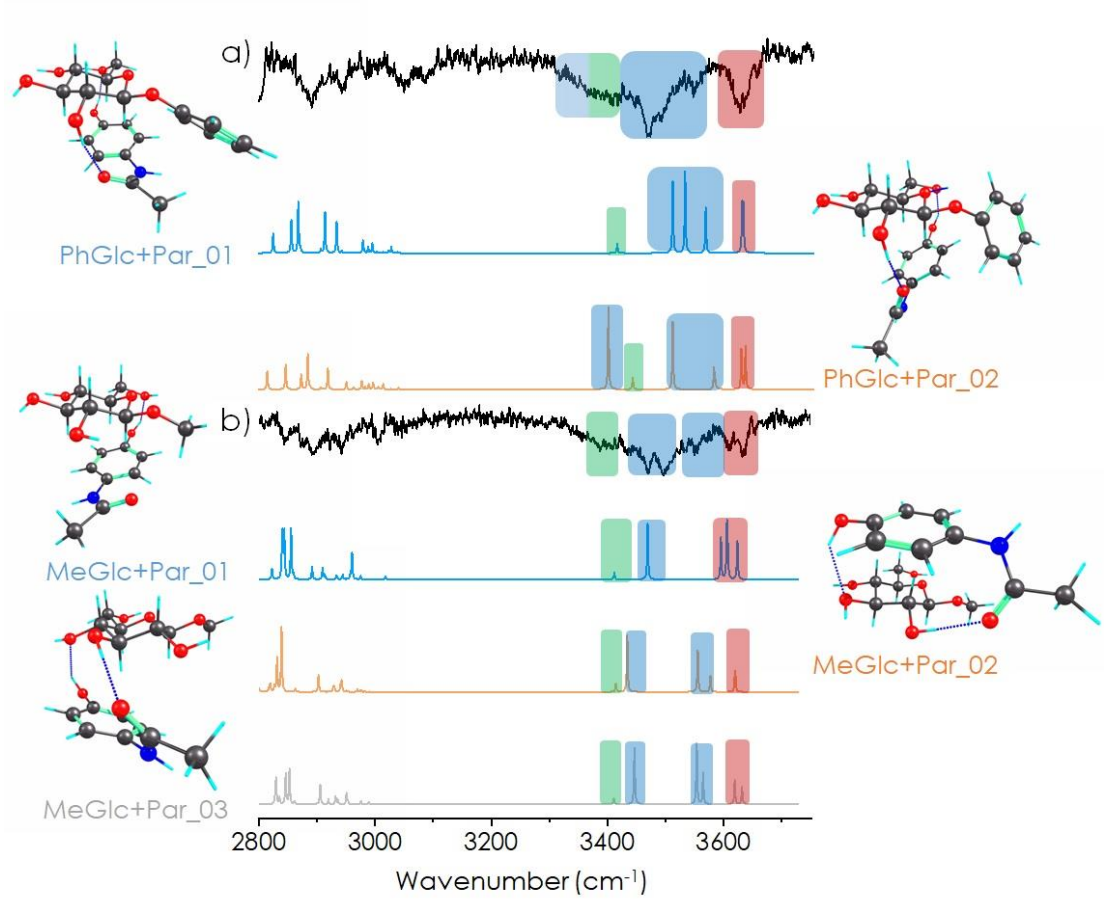

Figure 4.9: IDIR spectrum of a) PhGlc+Par and b) MeGlc+Par compared to theoretical spectra of their most stable structures, computed at M06-2X/6-311++G(d,p). A correction factor of 0.939 and 0.953 was used to account for the anharmonicity of OH/CH and NH groups, respectively. Color blocks are used as an eye guide: red color indicates free OH stretches, blue color bonded OH stretches and green color NH group stretches.

Figure 4.9 shows the comparison between the experimental and theoretical IR spectra of PhGlc+Par and MeGlc+Par complexes. In both systems, the experimental traces present some similarities: the free OH stretching of glucose are grouped around 3620 cm^{-1}, and the vibrational bands of those OH groups involved in a HB appear over a broad background between 3300-3500 cm^{-1}. Due to its low intensity compared to the absorption of OH bands, the free NH band of Par it is hidden by the broad absorption of the bonded bands. On top of such absorption, some transitions are visible, although the complexity of the spectrum and the abundance of bands makes the assignment tentative.

A first comparison with the theoretical predictions of the most stable isomers of each complex shows that none of the predicted spectrum for the computed structures can explain the experimental bands. In the case of PhGlc+Par, the most stable structure (PhGlc+Par_01) well reproduces the overall experimental spectrum. However, the prediction for the second most stable structure (PhGlc+Par_02) would explain the appearance of the most red-shifted OH band around 3400 cm^{-1}. As they are basically the same isomer, but with different orientation of the paracetamol respect to PhGlc and they are very close in energy, is highly probable to find both isomers populated under our experimental conditions.

For MeGlc+Par dimer, the combination of the three most stable isomers well reproduces the overall experimental trace. Structure MeGlc+Par_01 not only reproduces the free OH band, but also one of the most intense transition built over the broad absorption (~3500 cm^{-1}), which can be assigned to the strong $O_{Par}H\cdots O6H$ interaction. The resto of the bands, especially the group of free OH and the broad absorption, can be explained with structures MeGlc+Par_02 and MeGlc+Par_03. These latter structures present different interactions, where paracetamol's hydroxyl group is acting as a donor to O4H and O3H, respectively. Besides, the C=O group of Par is acts as a proton acceptor, as observed in PhGlc+Par.

Finally, a comparison with the previously studied complexes is mandatory. Figure 4.10 summarizes the assigned structures for paracetamol complexes studied in this section and previously mentioned PhGlc+mAct dimer. Additionally, results from recent studies on PhGlc+P complexes[1,3] were also included in order to compare its interaction preferences with the ones observed in paracetamol clusters.

Two different interactions were detected in PhGlc+mAct complex. None of these structures showed an interaction with O3H and O4H moieties of the sugar, highlighting

a preference of the peptide fragment to interact with O6H and O2H groups. Besides, extensive dispersive interaction with the π electronic cloud of PhGlc aromatic ring add extra stability to the complex.

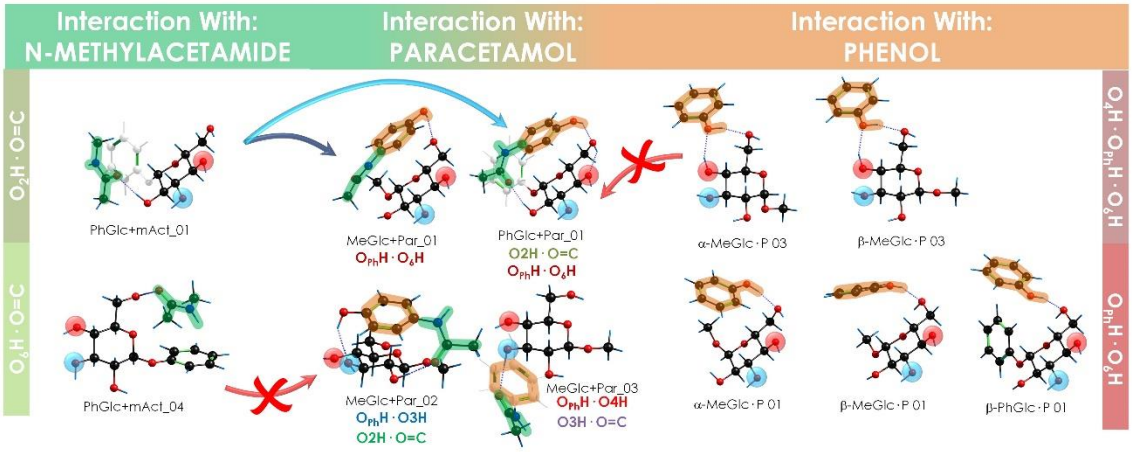

Figure 4.10: Assigned structures of different glucose complexes studied in this work.

Phenol gives rise to a completely different set of interactions compared to mAct, because the former is an aromatic ring with a hydroxyl group, while the latter has NH and C=O groups as spots to establish intermolecular interactions. The results were revealing: PhGlc+P produced only structures where both aromatic rings interact together, with the phenolic hydroxyl group attached at the O6H position (PhGlc+P_01). Other structures with hydrogen bonds set in different positions where predicted higher in energy and, accordingly, they were not found in the experiments. Surprisingly, the substitution of the aromatic ring in O1 position by a methyl group resulted in a competition between conformers similar to the ones with PhGlc, and additional ones were the phenolic OH group acted as proton acceptor from the O4H moiety. This is true for both α-MeGlc and β-MeGlc complexes with phenol.

It is interesting that a similar behavior to the above-described interactions was observed for paracetamol clusters. While the carbonyl group of the amide part is accepting the O2H protons (as in mAct), the interaction of the phenolic hydroxyl group with O6H predominated compared to the rest of the free OHs of the sugar. Once more, removing the aromatic ring from the sugar resulted in a competition of interactions, where $O_{Par}H\cdots O6H$ is not the preferred interaction. Hence, dispersive forces involving the aromatic rings play an important role in the interactions formed, favoring the interacting with the O6H and O2H groups of the sugar.

4.4. β-Phenyl-D-glucopyranoside and β-phenyl-D-galactopyranoside dimers: small structural differences but very different interactions

The studies presented in the sections above highlighted the aggregation preferences of glucose derivatives with other small molecules. Examination of the dimers formed by the sugar derivative with different partners led us to conclude that there is a strong preference towards interacting with the O6H and O2H hydroxyl groups. We will explore here the impact that a modification in the sugar has in the aggregation preferences.

Previously published works on glucose dimers[3,8] showed that the anomeric conformation of glucose bound to a voluminous group is transmitted through the whole molecule due to the formation of a cooperative hydrogen bond network that involves interactions between all the hydroxyl groups. Thus, the intramolecular hydrogen bonds act as an amplifier of the changes in the orientation of the anomeric substituent, which is at one of the ends of the network. Here, we explore if such mechanism also plays a role when the modification takes place in a different carbon atom, by forming the homodimers of glucose and galactose derivatives. These two monosaccharides, depicted in Figure 4.11, differ in the position of the hydroxyl in carbon 4, which is in the equatorial position in glucose and in the axial position in galactose.

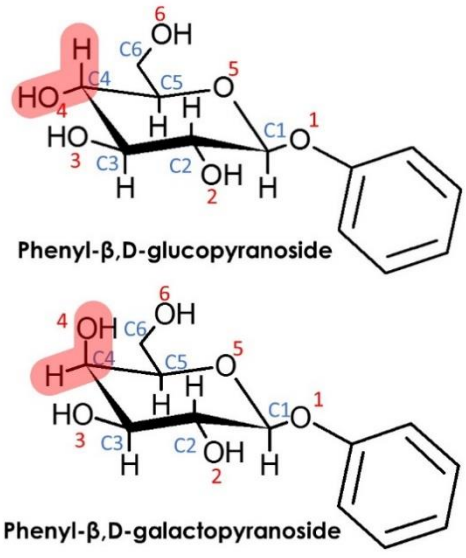

Figure 4.11: β-Phenyl-D-glucopyranoside and β-phenyl-D-galactopyranoside molecules. The position of the O4H group is highlighted in red.

The spectroscopy of β-PhGal and the previously shown β-PhGlc was first characterized by Simons and coworkers.[2,9] They concluded that the conformational landscape of β-

PhGlc presents three stable isomers at the conditions of the molecular expansion. These structures are collected in Figure 4.12 and show that the structural differences between them lie in the orientation of the hydroxymethyl group.

Likewise, β-PhGal also presents several conformers with the global minimum being very similar in both systems. On the other hand, the effect of the epimerization at C_4 is already present by changing the conformational energetic ordering: for example, β-PhGal-02 is of the same type as β-PhGlc-03 but it is relatively more stable in β-PhGal.

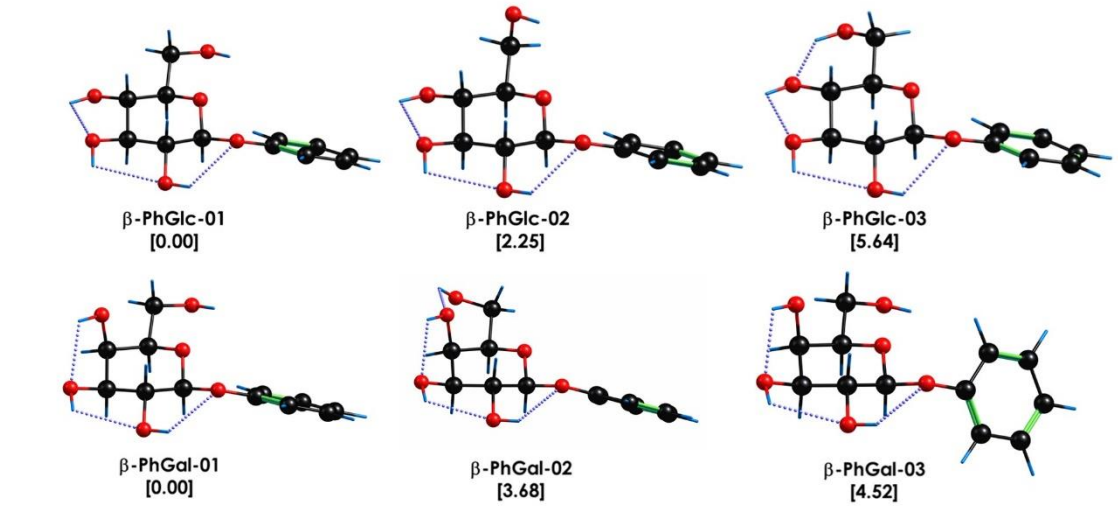

Figure 4.12: Most stable conformational isomers of β-PhGlc and β-PhGal, together with their relative stability in kJ/mol computed at M06-2X/6-311++G(d,p).

Although PhGlc and PhGal monomers were accurately characterized, dimers resulted to be a very challenging system from the experimental point of view. Figure 4.13 shows the REMPI spectrum of the homodimers. Their formation resulted in broad absorptions, as expected for such complicated systems. However, no strong shift in the electronic absorption was observed, pointing to similar aggregation energies in the two electronic states implicated in the transition. The absence of discrete transition in the electronic spectra complicates the study, as it hampers the use of double resonance techniques (UV/UV Hole Burning) to unveil the presence of several conformational isomers of each aggregate. Instead, the broad absorptions were probed with the UV laser to record IDIR spectra, looking for changes in the shape of the IR spectrum.

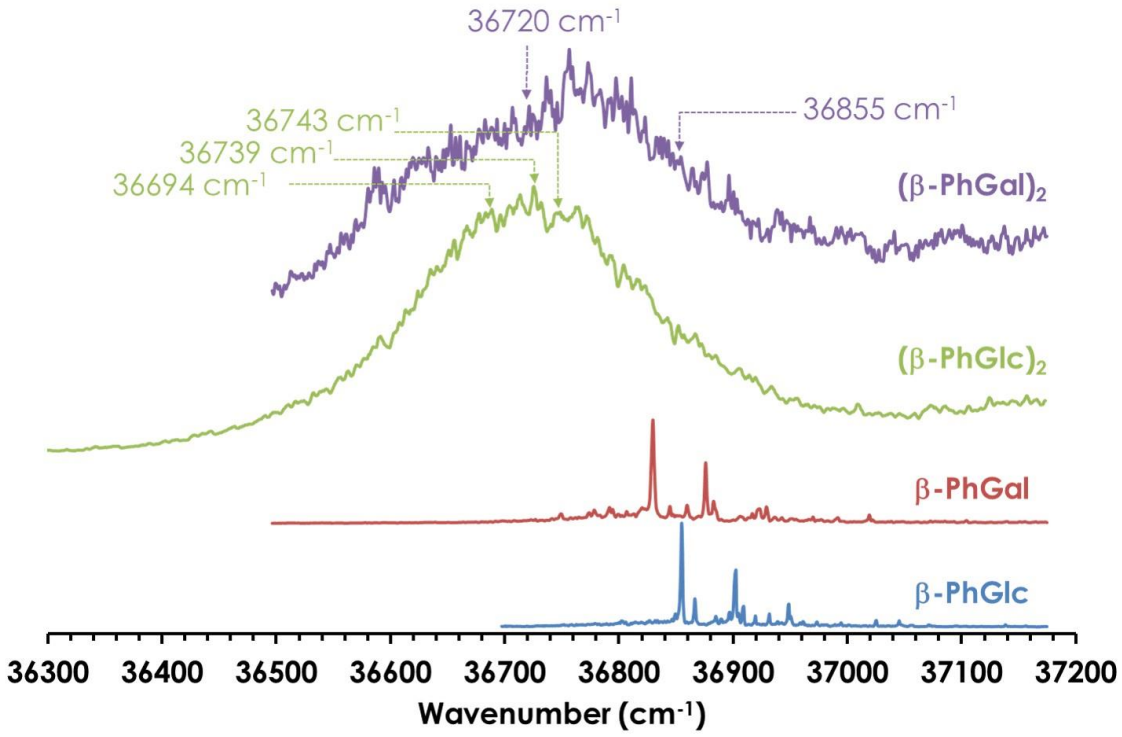

Figure 4.13: One-color REMPI spectra of β-PhGlc, β-PhGal, $(\beta\text{-PhGlc})_2$ and $(\beta\text{-PhGal})_2$ systems. The arrows indicate the wavelengths probed to record the IR spectra.

Figure 4.14 shows the experimental IR spectra for both PhGlc and PhGal dimers, compared to the predictions from structure minima. As we can observe from $PhGlc_2$ (Figure 4.14a), different IR spectra were recorded tuning the UV laser at 36694, 34739 and 36743 cm^{-1}. The shape of the IR spectrum changes depending on the wavenumber probed by the UV laser, indicating that at least two different isomers contribute to the REMPI spectrum. There are some key regions in the spectrum which give powerful structural information: the bands around _3650 cm^{-1} are due to the stretches of the OH moieties with weak interactions (probably only intramolecular interactions). The peak shifts to the red as the interaction of the involved. group gets stronger. Thus, the bands between 3450 and 3550 cm^{-1} are due to the stretching modes of those OHs involved in moderate-strong interactions. Finally, those peaks in the 2850 - 3100 cm^{-1} interval are due to the CH stretching modes

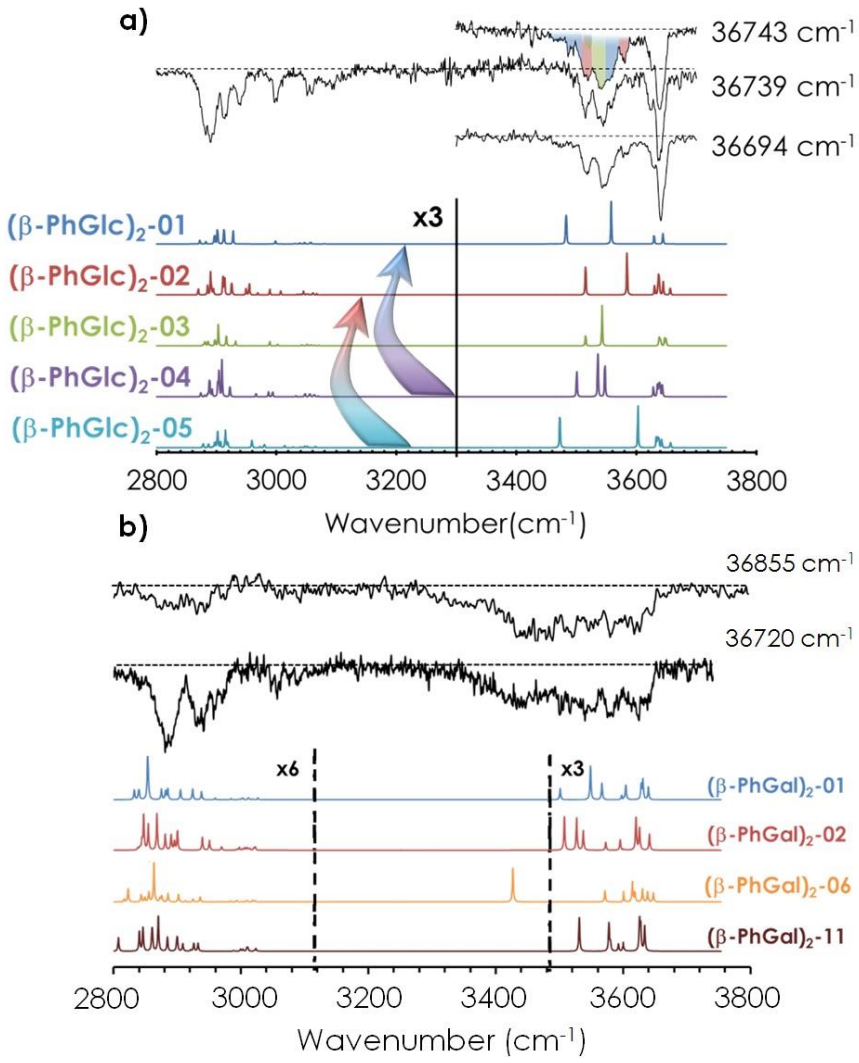

Figure 4.14: Comparison between the IDIR spectra of a) (β-PhGlc)$_2$ and b) (β-PhGal)$_2$ and the predicted spectra for the most stable structures, computed at M06-2X/6-311++G(d,p). To account for the anharmonicity a correction factor of 0.939 was employed for OH groups, and 0.953 for NH/CH groups. Arrows highlight possible isomerization pathways of less favorable isomers into deeper minima. The dashed line indicates the baseline.

As expected for β-PhGlc dimer, the number of shoulders in the observed bands is larger than the number of bands that a single isomer predicts, confirming that several conformational isomers were formed in the expansion. The two most stable isomers are required at least to reproduce the experimental trace, but the presence of the third most stable structure cannot be easily discarded, as its simulated spectrum is close to that of (β-PhGlc)$_2$-01. Other structures are energetically very high and are not expected to be populated enough or they can isomerize into the most stable structures.

In the case of (β-PhGal)$_2$, the spectroscopy is significantly more complex (see Figure 4.14b): instead of the presence of bands and shoulders, the OH stretches group into a

single, unstructured absorption that extends through the 3400-3650 cm^{-1} region. Comparison with the computational predictions explains the apparent lack of structure of the spectrum: against what was observed for $(\beta\text{-PhGlc})_2$, the OH stretches of the spectra predicted for the different $(\beta\text{-PhGal})_2$ isomers are spread along approximately the same region that in the experimental trace. Assuming that more than one isomer is contributing to the experimental trace, the computed spectra would be in good agreement with the experimental spectrum. In this case, it is only possible to estimate a lower limit for the number of isomers formed: no single conformer is able to solely reproduce the whole absorption in the 3400-3650 cm^{-1} region and therefore at least two species would be required to build the experimental spectrum, but the presence of additional species cannot be ruled out.

The study of relative Gibbs free energy diagrams for the computed species (see Figure 4.15) provide more evidences for the assignment proposed. The assigned structures for $(\beta\text{-PhGlc})_2$ are almost isoenergetic at the temperature window reached in the jet (around 150-200K), and relative binding Gibbs free energy also shows that isomers $(\beta\text{-PhGlc})_2$-01 and $(\beta\text{-PhGlc})_2$-02 are the most tightly bound. Altogether, one would expect to have mainly isomers $(\beta\text{-PhGlc})_2$-01 and $(\beta\text{-PhGlc})_2$-02 in the molecular expansion, in good agreement with the experimental results shows in Figure 4.15. The most relevant structures are represented in Figure 4.16.

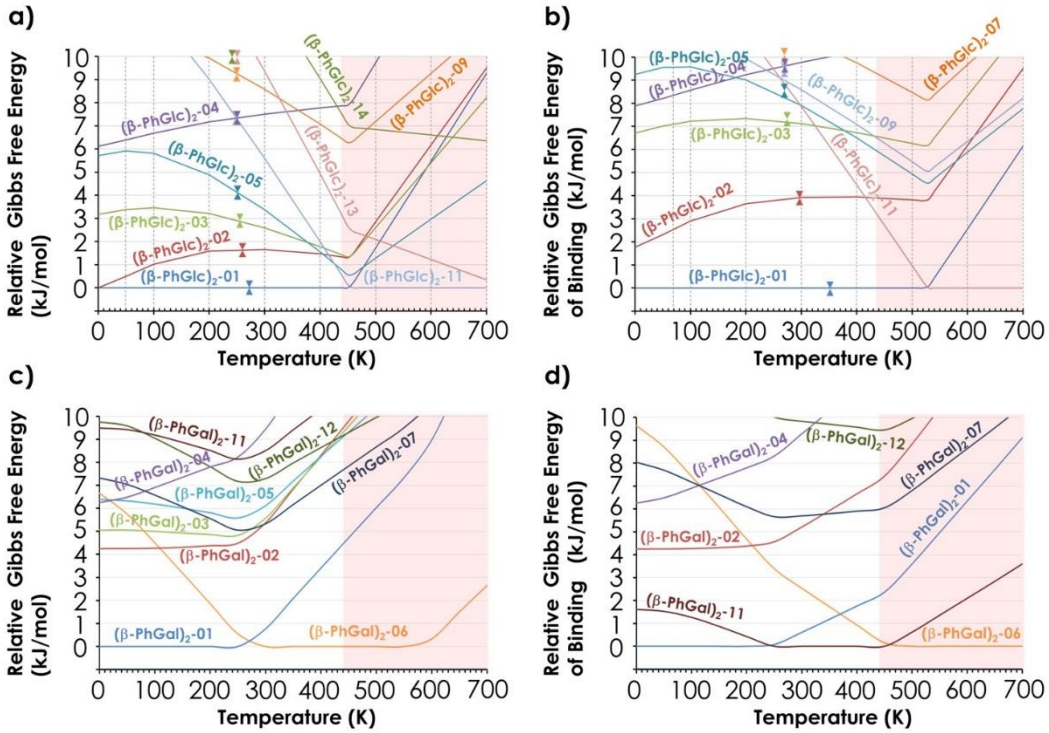

Figure 4.15: a) Relative Gibbs free energy of the 10 most stable (β-PhGlc)$_2$ computed species; b) Relative binding Gibbs free energy of the same species; c) Relative Gibbs free energy of the 10 most stable (β-PhGal)$_2$ computed species; d) Relative binding Gibbs free energy of the same species. All values are in kJ/mol and obtained from the structures computed at the M06-2X/6-311++G(d,p) level.

Regarding (β-PhGal)$_2$, the energetic situation is more interesting: (β-PhGal)$_2$-06 structure is entropically the most favored one, becoming close to the global minimum ((β-PhGal)$_2$-01) at the temperature of the beam. The presence of both isomers also explains all the features in the IR spectrum conforming the detection of these two conformers.

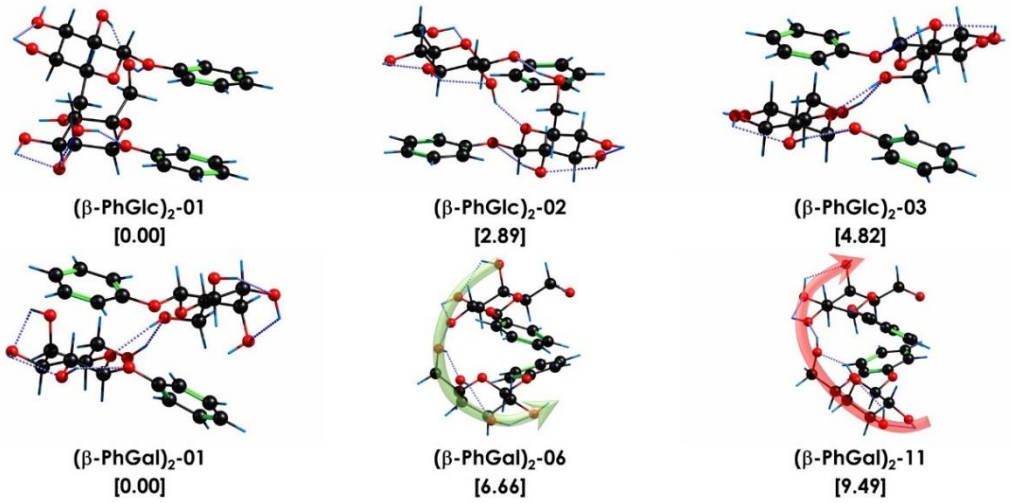

Figure 4.16: Assigned structures of (β-PhGlc)$_2$ and (β-PhGal)$_2$.

Besides, when the binding Gibbs free energy is taken into account, conformer (β-PhGal)$_2$-11 comes also into play, presenting a binding energy very similar to the global minimum. Actually, both conformers, (β-PhGal)$_2$-06 and (β-PhGal)$_2$-11, present very similar structures (see Figure 4.16), and the only difference between them is the orientation of the hydrogen bond network, that points in the opposite direction in conformer (β-PhGal)$_2$-11. In principle, the abundance of the monomer's conformer upon which the complex is based must be very small and it is unlikely that the aggregation energy can produce the isomerization into the least stable isomer and therefore, we can rule out the presence of isomer (β-PhGal)$_2$-11 in the expansion.

Previous studies concluded that the β anomer of glucose and its derivatives (methyl/phenyl-β-D-glucopyranoside) form very stable aggregates with the β anomer of other glucose derivatives, due to their ability to adopt symmetric structures, in which the hydroxymethyl group of each molecule integrates in the hydrogen bond network of the interaction partner. This same pattern can be also observed in the most stable structure assigned for (β-PhGlc)$_2$, which presents the two aromatic rings stacked and the glucose units interacting with each other. However, the structure of the rest of the isomers detected in the expansion breaks the mentioned symmetry. (β-PhGlc)$_2$-02 and (β-PhGlc)$_2$-03 also present stacked configurations, but the sugar units interact with the aromatic ring of the partner molecule. Therefore, the preferences of β anomers of glucose for forming the symmetric aggregates is lost in a great manner and we are able to observe at least one representative structure of each configuration.

The conformational landscape for galactose dimers is very different, as all the observed isomers are of the sugar-ring interaction type. Additionally, the structures assigned present extensive hydrogen bond networks, like the ones visible in (β-PhGal)$_2$-06. The global minimum of (β-PhGal)$_2$ is very similar to the third structure of glucose dimer, but the enantiomeric difference in the O4H group makes those structures more favorable due to an extra OH···π interaction which further stabilized the dimer. In the second structure of (β-PhGal)$_2$ detected, all the OH moieties but one are involved in a single network that jumps from one molecule to the other, resembling a spiral stairway. The (β-PhGal)$_2$ structures show an arrangement more based on intermolecular interactions, while (β-PhGlc)$_2$ structures are more based on intramolecular interactions with few intermolecular interactions. Another relevant information is that the binding energy of all three isomers of (β-PhGal)$_2$ presented in Figure 4.16 is a ~10% higher than for the (β-PhGlc)$_2$ species.

Concluding this study, the above results confirm the importance of the epimerization[10,11]. Several isomers were detected for each dimer. In the case of (β-PhGlc)$_2$, the most stable conformers show a competition between those structures with ring-ring/sugar-sugar interactions and those with sugar-ring interactions. Conversely, structures with just sugar-ring interactions where observed for (β-PhGal)$_2$. As a general trend, glucose dimers show arrangements more based in intermolecular interactions, while in galactose dimers the intramolecular interactions seems to govern the aggregation between species. Moreover, the computed binding energies of β-phenyl-D-galactopyranoside dimers are ~%10 higher than those of of β-phenyl-D-glucopyranoside dimers, confirming that the effect of the C_4 epimerization is amplified in the conformational behavior of the complexes. It is curious how a small difference between very similar molecules manifest a change in the interactions preference. This new information reinforces the idea that small structural changes between sugar units are amplified by formation of intra and intermolecular hydrogen bond networks that help other molecules (proteins, receptors) to easily read the sugar code of glycans.

4.5. The caffeine+phenyl-β,D-glucopyranoside molecular complex and its similarity with the interaction in A_{2A} receptor

In this section, we present an interesting example of how, despite the important differences between the environment in jets and that in biological systems, a perfect match between both situations is possible when particularly strong interactions are established. This situation takes place in the dimer between caffeine and β-phenyl-D-glucopyranoside.

Caffeine (Caf hereafter), is the fully methylated version of xanthine. Structurally rigid and planar, it is able to establish very stable stacking interactions, and due to its similarity to purine RNA/DNA bases, it can interfere with the metabolic system[12]. This molecule acts as a non-selective antagonist of the human adenosine receptor (A_1, A_{2A}, A_{2B} and A_3). Inside the orthosteric binding pockets of A_{2A} adenosine receptor, Caf mainly interacts with phenylalanine (F168) and asparagine (N253) residues, via stacking interactions and weak hydrogen bonds, respectively[13,14]. However, the specific chemical variables responsible of the molecular mechanisms underlying the effects of Caf have not been fully identified yet, although it is known that stacking interactions mediated by aromatic rings are pivotal in docking processes inside receptors[15–17]. Understanding them, may be

the key to characterize the interaction mechanisms of different biomolecules. Caffeine is a good model system to explore such kind of interactions, as recent studies reported the tendency of Caf to establish stacking interactions with saccharides[18]. In order to characterize the stacking preferences of Caf, its complex with β-phenyl-D-glucopyranoside was studied.

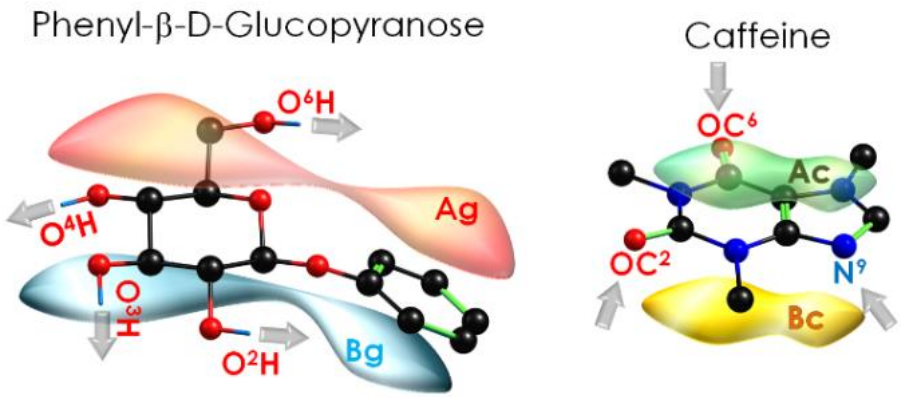

Figure 4.17: Phenyl-β-D-glucopyranoside (PhGlc) and Caffeine (Caf) structures. Main interaction sites of both molecules are highlighted by arrows. Note that the absence of symmetry in PhGlc results in several stacking combinations for the complex: AgAc, AgBc, BgAc, BgBc.

Figure 4.17 shows the structures of the monomers, with their main binding sites highlighted. While the aromatic heterocyclic ring of caffeine presents carbonyl and nitrogen groups that may serve as anchor points for the intermolecular interactions, PhGlc has a collection of hydroxyl groups that would enter in a tight competition with the aromatic ring for the interaction with caffeine.

In order to answer the questions of what the mechanism is that rules the biochemical behavior of Caf at molecular level, a good characterization is needed at both experimental and computational levels. For that reason, the experimental results obtained with double resonance spectroscopy techniques were complemented with an exhaustive computational study, in order to explore the binding competitions between π···π stacking and hydrogen bonds. Previous studies on Caf complexes[19,20] reported a rich collection of local minima in the iPES. The study of Caf+Phenol dimer[20] (Chapter 6) demonstrated that many standard computational methods have problems to reproduce the physical observables of systems in which the final shape is the result of a subtle balance between several weak interactions. In this study, two functionals were tested: The Minnesota functional (M06-2X), which provides an appropriate description of sugars, as demonstrated in previous studies,[4,8,21] and the Grimme's dispersion corrected B3LYP functional (B3LYP-GD3BJ) combined with the def2TZVP basis set level.

The latter has demonstrated to produce accurate predictions for molecular aggregates.[22,23]

A total of 108 optimized structures from the conformational search were classified in 13 families, which are summarized in the diagram in Figure 4.18. Structures were named according to the functional groups forming hydrogen bonds (O6H, O2H and O3H for PhGlc; OC2, OC6 and N9 for Caf). In those conformers with absence of hydrogen bonds, the faces of the two molecules with direct π···π interactions (see Figure 4.17) were used to label the structure.

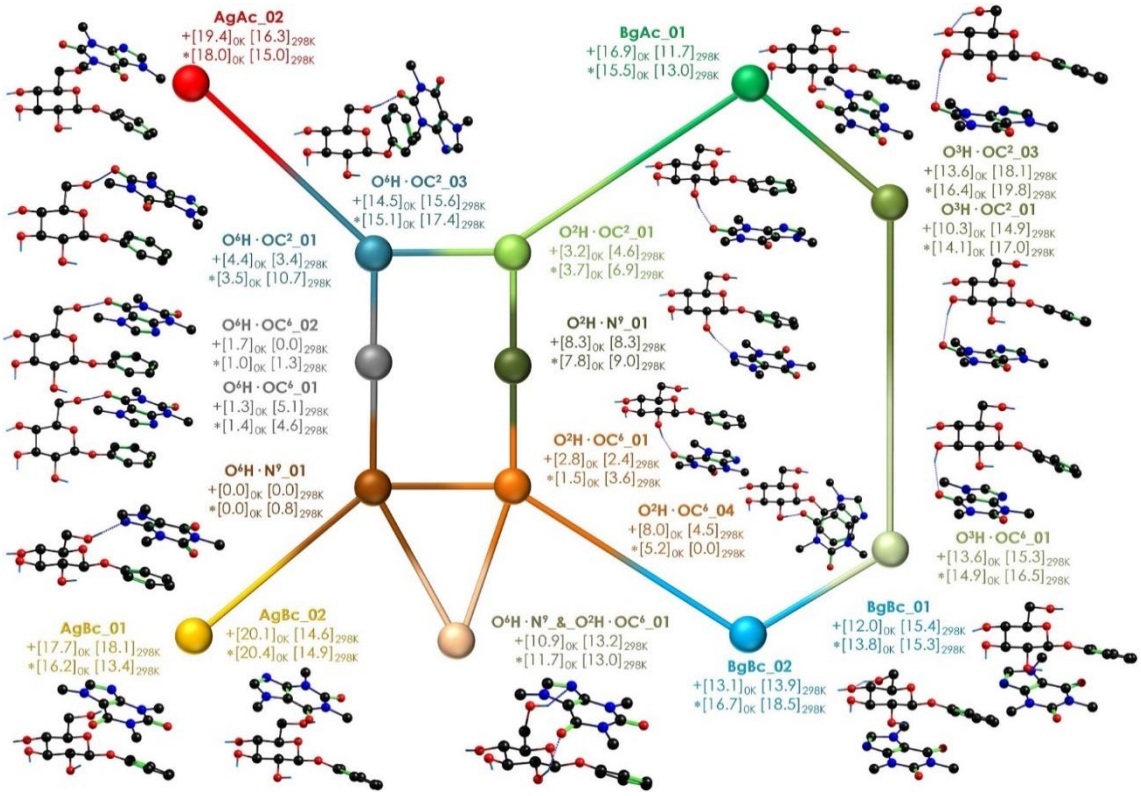

Figure 4.18: Interaction potential energy surface (iPES) of Caf+PhGlc. The isomers were classified by their interaction type, and connected to each other by isomerization pathways. Each structure is represented with its relative energy in two computational levels: +) M06-2X/6-311++G(d,p) and *) B3LYP-ED=GD3BJ/def2TZVP. Energy values are given in kJ/mol.

As can be observed, the conformational landscape of this system is quite diverse, even within each interaction family. As a general trend, all observed structures present stacking interactions. However, in many situations, stacking interactions are accompanied by an additional intermolecular hydrogen bond. For the sake of clarity, the most stable conformations with their relative energy are collected in Figure 4.19. The global energy minimum (RE) is highlighted in blue, and those structures with the highest binding energies (BE) are highlighted in green and orange).

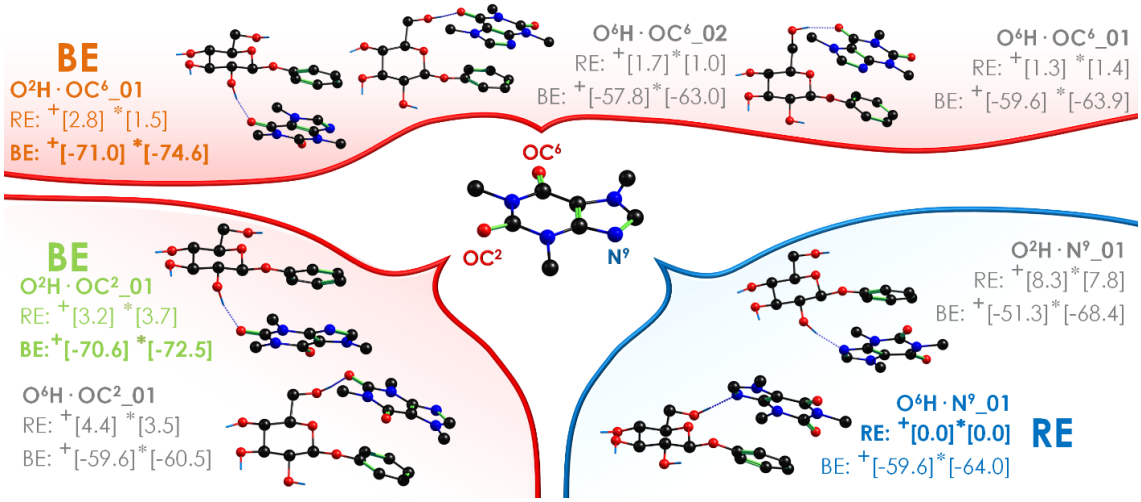

Figure 4.19: Most stable structures of Caf·PhGlc. Energy values (kJ/mol) are given for the two different computational methods used: (+) M06-2X/6-311++G(d,p) and (*) B3LYP-GD3BJ/def2TZVP. The first couple of values for each method refers to the relative energy (RE) while the second one is the binding energy (BE), calculated at 0 K. The label of each structure describes the main interaction forming the complex. The label of the most stable (RE: $O^6H{\cdot}N^9$_01) and that of the strongest bonded structures (BE: $O^2H{\cdot}OC^6$_01 with $O^2H{\cdot}OC^2$_01) are in bold.

The rich collection of structures displayed in the iPES resulted in a group of structures with similar energy, but with substantial differences in the binding strengths. This difference in the interactions is mainly caused by the flexibility of PhGlc and the multiple interaction sites in both molecules. Two possible situations arise: *(i)* a very stable conformation of the sugar gives rise to a less effective interaction with Caf; *(ii)* PhGlc adopts a less stable arrangement, but forming a strongly bonded complex. This causes a mismatch between the most stable structure and the tightly bounded one, as can be appreciated in Figure 4.19. Structures where a CO group of Caf is interacting with the sugar's O2H group ($O^2H{\cdot}OC^2$_01 and $O^2H{\cdot}OC^6$_01) are characterized by a stronger binding energy with respect to the rest, whereas the most stable structure ($O^6H{\cdot}N^9$_01) presents an interaction involving O6H and N9 groups. It is worth noting that both computational levels employed agree in predicting such structures as the most tightly bonded. The complete set of structures, together with the analysis of each family is reported in the appendix (see Figures A4.8-4.29).

PhGlc+Caf complex presented not only a sophisticated conformational landscape, but also a difficult spectroscopy to analyze. Figure 4.20 summarizes the REMPI spectrum obtained for the complex. A broad and unstructured absorption spectra was obtained for the complex, in clear contrast with those obtained from the monomers. The

chromophore in PhGlc was employed to excite the dimer, as it produced more signal. The most valuable structural information was obtained using IDIRS. Two excitation wavelengths were probed in order to look for additional isomers, but a similar spectrum was always obtained.

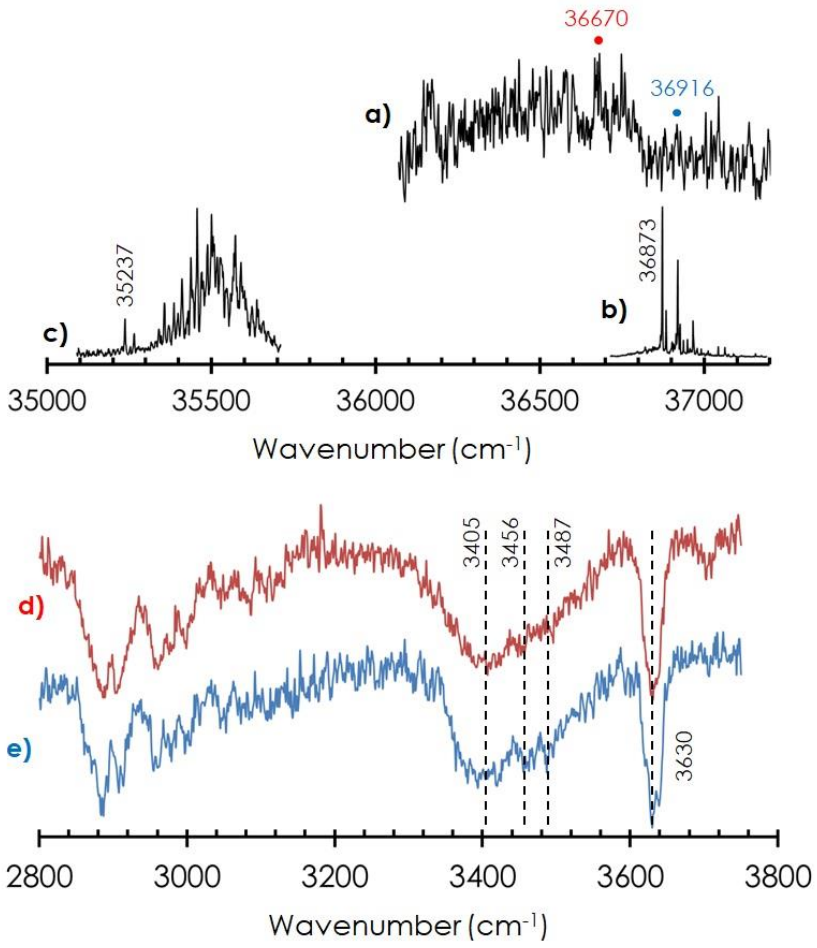

Figure 4.20: Experimental data for Caf+PhGlc system: One-color REMPI spectrum of a) Caffeine + Phenyl-β,D-glucopyranoside, b) Phenyl-β,D-glucopyranoside and c) Caffeine; d) IDIR spectrum of Caffeine + Phenyl-β,D-glucopyranoside, tuning the UV probe laser at 36670 cm^{-1}; e) IDIR spectrum of Caffeine + Phenyl-β,D-glucopyranoside, tuning the UV laser at 36916 cm^{-1}.

Figure 4.21 shows the comparison between the experimental IR spectrum and the theoretical predictions from the most stable families. First, there is a poorly resolved group of bands at ~3610 cm^{-1} due to the stretches of the glucose hydroxyl groups. Then, a broad absorption extends from 3300 to 3590 cm^{-1} and that very likely comprises the contribution from several OH moieties involved in different hydrogen bonds of variable strength. Finally, a complex group of transitions arises between 2800 and 3100 cm^{-1} due to the stretched of CH groups. No single species identified in the conformational analysis

can reproduce all the features observed. Even the combination of more than one structure from a family still fails.

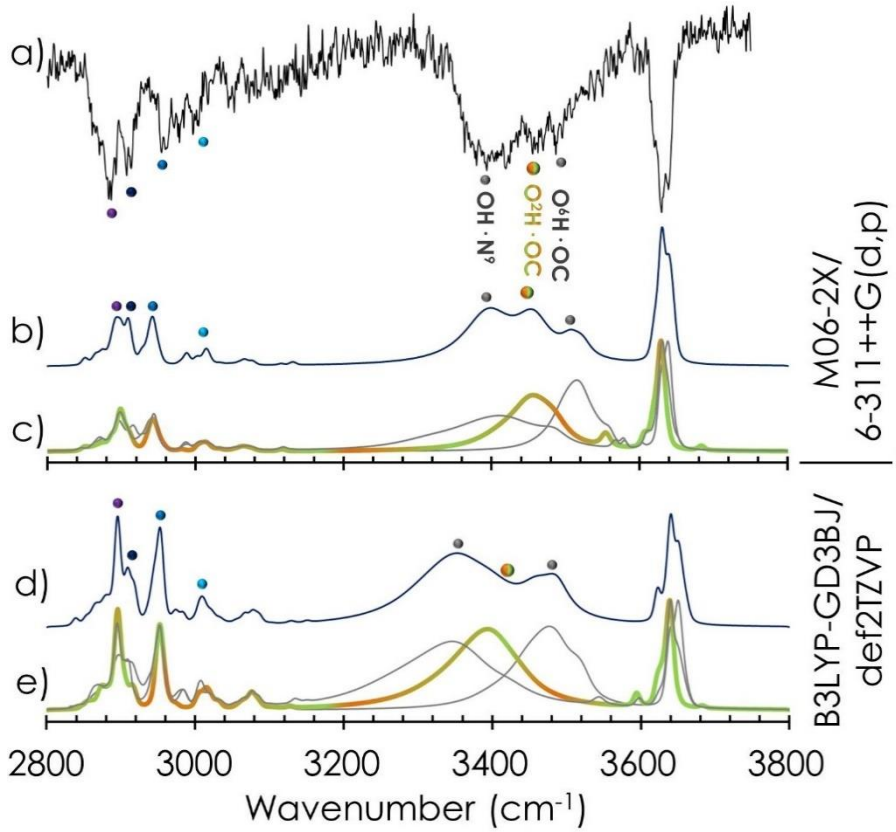

Figure 4.21: a) Experimental IDIR spectrum of Caf+PhGlc. b) Theoretical simulation at M06-2X/6-311++G(d,p) level. d) Theoretical simulation at B3LYP-ED=GD3BJ/def2TZVP level. c) and e) Averaged theoretical spectra of the main three interaction families ($O^6H{\cdot}OC$, $O^2H{\cdot}OC$ and $OH{\cdot}N^9$) at each theory level used to reproduce the experimental spectrum. For these averaged simulations, only those conformers of a given family below 5 kJ/mol were taken into account and their contributions were weighted using their relative population at the expected beam temperature of 150 K.

According to the computational simulations from both theory levels, at least three types of hydrogen bonds are required to reproduce the broad absorption on the central section of the spectrum: $O^6H{\cdot}OC$, $O^2H{\cdot}OC$ and $OH{\cdot}N^9$. Regarding the accuracy of the prediction, it is remarkable that not only the contribution of the global minimum structure ($OH{\cdot}N^9$ family) is needed to explain the experimental band, but also that of the two families with the strongest intermolecular interactions is mandatory ($O^2H{\cdot}OC$ and $O^6H{\cdot}OC$). Therefore, species presented in Figure 4.19 were employed to simulate the theoretical spectrum. Traces (c) and (e) show the individual contributions from the mentioned families, while traces (b) and (d) show the convoluted theoretical spectra of those families.

The assignment of the experimental spectrum reveals important information about the stacking behavior of Caf. Regardless of its direction when interacting with the π cloud of PhGlc, all the stacked orientations seem to be perfectly stable. Thus, Caf *floats* above the electronic cloud, adopting different orientations that are locked into place only when one of its proton-acceptor groups forms a hydrogen bond with a hydroxyl group of glucose.

Interestingly, the results obtained from this cluster can be used to better understand the non-selective antagonist behavior of Caf inside the adenosine receptor. A direct interaction between Caf and the phenyl group of the F168 residue was previously reported[13,14]. The purpose of this residue is to interact and accommodate hydrophobic and planar molecules, but in a somehow non-selective way. Thus, hydrogen bonds are responsible of that selectivity, as they can only be formed with molecules containing proton-acceptor groups in the correct position. Such behavior is quite similar to that observed experimentally in this Caf+PhGlc: there is no specificity in the stacking interactions between both molecules, but the structures detected present different hydrogen bonds. Additionally, the intermolecular interactions observed in the species detected (the most strongly bonded ones, $O^2H{\cdot}OC^6$_01 and $O^2H{\cdot}OC^2$_1) match exactly those in Caf+Phenol system[20].

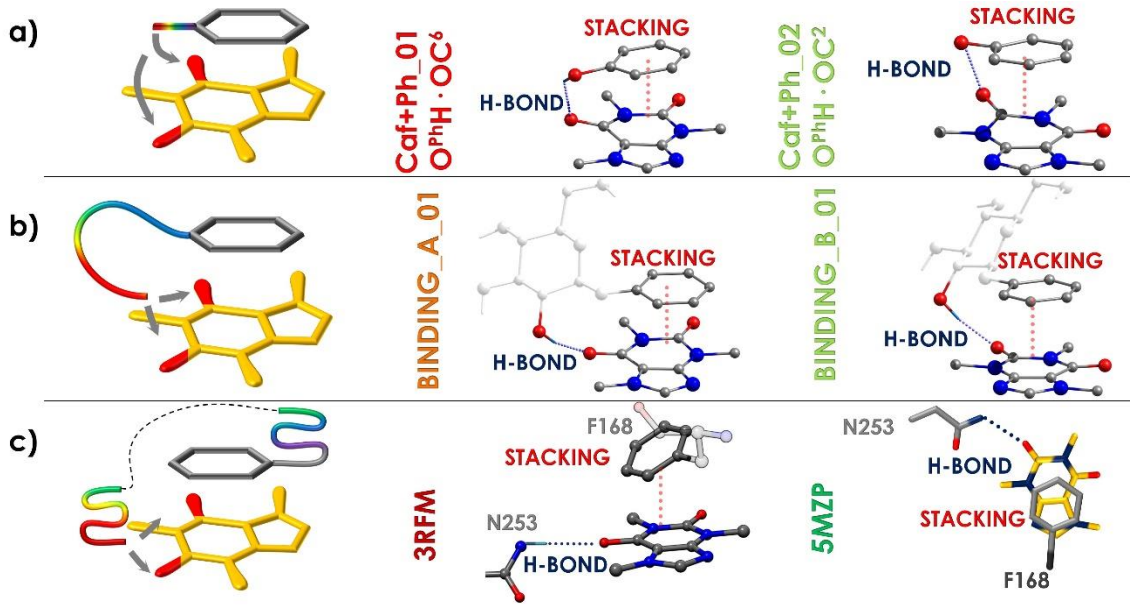

Figure 4.22: a) Most strongly bonded conformations of Caf+Phenol[20] complex. b) Most strongly bonded conformations of Caf+PhGlc ($O^2H{\cdot}OC^2$_01 and $O^6H{\cdot}OC^6$_01). c) Structural comparison with the caffeine interactions inside the A_{2A} receptor. PDB codes of the corresponding structures are 3RFM[14] and 5MZP[13].

Figure 4.22 presents a direct comparison between the structures of Caf+PhGlc, Caf+PhOH and the interactions of Caf inside the orthosteric site of A_{2A} receptor

uncovers surprising similarities, mainly that the non-covalent interaction pattern is maintained. In the case of Caf+PhGlc, the molecular flexibility of the partner (PhGlc) results in several families of structures, as demonstrated by the experimental spectrum. In particular, the two families ($O^2H{\cdot}OC^{6or2}$) stand out with significantly higher binding energy values, about 10 kJ/mol above that of the global minimum. Surprisingly, the same two families match with the conformational arrangement adopted by Caf inside the orthosteric site of the A_{2A} receptor.

Actually, it seems that the rules that determine the preference between stability and binding energy are the same that govern also the disposition of the ligand inside the receptor. In presence of water and at room temperature, the determinant factor in the docking process is how strongly the ligand can bind to the receptor, because such binding has to compensate the desolvation of both ligand and receptor. The isolation in this study, of the specific intermolecular interactions responsible for the most stable structural arrangements in an environment free of interferences, proved that the intramolecular stability can be *sacrificed* in favor of an increase in binding energy. This represents one of the few times in which this chemical behavior is clearly highlighted, thanks to the synergy between theory and experiment, and demonstrate the importance of considering not only the most stable structures, but also the most tightly bonded ones, in the extrapolation of the observations in isolated conditions to the real biological systems. The relevant conclusions reached in this work encourage us to continue with the study of molecular aggregation, using the powerful combination of supersonic expansion, laser spectroscopy and computational chemistry.

4.6. Discussion

In this chapter, we have explored the aggregation preferences of monosaccharides with other molecules and during dimerization. The interaction of glucose with mAct highlighted the preferred sites for the interaction with the glucose unit. The structures assigned demonstrated that insertion structures are not energetically favored. Similar conclusions were reached in the study of the dimers of β-PhGlc with phenol.[1] mAct does not have an aromatic ring, but still, the structures assigned present direct interactions with the aromatic substituent of the anomeric carbon (see Figure 4.23). As demonstrated in section 4.2 the two preferred sites for mAct to form hydrogen bonds are O2H and O6H. There are three reasons for this election: first, they are the terminal OH groups and therefore, the interaction with the partner molecule does not need of

breaking any intramolecular interaction; second, the flexibility of the hydroxymethyl group enables maximizing the interaction and third, the proximity of the aromatic ring results in additional secondary interactions with the aromatic cloud, that add some stability to the dimer (see NCI plot for β-PhGlc+mAct_01 in Figure 4.24).

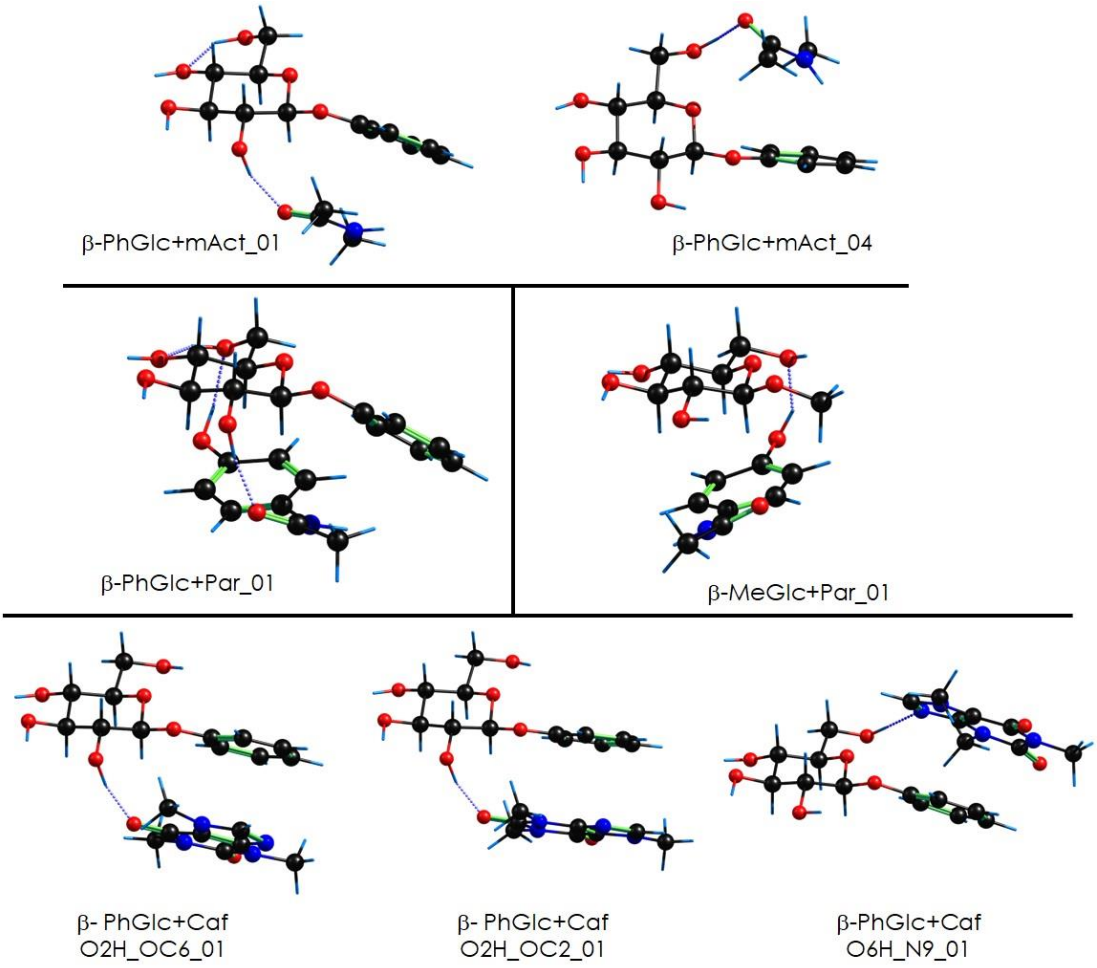

Figure 4.23: Assigned structures for the dimers formed between β-PhGlc and mAct, Par and Caf.

Comparison of β-PhGlc+mAct with β-PhGlc+Par allows us to estimate how solid the OH···O=C interaction observed in the former is. Besides, the sugar conformation did not change from β-PhGlc+mAct to β-PhGlc+Par dimers, which presents a cooperative HB network that starts in O6H and ends in the newly formed O2H···OC interaction. Par has an aromatic ring and a hydroxyl group that are also able to establish important interactions with β-PhGlc. Actually, the computed binding energy of β-PhGlc+mAct global minimum is 52.7 kJ/mol at 0 K, while that of β-PhGlc + Par is 70.5 kJ/mol (see Table 4.1). Interestingly, β-PhGlc+Par does not renounce to the appealing O2H···O=C interaction, and accommodates the rest of the interactions while pivoting around that anchor point. Coincidentally, the size of both molecules allow them to establish a second

hydrogen bond between the hydroxymethyl group of the sugar and the phenolic OH, while at the same time, the sugar stacks on top of the aromatic ring, exploiting the interactions due to dispersive forces. Interestingly, the strength of the dispersive interactions localized around the aromatic chromophore in the sugar seem to have decreased in comparison with mAct dimer, as observed in Figure 4.24. This observation points out a loss of the influence of the sugar's aromatic ring in the structure.

Table 4.1: Binding energies for the assigned structures of each sugar dimer studied, computed at M06-2X/6-311++G(d,p) level.

Dimer	Structure	Binding Energy 0 K (kJ/mol)	Binding Energy 298 K (kJ/mol)
β-PhGlc + mAct	1	-52.7	-4.5
	2	-49.6	3.0
	3	-47.2	4.4
	4	-45.8	5.0
β-PhGlc + Par	1	-70.5	-18.4
	2	-66.9	-16.8
β-MeGlc + Par	1	-51.0	-2.2
	2	-46.9	-0.7
	3	-47.2	-0.01
β-PhGlc + Caf	$O^2H\cdots OC^6$_01	-71.0	-1.4
	$O^2H\cdots OC^2$_01	-70.6	0.7
	$O^6H\cdots N^9$_01	-59.6	7.7
$(\beta\text{-PhGlc})_2$	1	-67.1	-21.1
	2	-65.3	-15.9
$(\beta\text{-PhGal})_2$	1	-75.2	-28.6
	6	-67.9	-23.1

This latter observation is reinforced by examining the structure of β-MeGlc+Par. Replacing the aromatic chromophore by a methyl group produces a reduction of 19.5 kJ/mol in the binding energy of the dimer. The removal of the aromatic substituent allows Paracetamol to adopt a different orientation in the global minimum of β-MeGlc+Par. In this arrangement, Par is maximizing the stacking, at expenses of the loss of O2H···O=C interaction, but it seems reluctant to lose the $O_{Ph}H\cdots$O6H anchor. Thus, as observed for other systems, some of them of very different nature,[24–27] formation of OH···O hydrogen bonds strongly drive aggregation of organic molecules, due to the directionality of such hydrogen bond and its relatively high strength.

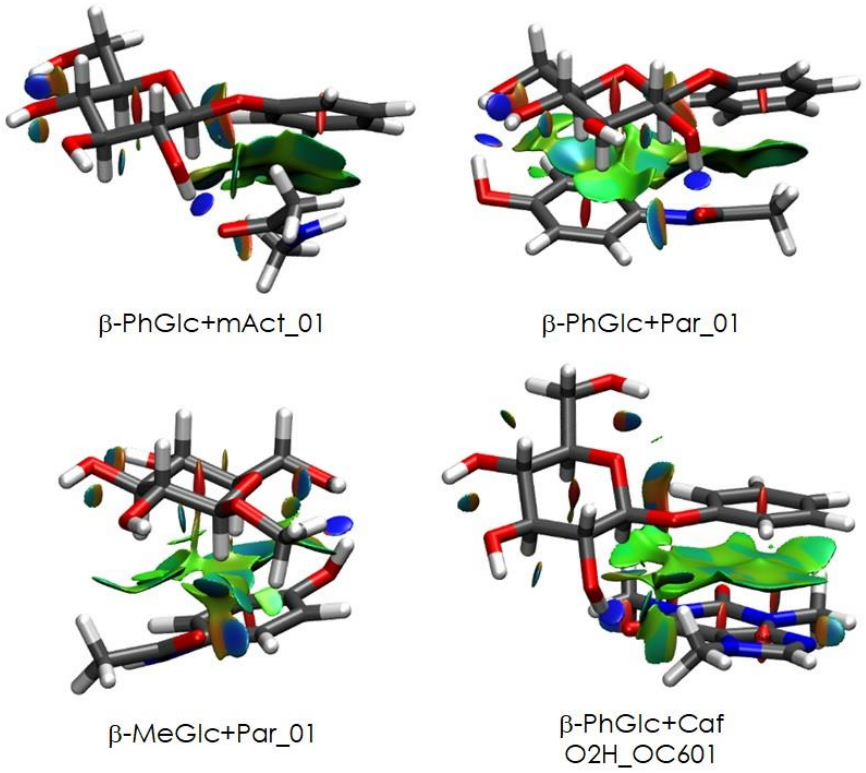

Figure 4.24: NCI plots for the most stable structures of β-PhGlc+mAct, β-PhGlc+Par, β-MeGlc+Par and β-PhGlc+Caf dimers.

Continuing with the analysis of the strength of the interactions forming the dimers studied in this chapter, β-PhGlc+Caf allowed us to explore the strength of the stacking interaction. Interestingly, the computed binding energies for the most tightly bounded families (O2H···$OC^{2\&6}$) are ~70 kJ/mol, which is similar to the interaction energy in β-PhGlc+Par global minimum. In comparison with mAct, which is the smallest dimer with the O2H···OC HB, the π-π interactions between Caf and the aromatic ring at O1 produces a binding energy increase to achieve similar numbers to those for β-PhGlc+Par, having the latter additional O_{Par}H···O6H and CH···π interactions. Thus, this comparison evidences the magnitude of the stacking interactions, whose relative strength[28] and flexibility makes them pivotal in molecular recognition processes, such as in the carbohydrate-protein interactions.[29–32]

Characterization of β-PhGlc and β-PhGal dimers also highlighted the importance of the stacking interaction in sugars. The binding energy of the assigned conformers was between 65-75 kJ/mol, which is very similar to that predicted for β-PhGlc+Par dimer. In addition, comparison between the structure of both systems emphasizes how a small structural modification results in large changes in the final shape of the aggregate. The

difference in the position of a single OH, from equatorial to axial, resulted in completely different aggregation tendencies. Combined with a strong OH···O interaction, mainly CH···π interactions where observed in (β-PhGal)$_2$, whereas in (β-PhGlc)$_2$ the most stable arrangements show a competition between structures formed by CH···π interactions between sugar and the aromatic rings; or π-π between aromatic rings. In fact, the most stable conformation for (β-PhGal)$_2$ present binding energies about 10% higher than those conformations for (β-PhGlc)$_2$, highlighting the influence in the change of C_4 hydroxyl group position upon intramolecular interaction.

4.7. Conclusions

Through this chapter, we characterized several sugar complexes in order to explore the interaction surface with different target molecules. The isolation provided by the supersonic expansion and the high resolution from the mass-resolved laser spectroscopy techniques allowed to extract valuable information about the conformational preferences of monosaccharides in several situations.

These studies showed that, in particular, phenyl-β,D-glucopyranoside clearly presents predominant binding groups upon the interaction with different molecules. Complexes with N-methylacetamide, paracetamol, and the comparison with previously reported phenol complexes evidences a clear preference to form hydrogen bonds involving O2H and O6H hydroxyl groups. Additionally, the role of the aromatic ring (or probably another big-size substitution) seemed to be the support for these interactions, as in its absence, O2H and O6H groups losses its preference for interaction. Furthermore, the epimerization effect of the C_4 was observed in β-PhGlc and β-PhGal sugar homodimers, where an interesting change in the intermolecular interactions was characterized. These systems demonstrated how a small structural change is able to alter the sensibility of the interaction preference of sugars.

Finally, a comparison between all the assigned structures allowed us to extract a general view of the relevance of aromatic interaction in sugars, and their influence in the final structure depending on its environment. The conclusions reached in this chapter revealed the true potential of mass-resolved laser spectroscopy techniques for the characterization of biologically relevant molecular systems, from where relevant structural information can be extracted in combination with powerful computational chemistry protocols.

4.8. References

[1] I. Usabiaga, J. González, P. F. Arnáiz, I. León, E. J. Cocinero and J. A. Fernández, Modeling the tyrosine-sugar interactions in supersonic expansions: glucopyranose-phenol clusters., *Phys. Chem. Chem. Phys.*, 2016, **18**, 12457–12465.

[2] F. O. Talbot and J. P. Simons, Sugars in the gas phase: the spectroscopy and structure of jet-cooled phenyl -D-glucopyranoside, *Phys. Chem. Chem. Phys.*, 2002, **4**, 3562–3565.

[3] I. Usabiaga, University of the Basque Country, 2017.

[4] A. Camiruaga, I. Usabiaga, A. Insausti, I. León and J. A. Fernández, Sugar–peptidic bond interactions: spectroscopic characterization of a model system, *Phys. Chem. Chem. Phys.*, 2017, **19**, 12013–12021.

[5] A. Camiruaga, I. Usabiaga, A. Insausti, E. J. Cocinero, I. León and J. A. Fernández, Understanding the role of tyrosine in glycogenin, *Mol. BioSyst.*, 2017, **13**, 1709–1712.

[6] J. M. Beames and A. J. Hudson, Jet-cooled spectroscopy of paracetamol., *Phys. Chem. Chem. Phys.*, 2010, **12**, 4157–64.

[7] W. Y. Sohn, S. Ishiuchi, M. Miyazaki, J. Kang, S. Lee, A. Min, M. Y. Choi, H. Kang and M. Fujii, Conformationally resolved spectra of acetaminophen by UV-UV hole burning and IR dip spectroscopy in the gas phase, *Phys.Chem.Chem.Phys.*, 2013, **15**, 957–964.

[8] I. Usabiaga, J. González, I. León, P. F. Arnaiz, E. J. Cocinero and J. A. Fernández, Influence of the Anomeric Conformation in the Intermolecular Interactions of Glucose, *J. Phys. Chem. Lett.*, 2017, **8**, 1147–1151.

[9] R. a. Jockusch, F. O. Talbot and J. P. Simons, Sugars in the gas phase, *Phys. Chem. Chem. Phys.*, 2003, **5**, 1502–1507.

[10] I. Peña, C. Cabezas and J. L. Alonso, Unveiling epimerization effects: a rotational study of -d-galactose, *Chem. Commun.*, 2015, **51**, 10115–10118.

[11] I. Usabiaga, A. Camiruaga, A. Insausti, P. Çarçabal, E. J. Cocinero, I. León and J. A. Fernández, Phenyl--D-glucopyranoside and Phenyl--D-galactopyranoside Dimers: Small Structural Differences but Very Different Interactions, *Front. Phys.*, 2018, **6**, 3.

[12] A. Nehlig, J.-L. Daval and G. Debry, Caffeine and the central nervous system: mechanisms of action, biochemical, metabolic and psychostimulant effects, *Brain Res. Rev.*, 1992, **17**, 139–170.

[13] R. K. Y. Cheng, E. Segala, N. Robertson, F. Deflorian, A. S. Doré, J. C. Errey, C. Fiez-Vandal, F. H. Marshall and R. M. Cooke, Structures of Human A1 and A2A Adenosine Receptors with Xanthines Reveal Determinants of Selectivity, *Structure*, 2017, **25**, 1275-1285.e4.

[14] A. S. Doré, N. Robertson, J. C. Errey, I. Ng, K. Hollenstein, B. Tehan, E. Hurrell, K. Bennett, M. Congreve, F. Magnani, C. G. Tate, M. Weir and F. H. Marshall, Structure of the Adenosine A2A Receptor in Complex with ZM241385 and the Xanthines XAC and Caffeine, *Structure*, 2011, **19**, 1283–1293.

[15] E. A. Kataev, T. A. Shumilova, B. Fiedler, T. Anacker and J. Friedrich, Understanding Stacking Interactions between an Aromatic Ring and Nucleobases in Aqueous Solution: Experimental and Theoretical Study, *J. Org. Chem.*, 2016, **81**, 6505–6514.

[16] S. Tsuzuki, CH/π interactions, *Annu. Rep. Prog. Chem.{,} Sect. C Phys. Chem.*, 2012, **108**, 69–95.

[17] J. L. Asensio, A. Ardá, F. J. Cañada and J. Jiménez-Barbero, Carbohydrate–Aromatic Interactions, *Acc. Chem. Res.*, 2013, **46**, 946–954.

[18] L. Tavagnacco, O. Engström, U. Schnupf, M.-L. Saboungi, M. Himmel, G. Widmalm, A.

Cesàro and J. W. Brady, Caffeine and Sugars Interact in Aqueous Solutions: A Simulation and NMR Study, *J. Phys. Chem. B*, 2012, **116**, 11701–11711.

[19] D. Kim, H. M. Kim, K. Y. Yang, S. K. Kim and N. J. Kim, Molecular beam resonant two-photon ionization study of caffeine and its hydrated clusters, *J. Chem. Phys.*, 2008, **128**, 134310.

[20] I. Usabiaga, A. Camiruaga, C. Calabrese, A. Maris and J. A. Fernández, Exploring Caffeine–Phenol Interactions by the Inseparable Duet of Experimental and Theoretical Data, *Chem. - A Eur. J.*, 2019, **25**, 14230–14236.

[21] I. Usabiaga, J. González, P. F. Arnáiz, I. León, E. J. Cocinero and J. A. Fernández, Modeling the tyrosine–sugar interactions in supersonic expansions: glucopyranose–phenol clusters, *Phys. Chem. Chem. Phys.*, 2016, **18**, 12457–12465.

[22] T. Forsting, H. C. Gottschalk, B. Hartwig, M. Mons and M. A. Suhm, Correcting the record: the dimers and trimers of trans-N-methylacetamide, *Phys. Chem. Chem. Phys.*, 2017, **19**, 10727–10737.

[23] B. Hartwig, M. Lange, A. Poblotzki, R. Medel, A. Zehnacker and M. A. Suhm, The reduced cohesion of homoconfigurational 1,2-diols, *Phys. Chem. Chem. Phys.*, 2020, **22**, 1122–1136.

[24] N. A. Seifert, A. L. Steber, J. L. Neill, C. Pérez, D. P. Zaleski, B. H. Pate and A. Lesarri, The interplay of hydrogen bonding and dispersion in phenol dimer and trimer: structures from broadband rotational spectroscopy, *Phys. Chem. Chem. Phys.*, 2013, **15**, 11468–11477.

[25] I. León, R. Montero, A. Longarte and J. A. Fernández, Influence of dispersive forces on the final shape of a reverse micelle, *Phys. Chem. Chem. Phys.*, 2015, **17**, 2241–2245.

[26] I. León, J. Millán, E. J. Cocinero, A. Lesarri and J. A. Fernández, Shaping Micelles: The Interplay Between Hydrogen Bonds and Dispersive Interactions, *Angew. Chemie Int. Ed.*, 2013, **52**, 7772–7775.

[27] M. Juanes, I. Usabiaga, I. León, L. Evangelisti, J. A. Fernández and A. Lesarri, The Six Isomers of the Cyclohexanol Dimer: A Delicate Test for Dispersion Models, *Angew. Chemie Int. Ed.*, 2020, **59**, 14081–14085.

[28] S. Tsuzuki, T. Uchimaru and M. Mikami, Magnitude and Nature of Carbohydrate–Aromatic Interactions in Fucose–Phenol and Fucose–Indole Complexes: CCSD(T) Level Interaction Energy Calculations, *J. Phys. Chem. A*, 2011, **115**, 11256–11262.

[29] K. L. Hudson, G. J. Bartlett, R. C. Diehl, J. Agirre, T. Gallagher, L. L. Kiessling and D. N. Woolfson, Carbohydrate–Aromatic Interactions in Proteins, *J. Am. Chem. Soc.*, 2015, **137**, 15152–15160.

[30] N. P. Barwell and A. P. Davis, Substituent Effects in Synthetic Lectins - Exploring the Role of CH–π Interactions in Carbohydrate Recognition, *J. Org. Chem.*, 2011, **76**, 6548–6557.

[31] A. G. Santana, E. Jiménez-Moreno, A. M. Gómez, F. Corzana, C. González, G. Jiménez-Oses, J. Jiménez-Barbero and J. L. Asensio, A Dynamic Combinatorial Approach for the Analysis of Weak Carbohydrate/Aromatic Complexes: Dissecting Facial Selectivity in CH/π Stacking Interactions, *J. Am. Chem. Soc.*, 2013, **135**, 3347–3350.

[32] J. Screen, E. C. Stanca-Kaposta, D. P. Gamblin, B. Liu, N. A. Macleod, L. C. Snoek, B. G. Davis and J. P. Simons, IR-Spectral Signatures of Aromatic–Sugar Complexes: Probing Carbohydrate–Protein Interactions, *Angew. Chemie Int. Ed.*, 2007, **46**, 3644–3648.

Chapter 5

Structural characterization of glycolipid model systems

Manuscript for publication in preparation

5.1. Introduction

In the previous chapter, we carried out a detailed analysis of the aggregation preferences of monosaccharides. However, the sugars explored (β-PhGlc and β-PhGal) only present one substitution, leaving the rest of the hydroxyl groups free to interact. One of the main conclusions was that O6H and O2H groups are the key to form stable non-covalent interactions in different environments. Additionally, the intramolecular hydrogen bond network played an important role in the final stability of the sugar. But, would the conformational preference of monosaccharides maintain with more substituted hydroxyl groups?

To shed light into the conformational preferences of substituted sugars, we explore here some lipid-substituted sugars in isolated phase. Compared to other model interactions, like peptide-carbohydrates,[1–5] lipids-glycan interactions remain largely unexplored, in spite of the large domain of application they cover. For instances, they are used as (glyco)-lipidic antigens and incorporated into vaccines to train the human immune system.[6–8] Structural information on such systems[9] is needed in order to better understand their mechanism of action and how glycolipidic systems might behave in non-natural environments.

The model glycolipids in this study are depicted in Figure 5.1. As can be observed, in GL1, the hydrogen atom in O3 is substituted by a voluminous lipid group, which contains a six–membered alkyl chain and an additional carbonyl group (C=O). Moreover, the chromophore needed for excitation spectroscopy in the anomeric carbon is now in α position (axial), and it consists of a catechol ring (a phenol ring with an OH group in the *ortho* position).

The second glycolipid, GLOMe, presents the same substitutions as the first one, but with a guaiacol instead of a catechol. In this way, the effects of that additional hydroxyl group in the sugar conformation can be isolated. The goal here is to elucidate the structural preferences of GL1 and GLOMe substituted monosaccharides, through recording their electronic and vibrational spectra of the monomers and their hydrated complexes in isolated phase. The study is challenging, specially taking into account the large size of the monomers and the flexibility of the aliphatic chain of the fatty acid.

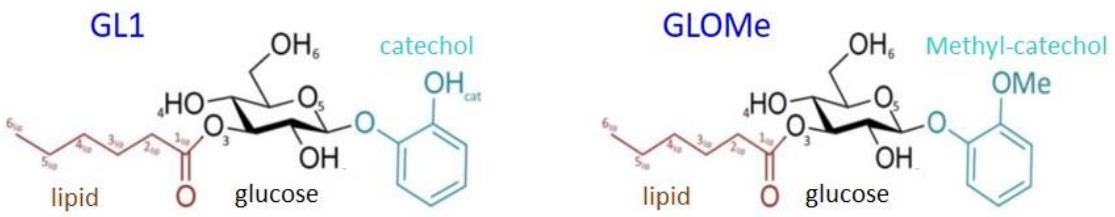

Figure 5.1: Schemes of GL1 and GLOMe monosaccharides.

5.2. The role of the lipid group in the sugar conformation: spectroscopic characterization of glycolipids in isolated phase

5.2.1. Computational exploration of the conformational landscapes

The computational exploration of these substituted monosaccharides started with a full conformational search based on molecular mechanics, combining different force fields. However, due to the systems having many torsional angles and the high flexibility of the lipid chain, the high amount of conformers obtained with such protocol, transferring the results directly to the optimization stage using quantum mechanics (specially knowing that many of them would probably end in redundant conformations) was impractical. The main responsible for such abundance of stable structures is the lipid chain flexibility, as these conformational searches showed it can arrange in many different ways without disturbing the intramolecular interactions of the sugar. Thus, a different approach was needed in order to extract more information about the non-covalent bond competition for the spectroscopic characterization of the systems.

The approach employed to find the representative structures for the glycolipids systems was divided in two steps. The lipid and the sugar conformations were decoupled, in the sense that for each sugar conformation a large number of lipid conformations are stable. First, the possible sugar conformations were explored by replacing the lipid chain by a methyl group. This made the quantum geometry optimizations substantially more efficient in terms of computational resources, and allowed us to explore a vast number of possible sugar conformations. Then, among the most stable conformations obtained by DFT studies, a pre-assignment was performed based on the agreement of their calculated spectra with the experimental ones. Finally, the selected conformations were reconstructed with the lipid and performed a conformational search on the lipid coordinates only.

This split approach shed light into an easily partitioned conformational landscape, as we can observe in Figure 5.2. As mentioned before, the lipid and sugar conformations may seem decoupled. The relative energy of the conformation is first dominated by the interactions in the sugar and is modulated by the lipid conformation. The effect of the lipid structure on the calculated frequencies of the OH stretching modes is insignificant, taking into account the precision of frequency calculations. Most of the sugar conformations are divided in two families, depending on the interaction involving the carbonyl group as an H acceptor of either O2H (O2H···OC; Figure 5.2a) or O4H (O4H···OC; Figure 5.2b). Additionally, for each of the above possibilities, the hydroxymethyl moiety can adopt three already known positions (Figure 5.2c).[10] Although the conformational possibilities of the lipid are virtually infinite (Figure 5.2d), clustering over the first two torsional angles of the lipid revealed three different situations: the lipid adopts an extended all *trans* conformation (Figure 5.2e pink), or it adopts a folded conformation. In the folded conformations, a quasi-continuum of combinations of the torsional angles of the lipid makes the conformational landscape difficult to summarize. However, considering only the first two torsions of the aliphatic chain makes possible distinguishing two major families: where the lipid folds towards either OH4 (Figure 5.2e green) or OH2 (Figure 5.2e orange).

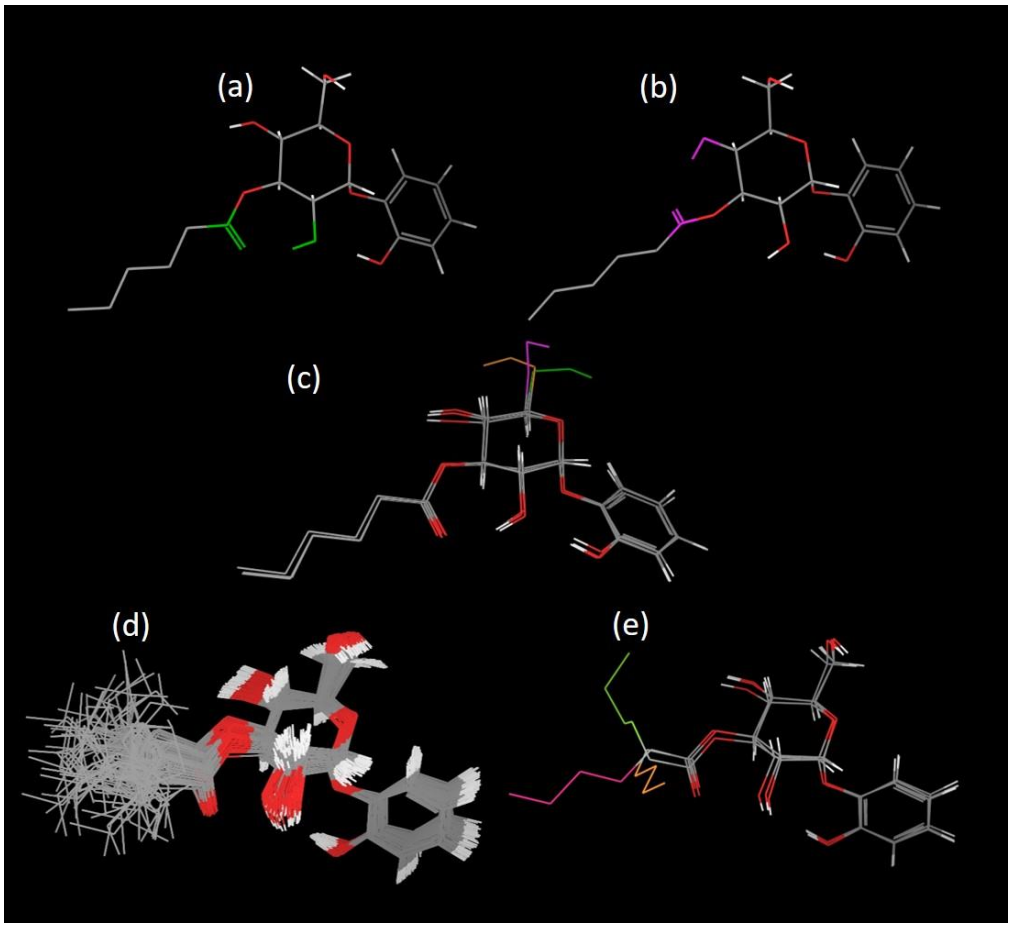

Figure 5.2: Conformation categories for the GL1 glycolipid, illustrating (a) and (b) the two main orientations of C=O, (c) the three orientations of hydroxymethyl moiety, and (d) the diversity of conformations of the lipid chain, which can be portioned in (e) three orientations.

After following the above-mentioned protocol, structures of both GL1 and GLOMe systems were optimized at the DFT level. Figure 5.3 shows the most stable structures found for the first glycolipid analyzed, GL1. The most stable conformations are those where a hydrogen bond network is formed starting from the catechol OH group and ending in the carbonyl group (O_{cat}H···O2H···O=C). Different arrangements for the lipid chain and the hydroxymethyl group appear with this HB network, forming the so-called O2H···OC structure family. As can be observed, the lipid moiety appears folded to both O2H and O4H groups, and also in a linear position with all its dihedral angles in *trans* conformation. Each of these lipid conformations appear also with the different arrangements of the O6H moiety. Due to the above-mentioned degrees of freedom, GL1 presents a rich conformational landscape at low energies. Moreover, one would expect that several conformations to coexist, as the energy difference between different lipid arrangements is low enough.

At higher energies, a second interaction family appears, in which the carbonyl group interacts with the O4H group, disrupting the HB network formed in the first family. As discussed for the most stable family, the O6H moiety may also adopt different orientations that lay close in energy.

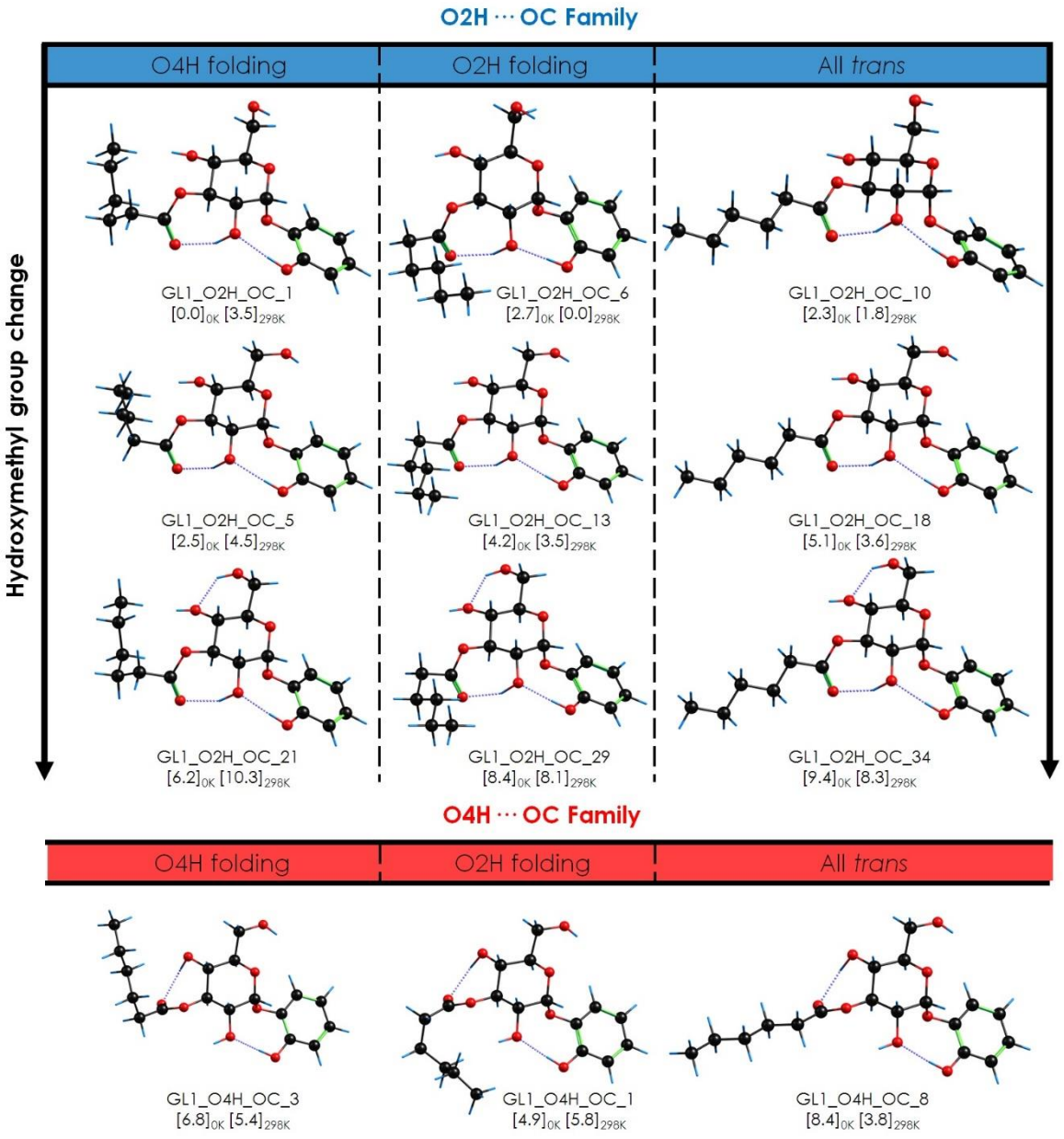

Figure 5.3: Most stable conformations found for GL1. Structures were classified and named depending on the main intramolecular interactions. Relative energy values at 0 and 298K computed at B3LYP-ED=GD3/cc-pVTZ level are given in kJ/mol,

The computational exploration of the conformational landscape of GLOMe is very different from that of GL1. In GL1 the most stable conformations are stabilized by a cooperative $O_{cat}H\cdots O2H\cdots O{=}C$ interaction chain. This type of conformation is not possible in GLOMe because of the absence of $O_{cat}H$. As can be observed in Figure 5.4, the

methylation of the catechol hydroxyl group favors the interaction between the O2H group and the catechol oxygen, forming O2H···O_{cat} bonds. Consequently, the interaction between the carbonyl and O4H (O4H···O=C) groups becomes more stable. In fact, the most stable structures of GLOMe presents this above-described O2H···O_{cat}/O4H···O=C pattern. Again, the hydroxymethyl group can adopt in three different orientations inside this family of structures, and different lipid chain conformations lay in very close energies. Note that in this case, the most stable lipid folding for GLOMe is towards O2H group, the opposite site in comparison with GL1.

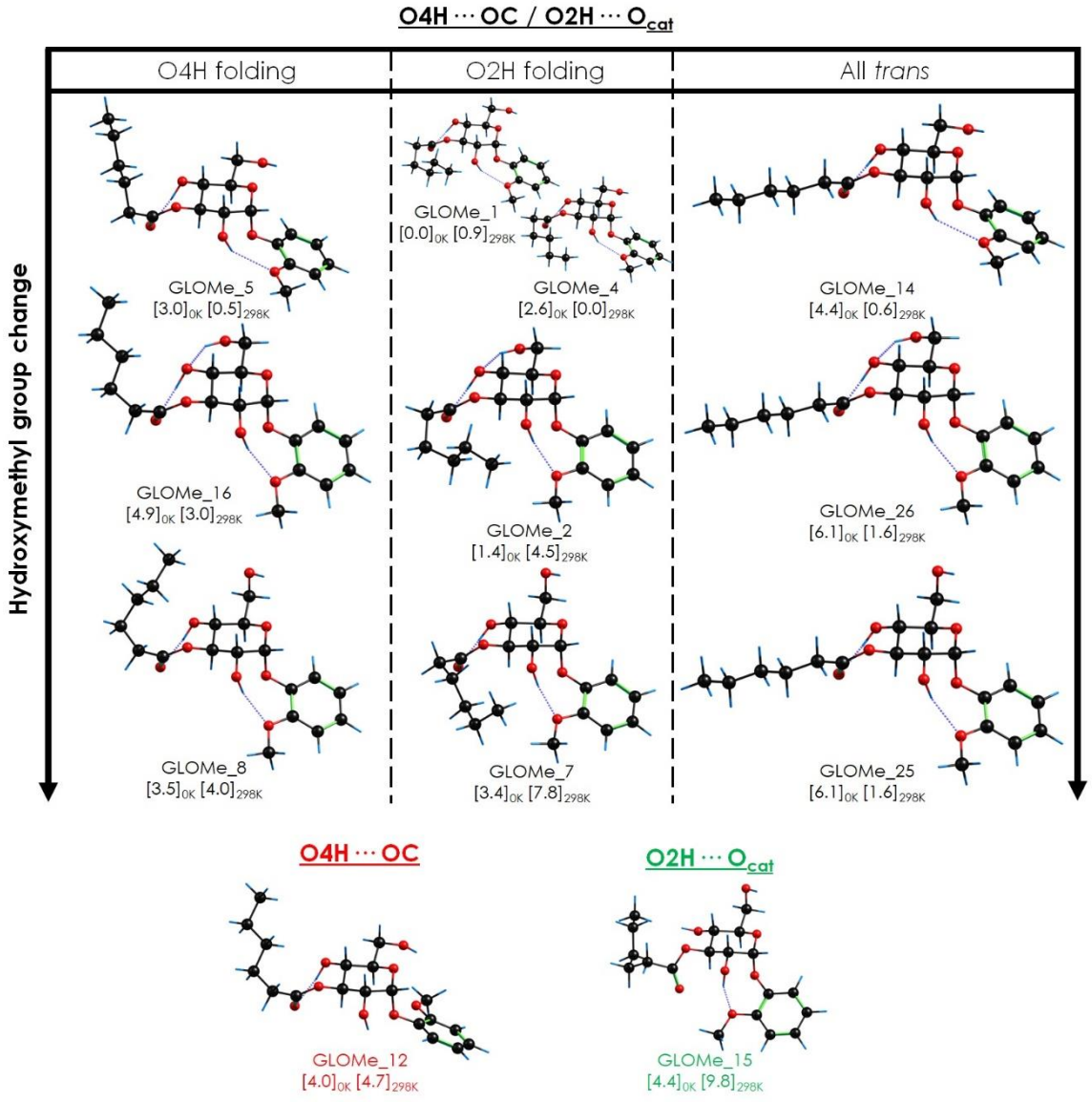

Figure 5.4: Most stable conformations found for GLOMe. Relative energy values at 0 and 298K computed at B3LYP-ED=GD3/cc-pVTZ level are given in kJ/mol.

5.2.2. Conformational assignment

Figure 5.5 collects the REMPI spectra of GL1, GLOMe and their monohydrated clusters. As can be observed, they present a broad and unstructured absorption, despite previous studies on catechol chromophore showed a well-resolved REMPI spectrum.[11,12] However, the addition of the glycolipid to the catechol can influence in many ways the chromophore in the ground and excited states, causing the unresolved absorption observed in the UV.[13,14]

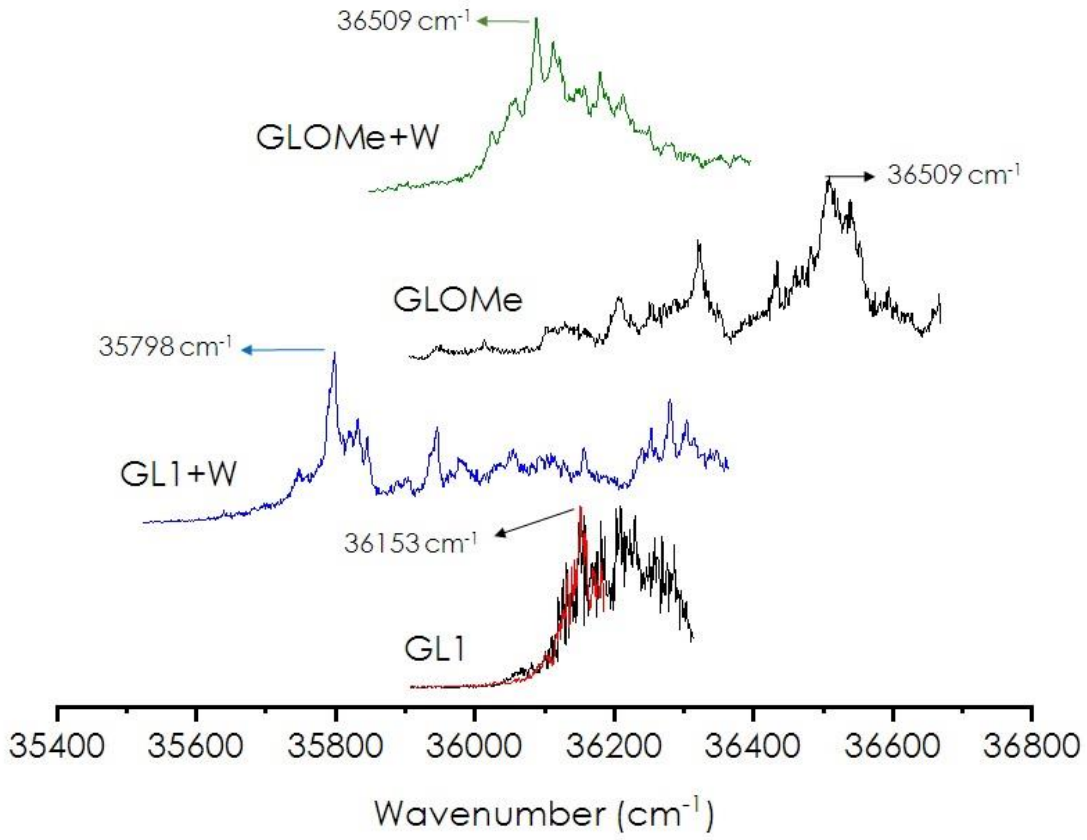

Figure 5.5: One-color REMPI spectra of GL1, GL1+W, GLOMe and GLOMe+W molecular systems. Wavelength marked with an arrow were used as probe in IR/UV double resonance experiments.

For all the systems, IR/UV double resonance was employed by probing several regions of the REMPI spectrum, although the same IDIR spectrum was obtained. Given the low selectivity induced by the unstructured REMPI spectra, it is very possible that several conformers contribute to the probed signal, and hence, to the IDIR spectra (see Figure 5.6).

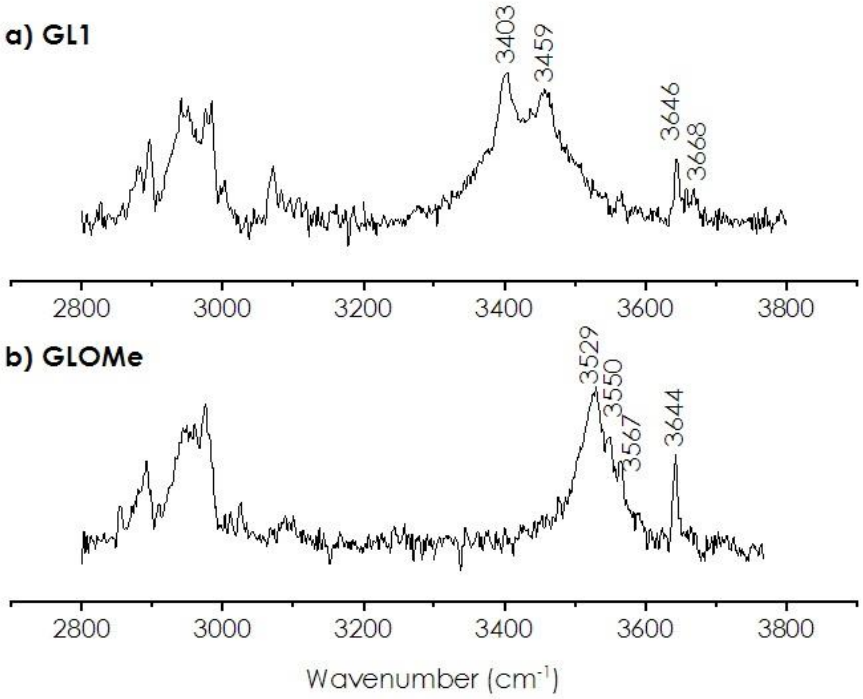

Figure 5.6: IDIR experimental spectra of a) GL1 and b) GLOMe.

The qualitative analysis of these spectra provides already valuable information before the comparison with the computational data. The OH bands above 3600 cm^{-1} correspond to the OH stretches of the sugar involved in relatively weak interaction. Then, we observe a strong and broad band in both GL1 and GLOMe systems, which probably contains more than one bonded OH stretch involved in stronger non-covalent interactions. A closer look to the position of these strong features may help one to clarify the structural differences between GL1 and GLOMe: the broad band in GL1 is centered in 3430 cm^{-1}, which is red-shifted in comparison with the bonded bands in GLOMe, that appear between 3500 and 3600 cm^{-1}. This indicates that methylation of the catechol OH affects the nature of the adopted conformations. Additionally, the strong band of GL1 presents a longer red-shift in comparison to the spectra of the glucose conformers, which only present above 3600 cm^{-1},[10] indicating the presence of a strong intramolecular hydrogen bond, probably involving the carbonyl group.

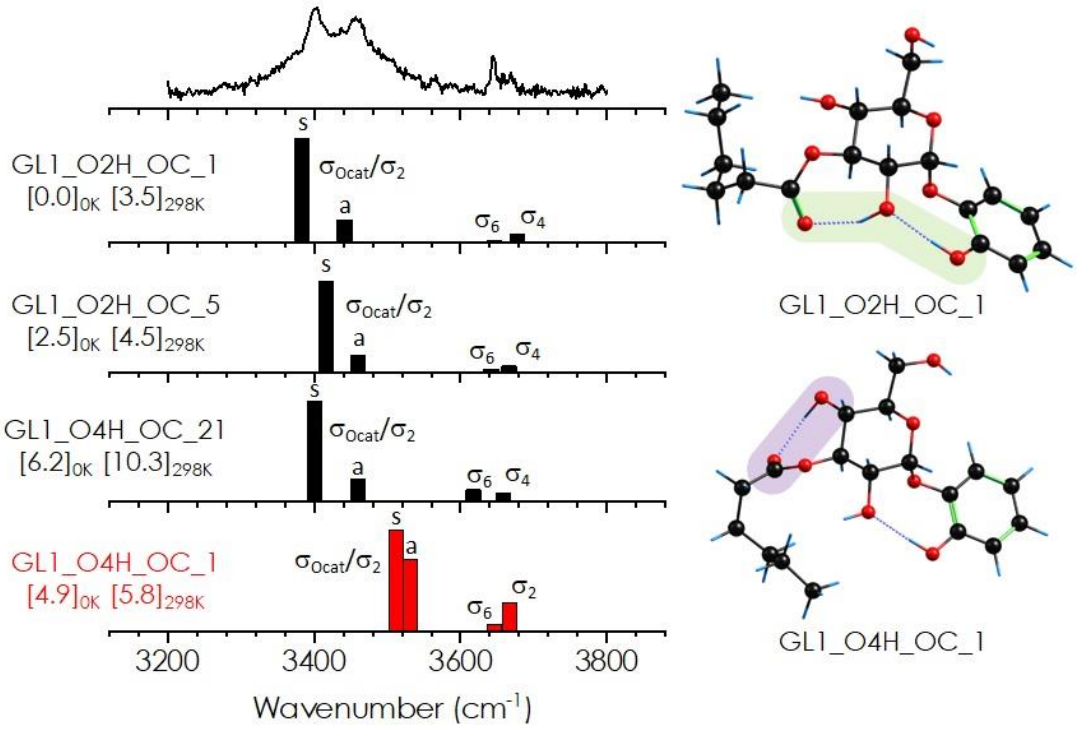

Figure 5.7: IDIR spectrum of GL1 compared to the predicted spectra for the most stable structures of O2H_OC family and O4H_OC family. A scaling factor of 0.96 was used to account for the anharmonicity of OH stretches. σ refer to the OH stretching mode of the corresponding OH group. The symmetric and antisymmetric stretching modes of the groups involved in the intermolecular hydrogen bonds are labelled *s* and *a*, respectively.

Figure 5.7 shows a comparison between the most stable structures of GL1 and the experimental IDIR spectra, obtained by probing at 36153 cm^{-1}. The spectra predicted for the structures within the O2H···OC family reproduce very well the experimental bands. Structures GL1_O2H_OC_1, 5 and 21 show the predictions for the sugar conformations with different O6H group positions. In spite of the difference in stability, the calculated spectra are very similar, and hence, distinguishing between hydroxymethyl group arrangements is not an easy task. A comparison between the predictions of different lipid arrangements inside a sugar conformation and the experimental spectrum can be found in Figure A5.1 of the appendix.

There is a clear difference with the spectra of those structures that contain the O4H···OC interaction, where the shift of the bonded OH groups does not reproduce the position of the bands in the experimental trace. This comparison allows one to discard structures containing the O4H···OC bond. This spectral assignment is consistent with the computed energies for GL1, as the structures with O_{cat}H···O2H···O=C HB network are the most stable ones, including the global minimum.

The assignment of the GL1 structure further confirms the nature of the observed band around 3450 cm^{-1}. The O2H group *trans* configuration (C1-C2-O2-H2 dihedral angle) allows $O_{cat}H$ to interact with it, and also to form the O2H···OC bond, resulting in a strong cooperative chain of intramolecular bonds. This leads to the symmetric and antisymmetric stretching modes of O2H/$O_{cat}H$ to be strongly red-shifted, appearing at 3403 and 3459 cm^{-1}, a spectral region never reached for monosaccharides bands with intramolecular interactions. This illustrates how strong the attraction of the carbonyl group is, and the cooperative effect induced by the hydrogen bond network. The bands observed at 3630 and 3650 cm^{-1}, in the usual spectral region for monosaccharides O-H stretching modes, correspond to the stretching modes of O4H and O6H, in constrained intramolecular interaction with O3 and O5, respectively. In this same region, a third band can be observed as a little shoulder close to the band at 3630 cm^{-1}. This is the indication of the population of at least an additional conformer of the same family. The calculated relative energies at 0 and 298K are consistent with the population of GLOMe_1 and GLOMe_4.

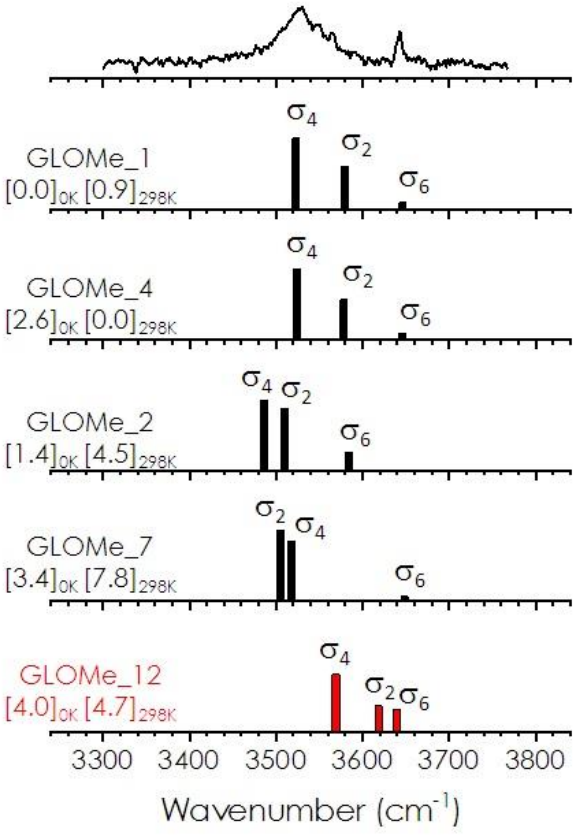

Figure 5.8: IDIR spectrum of GLOMe compared to the predicted spectra for the most stable structures. A scaling factor of 0.96 was used to account for the anharmonicity of OH stretches. σ refers to the OH stretching mode of the corresponding OH group.

Figure 5.8 shows a comparison between the computed spectra of the most stable structures of GLOMe and the experimental spectra. As the previous exploration of the conformational landscape revealed, most stable conformations show O4H···O=C/O2H···O_{cat} double hydrogen bonds. Simulated spectra of these structures well reproduces the observed experimental trace, specially the first two conformations (GLOMe_1 and GLOMe_4). The free OH stretch is also well predicted, but the prediction for a different O6H group arrangements in structure GLOMe_2 is shifted compared to that of the global minimum. Nevertheless, due to the broad absorption and the small energy difference between structures, an unequivocal assignment of the sugar conformation is too speculative. As in the case of GL1, probably there are more than one conformer contributing to the IR spectra, due to the flexibility of the lipid chain and the available orientations for the O6H group. Structure GLOMe_12, which is the most stable form of the family of structures with only O4H···OC bond, does not fit well with the experimental spectrum, due to the presence of the free O2H band. Therefore, we can discard structures within this family under our experimental conditions.

As demonstrated by the experimental assignment, there is a strong structural change due to the methylation of the catechol's hydroxyl group. The disruption of the strong cooperative hydrogen bond network observed in GL1 produces a qualitative difference in the band shift that can be appreciated in GLOMe spectrum. In the observed structures of GLOMe, O2H no longer interacts with the carbonyl group as it is forming new bonds with O_{cat}. Therefore, the cooperative effect is banished in this conformation, leading to weaker electrostatic interactions. This is why the most red-shifted band in the IR spectrum of GLOMe is above 3500 cm^{-1}, while the bonded stretching modes of GL1 lie below 3500 cm^{-1}.

5.3. Analysis of the monohydrated complexes of GL1 and GLOMe

After the spectroscopic characterization of the glycolipid monomers in the isolated phase, we proceeded with the study of their water complexes. In order to ease the interpretation of the observed spectra and obtain more accurate structural information, complexes with heavy water were also formed and recorded in a different mass-channel. Figure 5.5 shows the REMPI spectra of the monohydrated versions of GL1 and GLOMe. Their spectra present broad and unstructured absorption, similar to those of the

monomers, but with the origin of the UV absorption shifted to lower energies. Despite several excitation wavelengths were probed, a single IR spectrum was obtained for each complex.

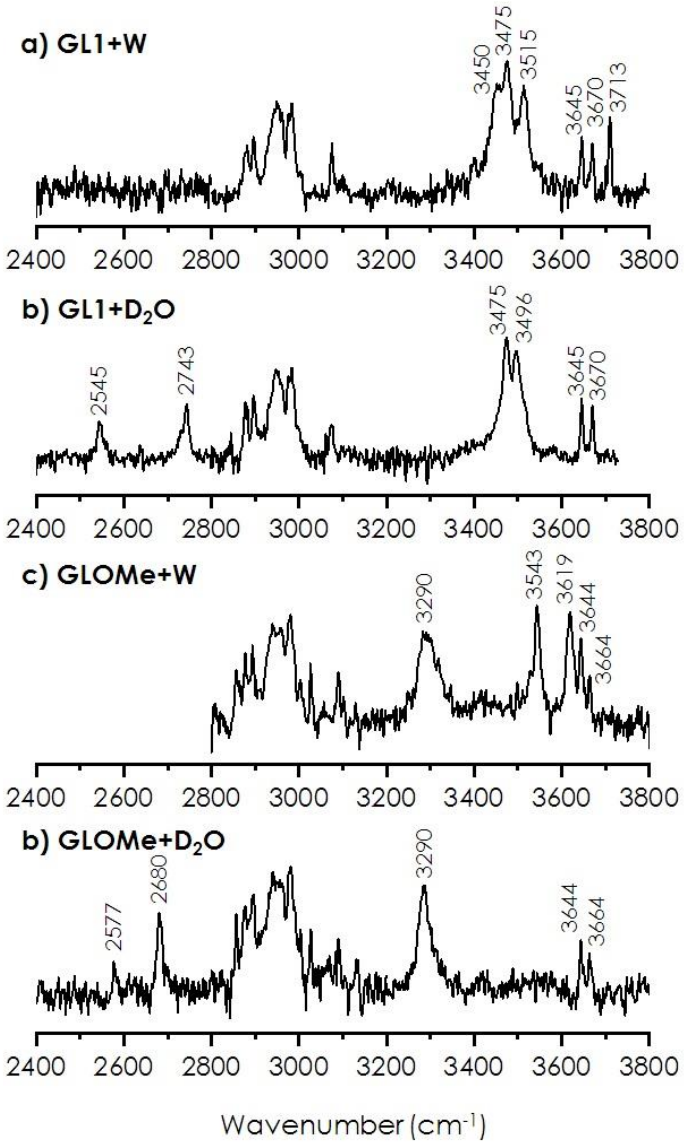

Figure 5.9: IDIR experimental spectra of a) GL1+W, b) GL1+D_2O, c) GLOMe+W and d) GLOMe+D_2O complexes.

Figure 5.9 collects the IR spectra of GL1+W and GLOMe+W complexes, recorded in the CH and OH stretching regions for the water complex, and in the OD stretching region for the heavy-water complexes.

The IR spectrum of GL1+W complex corresponds to a typical water insertion in the monosaccharide structure, acting simultaneously as a single HB donor and acceptor.[15] One of the water OH bonds is forming part of the intramolecular hydrogen bond network, as indicated by the position of its stretching: close to the broad bands around

3450 cm^{-1}. The other one appears around 3720 cm^{-1}, corresponding to the free OH stretching. This observation is further confirmed by the observed shifts in the experimental bands of the heavy-water complex, where both free and bonded OD stretching bands can be observed between 2500-2800 cm^{-1}. Usually, in monohydrated monosaccharides, water molecules inserts into the H bond network of the molecule to replace weak intramolecular interaction by much stronger intermolecular interactions, indicated by strong red-shifts in the OH spectra of the complexes.[15,16] It is worth to mention that the most red-shifted OH band in GL1 is higher in energy than the bands assigned to the symmetric and antisymmetric stretching motions of O2H and $O_{cat}H$ in the most stable conformation of GL1. This indicate that the hydration site is probably different as the usual insertion site where the water molecule is intercalated between a donating OH and an accepting OH of the sugar.

GLOMe+W spectrum is very different from that of GL1+W and previously reported sugar-water complexes.[15] On one hand, the absence of a free OH stretching band is striking. This would discard any insertion–type structure, indicating that the water molecule must adopt a bridging position where both hydroxyl groups are donors. On the other hand, an OH stretching band appears around ~3300 cm^{-1}. This band present quite a strong red shift in comparison with the rest of the OH bands observed in these glycolipids, which predicts a very strong intra/inter-molecular interaction. Furthermore, this red-shifted band is maintained in the heavy-water complex, which indicates that it corresponds to one of the hydroxyl groups of GLOMe involved in a strong interaction.

The exploration of the conformational landscape of the hydrated complexes was performed using the same approach described for the monomers. The exploration without the lipid moiety allowed isolating the most stable intermolecular interactions with the water molecules, which resulted to be the insertion of the water molecule between O2H and carbonyl groups, forming a new HB network. Then, for the most stable sugar-water interactions, the conformation of the lipid moiety was explored.

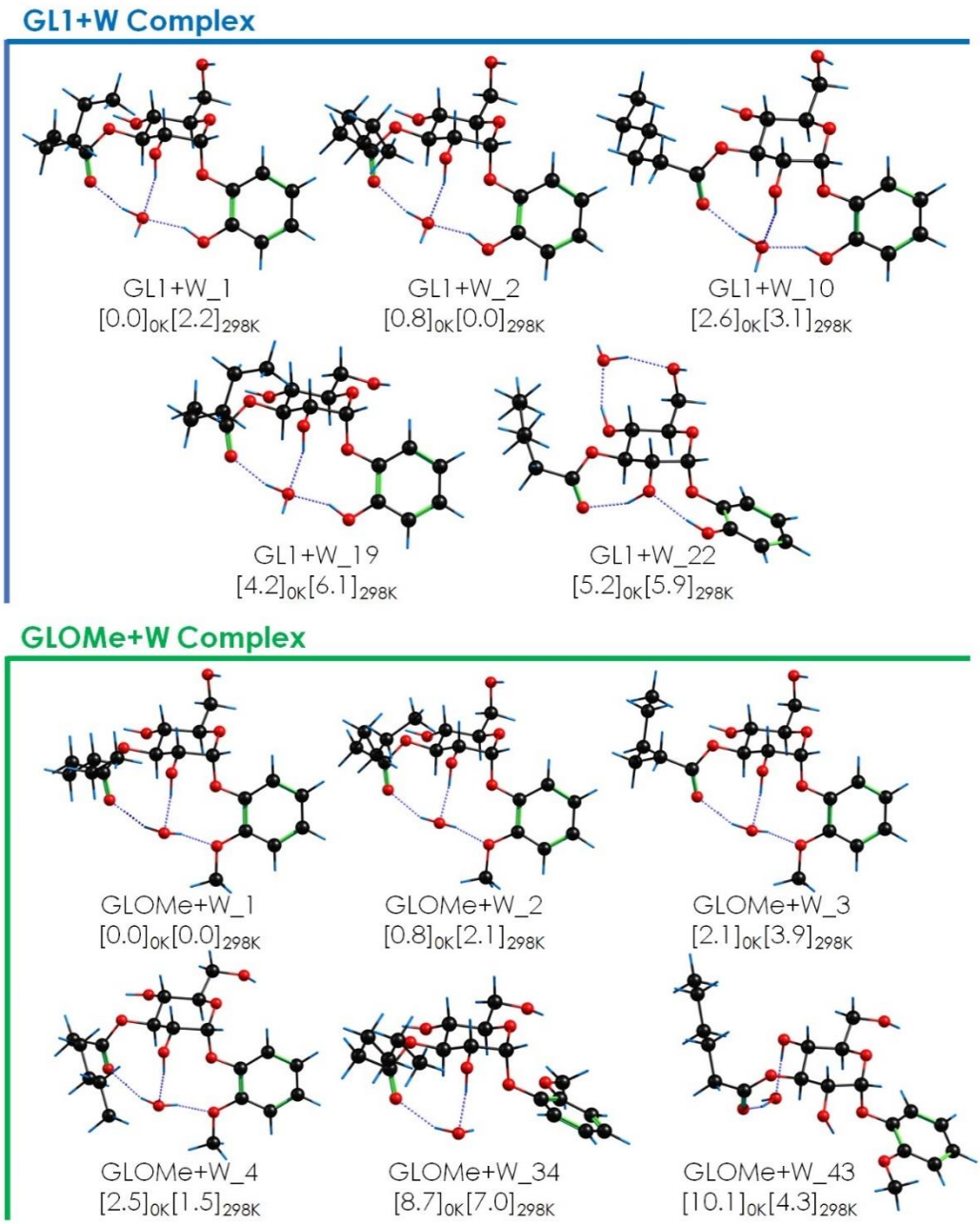

Figure 5.10: Most representative conformations of GL1+W and GLOMe+W complexes, computed at B3LYP-ED=GD3/cc-pVTZ level. Energy values at 0 and 298K are given in kJ/mol.

Figure 5.10 collects the most representative structures for the GL1+W and GLOMe+W complexes. The conformational preferences of GL1+W and GLOMe+W, as revealed by the computational exploration, are in good agreement with the qualitative analysis of the experimental IR spectra. Most stable GL1+W structures present the water molecule inserted in the glycolipid, with one of its OH groups free. Besides, most stable structures of GLOMe+W presents a tri-coordinated water molecule inserted as a double donor, forming a three-fold HB network between the C=O group, O_{cat}, and the O2H group. Such a network is not common in hydrated monosaccharides. Although it is not associated

with a red-shift signature in the IDIR spectrum, the water molecule still contributes to a global stabilization of the complex. To achieve such an arrangement, the $O_{cat}H\cdots O2H\cdots O{=}C$ chain is replaced by a tridentate interaction of water acting as double acceptor and donor with the catechol chromophore orientation being adapted to optimize this interaction. As observed for the monomers, other O6H group arrangements are possible within these conformations. However, it is intriguing that the most stable interactions with water are by far those involving the C=O, O2H and $O_{cat}H$ groups, anticipating formation of a possible water pocket in the glycolipid.

Regarding to the lipid moiety, the conformational distribution is similar to that observed for the monomers. However, in this case, the most stable conformation presents the lipid chain folded towards the O2H group in both glycolipids.

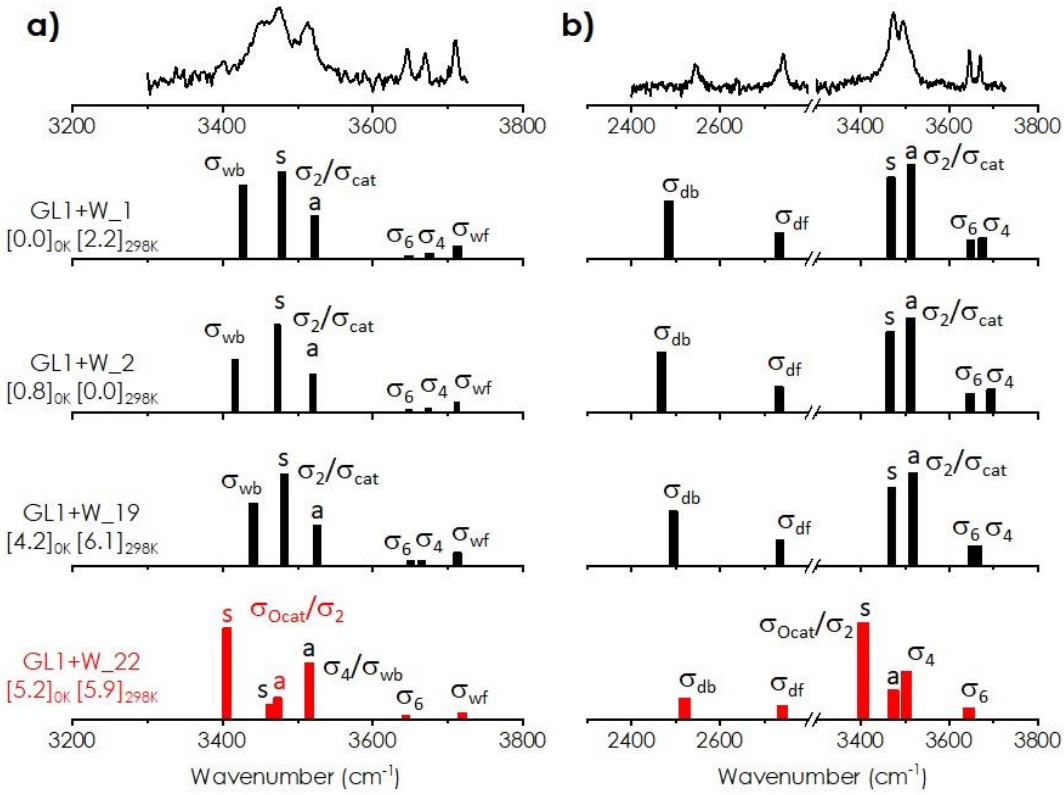

Figure 5.11: IDIR spectra of GL1+W/D_2O complex compared to the predicted spectra for the most stable conformations, computed at B3LYP-ED=GD3/cc-pVTZ. A scaling factor of 0.96 was used to account for the anharmonicity of free OH stretches, and 0.97 to the intermolecular donating groups. Predictions plotted in red correspond to different water interactions. σ refers to the OH stretching mode of the corresponding OH group; and σ_{wf} and σ_{wb} correspond to the free and bonded OH stretching of the water, respectively ("d" used in the case of heavy water).

Figure 5.11 shows a comparison between the simulated spectra of the most stable structures of GL1+W and the experimental IDIR spectrum. The calculated spectra of the

two most stable conformations (GL1+W_1 and GL1+W_2) reproduce very well the experimental bands of both OH and OD stretching regions. This assignment also comes in good agreement with the previous qualitative analysis of the experimental spectrum, as the assigned free OH/OD bands unequivocally reveals that the water in inserted as a single donor. Interestingly, water is inserted in between the $O_{cat}H$, O2H and C=O groups, disrupting the previously formed strong HB network in GL1. However, the observed red shift is comparable to that observed in the monomer, indicating that the newly formed HB network with the water molecules is strong. As occurred with the monomer, the orientation of the O6H group in GL1+W19 structure also explains the experimental bands, and thus, its presence in the jet cannot be discarded despite is higher in energy.

Conformation GL1+W_22 shows a different prediction, where the water molecule forms a new network with O4H and O6H groups. However, the theoretical prediction of this structure does not fit well with the observed bands, especially for the free OH stretching of the sugar. On the light of these results, conformation GL1+W_22 can be discarded.

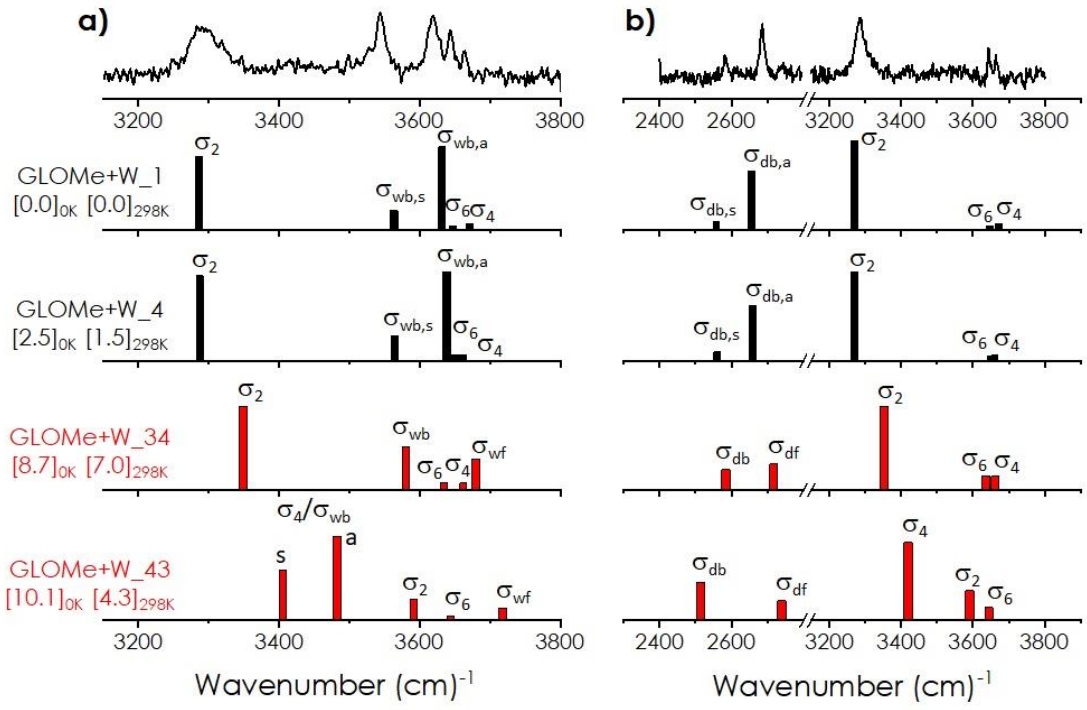

Figure 5.12: IDIR spectra of GLOMe+W/D_2O dimers compared to the predicted spectra for the most stable conformations, computed at B3LYP-ED=GD3/cc-pVTZ level. A scaling factor of 0.96 was used to account for the anharmonicity of free OH stretches, and 0.97 for the intermolecular donating groups. Predictions plotted in red correspond to different water interactions. σ refers to the OH stretching mode of the

corresponding OH group; and σ_{wf} and σ_{wb} correspond to the free and bonded OH stretching of the water, respectively ("d" used in the case of heavy water).

Figure 5.12 shows the experimental IDIR spectrum of GLOMe+W compared to the predictions of the most stable computed conformations. There is a very good agreement between the experiment and the theoretical spectra of the most stable conformations of GLOMe+W. These structures, as observed in the previous conformational exploration, present the water molecule in a bridging position, which is further confirmed by the absence of any free OH stretches of the water around 3710-3720 cm^{-1}. Instead, the water bands appear slightly below the sugar's free OH groups, and completely disappear in the heavy-water complex, leaving a clear spectrum where all OH bands can be easily identified.

The most red-shifted band of GLOMe+W, around 3300 cm^{-1}, can be assigned to the O2H group of the sugar involved in a very strong hydrogen bond with water. Because of the double donor behavior of water, the oxygen atom becomes more electronegative, and thus, the O2H group is more tightly bound. It is worth noting that this change in the bond strength is well captured by the theory, as can be appreciated in the predictions of structures GLOMe+W_1 and GLOMe+W_4.

The tricooordinated water between C=O, O2H and O_{cat} groups seems to be the most stable form in the computed complexes. Conformations GLOMe+W_34 and GLOMe+W_43 show a different insertion of the water molecule: in the former, there is no HB between water and O_{cat} as the conformation of the catechol ring respect to the sugar is completely different; while in the latter, water inserts between the C=O and O4H groups. These conformations are substantially high in energy, and their predictions did not fit well with the observed bands. Therefore, the experimental assignment finally reveals that the monohydrated aggregation of GLOMe is mainly dominated by a strong HB network formed with water between the C=O, O2H and O_{cat} groups.

5.4. Discussion

The comparison between the experimental results with the ones from the computational exploration revealed clear differences in the conformational preferences of the studied glycolipids. As expected, the esterification in the O3 position and the catechol's hydroxyl group affect significantly the intramolecular interaction roadmap in the monosaccharide. The structures assigned for GL1 present a strong

intermolecular hydrogen bond network that starts in the $O_{cat}H$ group, and ends in the C=O group of the lipid (see Figure 5.13). This interaction is by far the most stable arrangement in the isolated sugar. Moreover, we clearly evidenced the interaction site of the C=O group in GL1, as the strong cooperative effect is experimentally captured in the strong red shift of the bounded OH stretch.

Upon methylation of the hydroxyl group of the catechol ring, the previous panorama changed. The HB network seen in GL1 is no longer possible and the cooperative effect is lost, resulting in a re-arrangement of the sugar OH groups. The assignment provided by the comparison of the experimental and theoretical data revealed that the C=O group changes its position to interact with O4H. We could expect a competition between the O4H···O=C and O2H···O=C interactions, but it seems that the O2H groups prefers interacting with the lone pairs of O_{cat}, and the carbonyl group binds to O4H group. This intramolecular arrangement is by far the most stable for the GLOMe conformation.

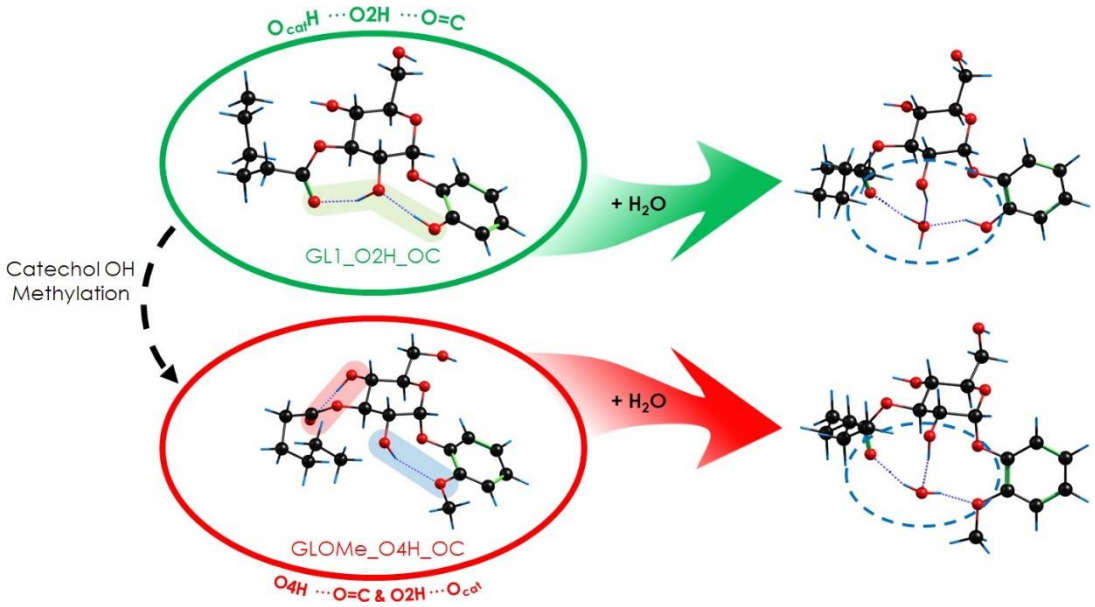

Figure 5.13: Experimentally assigned conformers of the studied monomers and water complexes.

The intramolecular polar interactions involving the OHs and the CO groups have been precisely characterized in the glycolipids from the analysis and interpretation of the experimental data. For the lipid chain conformation, the OH stretching frequency predictions do not provide any information. Despite all the possible arrangements of the lipid chain inside a specific conformation (intramolecular polar interactions) were analyzed, all of them produced similar spectra in the OH stretches region and the energetic order of the interaction families was within the computation error. Thus, we

can conclude that the influence of the lipid chain in the sugar conformation is negligible, and *vice versa*. It is worth nothing that there might be some secondary interactions that produce small variations on the overall stability of the conformations, as the most stable lipid arrangement revealed by theory for both GL1 and GLOMe systems is not the all *trans* conformation, in comparison with previous alkyl chain studies on isolated phase.[17] The CH stretching modes, between 3200 and 2800 cm^{-1} may encode some information on the lipid chain conformation. However, due to the lack of precision of the predictions for CH stretches and also due to the congested bands in that region of the IR spectrum, it is difficult to perform a clear assignment for the lipid conformation. Thus, as it happens with the O6H group of the sugar, the existence of multiple lipid chain conformations with the assigned intramolecular interactions must be assumed.

Nevertheless, theoretical exploration of the conformational landscapes revealed energy differences between the lipid chain folding between GL1 and GLOMe. Figure 5.14 summarizes the relative energy of the most stable folding in each sugar conformation (same interactions but different arrangement of the free O6H group). As can be observed, most stable folding at GL1 is towards O4H group at 0 K, whereas in GLOMe it changes to the O2H group. Near room temperature, changes in the stability order can be appreciated, but especially for the *all trans* conformation, which is entropically more favored.

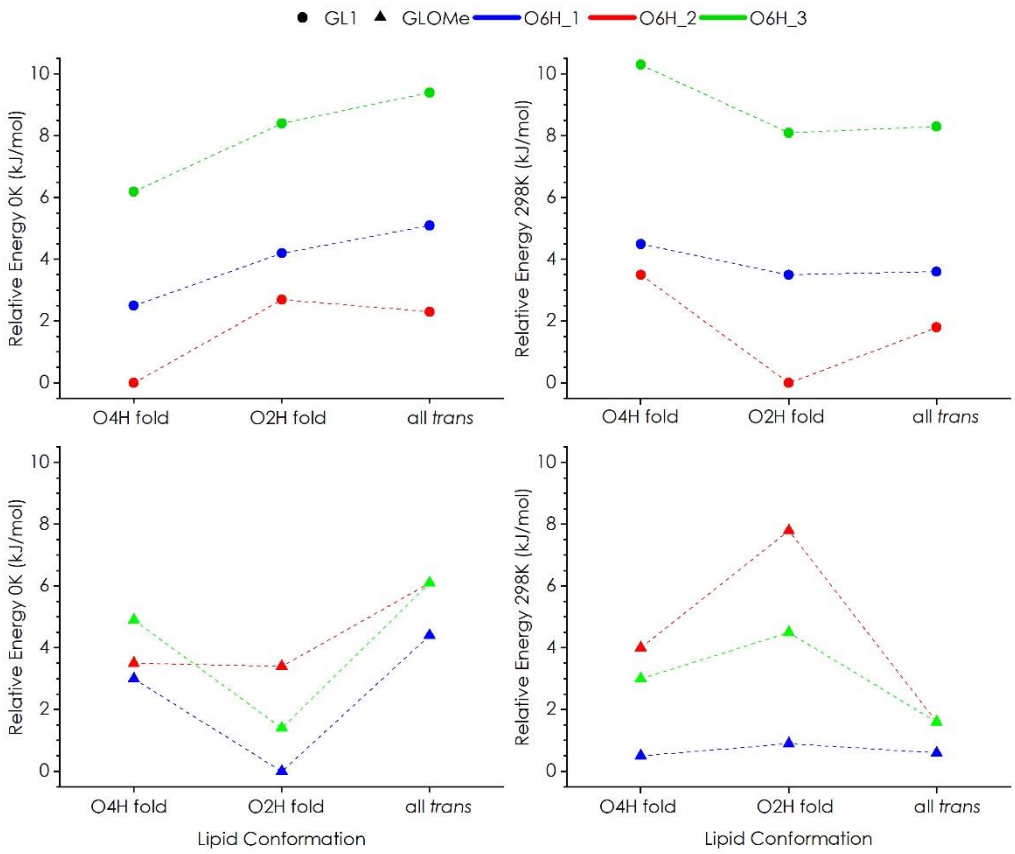

Figure 5.14: Diagrams for the relative energies of different lipid conformations in GL1 and GLOMe. Blue, red and green colors represent the different orientations of O6H for each system: O6H_1 (blue) refers to the hydroxymethyl group looking towards O5, O6H_2 (red) when is in *p* position, and O6H_3 (green) when it points towards O4H.

The above-mentioned stability change regarding to the lipid folding could be trapped in the experimental spectra in the CH stretching regions. As can be observed in Figure 5.6, there is a narrow CH stretch around 3100 cm^{-1} in GL1 IR spectrum that disappears in the GLOMe spectrum. This experimentally observed change could be related to the lipid folding change, as we demonstrated that GLOMe presents different intramolecular interactions and a change in the C=O group orientation, favoring the lipid folding towards O2H.

Furthermore, there is no significant changes in the CH band shape between GL1 and GL1+W complexes. However, in GLOMe+W the above-mentioned CH stretch around 3100 cm^{-1} appears again, indicating a change in the lipid chain during the hydration process. As revealed by theory, energy difference between O2H and O4H folding is reduced in both GL1+W and GLOMe+W. This fact would be related to the orientation of the C=O group, which is in mid-way between the two conformations assigned in the

monomers. Therefore, the population of both O2H and O4H foldings in the water complexes would explain the appearance of the 3100 cm^{-1} band for GLOMe+W.

Regarding to the sugar conformation, the panorama dramatically changed upon the hydration of the glycolipids. The assigned structures resulted to be quite atypical, in comparison with previous sugar-water complexes. In non-substituted monosaccharides, hydration sites are located at the weakest points of the intramolecular hydrogen bond network of the monomer, which is usually between the O4H and O6H groups of the sugar.[15] Structures with such interactions are calculated at least 6-8 kJ/mol higher than the most stable conformation for GL1+W and GLOMe+W, respectively, and the agreement between their predicted spectra and the experimental one is poor. In the present case, the C=O group is such a strong H acceptor that the water is lured to this binding pocket, disrupting any previous bonds inside the sugar. This behavior is comparable to the favored hydration site observed for GlcNac systems.[18] It can be said that the lipid moiety in the glycolipids create a very electronegative region that attracts water, as the interaction site did not change from GL1 to GLOMe complexes.

Figure 5.15 shows the mapping of the NCIs in the most stable conformations for GL1+W and GLOMe+W. In both cases, multiple vdW interactions can be observed around the water pocket and between the lipid chain and the O2H group (green-yellow colored surface), along with the strong HBs formed between the hydroxyl groups of the sugar and water molecules (blue colored surfaces). In GL1+W complex, experiments revealed that water molecule is inserted between $O_{cat}H$, O2H and C=O groups, creating a new strong, cooperative HB network, similar to the one observed in the monomer.

When methylation occurs in GLOMe, $O_{cat}H\cdots O_w$ bond is replaced by an $O_wH\cdots O_{cat}$ interaction. In this situation, water molecule changes its role from a single donor to a double donor, in a bridging position between C=O and O_{cat} groups. Due to this double donor behavior, electronic density around O_w is more polarized, becoming more receptive for hydrogen bonds. This effect was clearly observed by the experiment, as the IR band for the $O2H\cdots O_w$ interaction appears 160 cm^{-1} red shifted in comparison with the same interaction in GL1+W. Theory also captures this bond strength change in the frequency predictions. As can be observed in the RDG vs sign(λ_2) diagram (see Figure 5.15), there is a strong density gradient reduction for $\rho < -0.03$ values, which indicates the formation of strong $O2H\cdots O_w$ interaction in both complexes (red plot for GL1+W, and green plot for GLOMe+W). Moreover, the strength of this interaction is different, as

values of reduced density gradient for GLOMe+W are lower than those in GL1+W, indicating that water is more tightly bound to O2H group of GLOMe.

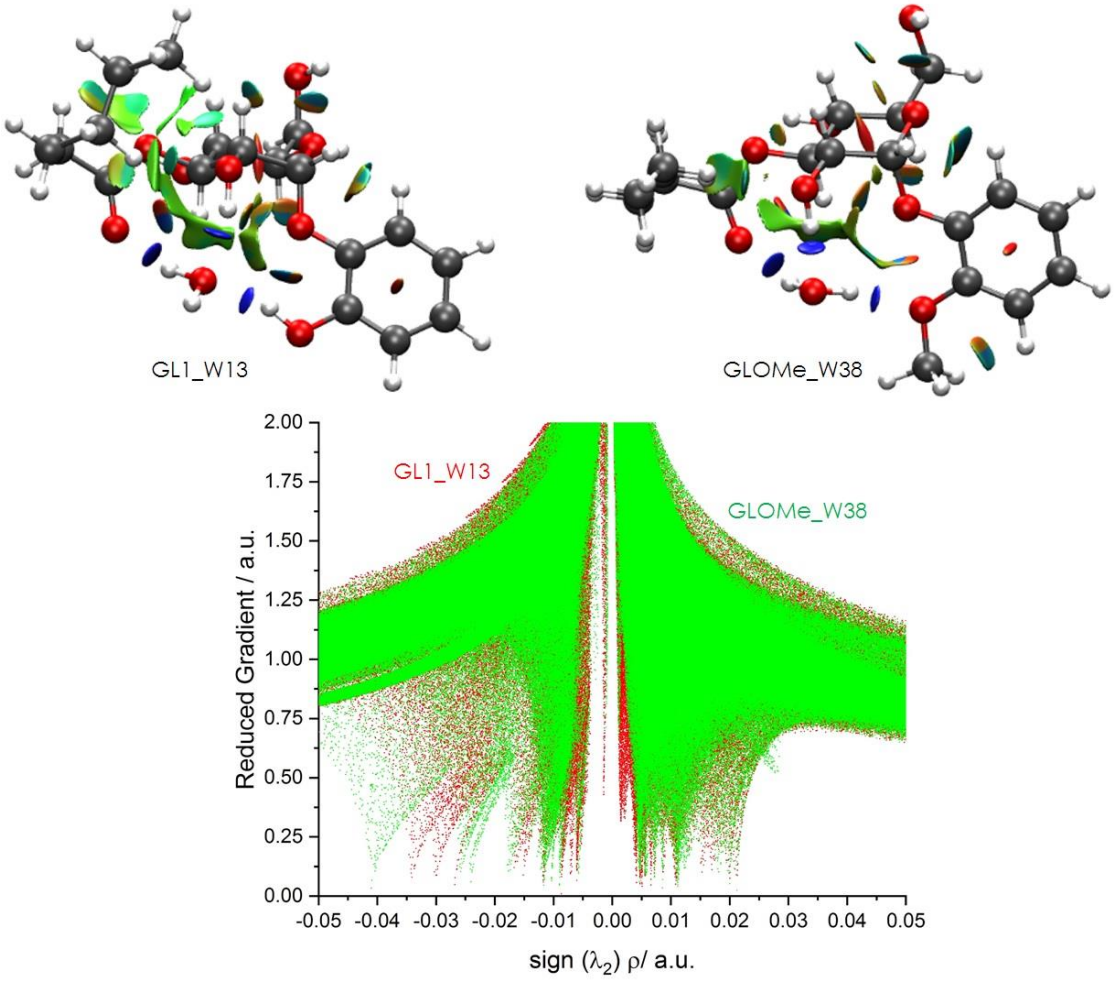

Figure 5.15: NCI plots of the most stable assigned water complexes of GL1 and GLOMe.

5.5. Conclusions

This chapter presents the study of conformational preferences of lipid-substituted monosaccharides in isolated phase. Thanks to the combination of mass-resolved laser spectroscopy and powerful computational methods, we fully characterized the intramolecular interactions that drives the final structures of GL1 and GLOMe glycolipids. Furthermore, water complexes of both sugars where obtained and precisely assigned thanks to the isotopic substitution of water.

The analysis of the assigned structures for the sugar monomers revealed the big influence of the carbonyl group substitution. In comparison with non-substituted

monosaccharides in isolated phase, where all hydroxyl groups orient themselves in a continuous HB network, the presence of C=O group disrupted those interactions. A O_{cat}H···O2H···O=C hydrogen bond network was formed in GL1, and it is disrupted in GLOMe due to the methylation of the catechol's hydroxyl group. The analysis of different lipid folding and the comparison with the predicted spectra revealed that the influence of the lipid chain in the sugar is negligible, and *vice versa*. However, small structural changes were detected in the experimental spectra, related to a change in the lipid conformation from GL1 to GLOMe glycolipids and upon single hydration of GLOMe.

Regarding to the monohydrated complexes, both GL1 and GLOMe presented unexpected interactions, which were mainly located around the lipid group and the substituted aromatic ring. The observed strong binding site for the water molecule is very different from those reported for non-substituted sugar-water complexes. Therefore, we conclude that the substitution in O3 position of a carbonyl group at the beginning of the lipid chain strongly affects the aggregation preferences of the sugar monomers with water.

The spectroscopic study of GL1 and GLOMe substituted monosaccharides revealed a new interesting conformational panorama, where the insertion of voluminous groups could change the preferences for both intra- and inter-molecular interactions of the sugars.

5.6. References

[1] E. J. Cocinero, P. Çarçabal, T. D. Vaden, J. P. Simons and B. G. Davis, Sensing the anomeric effect in a solvent-free environment., *Nature*, 2011, **469**, 76–79.

[2] J. P. Simons, R. A. Jockusch, P. ÇarÇabal, I. Hünig, R. T. Kroemer, N. A. Macleod and L. C. Snoek, Sugars in the gas phase. Spectroscopy, conformation, hydration, co-operativity and selectivity, *Int. Rev. Phys. Chem.*, 2005, **24**, 489–531.

[3] E. J. Cocinero, C. Pierre, T. D. Vaden, B. G. Davis and J. P. Simons, Exploring Carbohydrate - Peptide Interactions in the Gas Phase: Structure and Selectivity in Complexes of Pyranosides with N -Acetylphenylalanine Methylamide, 2011, 4548–4557.

[4] J. Screen, E. C. Stanca-Kaposta, D. P. Gamblin, B. Liu, N. A. Macleod, L. C. Snoek, B. G. Davis and J. P. Simons, IR-Spectral Signatures of Aromatic–Sugar Complexes: Probing Carbohydrate–Protein Interactions, *Angew. Chemie Int. Ed.*, 2007, **46**, 3644–3648.

[5] I. Usabiaga, J. González, P. F. Arnáiz, I. León, E. J. Cocinero and J. A. Fernández, Modeling the tyrosine-sugar interactions in supersonic expansions: glucopyranose-phenol clusters., *Phys. Chem. Chem. Phys.*, 2016, **18**, 12457–12465.

[6] V. Makarov, G. Manina, K. Mikusova, U. Möllmann, O. Ryabova, B. Saint-Joanis, N. Dhar, M. R. Pasca, S. Buroni, A. P. Lucarelli, A. Milano, E. De Rossi, M. Belanova, A. Bobovska, P. Dianiskova, J. Kordulakova, C. Sala, E. Fullam, P. Schneider, J. D. McKinney, P. Brodin, T.

Christophe, S. Waddell, P. Butcher, J. Albrethsen, I. Rosenkrands, R. Brosch, V. Nandi, S. Bharath, S. Gaonkar, R. K. Shandil, V. Balasubramanian, T. Balganesh, S. Tyagi, J. Grosset, G. Riccardi and S. T. Cole, Benzothiazinones Kill Mycobacterium tuberculosis by Blocking Arabinan Synthesis, *Science (80-.).*, 2009, **324**, 801 LP – 804.

[7] P.-H. Lambert, T. Hawkridge and W. A. Hanekom, New Vaccines Against Tuberculosis, *Clin. Chest Med.*, 2009, **30**, 811–826.

[8] M. Gilleron, S. Stenger, Z. Mazorra, F. Wittke, S. Mariotti, G. Bo hmer, J. Prandi, L. Mori, G. Puzo and G. De Libero, Diacylated Sulfoglycolipids Are Novel Mycobacterial Antigens Stimulating CD1-restricted T Cells during Infection with Mycobacterium tuberculosis , *J. Exp. Med.*, 2004, **199**, 649–659.

[9] C. Kirschbaum, K. Greis, E. Mucha, L. Kain, S. Deng, A. Zappe, S. Gewinner, W. Schöllkopf, G. von Helden, G. Meijer, P. B. Savage, M. Marianski, L. Teyton and K. Pagel, Unravelling the structural complexity of glycolipids with cryogenic infrared spectroscopy, *Nat. Commun.*, 2021, **12**, 1201.

[10] F. O. Talbot and J. P. Simons, Sugars in the gas phase: the spectroscopy and structure of jet-cooled phenyl -D-glucopyranoside, *Phys. Chem. Chem. Phys.*, 2002, **4**, 3562–3565.

[11] H. Mitsuda, M. Miyazaki, I. B. Nielsen, P. Çarçabal, C. Dedonder, C. Jouvet, S. Ishiuchi and M. Fujii, Evidence for Catechol Ring- Induced Conformational Restriction in Neurotransmitters, *J. Phys. Chem. Lett.*, 2010, **1**, 1130–1133.

[12] T. Bürgi and S. Leutwyler, O–H torsional vibrations in the S0 and S1 states of catechol, *J. Chem. Phys.*, 1994, **101**, 8418–8429.

[13] A. Longarte, C. Redondo, J. A. Fernández and F. Castaño, IR/UV and UV/UV double-resonance study of guaiacol and eugenol dimers, *J. Chem. Phys.*, 2005, **122**, 164304.

[14] A. Longarte, I. Unamuno, J. A. Fernández, F. Castaño and C. Redondo, Experimental and theoretical study of the structures and binding energies of eugenol (H2O)n, n=0–2, *J. Chem. Phys.*, 2004, **121**, 209–219.

[15] P. Çarçabal, R. A. Jockusch, I. Hünig, L. C. Snoek, R. T. Kroemer, B. G. Davis, D. P. Gamblin, I. Compagnon, J. Oomens and J. P. Simons, Hydrogen Bonding and Cooperativity in Isolated and Hydrated Sugars: Mannose, Galactose, Glucose, and Lactose, *J. Am. Chem. Soc.*, 2005, **127**, 11414–11425.

[16] E. J. Cocinero and P. Çarçabal, eds. A. M. Rijs and J. Oomens, Springer International Publishing, Cham, 2015, pp. 299–333.

[17] D. M. Hewett, S. Bocklitz, D. P. Tabor, E. L. Sibert III, M. A. Suhm and T. S. Zwier, Identifying the first folded alkylbenzene via ultraviolet, infrared, and Raman spectroscopy of pentylbenzene through decylbenzene, *Chem. Sci.*, 2017, **8**, 5305–5318.

[18] E. J. Cocinero, E. C. Stanca-Kaposta, M. Dethlefsen, B. Liu, D. P. Gamblin, B. G. Davis and J. P. Simons, Hydration of Sugars in the Gas Phase: Regioselectivity and Conformational Choice in N-Acetyl Glucosamine and Glucose, *Chem. – A Eur. J.*, 2009, **15**, 13427–13434.

Chapter 6

Exploration of Caffeine-Phenol interactions

Adapted from: I. Usabiaga, A. Camiruaga, C. Calabrese, A. Maris and J. A. Fernández, *Chem. – A Eur. J.*, 2019, **25**, 14230–14236.

6.1. Introduction

The systems studied in previous chapters demonstrated the interplay that exists between theory and experiments in the study of molecular aggregates: experimental data can only be interpreted on the light of the computational predictions. But at the same time, development and test of the computational methods require of a large body of data to fine tune the quantum chemistry calculation levels. We present here a particularly difficult system from the computational point of view: the caffeine-phenol dimer (Caf+Ph). Caffeine (Figure 6.1) is a methylxanthine present in coffee and responsible for its stimulant effects.[1] Its structure contains four nitrogen atoms, two oxygen atoms, and an aromatic system, and therefore, exhibits multiple interaction sites for other molecules. Conversely, phenol is a simple molecule formed by a benzene ring with a hydroxyl substituent. It is known to be one of the components of tobacco smoke,[2] and therefore, both molecules may come into contact in the blood of coffee-drinking smokers, and their aggregation may even alter the way in which they interact with different receptors in the cells.[3–6] However, the main goal of this work is not to explore such health-related issues, but to use the spectroscopic information recorded from the aggregates to explore the ability of several computational levels to model the interactions by analyzing the coherence/incoherence of their predictions. This comparison will help us to understand where there are limits for the interpretation of theoretical predictions.

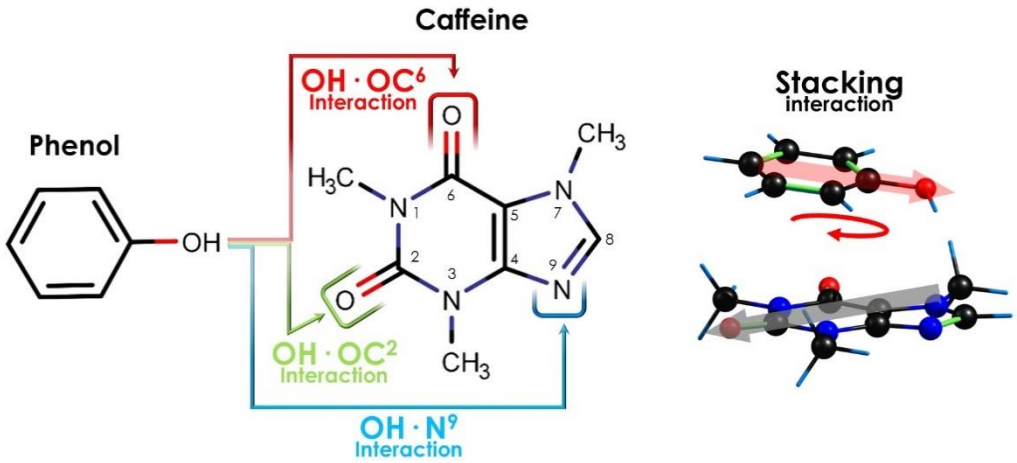

Figure 6.1: Structure of phenol and caffeine (with atom numbering). The four main interacting sites, OH·OC6, OH·OC2, OH·N9, and the stacking interaction, are highlighted.

Figure 6.1 shows the structures of phenol and caffeine. As can be observed, caffeine contains several anchor points where phenol can form hydrogen bonds. The stability of these interactions will also be modulated by π···π stacking interactions between the

aromatic rings, or additional CH···π interactions between the methyl groups of caffeine and phenol's aromatic ring. As these interactions can stabilize both molecules in many different ways, leading to a large number of possible conformational isomers that are very close in stability.

The methodology followed in this work was the same as the rest of the studies presented in this thesis, but with an increased computational exploration involving different methods and basis sets. We used four different computational methods, combining pure DFT, hybrid methods and pure ab initio: M06-2X, MN15, B3LYP and MP2. M06-2X, as we observed in previous chapters, yielded good results in different situations.[7,8] However, evidences have appeared regarding the performance of this functional, especially when there is a close competition between several weak interactions.[9] Thereby, we employed MN15, the latest version of this functional at the time this work was done, which was also developed by Thrular's group.[10] We also included the empirical dispersion corrected B3LYP functional (ED=GD3BJ),[11] which was also previously used in this thesis. This functional yielded outstanding results for systems attached by non-covalent interactions.[12,13] Finally, we included the MP2 ab initio method, to compare the predictions for dispersive forces with the above-mentioned DFT methods. Both triple-ζ basis sets of Pople and Aldrich where used for each functional, except for MP2, where only 6-311++G(d,p) basis set was employed due to the high computational cost of this ab initio method.

6.2. Conformational landscape of Caffeine-Phenol complex

The interaction potential energy surface (iPES) of Caf+Ph was built by analyzing all the optimized structures from the conformational search. As four computational methods were used, optimization processes took different paths, but most of the most stable structures ended in the same geometry. A RMSD comparison between the structures optimized by different levels allowed an easy comparison of the local minima. The analysis of the conformational landscape of Caf+Ph dimer revealed the existence of several possible isomers for phenol interacting with each interaction site of caffeine. The differences between them are due to the secondary interactions, which are maximized in each case. For example, as shown in Figure 6.2, if phenol interacts with OC6, it can also interact with the aromatic ring (isomers 1 and 6) or with one of the methyl groups (isomer 7, 17), or just maximize the OH· · · O interaction, by positioning the phenolic ring away from caffeine (isomer 12, see also Figures A6.1-6.4 in Appendix 6). It is very likely

that many of the computed structures are connected by low potential-energy barriers, and therefore, the whole system simplifies during the cooling process, leading to a reduced number of structures in the expansion. Thus, information on the relative stability of the computed structures may be helpful for the assignment of experimental spectra.

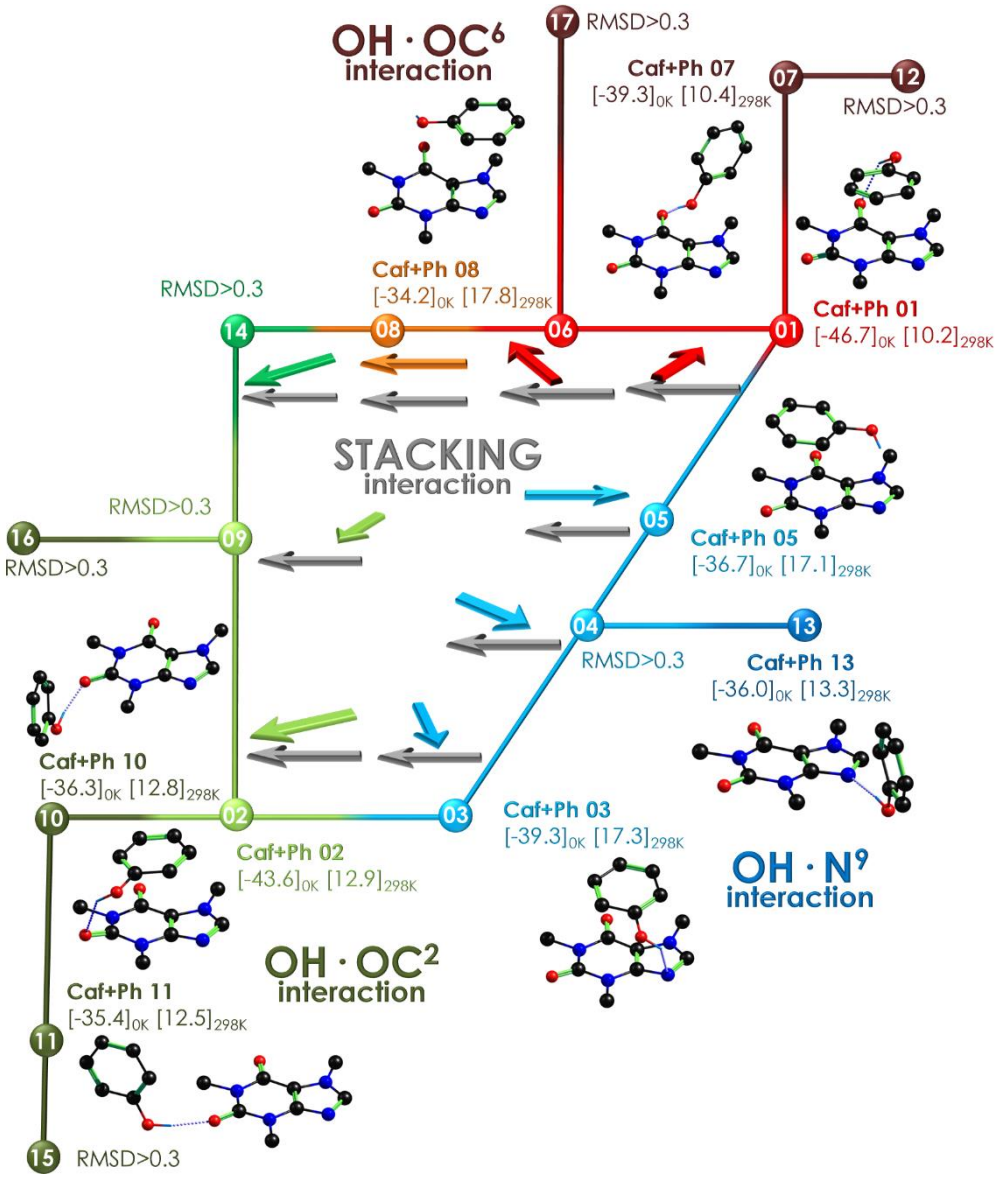

Figure 6.2: Computed structures of Caf+Ph, which are sorted according to similarity and interaction site. Binding Gibbs free energy values DDG [kJ·mol^{-1}] are given at 0 and 298 K, and they are the average of the six theoretical methods, considering only structures with a root-mean-square deviation (RMSD) of atomic positions (counting only C and O atoms) of ‹0.3. MP2 was not included because several of the structures predicted by the other methods converged to the same conformer upon optimization at MP2. The arrows depict the relative orientation of the two molecules in stacking. All hydrogen atoms attached to a carbon atom were hidden for the sake of clarity. More elaborate versions of this figure, with the relative stability of the structures calculated at each computational level, can be found in Appendix 6.

In this complex, binding energy is directly related to the stability of the structure, as the monomers present a single conformation. Figure 6.3 presents the $\Delta\Delta G_B$ values at 0 and 298 K averaged over the six theory levels employed in this study. Only those structures with a root-mean-square deviation (RMSD) of atomic positions of ‹0.3 were considered. This means that if optimization of one isomer resulted in very different structures at two computation levels, it was discarded from the rest of the analysis.

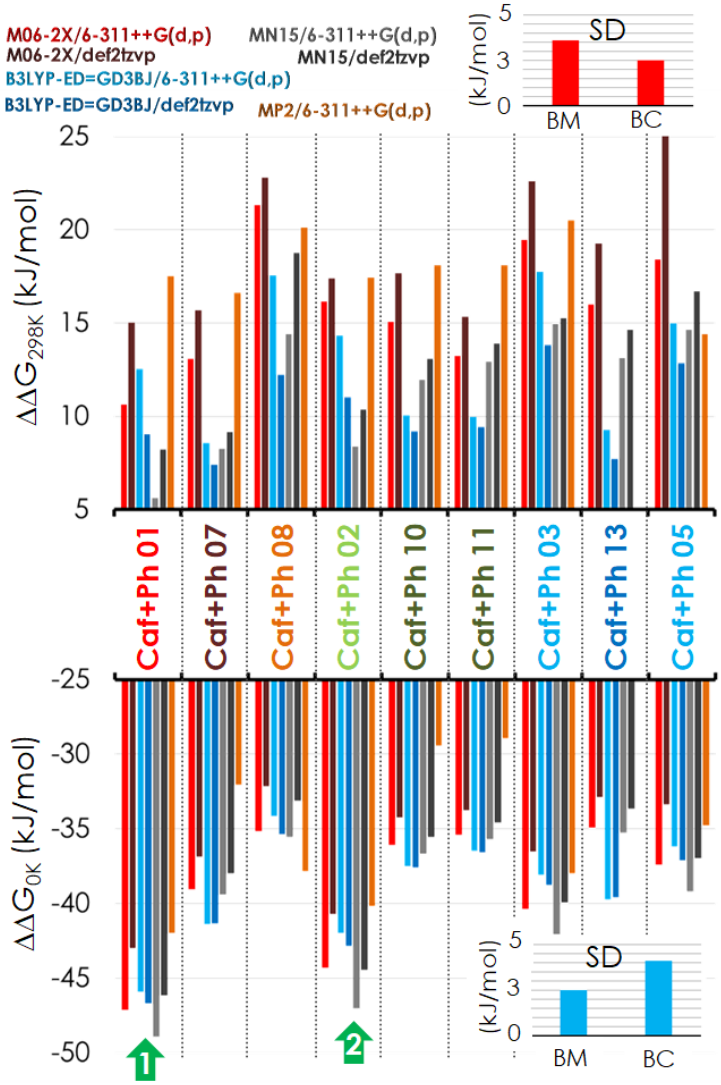

Figure 6.3: Relative binding Gibbs free energy ($\Delta\Delta G_B$) diagram at 0 and 298 K for the conformers of Caf+Ph with RMSD of atomic positions ‹ 0.3. $\Delta\Delta G$ is defined as the difference in ΔG of a given specie with the global minimum. SD= standard deviation, BM= between methods, BC = between conformers.

Figure 6.3 collects the binding Gibbs free energies ($\Delta\Delta G_B$) of Caf+Ph conformers, computed at 0 and 298 K at all the theory levels employed. All theoretical approaches point to isomer 1 as the most stable structure at 0K followed by isomer 2. However, some discrepancies in the relative energetic order of the rest of the structures were

found: the standard deviation (SD) of $\Delta\Delta G_B$ between the seven computational methods (labelled as BM) is larger than the SD of $\Delta\Delta G_B$ between conformers (labelled as BC), which means that the energy difference between most of the conformers is within the computational error. All of these error estimations were performed without considering the structures with a RMSD in the atomic positions of >0.4, since, for those conformers, the optimization step resulted in very different structures. Surprisingly, the same trends were observed for calculations with MP2, regarding dispersion of the computed values and it presented one of the highest SDs. Optimization with MP2 also resulted in a reduced number of isomers because some of the conformers found by the other calculation levels converged in a single structure under MP2 calculations (see Table A6.1 in Appendix 6).

The discrepancies are maximized at higher temperatures. For example, at 298K, the ratio between BM and BC SDs is inverted, which means that the computational error is larger than the energy difference between conformers. Therefore, it is more convenient to consider only families of structures and trends instead of isolated conformations. Other evidence of this facts can be found in Figure A6.5, in which the Gibbs free energy diagrams for the seven theory levels are presented.

On the light of the above-mentioned trends, all computational methods point that the most stable families always present strong OH···OC interactions. The isomers that present such interactions are 10, 11, 15 and 16 for the OH·OC^2 family; and isomers 07, 12 and 17 for the OH·OC^6 family.

6.3. Spectroscopy of caffeine-phenol complex

The first step was to record the REMPI spectra of the monomers. Figure 6.4 shows the UV absorptions of caffeine, phenol, and Caf+Ph dimer. As can be observed, both phenol and caffeine present discrete, well-resolved vibronic transitions, in very good agreement with previous studies.[14–17] However, owing to the presence of two chromophores, a short lifetime of the excited state, or multiple conformational isomers of the dimer with numerous low-frequency vibrations, the REMPI spectrum of Caf+Ph is a structureless absorption starting about 35200 cm^{-1}. For example, in a pioneering study, de Vries and co-workers reported the one-color REMPI spectra of 7-methylxanthine and theobromine homodimers and, in both cases, the result was a broad absorption, similar to that reported herein for caffeine.[14]

The absence of a discrete spectrum precluded the use of isomer-specific spectroscopic techniques, such as UV/UV hole burning. However, it is still possible to estimate the number of isomers that contribute to the REMPI trace by recording the IR/UV spectrum to probe different wavelengths with the UV laser.

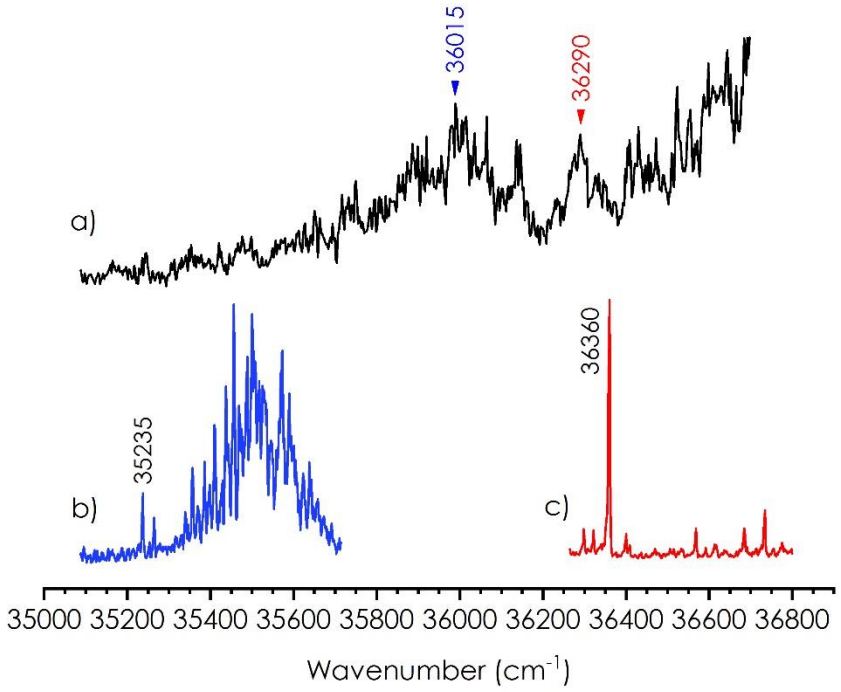

Figure 6.4: One-color REMPI spectra of a) Caffeine+Phenol, b) Caffeine and c) Phenol.

Figure 6.5 shows the experimental IDIR spectra in the OH/CH stretching regions obtained for phenol, caffeine and Caf+Ph dimer, with the probe laser tuned at 36015 and 36290 cm^{-1}. The IR spectra of phenol and caffeine are in good agreement with previous publications:[14,18] caffeine exhibits only CH stretches that appear as a single broad band located at 2960 cm^{-1}, whereas phenol presents some weak CH stretch absorptions around 3062 cm^{-1} and a stronger transition corresponding to its single OH stretching band, at 3662 cm^{-1}. The observed OH band in Caf+Ph complex is 200 cm^{-1} red-shifted from that of the monomer, which is between the observed shifts in phenol-water and phenol-ammonia.[19]

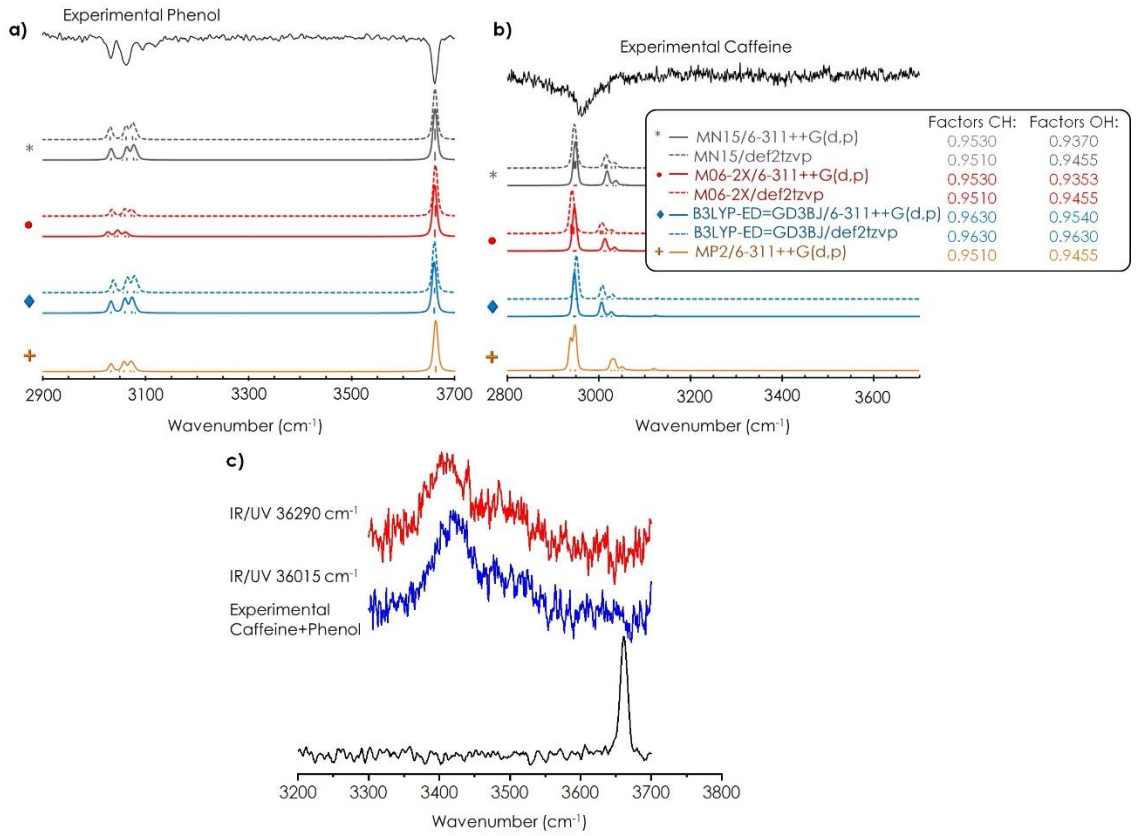

Figure 6.5: Experimental IDIR spectra of a) Phenol, b) Caffeine and c) Caf+Ph complex. A comparison with the computational predictions in the monomers allowed us to determine the value of the factors to account for anharmonicity.

The IR spectra of the monomers were used to test and adjust the correction factors to account for anharmonicity in the computed frequencies. As can be observed, all computational levels produced very similar predictions, and accurately reproduced the experimental observations. However, the anharmonicity factors required were significantly different for each computational level. Interestingly, a more similar factor for both CH and OH stretches was required for computations with def2tzvp and a single value for both types of stretches was required at the B3LYPED=GD3BJ/def2tzpv level.

As observed in Figure 6.5, the two IR spectra of Caf+Ph obtained upon probing two different wavelengths are noisy, but still they present small but noticeable differences; thus indicating population changes with the UV wavelength and providing evidence of the contribution of several isomers to the spectrum. Furthermore, only the OH stretch is expected to appear in that spectral region, while the broad absorption presents a shoulder, which may be due to the existence of additional isomers or to fragmentation from larger clusters. However, the weak signal of the dimer and the absence of signals in the mass spectrum that could be attributed to the trimer exclude such a possibility.

The other possible fragmentation source is water complexes, but in this experimental arrangement the formation of water complexes is so disfavored that even phenol+water or caffeine+water complexes are hard to detect.

Assignment of the IR spectrum requires a comparison with the computational predictions, but the shift in the OH stretch of phenol clearly indicates that the participant molecules form a moderately strong hydrogen bond.

Figure 6.6 collects the predictions for all the structures of Caf+Ph at all the seven computational methods, compared to the experimental IDIR spectra. The discrepancies between the computational methods are not only limited to the values of the relative stability, as we observed in the previous section, but also to the frequency prediction of the vibrational modes.

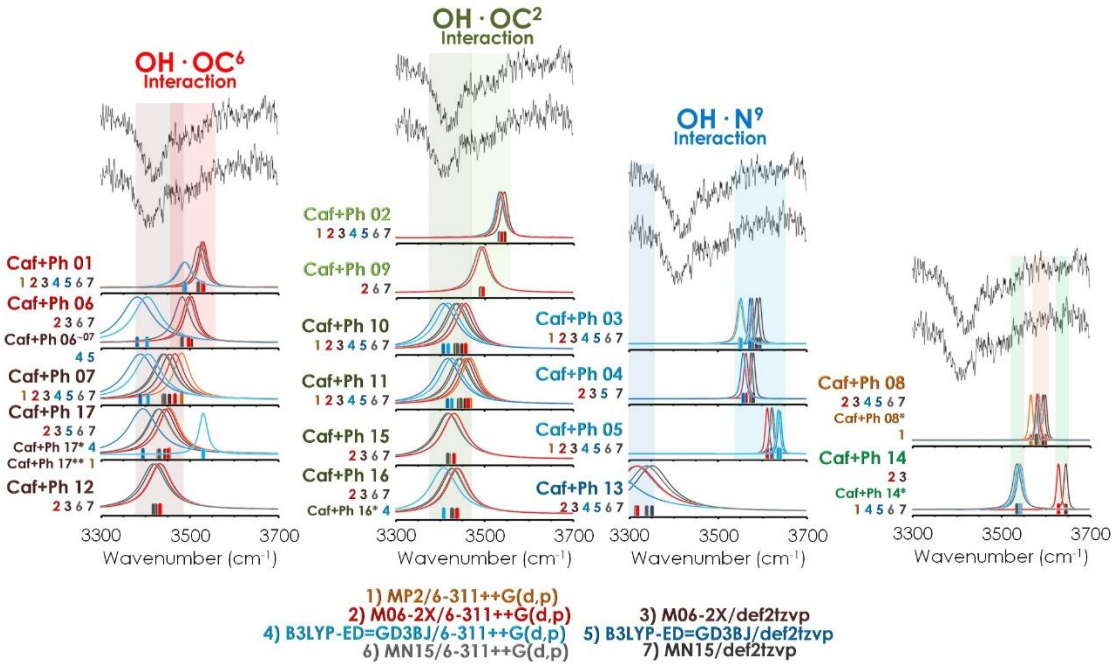

Figure 6.6: Comparison between the IR spectra of Caf+Ph and the computational predictions for the calculated structures. The structures are grouped by the type of interaction. The position of the bands is simulated by using gaussians that follow the color code of the computational level.

The comparison between experiment and predictions did not offer a univocal assignment, as no single isomer is able to reproduce the observed experimental trace. Clearly, those structures with phenol interacting with N^9 of caffeine can be discarded because they present absorptions that are either to the blue (Caf+Ph 03, 04 and 05) or to the red (Caf+Ph 13) of the experimental observations. Likewise, the predictions for isomer 8 are not in good agreement with the experimental spectrum. Thus, the mentioned isomers or isomer families can be discarded.

On the other hand, isomer 14 may reproduce the position of the shoulder at all levels apart from the two M06-2X level. This also correlates with the large RMSD deviation due to a large structural change during the optimization at the M06-2X level. Such structural changes also occur in other isomers, such as Caf+Ph 06, 08, 16, and 17, resulting in very different predicted IR spectra. The computed spectra for the rest of the species and families present transitions that are compatible with the experimental spectra. A more accurate assignment would also need to take into account, in addition to the relative stability of the structures, the shape of the potential-energy surface. However, the differences in the values offered by each computational level do not clarify which of the methods would yield the most accurate description of the conformational space, especially at 298 K. Notably, the families that are stabilized at higher temperatures are those that better reproduce the position of the strong absorption in the spectra (around 3450 cm^{-1}).

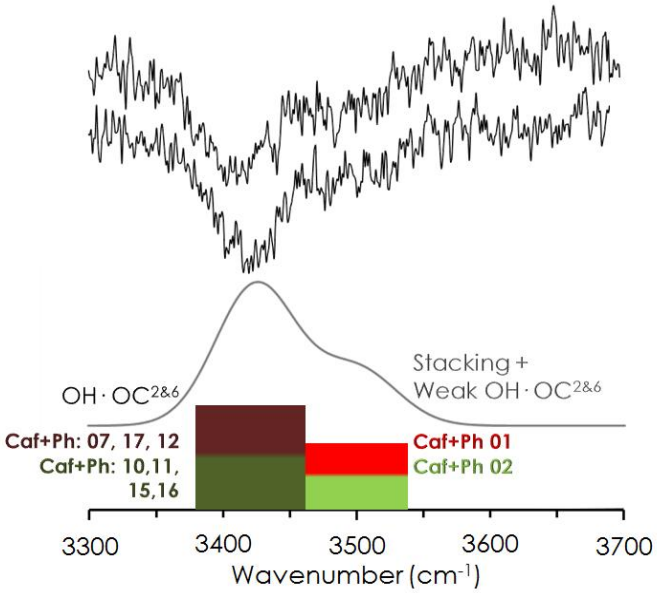

Figure 6.7: Simulation of the IR spectra with the contributions of the four main families of isomers assigned to Caf+Ph complex. The width of the bars indicated the uncertainty in the prediction of the band position.

Figure 6.7 summarizes the final assignment for Caf+Ph complex. The simulated spectrum is a convolution of the predictions from the four main families of isomers. The width of the bars represents the uncertainty in the position of the transition. Clearly, the whole experimental trace is explained by the transitions predicted for these families: the maximum of the absorption correlates very well with the OH stretching of those families that are stable at higher temperatures and present a strong OH···$OC^{2,6}$ hydrogen bond.

Likewise, the shoulder is well reproduced by the structures that are more stable at 0K and that present stacking interactions in addition to the OH·OC^{2,6} hydrogen bond.

There is a clear competition between OH···OC^{2} and OH···OC^{6} hydrogen bonds. The presence of both of them explain the experimental observations, and their difference in energy is not large enough to discard one of them. These latter interactions seem to be the leading forces in the aggregation of Caf+Ph, acting as anchor point for the hydroxyl group of phenol, as other HB possibilities (like OH·N^{9}) were experimentally discarded.

The topological analysis of the reduced electronic density gradient of Caf+Ph gives a graphical representation of the non-covalent interactions. Figure 6.8 shows the NCI plots for the most stable isomers (Caf+Ph 01 and 02), responsible of the weaker shoulder in the IR spectrum, and for one of the isomers responsible of the strong absorption (Caf+Ph 07). The difference between isomers 01 and 02 is the change of the C=O group of caffeine that acts as proton acceptor. In both of them, the OH···O interaction is represented as a blue colored surface. Additionally, $\pi\cdots\pi$ interactions can be observed as a green surface between both aromatic rings. The strength of the dispersive forces in isomers 01 and 02 is nearly identical, as shown by the RDG vs sign(λ_2)ρ representation (red and green plots). However, the difference is clear when comparing these results with ones from isomer 07. The isosurface is completely different, with very limited presence of dispersive interactions. This fact can be also appreciated in the numerical representation of the reduced density gradient, as no low density, low gradient regions can be observed for isomer 07 (blue plot) near sign(λ_2)ρ zero values. Besides, there is a clear difference in the OH···O HB strength, as the low-density, low-gradient through this interaction appear at more negative values in comparison with isomers 01 and 02.

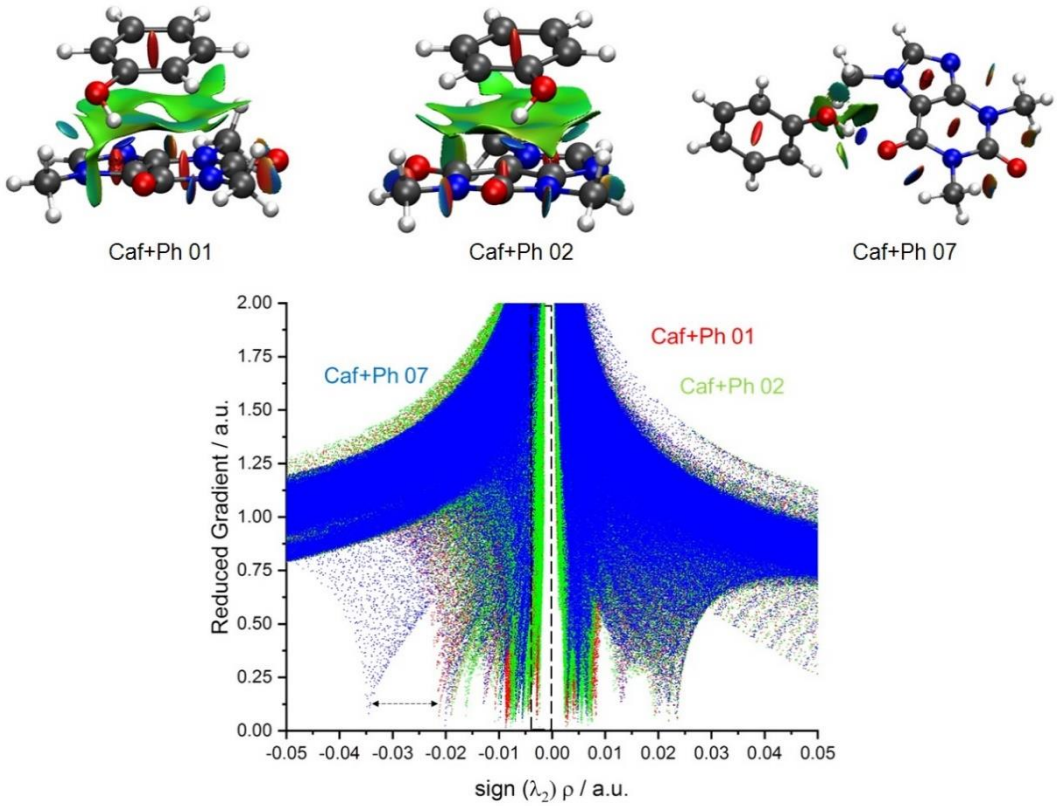

Figure 6.8: NCI plots of the assigned isomers with the main interaction in Caf+Ph complex.

On the light of these results, it is clear that the conformational landscape of Caf+Ph complex resulted to be a difficult case to model. It seems like phenol is floating around caffeine, maximizing hydrogen bonds and stacking interactions separately depending on the structure adopted. Additionally, differences in the coefficients of the functionals employed to describe weaker interactions result in fuzzy predictions of the local minima, especially when temperature raises. All of the above highlights the importance of taking into account not only the most stable isomer, but also other relatively stable conformations, especially if attractive forces are a balance between several weak interactions.

6.4. Conclusions

In this chapter we present a combined computational and experimental examination of Caf+Ph aggregate. The reduced size of the complex is not related to its complexity, which finally resulted to be substantially difficult to model. Caffeine presented multiple interaction sites for phenol, with numerous local minima, resulting from the balance

between CH···π and π···π dispersive forces, and different hydrogen bond possibilities of similar strength. Four different functional were employed for the computational exploration: M06-2X, MN15, B3LYP and MP2. Three of them where combined with both 6-311++G(d,p) and def2TZVP bases, making a total of seven computational levels. All of them agreed that conformer 1 is the most stable structure, followed by isomer 2. In such conformers, phenol interacts with caffeine through π···π interactions and hydrogen bonds with $OC^{2,6}$. This assignment is in agreement with previous studies on caffeine-water, in which water was also found to interact preferentially with the carbonyl groups of caffeine.[16,17,20] However, no consensus was found between them for the relative stability of the local minima. This seems to indicate that the methods used are able to accurately model stronger interactions, but they balance other weaker interactions in different ways. The magnitude of the discrepancies between the predictions is assumed to be due to differences in the strengths of the secondary interactions, and therefore, in the low-frequency modes.

The panorama resulting from this work warns about overinterpreting the results of these kind of studies, as the limited amount of experimental information and implicit precision of the computations limit the conclusions that one can extract. We can affirm that phenol preferentially interacts with OC^{6} and that the most likely secondary interaction site is OC^{2}. Such interactions result in a broad absorption centered at around 3450 cm^{-1}. Other isomers may also contribute to the spectrum, with the interaction with the same oxygen atoms as a leading force, but with a different ratio of contributions of other secondary interactions (mainly stacking and CH···π). The discrepancies observed in a small system like Caf+Ph may be amplified in larger systems, such as protein folding or protein-ligand aggregates, in which the interactions due to dispersive forces play a determining role in the final shape of the system.

6.5. References

[1] A. Nehlig, J.-L. Daval and G. Debry, Caffeine and the central nervous system: mechanisms of action, biochemical, metabolic and psychostimulant effects, *Brain Res. Rev.*, 1992, **17**, 139–170.

[2] A. Rodgman and T. Perfetti, *The Chemical Components of Tobacco and Tobacco Smoke*, CRC Press, Boca Raton, 2nd Editio., 2013.

[3] T. T. Lang, J. D. Young and C. E. Cass, Interactions of Nucleoside Analogs, Caffeine, and Nicotine with Human Concentrative Nucleoside Transporters 1 and 2 Stably Produced in a Transport-Defective Human Cell Line, *Mol. Pharmacol.*, 2004, **65**, 925 LP – 933.

[4] B. B. Fredholm, K. Bättig, J. Holmén, A. Nehlig and E. E. Zvartau, Actions of Caffeine in the

Brain with Special Reference to Factors That Contribute to Its Widespread Use, *Pharmacol. Rev.*, 1999, **51**, 83 LP – 133.

[5] S. Zevin and N. L. Benowitz, Drug Interactions with Tobacco Smoking, *Clin. Pharmacokinet.*, 1999, **36**, 425–438.

[6] J. Istvan and J. D. Matarazzo, Tobacco, alcohol, and caffeine use: A review of their interrelationships., *Psychol. Bull.*, 1984, **95**, 301–326.

[7] I. Usabiaga, J. González, P. F. Arnáiz, I. León, E. J. Cocinero and J. A. Fernández, Modeling the tyrosine–sugar interactions in supersonic expansions: glucopyranose–phenol clusters, *Phys. Chem. Chem. Phys.*, 2016, **18**, 12457–12465.

[8] A. Camiruaga, I. Usabiaga, A. Insausti, I. León and J. A. Fernández, Sugar–peptidic bond interactions: spectroscopic characterization of a model system, *Phys. Chem. Chem. Phys.*, , DOI:10.1039/C7CP00615B.

[9] C. Pérez, I. León, A. Lesarri, B. H. Pate, R. Martínez, J. Millán and J. A. Fernández, Isomerism of the Aniline Trimer, *Angew. Chemie Int. Ed.*, 2018, **57**, 15112–15116.

[10] H. S. Yu, X. He and D. G. Truhlar, MN15-L: A New Local Exchange-Correlation Functional for Kohn–Sham Density Functional Theory with Broad Accuracy for Atoms, Molecules, and Solids, *J. Chem. Theory Comput.*, 2016, **12**, 1280–1293.

[11] S. Grimme, J. Antony, S. Ehrlich and H. Krieg, A consistent and accurate ab initio parametrization of density functional dispersion correction (DFT-D) for the 94 elements H-Pu, *J. Chem. Phys.*, 2010, **132**, 154104.

[12] I. Usabiaga, A. Camiruaga, C. Calabrese, A. Maris and J. A. Fernández, Exploring Caffeine–Phenol Interactions by the Inseparable Duet of Experimental and Theoretical Data, *Chem. – A Eur. J.*, 2019, **25**, 14230–14236.

[13] E. Caldeweyher, C. Bannwarth and S. Grimme, Extension of the D3 dispersion coefficient model, *J. Chem. Phys.*, 2017, **147**, 34112.

[14] M. P. Callahan, Z. Gengeliczki, N. Svadlenak, H. Valdes, P. Hobza and M. S. de Vries, Non-standard base pairing and stacked structures in methyl xanthine clusters, *Phys. Chem. Chem. Phys.*, 2008, **10**, 2819–2826.

[15] A. Oikawa, H. Abe, N. Mikami and M. Ito, Solvated phenol studied by supersonic jet spectroscopy, *J. Phys. Chem.*, 1983, **87**, 5083–5090.

[16] D. Kim, H. M. Kim, K. Y. Yang, S. K. Kim and N. J. Kim, Molecular beam resonant two-photon ionization study of caffeine and its hydrated clusters, *J. Chem. Phys.*, 2008, **128**, 134310.

[17] P. B. Balbuena, W. Blocker, R. M. Dudek, F. A. Cabrales-Navarro and P. Hirunsit, Vibrational Spectra of Anhydrous and Monohydrated Caffeine and Theophylline Molecules and Crystals, *J. Phys. Chem. A*, 2008, **112**, 10210–10219.

[18] E. Aguado, I. León, E. J. Cocinero, A. Lesarri, J. A. Fernández and F. Castaño, Molecular recognition in the gas phase: benzocaine–phenol as a model of anaesthetic–receptor interaction, *Phys. Chem. Chem. Phys.*, 2009, **11**, 11608–11616.

[19] A. Iwasaki, A. Fujii, T. Watanabe, T. Ebata and N. Mikami, Infrared Spectroscopy of Hydrogen-Bonded Phenol–Amine Clusters in Supersonic Jets, *J. Phys. Chem.*, 1996, **100**, 16053–16057.

[20] V. B. Singh, Spectroscopic signatures and structural motifs in isolated and hydrated caffeine: a computational study, *RSC Adv.*, 2014, **4**, 58116–58126.

Chapter 7

Spectroscopy of xanthine derivatives: theobromine and theophylline

Adapted from: A. Camiruaga, I. Usabiaga, V. C. D'mello, G. A. García, S. Wategaonkar and J. A. Fernández, *Phys. Chem. Chem. Phys.*, 2019, 21, 26430-26437.

7.1. Introduction

The interest of the studies about the photophysical and photochemical properties of biological molecules is increasing, due to the undesired effect that exposure of unprotected skin may have on health, such as the appearance of melanoma or skin aging caused by production of highly oxidative species. It is well known that DNA-UV photon interaction is may result in harmful mutations. Indeed, eukaryotic cells have developed an elaborate machinery to correct such mutations. Some theories even speculate that the DNA bases have evolved to present very short-lived electronic excited states as a mechanism to minimize UV radiation damage.[1–5]

In this context, the interaction of UV radiation with other metabolites has attracted significantly less attention, despite some of them being structurally related to DNA. Such is the case of xanthine and its derivatives. Their biological activity is very likely connected to the structural similarity with DNA bases, and their ability to form similar non-covalent interactions.[6–8] With the same purine aromatic backbone, xanthine includes N-H and C=O groups in a similar disposition to that of thymine, a resemblance that enables its docking to the same receptors, with certain degree of affinity. Two derivatives of xanthine, theobromine (TB) and theophylline (TP) also present biological activity. The difference between TP and TB is the position of a single methyl group, which is attached to N7 in the former and to N1 in the latter. Such a simple modification is enough to substantially alter the biological properties of the molecule.

The spectroscopy of TP and TB has already been explored: Callahan *et. al.* reported for the first time the REMPI spectra of 7-methylxanthine, TP, TB and caffeine,[9] and in a recent work, Kim *et. al.* reported spectra in agreement with those from de Vries group,[10] but substantially more crowded. The authors reported the bandwidths of the origin bands of TP and TB as 150 and 120 cm^{-1}, respectively, compared with 7 cm^{-1} for caffeine and that such large bandwidths could not be reduced by changes in the "backing pressure, temperature, carrier gas, or laser power". To explain such observations, Kim's group explored the impact that the structural changes on electronic excitation may have in the spectrum.[10] Here, we explore the effect of the position of the methyl group has on the dynamics of excited electronic states and on the ionization process of TP and TB in supersonic jets. For that purpose, in a collaboration work with TIFR[11] and the DESIRS beamline (SOLEIL Synchrotron, St. Aubin, France),[12] we recorded the zero-electron kinetic energy (ZEKE) and the threshold photoelectron spectra (TPES) to obtain precise ionization energies and the vibronic structure of the respective cations near their

first ionization threshold. The experimental results were complemented with computations on the electronic ground and the first excited state of the molecules and the ground state of the respective cations.

7.2. Conformational landscape

The conformational landscape of TB and TP is composed of several tautomers and rotamers. Figure 7.1 shows the relative stability of the tautomers of TB and TP, with an estimation of the unidimensional tautomerization potential energy barrier. For the case of theobromine, its most stable form corresponds to the di-keto tautomer, with the hydrogen bond attached to N1. Transferring that hydrogen atom to one of the two O atoms of the carbonyl groups results in two possible enol tautomers. Furthermore, each enol conformation has two possible rotamers, depending on the orientation of the OH moiety. According to the calculations, the most stable rotamer of the enol forms is about 80 $kJ \cdot mol^{-1}$ above the keto form, and therefore, it will be present in very low abundance in the jet. All these predictions are in agreement with those in previous publications.

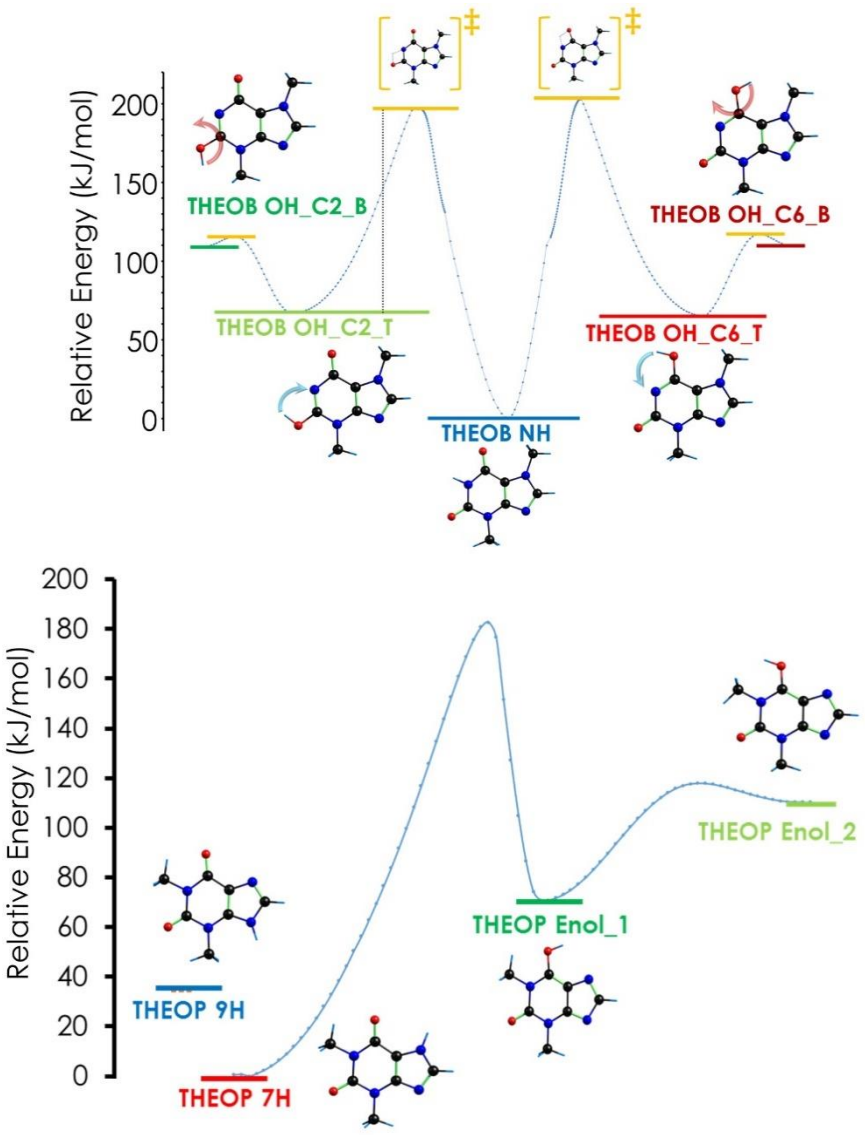

Figure 7.1: Upper panel: relative stability of TB tautomers, with estimated unidimensional barriers; lower panel: relative stability of the most stable TP tautomer, with estimated unidimensional tautomerization barriers. Barrier estimation was done re-optimizing the structure at each point (relaxed potential energy scan). All calculations were done at M06-2X/6-311++G(d,p) level.

For TP, there are two possible di-keto forms, depending if the H atom is attached to either N7 or N9. The most stable form is the N7H tautomer, with a relative energy difference of about 36 kJ·mol^{-1}. H transposition can produce an enolic form, but through a very high energy barrier. Hence, only the N7H tautomeric form of TP is expected to be populated in the beam.

The hindered rotation of the methyl groups may also result in several rotamers, although they are of very similar stability and the low barriers between them can be surmounted during the cooling stage. The computations run to explore the potential energy surface for the rotation of the methyl groups are summarized in Figure 7.2. As

can be observed, the rotation barriers for TB are between 10 cm^{-1} for the methyl group attached to N3 and 180 cm^{-1} for that attached to N7, in good agreement with previous computations by Kim's group.[10] In the case of TP, the difference between the rotation barriers between the methyl groups attached to N1 and N3 is smaller, because the free rotation of the N1 methyl group is more restricted by the C=O groups. Nevertheless, these values are of the order of what one would expect for the rotation of a methyl group attached to an aromatic ring,[13,14] and hence, one can expect several TB and TP rotamers in the jet.

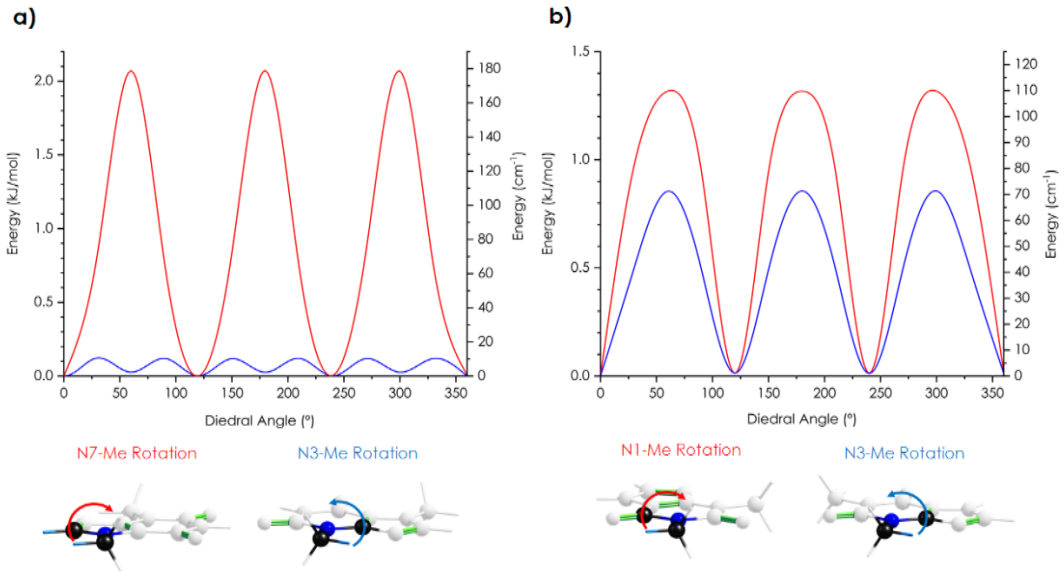

Figure 7.2: Rotational energy barriers of the methyl groups of a) TB and b) TP, computed at M06-2X/6-311++G(d,p) level.

7.3. Spectroscopy of Theobromine and theophylline

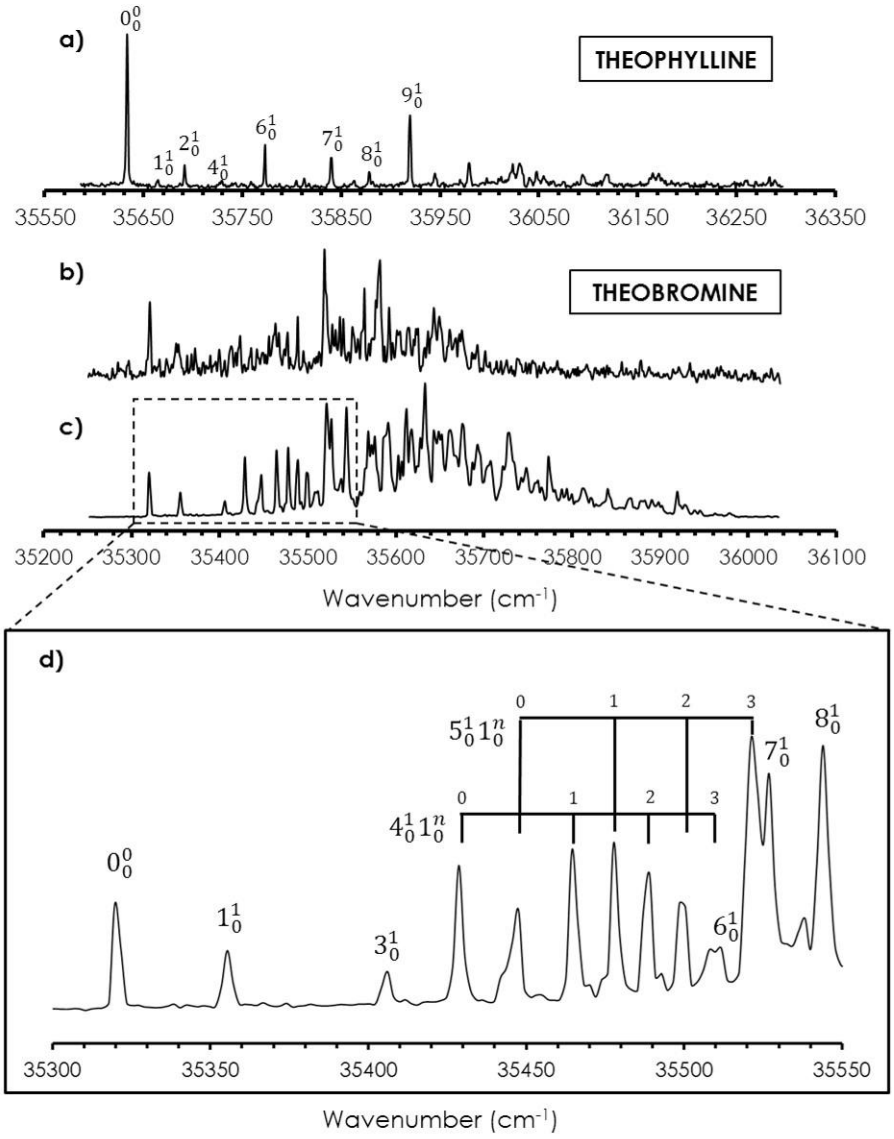

Figure 7.3: REMPI spectrum of a) TP; b) TB obtained using laser desorption; c) TB obtained using heating nozzle; d) zoom into the first 250 cm^{-1} of (c) with a tentative assignment of the main transitions. Relevant spectroscopic values may be found in Table 7.1. Assigned transitions are collected in Tables A7.1 and A7.2 of Appendix 7.

Despite their structural similarity, TB and TP present clear differences in their absorption spectra (Figure 7.3). The 0_0^0 transition of the latter carries most of the strength. In addition, several discrete transitions corresponding to the low frequency modes are clearly visible. The overall spectrum loses intensity ~400 cm^{-1} from the origin, until it fades away beyond 36200 cm^{-1}. In contrast, the spectrum of TB presents a low intensity 0_0^0 transition, on top of which several progressions are built. ν_1 (35.6 cm^{-1}) is an especially

active mode that couples to ν_4 (109.1 cm^{-1}) and ν_5 (127.9 cm^{-1}). Unfortunately, following the progressions above the fourth member is not easy due to spectral congestion.

The spectrum of TB presented here is closer to that obtained by de Vries' group[9] than to the one reported by Kim *et. al.*,[10] which seems to be significantly hotter, hampering the identification of individual transitions. Interestingly, the spectrum reported by de Vries' group presents a lesser number of transitions with respect to that in Figure 7.3, and the positions of the bands in the first ~200 cm^{-1} do not exactly match those in our spectra. A possible explanation is a different jet temperature, resulting in different rotamer populations, perhaps combined with some laser saturation in our experiment. Lifetime broadening may be excluded, as already discussed by Kim's group.[10] We also recorded the spectrum of TB using a laser desorption source (Fig. 7.3b) and although the overall spectrum presented a substantially reduced S/N ratio, the prominent bands in both spectra were in good agreement.

To test if additional species could be contributing to the absorption spectra, we also recorded the IDIR spectra of TB and TP, tuning the UV laser at different transitions and outside resonance. Figure 7.4 shows the comparison between the experimental spectra and those obtained from the computations. Clearly, the experimental spectrum corresponds to the most stable species, which are the N7H-keto form of TP and the di-keto form of TB. However, it seems that the spectrum of TB could contain some contribution from the two enol tautomers, as there is a very weak absorption, almost indistinguishable from the background, but which matches very well with the predicted position of the OH stretches. Nevertheless, additional experiments would be required to confirm this assignment, and for now we will only take into consideration the existence of the keto tautomer.

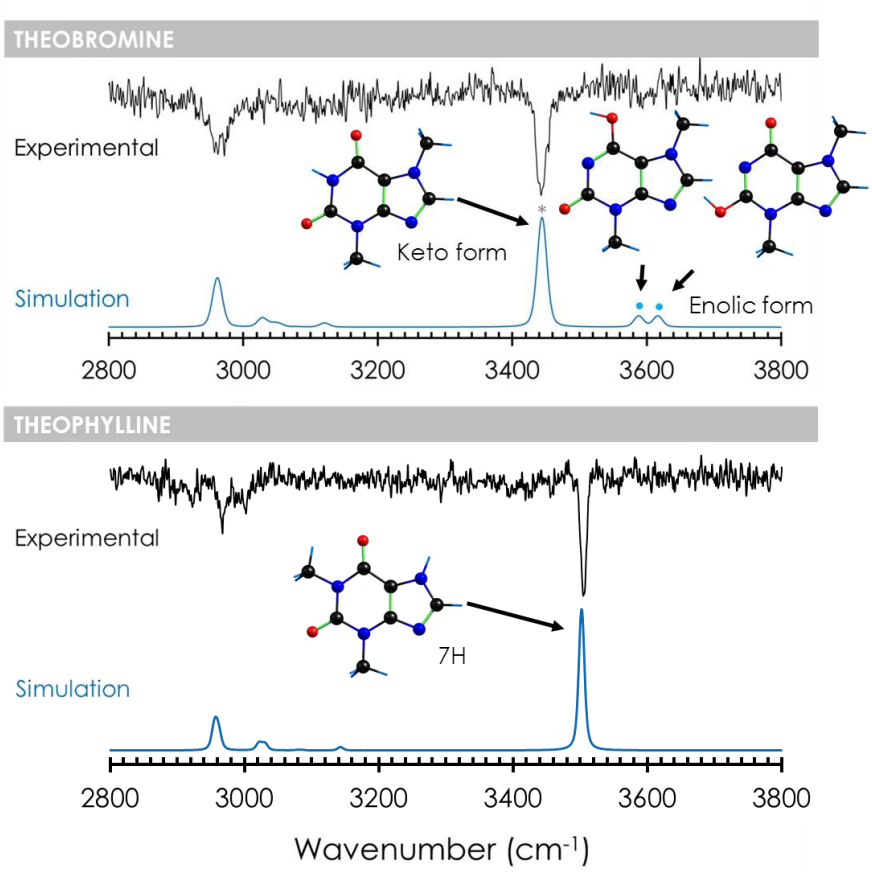

Figure 7.4: Comparison between the IDIR spectra of TB (upper panel) and TP (lower panel) and the simulated spectra computed at M06-2x/6-311++G(d,p). Correction factors of 0.962 (CH stretches), 0.936 (OH stretches) and 0.953 (NH stretches) were used to account for anharmonicity.

To further explore the effect that the small structural differences between TB and TP have on their electronic structure, we used ZEKE and TPES photoelectron spectroscopy. Figure 7.5 compares the ZEKE trace of both molecules, obtained by tuning the first color to their 0_0^0 transitions.

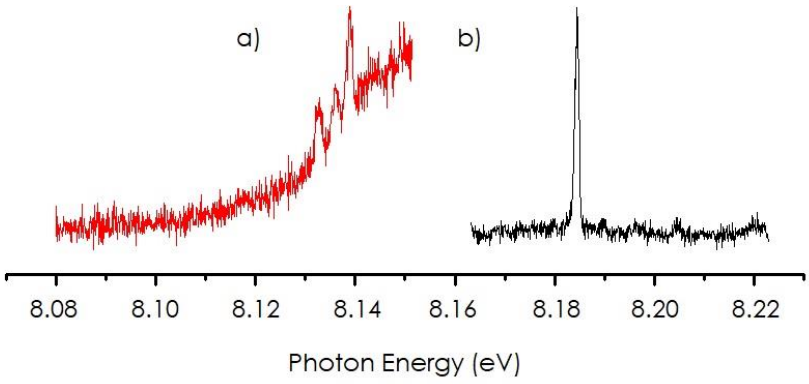

Figure 7.5: Experimental ZEKE spectra of a) TB and b) TP.

Once again, substantial differences were found between the experimental data of both molecules. TP present a sharp adiabatic ionization threshold at 66011 cm^{-1} (8.184 eV), while in the case of TB, the spectrum presents several peaks on top of a broad continuum. The first sharp peak appears at 65601 cm^{-1} (8.133 eV) and is taken as the value of the adiabatic ionization threshold. Relevant spectroscopic data of the UV origin bands and adiabatic ionization energies of TB and TP are collected in Table 7.1, along with the theoretical ionization energies obtained from different computational levels. The use of a soft extraction field in the ZEKE experiment usually results in higher (more realistic) ionization threshold when compared with REMPI or photoelectron spectroscopy. In addition, the technique enables recording it as a well-resolved transition, resulting in an accurate determination of the adiabatic threshold.

Table 7.1: Relative stability and spectroscopic values of theobromine and theophylline.

	Theobromine			**Theophylline**	
	Keto	*C2-Enol*	*C6-Enol*	*7H*	*9H*
Relative Stability (kJ/mol)	0	69.3	65.4	0	36.3
0-0 transition (cm^{-1})	35319.8	-	-	35633.3	-
Adiabatic Ionization Energies (eV)					
Experimental					
IP	8.120	-	-	8.170	-
ZEKE	8.133	-	-	8.184	-
TPEPICO	8.137	-	-	8.187	-
Theory					
M06-2X/6-311++G(d,p)	8.217	8.169	8.078	8.266	8.235
M06-2X/aug-cc-pVDZ	8.120	8.074	7.975	8.165	8.147
PBE0/aug-cc-pVDZ	8.088	8.010	7.921	8.113	8.065
CCSD(T)/cc-pVTZ	7.961	7.928	7.832	8.009	7.989

The values reported here, although higher probably because of the experimental electrostatic conditions, are in good agreement with those reported by Kim *et.al.* (8.10 and 8.06 eV for TP and TB respectively).[10] From the theoretical point of view, the match with the experimental values is not perfect. The method that nearly reproduces the experimental values is M06-2X/aug-cc-pVDZ. Interestingly, although the values from M06-2X/6-311++G(d,p) are almost 0.1 eV too high, it predicts the ionization threshold of TP to be 49 meV higher than that of TB, in excellent agreement with the 50 meV difference observed experimentally. Better predictions could be obtained using costly computational methods,[15] which is away of the scope of the present work. Nevertheless, all theory methods predict that theophylline's ionization threshold is slightly higher than that of theobromine, as observed experimentally.

To obtain a broader view of cation spectroscopy we have used VUV tunable synchrotron radiation to record the TPES of both TP and TB, shown in Figure 7.6. Although the resolution is inferior to that of ZEKE technique, there is a rich vibronic structure in the spectra of both molecules, which can be assigned with the help of calculations that take into account the structural changes between the neutral and ion electronic ground states.

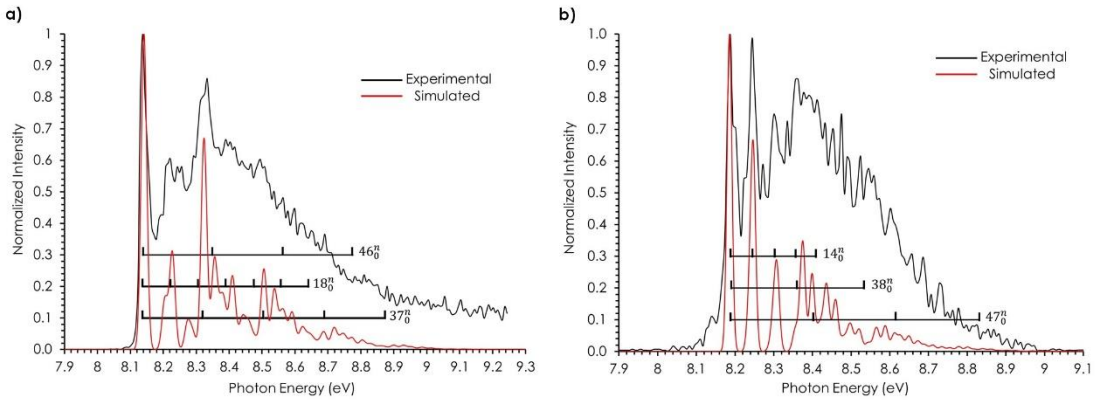

Figure 7.6: Threshold photoelectron spectra (TPES) of a) TB and b) TP, compared to the simulated traces obtained from the multidimensional Franck-Condon calculations. The three main progressions are highlighted. The computed spectra were shifted 0.083 and 0.085 eV respectively to match the experimental spectra. See Tables A7.3 and A7.4 in the appendix for the assignment of the vibrational transitions.

The photoelectron spectra were simulated using computational data from the optimized geometries as input for PGOPHER, as described in the computational section.[16,17] A multidimensional calculation of the Franck-Condon factors was performed with the neutral and ionic structures of TB and TP obtained at PBE0/aug-cc-pVDZ level. As can be observed in Figure 7.6, the simulated spectra correctly predicted the positions of the main absorption bands in the experimental trace. Furthermore, the three modes that are responsible for the observed bands are in-plane ring vibrations, which are consistent with the ionization process that involves ejecting an electron from the aromatic system, causing weakening and expansion of the rings. Therefore, one would expect that the Franck-Condon factors would favor the appearance of progressions in such modes. Note that the agreement between theory and experiment is not complete due to the appearance of a broad background in the TPES spectrum, which is common in this type of experiments and is attributed to auto-ionization processes.

7.4. Discussion

The spectroscopic data obtained allow us to evaluate the influence of the position of a single methyl group in two biologically relevant molecules, TP and TB. The REMPI spectra point to a strong influence of the position of the methyl group on electronic excitation. The spectrum of TP presents a very limited number of bands that do not seem to build any progression. In contrast, the spectrum of TB is more congested, with several coupled vibronic modes, and therefore it is risky to offer any assignments for the bands beyond ~ 0_0^0 + 200 cm^{-1}. Mode ν_1 (35.6 cm^{-1}) seems to be responsible for most of the congestion, as it seems to couple with other vibrations in a facile manner.

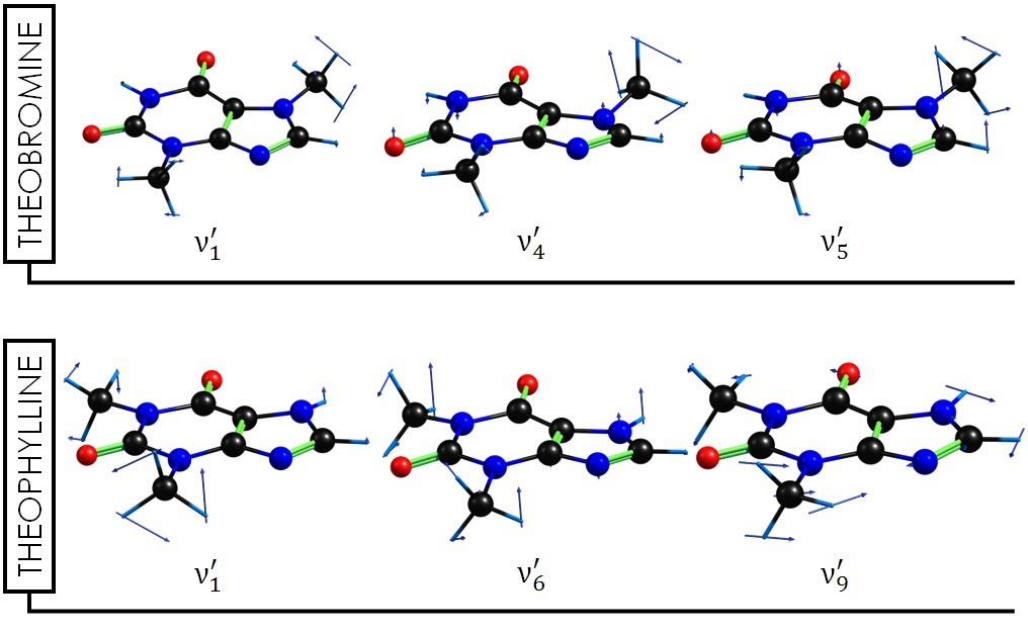

Figure 7.7: Comparison between the most active vibrational modes in the REMPI spectra of TB and TP. Calculations correspond to the S_1 state and were carried out at the CAM-B3LYP/aug-cc-pVDZ level.

Figure 7.7 depicts the three modes that give rise to the two assigned progressions in the REMPI spectrum of TB and the equivalent modes in TP. Mode ν_1 seems to be the responsible for most of the couplings, and it corresponds to the torsion of the two methyl groups. This mode is strongly coupled with ν_4 and ν_5, which involve torsion of the methyl groups, together with ring deformations. Such a ring deformation coordinate matches very well with the ring deformations that takes place upon electronic excitation. In fact, a pyramidalization of N7 in the excited state has been reported,[10,18] which may explain the rich vibrational activity in the REMPI spectrum of TB. Similar methyl group torsions in TP (ν_1) are coupled to ν_6 and ν_9. However, these modes are not as active as in the case of TB, mainly due to the absence of the above-mentioned ring

deformation, in good agreement with the modest vibrational activity observed in the REMPI spectrum of TP.

Further confirmation of this explanation is offered by the ZEKE spectra in Figure 7.5, where the well-defined origin band in the ZEKE spectrum of TP is in sharp contrast with the slow rising continuum observed for TB, whose origin is very likely to be due to a second structural change, i.e., the pyramidalization observed in S_1, probably related to the anti-aromaticity of this state,[19] which is reverted in the ion.

Further validation of the influence of the S_1 intermediate state is found in the photoelectron spectra shown in Fig. 7.6. Here, the ionization is achieved directly from the neutral S_0 ground state. The vibronic structures of both spectra is very similar, meaning that the differences observed in the ZEKE spectra, and therefore also in the REMPI traces, must be due to the different nature of the S_1 states. Computations qualitatively reproduce the general shape of the TPES spectra, and show that the most active vibrations in both TP and TB ions are in-plane ring vibrations (see Figure 7.8). Indeed, extraction of one electron from the aromatic system results in an overall reduction in the electronic density and an enlargement of the C–C and C–N bonds, with the subsequent activation of these modes and their appearance in the spectrum as progressions.

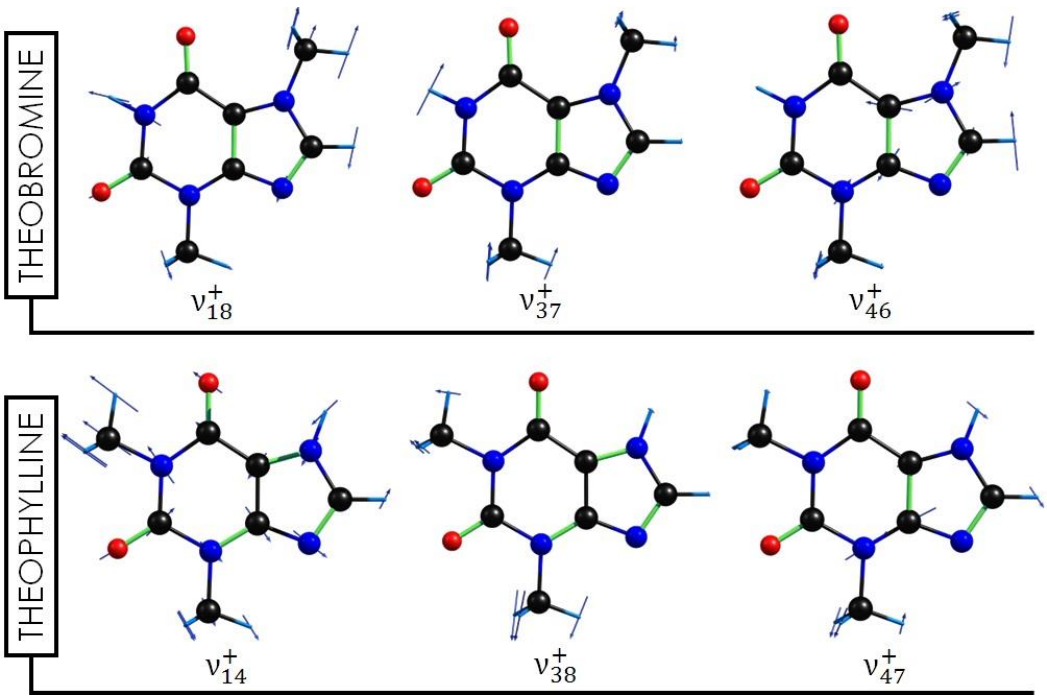

Figure 7.8: Comparison between the most active vibrational modes in the PEPICO spectra of TB and TP. Calculation were carried out at the PBE0/aug-cc-pVDZ level.

The above observations are in clear contrast with data on the excited dynamics of nucleobases.[5] Both experimental and computational experiments concluded that electronic excitation induces a ring deformation on both purine and pyrimidine nucleobases. However, the deformation takes place along different set of coordinates, which also depend on the substituent. For example, the deformation coordinate is C5=C6 in the case of pyrimidine bases; inclusion of an amino group in C4 induces a second deformation in C2.[20–29] If the amino group is introduced in C2, the deformation at that position is suppressed. On the other hand, methylation of guanine's C1 results in ns lifetimes, because of the removal of the $n\pi^*$-$\pi\pi^*$ conical intersection.[30]

The results in this work indicate that the position of the methyl group significantly alters the excited state dynamics and that there is an efficient coupling of the methyl torsion with the ring puckering when the methylation takes place in N7. However, this may also be consequence of the different stability of the $n\pi^*$ state, which is built by excitation of the lone pair of one of the N atoms.[31] This means that a different lone pair is excited in TB than in TP, changing the spacing between the two first excited states and enabling a better coupling between them in TB. Therefore, methylation may alter the excited electronic state dynamics in two different ways: by enabling coupling between the methyl torsion and the ring puckering vibration and by modifying the position of the excited electronic states.

Coupling of methyl torsion with molecular vibrations also affects the photophysics of the molecules, and strongly favors intramolecular vibrational energy redistribution, due to the direct connection between torsional levels and the vibrational ladder.[13,14,32–36]

The difference in the behavior observed in nucleobases compared with xanthines may be due to a very different location of the $n\pi^*$ state, which already overlaps with the first electronic excited state, even in the absence of methylation. Also, it seems to be connected with the N–H bond dissociation, which is not possible in the present xanthine molecules.[37] In any case, the results presented here indicate the importance of taking into account nucleobase modifications in the studies of their photophysics.

7.5. Conclusions

In this chapter, we present a detailed spectroscopic study of theophylline and theobromine. The only difference between them is the position of the methyl group. However, such a small modification strongly influenced the excitation spectrum. Due to

the coupling of the torsion of the methyl group in N7 with ring modes, the REMPI spectrum of theobromine presents a rich spectroscopy that is not present in that of theophylline. Although their adiabatic ionization energies are very similar, as shown in both ZEKE and TPE spectra, again there is a richer structure in the ZEKE spectrum of TB, which is attributed to a geometry change in the S_1 intermediate state. Both molecules show a significant vibrational activity in the PEPICO spectra due to the geometry changes in the cation, which are mainly attributed to the ring breathing following the removal of the electron from the aromatic system.

The results presented here are in contrast with the observed increase in excited state lifetime upon methylation and point to a different mechanism, for example, methylation restricts the lone pair excitation that will result in the formation of the $n\pi^*$ state and therefore, its overlap (or not) with the $\pi\pi^*$ state. Additionally, they underline the importance of taking into account nucleobase modifications in the photophysical studies.

7.6. References

[1] A. C. Rios and Y. Tor, On the Origin of the Canonical Nucleobases: An Assessment of Selection Pressures across Chemical and Early Biological Evolution, *Isr. J. Chem.*, 2013, **53**, 469–483.

[2] S. Mondal and M. Puranik, Ultrafast structural dynamics of photoexcited adenine, *Phys. Chem. Chem. Phys.*, 2017, **19**, 20224–20240.

[3] A. A. Beckstead, Y. Zhang, M. S. de Vries and B. Kohler, Life in the light: nucleic acid photoproperties as a legacy of chemical evolution, *Phys. Chem. Chem. Phys.*, 2016, **18**, 24228–24238.

[4] M. M. Brister, M. Pollum and C. E. Crespo-Hernández, Photochemical etiology of promising ancestors of the RNA nucleobases, *Phys. Chem. Chem. Phys.*, 2016, **18**, 20097–20103.

[5] C. E. Crespo-Hernández, B. Cohen, P. M. Hare and B. Kohler, Ultrafast Excited-State Dynamics in Nucleic Acids, *Chem. Rev.*, 2004, **104**, 1977–2020.

[6] K. Nemeková, J. Labuda, V. Milata, J. Blakoviová and J. Sochr, Interaction of DNA and mononucleotides with theophylline investigated using electrochemical biosensors and biosensing, *Bioelectrochemistry*, 2018, **123**, 182–189.

[7] G. R. Zimmermann, R. D. Jenison, C. L. Wick, J.-P. Simorre and A. Pardi, Interlocking structural motifs mediate molecular discrimination by a theophylline-binding RNA, *Nat. Struct. Biol.*, 1997, **4**, 644–649.

[8] G. M. HILL, D. M. MORIARITY and W. N. SETZER, *Sci. Pharm.*, 2011, 79.

[9] M. P. Callahan, Z. Gengeliczki, N. Svadlenak, H. Valdes, P. Hobza and M. S. de Vries, Non-standard base pairing and stacked structures in methyl xanthine clusters, *Phys. Chem. Chem. Phys.*, 2008, **10**, 2819–2826.

[10] D. Kim, K. Y. Yang, H. M. Kim, T.-R. Kim, N. J. Kim, S. Shin and S. K. Kim, Site-dependent

effects of methylation on the electronic spectra of jet-cooled methylated xanthine compounds, *Phys. Chem. Chem. Phys.*, 2017, **19**, 22375–22384.

[11] A. Bhattacherjee and S. Wategaonkar, Conformational preferences of monohydrated clusters of imidazole derivatives revisited, *Phys. Chem. Chem. Phys.*, 2015, **17**, 20080–20092.

[12] L. Nahon, N. de Oliveira, G. A. Garcia, J.-F. Gil, B. Pilette, O. Marcouillé, B. Lagarde and F. Polack, DESIRS: a state-of-the-art VUV beamline featuring high resolution and variable polarization for spectroscopy and dichroism at SOLEIL, *J. Synchrotron Radiat.*, 2012, **19**, 508–520.

[13] A. M. Gardner, W. D. Tuttle, L. Whalley, A. Claydon, J. H. Carter and T. G. Wright, Torsion and vibration-torsion levels of the S1 and ground cation electronic states of para-fluorotoluene, *J. Chem. Phys.*, 2016, **145**, 124307.

[14] L. D. Stewart, J. R. Gascooke and W. D. Lawrance, A strong interaction between torsion and vibration in S0 and S1 m-fluorotoluene, *J. Chem. Phys.*, 2019, **150**, 174303.

[15] H. Y. Zhao, K.-C. Lau, G. A. Garcia, L. Nahon, S. Carniato, L. Poisson, M. Schwell, M. M. Al-Mogren and M. Hochlaf, Unveiling the complex vibronic structure of the canonical adenine cation, *Phys. Chem. Chem. Phys.*, 2018, **20**, 20756–20765.

[16] C. M. Western, PGOPHER: A program for simulating rotational, vibrational and electronic spectra, *J. Quant. Spectrosc. Radiat. Transf.*, 2017, **186**, 221–242.

[17] C. M. Western and B. E. Billinghurst, Automatic and semi-automatic assignment and fitting of spectra with PGOPHER, *Phys. Chem. Chem. Phys.*, 2019, **21**, 13986–13999.

[18] D. Kim, H. M. Kim, K. Y. Yang, S. K. Kim and N. J. Kim, Molecular beam resonant two-photon ionization study of caffeine and its hydrated clusters, *J. Chem. Phys.*, 2008, **128**, 134310.

[19] H. Ottosson, Exciting excited-state aromaticity, *Nat. Chem.*, 2012, **4**, 969–971.

[20] C. Plützer and K. Kleinermanns, Tautomers and electronic states of jet-cooled adenine investigated by double resonance spectroscopy, *Phys. Chem. Chem. Phys.*, 2002, **4**, 4877–4882.

[21] C. Plützer, E. Nir, M. S. de Vries and K. Kleinermanns, IR–UV double-resonance spectroscopy of the nucleobase adenine, *Phys. Chem. Chem. Phys.*, 2001, **3**, 5466–5469.

[22] J. Andréasson, A. Holmén and B. Albinsson, The Photophysical Properties of the Adenine Chromophore, *J. Phys. Chem. B*, 1999, **103**, 9782–9789.

[23] S. K. Mishra, M. K. Shukla and P. C. Mishra, Electronic spectra of adenine and 2-aminopurine: an ab initio study of energy level diagrams of different tautomers in gas phase and aqueous solution, *Spectrochim. Acta Part A Mol. Biomol. Spectrosc.*, 2000, **56**, 1355–1384.

[24] D. C. Lührs, J. Viallon and I. Fischer, Excited state spectroscopy and dynamics of isolated adenine and 9-methyladenine, *Phys. Chem. Chem. Phys.*, 2001, **3**, 1827–1831.

[25] H. Kang, B. Jung and S. K. Kim, Mechanism for ultrafast internal conversion of adenine, *J. Chem. Phys.*, 2003, **118**, 6717–6719.

[26] A. L. Sobolewski and W. Domcke, On the mechanism of nonradiative decay of DNA bases: ab initio and TDDFT results for the excited states of 9H-adenine, *Eur. Phys. J. D - At. Mol. Opt. Plasma Phys.*, 2002, **20**, 369–374.

[27] M. Barbatti and H. Lischka, Can the Nonadiabatic Photodynamics of Aminopyrimidine Be a Model for the Ultrafast Deactivation of Adenine?, *J. Phys. Chem. A*, 2007, **111**, 2852–2858.

[28] I. Hünig, C. Plützer, K. A. Seefeld, D. Löwenich, M. Nispel and K. Kleinermanns,

Photostability of Isolated and Paired Nucleobases: NH Dissociation of Adenine and Hydrogen Transfer in its Base Pairs Examined by Laser Spectroscopy, *ChemPhysChem*, 2004, **5**, 1427–1431.

[29] C. M. Marian, A new pathway for the rapid decay of electronically excited adenine, *J. Chem. Phys.*, 2005, **122**, 104314.

[30] C. M. Marian, The Guanine Tautomer Puzzle: Quantum Chemical Investigation of Ground and Excited States, *J. Phys. Chem. A*, 2007, **111**, 1545–1553.

[31] M. S. de Vries, eds. A. M. Rijs and J. Oomens, Springer International Publishing, Cham, 2015, pp. 271–297.

[32] W. D. Tuttle, A. M. Gardner, L. E. Whalley and T. G. Wright, Vibration and vibration-torsion levels of the S1 state of para-fluorotoluene in the 580–830 cm−1 range: Interactions and coincidences, *J. Chem. Phys.*, 2017, **146**, 244310.

[33] D. J. Kemp, E. F. Fryer, A. R. Davies and T. G. Wright, Vibration-modified torsional potentials and vibration-torsion ("vibtor") levels in the m-fluorotoluene cation, *J. Chem. Phys.*, 2019, **151**, 84311.

[34] D. J. Kemp, L. E. Whalley, A. M. Gardner, W. D. Tuttle, L. G. Warner and T. G. Wright, Complexity surrounding an apparently simple Fermi resonance in p-fluorotoluene revealed using two-dimensional laser-induced fluorescence (2D-LIF) spectroscopy, *J. Chem. Phys.*, 2019, **150**, 64306.

[35] J. R. Gascooke, L. D. Stewart, P. G. Sibley and W. D. Lawrance, Pervasive interactions between methyl torsion and low frequency vibrations in S0 and S1 p-fluorotoluene, *J. Chem. Phys.*, 2018, **149**, 74301.

[36] J. R. Gascooke, E. A. Virgo and W. D. Lawrance, Torsion-vibration coupling in S1 toluene: Implications for IVR, the torsional barrier height, and rotational constants, *J. Chem. Phys.*, 2015, **143**, 44313.

[37] M. Zierhut, W. Roth and I. Fischer, Dynamics of H-atom loss in adenine, *Phys. Chem. Chem. Phys.*, 2004, **6**, 5178–5183.

Chapter 8

Intermolecular interactions in xanthine-nucleobase aggregates

Manuscript for publication in preparation

8.1. Introduction

This chapter continues the exploration of the interaction preferences in xanthines, and their role in several biological processes. Specially, we deal with the possible implication of methylxanthines in the origins of life. One of the conditions that a molecule must fulfil to become a valid nucleobase is to present the appropriate collection of intermolecular interactions. The nucleobases must selectively couple with their complementary base, but at the same time, they must present additional functional groups for the interaction with other molecules (like proteins), that are part of the complex transduction machinery of the cell. Following these thoughts, we are engaged in the study of the interaction landscape of the nucleobases and other structurally related biomolecules, but that were not chosen to form part of DNA/RNA, even when some of them are found in living beings.

Xanthines are found in human body as part of the guanine metabolism.[1] Some of their methylated derivatives, like theobromine (TB), present biological activity due to the similarity of their structure to that of other metabolites. Actually, its structure is a mixture between the CONHCO motif of thymine (T) and the purine scaffold of adenine (A). In the previous chapter, we analyzed the effects of the methylation in the excited state of methylxanthines, where it was evidenced how the position of a single methyl group influenced the dynamics of the excited electronic state. Furthermore, previous spectroscopic studies on TB demonstrated that its interaction with water is similar to those of the canonical nucleobases.[2] Besides, its tautomeric equilibrium is altered by the interaction with the water molecule in the same way as in the nucleobases.[2]

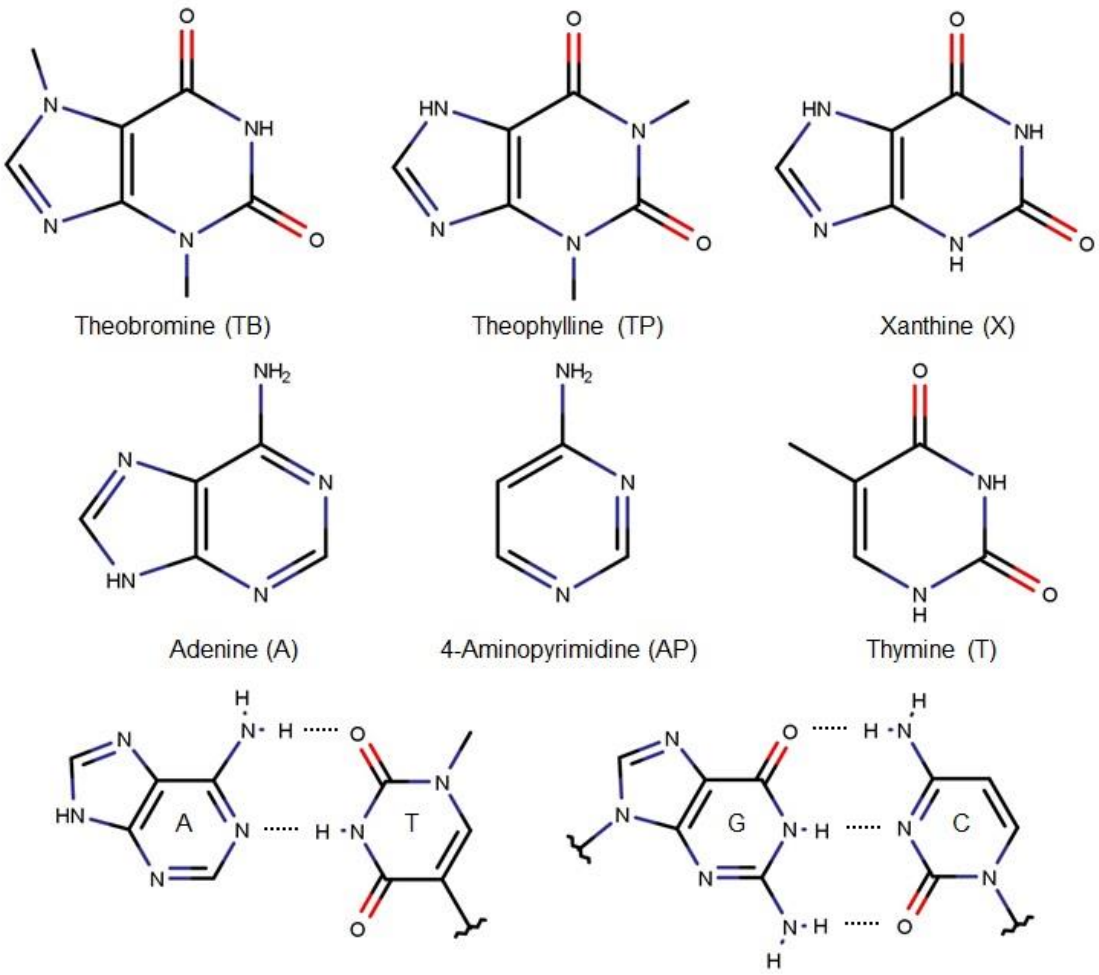

Figure 8.1: Structure of theobromine, theophylline, xanthine, adenine, 4-aminopyrimidine, thymine and Watson-Crick interactions for the canonical nucleobases.

In order to explore the aggregation preferences of xanthines, we explored their spectroscopy forming DNA base-xanthine aggregates in the beam. As a starting point for this study, adenine was complexed with different xanthines and the structure and binding energy of the aggregates was compared to the aggregation preferences of the canonical pair adenine-thymine (A+T). Caffeine, previously complexed with phenol (see Chapter 6) was excluded from these studies, as its methylation level prevents the formation of hydrogen bonds with DNA/RNA nucleobases.

8.2. Theobromine + Adenine and Theobromine + 4-aminopyrimidine dimers

Theobromine (TB) and xanthine have a very similar chemical structure to DNA nucleobases: they present the purinic scaffold of adenine (A) with the CONHCO binding motif of thymine. Such similarities, allow them to establish intermolecular interactions similar to those of adenine and thymine. In this section we explore the complex between TB and A, in order to compare them with those in the nucleobases and to test the ability of TB to mimic the intermolecular interactions of nucleobases. The study was complemented with the characterization of the theobromine+4-aminopyrimidine dimer (TB+AP). AP has the same NH_2 motif as A, and therefore one would expect that the aggregates formed by this dimer resemble those of A+T, but with the purinic-pyrimidinic structure reversed. Hence, comparison of the structure and binding energy of TB+AP with A+T allow us to understand the role of A+T interactions in other nucleobase candidates.

The presence of several proton donor and acceptor groups in the interacting molecules results in a rich collection of conformational isomers. Consequently, careful exploration of the potential energy surface is required to locate all the relevant minima. Figure 8.2 collects a simplified version of the iPES build for TB+A dimer. The complete set of structures can be found in Figure A8.1 and Table A8.1. Structures were classified depending on their interaction type, together with their relative stability computed at M06-2X/6-311++G(d,p) and B3LYP-ED=GD3BJ/def2TZVP levels.

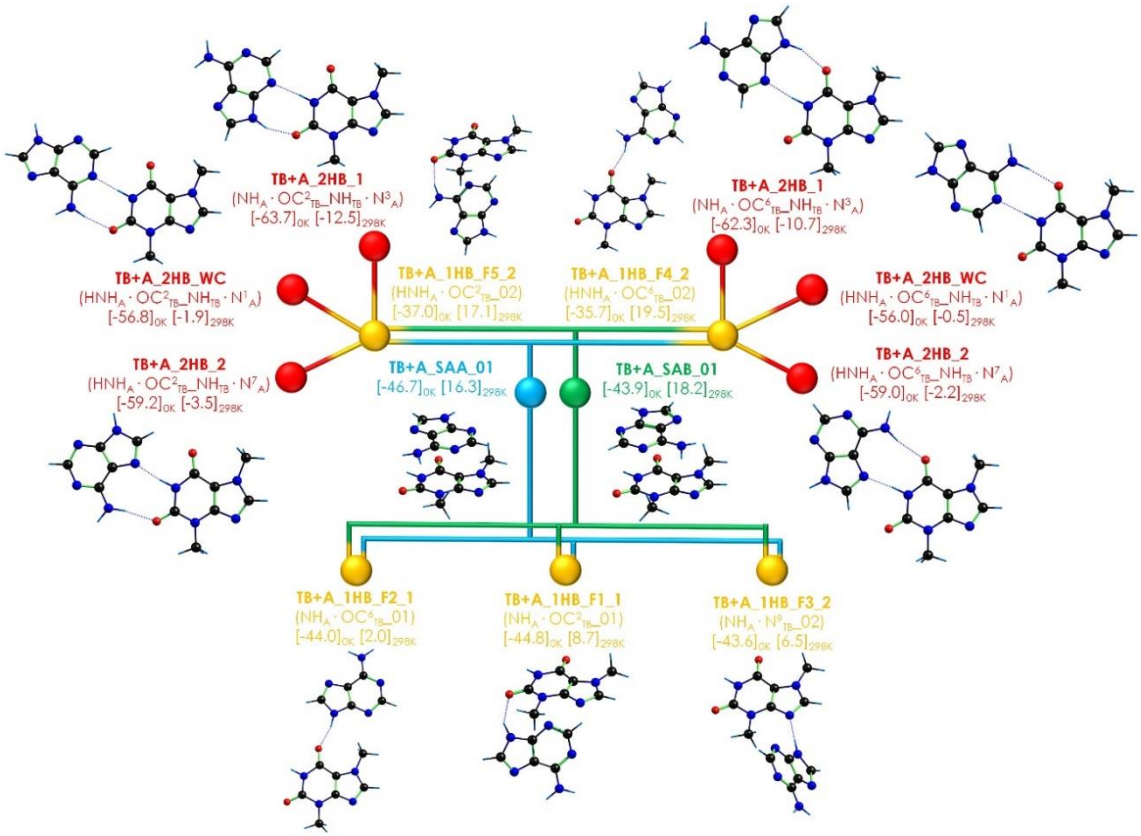

Figure 8.2: Simplified interaction potential energy surface (iPES) between theobromine and adenine. Conformers were classified and named depending on the type of intermolecular interaction. The connections between conformers highlight the similarities in structure and type of interaction. For each conformer, the optimization was performed at two different computational levels: M06-2X/6-311+G(d,p) and B3LYP-ED=GD3BJ/def2TZVP. The values of the binding energies (with ZPE and BSSE corrections) at 0 and 298 K are given under each structure. The energy values are the average of the values obtained at the two computational methods.

An exhaustive exploration of the iPES revealed three different families of interactions: (i) structures bounded by two strong HBs, (ii) single HB structures and (iii) isomers mainly attached by π···π stacking interactions. It is worth nothing that due to the low flexibility of the systems, relative stability and binding energy are directly related. As can be observed, the most stable conformations of TB+A dimer present two strong HBs. Figure 8.3 summarizes the six most stable isomers for TB+A, together with their binding energies at 0 and 298 K.

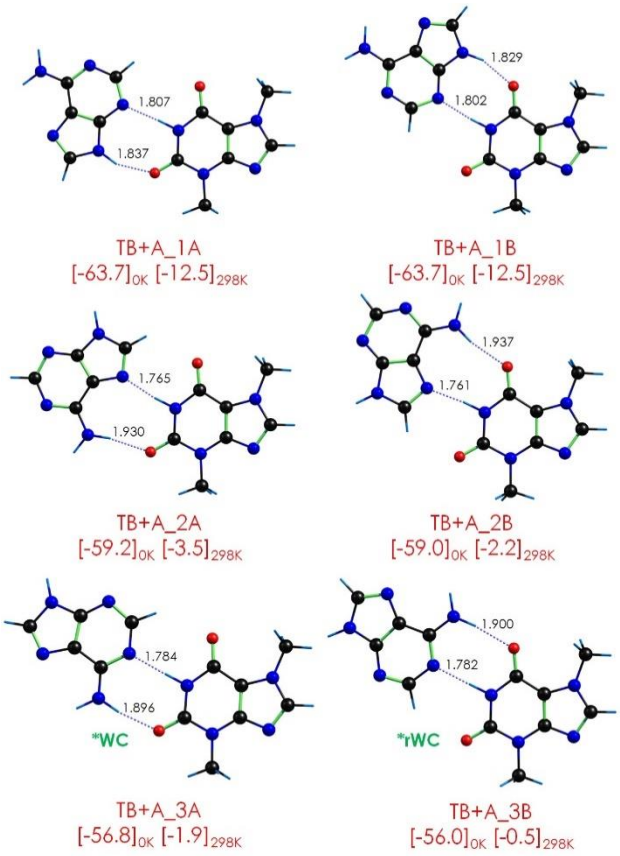

Figure 8.3: Six most stable conformational isomers of theobromine+adenine, together with their binding energy at 0 and 298 K. The binding energy values (kJ/mol) is the average of the two values computed at M06-2X and B3LYP methods. Hydrogen bond distances are those computed at the B3LYP-ED=GD3BJ/def2TZVP level.

The most favorable interaction is the formation of a double C=O···HN/N-H···N HB. Such interactions can be established with either of the two carbonyl groups in TB, resulting in pairs of (almost) degenerate structures (labelled as A and B in Figure 8.3). Due to the similarity of those pairs, they are indistinguishable in our experimental system, as they present an almost identical spectroscopic signature. Therefore, we will refer to each pair as a single isomer, although both structures can be present in the expansion. In tight competition with the above-mentioned interaction, formation of C=O···HNH/N-H···N HBs is also possible, with a small reduction in the binding energy. Depending on the relative orientation of the two molecules, the resulting structure resembles the Watson-Crick (W-C) complex of A+T. Following the W-C nomenclature, isomer TB+A_3A would correspond to a W-C conformation, while TB+A_3B would correspond to a reverse W-C conformation (rWC). Additional DNA-analogue interactions can be identified, since structures TB+A_2A/B correspond to the Hoogsteen base pairing between adenine and thymine.

Transition from a puric to a pyrimidinic base resulted in a substantially simpler conformational landscape. Figure 8.4 shows a simplified version of the iPES for TB+AP dimer, while the complete set of structures can be found in Figure A8.2 and Table A8.2.

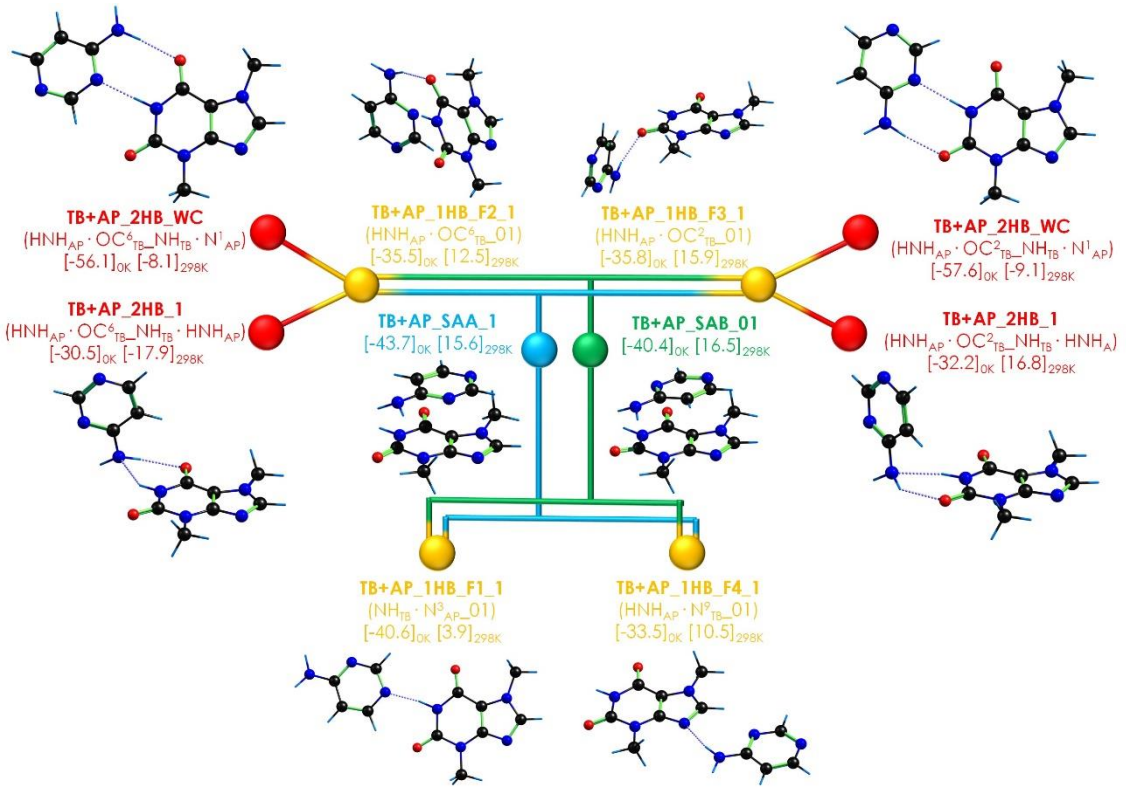

Figure 8.4: Simplified iPES between theobromine and 4-aminopyrimidine. Conformers were classified and named depending on the type of intermolecular interaction. The connections between conformers highlight the similarities in structure and type of interaction. For each conformer, the optimization was performed at two different computational levels: M06-2X/6-311++G(d,p) and B3LYP-ED=GD3BJ/def2TZVP. The values of the binding energies (with ZPE and BSSE corrections) at 0 and 298K are given under each structure and are the average of the two computed values.

Compared to the conformational landscape of TB+A, the lack of N7H group in AP reduced the number of possible families, especially for those structures bound by one HB. Two quasi-degenerate structures dominate the iPES of TB+AP, summarized in Figure 8.5 Interestingly, both isomers, but specially TB+AP_1A reproduce the WC configuration of A+T.

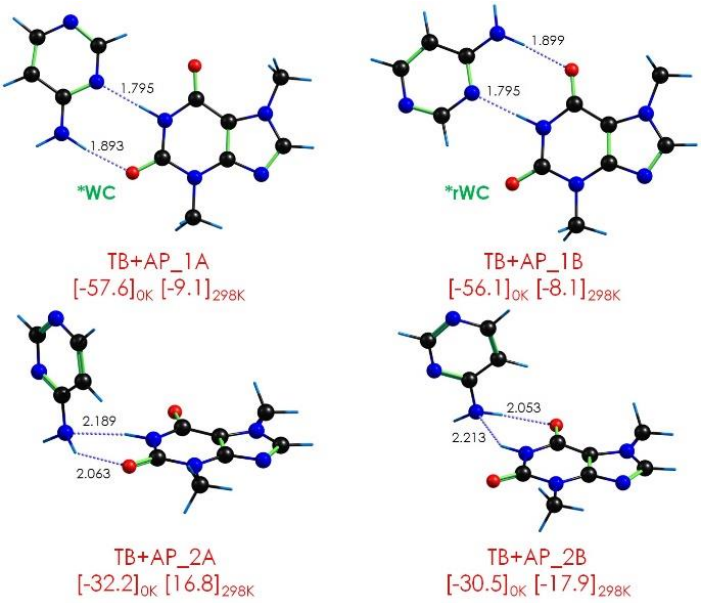

Figure 8.5: Four most stable conformational isomers of theobromine+4-aminopyrimidine, together with their binding energy at 0 and 298 K. The binding energy values (kJ/mol) are the average of the two values computed at M06-2X and B3LYP methods. Hydrogen bond distances are those computed at the B3LYP-ED=GD3BJ/def2TZVP level.

One of the main difficulties in the study of these systems is the short lifetimes of their electronic excited states,[3–5] which result in low signal intensity. Furthermore, the transfer of these molecules into gas phase requires of sophisticated set ups, such as laser desorption systems, that also increase the signal/noise ratio.

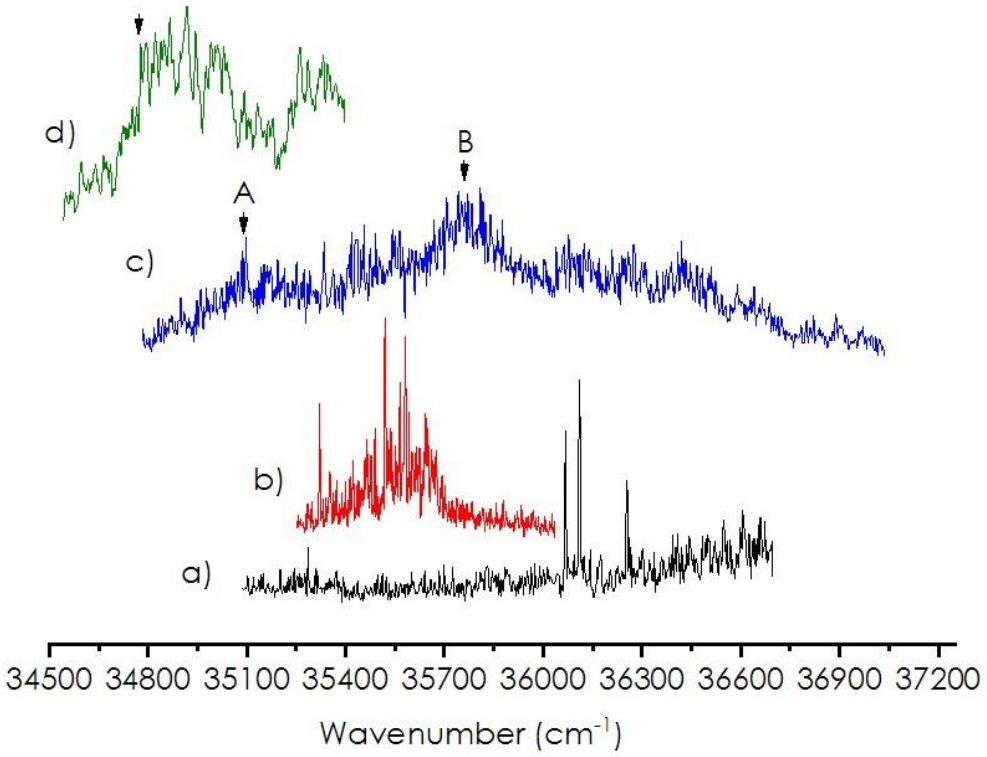

Figure 8.6: One-color REMPI spectra of a) Adenine, b) Theobromine, c) Adenine+Theobromine dimer and d) 4-aminopyrimidine+Theobromine dimer. Excitation wavelengths employed for IR/UV double resonance experiments are marked by an arrow in each complex.

Figure 8.6 shows the mass-resolved REMPI spectra of TB and A, and the TB+A and TB+AP dimers. The REMPI spectrum of the monomers is in very good agreement with previous studies.[6–8] While the spectrum of TB presents a large number of vibronic transitions due to the activation of several out of plane vibrations,[9] the spectrum of A in the 36000-36700 cm^{-1} region contains only three bands built over a background. The short lifetime of A, 0.18 ps,[10] makes the two-photon ionization process very inefficient, seriously reducing the overall sensibility of the experiments. Likewise, AP presents a short excited electronic state lifetime (400 fs)[11] hampering the recording of its excitation spectrum. The study of the dimer was possible using TB chromophore to record the spectrum of TB+AP, despite the low-intensity signal. The REMPI spectra of both dimers are broad and unstructured absorptions, precluding the use of hole-burning experiments to identify the contribution from different isomers. The Arrows in Figure 8.6 mark the excitation wavelengths used to record IDIRS spectra, in order to find different conformational isomers.

Figure 8.7 shows the comparison between the IDIRS spectra of TB+A, together and the predictions for the most stable isomers, computed at the two theory levels. The experimental IR spectra of TB+A clearly shows the presence of at least two isomers, as

the number of bands cannot be reproduced by the presence of a single conformational isomer. It is interesting to note that some of the bands are broad absorptions and present a large red shift, probably due to the formation of strong HBs or even to the possibility of concerted double proton transfer between the two molecules.[6,12–14] Additionally, a different experimental trace was obtained for the free NH stretching region when changing the excitation wavelength (trace (a)). This spectrum lacks of two free NH bands (marked as blue dots), that can be assigned to the symmetric and anti-symmetric stretching modes of the NH_2 group of adenine (see Figure A8.3 in Appendix 8). Hence, the NH_2 group of adenine of the conformer in the spectrum (a) must be taking part in a direct interaction.

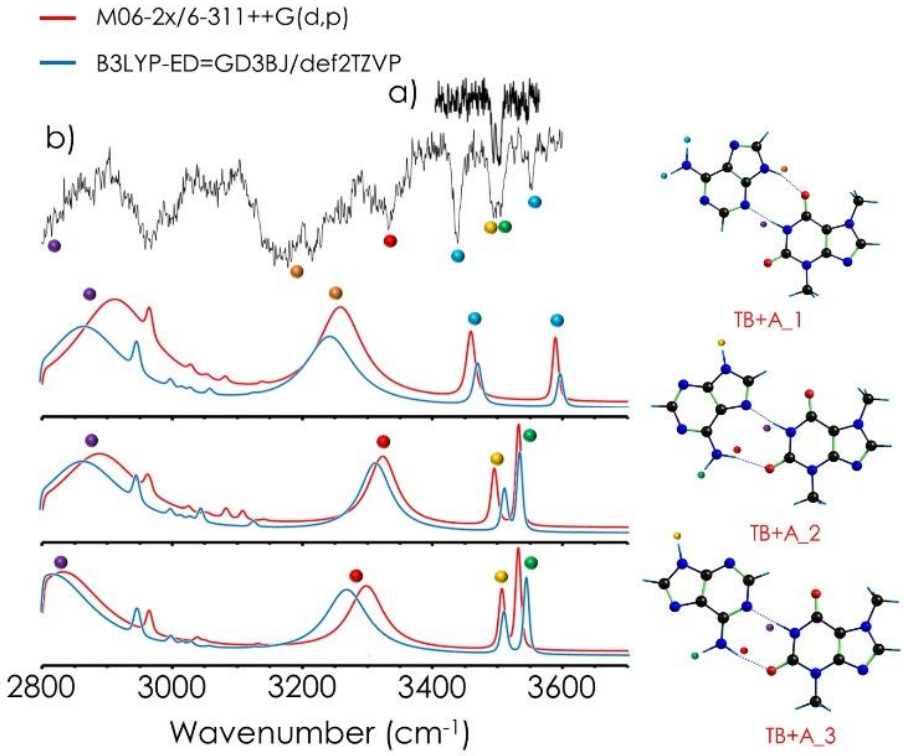

Figure 8.7: Comparison between the experimental IDIRS spectra of TB+A and the predictions for the most stable computed structures. Experimental traces were recorded at a) 35097 cm^{-1} and b) 35769 cm^{-1} excitation wavelengths.

Despite the rich conformational landscape of TB+A dimer, a first look at the experimental IR spectra clearly discards two of the observed interaction families: no structure with a single HB can explain both free and bounded NH bands, and the absence of the free NH band of TB discards all the stacking possibilities. Further information of the predicted spectra of all conformers can be found in Figure A8.4 and A8.5.

Comparison between the IDIRS spectrum of TB+A and the predictions for the most stable computed structures shows that the spectrum of the global minimum fits very well with the experimental trace, but the presence of an additional isomer is required to explain those transitions marked with yellow, green and red dots in Figure 8.7. Actually, de prediction for the second most stable isomer faithfully reproduces the position of the second set of bands around 3500 cm^{-1}. The prediction for the W-C conformer (TB+A_3) is also consistent with the spectrum of the second experimental conformer, but is higher in energy. The most likely explanation is that the two formed isomers correspond to the two most stable structures. Nevertheless, the structure of TB+A_3 is very similar to that of TB+A_2, and therefore, its presence in the beam cannot be totally discarded.

The IDIRS spectrum of TB+AP, Figure 8.8, contains less and broader bands. The spectral signatures of the formation of strong HBs are also clearly visible in the red shift of the transitions. These features are well predicted in the computed spectrum of the two most stable isomers. The computed spectrum of the W-C isomer (TB+AP_1) reproduces very well the position of the stretching frequency of the free NH and part of the observed broad transitions. Apparently, there are some extra bands (yellow and orange dots) that require of a second isomer for their assignment. In this second isomer, AP would adopt a position perpendicular to the plane of TB. Such structure is ~26 kJ/mol less stable that the global minimum, suggesting the presence of high energy barriers for isomerization.

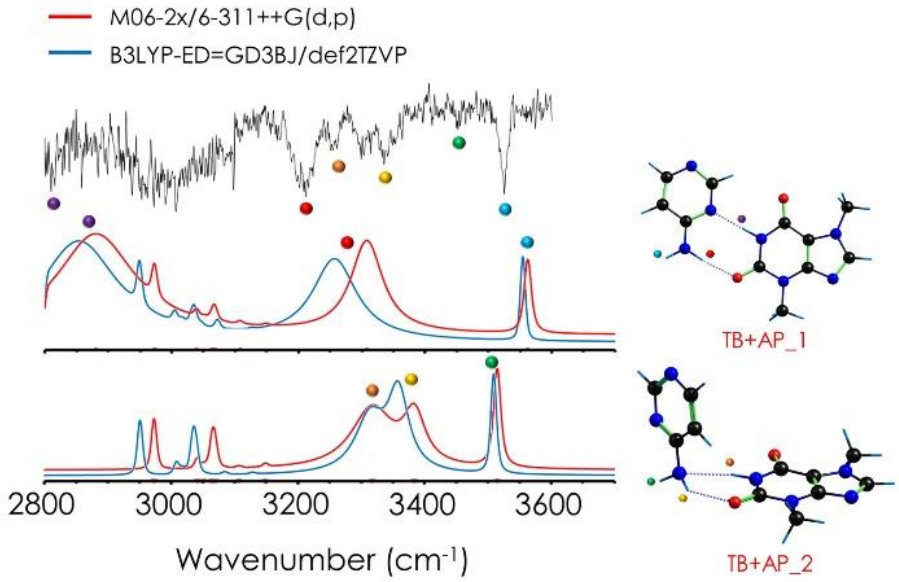

Figure 8.8: Comparison between the experimental IDIRS spectrum of TB+AP, recorded at 34794 cm^{-1}, and the prediction for the two most stable structures.

The two main conclusions that one can extract from the assigned structure are that both TB+A and TB+AP systems present very similar interactions to those found in the

canonical nucleobases in an environment free from external perturbations. In the case of TB+AP, the global minimum is of the W-C type, against what was observed in gas phase for CGAT.[15] To further understand the results in the context of DNA base aggregates, we examined the results obtained on these aggregates on the light of those in the literature regarding the canonical W-C nucleobase pairs.

Table 8.1 collects the binding energy values of the WC analogue's species detected and identified in this work and compares them with the computed values for similar systems studied by other authors. To carry out such comparison, the structures reported in the literature were optimized at B3LYP-ED=GD3BJ/def2TZVP level. For the sake of comparison, Figure 8.9 presents the computed structures of the dimers reported in Table 8.1.

Table 8.1: Binding energies for several dimers mimicking the Watson-Crick interactions computed at the B3LYP-ED=GD3BJ/def2TZVP level.

Complex	Binding energy 0 K[a]	Binding energy 298 K[a]
TB+A	60.6/59.9	8.2/6.0
TB+AP	60.7/59.4	10.3/9.3
T+A	61.6/60.3	8.0/6.9
AP+1-methylthymine[b]	61.9/59.5	11.2/9.6
AP+6-methyl-4-pyrimidinone (M4PMN)[b]	67.8	17.9
9-methylamine+2-pyridinone (9mA+2PY)[c]	67.8	16.6
AP+2-pyrimidinone (AP+2PY)	67.8	18.1
TB+2,4-aminopyridine (2,4AP)[c]	72.9/73.4	18.3/18.8
G+C	117	59.9

[a] Binding energy values given in kJ/mol. For the case of two different values, they correspond to the WC and rWC structures, respectively. [b] Ref 16. [c] Ref 12. [d] Ref 13.

Close examination of the binding energies of the systems in Table 8.1 show that the interaction energy values of TB+A and TB+AP are of comparable strength to that of T+A (around 60 kJ/mol at 0 K and 9 kJ/mol at 298 K). However, interaction energy values for G+C are nearly twice stronger than those for T+A dimers and analogue interactions, due to presence of formation of three HBs instead of two, in good agreement with previous theoretical studies about DNA base pairs.[17] In between are the values for several similar systems that could have existed in the prebiotic environment. Binding energies for W-

C-like interactions in AP+M4PMN, 9mA+2PY and AP+2PY are slightly larger than those predicted for TB+A and TB+AP, but still far from those interaction values predicted for G+C.

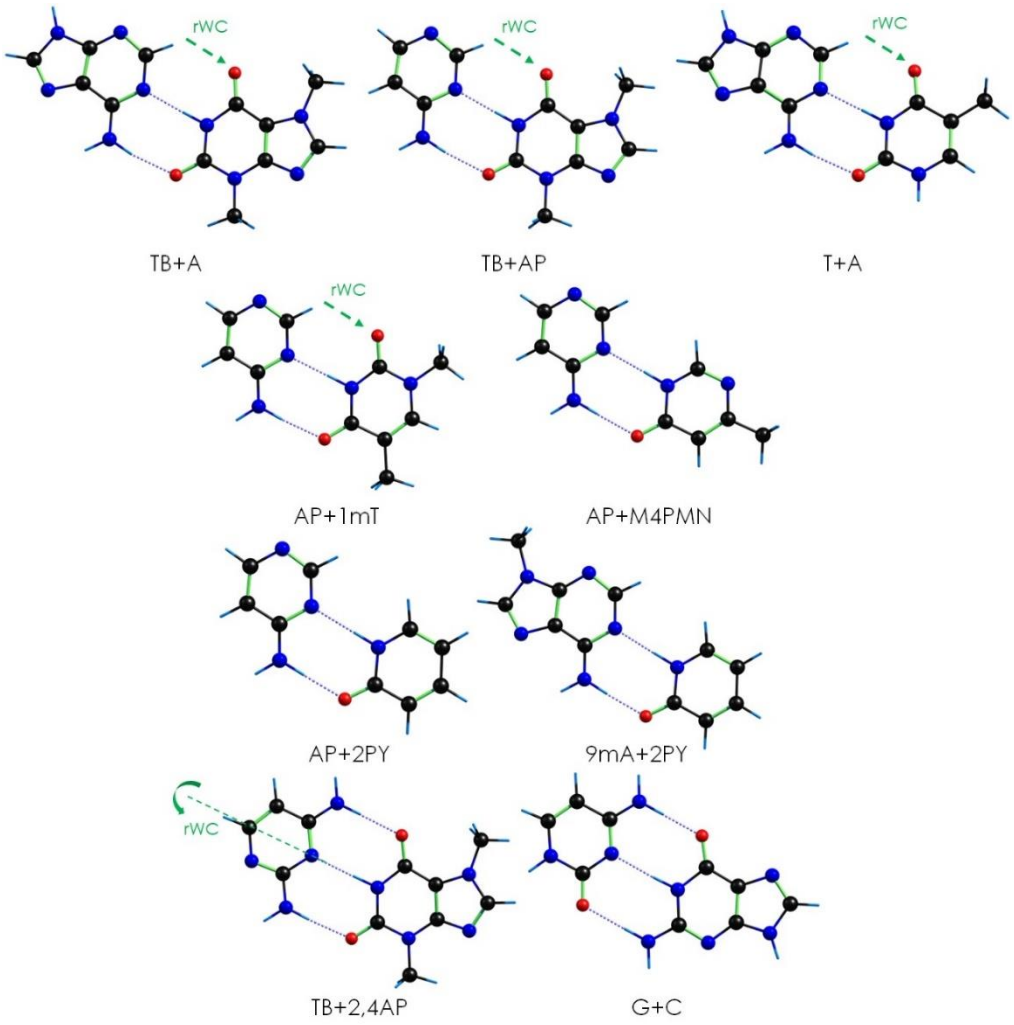

Figure 8.9: Structures of different dimers forming W-C-type interactions, computed at B3LYP-ED=GD3BJ/def2TZVP. Reverse W-C interaction sites (rWC) are labelled in green.

The data in Table 8.1 offer a complex panorama. Indeed, A+T Watson-Crick analogue's interaction energies are very close, which points out a possible competition for binding to adenine. If the interaction energy were the only selection pressure, only those systems able to establish three HBs, such as G+C would have survived this selection stage. Clearly, in an environment with a rich chemistry and large variety of species, the ability to form strong HBs would have offered a clear advantage. Thus, the most likely explanation is that the first biomolecules were formed by single strands.[18] The limiting factor to form a successful single strand would be the probability of formation of a given species and its stability in the medium. Further refinement of the molecules that

composed such strands resulted in today's well-known CGAT sequence. Therefore, if the intermolecular interaction played a role in the selection of CGAT it had to be in this second stage.

8.3. Exploring the spectroscopy of Adenine-Theophylline and Adenine-Xanthine dimers

We continued with the exploration of the aggregation preferences of nucleobases and related molecules with the study of the dimers of adenine (A) with theophylline (TP) and xanthine (X). As explained in previous chapters, the only difference between TP and TB is the position of a methyl group (see Figure 8.1). The absence of methyl groups in X multiplies the number of possible interactions with adenine, resulting in a rich conformational landscape.

The conformational landscape of TP was already explored in Chapter 7. Among all the possible tautomers, the most stable one (7H) was assigned experimentally. Xanthine presents more tautomeric forms, but they are significantly less stable compared to the *di-keto* forms (see Figure 8.10a). The energy difference between the two most stable isomers of X is ~30 kJ/mol at M06-2X/6-311++G(d,p), which is high enough to safely rule out the possibility of having both isomers populated in the supersonic expansion. Moreover, previous spectroscopic studies confirmed the presence of the *diketo*-7H tautomer.[19] The IDIR spectrum obtained probing the band at 36733 cm^{-1} in the REMPI spectrum of xanthine (Figure 8.10b) is in good agreement with those previous publications and with the prediction for the diketo-7H tautomer. Thus, we assumed that most of the population of xanthine in the beam is in *diketo*-N7H form, and therefore, only those conformers based on the *diketo*-7H tautomer were taken into account during the conformational exploration.

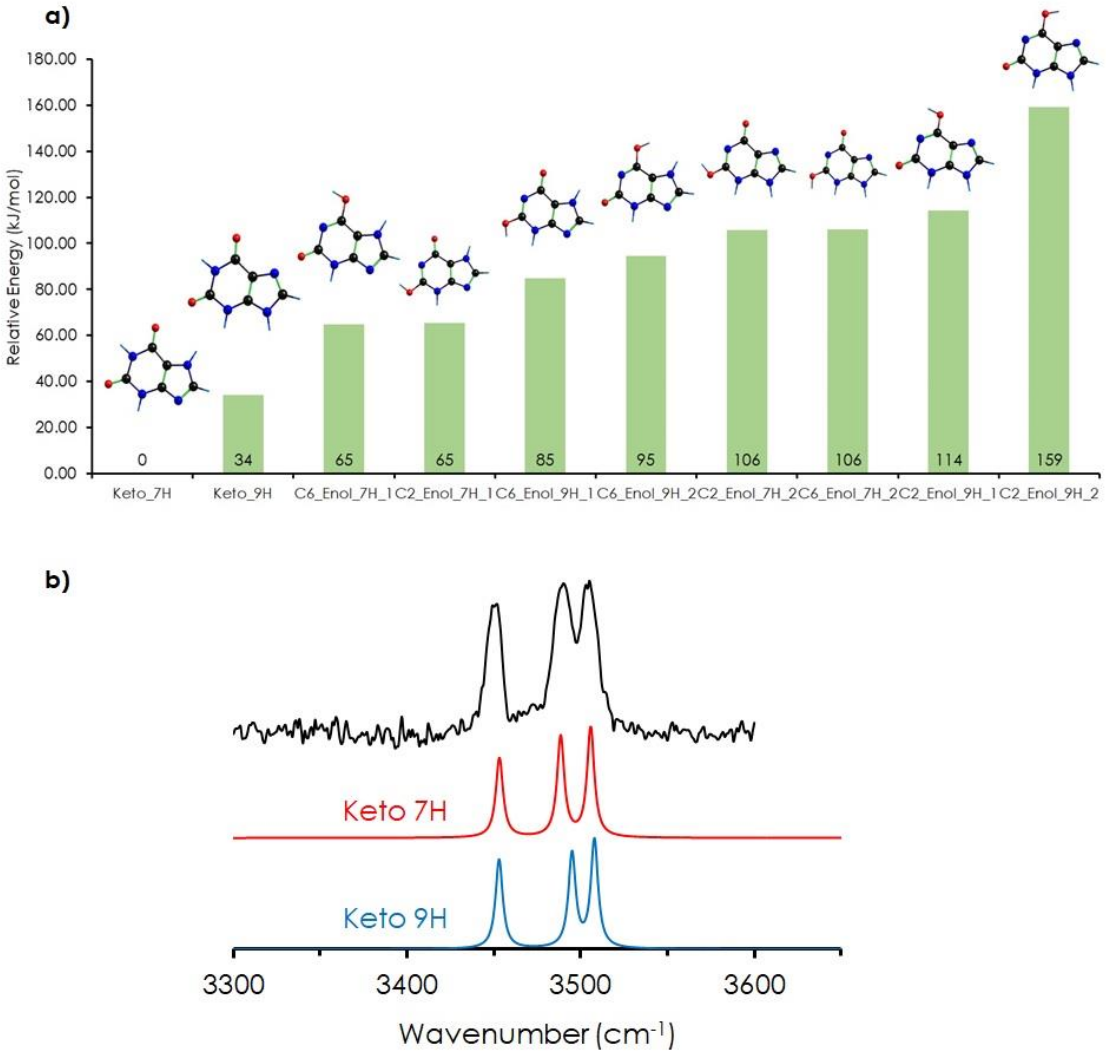

Figure 8.10: a) Relative energies for xanthine tautomeric forms, computed at M06-2X/6-311++G(d,p) level. b) IDIR spectrum of xanthine compared to the predictions for the most stable tautomeric forms, at M06-2X/6-311++G(d,p) level. IR spectra was obtained probing the band at 36733 cm^{-1}.

Figure 8.11 collects a simplified version of the iPES for TP+A dimer. The complete set of structures can be found in Figure A8.8 and Table A8.3. The structures were classified depending on their interactions, and are collected together with their relative stability computed at M06-2X/6-311++G(d,p) and B3LYP-ED=GD3BJ/def2TZVP levels.

The exploration of the iPES also revealed three different families of interactions for TP+A: (i) structures bounded by two strong HBs, (ii) single HB structures and (iii) isomers mainly attached by π···π stacking interactions. However, compared to TB+A, the number of structures inside the 2HB family is smaller. This is mainly caused by the methylation of the N1H group of TP. Consequently, HBs can only be formed with the N7H as donor, and with the nearby carbonyl group acting as proton acceptor.

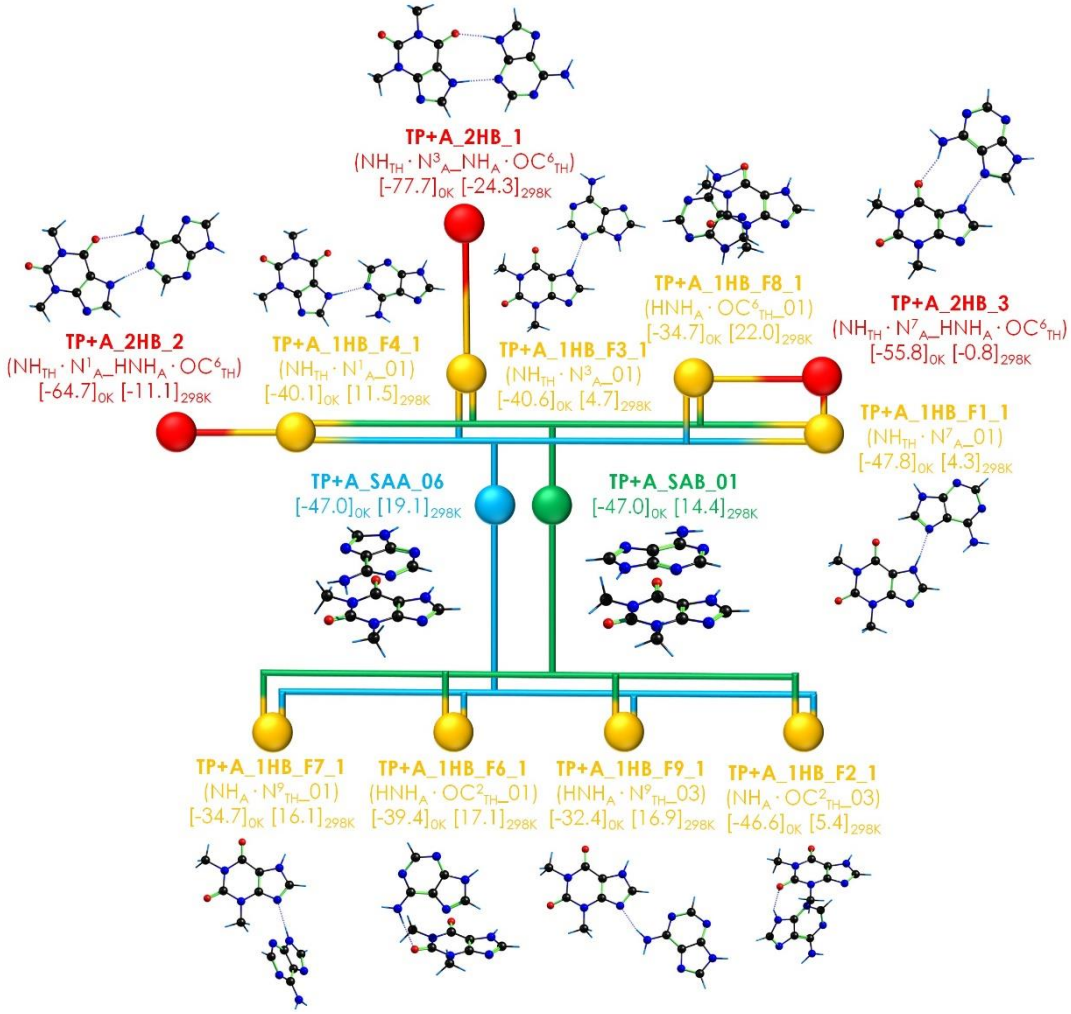

Figure 8.11: Simplified iPES for theophylline+adenine. Conformers were classified and named according on the type of intermolecular interaction. The connections between conformers highlight the similarities in structure and type of interaction. The optimizations were performed at two different computational levels: M06-2X/6-311+G(d,p) and B3LYP-ED=GD3BJ/def2TZVP. The values of the binding energies (with ZPE and BSSE corrections) at 0 and 298 K are for each structure and are the average of the values computed at the two methods.

Figure 8.12 summarizes the three most stable isomers for TP+A, together with their binding energies at 0 and 298 K. As can be noticed, the difference between these three structures is the orientation of A respect to TP. The most stable interaction is formed by a double NH···N/NH···OC bond that leaves the NH_2 group of adenine unbound. The change in the binding site in TP+A dimer compared to TB+A resulted in a slightly larger binding energy.

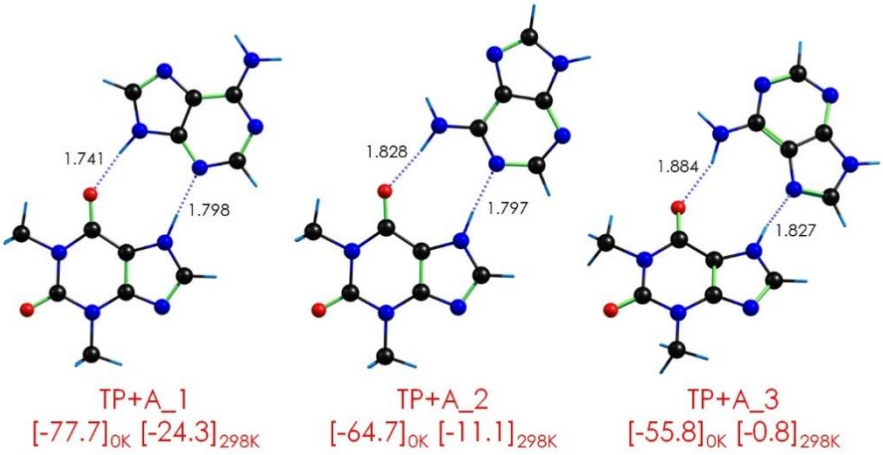

Figure 8.12: Three most stable conformational isomers of theophylline+adenine, together with their binding energy at 0 and 298 K. The binding energy values (kJ/mol) are the average of the two values computed at M06-2X and B3LYP methods. Hydrogen bond distances are those computed at the B3LYP-ED=GD3BJ/def2TZVP level.

Transition from TP to the non-methylated xanthine significantly changes the conformational panorama. Figure 8.13 shows iPES for X+A. As expected, the number of double hydrogen bonded structures increased for this dimer, compared to the previous methylxanthine-adenine systems. Thus, a careful exploration of the 2HB family was performed, which resulted in 14 stable conformations.

Interestingly, all the conformers found for TB+A and TP+A were also found for X+A, thanks to the absence of methylations. In some sense, characterization of this dimer enables a direct comparison between the interaction sites previously explored for the dimers of methylated xanthines. W-C interactions similar to those of the canonical A+T pair are now possible, as can be noticed in structures X+A_2HB_WC and X+A_2HB_rWC. Moreover, the most stable interaction is not the same as in TB+A dimer (X+A_2HB_4, with a double C=O···HN/N-H···N hydrogen bond), but that predicted for the most stable conformation of TP+A (X+A_2HB_1, with NH···N/NH···OC bonds). There is a clear competition between a number of structures for building the most stable conformation.

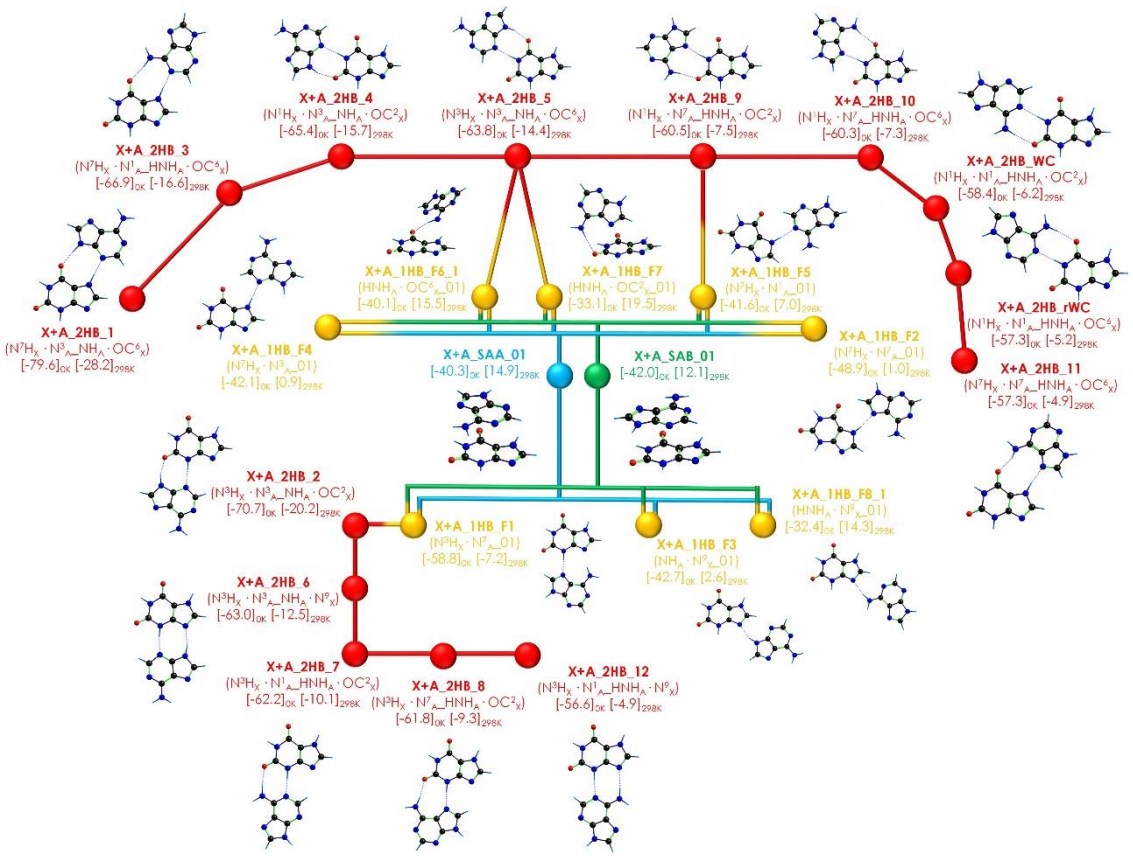

Figure 8.13: Simplified iPES for xanthine+adenine. Conformers were classified and named according on the type of intermolecular interaction. The connections between conformers highlight the similarities in structure and type of interaction. The optimizations were performed at two different computational levels: M06-2X/6-311+G(d,p) and B3LYP-ED=GD3BJ/def2TZVP. The values of the binding energies (with ZPE and BSSE corrections) at 0 and 298 K are for each structure and are the average of the values computed at the two methods.

Regarding the spectroscopic exploration of TP+A and X+A systems, the low signal intensity of the dimers compared to that of the monomers seriously hampered the study. The change in the excited state lifetimes, the difficulties on transferring the molecules to gas phase by ablation and the narrow set of conditions to form the dimers resulted in weak signal intensity and noisy backgrounds. Figure 8.14 shows the mass-resolved one-color REMPI spectra of TP+A and X+A complexes, together with that of the monomers.

The REMPI spectra of TP (which was analyzed in depth in Chapter 7) and X are in good agreement with those reported in previous studies.[6,19] The spectrum of TP shows a clearly defined vibronic progression, while X only exhibits a single band built over a broad absorption. In clear contrast with the monomer's spectra, TP+A and X+A dimers present broad absorptions through a wide spectral region. The low-signal intensity and the unresolved nature of the excitation spectra precluded performing hole-burning

experiments. Instead, different wavelengths were probed (marked by arrows in Figure 8.14) in order to look for isomers of the dimer.

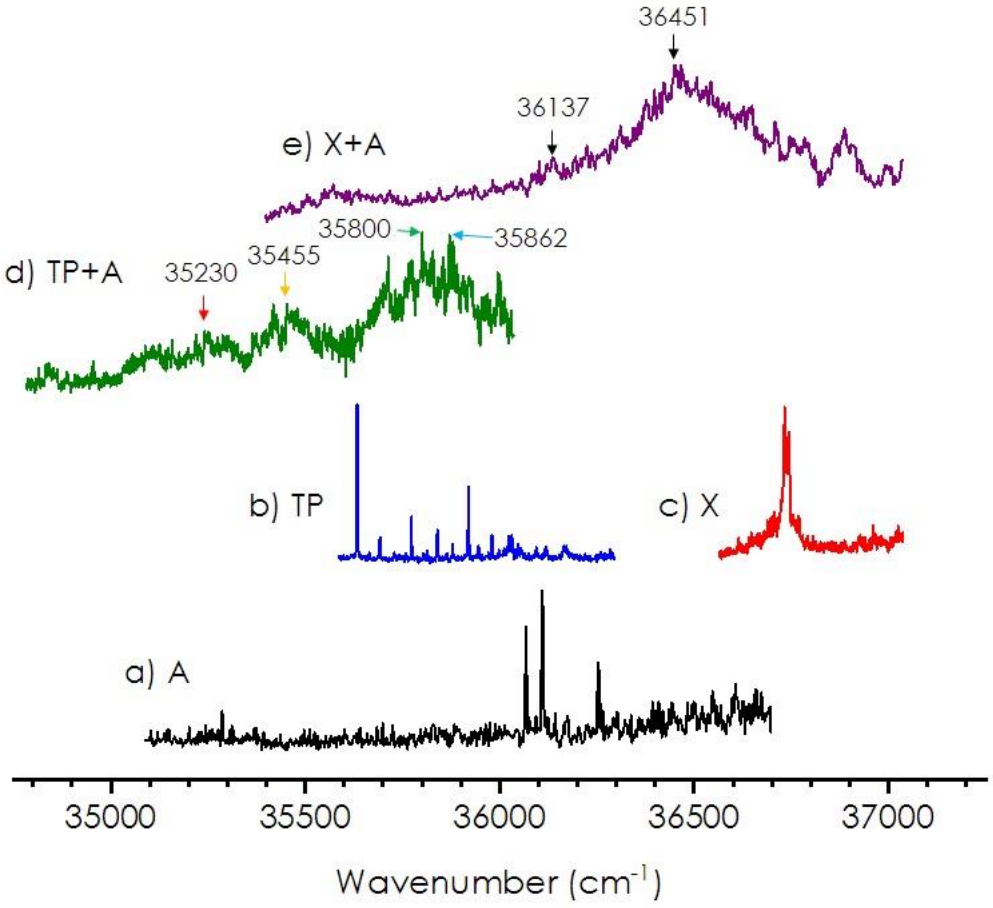

Figure 8.14: One-color REMPI spectra of a) Adenine, b) Theophylline, c) Xanthine, d) Theobromine + Adenine dimer and e) Xanthine + Adenine dimer. Excitation wavelengths employed for IR/UV double resonance experiments are marked by arrows.

Figure 8.15 show the IR spectra obtained for TP+A at several excitation wavelengths. The same trace was obtained in all the probed transitions, but with different S/N ratios, indicating that a single isomer contributes to the REMPI spectrum, at least in the observed spectral range. For this type of rigid dimers, the comparison with the monomer's IR spectra enables a preliminary assignment, as the NH stretching bands remains nearly unperturbed if they do not take part in intermolecular interactions.

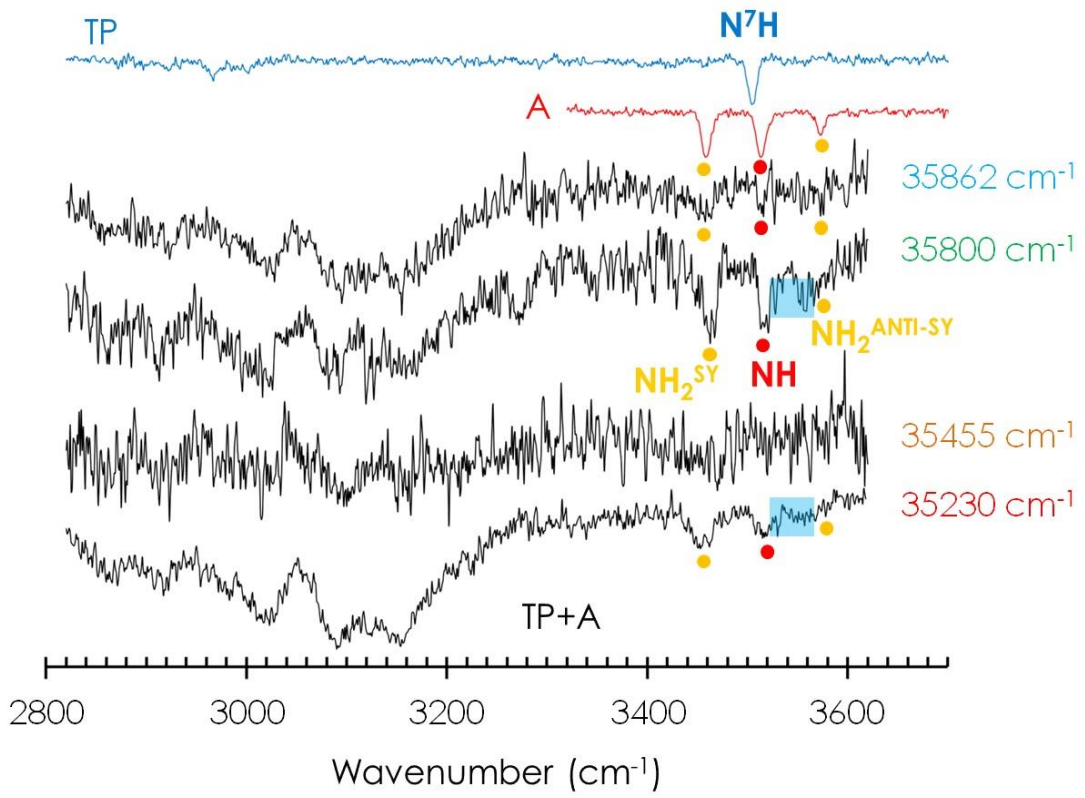

Figure 8.15: IDIR spectra of Theophylline + Adenine dimer recorded at different excitation wavelengths, and compared to the experimental IR spectra of the monomers. Color code of the excitation wavelengths follows that of the arrows in Figure 8.14.

The free NH band of TP is not present in the TP+A spectra, indicating that it must be forming a HB as a donor. Besides, both the symmetric and anti-symmetric stretching modes of the NH_2 group of A are present in TP+A. This means that at least in one isomer, adenine's NH_2 group does not take part in the intermolecular interactions. Likewise, the free N9H stretching band in the dimer and the shoulder on the blue side of the transition, evidence the presence of an isomer interacting with the NH_2, leaving the other N9H of adenine free. Thus, the qualitative analysis of the IDIR spectra revealed that there must be at least two different isomers contributing to the dimer's spectrum.

Figure 8.16 shows a comparison between the IDIR experimental spectrum of TP+A, together with the predictions for the most stable isomers. The assignment of the most stable TP+A structures is in very good agreement with the previous qualitative analysis: the most stable conformation, TP+A_1, is required to explain the observed symmetric and anti-symmetric bands (red and blue dots) of the free NH_2 group. The rest of the bands are explained by TP+A_2: the free NH of adenine (orange dot) and its shoulder (green/yellow). The latter is assigned to the remaining anti-symmetric stretch of the

bounded NH_2. The broad and intense bands bellow 3300 cm^{-1}, which present a large red-shift, correspond to the NH groups involved in strong HBs. However, due to their broadening and close distance, it is difficult to assign their origin to their corresponding structures. The predicted spectrum for TP+A_3 also fits well with the position of the free NH stretches, but the position of the transition corresponding to one of the bonded NHs is predicted to be around 3200 cm^{-1}, while no absorption was observed in that region in the experimental spectrum.

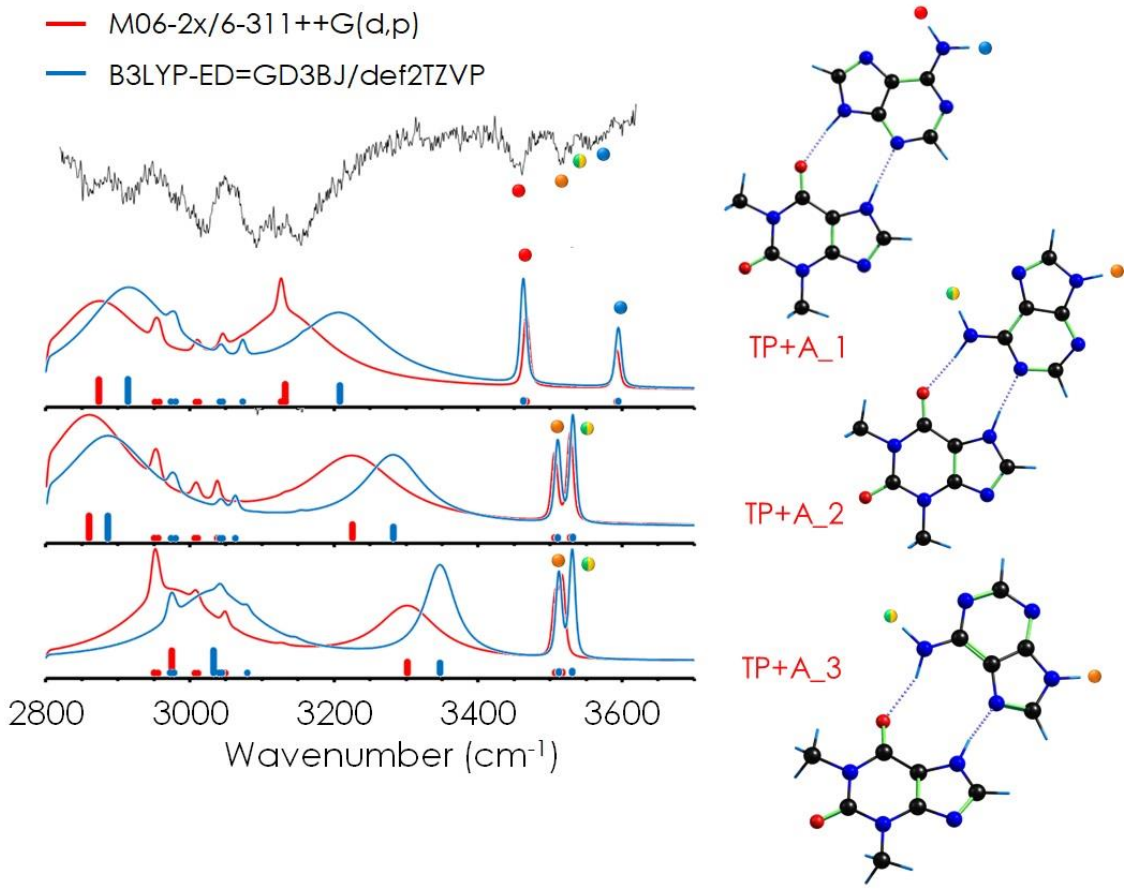

Figure 8.16: Comparison between the experimental IDIRS spectra of TP+A and the predictions for the three most stable computed structures. The experimental trace used in the comparison was recorded at 35230 cm^{-1}.

Concluding with the experimental analysis of TP+A dimer, we confirmed the presence of the most tightly bounded structure TP+A_1. In addition, contribution from TP+A_2 is also required in order to explain the rest of the experimental bands.

Regarding the second system studied in this section, X+A dimer, its experimental IR spectrum presents a congested free NH stretching region. Figure 8.17 collects the IDIR spectra for X+A dimer, together with those of the monomers. There is a perfect match for the free N7H band of X in the dimer, and also for the anti-symmetric stretch of the NH_2 group. However, the symmetric stretch of the latter is slightly displaced, and it

seems to be overlapped with the free N1H band of X. Thus, the origin of this band remains unexplained. Additionally, there is a weak transition to the blue of the N7H band in the dimer (green dot), which is hardly visible over the noisy background and that may correspond to the bounded anti-symmetric stretch of NH_2, as previously observed in TP+A, TB+A and TB+AP complexes. Interestingly, a band in the spectrum of the dimer slightly shifted to the red of the N3H stretch of X could be indicating a small perturbation on that group. Although the origin of some bands was identified, the comparison with the monomer's IR spectra is not enough to perform a preliminary assignment, or even for predicting the number of isomers. Thus, comparison with computational data is mandatory in order to correctly assign the spectrum of X+A dimer.

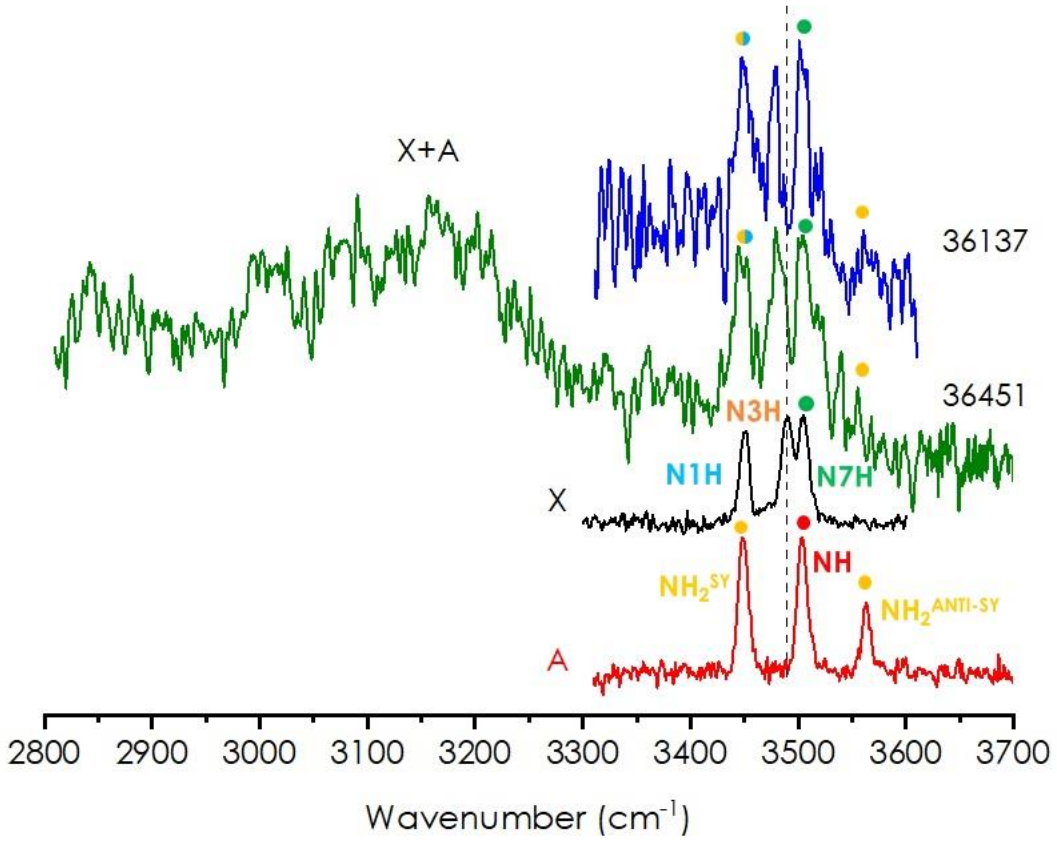

Figure 8.17: IDIR spectra of xanthine, adenine and Xanthine + Adenine dimer recorded at different excitation wavelengths.

Figure 8.18 shows a comparison between the IDIR spectra of X+A, together with the predictions for the most stable isomers, computed at the two theory levels.

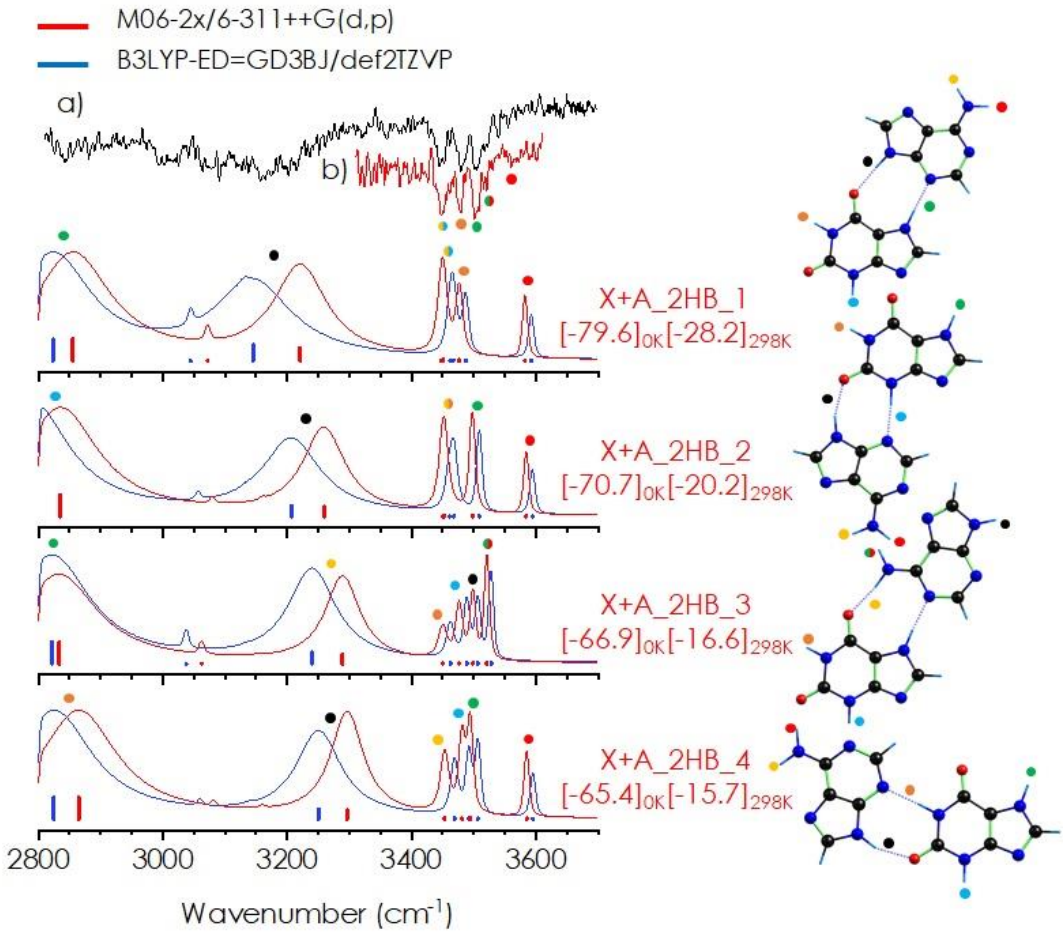

Figure 8.18: Comparison between the experimental IDIR spectra of X+A and the predictions for the most stable computed structures. Experimental traces were recorded at a) 36451 cm^{-1} and b) 36137 cm^{-1} excitation wavelengths.

As can be observed, none of the computed spectra is able to reproduce the experimental trace. At least two isomers are needed to explain all the bands. Additionally, the bands of the stretches of the bonded NH groups are so broad that they contain an undetermined number of contributions. Nevertheless, the comparison allows us to tentatively assign the spectrum, using only the free NH stretching region. As we mentioned above, the unperturbed position of the anti-symmetric stretching band of the NH_2 fits very well with the presence of the global minimum, X+A_2HB_1. In addition, the shoulder marked with a green/red dot could be assigned to the stretch of the bonded NH_2 group, and it is well reproduced by the predicted bands in the computed spectrum of X+A_2HB_3. This isomer would be in lower abundance, as this is the (predicted) strongest band in this spectral region and it appears as a weak shoulder. Finally, as the N7H band of xanthine remains nearly unperturbed, as in the spectrum of X+A_2HB_2. All together, the experimental trace needs of the presence of the three

most stable isomers to be completely assigned. It is worth noting that there is a substantial difference in relative stability between the three assigned structures. They also present very different interaction patterns, which evidences the high competition and isomerization barriers in the formation of this complex.

8.4. Adenine – Theobromine heterotrimers

On the light of previous results, formation of xanthine-adenine dimers was driven by to strong HBs. In this section, we explore the aggregation of a third molecule. The process is significantly more complex, as the number of possibilities grows exponentially with the number of molecules. Besides, from an experimental point of view, recording of the spectra is also complicated due to the further reduction in signal intensity.

Before analyzing the experimental data, a careful exploration of the conformational landscape is needed. Following the same methodology as in previous sections, the conformational landscape was structured by families of structures formed by double HBs, single HB or stacking interactions. The number of structures inside each family depended on the available binding sites. Therefore, the addition of a third molecule to the previous dimers strongly complicated the conformational landscape.

The iPES for this system is too complex. Thus, we focused on the exploration of the most stable structures computed for each trimer. To classify and easily identify the conformers, we employed a similar notation used in previously published theoretical exploration of DNA trimers by Hobza and coworkers.[20] This notation is based on the HBs formed between the bases and the position of the stacking ones: HB/HB family refers to those structures only formed by double HBs, and that are planar. Then, S (stacked) or T(T-shaped) denotes the orientation of a molecule that is forming a single HB or linked by π-stacking interactions.

Due to the relatively large size of the complex, the computational cost of the optimization step and taking into account the accurate predictions obtained for de dimers using M06-2X/6-311++G(d,p), optimization was only carried out at this computation level. Certainly, the study would benefit from addition of the predictions obtained using a second computational level and it will be considered for future studies.

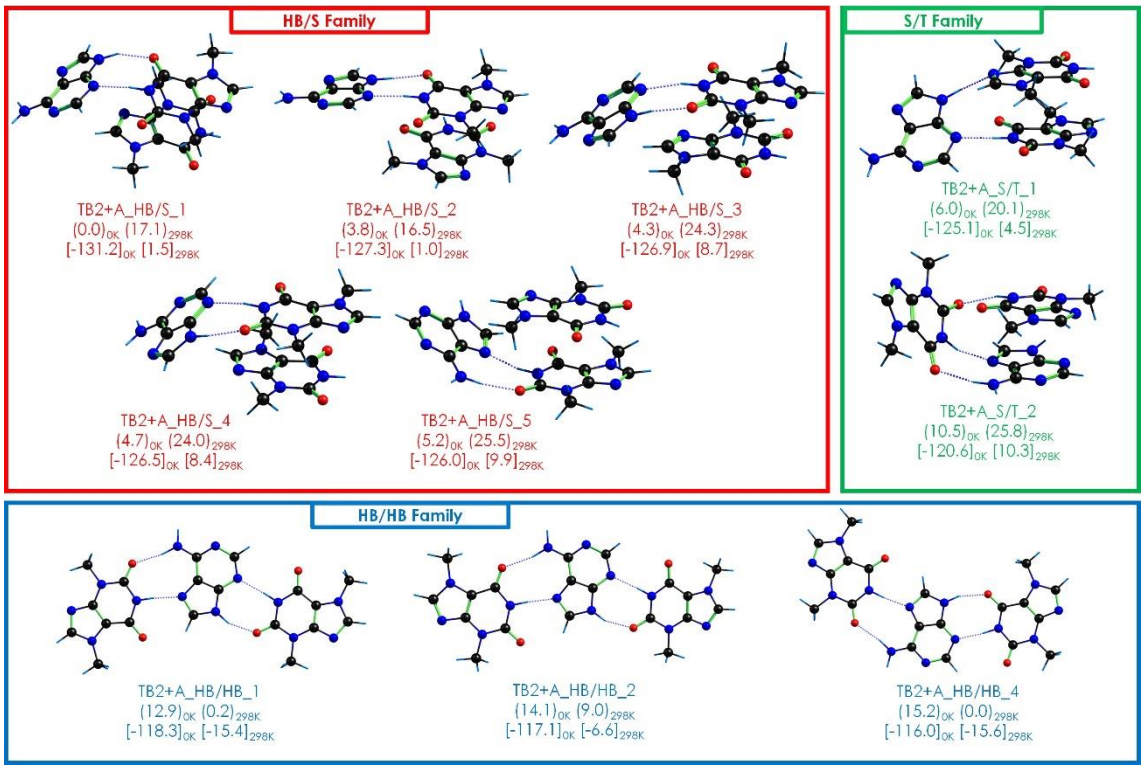

Figure 8.19: Most stable conformations found for the TB2+A trimer, computed at M06-2X/6-311++G(d,p). The structures were classified according to the intermolecular interactions: double hydrogen bonded (HB), stacked (S) or T-shaped (T). Relative energy values in kJ/mol are given in parenthesis, and interaction energies in brackets. All energy values are ZPE and BSSE corrected. The data for the complete set of structures may be found in Table A8.5.

Figure 8.19 collects the most stable conformations found for the TB2+A complex. As can be appreciated, the most stable structures are those from the HB/S family, which are formed by a double H-bonded TB+A dimer and an additional TB in a stacked position. Stacked/T-shaped structures (S/T family) are higher in energy. In this family, either TB or A is forming a HBs with each of the other two molecules, which are stacked. This family is composed by a large number of structures, as it offers a wide variety of possible interactions. The third family exclusively contains planar structures, in which a central molecule establishes two HBs with each of the other two monomers.

Interestingly, previously assigned TB+A dimers in 8.2 section can be identified as forming the kernel for the trimer in HB/S and HB/HB families. In particular, TB+A_1A/B and TB+A_2A/B are readily identified as being part of the trimer. TB+A_3A/B interactions (the W-C-type structure) were found higher in energy (see Table A8.5).

Structure TB2+A_HB/S_1 is the global minimum at 0 K, and also presents the highest interaction energy. This trimer is formed by an A and TB linked by a double C=O···HN/N-H···N HB (type TB+A_1A). The additional TB molecule is stacked above the other TB. The

rest of the structures inside this family present the same interaction pattern, except TB2+A_HB/S_5, which present a TB+A_2A-type double HB interaction.

One must take into account that the structures inside the HB/HB family are the most stable ones at 298 K, while they are more than 10 kJ/mol higher in energy at 0 K respect to the global minimum. The experimental data could therefore indicate if the nucleation of the trimer follows a kinetic or a thermodynamic pathway.

Exploration of the TB+A2 heterotrimer resulted in a very similar conformational landscape. Figure 8.20 presents the most stable conformations found for TB+A2. The most stable structures are those in HB/S, S/T and HB/HB families, as observed for TB2+A. However, there is a substantial change in the global minimum: the most stable structure at both 0 and 298K present a planar arrangement, linked by double HBs.

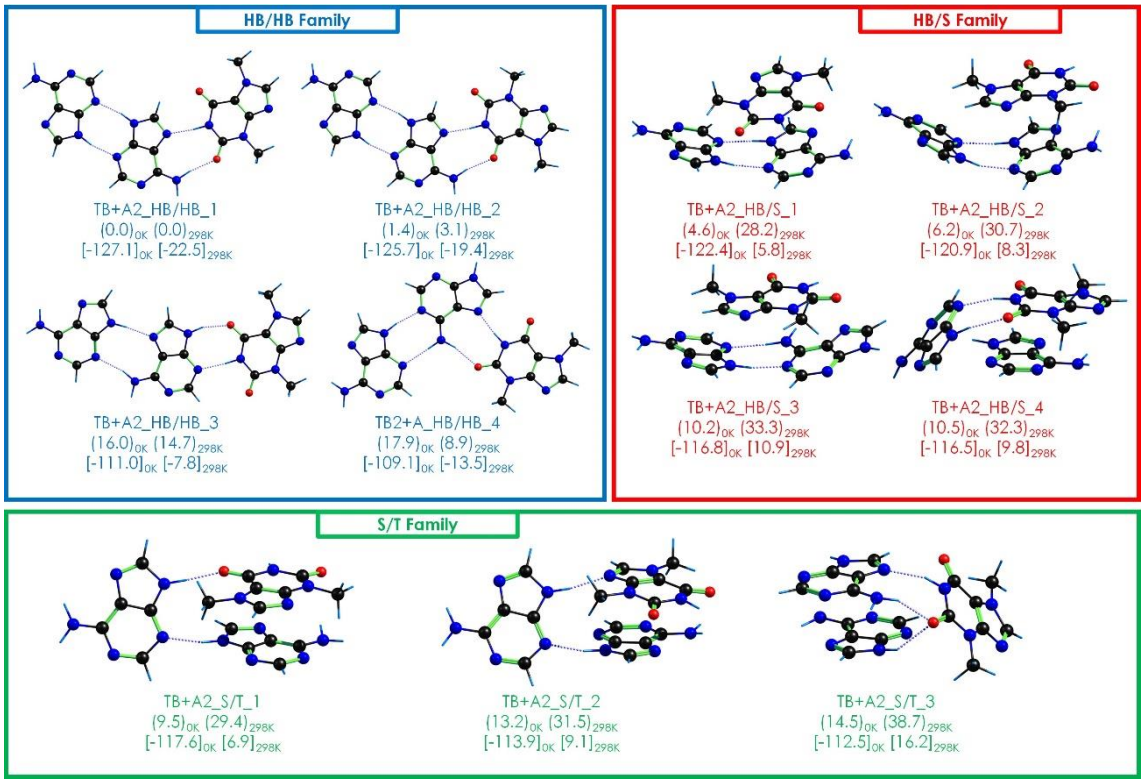

Figure 8.20: Most stable conformations found for TB+A2 complex, computed at M06-2X/6-311++G(d,p). Structures were classified according to their intermolecular interactions: double hydrogen bonded (HB), stacked (S) or T-shaped (T). Relative energy values in kJ/mol are given in parenthesis, and interaction energies in brackets. All energy values are ZPE and BSSE corrected. The complete set of structures are collected in Table A8.6.

A closer look at the interactions in the most stable structures revealed that both adenine molecules tend to interact. The most stable A_2 dimer is formed by a double

NH···N/N···HN HB. This dimer can be found as part of TB+A2_HB/HB_1 and _2, and also in TB+A2_HB/S_1 and _2. It is worth noting that in this case, the HB/S and S/T families are very high in energy at 298 K compared to HB/HB structures. This indicates that for the TB+A2 trimer, planar structures are also favored by entropy.

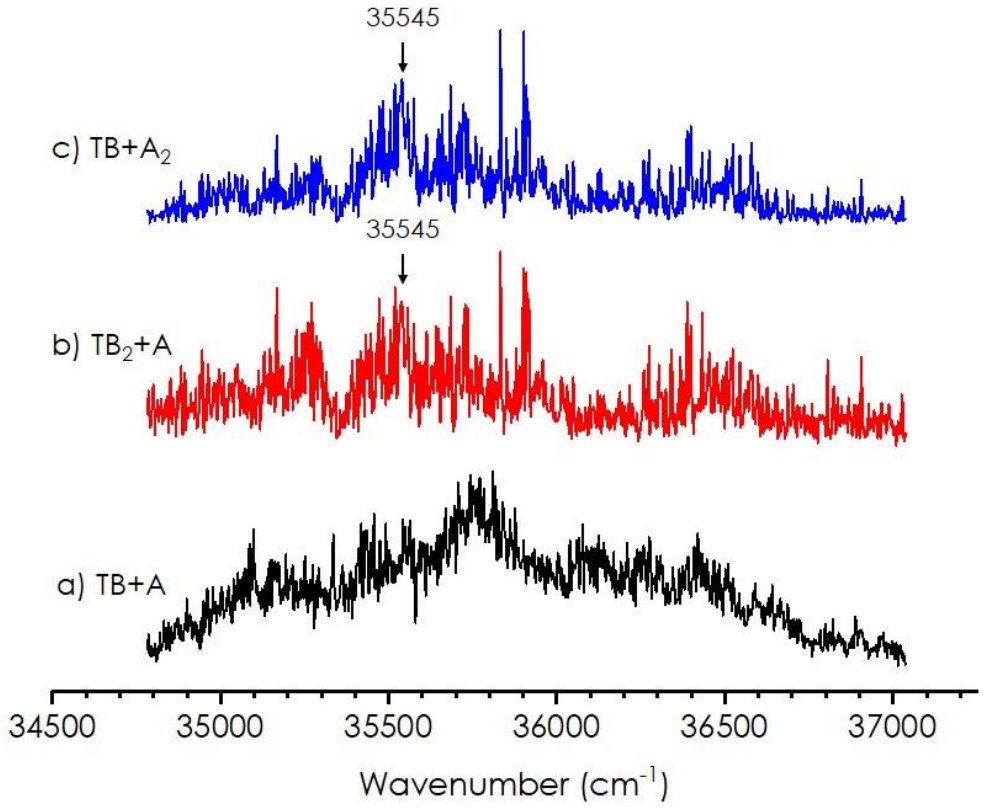

Figure 8.21: One-color REMPI spectra of a) Adenine + Theobromine, b) Adenine + Theobromine$_2$, c) Adenine$_2$ + Theobromine. Excitation wavelengths employed for IR/UV double resonance experiments are marked by an arrow in each complex.

Figure 8.21 shows the REMPI spectra of TB2+A and TB+A2 heterotrimers. The absorption spectra are nearly identical, with very little changes in transition intensities. Due to the low intensity and instability of the signal, IDIRS spectra were only probed at a single wavelength (35545 cm^{-1}). Despite having similar UV absorptions, the recorded IR spectra present substantial differences.

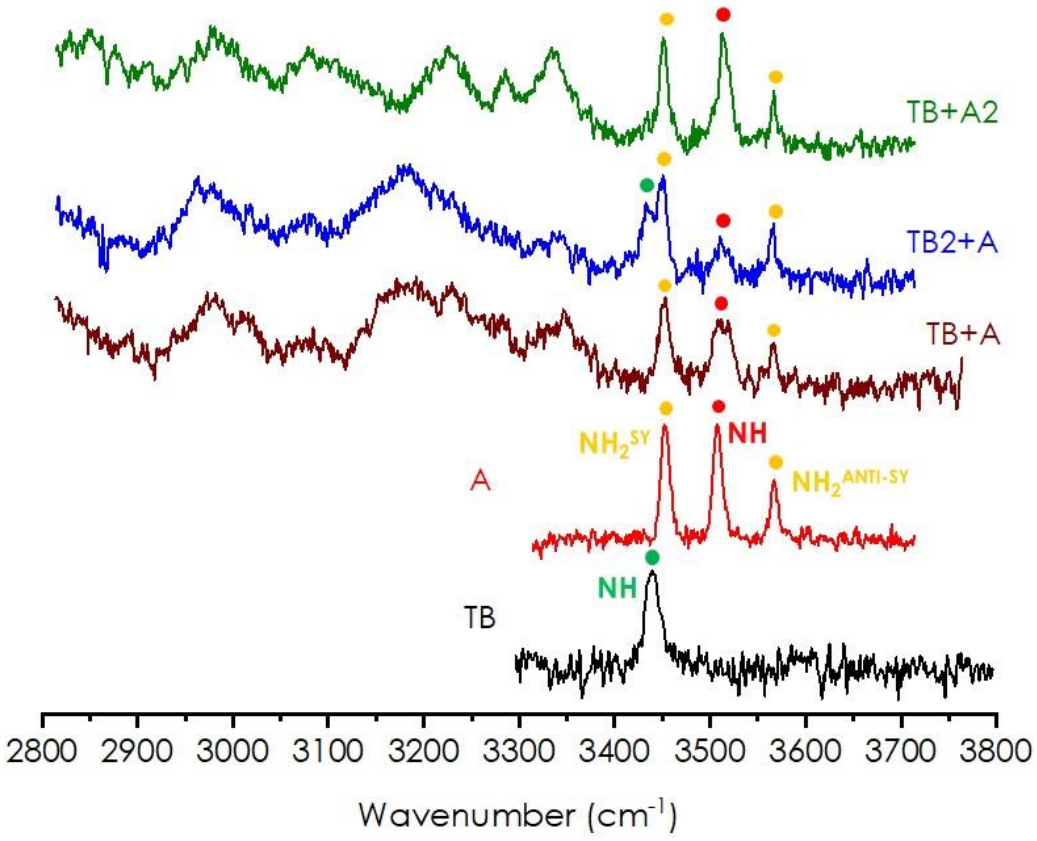

Figure 8.22: IDIR spectra of TB2+A and TB+A2, recorded at 35545 cm^{-1}, compared to the spectra of adenine and theobromine monomers and TB+A dimer.

The IR spectra obtained for TB2+A and TB+A2 may be found in Figure 8.22, together with those of the monomers, in order to identify the unperturbed vibrational bands. As can be appreciated, the free NH band of TB only appears in TB2+A complex, indicating that there must be a conformer where one TB molecule does not form a hydrogen bond as proton donor, probably forming stacking interactions. Note that both NH bands of TB and the NH_2 symmetric band of A are distinguishable in the IR spectrum of TB2+A, where the former appears as a shoulder. For the case of A, however, both symmetric and anti-symmetric stretching modes of the NH_2 group are visible in both trimers. Therefore, both trimers must present at least one conformation where adenine is not forming HBs involving the NH_2 group.

Interestingly, there is a change in the relative intensity of the transitions, from the monomers to the trimers, indicating that several conformers may be contributing to the spectrum, with different relative populations. Moreover, the trace of TB+A dimer is present in the trimers absorptions, especially in the bonded NH and CH stretching regions, which indicates that in the trimers the same interactions, or interactions with

similar strength compared to those seen in the dimer, are present. Further comparison with the theoretical predictions are needed in order to assign the experimental spectrum.

Figure 8.23 shows the comparison between the IDIR spectra of TB2+A and the predictions for the most stable isomers. A quick look at the theoretical simulations shows that no single conformer is able to explain the observed bands in the free NH stretching region. At least two conformations, with different interacting groups, are needed in order to fully assign the experimental trace.

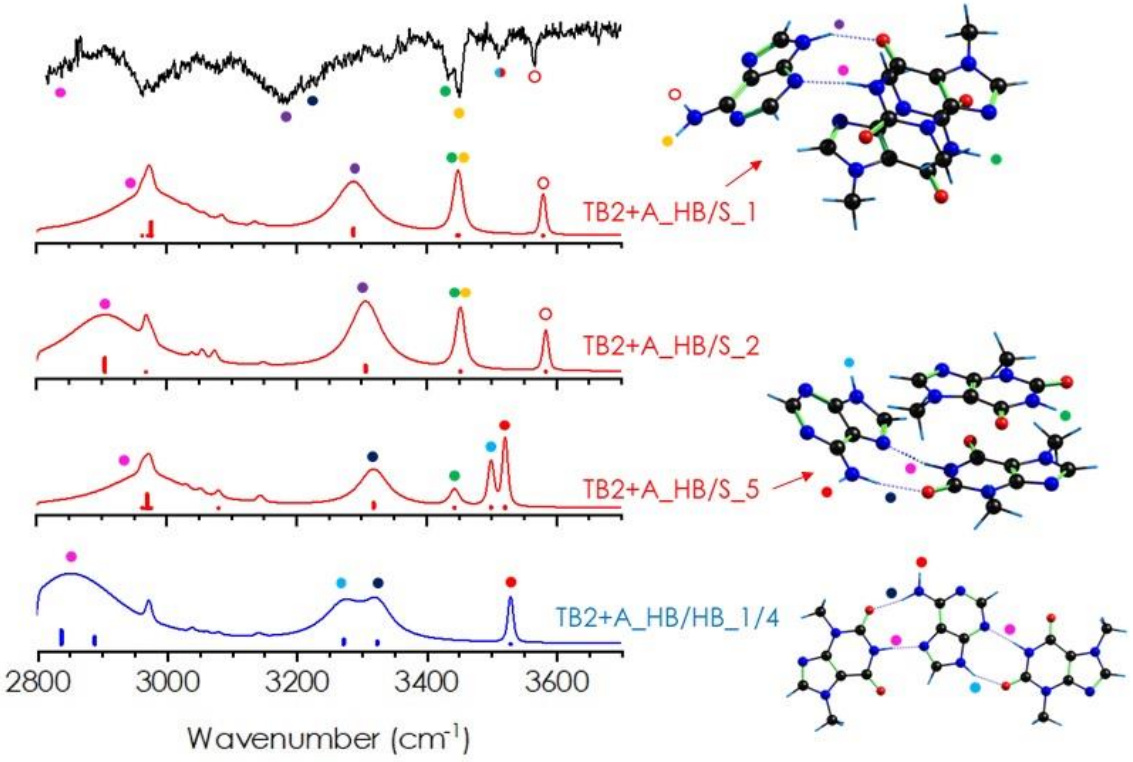

Figure 8.23: Comparison between the experimental IDIR spectrum of TB2+A and the predictions for the most stable structures computed at M06-2x/6-311++G(d,p) level. Colored dots are used to guide the assignment for each structure.

The simulated spectrum ofTB2+A_HB/S1, which is the most stable conformation at 0 K, well reproduces the NH_2 group symmetric and anti-symmetric stretches, and also the free NH of the stacked TB (predicted to be very close to the anti-symmetric stretch of NH_2 at this level of theory). However, an additional conformation is needed in order to explain the weak absorption around 3500 cm^{-1}. This band is well predicted by structure TB2+A_HB/S_5, where different HBs are formed between A and TB (type TB+A_2A dimer). However, planar structures, such as HB/HB_1 or its degenerate HB/HB_4, could also explain the appearance of that absorption. Besides, these planar structures are the

most stable ones at 298 K, and their formation cannot be fully discarded. Structures TB2+A_HB/S_1-4 present very similar predictions, as they only differ in the position/rotation of the stacked TB and in the orientation of the double HBs formed with adenine (degenerate dimers, as we observed in section 8.2).

Regarding TB+A2 heterotrimer, Figure 8.24 shows the comparison between the IDIR spectrum of TB+A2, together with the predictions for the most stable isomers. In this case, planar structures are the most stable ones. Structure TB+A2_HB/HB_1, the global minimum, well reproduces most of the experimental bands. TB+A2_HB/HB_2, which is a degenerate structure (the only difference is the orientation of the carbonyl groups of TB), also presents a similar prediction. NH_2 bands in both free (red and yellow dots) and bounded states (blue and dark blue dots) are clearly visible. Besides, theory well predicts the band displacement corresponding to the double NH···N/N···HN HBs between adenine molecules (purple dot), and to the strong NH···N interaction (magenta dot) between theobromine and adenine.

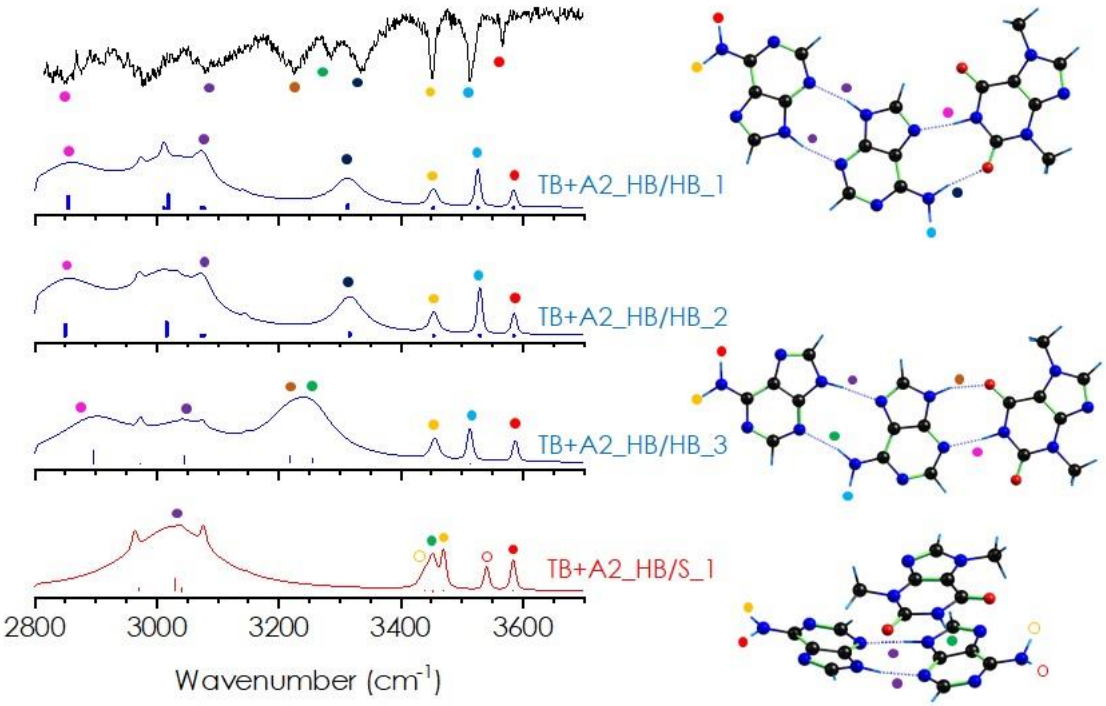

Figure 8.24: Comparison between the experimental IDIRS spectrum of TB+A2 and the predictions for the most stable structures computed at M06-2x/6-311++G(d,p) level. Colored dots are used to guide the assignment for each structure.

However, there are still some bounded bands, marked in green and brown, that need an assignment. To explain those absorptions, a third structure must be taken into account, being TB+A2_HB/HB_3 the best candidate. In this conformer, additional bands appear due to secondary HB arrangement between A-A dimer and between A and TB. More precisely, the stretching vibrations of the groups involved in the HNH···N interaction in A-A dimer (green dot), and in the N9H···O=C hydrogen bond (brown dot) can be assigned to the broad bands around 3250 cm^{-1}. Conversely, the prediction for the most stable structure of the next family, HB/S, does not reproduce the experimental observation. Thus, we can discard the existence of stacked trimers.

8.5. Discussion

In previous sections we presented an exhaustive spectroscopic and computational analysis of xanthine/methylxanthine-adenine complexes. In general terms, aggregation between these compounds is dominated by strong NH···N and NH···O=C HBs. All the assigned dimers presented two HBs, similar to those observed in DNA/RNA between purine and pyrimidine bases. Interestingly, no stable stacking interactions were observed in any of the dimers, which evidences a clear preference to form strong and cooperative double HBs in absence of external perturbations. In fact, the observed HBs between TB, TP or X with A are extraordinarily strong, as reflected by the width of the IR transitions and the large red shift: the stretches of the hydrogen bonded NHs appear in the region of the CH stretches.

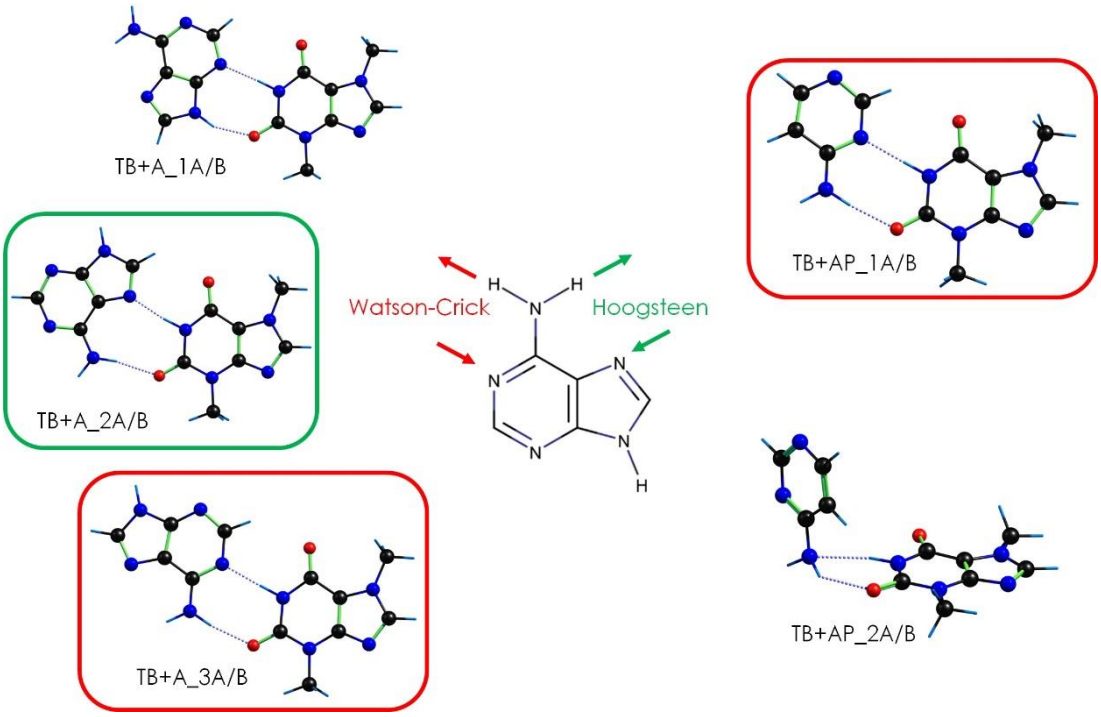

Figure 8.25: Experimentally assigned structures for TB+A and TB+AP dimers.

Due to its resemblance with thymine base, especially in its CONHCO binding motif, the conformational landscape of TB+A dimer revealed structures with analogue interactions to those in T+A. Figure 8.25 shows the assigned structures of TB+A and TB+AP dimers. The most stable conformer,TB+A_1, is formed by two $N_{TB}H\cdots N^3_A$ and $N_AH\cdots O{=}C$ HBs. However, additional features in the spectrum needed of the presence of conformers TB+A_2 and 3. These conformers also show double HBs, but with the adenine in a different orientation and establishing intermolecular interactions similar to those observed in DNA. For example, TB+A_2 dimer presents $N_{TB}H\cdots N^7_A$ and $HNH\cdots O{=}C$ HBs, similar to those observed in Hoogsteen alternative base pairing[21,22] in triple-stranded DNA structures.[23,24] Furthermore, conformer TB+A_3 is of the W-C type, with $N_{TB}H\cdots N^1_A$ and $HNH\cdots O{=}C$ HBs. Conversely, the TB+AP global minimum is of the W-C type. Although we confirmed its presence in the jet, to completely explain the experimental spectrum, the presence of conformer TB+AP_2 was also required to assign all the bands in the spectrum. In this conformer, AP adopts a T-shaped position, while is forming HBs with its NH_2 group acting both as proton donor and acceptor.

Methyl group change (or removal) in TP+A and X+A complexes strongly affected the hydrogen bond patterns, in comparison with TB+A. Figure 8.26 collects the experimentally assigned structures for all the dimers here studied. X+A dimer resulted to be the paradigm of the interactions between xanthine family and adenine, as the lack of substituted NH groups expanded its conformational landscape with all the possible

combinations. Therefore, the two molecules are free to find the most stable interaction, reaching a 80 kJ/mol binding energy. The methylation of TP does not block the groups involved in the preferred interaction and therefore, they form a structure that resembles that of X+A and present similar binding energy. However, the position of the methyl group in TB blocks such conformation, forcing adenine to interact with the NH/CO motif of TB and reducing the binding energy to ~64 kJ/mol.

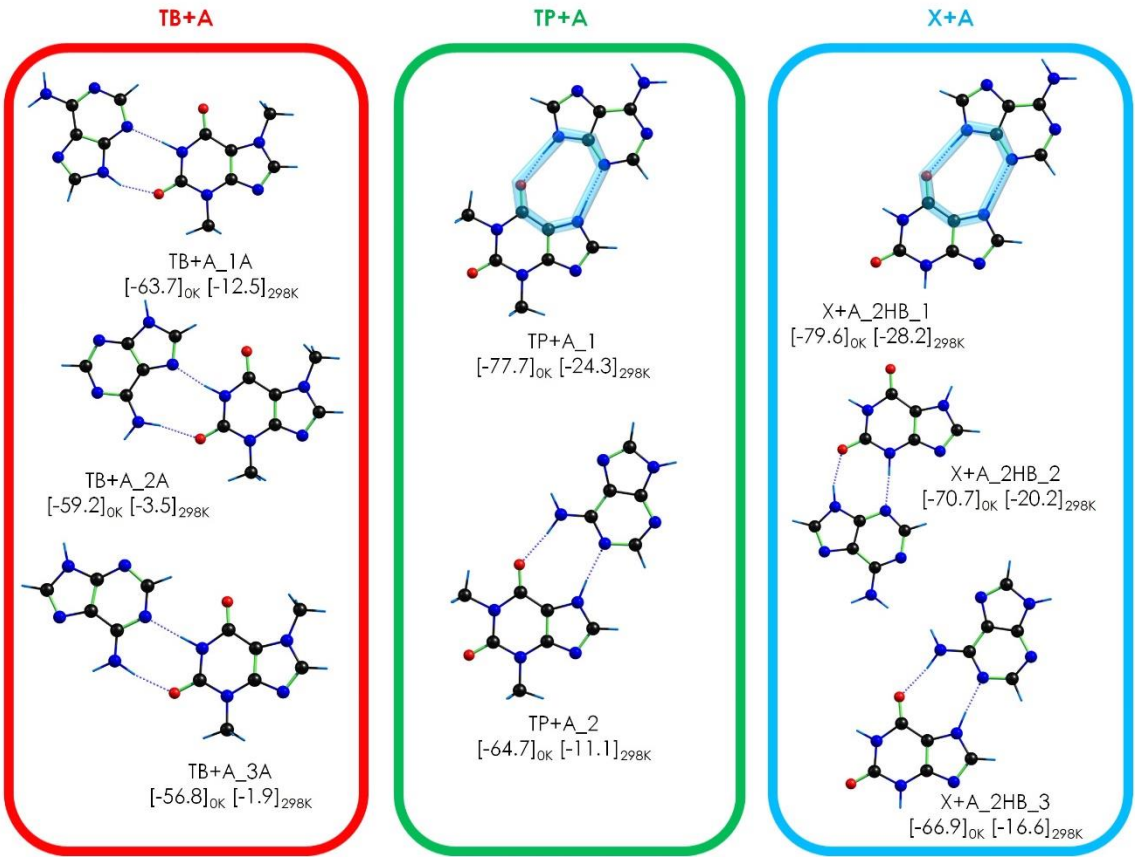

Figure 8.26: Comparison between the assigned conformations of TB+A, TP+A and X+A, together with their computed interaction energies. The energy values are the average of the two values computed using the M06-2X and B3LYP functionals.

The comparison between the assigned structures of TB+A, TP+A and X+A, together with their computed interaction energies, evidences that the methylation in xanthine derivatives modulates the interaction energy of the dimers. Interaction energies for the most stable TP+A and X+A dimers are 77.7 and 79.6 kJ/mol, respectively, while in the most stable structure of TB+A is 63.7 kJ/mol. This binding energy modulation through the methylation could be the reason behind the binding affinity of xanthine derivatives. For example, a study in the RNA binding affinity with different xanthine compound revealed a stronger binding affinity for theophylline rather than for theobromine,

among others.[25] Additional studies between xanthine derivatives and different DNA bases could provide more information about the possible specificity of the interactions.

Cluster growth in TB+A system revealed an interesting panorama. As a general trend, all the assigned and stable structures for the trimer show the same interactions observed in TB+A dimers (see Figure 8.25). More precisely, the interaction between TB+A pairs in the trimer correspond to those in TB+A_1 and TB+A_2 dimers. This indicates that, very likely, the formation of the trimers comes from the addition of a third molecule (A or TB depending on which heterotrimer is formed) to the most stable and previously formed dimers in the supersonic expansion. A similar tendency was already observed in cluster growth with cytosine homoaggregates.[26]

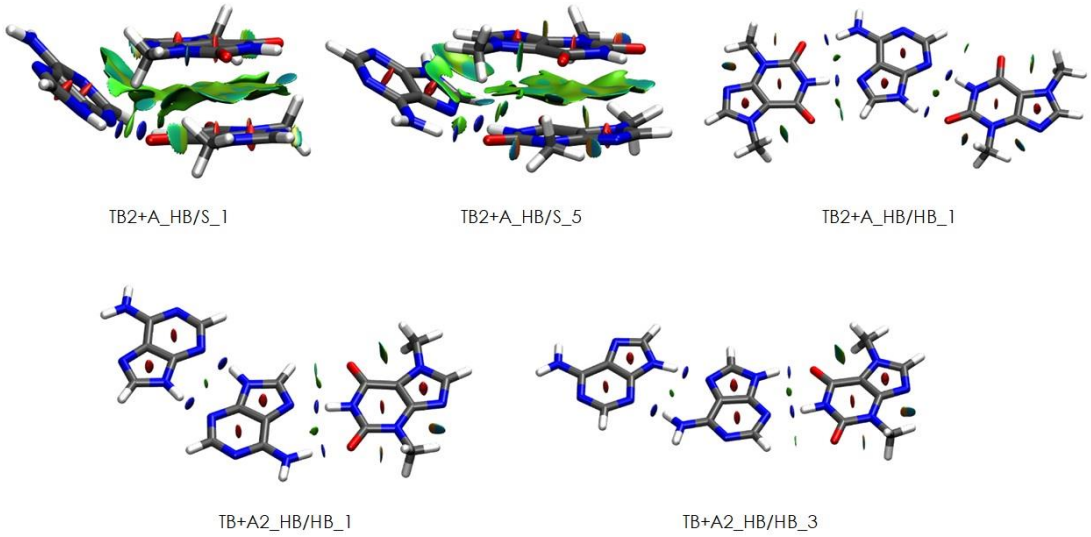

Figure 8.27: NCI plots for the assigned structures of TB2+A and TB+A2 trimers.

Figure 8.27 shows the NCI plots of the assigned TB2+A and TB+A2 trimers. The presence of TB2+A trimers formed by both double HBs and stacking interactions (see structures TB2+A_HB/S_1 and 5) were required to explain the experimental spectrum. As revealed by the isosurface representation, the stacked molecule presents interactions due to dispersive forces with the other two molecules. Moreover, TB shows a preference towards forming stacking interactions with TB rather than with A. This observation is in good agreement with the previous studies about the stacking preferences of TB in homodimers and homotrimers.[6,27] However, planar structures (TB2+A_HBHB_1) may also be formed in the expansion, and are energetically favored at higher temperatures, becoming the global minimum above 298 K. Therefore, they could be trapped during

the first stages of the expansion, indicating the prevalence of a kinetic cooling process instead of a thermodynamic one. Relaxation of the planar structures to more stable conformers in that case would be unlikely, as the energy needed to break two strong HBs is higher than that provided by the inelastic collisions between the molecules and/or the carrier gas.

In clear contrast with the previous trimer, TB+A2 showed a preference to form planar structures, in which A and TB adopt the most stable conformation observed in the dimer, plus an additional A=A interaction. This observation revealed that A tends to form hydrogen bonds rather than to stack over itself or above TB. Previous studies in supersonic expansions also revealed this tendency, as no stacking interactions where found in isolated adenine dimers.[28] No spectroscopic signatures for the HB/S family were found for this trimer. In fact, the most stable structure inside this family presents a TB stacked over an A=A dimer. Structures with a stacked A molecule (TB+A2_HB/S_4), which resembles to the most stable conformer in TB2+A, presents interaction energies about 15 kJ/mol lower than its brother system. Altogether, this observation points out the low interaction preference of the adenine to perform stacking interactions. Characterizing these interaction preferences in a stepwise nucleation is crucial not only to better understand the NCI preferences in DNA, but also for the development of new supramolecular materials that exploit the force of the above-studied interactions.[29]

8.6. Conclusions

In this chapter, we present the first and extensive spectroscopic study of the aggregates between xanthines and DNA bases. Interpretation of the experimental spectra on the light of the computational predictions revealed that both TB+A and TB+AP systems present very similar interactions to those found in the canonical nucleobases in an environment that is free from external perturbations. W-C interaction between A-T was observed in TB+AP. In its brother systems TB+A, that particular interaction can only be tentatively assigned, though. Comparison of the binding energy of these systems with those from similar systems, including those formed by the canonical nucleobases shows a wide range of values, with G+C forming the strongest dimers. This means, on the one hand, that election of T and A as nucleobases was not based (or at least exclusively based) on the strength of the intermolecular interactions, and on the other, that the canonical nucleobases had to compete with other interacting partners for the formation of the proto-information polymers.

Forming aggregates between A and different xanthine derivatives, such as TP and X, revealed that the methylation can modulate the binding energy of the system. Interestingly, the most stable structures assigned for TP+A and X+A present the same interaction. Finally, we characterized the interaction preferences in heterotrimers formed between A and TB. Despite the complex and extended conformational landscape of the trimers, the most stable families were detected in the beam. Interestingly, all assigned trimers present the same interactions previously found in TB+A dimer, confirming that the aggregation process of these adenine-xanthine complexes follows a sequential growth. Addition of a second adenine results in planar arrangements, while TB2+A prefers formation of 3D structures, including with stacking interactions.

8.7. References

[1] P. J. Marro, S. Baumgart, M. Delivoria-Papadopoulos, S. Zirin, L. Corcoran, S. P. McGaurn, L. E. Davis and R. R. Clancy, Purine Metabolism and Inhibition of Xanthine Oxidase in Severely Hypoxic Neonates Going onto Extracorporeal Membrane Oxygenation, *Pediatr. Res.*, 1997, **41**, 513–520.

[2] I. Usabiaga, A. Camiruaga, C. Calabrese, A. Veloso, V. C. D'mello, S. Wategaonkar and J. A. Fernández, Exploration of the theobromine–water dimer: comparison with DNA microhydration, *Phys. Chem. Chem. Phys.*, 2020, **22**, 15759–15768.

[3] T. Schultz, E. Samoylova, W. Radloff, I. V Hertel, A. L. Sobolewski and W. Domcke, Efficient Deactivation of a Model Base Pair via Excited-State Hydrogen Transfer, *Science (80-.).*, 2004, **306**, 1765 LP – 1768.

[4] A. L. Sobolewski, W. Domcke and C. Hättig, Tautomeric selectivity of the excited-state lifetime of guanine/cytosine base pairs: The role of electron-driven proton-transfer processes, *Proc. Natl. Acad. Sci. U. S. A.*, 2005, **102**, 17903 LP – 17906.

[5] Z. Gengeliczki, M. P. Callahan, N. Svadlenak, C. I. Pongor, B. Sztáray, L. Meerts, D. Nachtigallová, P. Hobza, M. Barbatti, H. Lischka and M. S. de Vries, Effect of substituents on the excited-state dynamics of the modified DNA bases 2,4-diaminopyrimidine and 2,6-diaminopurine, *Phys. Chem. Chem. Phys.*, 2010, **12**, 5375–5388.

[6] M. P. Callahan, Z. Gengeliczki, N. Svadlenak, H. Valdes, P. Hobza and M. S. de Vries, Non-standard base pairing and stacked structures in methyl xanthine clusters, *Phys. Chem. Chem. Phys.*, 2008, **10**, 2819–2826.

[7] C. Plützer, E. Nir, M. S. de Vries and K. Kleinermanns, IR–UV double-resonance spectroscopy of the nucleobase adenine, *Phys. Chem. Chem. Phys.*, 2001, **3**, 5466–5469.

[8] C. Plützer and K. Kleinermanns, Tautomers and electronic states of jet-cooled adenine investigated by double resonance spectroscopy, *Phys. Chem. Chem. Phys.*, 2002, **4**, 4877–4882.

[9] A. Camiruaga, I. Usabiaga, V. C. D'mello, G. A. García, S. Wategaonkar and J. A. Fernández, Revisiting the spectroscopy of xanthine derivatives: theobromine and theophylline, *Phys. Chem. Chem. Phys.*, 2019, **21**, 26430–26437.

[10] B. Cohen, P. M. Hare and B. Kohler, Ultrafast Excited-State Dynamics of Adenine and

Monomethylated Adenines in Solution: Implications for the Nonradiative Decay Mechanism, *J. Am. Chem. Soc.*, 2003, **125**, 13594–13601.

[11] G. Zechmann and M. Barbatti, Ab initio study of the photochemistry of aminopyrimidine, *Int. J. Quantum Chem.*, 2008, **108**, 1266–1276.

[12] J. A. Frey, A. Müller, H.-M. Frey and S. Leutwyler, Infrared depletion spectra of 2-aminopyridine2-pyridone, a Watson–Crick mimic of adenineuracil, *J. Chem. Phys.*, 2004, **121**, 8237–8245.

[13] Z. Gengeliczki, M. P. Callahan, M. Kabelá, A. M. Rijs and M. S. de Vries, Structure of 2,4-Diaminopyrimidine–Theobromine Alternate Base Pairs, *J. Phys. Chem. A*, 2011, **115**, 11423–11427.

[14] J. A. Frey, P. Ottiger and S. Leutwyler, Watson-crick and sugar-edge base pairing of cytosine in the gas phase: UV and infrared spectra of cytosine·2-pyridone, *J. Phys. Chem. B*, 2014, **118**, 682–691.

[15] C. Plützer, I. Hünig, K. Kleinermanns, E. Nir and M. S. De Vries, Pairing of isolated nucleobases: Double resonance laser spectroscopy of adenine-thymine, *ChemPhysChem*, 2003, **4**, 838–842.

[16] V. Nosenko, M. Kunitski, T. Stark, M. Göbel, P. Tarakeshwar and B. Brutschy, Vibrational signatures of Watson–Crick base pairing in adenine–thymine mimics, *Phys. Chem. Chem. Phys.*, 2013, **15**, 11520–11530.

[17] P. Jureka and P. Hobza, True Stabilization Energies for the Optimal Planar Hydrogen-Bonded and Stacked Structures of Guanine···Cytosine, Adenine···Thymine, and Their 9- and 1-Methyl Derivatives: Complete Basis Set Calculations at the MP2 and CCSD(T) Levels and Comparison with E, *J. Am. Chem. Soc.*, 2003, **125**, 15608–15613.

[18] G. von Kiedrowski, A Self-Replicating Hexadeoxynucleotide, *Angew. Chemie Int. Ed.*, 1986, **25**, 932–935.

[19] M. P. Callahan, B. Crews, A. Abo-Riziq, L. Grace, M. S. de Vries, Z. Gengeliczki, T. M. Holmes and G. A. Hill, IR-UV double resonance spectroscopy of xanthine, *Phys. Chem. Chem. Phys.*, 2007, **9**, 4587–4591.

[20] M. Kabelá, E. C. Sherer, C. J. Cramer and P. Hobza, DNA Base Trimers: Empirical and Quantum Chemical Ab Initio Calculations versus Experiment in Vacuo, *Chem. – A Eur. J.*, 2007, **13**, 2067–2077.

[21] K. Hoogsteen, The crystal and molecular structure of a hydrogen-bonded complex between 1-methylthymine and 9-methyladenine, *Acta Crystallogr.*, 1963, **16**, 907–916.

[22] G. Ghosal and K. Muniyappa, Hoogsteen base-pairing revisited: Resolving a role in normal biological processes and human diseases, *Biochem. Biophys. Res. Commun.*, 2006, **343**, 1–7.

[23] S. Rhee, Z. Han, K. Liu, H. T. Miles and D. R. Davies, Structure of a Triple Helical DNA with a Triplex–Duplex Junction, *Biochemistry*, 1999, **38**, 16810–16815.

[24] J. Bernués and F. Azorín, eds. F. Eckstein and D. M. J. Lilley, Springer Berlin Heidelberg, Berlin, Heidelberg, 1995, pp. 1–21.

[25] I. M. Johnson, S. G. B. Kumar and R. Malathi, RNA Binding Efficacy of Theophylline, Theobromine and Caffeine, *J. Biomol. Struct. Dyn.*, 2003, **20**, 687–692.

[26] J. González, I. Usabiaga, P. F. Arnaiz, I. León, R. Martínez, J. Millán and J. A. Fernández, Competition between stacked and hydrogen bonded structures of cytosine aggregates, *Phys. Chem. Chem. Phys.*, 2017, **19**, 8826–8834.

[27] I. Usabiaga, University of the Basque Country, 2017.

[28] C. Plützer, I. Hünig and K. Kleinermanns, Pairing of the nucleobase adenine studied by IR-UV double-resonance spectroscopy and ab initio calculations, *Phys. Chem. Chem. Phys.*, 2003, **5**, 1158–1163.

[29] J. Pascual-Colino, G. Beobide, O. Castillo, I. da Silva, A. Luque and S. Pérez-Yáñez, Porous Supramolecular Architectures Based on π-Stacking Interactions between Discrete Metal-Adenine Entities and the Non-DNA Theobromine/Caffeine Nucleobases, *Cryst. Growth Des.*, 2018, **18**, 3465–3476.

Chapter 9

Conclusions & Future Perspectives

9.1. Conclusions

The aggregation mechanisms, the non-covalent forces that govern these process and the structure characterization of different model systems containing biologically relevant functional groups have been explored in several biologically-relevant systems, using a combined approach of experimental and theoretical methodologies. The results achieved demonstrate the efficacy of such approach. The continuous evolution of computational methods and the improve of their accuracy in the predictions encourages the exploration of molecular aggregates of increasing complexity.

The study of the aggregation of aromatic alcohols, benzyl alcohol and 2-phenylethanol, revealed that formation of OH···O HBs is the leading interaction in the aggregation process, whereas secondary OH···π and π-πinteractions shaped the final structure of the clusters. Increasing the number of molecules, allowed us to locate the transition from linear structures to cyclic ones. The trimer still presents OH···OH···OH···π linear interactions, due to the relative strength of the OH···π interaction and that it is less demanding in the angle of attack of the donor molecule. Thus, the molecules can accommodate their relative positions to maximize the rest of the interactions. Adding the fourth molecule allows the monomers to form a cyclic HB network due to the reduced strain of the angles. This type of structures gain stability from the cooperative effects, substantially increasing the overall stability of the aggregate.

Characterization of the aggregation preferences of sugar derivatives is very interesting due to the high flexibility that their multiple hydroxyl groups present, which is related to their implication on the immune system. In Chapter 4, phenyl-β,D-glucopyranoside was complexed with different molecules, in order to understand its interaction with other molecules

Complexes with N-methylacetamide, paracetamol or phenol revealed a clear preference to form hydrogen bonds with O2H and O6H hydroxyl groups. Additionally, the aromatic ring substituent seemed to reinforce these interactions. Comparison between the binding energy of β-PhGlc+Par and β-MeGlc+Par demonstrated that the addition of the aromatic ring increased the binding energy in ~20 kJ/mol, from 51 kJ/mol to 70.5 kJ/mol. Thus, the aromatic ring introduces a non-negligible modulation in the aggregation of Glc. This indicates that the substitution in O1 of a big group can change the interaction preference of the sugar. A similar change in the interaction preference was observed for β-PhGlc and β-PhGal homodimers, where a small structural change in

C_4, switching the OH group from axial to equatorial position, strongly modifies the structure of the dimer.

Finally, we explored the propensity of sugar units to form stacking interactions in the Caf+PhGlc dimer. Clearly, the stacking interaction is highly unspecific and it has to be combined with hydrogen bonds to favor a given orientation.

The studies on sugar aggregation served as a base to move to substantially larger clusters. GL1 and GLOMe are complex molecules that may be taken as a model of the conformational preferences in glycolipids. In this systems, the O3H group was substituted by a fatty acid. The results showed that the influence of the carbonyl group disrupted the typical cooperative HB network formed in non-substituted monosaccharides. Besides, the presence of the voluminous alkyl chain did not alter the binding preference on hydroxyl groups. Unexpected interactions were observed in the monohydrated complexes of the glycolipids. The presence of the carbonyl groups strongly altered the water's binding preference, creating a "hot spot" or a binding pocket very different from those reported for non-substituted sugar-water complexes.

In the last sections of this thesis, the spectroscopy of the aggregates of xanthines was explored. Caf+Ph, resulted to be a complex system. Thus, an extended computational methodology was used in order to model the non-covalent forces forming Caf+Ph complex. We concluded that phenol interacts with caffeine through π-π stacking interactions and with relatively strong HBs with the carbonyl groups of caffeine. Comparison with the experimental results highlighted the problems that the computational methods have to describe systems formed by an equilibrium between different non-covalent interactions.

Exploration of the interactions of xanthines with other molecules allowed us to speculate with the role that non-covalent interactions played in the first instants of the pre-biotic chemistry. No substantial differences between the aggregation of nucleobases and that of xanthine derivatives was observed. The results presented in this work even demonstrate that formation of trimers between adenine and theobromine may result in stacked structures. Such tendency towards formation of stacked structures that resemble those in DNA double strands would be boosted in solution, taking into account the hydrophobic nature of these molecules. These results depict a complex pre-biotic landscape in which a myriad of organic compounds compete to form stable aggregates and somehow autocatalyze new molecules.

9.2. Annex: Future perspectives and additional experimental results

Although we present here a joined experimental and computational analysis of the aggregation of several systems, the central part of this thesis are the experimental results. The techniques used in this work, based on mass-resolved laser spectroscopy, entails a complicated methodology. For each experiment to be reproducible, laser alignment, maintenance, correct function of electronic devices and accurate optimization of the experimental conditions is needed. Many factors affect the experimental measurements. The ambitious objectives of this project pushed us to take the technique to its limits in order to extract information from systems of increasing complexity.

Only those experimental results that were fully analyzed were presented in previous chapters. But in addition, several other systems were also explored and the results still wait for the computational data to be understood. In this section, we briefly present some of the spectra obtained from those systems. As it will be shown, very challenging systems were explored and they will also be the objective of future thesis.

9.2.1. Microhydration of aromatic alcohol aggregates

Chapter 3 collects the results obtained for benzyl alcohol (BnzA) and 2-phenylethylalcohol (PEAL) clusters. The extensive exploration of their aggregates up to the tetramer allowed us to characterize the effects of the alkyl chain in the interplay between dispersive forces and HB networks. Additionally, the hydrated clusters of BnzA aggregates were spectroscopically explored.

Those complexes were sometimes detected through fragmentation processes in the electronic spectrum of the aggregate (dimer, trimer, etc.), or by detecting signal in their corresponding mass-channels, if the population of the hydrated complex is high enough. Such was the case for PEAL dimer, where its hydrated clusters were detected, allowing us to carry out their spectroscopic study. Thus, experimental data were obtained for $PEAL_2$+W_n (n=1-3) aggregates.

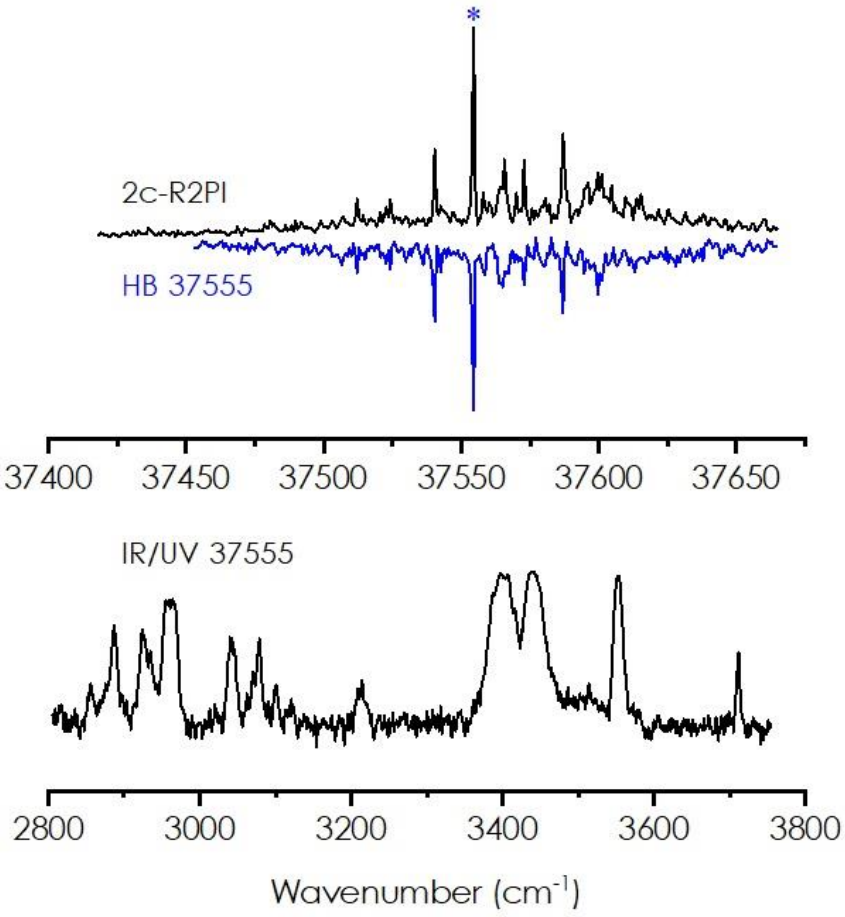

Figure 9.1: Upper trace: two-color REMPI spectrum of $PEAL_2+W_1$, compared to the UV/UV Hole Burning spectrum, obtained setting the UV pump laser to 37555 cm^{-1}. Lower trace: IDIRS experimental spectrum of $PEAL_2+W_1$, obtained at 37555 cm^{-1}.

Figure 9.1 shows the REMPI spectrum for $PEAL_2+W_1$. As can be observed, it presents some well resolved vibronic transitions, which become broader as the spectrum progresses to the blue. UV/UV Hole Burning double resonance experiments revealed the presence of a single conformation. This was further confirmed by IR/UV experiments, in which a single IR trace was obtained. As can be seen, the IR spectrum is similar to that reported for PEAL dimer, but with two additional OH stretches corresponding to the additional water molecule.

Despite computational work is still in progress, some qualitative analysis can be performed with the actual experimental data. There is a single OH band around 3700 cm^{-1}, which may correspond to the free anti-symmetric mode of water. This already indicates that water is inserted as a single donor, and those arrangements where water is in a bridged position can be discarded.

The band at ~3580 cm^{-1} would correspond to an OH···π HB type, similar to the ones observed in BnzA and PEAL complexes in Chapter 3. Finally, two bands are clearly visible around 3410 cm^{-1}, that are in good agreement with the presence of two strong OH···O HBs: one corresponding to the interaction between PEAL molecules, and the other one coming from the water attached to one PEAL molecule. Thus, we can speculate about a possible conformation with an OH···OH···OH···π HB network. However, further comparison with computational predictions is necessary in order to assign the complex, as there can be other conformational arrangements, like cyclic structures, previously reported in similar microhydrated alcohol dimers.[1,2]

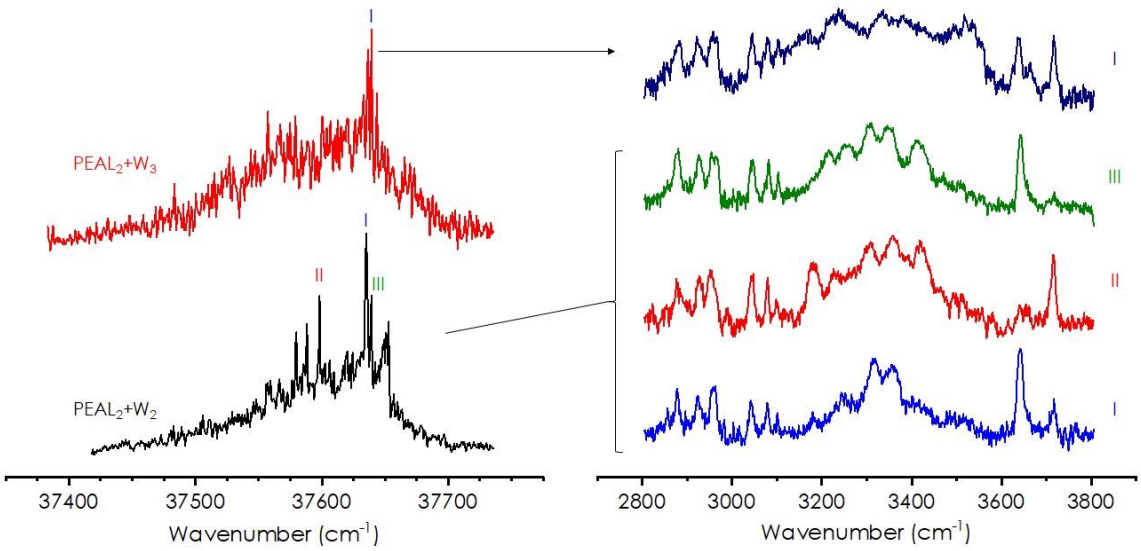

Figure 9.2: Left: Two-color REMPI spectra of $PEAL_2+W_2$ and $PEAL_2+W_3$ complexes. Right: IDIR spectra of $PEAL_2+W_2$ and $PEAL_2+W_3$ complexes. Different excitation wavelengths were proved for $PEAL_2+W_2$, in order to find different conformations.

Figure 9.2 collects the experimental results obtained for PEAL dimer with two and three water molecules. Compared to the monohydrated complex, the REMPI spectra are significantly broader. Regarding to the IR spectra, we also observed additional bands in the OH stretching region, compared to the spectrum in Figure 9.1. It is interesting that in $PEAL_2+W_2$ complex, different IR traces were obtained when changing the excitation wavelength, specially revealing are the intensity changes in the OH stretches between 3600-3700 cm^{-1}. However, the spectral region corresponding to the bonded OH bands is substantially congested, especially in the $PEAL_2+W_3$ complex. In this case, comparison with theoretical predictions is mandatory in order to offer a preliminary assignment of the systems.

9.2.2. Sugar-Aromatic complexes

The initial exploration of the interaction potential energy surface of sugars was extended also to different monosaccharides. This is the case of some experiments with α/β-MeGal and phenol complexes. The aim of these studies is to characterize the HB modulation by the structural changes in C_4, and to compare the obtained data with previous results on MeGlc+Ph anf PhGlc+Ph complexes.

Figures 9.3 and 9.4 show the experimental spectra obtained for α-MeGal+Ph and β-MeGal+Ph aggregates respectively. The predicted spectra for the preliminary computational exploration are also presented. These structures present the phenol ring acting as a HB donor to O6H and O2H groups of the galactose molecules. Additional CH···π interaction between the methyl group of the sugar and phenol might stabilize the final structure.

As can be observed, the predictions for the two conformations shown in each aggregate are in good agreement with the experimental spectra. However, computational results are preliminary, as many families with different HBs are very close in energy. Further work is needed to accurately define the subtle balance between HBs and stacking interactions, in order to characterize the interaction preferences of galactose.

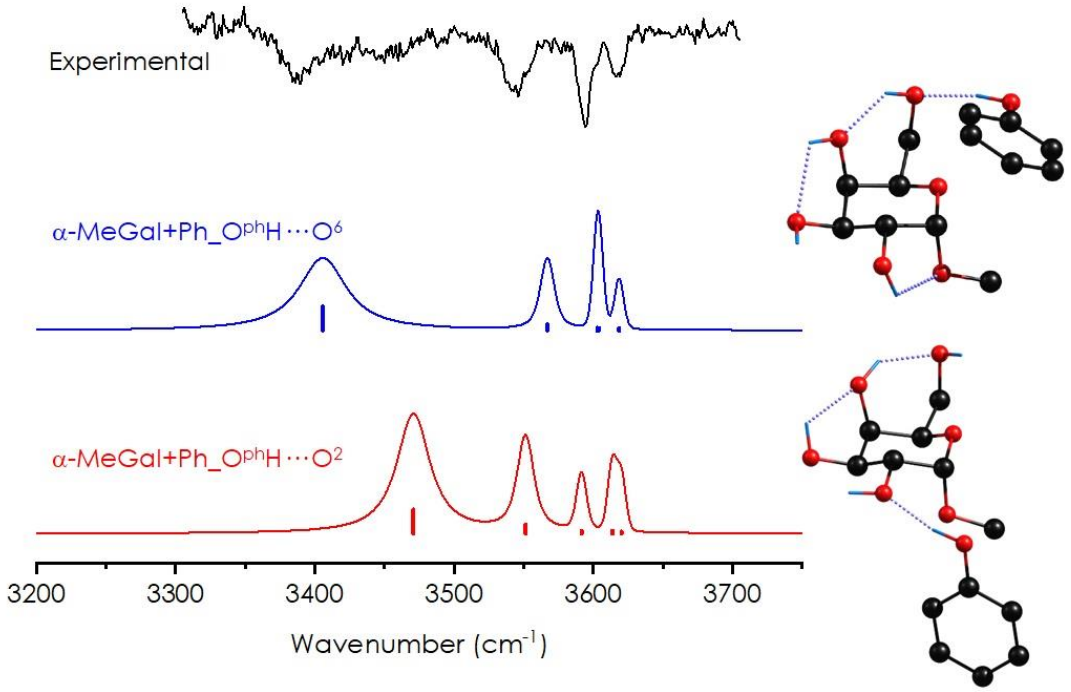

Figure 9.3: IDIR spectrum of α-MeGal+Ph complex, compared to the preliminary results from the computational exploration, at M06-2X/6-311++G(d,p) level.

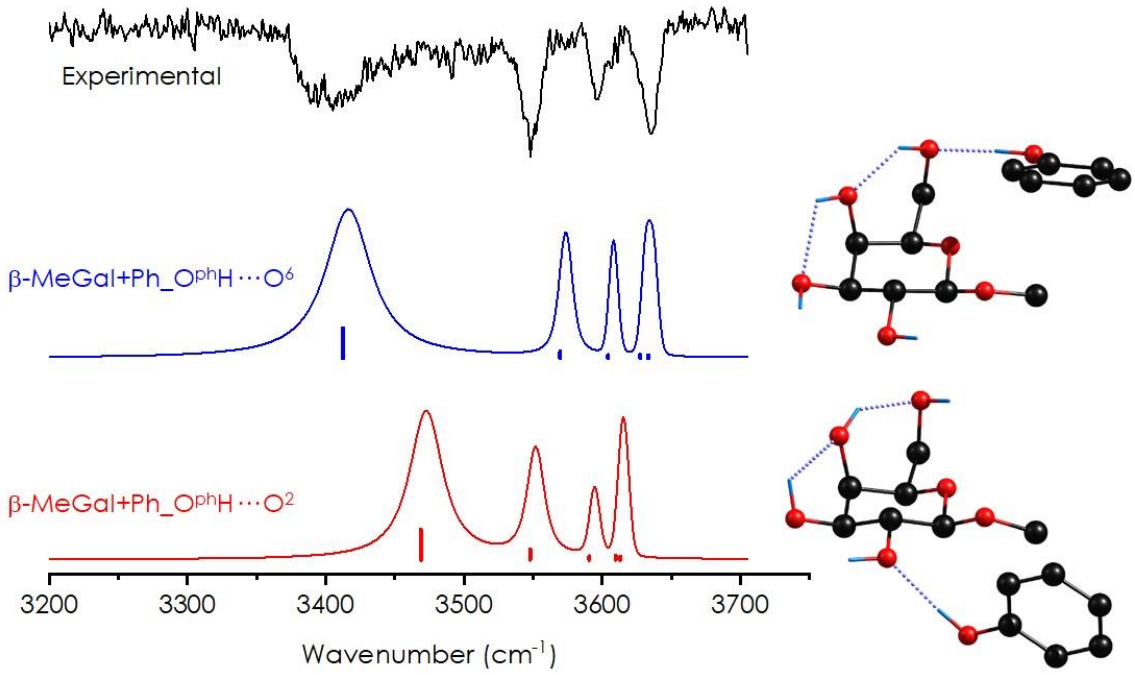

Figure 9.4: IDIR spectrum of β-MeGal+Ph complex, compared to the preliminary results from the computational exploration, at M06-2X/6-311++G(d,p) level.

Dispersive interactions, mainly CH···π interactions, between sugars and aromatic compounds are of great interest, as they play an important role in recognition processes, such as in lectin-sugar or protein-glycolipid systems.[3] Following these studies, we combined the flexibility of phenyl-β,D-glucopyranoside with adenine, in a kind of flexible-rigid nucleation. Figure 9.5 collects the absorption and IR spectra obtained for PhGlc+A complex. Different excitation wavelengths were probed in order to find all possible conformations. However, it seems that the obtained IR traces are very similar. Computational work is still needed in order to assign this complex, as both PhGlc and A molecules present multiple functional groups that could act as binding points.

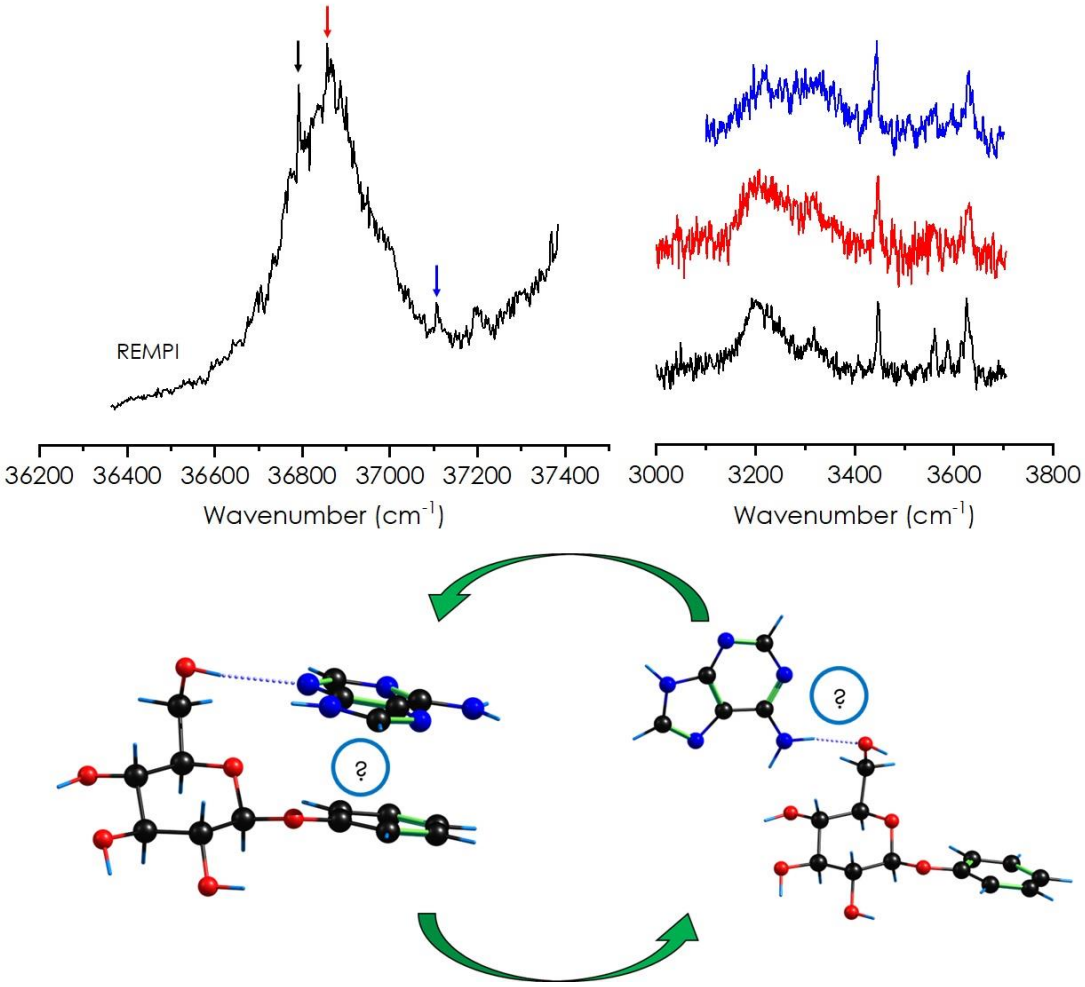

Figure 9.5: Left: One-color REMPI spectrum of PhGlc+A complex. Right: IDIR spectra of PhGlc+A complex, obtained at different excitation wavelengths. The color of the traces match those of the arrows, indicating the origin of each spectrum. Bottom: Representative scheme of the possible interactions between PhGlc and A molecules. Further computational work is needed in order to characterize the most stable conformation.

9.2.3. Microhydrated peptides

In order to characterize non-covalent interactions in different biological building blocks, we also explored the spectroscopy of peptides and its hydrated clusters. Water-peptide interactions are of great, since they play an important role in the final peptide structure and function. We started by exploring aspartame, which is the methyl ester of a dipeptide formed by aspartic acid and phenylalanine. As phenylalanine contains an aromatic ring that acts as a chromophore, we were able to use laser spectroscopy to explore it. Figure 9.6 collects the REMPI spectra obtained for aspartame and its mono- and di-hydrated complexes. As can be observed, most of the vibronic activity of

aspartame is concentrated in a narrow spectra region, which presents several discrete transitions. Interestingly, absorptions in the water complexes are close to those of the monomer.

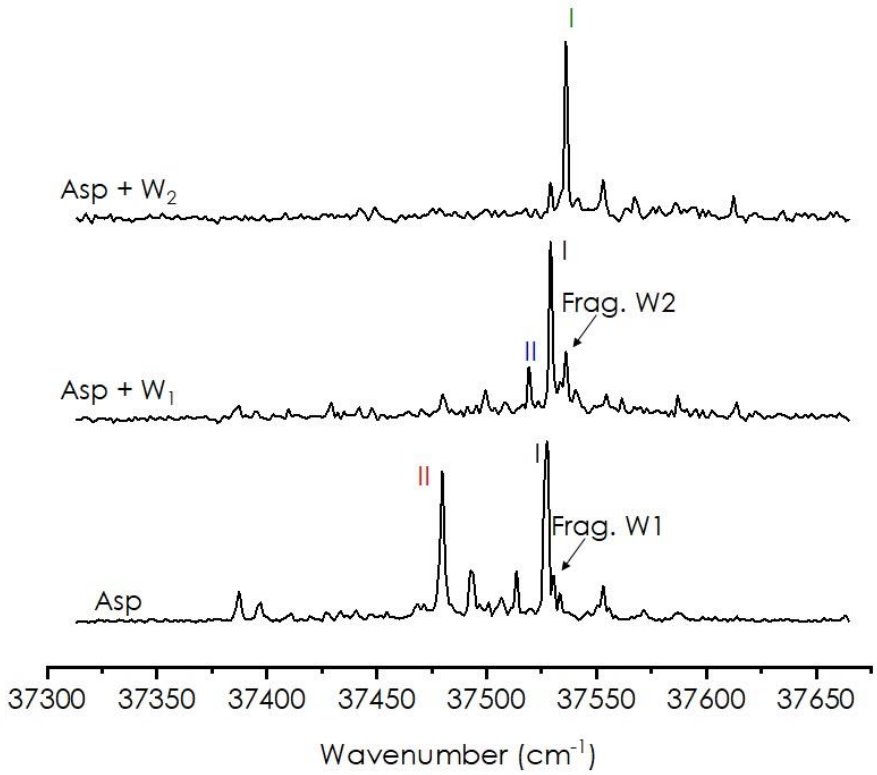

Figure 9.6: One color REMPI spectra of aspartame and its microhydrated complexes. Roman number mark the transitions probed to obtain IDIR spectra.

Roman numbers in Figure 9.6 mark the different excitation wavelenghts probed in order to find different conformations. Figure 9.7 shows the two IDIR spectra obtained for aspartame, compared to the best match from a preliminary computational exploration. As can be observed, there is a shift in the absorption bands around 3400 cm^{-1}. That could indicate that both isomers present similar structures.

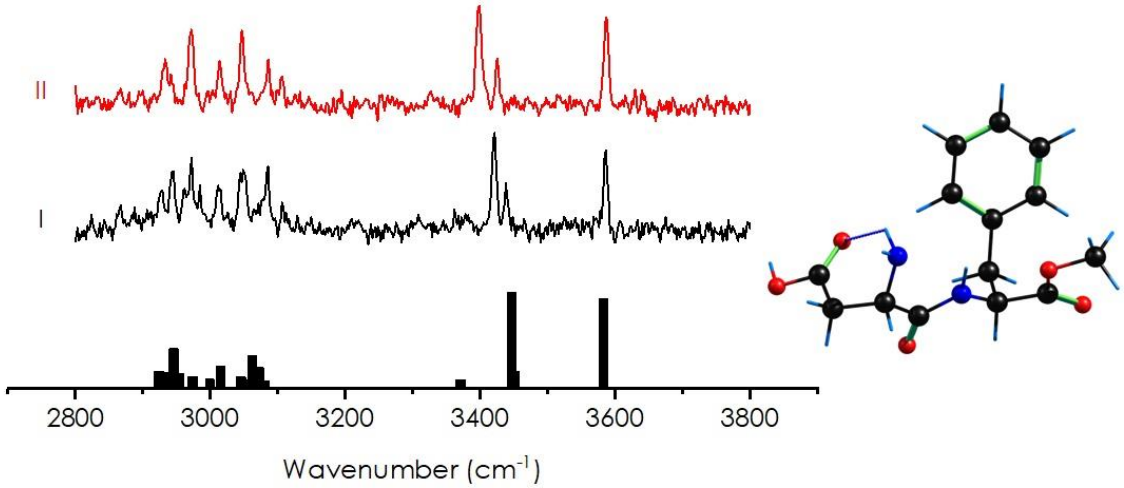

Figure 9.7: IDIR spectra of aspartame, compared to predictions from a preliminary computational exploration at B3LYP-ED=GD3BJ/def2TZVP level.

Figure 9.8 collects the IDIR spectra obtained for aspartame-water complexes. For Asp+W_1, two very different IR spectra were obtained, pointing to a different water-insertion structures in the cluster. However, for Asp+W_2, a single IR spectra was obtained. Further computational exploration and comparison with experimental data is needed in order to offer an assignment for these complexes.

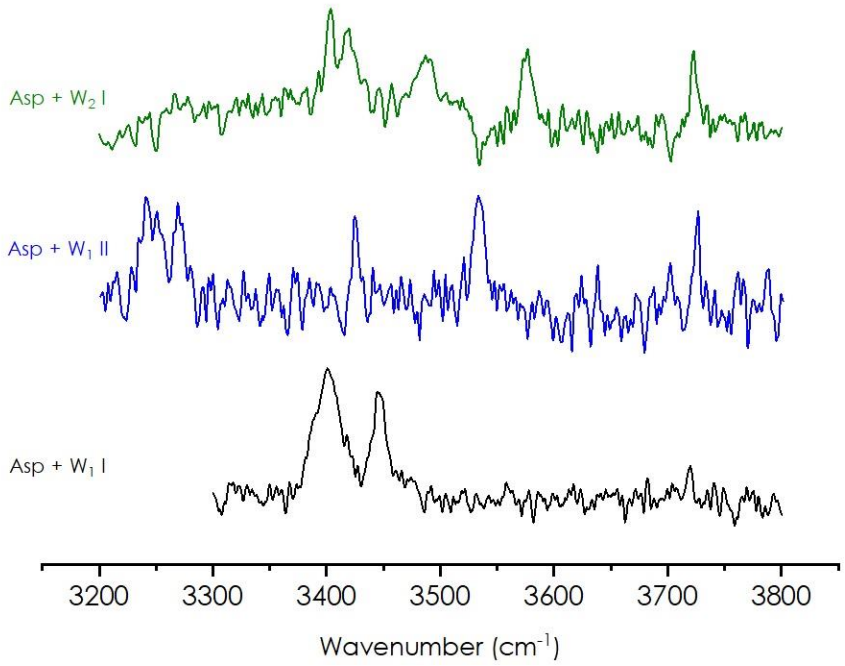

Figure 9.8: IDIR spectra of Aspartame+W_1 and Aspartame+W_2 complexes.

9.2.4. Xanthine + DNA-base aggregates

Continuing with the xanthine-DNA base aggregates studied in Chapter 8, we explored the interactions inside the dimer formed by theophylline (TP) and cytosine (C). This complex is quite interesting, as some studies revealed that theophylline is specifically recognized by a RNA aptamer.[4,5] In such complex, there is a preference for theophylline to form interactions with cytosine and uracil bases. Here, we explored the theophylline-cytosine interaction in an environment free of external perturbations. Figure 9.9 shows the IDIR spectra obtained for TP+C, compared to the predictions for the most stable structures. This preliminary comparison allowed us to identify the most stable interactions formed in this dimer, that match with those observed in the complex between TP and the RNA aptamer.

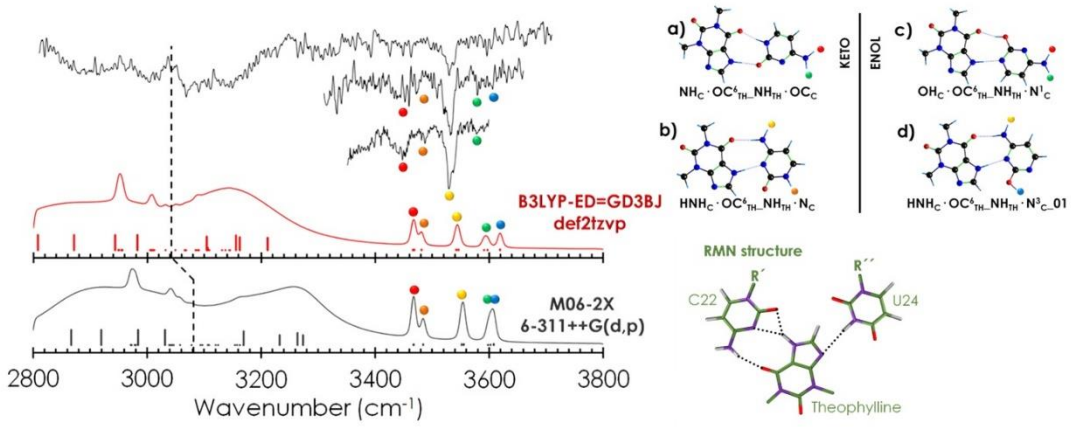

Figure 9.9: IDIR spectra of TP+C dimer compared to the predictions for the most stable structures. The theoretical spectra are a combolution of the four most stable isomers.

Additional methylxanthine-DNA base complexes were explored. Continuing with the studies in the interaction preferences of theobromine (TB), dimers with cytosine and guanine (G) were explored in supersonic expansions. Figure 9.10 shows the preliminary experimental data obtained for TB+C and TB+1MeC. Different IR traces were obtained in for TB+C, in which the only difference is the shape of the broad absorption around 3150 cm^{-1}. The spectrum for the complex with 1-methylcytosine (1MeC), the S/N ratio is lower due to the low signal of the complex. Extensive computational explorations are needed to assign these complexes, as different tautomeric forms of cytosine could coexist in the jet.

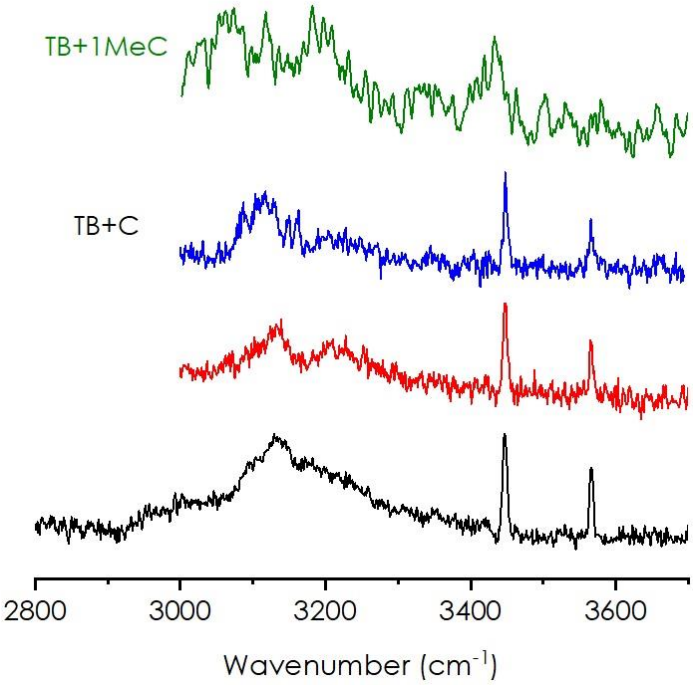

Figure 9.10: IDIR spectra of TB+C, probed at different excitation wavelengths (black, red and blue traces), and TB+1MeC (green trace).

Similar experiments were done over the TB+G dimer. As can be observed in Figure 9.11, the IDIR spectrum obtained for the dimer is very congested, with multiple free and bounded NH/OH stretches. Once more, different tautomeric forms of G complicate the experimental assignment, and further experimental results or computational studies are needed.

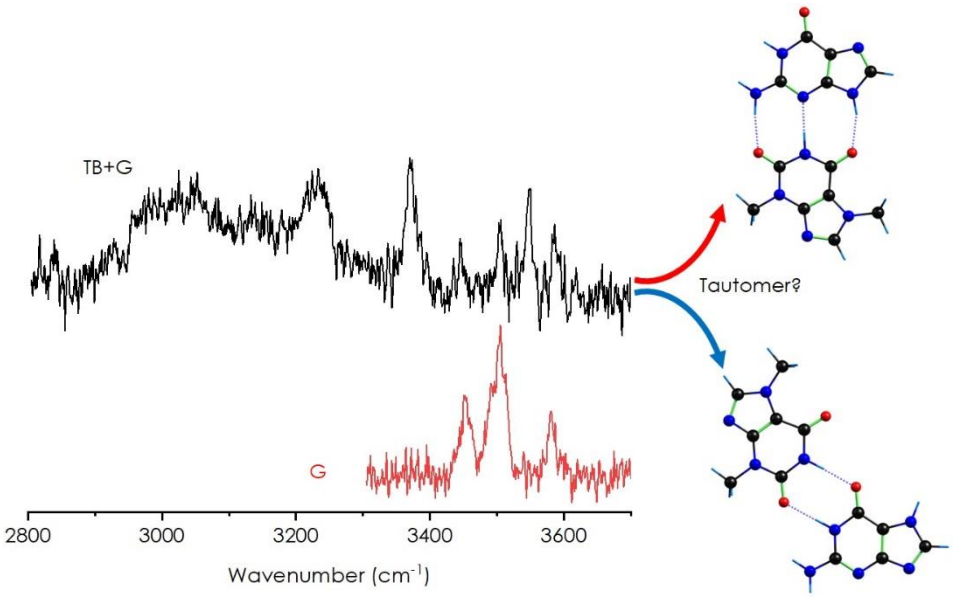

Figure 9.11: IDIR spectrum of TB+G dimer, compared to the experimental IR spectra of G monomer.

9.2.5. Nucleotide aggregates

Finally, increasing the level of complexity of previous aggregates, we started some studies about non-covalent interactions in nucleotide complexes. Characterizing NCI preferences in these type of compounds is intriguing, as they present multiple interactions sites in both sugar and nucleobase moieties. We started the spectroscopic exploration of these biologically relevant compounds with 2-deoxyadenosine. Experiments were not easy to carry, as due to the cluster size, low signals were obtained in the complexes here presented. Figure 9.12 presents the single IR spectrum obtained for 2-deoxyadenosine dimer. As can be observed, some weak absorptions appear in the free OH and NH stretching regions, followed by two strong and broader absorptions that would probably come from the formation of hydrogen bonds. Preliminary simulations for the most stable conformations are in good agreement with the overall experimental spectra. Such conformations show an interesting stacking between adenine bases, while the amino groups of them are interacting with the OH groups of the neighbor nucleotide. These stacked arrangements are different from those observed in previous adenosine complexes in isolated phase.[6]

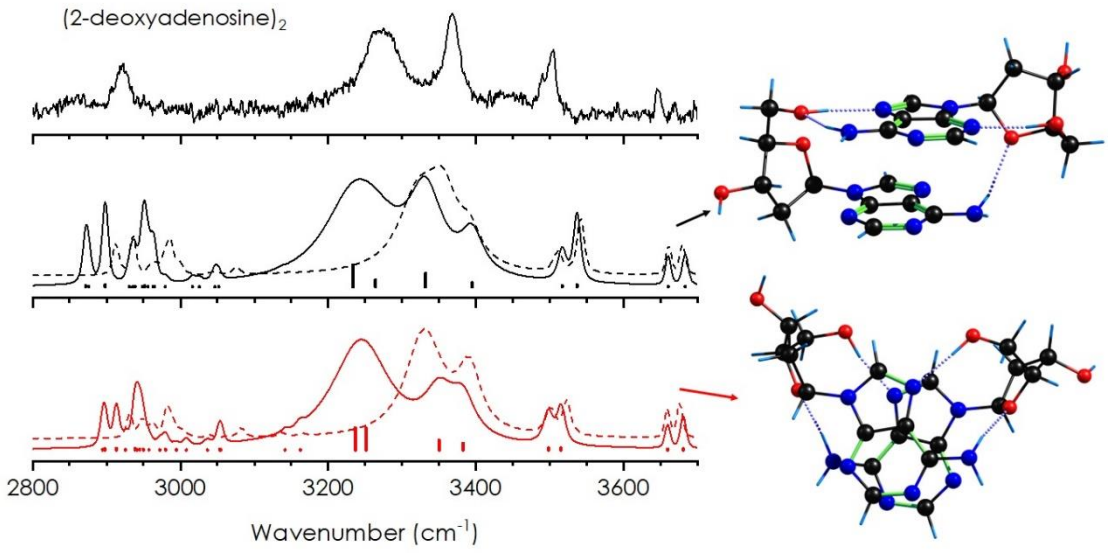

Figure 9.12: IDIR spectrum of 2-deoxyadenosine dimer, compared to the computational predictions for the most stable conformations. Dashed trace correspond to the predictions at M06-2X/6-311++G(d,p) level, whereas the filled trace correspond to the predictions at B3LYP-ED=GD3BJ/def2TZVP level.

Pushing the experimental conditions to its limit, we were able to measure the IDIR spectra of 2-deoxyadenosine+TB and 2-deoxyadenosine+β-PhGlc dimers. Compared to the previously observed 2-deoxyadenosine dimer, the IR spectra are more crowded. Further computational work is needed in order to offer an assignment of such

complexes. 2-deoxyadenosine+TB dimer is of special interest, as it can be considered as a continuation of the TB+A complex previously shown in Chapter 8.

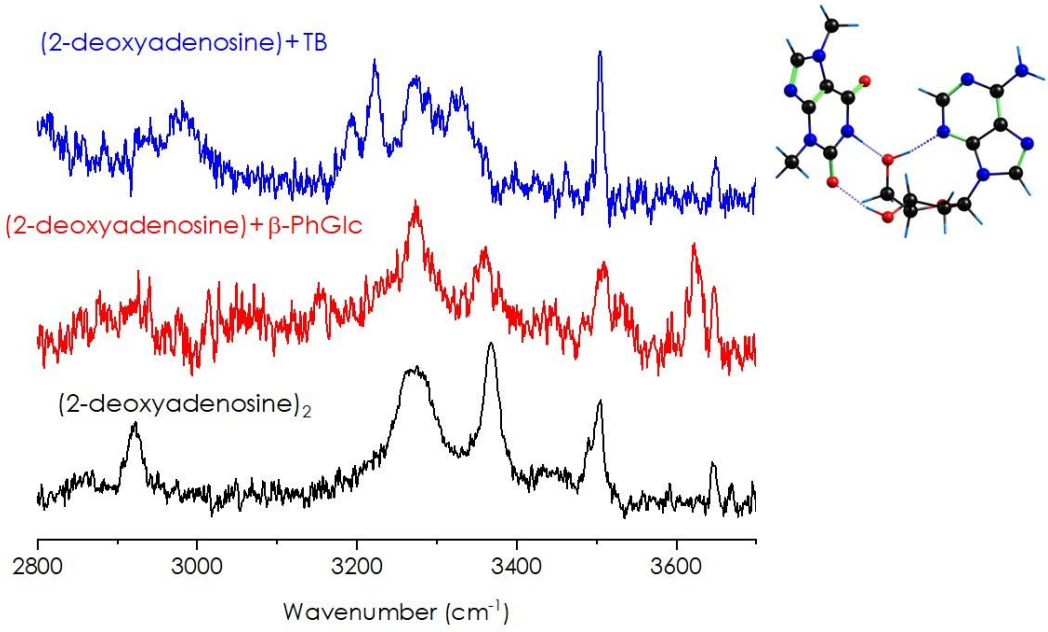

Figure 9.13: IDIR spectra of 2-deoxyadenosine+β-PhGlc and 2-deoxyadenosine+TB, compared to the IR spectrum obtained for 2-deoxyadenosine dimer.

9.3. References

[1] I. León, J. Millán, E. J. Cocinero, A. Lesarri and J. A. Fernández, Transition from Planar to Nonplanar Hydrogen Bond Networks in the Solvation of Aromatic Dimers: Propofol2-(H2O)2–4, *J. Phys. Chem. A*, 2013, **117**, 3396–3404.

[2] I. León, J. Millán, F. Castaño and J. A. Fernández, A Spectroscopic and Computational Study of Propofol Dimers and Their Hydrated Clusters, *ChemPhysChem*, 2012, **13**, 3819–3826.

[3] M. Maresca, A. Derghal, C. Carravagna, S. Dudin and J. Fantini, Controlled aggregation of adenine by sugars: physicochemical studies, molecular modelling simulations of sugar–aromatic CH–π stacking interactions, and biological significance, *Phys. Chem. Chem. Phys.*, 2008, **10**, 2792–2800.

[4] G. R. Zimmermann, R. D. Jenison, C. L. Wick, J.-P. Simorre and A. Pardi, Interlocking structural motifs mediate molecular discrimination by a theophylline-binding RNA, *Nat. Struct. Biol.*, 1997, **4**, 644–649.

[5] P. C. Anderson and S. Mecozzi, Unusually short RNA sequences: Design of a 13-mer RNA that selectively binds and recognizes theophylline, *J. Am. Chem. Soc.*, 2005, **127**, 5290–5291.

[6] H. Asami, K. Yagi, M. Ohba, S. Urashima and H. Saigusa, Stacked base-pair structures of adenine nucleosides stabilized by the formation of hydrogen-bonding network involving the two sugar groups, *Chem. Phys.*, 2013, **419**, 84–89.

eman ta zabal zazu
Universidad del País Vasco
Euskal Herriko Unibertsitatea
FACULTY OF SCIENCE AND TECHNOLOGY
UNIVERSITY OF THE BASQUE COUNTRY

Agregatu molekularren laser-karakterizazio espektroskopikoa

Doktoretza-tesia

Ander Camiruaga Leza

Zuzendariak:

Dr. José Andrés Fernández González

Dr. Imanol Usabiaga Gutierrez

Kimika Fisikoa Saila

Leioa, 2021

Ander Camiruaga-k Eusko Jaurlaritzak ikertzaileak prestatzeko doktoretza laguntza izan zuen. Ikerketa hau Espainiako Ekonomia eta Lehiakortasun Ministerioak (CTQ2015-68148-C2-1-P eta PGC2018-098561-B-C21) eta Eusko Jaurlaritzako Ekonomiaren Garapen eta Lehiakortasun sailak (IT1162-19) finantziatu zuten. Eskerrak ere SGIker (UPV/EHU) Laser eta Konputazio zerbitzuei.

Aurkibidea

Tesi honen eranskina formatu elektronikoan dago eskuragarri. Irakurleak online aurkitu dezake pdf gisa, hurrengo web estekan:

https://drive.google.com/file/d/1acMd16fyx4VlehX6Op6tQWatLANTkL0x/view?usp=sharing

1. Kapitulua

Sarrera

1.1. Sarrera

Kimikaren arlorik liluragarrienetako bat, elkarrekintza intermolekularren eta sistema supramolekularren egitura aztertzea da. Elkarrekintza ez-kobalenteek (*Non-Covalent Interaction*, NCI) naturan nonahikoak dira eta prozesu kimiko, industrial eta biologiko ugari gobernatzen dute, molekula-agregatu txikiak eratzetik eskala-handiko fenomeno fisiko supramolekularretara arte, hala nola, aerosolen sorkuntza, proteinen tolestura, ligatze-prozedurak edo seinale-ezagutza.[1] Elkarrekintza intra- eta intermolekular hauen natura guztiz kuantikoa da, hau da, horiek auzoko molekulen hodei elektronikoen arteko elkarreraginetik sortzen dira, elektroien korrelazio dinamikoan deritzon prozesu batean.[2-4] Sarritan, elkarrekintza horiek van der Waals (vdW) elkarrekintzetan (elektrostatikoak, dispertsio eta dipolo-dipolo) eta hidrogeno-loturetan sailkatzen dira. Lotura kobalentearekin alderatuz, talde atomiko desberdinen konbinazio posibleen aniztasun handiak eta muga energetiko eta estrukturalak NCI-ei lengoaia espezializatu bat sortzeko aukera ematen dio. Lengoaia hori agregazio molekularra gobernatzen du.[5] Sistema biologikoen agregazioan funtsezko papera jokatzen duten propietate batzuk, esate baterako, alboko molekulak "sentitzeko" eta denbora-eskala laburretan disoziatu daitezkeen lotura-ahulak sortzeko gaitasuna dira.

Aipatu ditugun NCI-ren artean, hidrogeno-loturek (*Hydrogen Bond*, HB) azpimagarrienak dira. Lotura mota hori buruz makina bat ikerketa dago , baina denak bizitzarako ezinbestekoa delakoan bat datoz, elkarrekintza intermolekularrak modulatzen dutelako: uraren egitura likidoaren eta solidoaren arduraduna da, baina, aldi berean, biokimikaren seinale-ezagutza prozesu konplexuak kontrolatzen ditu. Hortaz, ez da harritzekoa hidrogeno loturaren karakterizazioak interes zientifiko handia erakarri izana, bere ikerketarako prozedura esperimental eta konputazional sofistikatuak garatuz.

Azken hamarkadetako ikerketa esperimental eta teorikoen emaitzak Pauling-ek[6] eta Pimentel eta McCleallan-ek[7] sortutako hidrogeno loturaren formazioari buruzko kontzeptu klasikoaren definizio berri bat izatea iradokitzen zuten IUPAC-ren aldetik., Halaber, definio hori O, N edo S desberdinak diren beste atomo elektronegatiboen elkarrekintzak barneratu behar ditu:[8]

"*Hidrogeno lotura, lotura baten eraketaren frogaren bat dagoen, X-H motako molekula edo fragmentu molekular bateko eta molekula berdineko edo desberdineko atomo baten edo atomo batzuen arteko elkarrekintza erakargarri bat da non X hidrogenoa baino elektronegatiboagoa den atomo bat den.*"

Elkarrekintza honen izen hidrogeno atomo bat talde emaile eta hartzaileen artean partekatzetik dator. Tradizionalki, hidrogeno lotura X-H···Y bezala irudikatzen da, non X eta Y atomo elektronegatiboak diren. Ikuspuntu kuantiko batetik, Y atomoaren dentsitate elektronikoaren zati bat X-H taldearen orbital ez-lotzaileetara igarotzen da. Gainezarpen orbital horrek hidrogeno loturari nolabaiteko izaera kobalentea ematen dio, eta indar handia, bereziki.

O eta N atomoak dituzten hidrogeno loturak (O-H···O, O-H···N, N-H···O edo N-H···N) interesgarrienetakoak dira, naturan duten funtsezko jardueragatik. Van der Waals indarrekin batera, hidrogeno loturak makromolekula biologikoen egonkortasunean eta solbatazioan oinarrizkoak dira, hala nola DNA-n, RNA-n eta proteinetan.

Hala eta guztiz ere, elkarrekintza kobalenteekin alderatura, NCI-en izaera eta modulu ahula kontuan hartuz gero, ez da harritzekoa haien karakterizazioa lan konplexua dela. Haien ikerketa giro tenperaturan zaila da, disoziatzeko joera baitute eta soilik elkarrekintza sendoenak biziraun dezakete. Horrez gain, solbatazioa elkarrekintza horiek estali dezake, dinamikoa den eta etengabe aldatzen den ingurugiroa sortuz.[9] Hau guztia kontuan hartuta, NCI-en azterketa metodo esperimentalentzat zein teorikoentzat erronka bat da.[10-14]

Deskribapen molekular argi bat egiteko gai diren teknika esperimental ugari ez daude. Horregatik, gero eta interes handiagoa dago NCI-en bitartez lotutako sistema molekularren kalitate handiko datuak ematen dituzten metodologia esperimentalen eta teorikoen garapenean. Hasiera batean, kristal egituren X-izpien difrakzioak sortutako datu esperimentalak erreferentzia gisa erabili ziren. Alabaina, kristal sareek NCI-etan sortutako perturbazioak direla eta, egituren azterketa zuzena ekiditzen zuten. Teknika berrien sorpenarekin, eta erradiazio iturrien bereizmenean egindako aurrerapenei esker, teknika espektroskopikoak, batez ere, gas egoeran burutzen direnak, molekulen agregatuen egiturari buruzko datu esperimentalak emateko aukera sendoa bilakatu ziren.[15] Zehazki, 1980-ko hamarkadan, azterketa espektroskopikoak espantsio supersonikoetan erabateko iraultza izan ziren.[14,16-23] Espantsio supersonikoak usaian sortzen dira pultsuzko balbula batekin, zeinak gas nahaste bat zirrikitu estu batetik injektatzen duena huts handiko ganbara baten barruan. Bi aldeen arteko presio desberdintasun handia dela eta, espantsio adiabatiko bat sortzen da, zeinaren barruan molekulen barne energia errotazional eta bibrazionala energia translazionalean transferitzen dena gasa garraiatzailearekiko talkei esker.[19,24,25] Modu honetan, espantsioak dentsitate altuko izpi molekular "hotz" bat sortzen du, non molekulek guztiz

isolatuta bidaiatzen duten (kanpoko perturbaziorik gabe). Gainera, espantsio supersonikoak eskainitako giroak aztertzen ari den sistemaren espektroskopia ere sinplifikatu egiten du. Izan ere, banden zabalera eta pilaketa espektrala murrizten dira populazio baxuko energia-maila errotazionalei eta bibrazionalei esker. Hortaz, espantsioek sortutako baldintza bikainak hainbat teknika espektroskopikoekin konbinatuak izatea ahalbidetzen dute, hala nola, espektroskopia elektronikoa, bibrazionala edo errotazionala, besteak beste.[20,21,23,26-28]

Proiektu honetan, espantsio supersonikoak masan bereizgarriak diren laser espektroskopia teknikekin konbinatu egin dira, espantsioetan sortutako molekula agregatuen informazio elektroniko eta bibrazionala eskuratu ahal izateko. Are gehiago, masan bereizgarria den detekzioak tamaina desberdineko molekula agregatuen azterketa izugarri errazten du, nahi ez diren interferentziak saihesten direlako. Hala ere, isolatutako konposatuen ikerketa espektroskopikoen aurrerapen nagusienetariko bat laser desortzio sistemen barnerapena izan zen. Erraminta horrek molekula termolabilen desortzioa ahalbidetzen du, zeinak momentuan narrastuak izan ahal diren zabaltzen den gasean.[29-34] Tesi honetan, laser desortzio sistemak dituzten sistema esperimental konplexuak erabili dira (ikusi deskribapen zehatzago bat 2 Kapituluan) tenperatura altuetan degradazio termikoa pairatzen dituzten molekulen ikerketa burutzeko, hala nola, karbohidratoak, edota bapore-presio txikia duten konposatu biologiko garrantzitsuak, DNA nukleobaseen moduan.

Molekula agregatuak edukitzen duen eta espantsio supersoniko batean sortutako izpi molekularra ionizazio ganbara batera bideratzen da, non kitzikatu eta ionizatu egiten den erresonantziaren bidezko ionizazio multifotonikoari esker (*Resonance Enhanced Multiphoton Ionization,* REMPI). Ondoren, eremu elektrikoak erabilita, sortutako ioiak hegaldi-denbora (*Time of Flight,* TOF) masa espektrometro batera bideratzen dira. REMPI teknika infragorri (IR) laserrekin konbinatu daiteke (erresonantzia bikoitzeko IR/UV teknikak sortuz) ikertu nahi diren molekulen/molekula agregatuen IR espektroa lortzeko. Tesi honetan zehar, 2800-4000 cm^{-1} tarteko eremu espektrala luze aztertu da, hau da, egiturei buruzko informazio interesgarria eskuratzen da, NH/OH taldeek tarte horretan ingurumenarekiko duten sentsibilitatearen ondorioz. Lehen aipatu den moduan, talde atomiko horiek hidrogeno loturak sortzeko joera aurkezten dute. Elkarrekintza horiek sortutako perturbazioak luzaketa-bibrazio moduetan banden posizioaren lerrakuntza gisa agertzen dira. Azken lerrakuntza horretatik sortutako elkarrekintza intra- edo intermolekularrari buruzko informazioa lortu daiteke, hala nola, elkarrekintzaren indarra.

Espantsio supersonikoetan teknika espektroskopikoak erabiltzearen beste abantaila bat espektroak kimika konputazionaletik lortutako datuekin zuzenean aldera daitekeela da. Normalean, REMPI edo IR/UV laser espektroskopia tekniketatik lortutako informazioa ulertzeko zaila da. Sarritan, interpretazio horren zailtasuna molekula edo molekula agregatuen flexibilitatearekin guztiz erlazionatuta dago. Sistema molekular txikietan, edo flexibilitate baxuko sistemetan, egonkorrak diren isomero konformazionalen kopurua txikiagoa da, eta ondorioz, banda espektralen esleipena simulazio konputazionalekin alderatuz buru daiteke.

Hala ere, sistemaren tamaina hazi ahala, konformero posibleen kopurua ere bai handitzen da. Gertaera horrek espektro esperimentalaren interpretazioa zaila egiten du, zeinak familia konformazional bat baino gehiagoren kontribuzioak izan dezake, trantsizio bibrazionalen pilaketa bat aurkeztuz. Kasu horietan, energia-baxuko konformero posible guztien esplorazio konputazionala beharrezkoa da, datu esperimentalen interpretazio zuzena ahalbidetzeko.[35-41]

Elkarrekintza intermolekularrak karakterizatzeko estrategietako bat, txikiak eta sinpleak diren molekula multzotan aztertzea da (masa bereizmenarekin), aldez aurretik aukeratutako talde kimiko kopuru murriztua aurkezten dutelarik. Esate baterako, ur-agregatuen ikerketak biologikoki esanguratsua den O-H···O elkarrekintza finki karakterizatzeko aukera ematen du, kanpoko asaldurarik ezean, ur dekameroarekin bereziki ilustratu den moduan.[42,43] Talde kimiko gehigarriak sartzeak O-H···O hidrogeno lotura modulatzeko aukera ematen du. Bide hau jarraituz, O-H···O elkarrekintzaren karakterizazioa konplexutasun gero eta handiagoa duten sistemei esker burutu da, alkohol alifatiko[41,44-49] eta aromatikoetan,[50-55] batez ere. Alkohol agregatuetan eraztun aromatiko bat sartzeak bere panorama konformazionala erabat aldatzen du. Eraztunaren dentsitate elektroniko handiak elkarrekintza berrien sorpena ahalbidetzen du, hala nola, C-H···π, O-H···π edo π···π motako elkarrekintzak. Azken horiek interes handikoak dira, izan ere, eskala handiko edo agregazio makromolekularra baldintzatzen dutelako. Eraztun aromatikoek kromoforoak direnez gero, espektroskopia elektronikoaren erabilpena ahalbidetzen dute. Lehen aipatu egin den moduan, espektroskopia elektronikoaren abantaila masan bereizgarriak diren erresonantzia bikoitzeko teknikak erabiltzeko aukera ematen duena da, zeinak ikertzen ari diren espezieen kontrola hobetzen duten. Batek kontuan hartu behar du agregatuen espektroak tarte espektral berean agertzen direla, izan ere, agregatuak monomeroaren elkarrekintzaren baino perturbazio bat baino ez dira.

Tesi honen helburua sistema supramolekular desberdinen azterketa egitea da, masan bereizgarria den kitzikapen espektroskopiaren (*Mass Resolved Excitation Spectroscopy*, MRES) eta kimika kuantikoaren arteko konbinazioa erabiliz, molekulen agregazioaren mekanismoei buruzko egungo ezagutza areagotzeko.

Agregazio molekularrean ematen diren indar dispertsiboen eta OH···O motako hidrogeno loturen arteko elkarrekintzak aztertzeko, tesi honek, alkohol aromatiko ereduen agregazio lehentasunak ikertzeko 3.Kapitulua eskaintzen du.

Lehen aipatu den bezala, NCI-ak bereziki erabakigarriak dira organismo bizidunentzat. Milioika urteko eboluzioaren ondoren, molekulek hautapen-prozesu konplexu bat jasan dute, izaki bizidunen metabolismoan gertatzen diren rol espezializatuak antzezteko egokienak diren espezieak aukeratzeko. Horixe da sakaridoen kasua. Molekula hauek organismo fotosintetikoek sortzen dituzte batez ere, energia biltegiratzeko modu gisa.[56] Hala eta guztiz ere, zelulen metabolismoan jokatzen duten papera askoz haratago doa.[57,58] DNAn, kitinan edo zelulosan egitura-blokeak dira, baina immunitate-sistemaren parte ere baitira.[59-63] Adibidez, gluzidoak proteinetara eta lipidoetara lotutako polisakaridoak dira, mintz zelularraren kanpo aldean kokatzen direnak. Sistema immunologikoko zelulek gluzido horiek galdeketa egiteko errezeptore espezializatuak dituzte. Hortaz, gluzidoak antzeman daitekeen monosakarido sekuentzia faltan duenean, erantzun immunologiko bat ematen da.[60-63]

Sakaridoen flexibilitate altuak ingurumenari eraginkortasunez egokitzeko aukera ematen dio, baita helburu-hartzailearekiko elkarrekintza optimizatzeko ere, selektibitate altuko ezagutza prozesua sortuz. Izan ere, gluzidoen errezeptoreak ez daude soilik sekuentzia batean sakarido unitateak detektatzeko diseinatuta, baizik eta, haien adarkadurak eta elkarrekintza intermolekularrak detektatzeko gai dira.[64] Gluzido errezeptoreen selektibitatearen adibide bat odol taldeen kasuan aurki daiteke, non gluzidoaren azukre unitate baten hidroxilo talde baten orientazioaren aldaketak nahikoak dira errezeptorearekiko afinitatea aldatzeko.[65]

Prozesu horiek ulertzeko, elkarrekintza-mekanismoen ezaguera sakona beharrezkoa da, eskala molekularrean. Egoera likidoan, biomolekula horiek sor dezaketen elkarrekintza kopuru ia mugagabeak elkarrekintza ez-kobalenteen propietate intrintsekoen karakterizazioa izugarri zailtzen du. Bada literatura zabal bat azukreen lehentasun konformazionalari buruz, batez ere gas egoeran buruturiko espektroskopia errotazional[30,66] eta bibrazionalean.[37,67-71] Azken teknika honekin egindako ikerketek NCI-ak aztertzeko datu esperimental ugari sortu zituzten, tamaina handiko

biomolekulak edo molekulen konplexuak azter daitezke eta.[72,73] Tesi honen helburuetako bat azukre konplexuetan NCI-ak karakterizatzea da, MRES eta kimika konputazionalaren arteko konbinazioa erabilita. 4.Kapituluan, azukre deribatuen eta zenbait molekulen arteko elkarrekintzen miaketa zehatza aurkezten da. Bildutako datuek molekula hauen gaitasuna elkarrekintza anizkoitzak ezartzeko erakusten dute, haien hidroximetilo talde malguak egoera desberdinetan moldatzen dutelarik elkarrekintzen indarra maximizatzeko. Ikerketa horiek 5.Kapituluan jarraitzen dute O3 taldea gantz-azido batekin esterifikatuta duten bi monosakaridoen karakterizazioarekin.

Elkarrekintza ez-kobalenteak berebiziko garrantzia dute nukleobaseek jokatzen duten rol biologikoan. Zitosina (C), guanina (G), adenina (A) eta timina (T) DNAn aurkitzen diren lau baseak dira. Bi edo hiru hidrogeno loturen bitartez pareetan lotuta aurkitzen dira, zeinak kateak eratzen dituzte azukre-fosfato hezurdurarekin konbinatuz. Lau base horiek "bizitzaren alfabetoa" deritzona eratzen dute, haien sekuentzien ordena informazio genetikoa kodifikatzen duelako.[57] Gainera, nukleotidoek metabolismo zelularrean hainbat rol jokatzen dute kode genetiko ezagunaz gain, hala nola, ATP/ADP energia-txanponen osagarriak izatea,[74] edo GTP/GDP osatzea G-proteinei atxikitutako errezeptoreen (GPCR) metabolismoan.[75] Hori guztia dela eta, zientziaren galdera zirraragarrienetako bat DNAren jatorria eta konposizio kimikoaren arrazoia ulertzea da. Naturak "bizitzaren alfabetorako" CGAT baseen aukera oraindik irekia dagoen galdera da. Hitzarmen orokor bat dago base horiek fase desberdinetan gertaturiko presio ebolutiboaren ondorio direla.[76] Hala ere, antzeko egitura kimikoak dituzten metabolitoak zelulan elkarri bizitzen dira, zeinean DNA baseen antzeko rolak jo dezaketeen.

CGAT baseetara eboluzionatu duten hasierako molekulek gaur egungo nukleobaseekin desberdintasun nabariak izan zitezkeen, arrazoi askoren artean, jatorrizko baldintza fisiko-kimikoak oso desberdinak ziren gaur egungokoekin alderatuta. Aurkitutako harri zaharrenak 3.6 bilioi urte dute, eta jadanik organismo zelularren hondakinak zituzten. Horren arabera, bizitza gure planetaren lehen 400 milioi urteetan garatu zen.[77–79] Garai hartan, oxigeno askearen kantitatea mesprezagarria zen, eta ziur aski, atmosfera erreduzitzeko ahalmen txikia zuen.[80] Hasieran, metanoa atmosferan lurrazalaren hozketa prozesuen arabera kantitate txikietan edo handietan aurki zitekeen.[81] Denbora pasa ahala, atmosferak, batez ere, CO, CO_2, H_2O, H_2 eta N_2 eduki ditzake, baina amoniakorik ez. [76,82] Baldintza horietan, HCN-ren kondentsazioa eta H_2CO-ren presentzia lehen molekula prebiotikoen agerpena sustatu ahal izan dute.[83]

Kondentsazio horren ondorioz ez soilik CGAT baseak, baizik eta bestelako purina, pirimidina eta gainerako konposatu heteroziklikoak sortu dira.[84-86] Beharbada, egonkortasun kimikoak faktore bat izan zitekeen ingurumen horretan konposatu jakin batzuen aberastasuna sustatzeko. Hala eta guztiz ere, ikerketak purina eta pirimidina konposatuen erdi-bizitzan CGAT baseen hautaketak faktore erabakigarria ez zela (edo faktore erabakigarri bakarra, behintzat) frogatu zuten. Izan ere, badira zenbait konposatu, 2,6-diaminopurina edo 2,4-diaminopirimidina alegia, zeinek nukleobaseen antzeko egonkortasun kimikoa aurkezten duten.[87-89]

Argiaren irradiazioa hautaketa-faktore garrantzitsua izan liteke. Egile askoren arabera, atmosfera primitiboaren UV erradiazioarekiko iragazkortasuna gaur egungoa baino askoz altuagoa zen.[90] Hortaz, erradiazioak erreakzio sintetikoetan eta produktu egonkorren hautaketan lagundu ahal izan zuen. De Vries,[91] Crespo-Hernández,[92] eta Hobza-ren[93,94] ikerketak nukleobaseen egoera elektroniko kitzikatuen erdi-bizitza laburra frogatu zuten. Datu hori argiak sortutako hondapenaren babespen mekanismo gisa hartu da. Hala ere, beste konposatu prebiotiko batzuek ere erdi-bizitza oso laburrak aurkezten dute, nukleobaseena baino laburragoak, alegia. Esaterako, hipoxantinaren egoera kitzikatuaren erdi-bizitza 0.13 ps-koa da,[95] adeninaren (0.18 ps)[96] edo guaninaren (0.16 ps)[97] balioetatik hurbil dagoena.

Naturak zergatik aukeratu zituen nukleobase kanonikoak ulertzeko arazoetako bat bizitzaren sorpenaren lehen aldiunetan aukeratu ez zirela da. Hauen eboluzioa lehen biopolimeroenarekin batera paraleloan eman zen. Rios eta Tos egindako aipamen batean hautaketa gerta zitekeen zenbait aldiune identifikatzen dute.[76] Egile hauen arabera, kimika prebiotikoari esker, sortutako konposatu kopuru aberatsak geroago lehen polimero informazionalen eraikierari, bizitzaren sorpen eta eboluzioari, eta azken aitzindari komun unibertsalari (*Last Universal Common Ancestor*, LUCA) esker findu zen. Gaur egun, badira zenbait autore, lau nukleobase baino gehiagoko sistemen izatearen ideiarekin hausnartzen direnak (ikusi 1.1 Irudia). Hipotesi horren aldean bakteriofagoetan aurkitutako nukleobase eraldatuen izatea dago,[98] edo alfabeto zabalagoak sortzeko aukera kimika sintetikoaren bitartez.[99]

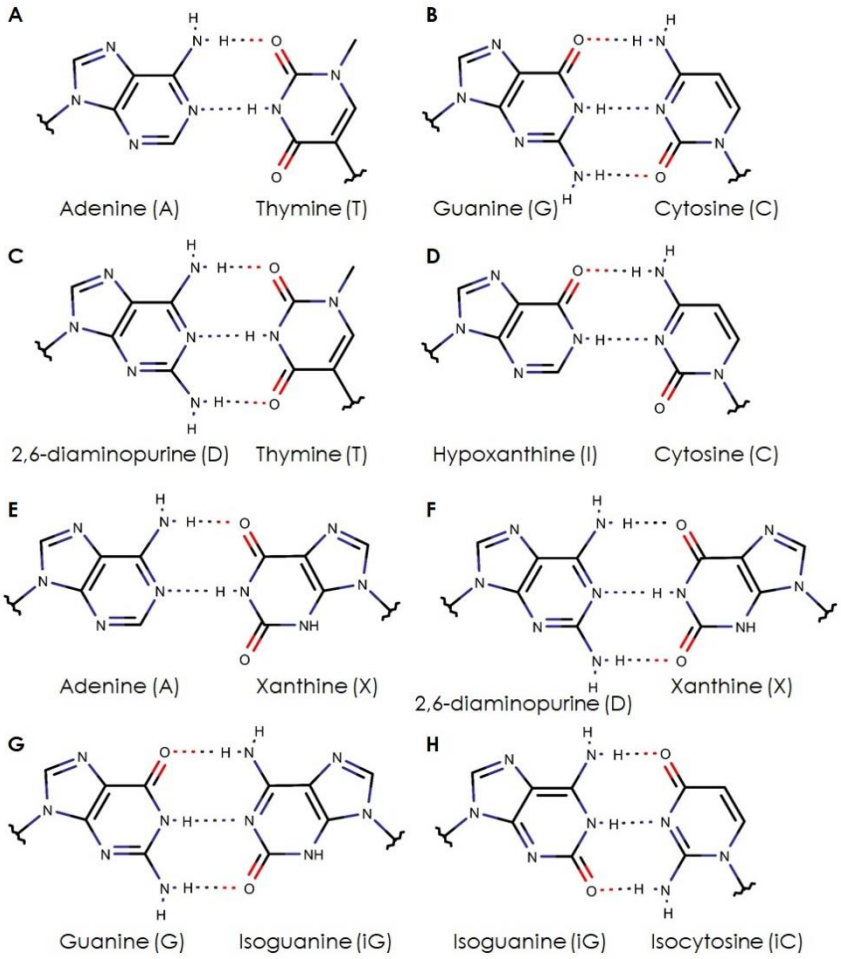

1.1 Irudia: (A-B) Watson-Crick elkarrekintzak nukleobase kanonikoen artean. (C-H) Watson-Crick antzeko elkarrekintzak zenbait nukleobase ez-kanonikoen artean.[82]

Siege eta Tor[86] aurkeztutako lan interesgarri batean, RNA base aitzindari (ikusi 1.2 Irudia) posible bat aipatzen dute, geroago ingurugiro akuosoan emandako hidrolisiari esker gaur egun ezagutzen diren C eta U baseetara eboluzionatzen duena. Base prebiotiko horren berezitasuna (D), lotura N-glukosidikoa amina talde exo-ziklikoaren bitartez ematen dela da. Hasierako konfigurazio horrek mutazioen bitartez eboluzionatu liteke A edo G base purikoak sartzeko.

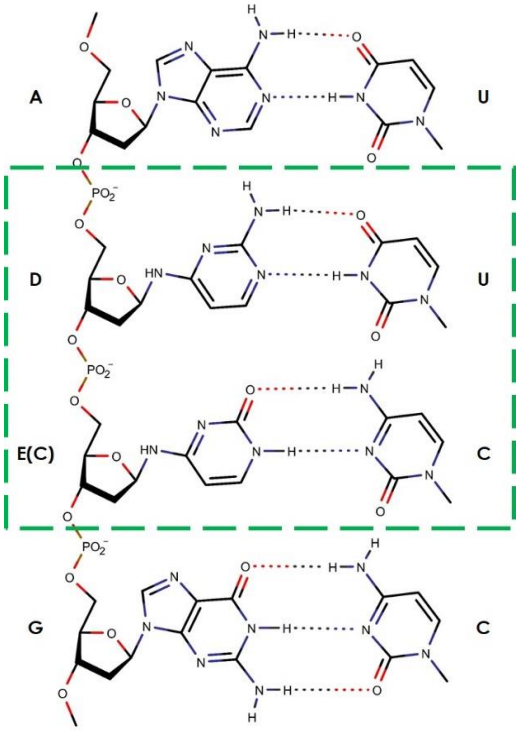

1.2 Irudia: Siege eta Tor-ek proposaturiko proto-RNA baten sekuentzia, base parekatze alternatibo batekin.[86]

Gorago deskribatutako bide ebolutiboaren faseei buruz, gure hipotesiaren arabera nukleobase kandidatuen hautaketan elkarrekintza ez-kobalenteek ere paper erabakigarria jokatu zuten. DNA baseetako talde funtzionalen konbinazio bereziak aukera ematen die pare osagarriak osatzeko, baina, gainera, talde funtzionalek beste biomolekula batzuekin elkarrekintzak sortzeko aukera eman dezakete, proteinekin esaterako. Gai hori lantzeko, tesi honetan xantina familiaren nukleobase kandidatuei buruzko analisi esperimental eta konputazionala egiten da.

Xantinek konposatu familia oso interesgarri bat osatzen dute, zeinak guaninaren metabolismoaren atal moduan naturan edo giza gorputzean aurki daitezkeenak.[100] Haien purina hezurdurari esker (A edo G-ren antzekoa), eta talde funtzionalei esker (T edo U baseen antzeko CONHCO segida), metabolismoan rol desberdinak jokatzen dute. Izan ere, DNA/RNA baseekiko antzekotasuna halako da, DNA/RNA baseak parte hartzen duten ezagutza molekularraren prozesuetan oztopatzeko gaitasuna dutela.[101] Metilatutako xantinak bereziki interesgarriak dira ikuspuntu horretatik.[101-104] Adibidez, ikerketa batzuk teofilina RNA aptamero bategaz espezifikoki antzematua dela frogatu zuten (ikusi 1.3 Irudia).[104,105] Egitura horretan, teofilinak zitosina eta urazilo baseekin espezifikoki lotzen da hidrogeno loturen bitartez, eta π···π pilaketa elkarrekintza gehigarriak konplexua egonkortzen dute.

Teobrominak, aldiz, T edo U baseen loturak sortzeko gune berdina aurkezten du, eta ondorioz, DNA/RNA-an ikusten diren antzeko elkarrekintzak sor ditzake. Azkenik, guztiz metilatutako xantina, kafeina izenekoa, ezaguna den konposatu estimulatzailea da, zeinak giza burmuinaren adenosina errezeptoreen (A_1, A_{2A}, A_{2B}, eta A_3) antagonista ez-selektibo moduan jokatzen duen.[106,107] Xantinen selektibitatea eta funtzio biologikoak ulertzeko, prozesu horietan eragiten duten aldagaien azterketa beharrezkoa da eskala molekular batean.

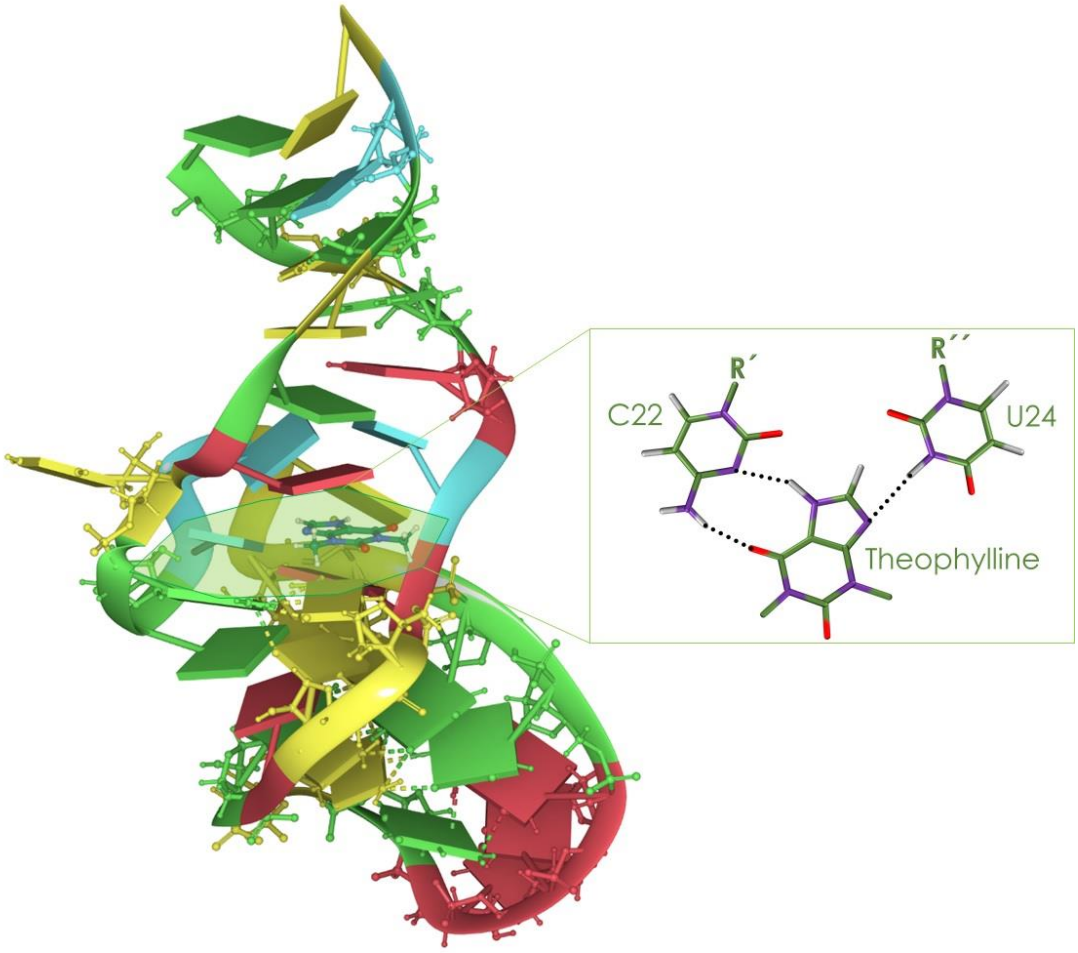

1.3 Irudia: RNA aptameroa, teofilinarekin batera konplexu bat sortuz (PDB: 1EHT).[104]

Tesi honen 6-8 Kapituluen helburu nagusiena xantina deribatuen elkarrekintza lehentasunak aztertzea da, DNA baseen eta xantinen arteko konplexuen egiturak lehen aldiz ikertuz. Alde batetik, 4 eta 6 Kapituluetan aurkeztutako emaitzak kafeinak azukre eta fenol deribatuekin dituen pilatzeko lehentasunak gailentzen dituzte. Dimero horiek elkarrekintza oso ahulen bitartez sortzen dira, eta ondorioz, oso zailak lantzeko. Bestetik,

7. eta 8. Kapituluek metilxantina monomeroen karakterizazioa eskaintzen dute; eta bere konbinazioak adeninarekin, DNA-ren Watson-Crick elkarrekintza sortzeko gaitasuna aurkezten dute eta. Horrez gain, teobromina 4-aminopirimidinarekin konbinatu egin da, Watson-Crick antzeko elkarrekintzak aztertzeko purina-pirimidina pare bat simulatuz. Watson-Crick antzeko elkarrekintza prebiotiko posibleen eta nukleobase kanonikoetan ematen diren elkarrekintzen arteko konparaketak, NCI-ak lehen polimero informazionalen eboluzioaren hautaketa-faktore gisa jokatu zuten ulertzeko lagun dezakete.

1.2. Erreferentziak

[1] H. Margenau and N. R. Kestner, *Theory of intermolecular forces*, Pergamon Press, Oxford, 2nd Editon., 1971.

[2] T. Steiner, The Hydrogen Bond in the Solid State, *Angew. Chemie Int. Ed.*, 2002, **41**, 48–76.

[3] J. Perlstein, The Weak Hydrogen Bond In Structural Chemistry and Biology (International Union of Crystallography, Monographs on Crystallography, 9) By Gautam R. Desiraju (University of Hyderabad) and Thomas Steiner (Freie Universität Berlin). Oxford University Press: , *J. Am. Chem. Soc.*, 2001, **123**, 191–192.

[4] P. Hobza and K. Müller-Dethlefs, *Non-covalent interactions: theory and experiment*, Royal Society of Chemistry, 2010, vol. 2.

[5] S. Scheiner, *Noncovalent forces*, Springer, 2015, vol. 19.

[6] L. Pauling and others, *The Nature of the Chemical Bond...*, Cornell university press Ithaca, NY, 1960, vol. 260.

[7] G. C. Pimentel and A. L. McClellan, *The hydrogen bond*, WH Freeman, 1960.

[8] E. Arunan, G. R. Desiraju, R. A. Klein, J. Sadlej, S. Scheiner, I. Alkorta, D. C. Clary, R. H. Crabtree, J. J. Dannenberg, P. Hobza, H. G. Kjaergaard, A. C. Legon, B. Mennucci and D. J. Nesbitt, Definition of the hydrogen bond (IUPAC Recommendations 2011), *Pure Appl. Chem.*, 2011, **83**, 1637–1641.

[9] A. S. Mahadevi and G. N. Sastry, Cooperativity in Noncovalent Interactions, *Chem. Rev.*, 2016, **116**, 2775–2825.

[10] I. Usabiaga, A. Camiruaga, C. Calabrese, A. Maris and J. A. Fernández, Exploring Caffeine–Phenol Interactions by the Inseparable Duet of Experimental and Theoretical Data, *Chem. - A Eur. J.*, 2019, **25**, 14230–14236.

[11] A. Poblotzki, H. C. Gottschalk and M. A. Suhm, Tipping the Scales: Spectroscopic Tools for Intermolecular Energy Balances, *J. Phys. Chem. Lett.*, 2017, **8**, 5656–5665.

[12] A. S. Christensen, T. Kubař, Q. Cui and M. Elstner, Semiempirical Quantum Mechanical Methods for Noncovalent Interactions for Chemical and Biochemical Applications, *Chem. Rev.*, 2016, **116**, 5301–5337.

[13] J. A. Frey, C. Holzer, W. Klopper and S. Leutwyler, Experimental and Theoretical Determination of Dissociation Energies of Dispersion-Dominated Aromatic Molecular Complexes, *Chem. Rev.*, 2016, **116**, 5614–5641.

[14] K. Müller-Dethlefs and P. Hobza, Noncovalent Interactions: A Challenge for Experiment

and Theory, *Chem. Rev.*, 2000, **100**, 143–168.

[15] O. F. Hagena and W. Obert, Cluster Formation in Expanding Supersonic Jets: Effect of Pressure, Temperature, Nozzle Size, and Test Gas, *J. Chem. Phys.*, 1972, **56**, 1793–1802.

[16] F. Biedermann and H.-J. Schneider, Experimental Binding Energies in Supramolecular Complexes, *Chem. Rev.*, 2016, **116**, 5216–5300.

[17] M. Becucci and S. Melandri, High-Resolution Spectroscopic Studies of Complexes Formed by Medium-Size Organic Molecules, *Chem. Rev.*, 2016, **116**, 5014–5037.

[18] O. Dopfer and M. Fujii, Probing Solvation Dynamics around Aromatic and Biological Molecules at the Single-Molecular Level, *Chem. Rev.*, 2016, **116**, 5432–5463.

[19] D. H. Levy, Laser Spectroscopy of Cold Gas-Phase Molecules, *Annu. Rev. Phys. Chem.*, 1980, **31**, 197–225.

[20] T. J. Balle and W. H. Flygare, Fabry–Perot cavity pulsed Fourier transform microwave spectrometer with a pulsed nozzle particle source, *Rev. Sci. Instrum.*, 1981, **52**, 33–45.

[21] B. H. Pate and F. C. De Lucia, Broadband Molecular Rotational Spectroscopy Special Issue, *J. Mol. Spectrosc.*, 2012, **280**, 1–2.

[22] S. Oswald, M. Wallrabe and M. A. Suhm, Cooperativity in Alcohol–Nitrogen Complexes: Understanding Cryomatrices through Slit Jet Expansions, *J. Phys. Chem. A*, 2017, **121**, 3411–3422.

[23] T. S. Zwier, Laser Spectroscopy of Jet-Cooled Biomolecules and Their Water-Containing Clusters: Water Bridges and Molecular Conformation, *J. Phys. Chem. A*, 2001, **105**, 8827–8839.

[24] T. A. Miller, Chemistry and Chemical Intermediates in Supersonic Free Jet Expansions, *Science (80-.).*, 1984, **223**, 545 LP – 553.

[25] M. V Johnston, Supersonic jet expansions in analytical spectroscopy, *TrAC Trends Anal. Chem.*, 1984, **3**, 58–61.

[26] J.-P. Schermann, *Spectroscopy and modeling of biomolecular building blocks*, Elsevier, 2007.

[27] T. S. Zwier, THE SPECTROSCOPY OF SOLVATION IN HYDROGEN-BONDED AROMATIC CLUSTERS, *Annu. Rev. Phys. Chem.*, 1996, **47**, 205–241.

[28] G. Meijer, M. S. de Vries, H. E. Hunziker and H. R. Wendt, Laser desorption jet-cooling of organic molecules, *Appl. Phys. B*, 1990, **51**, 395–403.

[29] J. L. Alonso, C. Pérez, M. Eugenia Sanz, J. C. López and S. Blanco, Seven conformers of l-threonine in the gas phase: a LA-MB-FTMW study, *Phys. Chem. Chem. Phys.*, 2009, **11**, 617–627.

[30] E. J. Cocinero, A. Lesarri, P. Écija, F. J. Basterretxea, J.-U. Grabow, J. A. Fernández and F. Castaño, Ribose Found in the Gas Phase, *Angew. Chemie Int. Ed.*, 2012, **51**, 3119–3124.

[31] I. Peña, C. Cabezas and J. L. Alonso, The Nucleoside Uridine Isolated in the Gas Phase, *Angew. Chemie Int. Ed.*, 2015, **54**, 2991–2994.

[32] F. O. Talbot and J. P. Simons, Sugars in the gas phase: the spectroscopy and structure of jet-cooled phenyl β-D-glucopyranoside, *Phys. Chem. Chem. Phys.*, 2002, **4**, 3562–3565.

[33] E. J. Cocinero, P. Çarçabal, T. D. Vaden, J. P. Simons and B. G. Davis, Sensing the anomeric effect in a solvent-free environment., *Nature*, 2011, **469**, 76–79.

[34] S. De Camillis, J. Miles, G. Alexander, O. Ghafur, I. D. Williams, D. Townsend and J. B. Greenwood, Ultrafast non-radiative decay of gas-phase nucleosides, *Phys. Chem. Chem. Phys.*, 2015, **17**, 23643–23650.

[35] I. León, E. J. Cocinero, J. Millán, A. M. Rijs, I. Usabiaga, A. Lesarri, F. Castaño and J. A. Fernández, A combined spectroscopic and theoretical study of propofol·(H2O)3, *J. Chem. Phys.*, 2012, **137**, 74303.

[36] J. González, I. Usabiaga, P. F. Arnaiz, I. León, R. Martínez, J. Millán and J. A. Fernández, Competition between stacked and hydrogen bonded structures of cytosine aggregates, *Phys. Chem. Chem. Phys.*, 2017, **19**, 8826–8834.

[37] I. Usabiaga, J. González, P. F. Arnáiz, I. León, E. J. Cocinero and J. A. Fernández, Modeling the tyrosine–sugar interactions in supersonic expansions: glucopyranose–phenol clusters, *Phys. Chem. Chem. Phys.*, 2016, **18**, 12457–12465.

[38] I. Usabiaga, J. González, I. León, P. F. Arnaiz, E. J. Cocinero and J. A. Fernández, Influence of the Anomeric Conformation in the Intermolecular Interactions of Glucose, *J. Phys. Chem. Lett.*, 2017, **8**, 1147–1151.

[39] I. Usabiaga, A. Camiruaga, C. Calabrese, A. Maris and J. A. Fernández, Exploring Caffeine–Phenol Interactions by the Inseparable Duet of Experimental and Theoretical Data, *Chem. – A Eur. J.*, 2019, **25**, 14230–14236.

[40] I. León, I. Usabiaga, P. F. Arnaiz, A. Lesarri and J. A. Fernández, Stepwise Nucleation of Aniline: Emergence of Spectroscopic Fingerprints of the Liquid Phase, *Chem. – A Eur. J.*, 2018, **24**, 10291–10295.

[41] M. Juanes, I. Usabiaga, I. León, L. Evangelisti, J. A. Fernández and A. Lesarri, The Six Isomers of the Cyclohexanol Dimer: A Delicate Test for Dispersion Models, *Angew. Chemie Int. Ed.*, 2020, **59**, 14081–14085.

[42] C. Pérez, S. Lobsiger, N. A. Seifert, D. P. Zaleski, B. Temelso, G. C. Shields, Z. Kisiel and B. H. Pate, Broadband Fourier transform rotational spectroscopy for structure determination: The water heptamer, *Chem. Phys. Lett.*, 2013, **571**, 1–15.

[43] C. Pérez, D. P. Zaleski, N. A. Seifert, B. Temelso, G. C. Shields, Z. Kisiel and B. H. Pate, Hydrogen Bond Cooperativity and the Three-Dimensional Structures of Water Nonamers and Decamers, *Angew. Chemie Int. Ed.*, 2014, **53**, 14368–14372.

[44] J. P. I. Hearn, R. V. Cobley and B. J. Howard, High-resolution spectroscopy of induced chiral dimers: A study of the dimers of ethanol by Fourier transform microwave spectroscopy, *J. Chem. Phys.*, 2005, **123**, 1–7.

[45] T. N. Wassermann and M. A. Suhm, Ethanol Monomers and Dimers Revisited: A Raman Study of Conformational Preferences and Argon Nanocoating Effects, *J. Phys. Chem. A*, 2010, **114**, 8223–8233.

[46] D. Loru, I. Peña and M. E. Sanz, Ethanol dimer: Observation of three new conformers by broadband rotational spectroscopy, *J. Mol. Spectrosc.*, 2017, **335**, 93–101.

[47] M. S. Snow, B. J. Howard, L. Evangelisti and W. Caminati, From Transient to Induced Permanent Chirality in 2-Propanol upon Dimerization: A Rotational Study, *J. Phys. Chem. A*, 2011, **115**, 47–51.

[48] A. K. King and B. J. Howard, A microwave study of the hetero-chiral dimer of butan-2-ol, *Chem. Phys. Lett.*, 2001, **348**, 343–349.

[49] A. Maris, B. M. Giuliano, D. Bonazzi and W. Caminati, Molecular recognition of chiral conformers: A rotational study of the dimers of glycidol, *J. Am. Chem. Soc.*, 2008, **130**, 13860–13861.

[50] N. A. Seifert, A. L. Steber, J. L. Neill, C. Pérez, D. P. Zaleski, B. H. Pate and A. Lesarri, The interplay of hydrogen bonding and dispersion in phenol dimer and trimer: structures from broadband rotational spectroscopy, *Phys. Chem. Chem. Phys.*, 2013, **15**, 11468–11477.

[51] J. Altnöder, S. Oswald and M. A. Suhm, Phenyl- vs cyclohexyl-substitution in methanol: Implications for the OH conformation and for dispersion-affected aggregation from

vibrational spectra in supersonic jets, *J. Phys. Chem. A*, 2014, **118**, 3266–3279.

[52] R. Medel and M. A. Suhm, Understanding benzyl alcohol aggregation by chiral modification: the pairing step, *Phys. Chem. Chem. Phys.*, 2020, **22**, 25538–25551.

[53] I. Leon, E. J. Cocinero, J. Millán, S. Jaeqx, A. M. Rijs, A. Lesarri, F. Castaño and J. A. Fernández, Exploring microsolvation of the anesthetic propofol, *Phys. Chem. Chem. Phys.*, 2012, **14**, 4398.

[54] I. Leõn, J. Millán, E. J. Cocinero, A. Lesarri and J. A. Fernández, Shaping micelles: The interplay between hydrogen bonds and dispersive interactions, *Angew. Chemie - Int. Ed.*, 2013, **52**, 7772–7775.

[55] I. León, A. Lesarri and J. A. Fernández, in *Intra- and Intermolecular Interactions Between Non-covalently Bonded Species*, ed. E. R. B. T.-I. I. I. B. N. B. S. Bernstein, Elsevier, 2021, pp. 143–188.

[56] P. M. Collins and R. J. Ferrier, *Monosaccharides: their chemistry and their roles in natural products.*, 1996.

[57] D. L. Nelson, A. L. Lehninger and M. M. Cox, *Lehninger principles of biochemistry*, Macmillan, 2008.

[58] D. Solís, N. V Bovin, A. P. Davis, J. Jiménez-Barbero, A. Romero, R. Roy, K. Smetana and H.-J. Gabius, A guide into glycosciences: How chemistry, biochemistry and biology cooperate to crack the sugar code, *Biochim. Biophys. Acta - Gen. Subj.*, 2015, **1850**, 186–235.

[59] B. Fiege, C. Rademacher, J. Cartmell, P. I. Kitov, F. Parra and T. Peters, Molecular Details of the Recognition of Blood Group Antigens by a Human Norovirus as Determined by STD NMR Spectroscopy, *Angew. Chemie Int. Ed.*, 2012, **51**, 928–932.

[60] S. Hakomori and Y. Igarashi, Functional Role of Glycosphingolipids in Cell Recognition and Signaling, *J. Biochem.*, 1995, **118**, 1091–1103.

[61] H.-J. Gabius, S. André, J. Jiménez-Barbero, A. Romero and D. Solís, From lectin structure to functional glycomics: principles of the sugar code, *Trends Biochem. Sci.*, 2011, **36**, 298–313.

[62] E. C. Stanca-Kaposta, D. P. Gamblin, E. J. Cocinero, J. Frey, R. T. Kroemer, A. J. Fairbanks, B. G. Davis and J. P. Simons, Solvent Interactions and Conformational Choice in a Core N-Glycan Segment: Gas Phase Conformation of the Central, Branching Trimannose Unit and its Singly Hydrated Complex, *J. Am. Chem. Soc.*, 2008, **130**, 10691–10696.

[63] H. Ghazarian, B. Idoni and S. B. Oppenheimer, A glycobiology review: Carbohydrates, lectins and implications in cancer therapeutics, *Acta Histochem.*, 2011, **113**, 236–247.

[64] M. del C. Fernández-Alonso, F. J. Cañada, J. Jiménez-Barbero and G. Cuevas, Molecular Recognition of Saccharides by Proteins. Insights on the Origin of the Carbohydrate–Aromatic Interactions, *J. Am. Chem. Soc.*, 2005, **127**, 7379–7386.

[65] A. P. Davis and R. S. Wareham, Carbohydrate recognition through noncovalent interactions: a challenge for biomimetic and supramolecular chemistry, *Angew. Chemie Int. Ed.*, 1999, **38**, 2978–2996.

[66] I. Peña, E. J. Cocinero, C. Cabezas, A. Lesarri, S. Mata, P. Écija, A. M. Daly, Á. Cimas, C. Bermúdez, F. J. Basterretxea, S. Blanco, J. A. Fernández, J. C. López, F. Castaño and J. L. Alonso, Six Pyranoside Forms of Free 2-Deoxy-D-ribose, *Angew. Chemie Int. Ed.*, 2013, **52**, 11840–11845.

[67] A. Camiruaga, I. Usabiaga, A. Insausti, I. León and J. A. Fernández, Sugar–peptidic bond interactions: spectroscopic characterization of a model system, *Phys. Chem. Chem. Phys.*, 2017, **19**, 12013–12021.

[68] A. Camiruaga, I. Usabiaga, A. Insausti, E. J. Cocinero, I. León and J. A. Fernández,

Understanding the role of tyrosine in glycogenin, *Mol. BioSyst.*, 2017, **13**, 1709–1712.

[69] I. Usabiaga, A. Camiruaga, A. Insausti, P. Çarçabal and M. D. Marshall, Phenyl- β -D-glucopyranoside and Dimers : Small Structural Differences but Very Different Interactions, 2018, **6**, 1–9.

[70] P. Çarçabal, E. J. Cocinero and J. P. Simons, Binding energies of micro-hydrated carbohydrates: measurements and interpretation, *Chem. Sci.*, 2013, **4**, 1830–1836.

[71] E. J. Cocinero and P. Çarçabal, in *Gas-Phase IR Spectroscopy and Structure of Biological Molecules*, eds. A. M. Rijs and J. Oomens, Springer International Publishing, Cham, 2015, pp. 299–333.

[72] R. A. Jockusch, R. T. Kroemer, F. O. Talbot, L. C. Snoek, P. Çarçabal, J. P. Simons, M. Havenith, J. M. Bakker, I. Compagnon, G. Meijer and G. von Helden, Probing the Glycosidic Linkage: UV and IR Ion-Dip Spectroscopy of a Lactoside, *J. Am. Chem. Soc.*, 2004, **126**, 5709–5714.

[73] I. A. Bermejo, I. Usabiaga, I. Compañón, J. Castro-López, A. Insausti, J. A. Fernández, A. Avenoza, J. H. Busto, J. Jiménez-Barbero, J. L. Asensio, J. M. Peregrina, G. Jiménez-Osés, R. Hurtado-Guerrero, E. J. Cocinero and F. Corzana, Water Sculpts the Distinctive Shapes and Dynamics of the Tumor-Associated Carbohydrate Tn Antigens: Implications for Their Molecular Recognition, *J. Am. Chem. Soc.*, 2018, **140**, 9952–9960.

[74] M. Klingenberg, The ADP and ATP transport in mitochondria and its carrier, *Biochim. Biophys. Acta - Biomembr.*, 2008, **1778**, 1978–2021.

[75] D. M. Rosenbaum, S. G. F. Rasmussen and B. K. Kobilka, The structure and function of G-protein-coupled receptors, *Nature*, 2009, **459**, 356–363.

[76] A. C. Rios and Y. Tor, On the Origin of the Canonical Nucleobases: An Assessment of Selection Pressures across Chemical and Early Biological Evolution, *Isr. J. Chem.*, 2013, **53**, 469–483.

[77] G. F. Joyce, RNA evolution and the origins of life, *Nature*, 1989, **338**, 217–224.

[78] R. Buick, J. S. R. Dunlop and D. I. Groves, Stromatolite recognition in ancient rocks: an appraisal of irregularly laminated structures in an Early Archaean chert-barite unit from North Pole, Western Australia, *Alcheringa An Australas. J. Palaeontol.*, 1981, **5**, 161–181.

[79] M. Schidlowski, P. W. U. Appel, R. Eichmann and C. E. Junge, Carbon isotope geochemistry of the 3.7 × 109-yr-old Isua sediments, West Greenland: implications for the Archaean carbon and oxygen cycles, *Geochim. Cosmochim. Acta*, 1979, **43**, 189–199.

[80] J. W. Schopf, *Earth's earliest biosphere: Its origin and evolution*, Princeton University Press, United States, 1983.

[81] S. Chang, D. J. Des Marais, R. Mack, S. L. Miller and G. Strathearn, *Earth's Earliest Biosphere: Its Origin and Early Evolution*, Princeton University Press, 1983.

[82] B. J. Cafferty and N. V Hud, Was a Pyrimidine-Pyrimidine Base Pair the Ancestor of Watson-Crick Base Pairs? Insights from a Systematic Approach to the Origin of RNA, *Isr. J. Chem.*, 2015, **55**, 891–905.

[83] Y. Nosenko, M. Kunitski, T. Stark, M. Göbel, P. Tarakeshwar and B. Brutschy, Vibrational signatures of Watson–Crick base pairing in adenine–thymine mimics, *Phys. Chem. Chem. Phys.*, 2013, **15**, 11520–11530.

[84] V. M. Kolb, J. P. Dworkin and S. L. Miller, Alternative bases in the RNA world: the prebiotic synthesis of urazole and its ribosides, *J. Mol. Evol.*, 1994, **38**, 549–557.

[85] R. Saladino, G. Botta, S. Pino, G. Costanzo and E. Di Mauro, Genetics first or metabolism first? The formamide clue, *Chem. Soc. Rev.*, 2012, **41**, 5526–5565.

[86] J. S. Siegel and Y. Tor, Genetic alphabetic order: what came before A?, *Org. Biomol. Chem.*,

2005, **3**, 1591–1592.

[87] M. Levy and S. L. Miller, The stability of the RNA bases: Implications for the origin of life, *Proc. Natl. Acad. Sci.*, 1998, **95**, 7933 LP – 7938.

[88] M. P. Robertson, M. Levy and S. L. Miller, Prebiotic synthesis of diaminopyrimidine and thiocytosine, *J. Mol. Evol.*, 1996, **43**, 543–550.

[89] C. H. House and S. L. Miller, Hydrolysis of Dihydrouridine and Related Compounds, *Biochemistry*, 1996, **35**, 315–320.

[90] C. Sagan, Ultraviolet selection pressure on the earliest organisms, *J. Theor. Biol.*, 1973, **39**, 195–200.

[91] S. Boldissar and M. S. de Vries, How nature covers its bases, *Phys. Chem. Chem. Phys.*, 2018, **20**, 9701–9716.

[92] C. T. Middleton, K. de La Harpe, C. Su, Y. K. Law, C. E. Crespo-Hernández and B. Kohler, DNA Excited-State Dynamics: From Single Bases to the Double Helix, *Annu. Rev. Phys. Chem.*, 2009, **60**, 217–239.

[93] H. Kang, K. T. Lee, B. Jung, Y. J. Ko and S. K. Kim, Intrinsic Lifetimes of the Excited State of DNA and RNA Bases, *J. Am. Chem. Soc.*, 2002, **124**, 12958–12959.

[94] M. M. Brister, T. Gustavsson and C. E. Crespo-Hernández, *Mol.*, 2020, 25.

[95] M. K. Shukla and J. Leszczynski, *Radiation Induced Molecular Phenomena in Nucleic Acids*, Springer Netherlands, 2008.

[96] B. Cohen, P. M. Hare and B. Kohler, Ultrafast Excited-State Dynamics of Adenine and Monomethylated Adenines in Solution: Implications for the Nonradiative Decay Mechanism, *J. Am. Chem. Soc.*, 2003, **125**, 13594–13601.

[97] J. P. Villabona-Monsalve, R. Noria, S. Matsika and J. Peón, On the Accessibility to Conical Intersections in Purines: Hypoxanthine and its Singly Protonated and Deprotonated Forms, *J. Am. Chem. Soc.*, 2012, **134**, 7820–7829.

[98] J. H.Gommers-Ampt and P. Borst, Hypermodified bases in DNA, *FASEB J.*, 1995, **9**, 1034–1042.

[99] H.-J. Kim, N. A. Leal and S. A. Benner, 2′-Deoxy-1-methylpseudocytidine, a stable analog of 2′-deoxy-5-methylisocytidine, *Bioorg. Med. Chem.*, 2009, **17**, 3728–3732.

[100] P. J. Marro, S. Baumgart, M. Delivoria-Papadopoulos, S. Zirin, L. Corcoran, S. P. McGaurn, L. E. Davis and R. R. Clancy, Purine Metabolism and Inhibition of Xanthine Oxidase in Severely Hypoxic Neonates Going onto Extracorporeal Membrane Oxygenation, *Pediatr. Res.*, 1997, **41**, 513–520.

[101] I. M. Johnson, S. G. B. Kumar and R. Malathi, RNA Binding Efficacy of Theophylline, Theobromine and Caffeine, *J. Biomol. Struct. Dyn.*, 2003, **20**, 687–692.

[102] R. D. Jenison, S. C. Gill, A. Pardi and B. Polisky, High-resolution molecular discrimination by RNA, *Science (80-.).*, 1994, **263**, 1425–1429.

[103] M. P. Latham, G. R. Zimmermann and A. Pardi, NMR chemical exchange as a probe for ligand-binding kinetics in a theophylline-binding RNA aptamer, *J. Am. Chem. Soc.*, 2009, **131**, 5052–5053.

[104] G. R. Zimmermann, R. D. Jenison, C. L. Wick, J.-P. Simorre and A. Pardi, Interlocking structural motifs mediate molecular discrimination by a theophylline-binding RNA, *Nat. Struct. Biol.*, 1997, **4**, 644–649.

[105] P. C. Anderson and S. Mecozzi, Unusually short RNA sequences: Design of a 13-mer RNA that selectively binds and recognizes theophylline, *J. Am. Chem. Soc.*, 2005, **127**, 5290–5291.

[106] R. K. Y. Cheng, E. Segala, N. Robertson, F. Deflorian, A. S. Doré, J. C. Errey, C. Fiez-Vandal, F. H. Marshall and R. M. Cooke, Structures of Human A1 and A2A Adenosine Receptors with Xanthines Reveal Determinants of Selectivity, *Structure*, 2017, **25**, 1275-1285.e4.

[107] A. S. Doré, N. Robertson, J. C. Errey, I. Ng, K. Hollenstein, B. Tehan, E. Hurrell, K. Bennett, M. Congreve, F. Magnani, C. G. Tate, M. Weir and F. H. Marshall, Structure of the adenosine A 2A receptor in complex with ZM241385 and the xanthines XAC and caffeine, *Structure*, 2011, **19**, 1283–1293.

2. Kapitulua

Metodologia

2.1. Sistema esperimentala

Lan honetan aurkezten diren sistema molekularrak ikertzeko sistema esperimental desberdinak erabili dira, laginaren prestakuntzaren arabera. Hala eta guztiz ere, erabilitako sistemak masan-bereizgarriak diren kitzikapen espektroskopia tekniketan (*Mass Resolved Excitation Spectroscopy*, MRES) oinarrituta daude.[1-3] Erraminta horiei esker, espantsio supersonikoetan isolatutako molekula edo molekula-agregatuen datu elektroniko zein bibrazionalak eskura daitezke (ikusi 2.1 Irudia).

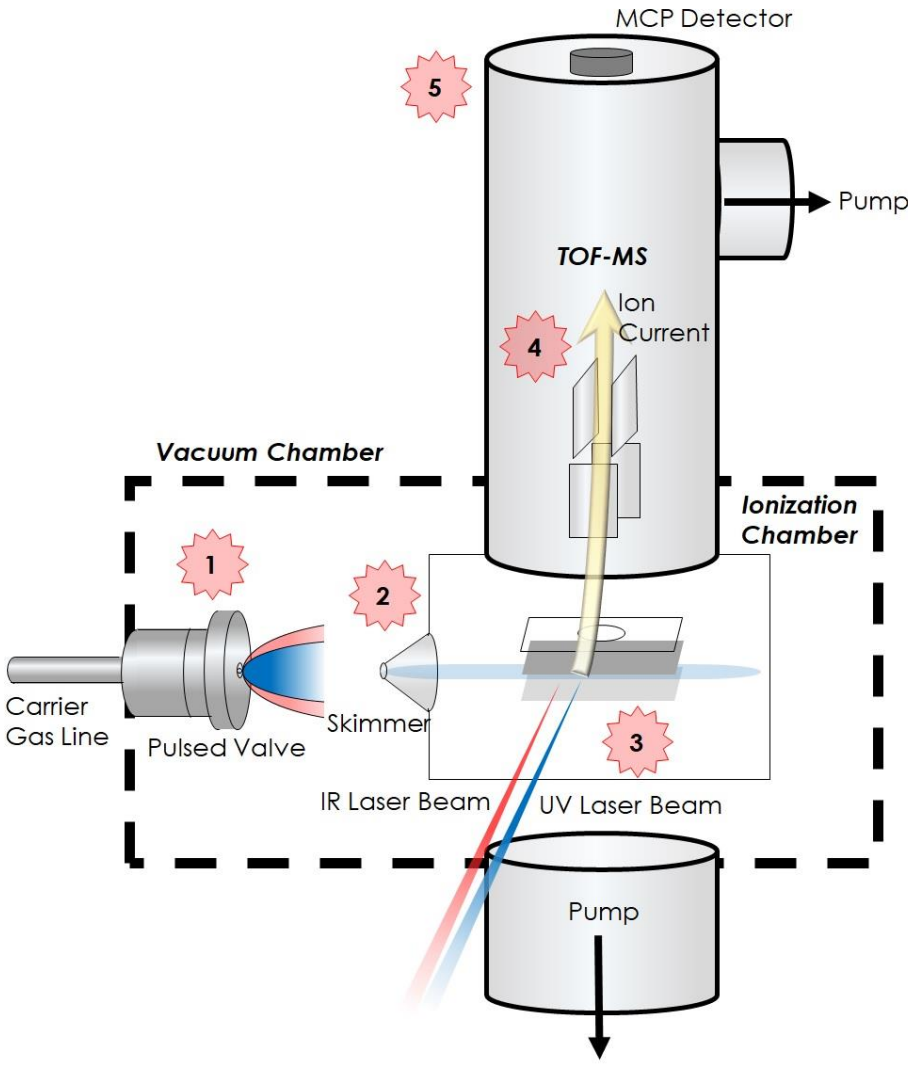

2.1 Irudia: MRES teknikan oinarrituriko sistema esperimental baten eskema orokorra. Huts maila altuko ganbara bati lotutako pultsuzko balbula (1) laginarekin nahastutako gas garraiatzailea (normalean He, Ne edo Ar) espantsio supersoniko bat bilakatzen du zirrikitu batetik (0.1 mm$^{\varnothing}$) pasatzean. Sortutako izpi molekularra ionizazio ganbarara iritzi baino lehen, atalik hotzena aukeratzen da kono baten laguntzaz (2). Izpi molekularra ionizazio eremura ailegatzean, molekulak edota molekula-agregatuak laser erradiazio iturriekin topo egiten dute. Sekuentzia sinkronizatu batean, ionizazio laserrak molekulen ioiak sortarazten ditu (3). Sortutako ioiak azelerazio bat jasaten dute tentsio altuko plaka batzuk eratzen duten eremu

elektrikoa dela eta. Modu honetan, ioiak hegaldi-denbora masa espektrometro batera (*Time of Flight*, ToF) bideratu eta azeleratzen dira (4). Ioiek aske hegan egiten dute espektrometroan zehar, bere masa eta kargaren arabera banantzen diren bitartean. MCP motako detektagailura ailegatzean (5), seinale elektriko bat sortarazten dute, monitorizatu daitekeena osziloskopio baten laguntzaz.

2.1.1. Laser iturriak

Ikertu nahi den eremu espektralaren arabera edota molekuletatik eskuratu nahi den informazio motaren arabera, laser bat edo gehiago erabili dira. Molekulak eta molekula-agregatuak beraien egoera kitzikatuera eramateko UV erradiazioa igortzen duten laserrak erabili dira. Aldiz, molekulak despopulatzeko erresonantzia bikoitzeko tekniketan, UV edo IR erradiazioak erabili dira. Azkenik, IR laserrek konposatu termolabilen laser desortzio sistemetan parte hartzen dute.

2.1.1.1. UV laser koloratzaileak

Tresnaren diseinu optikoa eta konfigurazioa fabrikatzailearen arabera alda daiteke. Halaber, orokorrean koloratzaile laser guztiek hurrengo 2.2 Irudian agertzen den diseinu optikoa jarraitzen dute. Laserra ionizazio ganbaretara garraiatzen da prisma, lente eta iris sorta bat erabilita. Lan honetan erabilitako laserrak hurrengoak dira:

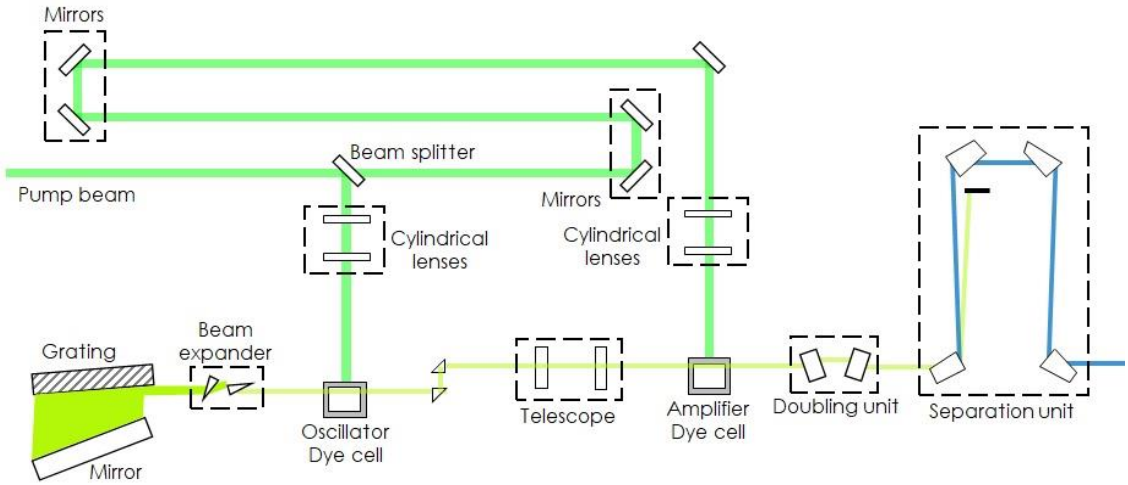

2.2 Irudia: Laser koloratzaile orokorren diseinu optikoaren eskema.

Q-Scan Dye Laser (Quantel): Nd:YAG ponpaketa laserrarekin (Q-Smart, Quantel, 220 mJ/pultsuko 355 nm-tan), 265-290 nm tartea ikertzeko Coumarin 540A koloratzailearekin.

Pulsare Pro-S Dye Laser (Fine Adjustment): Nd:YAG ponpaketa laserrarekin (Brilliant-b, Quantel, ~180 mJ/pultsuko 355 nm-tan) 250-270 nm tartea ikertzeko Coumarin 540A eta Coumarin 500 koloratzaileekin.

TDL-90 Dye Laser (Quantel): Nd_YAG ponpaketa laserrarekin (YG-980, Quantel, 500 mJ/pultsuko 532 nm-tan) 295-310 nm tartea ikertzeko Rhodamine 590, 600 eta 610 koloratzaileekin.

2.1.1.2. IR laserra

Erresonantzia bikoitzeko IDIRS (*Ion Dip InfraRed Spectroscopy*) esperimentuetan OPO/OPA (*Optical Parametric Oscillator/Optical Parametric Amplifier*) motako laser bat (LaserVison) erabili da IR erradiazio iturri gisa. Koloratzaile laserrekin alderatuta, laser horrek desberdintasun nabarmenak aurkezten ditu, egoera solidoko teknologian oinarrituta baitago. Nd:YAG laser bat (Continuum Surelite II; 500 mJ/pultsuko 1064 nm-tan) erabiltzen da OPO/OPA sistemaren ponpaketa egiteko. Maiztasun nahasketa ahalbidetzen duten kristalei esker, iterako erradiazioa 2500 eta 4000 cm^{-1} tartean finka daiteke (~5-10 mJ/pultsuko energiarekin, ~10 cm^{-1}-ko uhin zabalera izanda). Hurrengo 2.3 Irudian LaserVision OPO/A laserraren eskema orokorra antzeman daiteke.

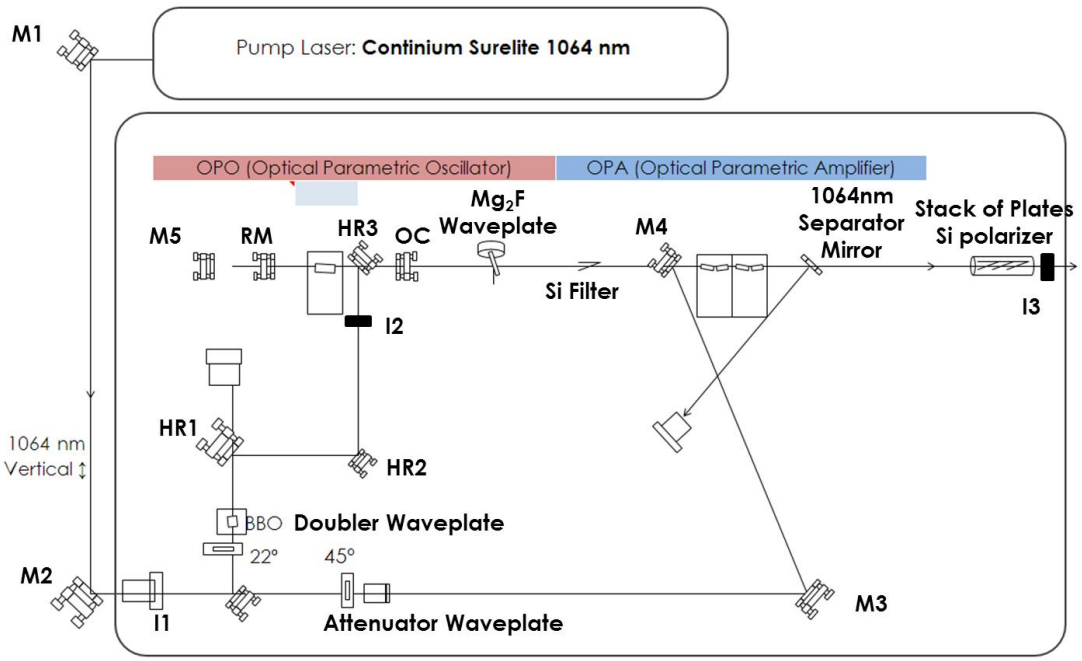

2.3 Irudia: Laservision OPO/OPA laserraren diseinu optikoaren eskema.

2.1.1.3. Desortzio laserrak

Konposatu termolabilen kasuan, molekulak gas egoerara eramatea ezinezkoa da beroketa prozesu sinpleak erabilita. Beraz, deskonposaketa termikoa ekiditeko, laser desortzio (LD) sistemak erabili dira. Tesi honetan zehar, laser desberdinak erabili dira laginen desortzio prozedurarako: Quantel Ultra bat (Quantel, 30 mJ/pultsuko 1064 nm-tan, 10 Hz-tan lan egiten duena, 8 ns pultsu zabalerarekin eta 3mm diametroko izpia sortzen duena), Minilite bat (Continuum, 30 mJ/pultsuko 1064 nm-tan, 10 Hz-tan lan egiten duena, ~5-7 ns pultsu zabalerarekin eta 3mm diametroko izpia sortzen duena) eta Brilliant-b bat (Quantel, 850 mJ/pultsuko 1064 nm-tan, 10 Hz-tan lan egiten duena, 6 ns pultsu zabalerarekin). Desortzio prozedura optimizatzeko, bukaeran sortutako argindarra eta izpiaren tamaina moldatu egin dira irisak eta CaF_2-zko lenteak erabiliz.

2.1.2. Tresna elektronikoak

MRES esperimentu arrakastatsu bat egiteko eskakizun zorrotzenetako bat esperimentuaren osagai guztien sinkronizazio egokia izatea da. Gertakizun guztiak (gas balbularen irekiera, desortzio laserra piztea, ionizazio laserra piztea eta detekzioa) denbora leiho estu batean sinkronizatu behar dira. Horretarako, laser iturri guztiak eta gailu elektroniko guztiak kanpotik kontrolatzen dira kanal askotako denbora kontrolagailuak erabilita. 2.4 Irudian esperimentu baten elementu desberdinen denbora eta pultsu sekuentziaren eskema bat aurkezten da. Esperimentu motaren arabera, aldaketa txikiak egin ahal dira denbora-leihoetan baldintzak optimizatzeko.

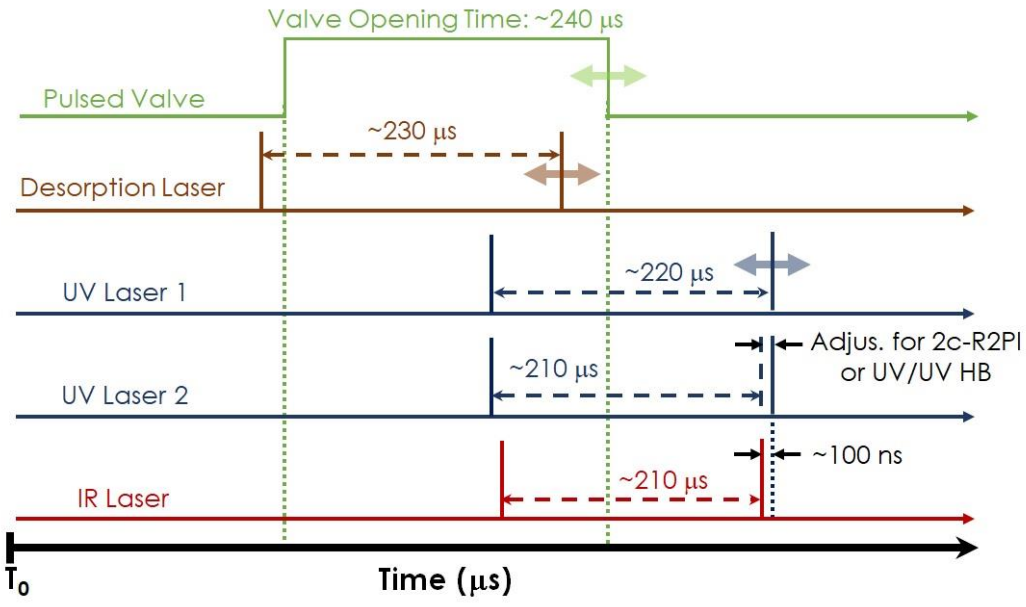

2.4 Irudia: Gertakizun esperimental baten denbora sekuentzien eskema.

2.1.3. Hegaldi-denbora masa-espektrometroak

Masa espektrometroak, MRES tekniketan, gailu giltzarriak dira. Espantsioan ionizatutako molekulen detekzioa eta banaketa bere masaren arabera ahalbidetzen dute. Horrez gain, ioi-zatiak eta espezie protonatuak monitorizatu ahal dira.[4,5] Masa espektrometro guztiak huts maila altuan lan egiten du, turbomolekular/errotatoria ponpa sistema bikoitz bati esker (ikusi deskripzio zehatzago bat behean). Bukaerako hutsa ganbaran $1 \cdot 10^{-7}$ mbar-koa da esperimentuen tartean, eta $10^{-6} - 10^{-4}$ mbar-koa gas balbula lan egiten duen bitartean (erabiltzen den gas garraiatzailearen arabera eta balbularekin irekiera denboraren arabera). Gehigarri gisa, espektrometroan ioi multzoa detektagailura ardaztu daiteke Einzel lente pare bati esker, amaierako seinalearen intentsitatea handitzeko eta erresoluzio espaziala handiagotzeko.

Bi masa espektrometro desberdin erabili dira EHU-n: tamaina txikiagoa duen espektrometro bat, zeinean ZEKE motako esperimentuak burutu ahal diren ioiak eta elektroiak detektatuz (Sistema esperimentala 1), eta luzeagoa den bigarren bat, masan bereizmen handiagoa duena eta gainera laser desortzio sistema batekin ekipatuta dagoena (Sistema experimentala 2). Horiez gain, hirugarren sistema esperimental bat erabili da Dr. Çarçabal-en ikerketa taldean egindako egonaldi batean zehar.

2.1.3.1. Sistema esperimentala 1

Sistema honetan,[6-8] ikertu nahi diren laginak balbularen kanpoaldean aurkitzen den konpartimentu batean kokatzen dira. Konpartimentua, gas lerroa eta balbula bero daitezke manta berogailu bati esker, laginaren bapore presioa handiagotzeko. Horrela, lurrundutako laginaz eta gas garraiatzaileaz (He, Ne edo Ar, normalean 0.5-3 bar-ko presioarekin) osatutako nahastea 0.5 mm-ko diametrodun zirrikitu batetik hedatu egiten da pultsuzko balbula bati esker (R. M. Jordan). Sortutako espantsio supersonikoaren atalik hotzena hautatzen da kono baten laguntzaz, eta isolatutako izpi molekularra hegaldi denbora masa espektrometrora (TOF-MS, R. M. Jordan, etxeko diseinua) bideratu egiten da. Huts sistema hiru ponpa turbomolekular (bi Pfeiffer Vacuum TMU 071, 200 m^3/h eta Pfeiffer Vacuum TMU 521 bat, 1870 m^3/h) eta ponpa errotatorio bakarra (Varian DS402, 20 m^3/h) osatzen dute. Lortutako ioiak erauziak dira 1 cm distantziara eta tentsio altuko sorgailuetara (PS350 High Voltage Power Supply, SRS Stanford Research Systems, IMC.) konektatuta dauden bi plaka metaliko sortutako eremu elektrikoari esker. Erauzitako ioiak azeleratu egiten dute 18 mm-dun plaka multikanaleko detektagailuaren (MCP) kontra. Sortutako erantzun elektriko detektagailuan jaso eta monitorizatu egiten da osziloskopio digital bat erabiliz

(Tektronics TDS 3032, 300 MHz). Azkenik, pultsuzko denbora-tarte sorgailuei (Stanford DG535/645) esker gertakizun guztien kontrol zehatza lortzen da. 2.5 Irudian sistema esperimentalaren argazki bat eta balbularen diagrama bat aurki daiteke.

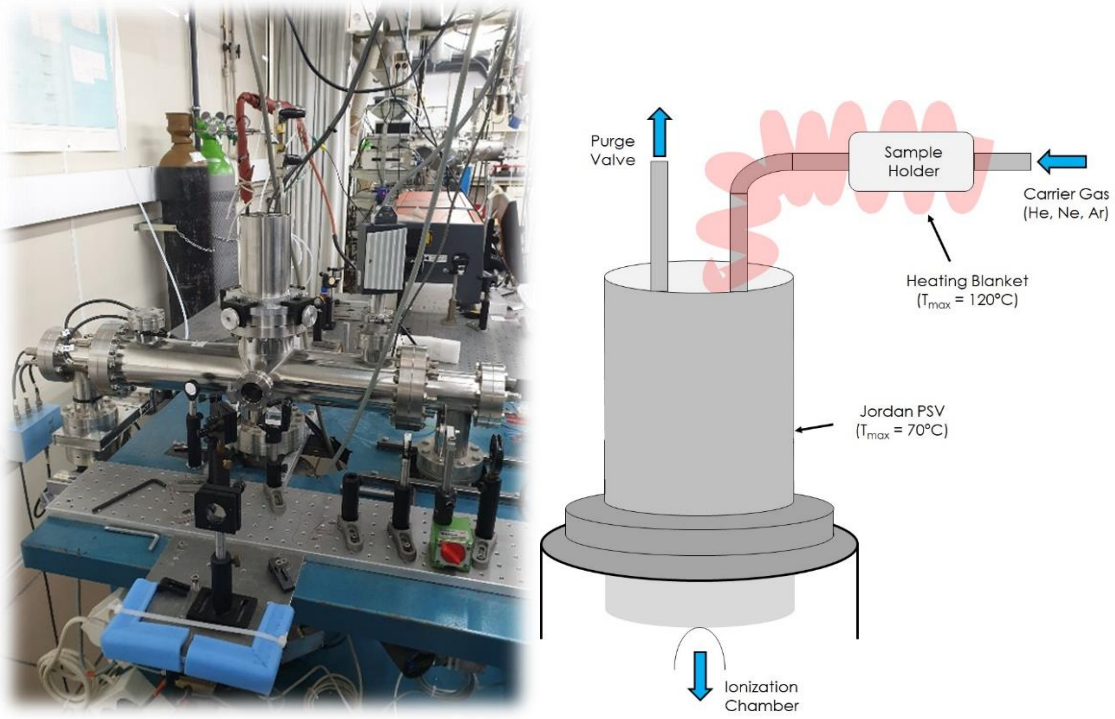

2.5 Irudia: (Ezkerraldean) Sistema esperimental 1; (Eskuinean) Pultsuzko balbularen beroketa sistemaren eskema.

2.1.3.2. Sistema esperimentala 2

Sistema esperimental honen hegaldi denbora masa espektrometro lineala (MS-TOF, R. M. Jordan) hegaldi tutu luzeago batekin ekipatuta dago, zeinak masa bereizgarriaren erresoluzioa handitzen duen. Ionizazio ganbararen diseinua Prof. J. Simons-en taldeak eginda da (Oxford unibertsitatea), geroago EHU-an aldatu egin dena.[9-10] Ganbarak sarrera ugari aurkezten ditu desortzio, ionizazio eta despopulazio laserrak barrualdera bideratzeko. Horrez gain, lagin solidoak mugitzeko pausuko motorra du, laser desortzioa burutzeko. Ganbarako huts maila mantendu egiten da ponpa errotatorio bati (Varian SD700, 27 m^3/h) konektatuta dauden bi ponpa turbomolekularrei (Leybold Turbovac 151, 145 l/s, eta Leybold TW 701, 680 l/s) esker. Gainontzeko gailu elektronikoak (tentsio sorgailuak, osziloskopioa, detektagailua eta pultsuzko denbora-tarte sorgailuak) sistema esperimental 1-ean deskribatutakoen antzekoak dira.

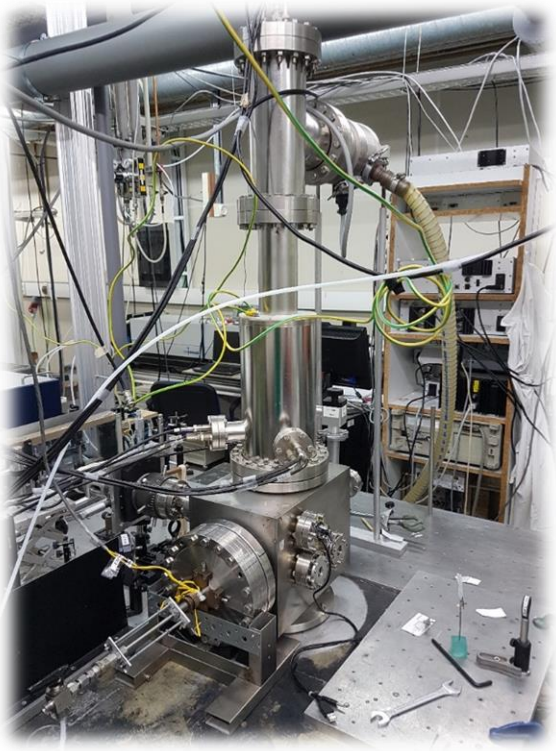

2.6 Irudia: Laser desortzio sistemara konektatuta dagoen hegaldi denbora masa espektrometroa.

Laser desortzio iturria sistema esperimental honen ezaugarririk nagusiena da, zeinak azukreen, peptidoen edo bestelako molekula termolabilak neurtzea ahalbidetzen duen. Laginaren zilindroa aldatutako pultsuzko balbula (General Valve, Series 9, 0.1 mm-ko zirrikituarekin) baten irteeran kokatu egiten da, 2.7 Irudian agertzen den bezala. Pausuzko motor bati esker (RS 440-442 pausuzko motorra, 1.8º/pausuko), laginaren zilindroa biratu daiteke, modu konstante batean lagina berrizteko. Desortzio laserra balbularen irekierarekin sinkronizatu egiten da. Modu horretan, solidotik gasera igaro diren molekulak espantsio supersonikoan harrapatuta geratzen dira. Hala ere, hozketa prozesua laser desortzioarekin ez da hain eraginkorra balbularekin batera datozen molekulen hozketarekin konparatuta. Hortaz, hozketa prozesuaren errendimendua hobetzeko, gas garraiatzailearen presio altuagoak erabiltzen dira (6-12 bar bitartean).

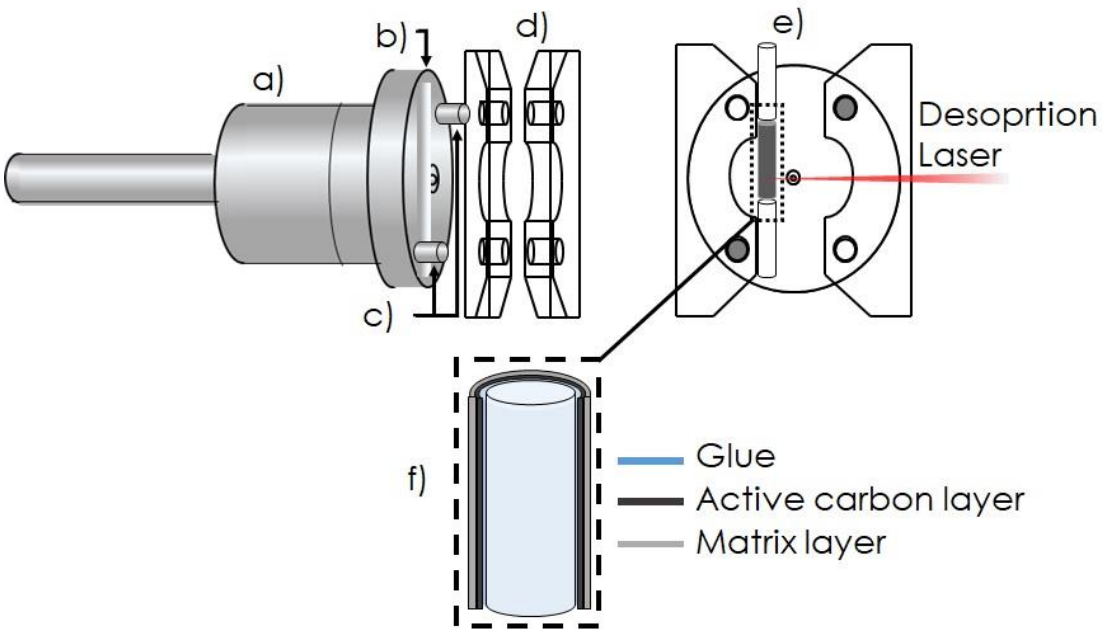

2.7 Irudia: Pultsuzko balbulari atxikitutako laser desortzio sistemaren eskema. a) General Valve Series 9, 28V, Kel-F "poppetarekin". b) Laginari lekua egiteko zuloa. c) Eusteko makilak. d) Bukaerako horma. e) Laginaren zilindroa, pausuzko motorrari eutsita. f) Zilindroa lagin nahastearekin.

Laser desortzio sistema horren lagin-prestaketa urrats delikatua da: desortzio prozedura laguntzen duen matrizearen eta laginaren arteko nahaste bat sortu behar da. Ondoren, nahastea zilindroan ezartzen da geruza homogeneo bat eratuz. Geruzan ezpurutasunak izanez gero, molekularen seinalean aldaketak nabarmenak dira, normalean esperimentuan martxan dagoelarik erraz zuzendu ezin direnak. Lehenik eta behin, neurtu nahi den konposatuaren eta karbonozko nano-tutuen (MWCNT, Cheaptubes Inc.) arteko nahaste homogeneoa prestatzen da. Ondoren, nahasketa grafitozko zilindro baten gainazalean ezartzen da. Azken pausu horretan, laginaren ezarpena bere testurarekin erlazionatuta dago, baina zilindroaren gainean karbono aktibozko geruza mehe baten ezarpenarekin hobe daiteke.

Bestalde, lagin batzuek biskositate maila altuak aurkezten dute, beraien maneiua oztopatzen duena. Hori da hain zuzen tesi honen 4.Kapituluan aztertutako N-metilazetamida/β-fenil-D-glukopiranosa konplexuaren esperimentuetan gertatzen dena. N-metilazetamida solido likatsua da, zeinaren fusio-puntua gelako tenperaturatik gertu dagoen (26 ºC). Matrizearekin nahastean, entropiaren igoera nahikoa da substantzia likatzeko, eta ondorioz, bere ezarpena zilindroaren gainazalean zaildu egiten da. Likidoa berotuz espantsioan sartzeko emaitza txarrak eman ditu, lurrunketa prozedurarekin eta laser desortzio prozedurarekin gas egoerara bidalitako bi molekulen konplexuak eratzeko baldintza esperimentalak paregabeak direlako gure sistema

esperimentalean. Ondorioz, laginak prestatzeko metodologia berria garatu zen (ikusi 2.8 Irudia). Lehenik eta behin, kola likidozko tanta bat zilindroaren gainazalaren gainean bota eta gainazal osoan zehar hedatu egiten da. Ondoren, aldez aurretik prestaturiko karbono nano-tutuen eta β-fenil-D-glukopiranosaren arteko nahastea zilindroan ezartzen da, honen gainazala nahastearen hautsaren kontra eginez. Azkenik, N-metilazetamidaren tanta batzuk botatzen dira zilindroaren gainean, eta kontu handiz gainazal osoan zehar sakabanatu egiten da.

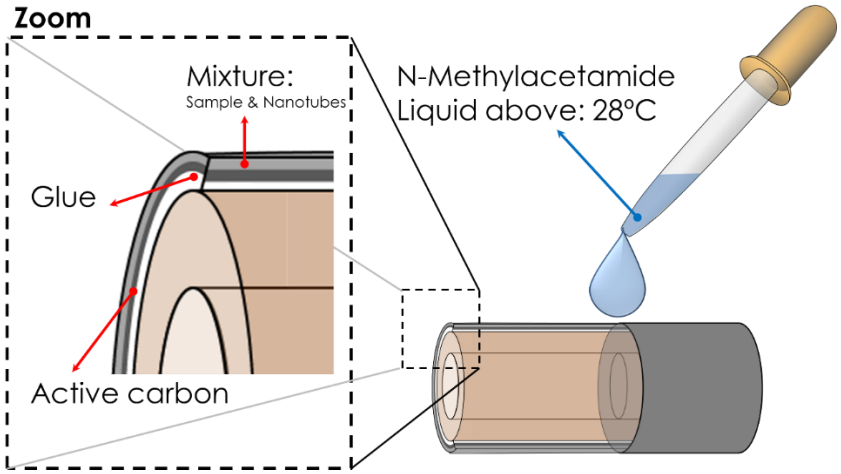

2.8 Irudia: Solido likatsuen lagin-prestaketa metodoaren eskema.

2.1.3.3. Carlotta masa-espektrometroa (ISMO)

ISMO (Institut des Sciences Moléculaires d'Orsay) laborategian egindako atzerriko egonaldian zehar, Dr. Pierre Çarçabal-en zaintzapean, hirugarren sistema esperimental bat erabili da. Honen diseinua EHU-n erabilitako esperimentuen antzekoa da, baina lagin-prestaketa desberdinarekin

Hasieran, laginaren hautsa grafitoarekin txikitu egiten da nahasketa homogeneo bat lortzeko. Gero, nahastea grafitozko barra baten gainazalaren gainean igurtzi egiten da, geruza mehe bat sortuz. Grafitozko barra, laginarekin batera, pultsuzko balbula baten irteeran finkatu egiten da (R. M. Jordan, 500 μm diametroko zirrikituarekin, 10 Hz-tan lan egiten duena, Ne edo Ar erabiliz 5 bar-ko atzerako presioarekin). Nd:YAG motako laser baten lehen harmonikoa (1064 nm, Minilite, Continuum) balbularen irekierarekin sinkronizatu egiten da laser desortzioa emateko. Espantsio supersonikoaren alde hotzena kono baten laguntzaz hautatzen da (Beam Dynamics), hegaldi denbora masa espektrometro (TOF-MS, R. M. Jordan) baten ionizazio ganbarara ailegatu baino lehen. Gainontzeko gailu elektronikoak (tentsio sorgailuak, osziloskopioa, detektagailua eta

pultsuzko denbora-tarte sorgailuak) sistema esperimental 1-ean deskribatutakoen antzekoak dira.

2.2. Metodologia Esperimentala

Isolatutako biomolekulen eta molekula-agregatuen informazio estruktural aipagarria eta zehatza lortzeko hainbat teknika erabili dira tesi honetan zehar. Guztiak ionizazio prozesu multifotonikoan oinarritzen dira (*MultiPhoton Ionization*, MPI), non fotoiak laser iturri desberdinetatik etor daitezkeen. Gai horri buruzko deskribapen zehatzagoak aurki daitezke hurrengo erreferentzietan.[11,12]

2.2.1. "Resonance Enhanced Multi-Photon Ionization" espektroskopia (REMPI)

REMPI teknika oinarrizko egoeratik (S_0) ioi egoerara (I_0^+) ailegatzeko gutxieneko bi fotoien absortzioan oinarritzen da, non molekula kitzikatu egiten da bitarteko egoera kitzikatu batetik (S_1) igaroz. Beraz, teknika horrek egoera elektroniko kitzikatuari buruzko informazioa ematen du. Horrez gain, ionizazioaren eraginkortasuna handitzen du, absortzio koherente puruarekin alderatuta. Hala eta guztiz ere, badira zenbait baldintza sisteman bete behar direnak REMPI prozesurako: *(i)* egoera elektroniko kitzikatu erreal bat izatea, ionizazio prozesua indartuta egoteko, *(ii)* trantsizio elektronikoaren momentua zero ez izatea eta *(iii)* egoera kitzikatuaren bizitza nahiko luzea izatea bigarren fotoi baten absortzioa emateko. Baldintza horiek betetzen badira, egoera kitzikatuaren espektroskopia mia liteke, bereizmen bibrazionala edo are errotazionalarekin, sortutako ioi korronteen aldakuntza aztertuz kitzikatze energiaren menpe (ikusi 2.9 eta 2.10 irudiak).

REMPI prozesuan[13,14] parte hartzen duten egoera elektronikoen arteko energia diferentziaren arabera, konfigurazio desberdinak aurki daitezke. Normalean, laser iturri bakarra erabiltzen bada fotoi-sorgailu gisa, prozesua kolore-bakarreko REMPI espektroskopia deitzen da (1c-REMPI). 1+1 eskemarekin deskribatzen da (fotoi bat kitzikapenerako, eta beste bat ionizaziorako), baina sistema molekularraren arabera, absortzio multifotonikoa bai kitzikapen zein ionizazio prozesuetan eman daiteke, 2+1 edo 1+2 kolore-bakarreko REMPI eskemak sortuz.

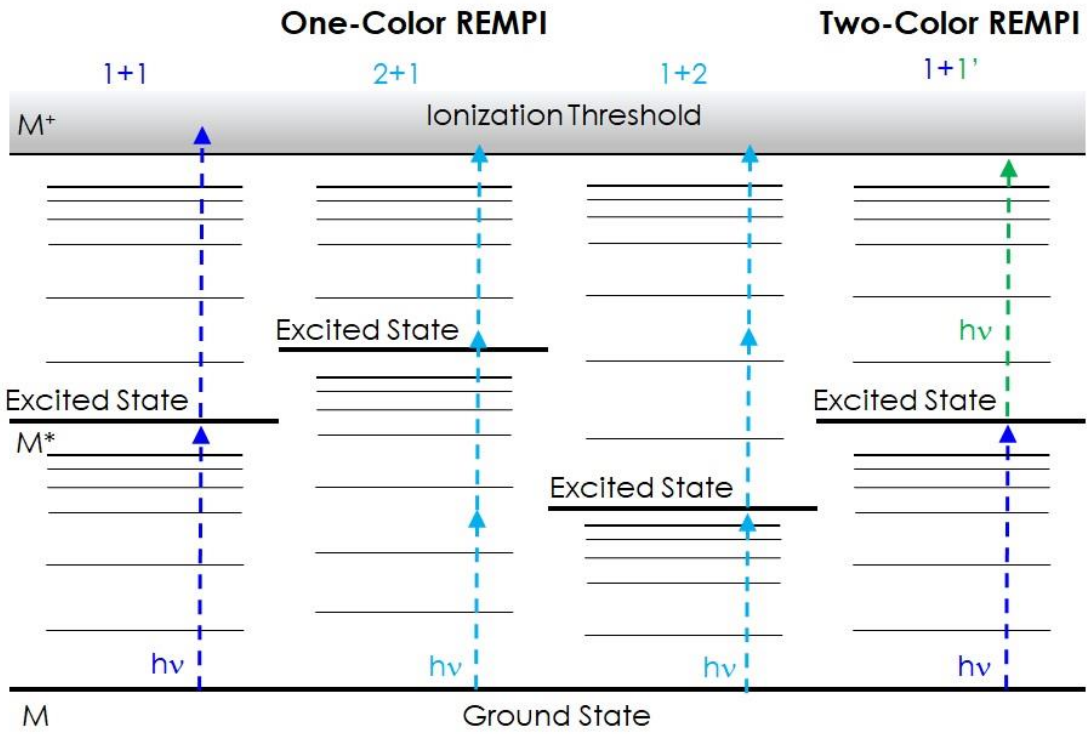

2.9 Irudia: Kolore-bakarreko eta bi-kolore REMPI espektroskopia tekniken eskemak.

Ionizaziora ailegatzeko fotoien energiaren doitze zehatza ezinezkoa da kolore-bakarreko REMPI espektroskopian. Ondorioz, normalean ioiak gehiegizko energiarekin sortzen dira. Honen zergatia, $S_1 \leftarrow S_0$ eta $I_0^+ \leftarrow S_1$ trantsizioen arteko energia desadostasuna da. Gehiegizko energia horrek ioien zatiketa sorta dezake. Ioi-zati horiek masa txikiagoko kanaletan detektatu egiten dira, zeinak askotan molekulen identifikazioa eta ikerketa zailtzen duten. Aipatutako prozesuak ekiditeko, bigarren laser iturri bat erabiltzen da $I_0^+ \leftarrow S_1$ trantsiziorako behar diren fotoiak sortarazteko. Teknika honen izena bi-koloreko REMPI espektroskopia da (2c-REMPI),[15,16] eta bi laser izpien gainezarpen espaziala eta tenporala behar ditu. Teknika horren bitartez eskuratutako espektro bibronikoa seinale/zarata erlazio hobea aurkezten ohi du, ionizazio energiaren doitzeak tamaina handiagoko konplexuen zatiketatik agertzen diren bandak desagertzeaz gain, ezpurutasunen edo gehiegizko potentzia erabiltzearen ondorioz sortzen diren bandak desagertzen direlako. Gainera, bi-koloreko REMPI teknika ionizazio atalase-maila eta egoera kitzikatuen erdibizitza eskuratzea ahalbidetzen du.

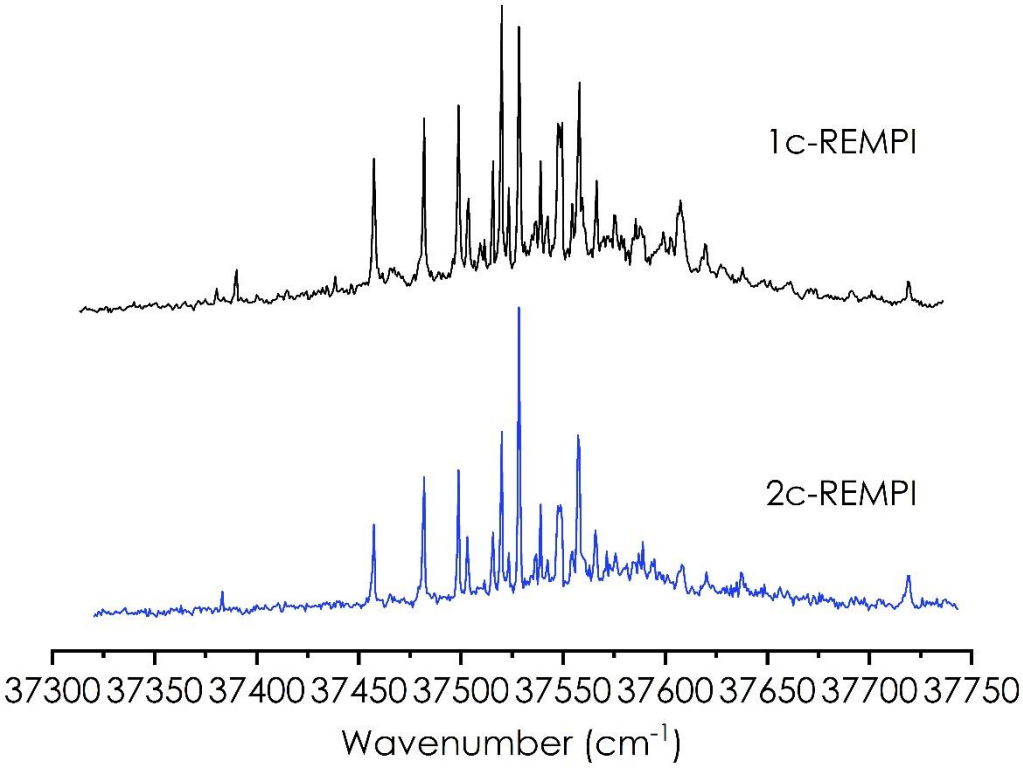

2.10 Irudia: Bentzil alkohol dimeroaren kolore-bakarreko eta bi-koloreko REMPI espektroak. Ikus daitekeen bezala, zenbait banda desagertu egiten dira bi koloreko espektroan.

REMPI espektroskopia teknika oso indartsua da, baina agregatuen ikerketan lehen pausua baino ez da. Sistema konplexuetan, REMPI espektroan hainbat isomero konformazionalen ekarpenak egon daiteke, erresonantzia bikoitzezko teknikekin (UV/UV hole burning edo IDIRS) soilik banan daitezkeenak.

2.2.2. "UV/UV Hole Burning" espektroskopia

Teknika honi esker REMPI espektro batean ekarpenak duten konformeroen zenbakia zehaztu daiteke, bi UV laser erabilita. Lehenengo laserra, ponpaketa laserra, REMPI espektroaren trantsizio zehatz batean finkatzen da. Usaian, gorrira dagoen trantsizioa jatorri moduan (0_0^0) hartzen da. Kasu batzuetan, jatorrizko trantsizioa oso ahula, edota espektroaren zaratarekin batera ateratzen da. Hortaz, kasu horietan trantsizio indartsuena aukeratzen da ponpaketa laserra finkatzeko. Ondoren, bigarren UV laser bat (zunda) eskaneatu egiten da REMPI espektroa agertzen den eremu espektralean. Aldi berean, ioi-korronteak sortutako seinalearen aldakuntzak neurtzen dira. Ponpaketa laserra zunda baino 100-200 ns lehenago pizten da. Modu honetan, zunda laserrak ponpatutako isomeroaren trantsizio berarekin topo egiten duenean, despopulazio bat

gertatzen da, eta ondorioz, zunda laserrak molekula gutxiago aurkitzen ditu kitzikatzeko, seinalean beherapen bat sortuz.

Teknika gehiago fintzeko, zunda laserra 5 Hz-tan erabili behar da ponpaketa laserra 10 Hz-tan lan egiten duen bitartean. Modu honetan, zuzenketa aktiboa buru daiteke, espektroen seinale/zarata erlazioa askoz handitzen duena (ikusi 2.11 Irudia). Erresonantzia bikoitzeko teknika hori oso erabilgarria da konformero bat baino gehiagoren presentzia erraz zehazteko, batez ere REMPI espektroa oso pilatuta badago.

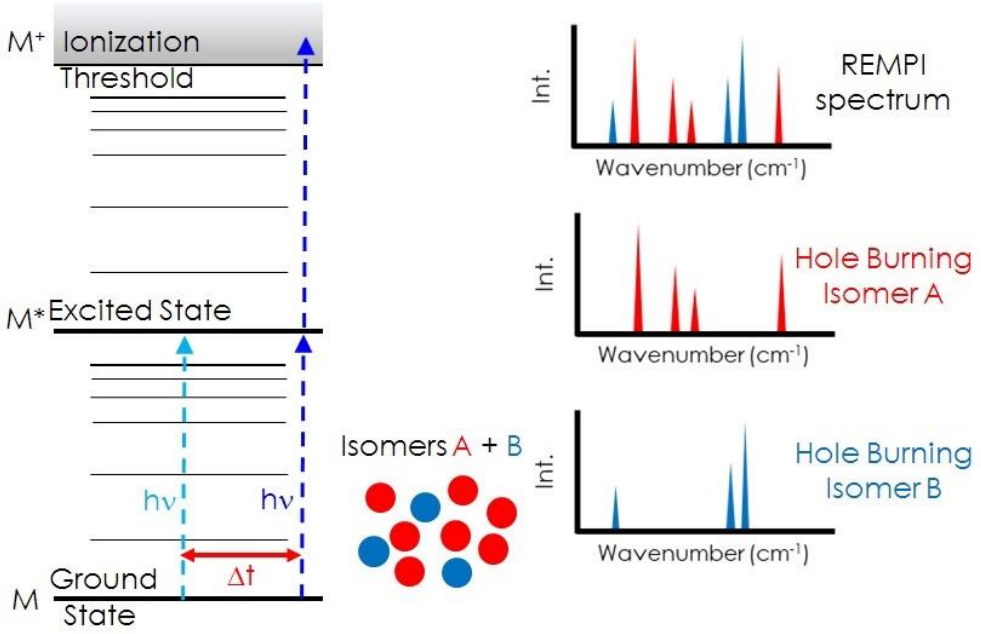

2.11 Irudia: Erresonantzia bikoitzeko "UV/UV Hole Burning" esperimentu baten eskema.

2.2.3. Ioi-Despopulazio Infragorri Espektroskopia (IDIRS)

Teknika hau, IR/UV erresonantzia bikoitza moduan ere ezaguten dena, isomero espezifiko bati dagokion IR espektroak eskuratzea ahalbidetzen du. Masan bereizgarria den detekzioarekin konbinatzean, IDIRS erraminta indartsuena bilakatzen da fase isolatuan agregatuen informazio estrukturala eskuratzeko.

Aurretik ikusitako "Hole Burning" espektroskopiaren antzeko konfigurazioa erabiltzen du IDIRS espektroskopia. Sintonizatu daitekeen IR laser bat ponpaketa gisa erabiltzen da, 5 Hz-tan lan egiten duena eta UV zunda laserra baino 100-200 ns baino lehenago pizten dena. UV zunda laserra aztertu nahi den isomeroaren trantsizio zehatz batean finkatzen da. Seinalea eta erreferentzia zuzenketa aktiboaren bitartez neurtzen dira, 5 Hz-tan. IR laserrak zundatutako isomeroaren trantsizio bibrazional batekin

erresonantea den bakoitzean, ioi seinalean despopulazio bat sortarazten du. Neurtutako erreferentzia espektroari despopulazio espektroa kenduz gero, isolatutako isomeroaren oinarrizko egoerako IR espektroa lortzen da.

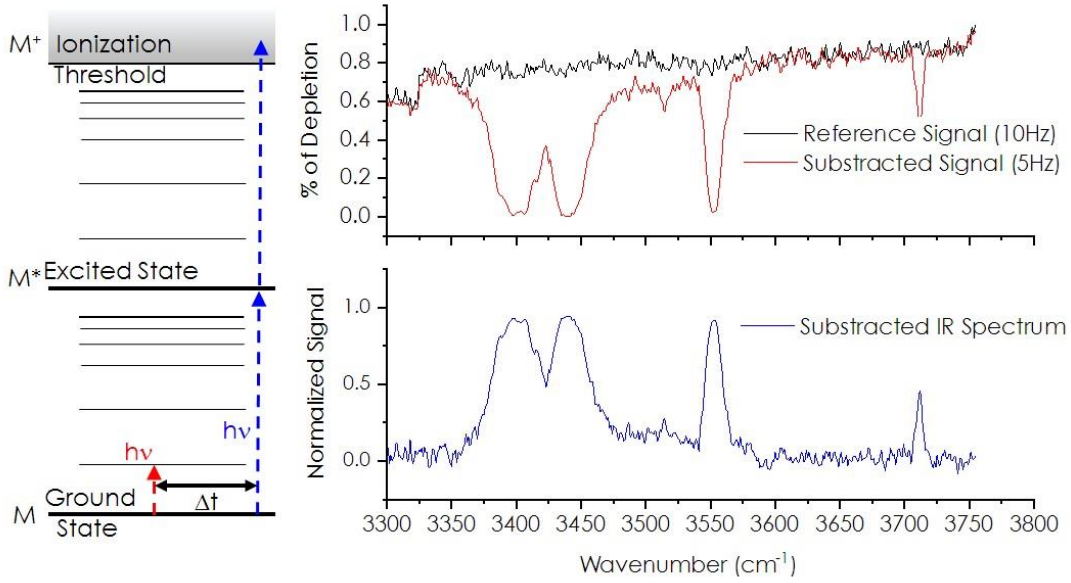

2.12 Irudia: IDIRS teknikaren eskema, zuzenketa aktiboaren adibide batekin.

2.2.4. "IR/UV Hole Burning" espektroskopia

Teknika honen helburua aurretik azaldutako "UV/UV Hole Burning" teknikaren berdina da, baina IR laser bat erabilita ponpaketa moduan. IR laserra ezaguna den trantsizio bibrazional bat kitzikatzen duen uhin-luzeran finkatzen da. Kitzikatutako trantsizioa partekatzen duten molekulek despopulazio bat jasango dute, eta ondorioz, UV zunda laserra eskaneatuz, isomeroaren REMPI espektroa lortzen da. Konfigurazioa teknika honetarako IDIRS esperimentuen antzekoa da, baina eskaneatu egiten den laserra IR-tik UV-ra aldatzen da.

2.3. Metodologia Teorikoa

Analisi teorikoaren helburu nagusiena ikertzen ari den sistemaren panorama konformazional osoaren miaketa da, minimo esanguratsuenak aurkitzeko eta horien energia erlatibo eta lotura-energia fidagarriak lortzeko. Horrez gain, aurkitutako minimoen IR espektro teorikoen simulazioak egiten dira, datu esperimentalen esleipena laguntzeko. Azken hamarkadetan, aurrerapenak konputazioaren potentzian eta metodo konputazional berrien ikerkuntzan zientzialari esperimentalen lanean pausu bat aurrera ematea ahalbidetu dute.[17-19]. Lan honetan, aurrerapen horiei esker, panorama konformazional konplexuak dituzten tamaina handiko molekula-agregatuak karakterizatu ahal izan dira.

Jarraitutako metodologia teorikoa hurrengo 2.13 Irudian aurkezten da. Laburbilduz, mekanika molekularrarekin panorama konformazionalaren bilaketa zabal bat burutzen da. Ondoren, aurkituriko egituren geometriak optimizatu egiten dira mekanika kuantikoa erabilita. Minimo baten benetako izaera bibrazio modu normalen analisian frekuentzia negatiborik ez dagoelako egiaztatzen da. Horrez gain, pausu horretan energia balio fidagarriak lortzen dira. Azkenik, IR espektroak, eta batzuetan UM espektroak ere, simulatu egiten dira datu esperimentalen esleipenean laguntzeko.

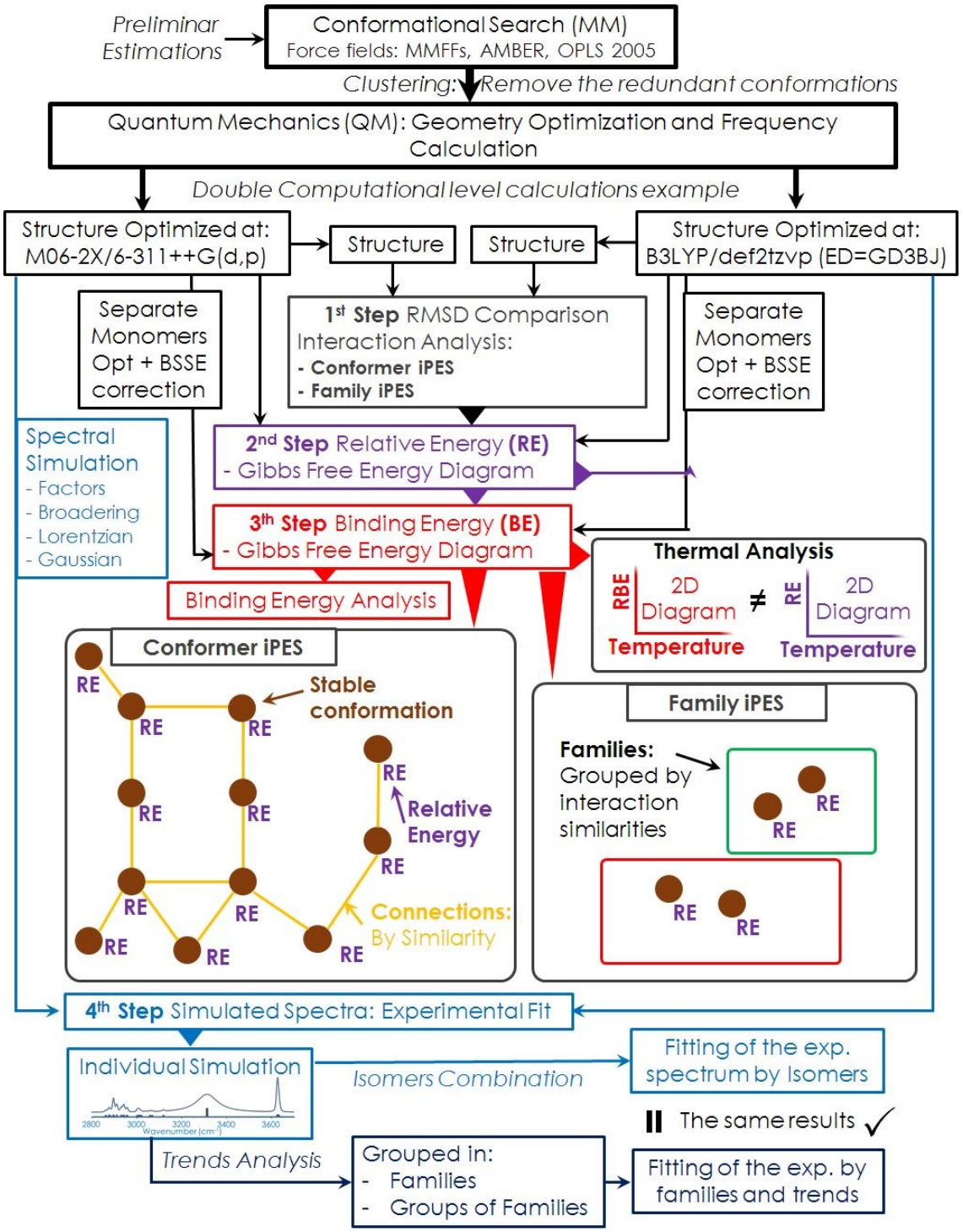

2.13 Irudia: Ikertutako sistemen analisi teorikoa egiteko jarraitutako protokolo teoriko orokorraren eskema

2.3.1. Bilaketa konformazionala

Molekulen panorama konformazionala eta elkarrekintza ez-kobalenteen dibertsitatea, hauek aurkezten duten flexibilitatearekin guztiz erlazionatuta daude. Angelu diedroen biraketa, talde funtzionalen tortsioa edota tautomerizazio prozesuak, minimo lokal

ugari aurkezten duen energia potentzialaren gainazala sortarazten dute. Tesi honetan landu diren sistema molekularren flexibilitateak eta konplexutasunak protokolo landu baten garapenera bultzatu du, bilaketa konformazionalean zehar egitura adierazgarrienak aurkitzen direla ziurtatzeko.

Lehenengo pausuan burutzen den bilaketa konformazional sakona mekanika molekularrean (MM) oinarritzen da. Metodo hauek askatasun gradu guztien miaketa egiten du, molekulak edo agregatuak har dezakeen konformazio posible guztien zerrenda sortaraziz.[20] Macromodel erramintaren (Schrödinger Suite)[21] Maestro softwarea bilaketa honetarako erabili da.

Egiturak Monte Carlo algoritmo baten bitartez sortzen dira, zeinak energia potentzialaren gainazalaren esplorazioa egiten duen lotura, angelu eta diedro guztietan aldaketak eginez. Ondoren, lortutako egiturak "mixed-torsional large scale low mode sampling" metodoarekin asaldatu egiten dira, minimo lokal berriak lortzeko. Azkenik, egituren energiaren minimizazioa egiten da konformero posible guztien zerrendara gehitu baino lehen. Nahiz eta erraminta aproposa izan panorama konformazional orokor bat modu azkar batean sortzeko, energiaren minimizazioak ez dira oso zehatzak, fisika klasikoan oinarritzen baitira. Hortaz, familia konformazional guztiak ezagutzeko intuizio kimikoa eta aldagai guztien analisia beharrezkoa da.

Badira zenbait erramintak konformero askoren zerrenda bat erraztu ditzaketenak. Adibidez, energia leiho bat aukeratuz, egituren kopurua nabarmenki murrizten da, energian oso altuak diren egiturak baztertzen direlarik. Gero, Maestro softwarearen klusterizazio metodoak erabil daitezke, geometriak beraien antzekotasunen arabera multzokatzeko. Honi esker, geometrien ikerketa egitura familietara sinplifikatzen da, egituren banakako azterketa egin beharrean. Familia horien egitura adierazgarrienak aukeratu egiten dira, ondoren DFT metodoekin optimizazio sakon bat jasateko. Molekularen edota agregatuen konformazio posibleak ez galtzeko, mekanika molekularraren indar eremu bat baino gehiago erabiltzea gomendagarria da. Lan honetan OPLS3,[22] MMFFs[23] eta AMBER[24,25] indar eremuak erabili dira.

2.3.2. Konputazio kuantikoa: Egituren optimizazioa eta bibrazio-maiztasunen kalkulua

Mekanika kuantikoak (MK) bilaketa konformazionalean (MM) lortutako egituren propietateen deskripzio zehatza ahalbidetzen dute. Metodo honetan, egiturak

geometriaren optimizazio sakon bati menderatuak dira, zeinaren zehaztasuna erabilitako maila konputazionalaren arabera dagoen. Lan honetan, dentsitate funtzionalaren teoria (DFT) metodo nagusiena izan da. Aurkitzen diren funtzional guztien artean, aukeratutakoak elkarrekintza dispertsiboak modu esplizituan kontuan hartzen dute. Funtzional ohikoenak ondokoak izan dira: M06-2X funtzionala, Truhlar-en taldeak[26] garatutakoa; eta B3LYP funtzionala, Grimme-ren dispertsio faktorearen (GD3-BJ) zuzenketarekin batera.[27] M06-2X funtzionalerako Pople-en doble eta triple ξ funtzio baseak (6-31+G(d) eta 6-311++G(d,p)) erabili dira; eta dispertsio-zuzendurako B3LYP funtzionalean, aldiz, def2tzvp funtzio basea erabili da. Aipatutako bi metodoak agregatuen propietate elektrikoen predikzio zehatzak burutzeko gaitasuna hainbat alditan frogatu dute.[10,28-30,31-36]

Optimizazio pausuaren ondoren, elkarrekintzen arabera egiturak familietan sailkatzen dira. Sistema molekularraren arabera, eta honek aurkezten duen flexibilitatearen arabera, 2.14. Irudian agertzen den antzeko konexio-diagramak eraiki ahal dira. Diagrama horrek elkarrekintza energia potentzial gainazalaren (*Interaction Potential Energy* Surface, iPES) irudikapena da, eta familia egonkorrenen edota adierazgarrienen arteko isomerizazio bideak laburbiltzen ditu.

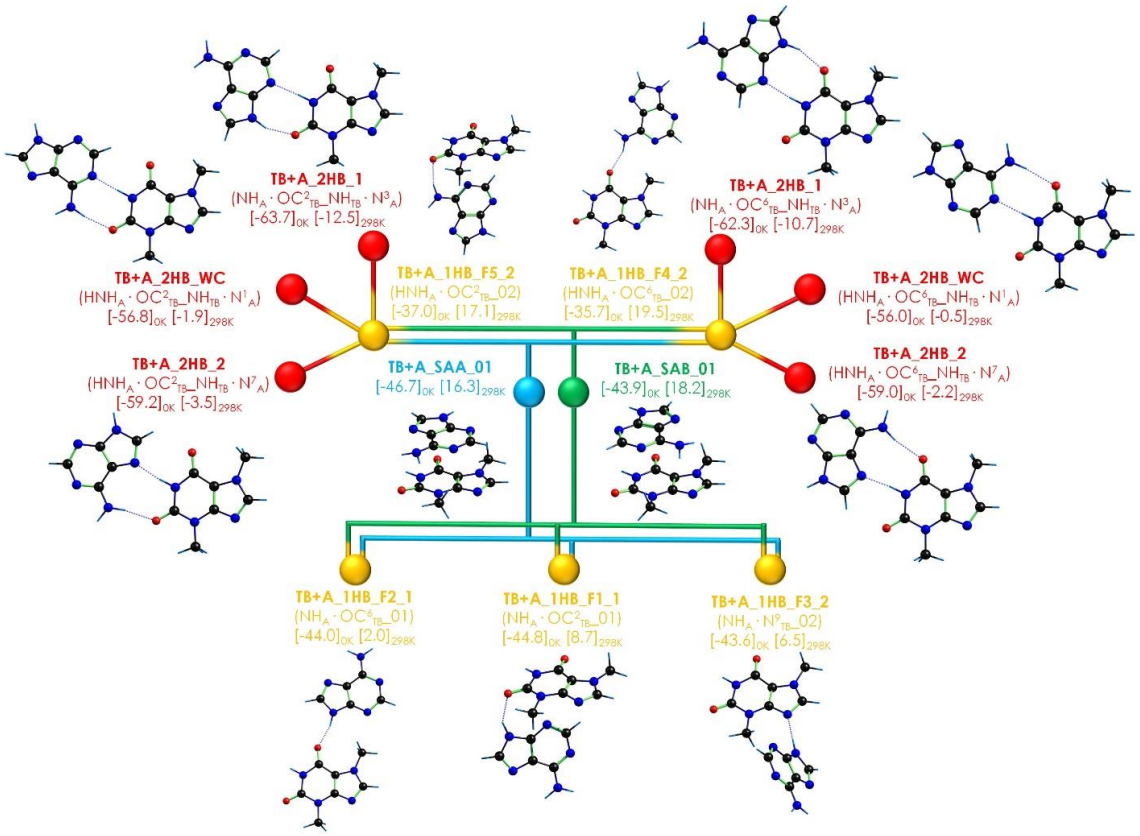

2.14 Irudia: Elkarrekintza energia potentzial gainazal (iPES) diagramaren adibidea. Elkarrekintza mota bakoitza kolore baten bidez adierazten da: bi hidrogeno lotura (gorria), hidrogeno lotura bakarra (horia) eta pilaketa elkarrekintzak (urdina edo berdea, elkarrekintzan parte hartzen duen molekularen aldearen arabera). Hurrengo pausuetan erabiltzen den kolore-kodea berdina da, datu konputazional guztiak dagokion egiturarekin erlazionatzeko.

Halaber, egituren energia elektronikoaren balioak ez dira beti esperimentalki isolatutako konformeroen adierazgarri. Hortaz, tesi honetan aurkezten diren molekula-agregatu askotan lotura-energia (*Binding Energy*, BE) erabili dira, aurrerako aurkeztuko diren kasu batzuen moduan, lotura-energia handiagoa duten espezieak detektatu direlako espezie egonkorrenak detektatu beharrean. Gainera, sistema desberdinen arteko lotura-energien konparaketak elkarrekintzaren naturari buruzko informazio garrantzitsua ematen du. Sistema baten energia erlatiboaren (RE) eta lotura energien kalkuluak hurrengo (1)-(5) ekuazioak erabiliz lortu dira:

$$E_{mono,i} = E_{Elec.} + E_{ZPE} + \Delta G_{TC,i} \quad (1)$$

$$E_i = E_{Elec.} + E_{ZPE} + E_{BSSE} + \Delta G_{TC,i} \quad (2)$$

$$RE_i = E_i - E_{GM} \quad (3)$$

$$BE_i = E_i - (E_{mono1,i} + E_{mono2,i}) \quad (4)$$

$$RBE_i = BE_i - BE_{SB} \quad (5)$$

Molekula bakar (monomero) baten energia bere energia elektroniko ($E_{elec.}$), zero-puntuko zuzenketa energia (ZPE) eta Gibbs energia askerako zuzenketa termikoaren (ΔG_{TC}) gehiketa gisa deskribatzen da (ikusi 1 Ekuazioa). Molekula-agregatu baten energiarako (2 Ekuazioa), funtzio-baseen gainezarpen akatsaren zuzenketa beharrezkoa da, Boys eta Bernardi garatutako "counterpoise" metodoarekin kalkulatzen dena.[37] Zuzenketa honek agregatuaren aparteko estabilizazioa kontuan hartzen du, agregatuaren osagai indibidualak definitzeko funtzio-base baino gehiago erabiltzeagatik sortua. Molekula-konplexu baten lotura energia (BE_i) agregatuaren energiari (E_i) bere osagaien energia kenduta lortzen da. Esaterako, dimero baten kasuan, $BE = E_{dimer} - (E_{mono1,I} + E_{mono2,I})$ (4 ekuazioa). Adieraztekoa da RE eta BE balioak orokorrean proportzionalak direla, monomeroek konformazio bat baino gehiago aurkezten duren kasuetan izan ezik. Nola konplexuen lotura energia bere osagaien konformazioen baitan dagoen, kasu konkretu batzuk eman ahal dira non bi egitura RE antzekoa duten baina BE desberdinak. Monomeroak lotura energia handiagoak sortzen dituen baina ezegonkorragoa den egitura bat hartzen duenean ematen da fenomeno hau (ikusi 2.15 Irudia azalpen eskematiko baterako). Azkenik, 5 ekuazioa erabil daiteke sistema bateko lotura energia guztiak alderatzeko, isomero besteen lotura energiari (BE_i) lotura indar handiena duen egituraren balioa (BE_{SB}) kenduz.

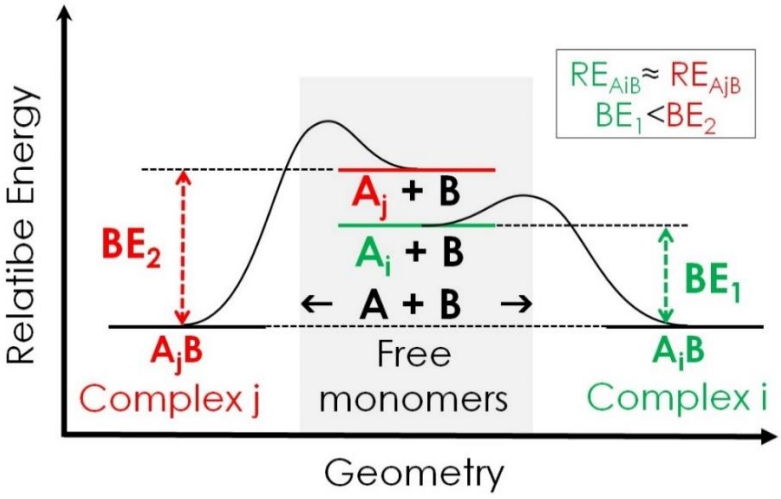

2.15 Irudia: Agregatu desberdinen lotura energien diagrama. Nahiz eta A_jB eta A_iB egonkortasun antzekoak izan, lotura energia desberdinak aurkezten dute.

Ikertutako sistema guztietan, molekulen egonkortasuna 0K baino tenperatura altuagotan kalkulatu egin da. Lan honetan zehar aurkeztutako emaitzak, molekulak baporizatzeko LD sistemak energia kantitate handiak sortzen dituela egiaztatu da. Talken bidezko hozketa prozesuan populazio "bero" honen zati bat atrapa dezake

minimo lokal gisa, zeinak tenperatura altuetan nolabaiteko egonkortasuna aurkezten duten. Hori dela eta, espezie horiek kontuan hartu behar dira emaitza esperimentalak doitzeko. Horretarako, agregatuen Gibbs energia askea eta Gibbs lotura energia askearen kalkuluak burutu dira, hurrengo ataletan azaltzen direnak.

2.3.3. Hozketa-konformazionala espantsio supersonikoan

Espantsio supersonikoen propietate nabarmenetako bat hozketaren eraginkortasun altua da. Hedatzen den gasa orekaz kanpoko egoera batetik igarotzen da, tenperaturaren atal errotazional eta bibrazionalen energia tenperatura translazionalera bihurtuz.[1] Orekatik kanpoko egoera hori lan honetan aztertutako sistemetan ere lortu da, laginak gas garraiatzailearekin espantsioan nahasten direnean. Metodologia esperimentalean azaldu den moduan, lagina berotuz gas egoerara pasatzen da, gas garraiatzailearekin nahastuz; edo laser desortzioaren bidez gas balbularen ostean, non hedatzen den gasa baporizatutako molekulak narrasten dituen. Balbula berotzen den sisteman, konformeroak oreka termodinamikoan aurkitzen dira balbularen zirrikituan. Egoera horretan, konformeroen populazioak Boltzmann banaketa bat jarraitzen dute tenperatura jakin baterako. Espantsio supersonikoan zehar, gas garraiatzailearekiko talkak molekulen maila errotazional eta bibrazionalen populazioak hozten dituzte, konformero egonkor batzuk harrapatuz.[38-40] Hala eta guztiz ere, espantsio supersonikoko azken konformero kopuruak bi alderdien araberakoa da: *(i)* populazioaren distribuzioa espantsioaren aurretik, eta *(ii)* isomerizazio energia-hesiaren altuera. Bigarren alderdiaren arabera, konformeroak harrapatuta gera daitezke energia-hesi altuak direla eta; edo konformeroen arteko isomerizazioa gerta daiteke molekulen eta gas garraiatzailearen arteko talka inelastikoek emandako energiari esker. Azaldutako egoera hauek hurrengo 2.16 Irudian aurkeztutako energia diagraman laburbilduta daude.

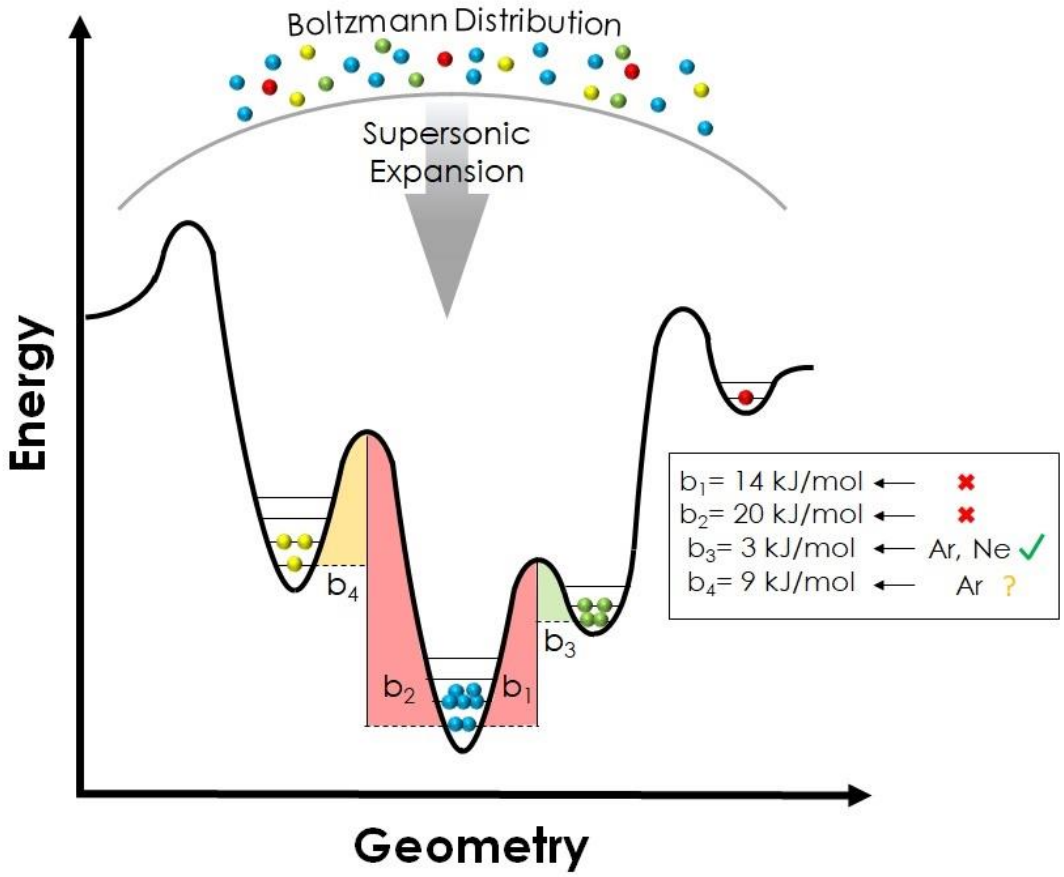

2.16 Irudia: Espantsio supersonikoan zehar ematen den hozketa konformazionalaren prozesuaren energia diagrama. Espantsioaren aurretiko banaketa konformazionala Boltzmann banaketa bati dagokio, tenperaturaren menpe. Kolorezko bolatxoak molekula baten konformero desberdinak irudikatzen dituzte, urdina egonkorren eta populatuen konformeroa izanda. Espantsio supersonikoa eman ondoren, gas garraiatzailearekiko talkak direla eta molekulak hozten dira, konformeroak harrapatuz energia-hesien artean. Kasu batzuetan, talkak emandako energia nahikoa izango da molekulak isomerizazio hesiak gainditzeko. Kontuan izanda gasaren abiadura espantsio supersonikoan ~Mach 2 dela, atomo bakar baten talka inelastikoak ematen duen energia zinetikoa b_3 eta b_4 hesiak zeharkatzea ahalbidetzen du.

Molekulak gas egoerara pasatzen direnean laser desortzio metodoen bitartez, ekuazioari ezezagun gehiago gehitzen dira, zeren eta ablazio luman molekulek tenperatura tarte zabalago bat aurkezten dutelako.[41] Tenperatura altu horiek beroketa prozesuaren antzeko isomerizazioak gertatzea ahalbidetzen du, nahiz eta lurrundutako molekulen hasierako tenperatura ezezaguna izan.

Tenperaturak konformeroen azken populazio mailan duen eragina aztertzeko, Gibbs energia askearen diagramak erabili dira, 0 eta 700 K-ko tenperatura tartean. Diagrama horiei esker tenperatura altuetan egonkor bilakatzen diren konformeroak aurkitzea ahalbidetzen dute, zeinek espektro esperimentalak azaltzeko garrantzitsuak izan liteke.

2.3.3.1. Gibbs lotura energia askea

6 eta 7 ekuazioak monomeroen Gibbs-en energia askeak determinatzeko erabili dira:

$$\Delta G_{Mono,i,T} = \Delta E_{Elec.,i} + \Delta E_{ZPE,i} + \Delta E_{ddH,i,T} - T \cdot \Delta S_{dS,i,T} \quad (6)$$

$$\Delta G_{Rel,Mono,i,T} = \Delta G_{Mono,i,T} - \Delta G_{GM,T} \quad (7)$$

6 ekuazioarekin, tenperatura (T) jakin batean i konformeroa duen molekula baten Gibbs energia askea lortzen da. Entalpiaren ekarpena ($\Delta E_{ddH,i,T}$) tenperatura bakoitzerako eta entropiaren ekarpena ($T \cdot \Delta S_{dS,i,T}$) zero puntuko zuzenketa duen energia elektronikoari gehitzen dira. Behin isomero guztien Gibbs energia askea lortuta, balio erlatiboak atera daiteke isomero bakoitzaren energiari ($\Delta G_{Mono,i,T}$) minimo globala ($\Delta G_{GM,T}$) kenduz gero. Gibbs energia askearen balio erlatiboak tenperaturaren funtzioan irudikatuz, 2.17 irudian agertzen den antzeko diagrama lortzen da. Horrez gain, ekuazio hauen erabilpena derrigorrezkoa da ondoren agregatuen Gibbs energia askea lortzeko.[42–44]

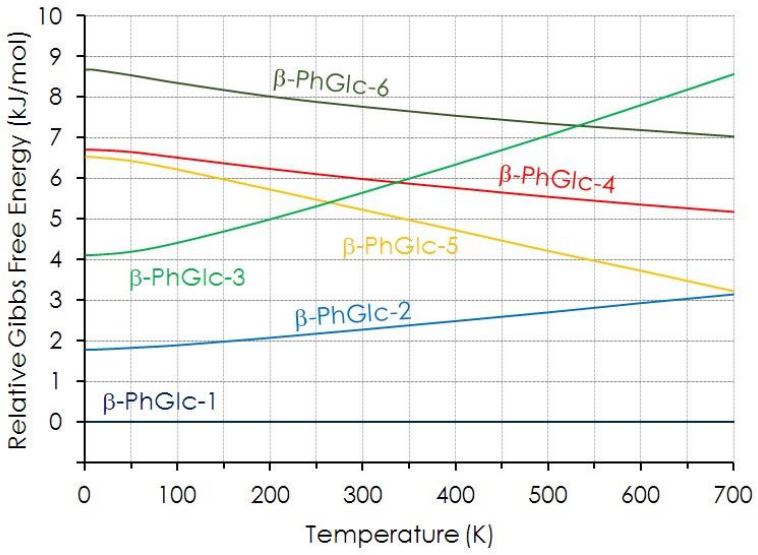

2.17 Irudia: PhGlc monomerorako Gibbs energia aske erlatibo diagramaren adibide bat. Konformazio bakoitzaren Gibbs energia askea 6 eta 7 ekuazioak jarraituz tenperatura desberdinetan kalkulatu da.

2.3.2 atalean azaldu den moduan, konplexu baten energia erlatiboaren kalkuluak bi egoera desberdinen arabera burutu daiteke: konplexua osatzen duten monomeroak konformazio bakarra dute, edo konformazio bat baino gehiago hartzen dute. Lehenengo kasuan, Gibbs energia aske erlatiboa ($\Delta\Delta G$) kenketa erraz batekin lortzen da. Baina, monomeroek konformazio bat baino gehiago izan ahal dutenean, termino berri bat sortzen da: Gibbs lotura-energia aske erlatiboa ($\Delta\Delta G_B$). Konplexu baten Gibbs energia askea hurrengo 8 ekuazioarekin kalkulatzen da. Antzeman daitekeen moduan,

monomeroen kasuan erabilitako terminoei BSSE zuzenketa kontuan hartzen duen terminoa gehitzen da:

$$\Delta G_{AB,i,T} = \Delta E_{Elec.,i} + \Delta E_{ZPE,i} + \Delta E_{BSSE,i} + \Delta E_{ddH,i,T} - T \cdot \Delta S_{dS,i,T} \quad (8)$$

Ondoren, balio erlatiboak lortu daiteke 9 ekuazioarekin, monomeroak konformazio bakarra aurkezten dutenean, edo 10 ekuazioarekin, monomeroak konformazio bat baino gehiago har dezaketenean:

$$\Delta\Delta G_{AB,i,T} = \Delta G_{AB,i,T} - (\Delta G_{A,T} + \Delta G_{B,T}) \quad (9)$$

$$\Delta\Delta G_{B\,AB,i,T} = \Delta G_{AB,i,T} - (\Delta G_{A,i,T} + \Delta G_{B,i,T}) \quad (10)$$

$$\Delta\Delta G_{Rel.,AB,i,T} = \Delta\Delta G_{AB,i,T} - \Delta\Delta G_{GM,AB,i,T} \quad (11)$$

11 ekuazioarekin lortzen diren datuak konplexu desberdinen egonkortasunen konparaketa ahalbidetzen du. Gibbs lotura-energia aske erlatiboa tenperaturaren funtzioan irudikatuz, 2.18 Irudian aurkezten diren diagramak lortzen dira. Diagrama hauei esker konformazio kopuru handi baten egonkortasunen konparaketa ahalbidetzen du tenperatura tarte zabal batean, zeinarekin espantsioan probabilitate altuarekin harrapatu ahal diren espezieen identifikazioa buru daitekeen.

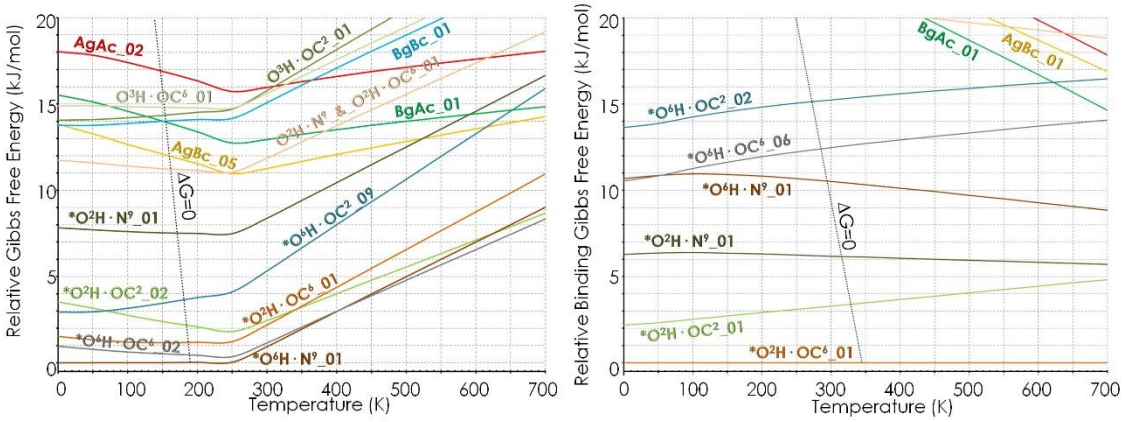

2.18 Irudia: Ezkerrean: Caf+PhGlc dimeroaren Gibbs energia aske erlatibo diagramaren adibidea. Kasu honetan, 9 ekuazioa erabili da. Eskuinean: Caf+PhGlc dimeroaren Gibbs lotura-energia aske erlatibo diagramaren adibidea, 10 ekuazioarekin lortuta. Ikusi nola nahiz eta konformero berdinak izan, bi metodoen artean egonkortasun erlatiboan desberdintasun handiak aurkezten diren.

2.3.4. Elkarrekintza ez-kobalenteen hurbilketa metodoa

Agregazio prozesuak gidatzen duten elkarrekintza intermolekularrak karakterizatzeko, mekanika kuantikoko kalkuluetatik lortutako dentsitate elektronikoa (ρ) aztertu daiteke. Elkarrekintza ez-kobalenteen (NCI) hurbilketa metodoa[45,46] elkarrekintza intermolekularrak ebaluatzen ditu dentsitate elektronikoan eta dentsitate gradiente murriztuan (s) oinarrituta. Azken honek dentsitate elektronikotik eta bere lehen deribatutik eskuratzen da:

$$s = \frac{1}{2(3\pi^2)^{1/3}} \frac{|\nabla\rho|}{\rho^{4/3}} \qquad (12)$$

Indar baxuko elkarrekintza inter-edo intramolekular daudenean, dentsitate gradiente murriztuan aldaketa nabarmen bat dago, dentsitate puntu kritikoak sortzen direlarik, zeinak minimo gisa agertzen diren. Hala ere, s vs ρ irudikatzean, dentsitate gradiente murriztuan agertzen diren minimoak azterketa sakonago bat behar dute, izan ere, elkarrekintza erakargarri eta aldaragarriak eremu berean agertzen direlako. Elektroi dentsitatearen matrize Heisiarraren bigarren balio propioaren (λ_2) zeinua gradientearen minimoaren natura azaltzen du: (-) elkarrekintza erakargarria denean, eta aldiz, (+) aldakorra denean.

Gradiente murriztua (s), dentsitate elektronikoaren (ρ) eta λ_2-ren zeinuaren arteko biderkaduraren funtzioan irudikatuz gero, 2.19 Irudian agertzen den moduko grafikoak lortzen dira. Matrize Heisiarraren bigarren balio propioaren zeinua positiboa edo negatiboa izan daiteke elkarrekintza motaren arabera: *(i)* lotura elkarrekintzak, hala nola, hidrogeno loturak, $\lambda_2 < 0$ denean agertzen dira; *(ii)* elkarrekintza ez-lotzaileak, hala nola, aldarapen esterikoak, $\lambda_2 > 0$ denean; eta *(iii)* elkarrekintza ahul deslokalizatuak, vdW elkarrekintzen kasuan, $\lambda_2 \leq 0$ denean. Hau guztia kontuan hartuta, λ_2 zeinuaren azterketa 2D NCI irudikapenetan elkarrekintza mota desberdinen identifikazioa ahalbidetzen du, ρ balioak elkarrekintzaren indarrari buruzko informazioa ematen duen bitartean.

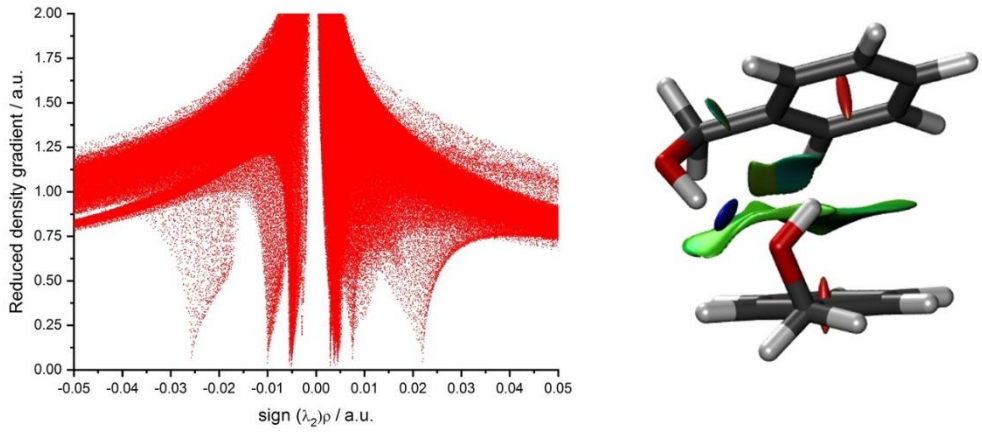

2.19 Irudia: Ezkerraldea: 2D NCI irudikapena. λ_2 balioak interakzio mota aurresaten du: elkarrekintza erakargarriak ezkerraldean agertzen dira, aldarakorrak eskuinaldean, eta vdW motako elkarrekintza ahulak zerotik hurbil. Eskuinaldea: Elkarrekintza ez-kobalenteen 3D-ko irudikapena. BGR kolore eskalarekin elkarrekintza motak sailkatzen dira. Adibide honetan, OH···O lotura urdin indartsu moduan agertzen da, bi eraztun aromatikoen arteko pilaketa elkarrekintzak gainazal berde baten moduan agertzen diren bitartean. Elkarrekintza aldarakorrak eraztun bakoitzaren barnealdean puntu gorri gisa agertzen dira. Gainazala s=0.5 balioarekin eraiki da, $-2.0 < \rho < 2.0$ au kolore eskalarekin.

Are gehiago, molekulen arteko elkarrekintza ez-kobalenteen 3D-ko irudikapen bat egin daiteke. Irudikapen hauetan, elkarrekintzak nukleoen arteko dentsitate gradiente murriztuaren gainazal gisa agertzen dira, daukaten indarraren arabera koloreztatuta BGR kode bat jarraituz: elkarrekintza eraginkorretarako kolore urdina, vdW elkarrekintza ahuletan berde kolorea, eta elkarrekintza aldarakorretan kolore gorria erabiltzen da. Kolorearen intentsitatea ematen den elkarrekintzaren sendotasuna adierazten du. Lan honetan aurkeztutako diagrama eta irudikapen guztiak NCI programarekin landu egin dira.

2.3.5. Espektroen simulazioa

DFT kalkuluen eta espektro esperimentalen arteko konparaketa laguntza handia da IR espektroen esleipena burutzeko. Ostera, konparazioak kalkuluen proba-banku gisa balio dute aldi berean, bien datuak egoera isolatuetatik lortzen baitira. MK kalkuluek optimizatutako geometrien bibrazio-maiztasun modu normalak ematen ditu. Hortaz, anharmonizitate eskala-faktore bat beharrezkoa esperimentuarekin konparaketa egin baino lehen. Faktore horiek metodo konputazionalen data-baseetatik eskuratu daiteke,[47] baina kasu honetan, zalantzarik gabeko esleipena duten molekulen datu esperimentalak erabiliz eskuratu dira faktore anharmonikoak.[48] Hurrengo 2.1 Taulan

maila OH, NH eta CH taldeen luzaketa-bibrazioetarako erabili diren eskala-faktoreak bildu dira, maila konputazional desberdinetan.

2.1 Taula: Anharmonizitatea kontuan hartzeko erabilitako eskala-faktoreak, maila konputazional desberdinetarako

Maila konputazionala (Metodoa/Base multzoa)	**OH eskala faktorea**	**NH eskala faktorea**	**CH eskala faktorea**
M06-2X/6-311++G(d,p)	0.935	0.953	0.953
M06-2X/def2TZVP	0.945	0.951	0.951
B3LYP-ED=GD3BJ/6-311++G(d,p)	0.954	0.963	0.963
B3LYP-ED=GD3BJ/def2TZVP	0.963	0.963	0.963
B3LYP-ED=GD3/cc-pVTZ	0.96	0.96	0.96
MN15/6-311++G(d,p)	0.937	0.953	0.953
MN15/def2TZVP	0.945	0.953	0.953
MP2/6-311++G(d,p)	0.945	0.951	0.951

Espektro esperimentalaren simulazio teorikoa burutzeko, zenbait pausu jarraitu dira. Lehenik, bibrazio-maiztasun bakoitza 5 cm^{-1}-ko zabalera duen funtzio Lorentziar batekin irudikatzen da. Ondoren, laserrak eragindako banda esperimentalen zabalera kontuan hartzen da. Nola erabilitako IR laserrak ~6cm^{-1} –ko profil Gaussiarra duenez, espektro teoriko osoa 6 cm^{-1}-ko zabalera duen funtzio Gaussiar batekin konboluzionatzen da. Azkenik, kontuan hartu behar da efektu anharmoniko sendoen edota energia maila txikiko modu bibrazionalen hozketa ez eraginkorrak sortutako banda esperimentalen zabalkuntza gehigarria. Fenomeno hau oso arrunta da agregatuetan, eta gorrirantzko lerrakuntzarekin areagotzen da (zeinak elkarrekintzaren indarrarekin erlazionatuta dagoen). Efektu hau simulazio teorikoan zuzentzeko, esperimentalki parametrizatutako funtzio koadratiko batetik lortutako zabalkuntza-faktorea erabili da (ikusi 2.20 Irudia).

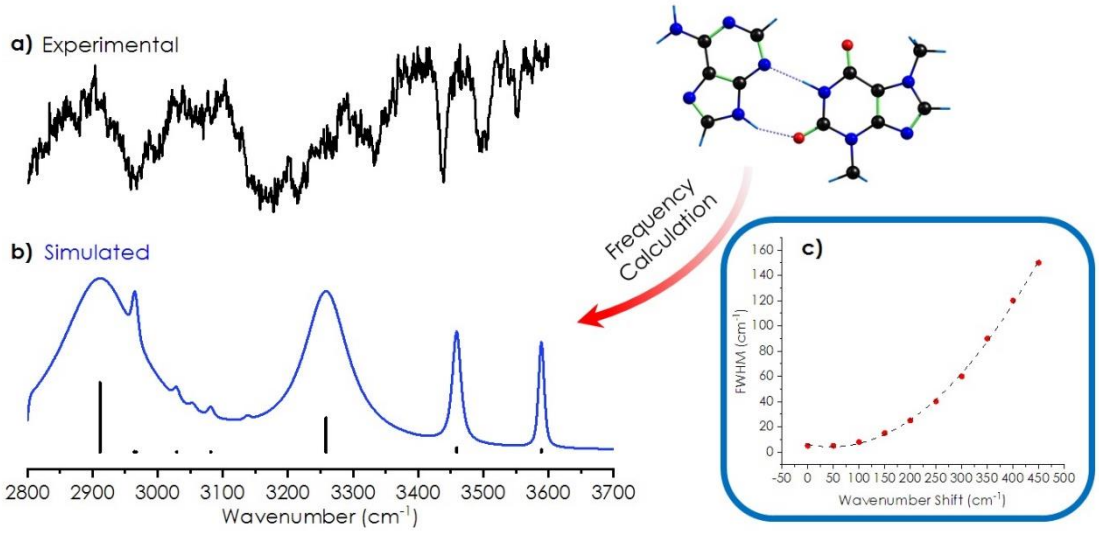

2.20 Irudia: Konformero baten espektro teorikoaren simulazioaren adibidea. Kalkulatutako bibrazio-maiztasunak funtzio Lorentziar (FWHM=5 cm^{-1}) batekin irudikatzen dira, geroago funtzio Gaussiar (FWHM=6 cm^{-1}) batekin konboluzionatu egiten dena. Azkenik, elkarrekintza batean parte hartzen duten modu bibrazionalen zabalkuntza funtzio koadratiko batetik (c) lortzen da.

2.4. Erreferentziak

[1] D. H. Levy, The spectroscopy of very cold gases., *Science*, 1981, **214**, 263–9.

[2] M. S. de Vries and P. Hobza, Gas-Phase Spectroscopy of Biomolecular Building Blocks, *Annu. Rev. Phys. Chem.*, 2007, **58**, 585–612.

[3] T. Ebata, Y. Inokuchi and A. Nakajima, in *Physical Chemistry of Cold Gas-Phase Functional Molecules and Clusters*, eds. T. Ebata and M. Fujii, Springer Singapore, Singapore, 2019, pp. 3–32.

[4] T. R. Rizzo and O. V Boyarkin, in *Gas-Phase IR Spectroscopy and Structure of Biological Molecules*, eds. A. M. Rijs and J. Oomens, Springer International Publishing, Cham, 2015, pp. 43–97.

[5] A. L. Patrick and N. C. Polfer, in *Gas-Phase IR Spectroscopy and Structure of Biological Molecules*, eds. A. M. Rijs and J. Oomens, Springer International Publishing, Cham, 2015, pp. 153–181.

[6] I. León, J. Millán, F. Castaño and J. A. Fernández, A Spectroscopic and Computational Study of Propofol Dimers and Their Hydrated Clusters, *ChemPhysChem*, 2012, **13**, 3819–3826.

[7] I. León, E. J. Cocinero, J. Millán, A. M. Rijs, I. Usabiaga, A. Lesarri, F. Castaño and J. A. Fernández, A combined spectroscopic and theoretical study of propofol·(H2O)3, *J. Chem. Phys.*, 2012, **137**, 74303.

[8] I. Leon, University of the Basque Country, 2011.

[9] I. Usabiaga, University of the Basque Country, 2017.

[10] I. Usabiaga, J. González, P. F. Arnáiz, I. León, E. J. Cocinero and J. A. Fernández, Modeling the tyrosine-sugar interactions in supersonic expansions: glucopyranose-phenol clusters., *Phys. Chem. Chem. Phys.*, 2016, **18**, 12457–12465.

[11] W. Demtröder, *Laser Spectroscopy*, 2003.

[12] J. M. Hollas, *Modern Spectroscopy*, 2004.

[13] D. M. Lubman and M. N. Kronick, Mass spectrometry of aromatic molecules with resonance-enhanced multiphoton ionization, *Anal. Chem.*, 1982, **54**, 660–665.

[14] R. Tembreull and D. M. Lubman, Use of resonant two-photon ionization with supersonic beam mass spectrometry in the discrimination of cresol isomers, *Anal. Chem.*, 1984, **56**, 1962–1967.

[15] J. Yao, H. S. Im, M. Foltin and E. R. Bernstein, Spectroscopy of Neurotransmitters and Their Clusters: Phenethylamine and Amphetamine Solvation by Nonpolar, Polar, and Hydrogen-Bonding Solvents, *J. Phys. Chem. A*, 2000, **104**, 6197–6211.

[16] R. T. Kroemer, K. R. Liedl, J. A. Dickinson, E. G. Robertson, J. P. Simons, D. R. Borst and D. W. Pratt, Conformationally Induced Changes in the Electronic Structures of Some Flexible Benzenes. A Molecular Orbital Model, *J. Am. Chem. Soc.*, 1998, **120**, 12573–12582.

[17] J. Leszczynski, Handbook of computational chemistry, *Handb. Comput. Chem.*, 2012, 1–1430.

[18] V. Barone, R. Improta and N. Rega, Quantum Mechanical Computations and Spectroscopy: From Small Rigid Molecules in the Gas Phase to Large Flexible Molecules in Solution, *Acc. Chem. Res.*, 2008, **41**, 605–616.

[19] J. F. Dobson, G. Vignale and M. P. Das, *Electronic Density Functional Theory*, Springer US, Boston, MA, 1998.

[20] K. Vanommeslaeghe, O. Guvench and A. D. MacKerell, Molecular Mechanics, *Curr. Pharm. Des.*, 2014, **20**, 3281–3292.

[21] L. Schro dinger, 2020.

[22] E. Harder, W. Damm, J. Maple, C. Wu, M. Reboul, J. Y. Xiang, L. Wang, D. Lupyan, M. K. Dahlgren, J. L. Knight, J. W. Kaus, D. S. Cerutti, G. Krilov, W. L. Jorgensen, R. Abel and R. A. Friesner, OPLS3: A Force Field Providing Broad Coverage of Drug-like Small Molecules and Proteins, *J. Chem. Theory Comput.*, 2016, **12**, 281–296.

[23] T. A. Halgren, Merck molecular force field. I. Basis, form, scope, parameterization, and performance of MMFF94, *J. Comput. Chem.*, 1996, **17**, 490–519.

[24] D. A. Case, T. E. Cheatham III, T. Darden, H. Gohlke, R. Luo, K. M. Merz Jr., A. Onufriev, C. Simmerling, B. Wang and R. J. Woods, The Amber biomolecular simulation programs, *J. Comput. Chem.*, 2005, **26**, 1668–1688.

[25] K. N. Kirschner, A. B. Yongye, S. M. Tschampel, J. González-Outeiriño, C. R. Daniels, B. L. Foley and R. J. Woods, GLYCAM06: A generalizable biomolecular force field. Carbohydrates, *J. Comput. Chem.*, 2008, **29**, 622–655.

[26] Y. Zhao and D. G. Truhlar, The M06 suite of density functionals for main group thermochemistry, thermochemical kinetics, noncovalent interactions, excited states, and transition elements: Two new functionals and systematic testing of four M06-class functionals and 12 other function, *Theor. Chem. Acc.*, 2008, **120**, 215–241.

[27] S. Grimme, J. Antony, S. Ehrlich and H. Krieg, A consistent and accurate ab initio parametrization of density functional dispersion correction (DFT-D) for the 94 elements H-Pu, *J. Chem. Phys.*, 2010, **132**, 154104.

[28] A. Camiruaga, I. Usabiaga, A. Insausti, I. León and J. A. Fernández, Sugar–peptidic bond interactions: spectroscopic characterization of a model system, *Phys. Chem. Chem. Phys.*, 2017, **19**, 12013–12021.

[29] I. Usabiaga, J. González, I. León, P. F. Arnaiz, E. J. Cocinero and J. A. Fernández, Influence of

the Anomeric Conformation in the Intermolecular Interactions of Glucose, *J. Phys. Chem. Lett.*, 2017, **8**, 1147–1151.

[30] I. Usabiaga, A. Camiruaga, A. Insausti, P. Çarçabal, E. J. Cocinero, I. León and J. A. Fernández, Phenyl--D-glucopyranoside and Phenyl--D-galactopyranoside Dimers: Small Structural Differences but Very Different Interactions, *Front. Phys.*, 2018, **6**, 3.

[31] E. Caldeweyher, C. Bannwarth and S. Grimme, Extension of the D3 dispersion coefficient model, *J. Chem. Phys.*, 2017, **147**, 34112.

[32] S. Grimme, S. Ehrlich and L. Goerigk, Effect of the damping function in dispersion corrected density functional theory, *J. Comput. Chem.*, 2011, **32**, 1456–1465.

[33] I. Uriarte, A. Insausti, E. J. Cocinero, A. Jabri, I. Kleiner, H. Mouhib and I. Alkorta, Competing Dispersive Interactions: From Small Energy Differences to Large Structural Effects in Methyl Jasmonate and Zingerone, *J. Phys. Chem. Lett.*, 2018, **9**, 5906–5914.

[34] T. Forsting, H. C. Gottschalk, B. Hartwig, M. Mons and M. A. Suhm, Correcting the record: the dimers and trimers of trans-N-methylacetamide, *Phys. Chem. Chem. Phys.*, 2017, **19**, 10727–10737.

[35] B. Hartwig, M. Lange, A. Poblotzki, R. Medel, A. Zehnacker and M. A. Suhm, The reduced cohesion of homoconfigurational 1,2-diols, *Phys. Chem. Chem. Phys.*, 2020, **22**, 1122–1136.

[36] F. Kollipost, K. E. Otto and M. A. Suhm, A Symmetric Recognition Motif between Vicinal Diols: The Fourfold Grip in Ethylene Glycol Dimer, *Angew. Chemie*, 2016, **128**, 4667–4671.

[37] H. S. Yu, X. He and D. G. Truhlar, MN15-L: A New Local Exchange-Correlation Functional for Kohn–Sham Density Functional Theory with Broad Accuracy for Atoms, Molecules, and Solids, *J. Chem. Theory Comput.*, 2016, **12**, 1280–1293.

[38] S. F. Boys and F. Bernardi, The calculation of small molecular interactions by the differences of separate total energies. Some procedures with reduced errors, *Mol. Phys.*, 1970, **19**, 553–566.

[39] R. Campargue, Progress in overexpanded supersonic jets and skimmed molecular beams in free-jet zones of silence, *J. Phys. Chem.*, 1984, **88**, 4466–4474.

[40] R. E. Smalley, L. Wharton and D. H. Levy, Molecular optical spectroscopy with supersonic beams and jets, *Acc. Chem. Res.*, 1977, **10**, 139–145.

[41] D. Patterson and J. M. Doyle, Cooling molecules in a cell for FTMW spectroscopy, *Mol. Phys.*, 2012, **110**, 1757–1766.

[42] R. Srinivasan and B. Braren, Ultraviolet laser ablation of organic polymers, *Chem. Rev.*, 1989, **89**, 1303–1316.

[43] P. Çarçabal, E. J. Cocinero and J. P. Simons, Binding energies of micro-hydrated carbohydrates: measurements and interpretation, *Chem. Sci.*, 2013, **4**, 1830–1836.

[44] P. D. Godfrey and R. D. Brown, Proportions of Species Observed in Jet Spectroscopy–Vibrational Energy Effects: Histamine Tautomers and Conformers, *J. Am. Chem. Soc.*, 1998, **120**, 10724–10732.

[45] http://www.nist.gov/mml/csd/informatics_research.

[46] J. Contreras-García, E. R. Johnson, S. Keinan, R. Chaudret, J.-P. Piquemal, D. N. Beratan and W. Yang, NCIPLOT: A Program for Plotting Noncovalent Interaction Regions, *J. Chem. Theory Comput.*, 2011, **7**, 625–632.

[47] R. Chaudret, B. de Courcy, J. Contreras-García, E. Gloaguen, A. Zehnacker-Rentien, M. Mons and J.-P. Piquemal, Unraveling non-covalent interactions within flexible biomolecules: from electron density topology to gas phase spectroscopy, *Phys. Chem.*

Chem. Phys., 2014, **16**, 9876–9891.

[48] NIST Standard Reference Database, Computational Chemistry Comparison and Benchmark DataBase, https://cccbdb.nist.gov/vibscalejust.asp.

[49] I. Usabiaga, A. Camiruaga, C. Calabrese, A. Maris and J. A. Fernández, Exploring Caffeine–Phenol Interactions by the Inseparable Duet of Experimental and Theoretical Data, *Chem. - A Eur. J.*, 2019, **25**, 14230–14236.

3. Kapitulua

Alkohol aromatikoen agregazioa

Argitaratzeko artikulua prestaketan

3.1. Sarrera

Elkarrekintza ez-kobalente garrantzitsuenetariko bat OH···O hidrogeno lotura da, hidroxilo taldea sarritan aurkitzen den funtsezko talde kimikoa delako. Era berean, OH···O elkarrekintza lotura indar handia aurkezten du, antzeko elkarrekintzekin alderatuta, hala nola, NH···N edo CH···O/N elkarrekintzak. Hortaz, elkarrekintza mota horren karakterizazioak garrantzi handia du sistema biologiko konplexuen agregazioak (azukreak, proteinak, etab.) ulertzeko. Atal honetan alkohol aromatikoen arteko agregazio prozesua deskribatzen da, non indar nagusia OH···O interakzioa da. Gainera, molekulen sinpletasun erlatiboak elkarrekintza isolatzeko eta haren egitura parametroak hobeto karakterizatzeko aukera ematen digu, espantsio supersonikoetan masan bereizgarriak diren laser espektroskopia teknikak eta kalkulu kuantikoak konbinatuz.

Kapitulu honetan, bentzil alkohol (BnzA) eta 2-feniletanol (PEAL) konposatuen agregazio prozesuaren karakterizazioa aurkezten dira. Biak alkohol alifatikoak dira, eraztun aromatiko bat txertatuta dutenak, eta haien azterketa fase isolatuan aurreko alkohol konplexuei buruzko ikasketen jarraipen gisa har daiteke.[1–5] Nahiz eta sinpleak izan, bi talde aipagarri aurkezten dute elkarrekintza ez-kobalenteak sortzeko: hidroxilo talde terminala, eta eraztun aromatikoa. Alde batetik, molekula horiek OH···O hidrogeno lotura sendoak eta hidrogeno-sare egonkorrak eratzea espero liteke. Antzinako ikerketak lotura-sare horiek ohikoak ez diren konplexu antolatuak eratzearen erantzule direla erakutsi zuten.[6,7] Bestetik, eraztun aromatikoko dentsitate elektroniko altua elkarrekintza gune deigarria ere bada, ez bakarrik π-π pilaketa elkarrekintzak sortzeko ahalmena duena, baizik eta OH···π motakoak sor ditzake. Azken horiek OH···O elkarrekintzak baino ahulagoak dira orokorrean, baina lotura sortzeko eskakizun gutxiago ditu hidroxilo taldearen erasoaren ikuspuntuari dagokionez.

Bi alkohol molekulen arteko desberdintasuna OH taldearen eta eraztun aromatikoaren bitarteko urrungailuaren luzera da: CH_2 bakarra BnzA-an, eta CH_2CH_2 PEAL-aren kasuan. Nahiz eta aldaketa txikia izan, PEAL-ari askatasun gradu eta malgutasun handiagoak ematen dio, panorama konformazional konplexuagoa eratuz. Zailtasun gehigarri gisa, bi molekulen estereoisomeria elkarrekintza familia baten konbinazio posibleen kopurua handitzen du. Gure helburua alkohol aromatiko horien agregatuak karakterizatzea da, OH/eraztun aromatiko lehiaketa eta alkil katearen luzeraren eragina aztertuz prozesu horretan zehar.

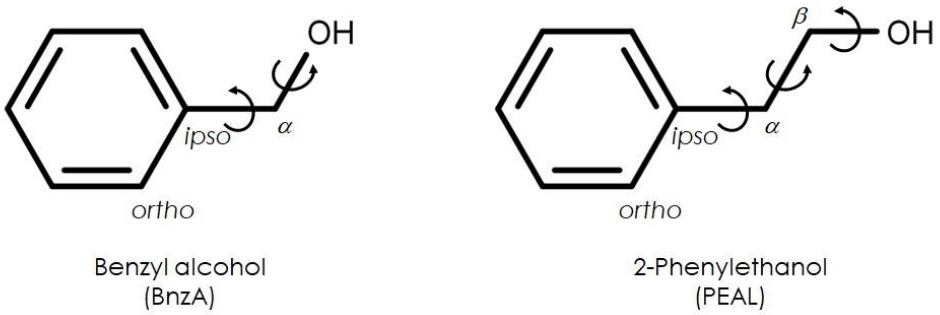

3.1. Irudia: Bentzil alkohol eta 2-feniletanol konposatuen eskema, atomoen izendapenarekin batera.

3.2. Bentzil alkoholaren espektroskopia

Atal honetan aurkeztutako emaitzak beroketa balbula bat erabiliz lortu ziren. Paper xurgatzaile zati bat bentzil alkohol (Sigma Aldrich, 98%) mL batzuekin busti eta balbularen lagin konpartimentuan kokatu zen. Kondentsazioa ekiditeko eta laginaren lurrunketa prozesua areagotzeko, lagin konpartimentua eta balbula 80°C-taraino berotu ziren. Gas garraiatzaile gisa He erabili zen, 1.5 bar-eko atzerako presioarekin.

3.2.1. Bentzil alkohol monomeroa

Bernstein et al.,[8] C.E.H. Dessent et al.[9] eta M. Mons et al. [10] BnzA eta bere homo-dimeroa aldez aurretik ikertu zuten MRES teknikarekin. BnzA-aren formarik egonkorrena hidroxilo taldea *gauche* konformazioan aurkezten zuela ondorioztatu zuten (ikusi 3.2. Irudia). Lan honen lehenengo pausua aurreko ikerketa horiek erreproduzitzea izan zen, gure esperimentuaren errendimendua egiaztatzeko eta baldintza esperimentalak optimizatzeko. Lortutako datu esperimentalak monomeroan DFT kalkuluak probatzeko erabili ziren.

BnzA bi angelu diedro ditu: $C_{ortho}C_{ipso}C_{\alpha}O$ and $C_{ipso}C_{\alpha}OH$. Beraz, BnzA-ren konformazioak $C_{ipso}C_{\alpha}$ eta $C_{\alpha}O$ loturen biraketen ondorioz lortzen dira. Kalkuluek bi konformazio egonkor baino ez dituzte erakusten. Minimo orokorrean, $-CH_2OH$ taldeak *gauche* antolamendua aurkezten du (ikusi BnzA_01 egitura 3.2 Irudian). Talde horrek eraztunarekiko sortzen duen angeluaren arabera, ispilu irudi bat agertzen da. Egitura honen egonkortasun gehigarria $C_{ortho}H\cdots O$ interakzio ahularen sorreratik dator.

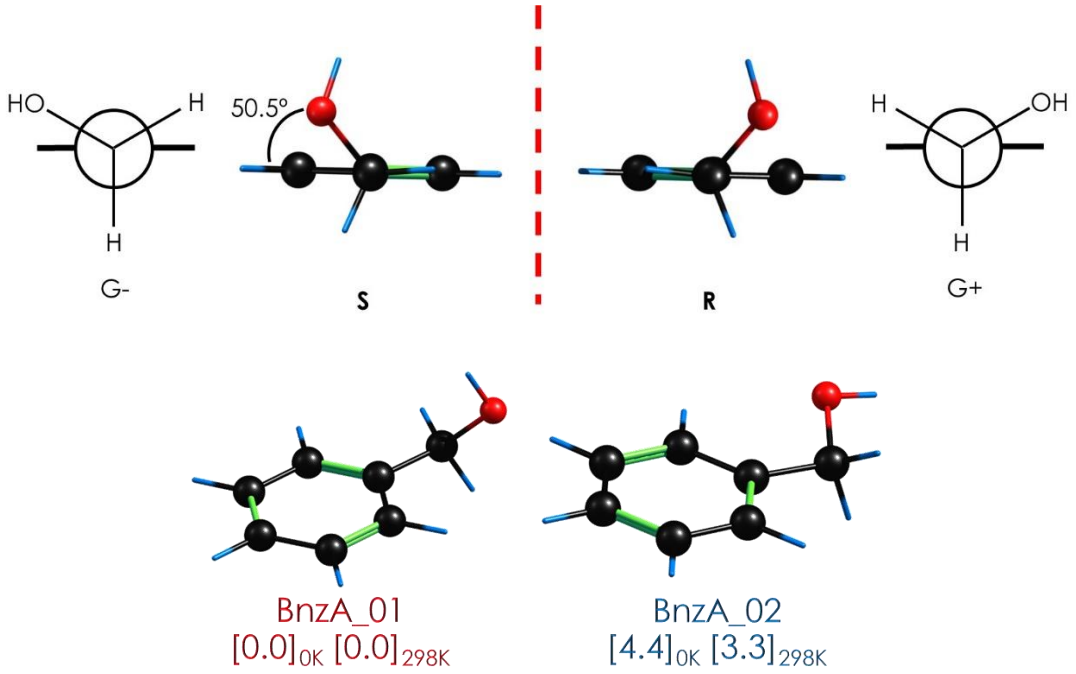

3.2 Irudia: Bentzil alkoholaren egitura egonkorrenak. B3LYP(ED=GD3BJ)/6-311++G(d,p) mailan kalkulatutako energia balioak kJ/mol-etan ematen dira.

Trans konformazioan (BnzA_02), hidroxilo taldeak eraztun aromatikoko kontrako aldera seinalatzen du, konformazio hedatu moduan ezagutzen dena.

BnzA-aren espektroskopia miaketa elektronikoaren emaitzak 3.3 Irudian aurkitzen dira. BnzA monomeroaren bi-koloreko REMPI espektroak jatorrizko banda (0_0^0) bat aurkezten du 37528 cm^{-1} uhin luzeran, aldez aurreko ikerketekin bat datozena.[8–10] Jatorrizko trantsizio horrek banda bibronikoz osatutako progresio batekin batera agertzen da. Gorrira agertzen diren intentsitate baxuagoko absortzioak erlaxatu gabeko modu bibrazionalei eta tamaina handiagoko konplexuen zatiketari dagozkie.[10]

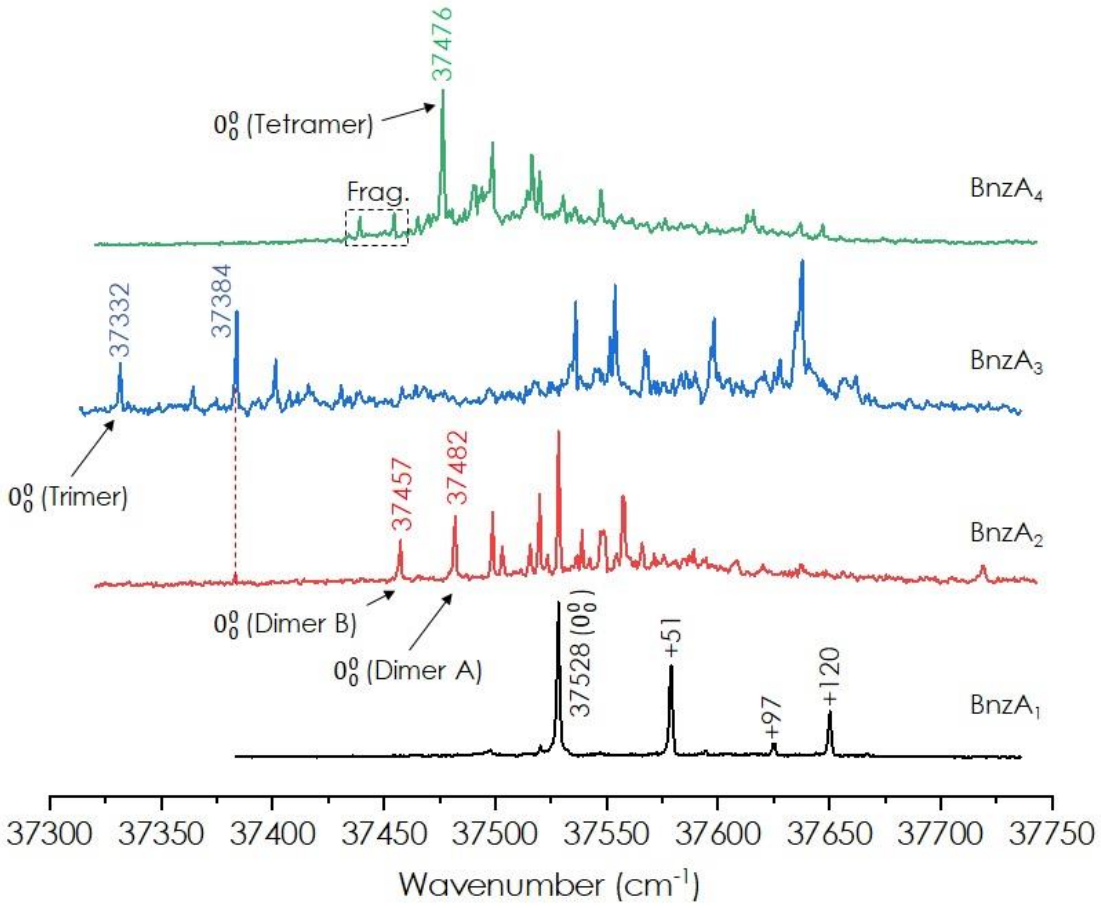

3.3 Irudia: BnzA eta tetramerorainoko konplexuen bi-koloreko REMPI espektroa, 37300 eta 37750 cm^{-1} tartean. Ionizazio laserra 35714 cm^{-1}-tan finkatu zen.

Absortzio espektro elektronikoa neurtu ondoren, IR/UV erresonantzia bikoitzeko teknika erabili egin da jatorrizko bandan frogatuz, IR espektroa lortzeko. Teknika horri esker lorturiko emaitzekin detektatutako espezien egitura esleitu eta metodo konputazionalak kalibratu ahal dira. Izan ere, elkarrekintza intermolekular baten ondorioz, OH trantsizio bibrazionalak pairatzen duten lerrakuntza gorrira eratutako loturaren indarrarekin zuzenean erlazionatuta dago.

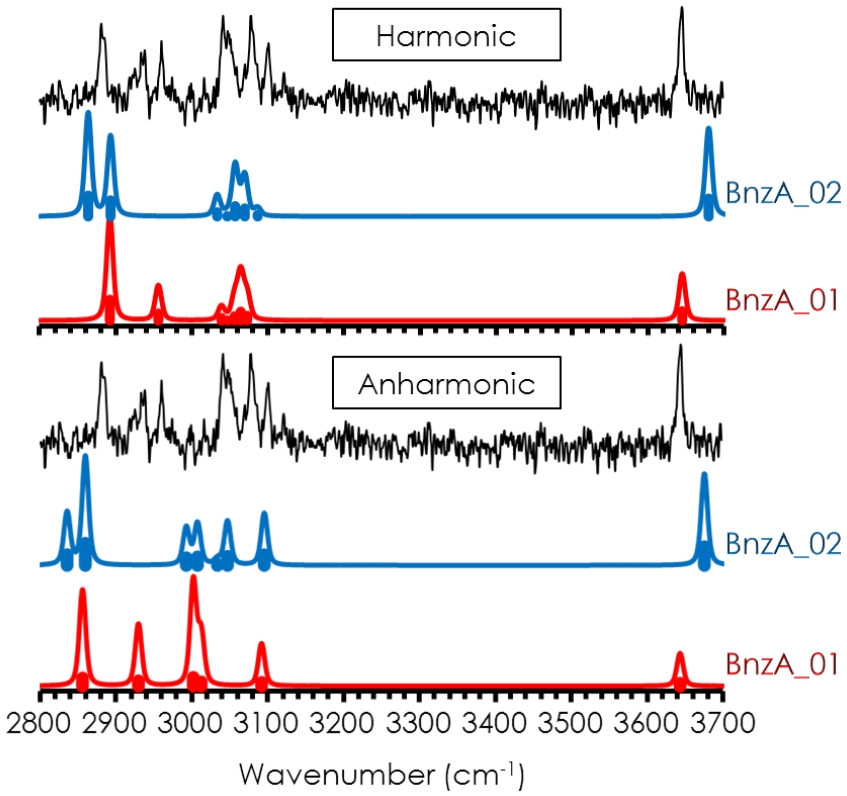

3.4 Irudia: Bentzil alkoholaren IDIR espektroak, kalkulu harmoniko eta anharmonikoekin alderatuta. Espektroen simulazioak B3LYP(ED=GD3BJ)/6-311++G(d,p) mailan egin dira. Kalkulu harmonikoen kasuan, 0.954-ko faktorea erabili egin da OH eta CH taldeen anharmonizitatea ekiditeko. Aldiz, kalkulu anharmonikoetan, inolako faktorerik ez ziren behar.

3.4 Irudian ikusi daitekeenez, CH eta OH taldeen luzaketa-bibrazioak barne hartzen ditu. OH eremuan, banda bakarra agertzen da 3645 cm^{-1}. Harrigarria da IR espektro esperimentalaren eta teorikoaren arteko adostasuna BnzA_01 egiturarako. Hortaz, 3645 cm^{-1} agertzen den banda OH taldearen luzaketa-bibrazioari esleitu egin da. Horrek esan nahi du banda hori etanolaren bibraziotik 25 cm^{-1}-ko lerrakuntza aurkezten duela, zeinak 3670 cm^{-1} inguru agertzen dena.[11] Hala ere, egindako esleipena aurretik argitaratutako ikerketekin bat datoz.[10] Behatutako lerrakuntza OH taldearen bibrazioan CH···O elkarrekintza ahul baten ondorioz, edota CO loturaren eta eraztun aromatikoaren arteko hiperkonjugazioaren ondorioz gerta daiteke.

Molekularen tamaina txikia abantaila moduan hartuta, bibrazio-maiztasun anharmonikoen kalkulua burutu da, Gaussian 16 programan ezarritako algoritmoak erabiliz.[12,13] Nahiz eta CH eremuaren predikzio teorikoen fidagarritasuna baxua izan, OH taldearen bibrazio-maiztasunen kalkuluak espektro esperimentalarekin duten adostasuna primerakoa da.

3.2.2. Bentzil alkohol dimeroa

Isolatutako BnzA-ren konformazioa gure baldintza esperimentaletan identifikatu ondoren, eta dimeroa aztertu baino lehen, monomeroaren kiralitatea kontuan hartu behar da. Jadanik 3.2 Irudian aurkeztu den moduan, ispilu-irudiak diren bi konformazio agertzen dira CH_2OH taldearen angeluaren arabera (G- eta G+ izendatuta). Enantiomero horiek espektroskopikoki berdinak dira, baina dimerizazioaren ondorioz, momentuko kiralitatea espektroskopikoki desberdindu daitekeen bi homo- edo hetero-dimeroak sortzen ditu. BnzA-ren *gauche* konformaziotik lau konbinazio posible daude: G-G+, G+G-, G+G+ eta G-G-, zeinak bikoteetan sailkatu ahal diren homo- eta hetero-dimeroetan, espektroskopikoki banan daitezkeen diastereoisomeroak direnak (3.5 Irudia).

BnzA dimeroaren energia potentzialaren gainazala (*Potential Energy Surface*, PES) B3LYP/6-311++G(d,p) maila konputazionalean aztertu egin da, eta optimizatutako egiturak elkarrekintza motaren arabera sailkatu egin dira. 3.6 Irudiak familia bakoitzaren egitura egonkorrenak aurkezten ditu. Arreta berezia jarri da lehen familiaren agregazio hetero-kiralean (kutxa gorria). Enantiomero puruak (CH_2OH taldearen eta eraztunaren inbertsioa) ez dira kontuan hartu, izan ere, espektroskopikoki bereizgarriak ez direlako. Antzeman daitekeen moduan, G-G+ egitura (BnzA2_dias1) ezegonkorra dirudi, eta honen optimizazioa minimo orokorrean amaitu da.

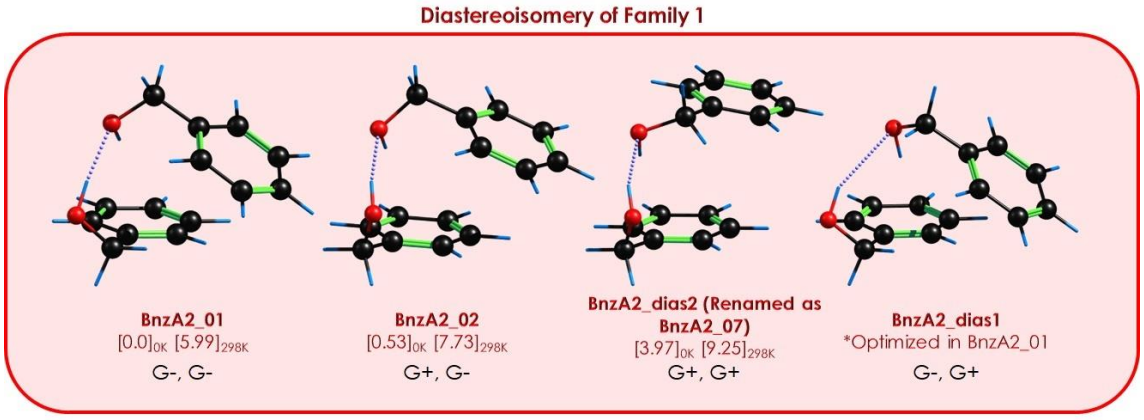

3.5 Irudia: $BnzA_2$ familia egonkorrenaren egitura diastereoisomerikoak, at B3LYP(ED=GD3BJ)/6-311++G(d,p) mailan kalkulatuta. Energia balioak kJ/mol-etan ematen dira.

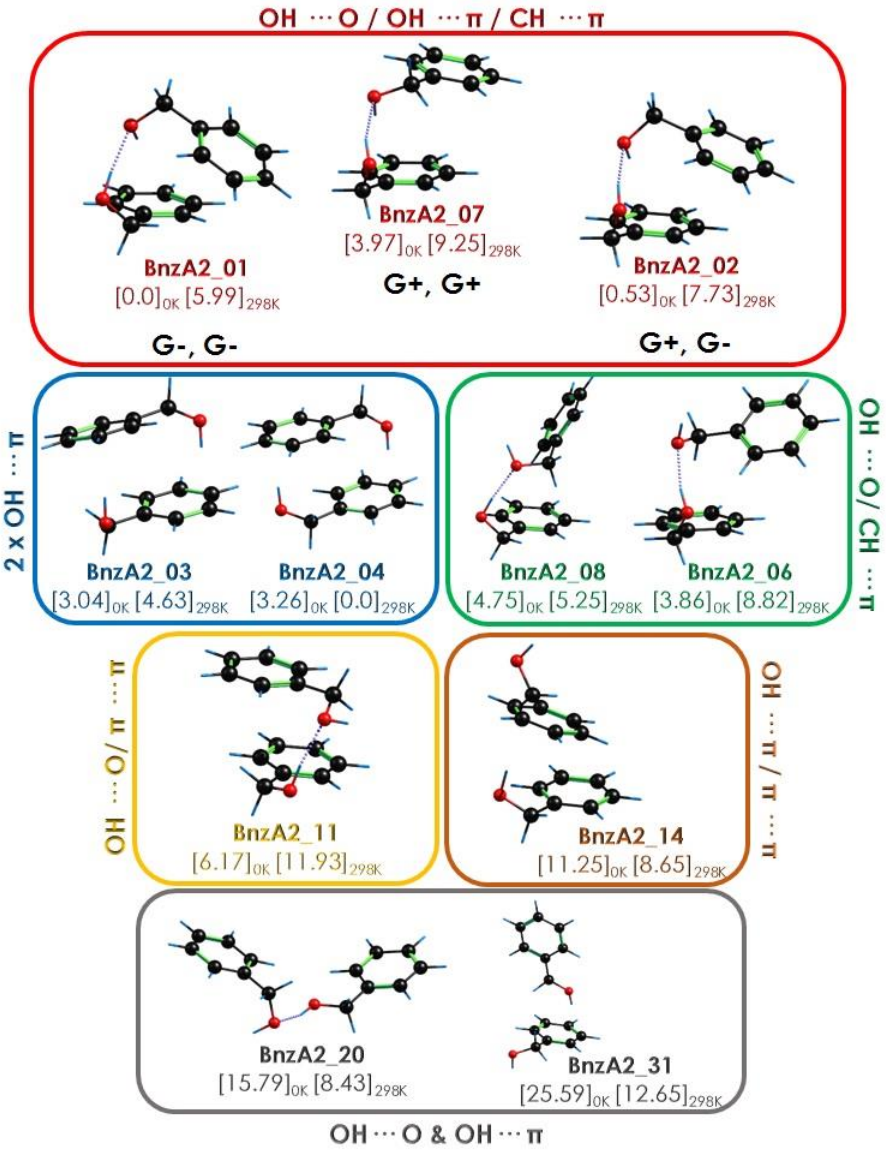

3.6 Irudia: Bentzil alkohol dimeroarentzako aurkitutako familien egitura esanguratsuenak. Bai egiturak zein familiak, aurkezten duten elkarrekintzen arabera sailkatu egin dira. Egitura guztiak B3YLP(ED=GD3BJ)/6-311++G(d,p) mailan optimizatu ziren. Balio energetikoak kJ/mol-etan ematen dira.

Ikusi daitekeenez, interakzio nagusia O-H···O hidrogeno lotura da, eta horrekin batera, bigarren hidroxilo taldeak eraztunarekin duen O-H···π elkarrekintza eta C(sp^2)-H···π elkarrekintza sekundarioa. Agian, O-H···π molekula emailearen eraso-angeluarekiko tolerantzia handiagoa duelako, edo O-H···O loturaren indar antzekoa dela eta, bi O-H···π elkarrekintzez osatutako isomeroak ez daude oso altu energian, minimo globalarekin konparatuz gero. BnzA2_06 eta BnzA2_08 egiturak interesgarriak dira, agregatua hazten ari den bitartean duten garrantziagatik (ikusi 3.2.3 atala). Egitura horietan, OH···π

elkarrekintza π···π pilaketa elkarrekintza bat ordezten du, OH···O hidrogeno lotura maximizatzen den bitartean.

3.7 Irudian BnzA dimeroaren bi koloretako REMPI espektroa aurkezten da. Monomeroaren absortzioarekin alderatuta, trantsizio bibroniko gehiago ditu. Horrelako banda-bilduma aberats bat jet supersonikoak konformazio egonkor bat baino gehiago isolatzetik edo espezie handiagoen zatiketatik sor daiteke. Konformero edo espezie kopurua determinatzeko, "UV/UV hole burning" teknika erabili da. Horren emaitza gisa, bi REMPI espektro lortu dira (lerro gorri eta urdina) laserra 37528 eta 37457 cm^{-1}-tan frogatuz gero, zeinak izartxo urdin eta gorriaz espektroan markatu direnak. Trantsizioak 37457 eta 37482 cm^{-1}-tan 1 eta 2 isomeroen jatorrizko banda moduan kontuan hartu dira, hurrenez hurren. Jatorrizko banda horiek gorrirantz desplazatuta daude (-71 cm^{-1} 1 isomerorako eta -46 cm^{-1} 2 isomerorako) monomeroaren jatorrizko bandarekin alderatuta (37528 cm^{-1}). Horrek eraztun aromatikoarekiko interakzio bat dagoela adierazten du, indar dispertsiboen eraginez. Gorrialderantz agertzen den lehen banda, 37383 cm^{-1}-tan kokatua, trimeroaren zatiketari dagokio, agregatu guztien REMPI espektroen konparaketan antzeman daitekeen moduan (ikusi 3.3 Irudia).

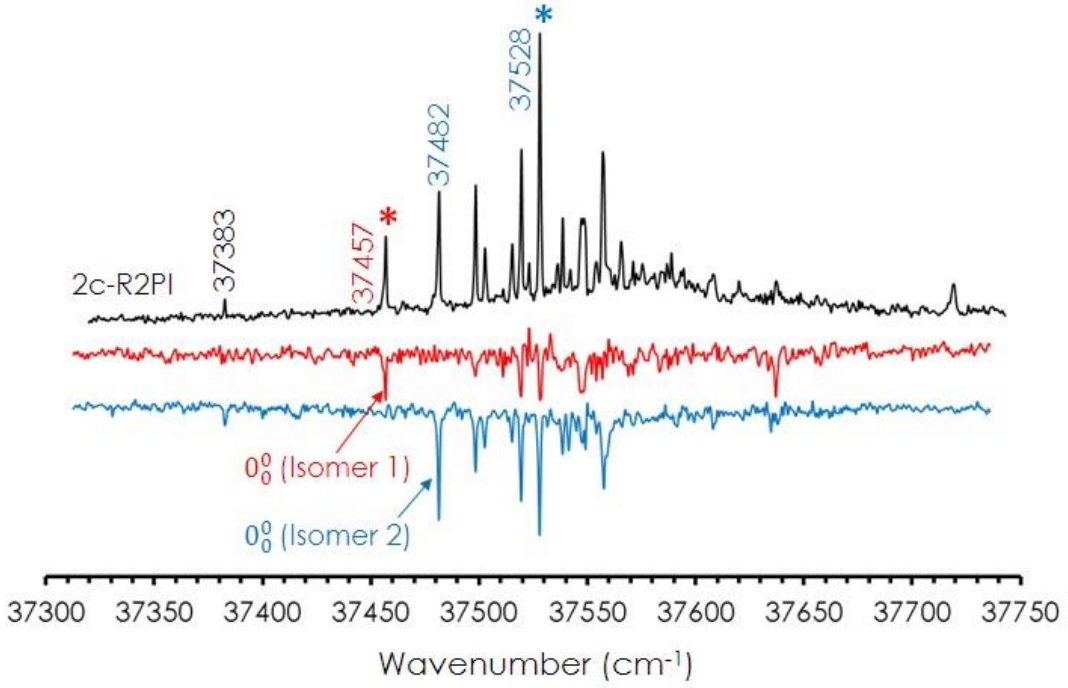

3.7 Irudia: Bentzil alkohol dimeroaren bi-koloreko REMPI espektroa, "UV/UV hole burning" esperimentuetan banandutako isomeroen REMPI espektroekin batera. Ionizazio laserra 35714 cm^{-1}-tan finkatu zen. 37457 eta 37528 cm^{-1} trantsizioak zundatu ziren "UV/UV hole burning" esperimentuetan lerro gorri eta urdinak lortzeko, hurrenez hurren

Egiturari buruzko ahalik eta informazio handiena ateratzeko, isolatutako bi dimeroen IDIR espektroa neurtu ziren OH eta CH luzaketa-bibrazio eremuan. Lortutako IR espektroak UV laserra 37457 cm^{-1}-tan (izartxo gorria) eta 37528 cm^{-1}-tan (izartxo urdina) zundatuz hurrengo 3.8 Irudian aurkezten dira. Gainerako trantsizioak ere aztertu ziren, baina guztiak jadanik aurkeztutako espektro berdinak aurkezten zuten.

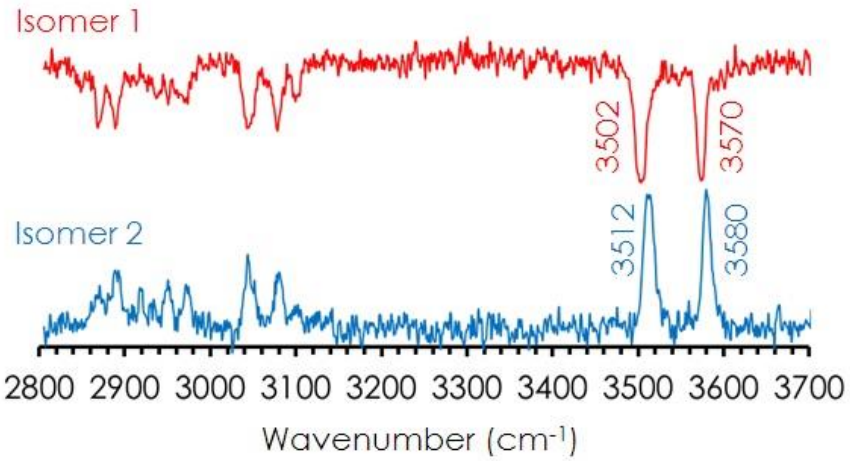

3.8 Irudia: Bentzil alkohol dimeroaren IDIR espektroak. Espektro urdina buelta emanda dago, bi espektroen banden arteko konparaketa hobetzeko.

Espektro horietan, OH eremuan bi banda agertzen dira, eta ondo ebatzitako CH banda batzuk ere behagarriak dira. Uhin-luzera altuetan begirada bat emanez gero, nabarmena den aldaketa txiki bat dago bi espektroen banden posizioan: espektro gorriaren OH bandak 10 cm^{-1} desplazatuta daude.

Datu teorikoekin edozein konparaketa egin baino lehen, datu esperimentalak erabili ahal dira dimeroen egiturari buruz hausnarketa bat egiteko. 1 isomeroaren espektroan bi OH banda argi ikus daitezke. Ziur aski, ~3580 cm^{-1}-tan agertzen dena interakzio ahulago bat aurkezten du ~3512 cm^{-1}-tan agertzen dena baino. Izan ere, OH bandaren lerrakuntza hidroxilo taldeak parte hartzen duen interakzioaren indarrarekin guztiz erlazionatuta dago. Hortaz, gorrialderantz gehiago lerrokatu den banda, ~3512 cm^{-1}-tan, OH···O motako elkarrekintza bati dagokiola; eta, aldiz, ~3580 cm^{-1}-tan agertzen den banda ahulagoa den OH···π elkarrekintza baten ondorioa dela esan daiteke.

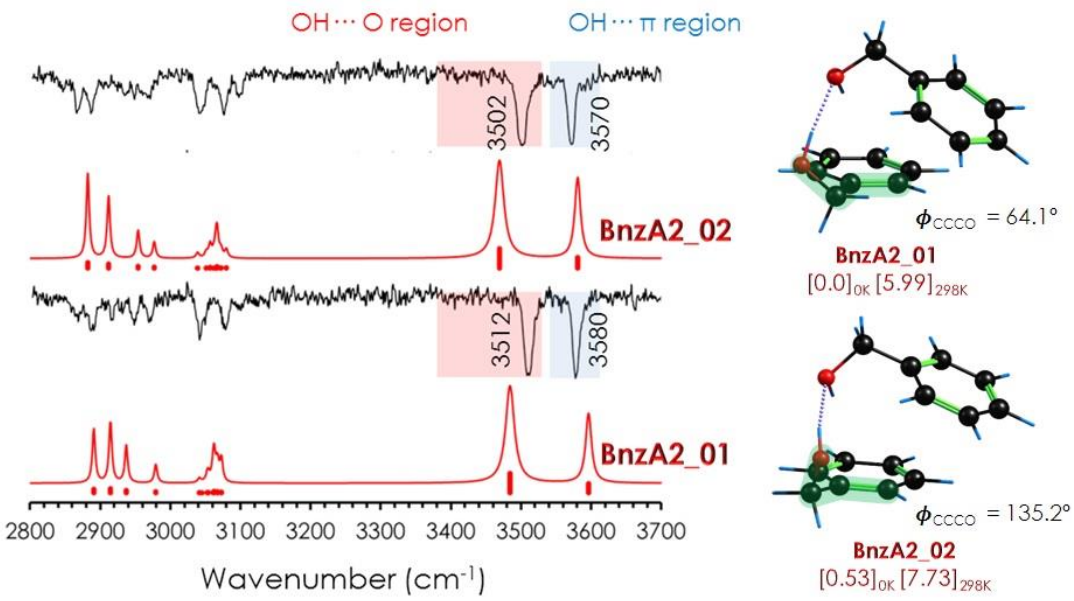

3.9 Irudia: $BnzA_2$-ren IDIR espektroa, egitura egonkorrenen simulazioekin alderatuta. Bibrazio-maiztasunen kalkulua B3LYP(ED=GD3BJ)/6-311++G(d,p) mailan burutu da, eta 0.954-ko eskala faktorea erabili da OH eta CH taldeen anharmonizitaterako.

3.9 Irudiak dimero egitura egonkorrenen simulatutako espektroen eta bi IR espektro esperimentalen arteko konparaketa aurkezten du. BnzA2_01 eta BnzA2_02 egiturek aurresaten duten espektroak ondo erreproduzitzen ditu OH eremuan agertzen diren bandak. Kontuan izan teoriak isolatutako bi isomeroen OH bandetan aipatutako aldaketa ere ondo erreproduzitzen duela. Esleitutako egiturei dagokionez, BnzA2_01 eta BnzA2_02 arteko desberdintasuna CH_2OH talde emaileren orientazioa da, zeinak elkarrekintzan parte hartzen duen oxigeno atomoaren elektroi bikote ez-parekatua ere aldatzen duen. Beraz, bi diastereoisomeroen (G-G-→BnzA2_01 eta G+G-→BnzA2_02) egituren arteko desberdintasunak OH luzaketa-bibrazio maiztasunetan perturbazio fin bat eragiten dute, esperimentalki zein teorikoki behatu dena.

Burututako esleipena frogatzeko, esleitutako bi egituren IR espektroak bi maila konputazional osagarritan kalkulatu dira: B3LYP/def2tzvp eta M06-2x/6-311++G(d,p) (ikusi 3.10 Irudia). Bitxia bada ere, Minnesota funtzionalaren konputazioak banden posizioa hobeto erreproduzitzen du, nahiz eta esleipen bera ekarri.

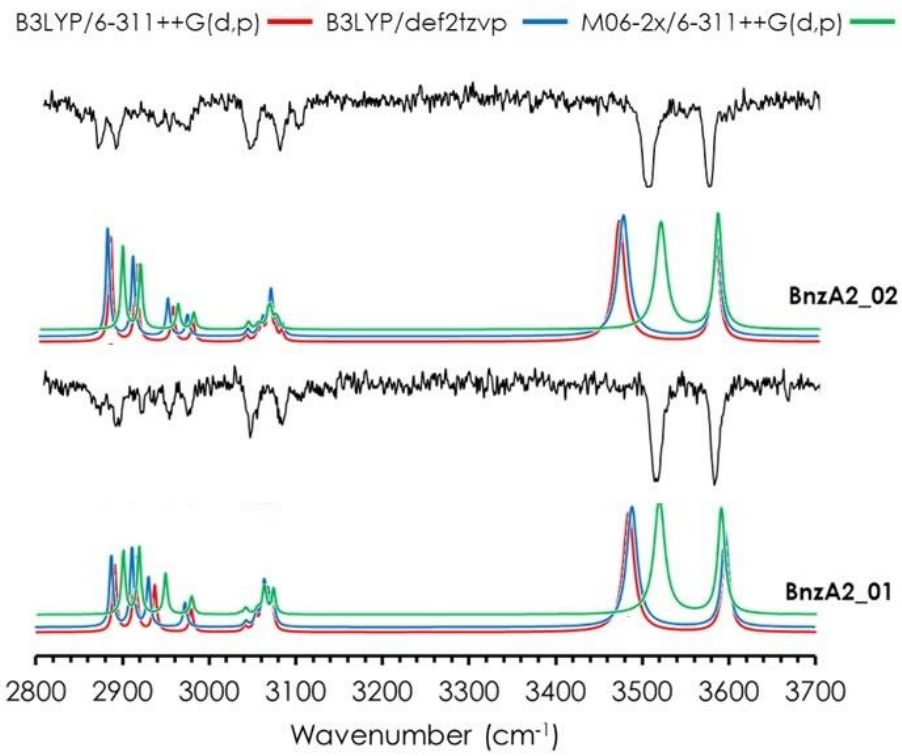

3.10 Irudia: $BnzA_2$ bi isomeroen IDIR espektro esperimentalen eta maila konputazional desberdinetan egindako egitura egonkorrenen simulazioen arteko konparaketa. OH taldeen eskala-faktorea 0.954 izan da B3LYP/6-311++G(d,p) mailan, 0.962 B3LYP/def2TZVP mailan eta 0.937 M06-2X/6-311++G(d,p) mailan. CH taldeen eskala-faktorea 0.962 izan da maila konputazional guztietan.

Familia bakoitzeko egitura egonkorrenen energia ere aztertu zen simulazioetan erabilitako maila konputazionaletan. Minnesota funtzionalak espektro esperimentalak hobeto erreproduzitu arren, BnzA2_01 eta BnzA2_02 egiturak ez ditu identifikatzen egonkorrenak bezala. Aldiz, BnzA2_03 eta BnzA2_04 (familia urdina) M06-2X mailak egitura egonkorrenak direla aurresaten du.

Dimero honetarako, Gibbs lotura energia aske erlatiboaren diagramak maila konputazional bakoitzean eraiki egin dira, tenperaturaren efektua familien egonkortasun erlatiboan aztertzeko. B3LYP metodoak familia gorria deskribatzen dute egonkorrena bezala tenperatura baxuetan, baina hau handitzean, pilatutako dimeroak faboratuak dirudi (ikusi A3.3 Irudia). Bitxia bada ere, M06-2X mailak guztiz kontrakoa aurresaten du, tenperatura altuetan familia gorria egonkorrena izanda.

Duela gutxi Medel eta Suhm-ek[14] argitaratutako emaitzekin alderatuta, akordio orokor bat dago: bi lanetan egitura berdinak aurkezten dira espezie egonkorrenak bezala, eta biak esperimentalki detektatu dira. Alabaina, lan horren egileek egitura gehigarri baten presentzia aurkezten dute, OH···π elkarrekintza bikoitz batez osatutako dimero hetero-

kirala (BnzA2_04 egitura). Gure espektroetan hirugarren isomero hori ez agertzea gure espantsioaren baldintzetan populazio txikia izatearen ondorioa izan daiteke. Hori dela eta, BnzA dimeroaren REMPI espektroa gas garraiatzaile desberdinekin neurtu da (ikusi 3.11 Irudia), espezie gehigarriak detektatzeko.

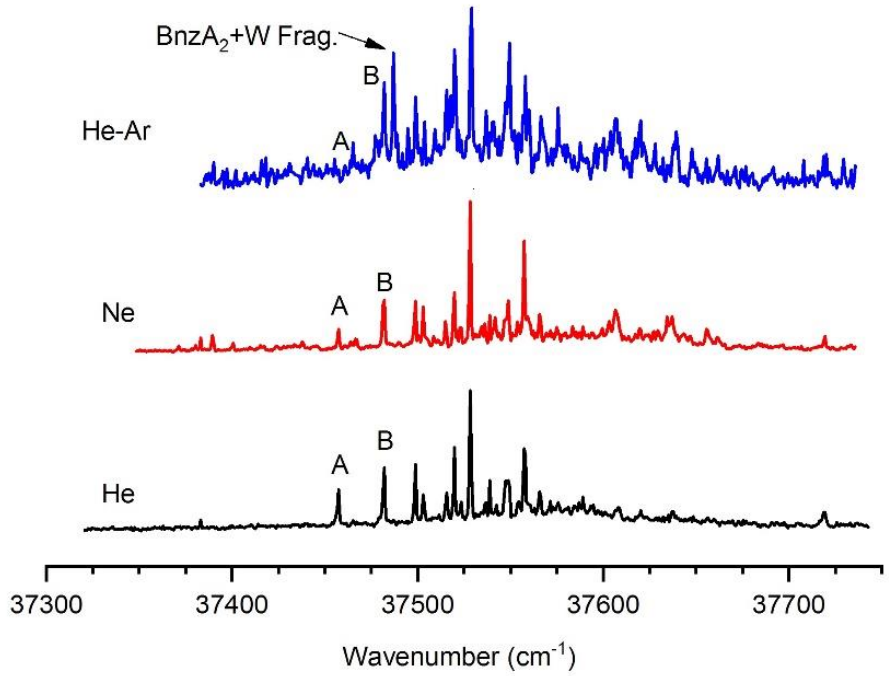

3.11 Irudia: BnzA dimeroaren REMPI espektroen konparaketa, He, Ne edo %10 Ar/He gas garraiatzaile gisa erabiliz.

3.11 Irudiko A eta B notazioak jadanik esleitutako BnzA2_02 eta BnzA2_01 egiturei dagozkie, hurrenez hurren. He ordez Ne jarriz gero, hozketa hobetu egiten da, eta egonkortasun gutxiagoko isomeroen populazioa harrapatzeko aukera ematen du. Horren ordez, %10 Ar/He erabiliz, hozketa eraginkorragoa lortzen da, baina Ar-ekin gertatzen diren talkak energetikoagoak dira ere, eta batzuetan gai dira minimo lokaletako populazioa isomero egonkorragotara transferitzeko.[15,16] Sistema honetan, He gasa Ne-rekin ordezkatzean asko lagundu zuen tamaina handiagoko konplexuen formazioan. Izan ere, seinaleak nonameroraino argi eta garbi ikusi ziren masa espektroan. Hala ere, dimeroaren espektroak ez zuten aldaketa nabarmenik erakusten. Banda sekundario batzuen intentsitate erlatiboan aldaketa bat antzematen da, trimeroaren edo BnzA:ura 2:1 konplexuaren zatiketaren ondorioz. Antza denez, hozketa hobetzeak isomero berririk harrapatzea ez zuen ahalbidetu. Isomero ezegonkorraren 0-0 trantsizioko intentsitate erlatiboa pixka bat jaitsi zela ikusi zen, izpi molekularraren tenperatura isomerikoaren jaitsiera bat eman dela adieraziz.

Ar/He nahastea gas garraiatzaile gisa erabiltzearen eragin nagusia BnzA:ura konplexuen zatiketaren areagotzeak izan zen. Espektroko banda guztien zundak isomero berrien harrapaketa ez dagoela erakutsi zuen. Isomero ezegonkorrenen jatorrizko trantsizioaren intentsitate erlatiboa nabarmen murriztu zen, zeinak ia ikusiezina den masa handiagoko agregatuen zatiketak sortutako zarataren gainean.

Dimeroarekin bukatuta, honen agregazioak O-H···O-H···π hidrogeno lotura sare kooperatibo batek bultzatzen duela ondorioztatu da, zeinak agregatua erdi pilatuta uzten duena.

3.2.3. Bentzil alkohol trimeroa

Agregatuaren hazkundeak eskuarki batuketa-prozesu bati jarraitzen dio, molekulak sekuentzialki metatuz aurreko egituraren gainean, zeinak nukleo gisa jokatzen baitu. Hala ere, molekularen adizioak aurreko egituraren berrantolaketa susta dezake. Ondorioz, BnzA-ren hazkunde naturalak molekula berri bat dimeroaren egitura egonkorrenari erantsiz jarraitzea espero da. Kasu horretan, hedapen horrek OH···OH···OH···π hidrogeno lotura sare lineala, edo hidrogeno lotura sare ziklikoa sor dezake. Horrela bada ere, literaturan agertzen diren sistema gehienek bigarren aukerarako joera orokorra dute.[17-19]

Kalkuluek panorama konformazional aberatsa erakutsi zuten BnzA-ren trimerorako, non makina bat egitura bi familia nagusitan bilduta agertzen diren, 20 kJ/mol-eko energia leihoan. PES-aren azterketa zehatza lan honen irismenetik haratago dago, eta, beraz, azterketa 3.12 Irudiko eta eranskineko A3.4 Irudiko familietara mugatu da.

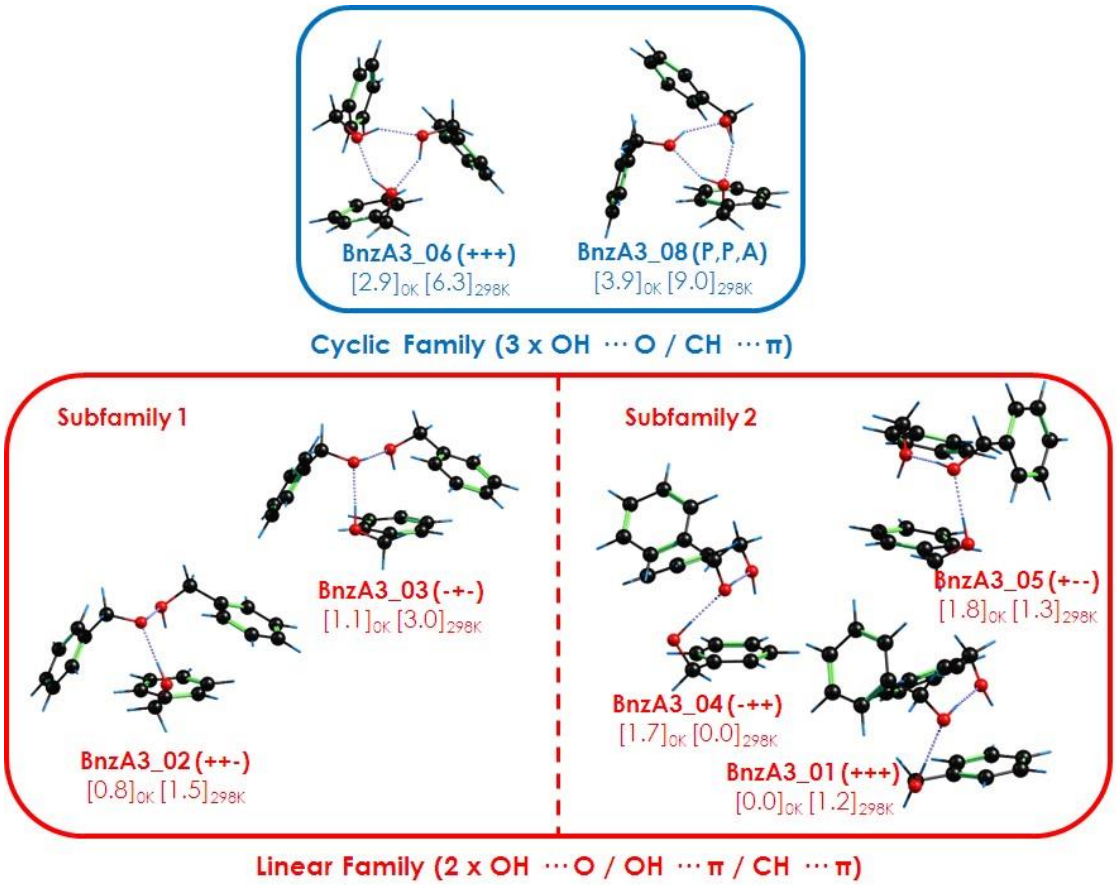

3.12 Irudia: $BnzA_3$-ren familia egonkorrenak, B3LYP(ED=GD3BJ)/6-311++G(d,p) mailan kalkulatuak. Energia balio erlatiboak egitura bakoitzaren azpian ematen dira, kJ/mol-etan. Egitura bakoitzaren izenari BnzA molekula bakoitzaren G konformazioaren angelu diedroaren orientazioa jarraitzen dio. Angelu diedroen analisia hidrogeno lotura sarearen sekuentzia jarraituz aztertu da, hau da, lehenengo seinua lehen protoi emaileari dagokio. BnzA3_08 egituraren kasuan, P eta A notazioak plano eta "anti" konformazioei dagozkie, hurrenez hurren.

Familia egonkorrenen (gorria eta urdina) arteko desberdintasun nagusia eraztun aromatikoen orientazioa da: horiek agregatuaren alboko aldeetan agertzen dira 1 azpifamilian, edo trinkoagoa den antolamendu batean 2 azpifamilian. Nolanahi ere, alde hori monomeroek hartutako konformazioaren ondorioz sortzen da, eta azkenean, familiako kide guztiek OH···OH···OH···π hidrogeno lotura sare bat aurkezten dute, $BnzA_2$-ren joera berari jarraituz. Bitxia bada ere, egitura egonkorrena G+G+G+ agregatu homo-kirala da.

Familia urdinari dagokionez, zeinak energia erlatiboan hurbil dagoen, hidrogeno lotura sare zikliko bat aurkezten du. Aipatzekoa da BnzA3_06 egituraren simetria altua, zeinak C3 ardatz simetriko bat aurkezten duen, non monomero guztiak G+ konformazioa duten. Hortaz, egitura horrek homo-kirala da ere, minimo orokorraren antzera.

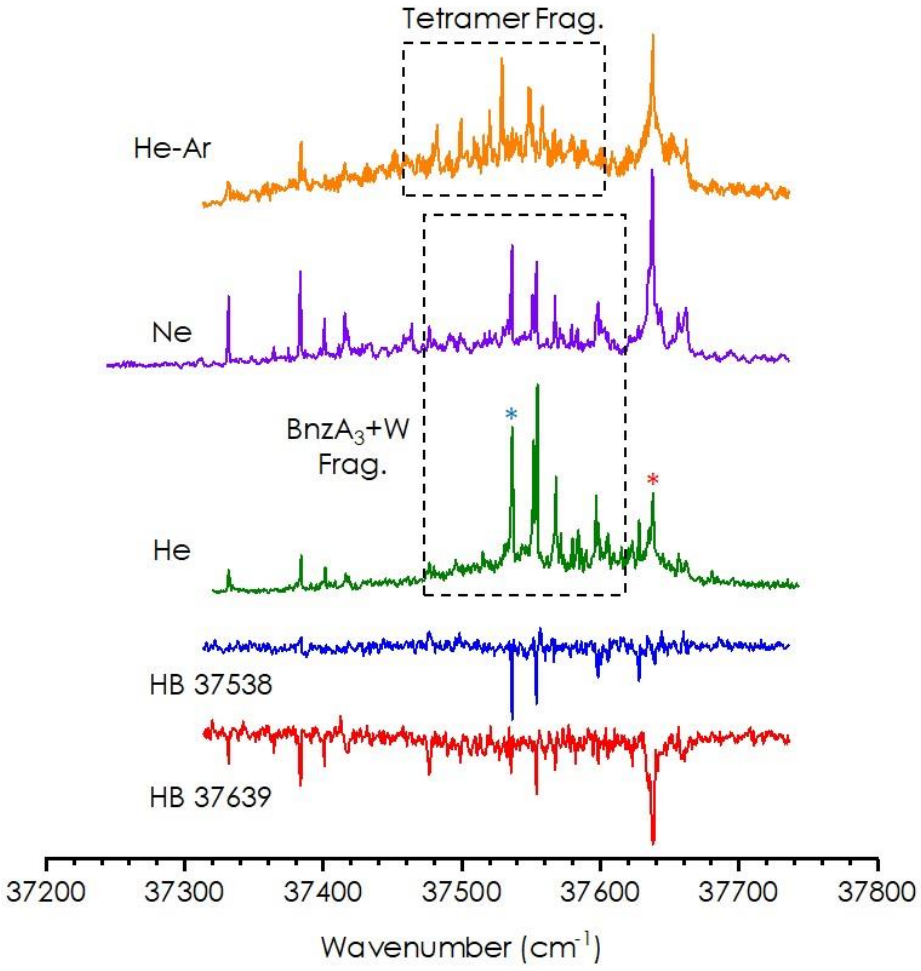

3.13 Irudia: Bentzil alkohol trimeroaren bi koloreko REMPI espektroa, 37538 and 37639 cm^{-1}-tan lortutako "UV/UV hole burning" espektroekin batera (izartxo urdin eta gorria, hurrenez hurren). Ionizazio laserra 35714 cm^{-1}-tan finkatu da espektro guztietarako.

3.13 Irudiak $BnzA_3$-ren bi koloreko REMPI espektroak biltzen ditu, gas garraiatzaile desberdinekin neurtuta. Espektro hauek konplexuak dira, eta urdinerantz joan ahala intentsitatea irabazten dute. Espantsioaren baldintzen arabera, tamaina handiagoko agregatuak edo urarekin sortutako konplexuak areagotzen ziren. Hala ere, baldintza optimoetan, BnzA:ura 3:1 konplexuaren zatiketa ere ezin izan zen saihestu.

"UV/UV hole burning" esperimentuak 37538 eta 37639 cm^{-1} bandak zundatuz egin ziren, 3.13 Irudian izartxoekin markatuta daudenak. UV laserra 37538 cm^{-1}-tan finkatzean lortutako espektroan 3:1 ur-konplexutik datozen bandak behagarriak dira. Aldiz, UV laserra 37639 cm^{-1}-tan finkatzean lortutako espektroan BnzA trimeroaren bandak aurkezten ditu. Isomero horren jatorrizko bandak 125 cm^{-1}-ko lerrakuntza aurkezten du gorrialdera, dimeroarenarekin alderatuz gero. Fenomeno horrek hidrogeno lotura sare

lineal baten presentzia adierazten du, kalkuluek aurresaten duten minimo orokorraren modukoa. Isomero gehiagoren bilaketa REMPI espektroaren gainontzeko trantsizioetan emaitza negatiboak eman zituen, egitura ziklikoen formazioa ezeztatuz.

Bitxia bada ere, 37332 eta 37384 cm^{-1}-ko trantsizioak zundatzean, bi IDIR espektro desberdin lortu ziren. Horrek esan nahi du bi isomeroek trantsizioak partekatzen dituztela UV espektroan, eta, beraz, haien ekarpenak bereizi ezin direla erresonantzia bikoitzeko UV/UV teknika erabiliz.

3.14 Irudiak 37325 (A) eta 37378 cm^{-1} (B) trantsizioetan zundatutako espektroen eta simulatutako egitura egonkorrenen espektroen arteko konparaketa aurkezten du. Espektro bakoitzean agertzen diren OH banden kopurua ez datoz bat isomero bakar baten predikzioarekin. Hortaz, 3.14 Irudian aurkeztutako espektroetan isomero bat baino gehiagoren presentzia espero da.

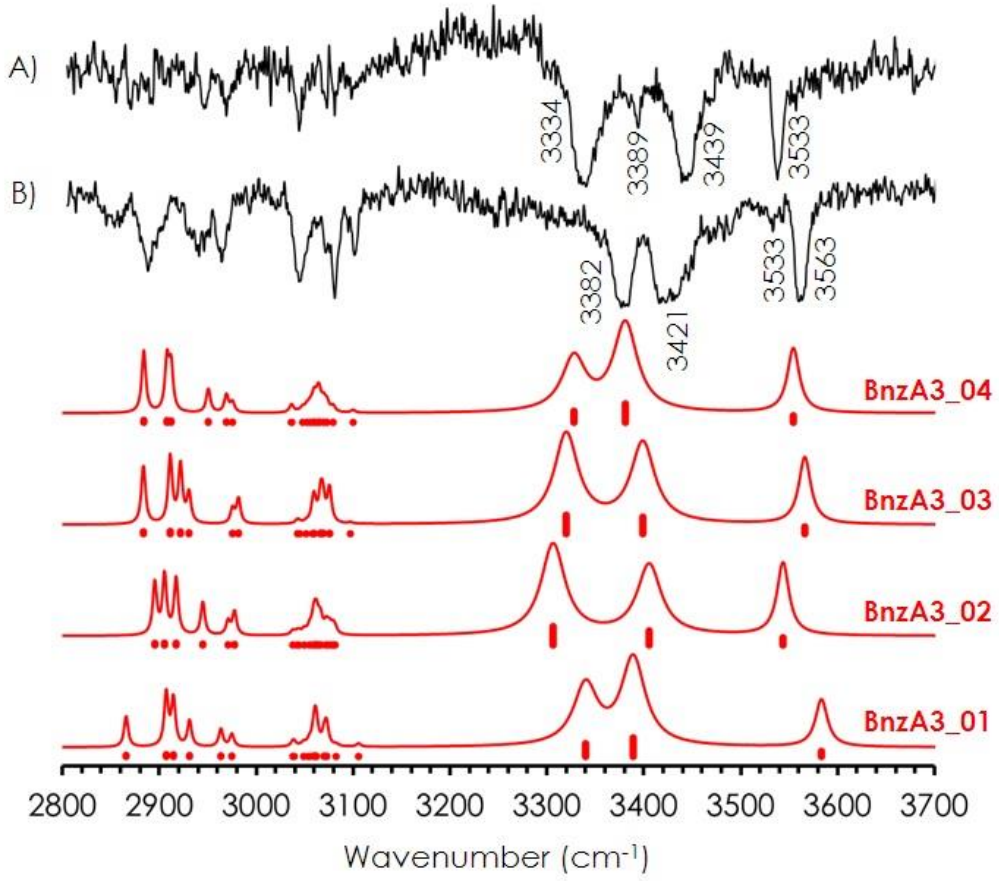

3.14 Irudia: $BnzA_3$-ren IDIR espektroen eta familia linealaren egitura egonkorrenen simulazioen arteko konparaketa. Bibrazio-maiztasunen kalkulua B3LYP(ED=GD3BJ)/6-311++G(d,p) mailan burutu da, eta

0.954-ko eskala-faktorea erabili da OH eta CH taldeen anharmonizitatea zuzentzeko. (A) eta (B) lerroak 37332 eta 37384 cm^{-1}-ko bandak zundatuz lortu dira, hurrenez hurren.

OH luzaketa-bibrazio banden arteko banaketa 3.14 Irudian OH talde bakoitzaren ingurumen desberdinak adierazten ditu. Adostasun on batekin, portaera hori erreproduzitu dezaketen isomeroak 2 familiakoak dira (ikusi 3.12 Irudia), non OH···π elkarrekintza batean amaitzen den hidrogeno lotura sare lineala eratzen baita. Egitura horiek oso hurbil daude energian (2 kJ/mol baino gutxiago), eta, ondorioz, jetan batera egon daitezke. BnzA3_01 egitura beheko espektroari esleitzen zaio; eta BnzA3_02 eta BnzA3_03 egiturekin, berriz, goiko espektroaren behin-behineko esleipena burutu daiteke. Bi esleipen horien arteko aldea eraztun aromatikoen antolamenduan dago, agregazio hetero-kiralaren ondorioz.

Detektatutako beste isomeroaren UV espektroaren trantsizio guztien zundaketa hurrengo 3.15 Irudian aurkezten den espektroan amaitzen zuten. Ikusi daitekenez, OH luzaketa-bibrazio modu guztiak batera agertzen dira, OH talde guztiek antzeko indarra duten hidrogeno loturak sortzen dutela adieraziz. Behaketa hau hidrogeno lotura sare ziklikoak sortzen duten isomeroekin aldera daiteke. Hala ere, gainontzeko banda bat agertzen da 3700 cm^{-1} inguruan, uraren OH askearen bibrazioarekin bat etortzen dena. Horrek adierazten du lortutako espektroa ur-konplexu baten zatiketari dagokiola.

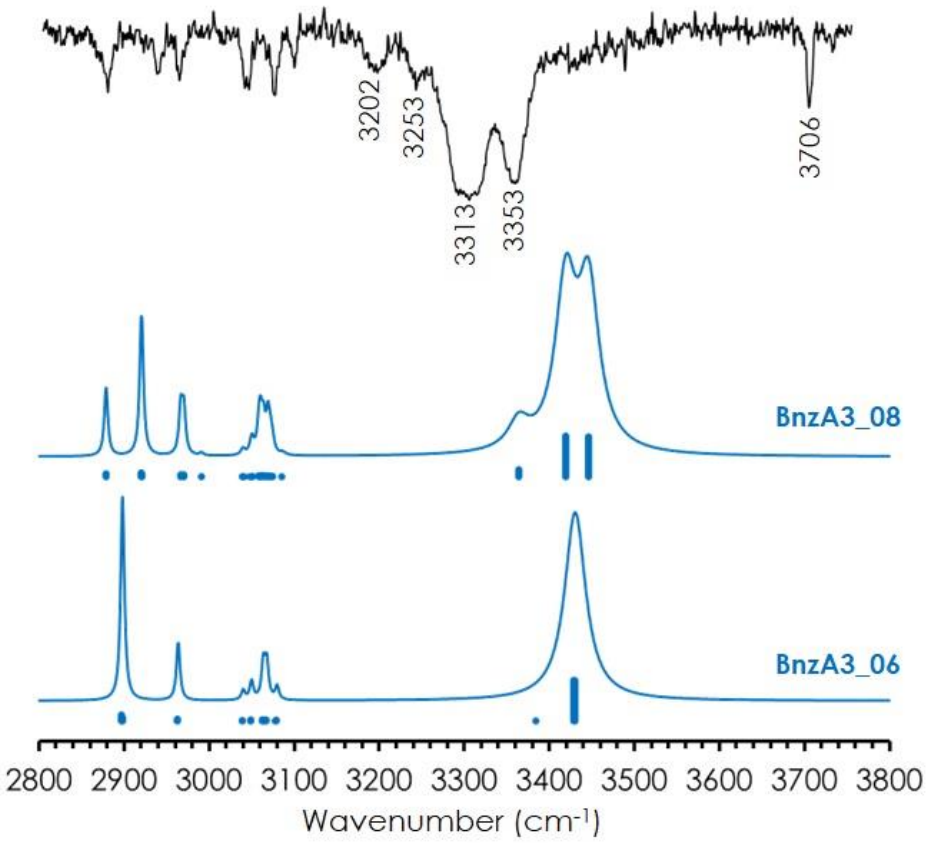

3.15 Irudia: $BnzA_3+W_1$-ren IDIR espektroaren eta BnzA trimeroaren familia ziklikoaren egitura egonkorrenen simulazioen arteko konparaketa. Bibrazio-maiztasunen kalkulua B3LYP(ED=GD3BJ)/6-311++G(d,p) mailan burutu da, eta 0.954-ko eskala-faktorea erabili da OH eta CH taldeen anharmonizitatea zuzentzeko. Espektroa 37536 cm^{-1}-ko banda zundatuz lortu egin da.

Dimeroan egin zen antzera, trimeroaren PES-aren egitura adierazgarrienak B3LYP/def2tzvp eta M06-2x/6-311++G(d,p) metodoetan kalkulatu ziren, burutako esleipen esperimentala frogatzeko. Hiru metodo konputazionalen emaitzak adierazten duten energia diagramak eranskinetan aurkitu ahal dira (ikusi A3.6 eta A3.7 Irudiak), espektroen simulazioekin batera. Orokorrean, esleipena ondo erreproduzitzen da B3LYP/def2tzvp eta M06-2x/6-311++G(d,p) maila konputazionaletan.

3.2.4. Bentzil alkohol tetrameroa

Tetrameroaren azterketa askoz zailagoa da, agregatuaren hazkundearekin batera doan seinalearen intentsitatearen murrizketa dela eta. Horrez gain, baldintza esperimentaletan soilik aldaketa estuak egin ahal dira, tetrameroaren seinalearen detekzioa maximizatzean, hala handitzen dira zatiketa prozesuak. Gertakisun horiek guztiak "UV/UV hole burning" espektroen neurketa eragotzi zuten.

3.16 Irudian tetrameroaren REMPI espektroa aurkezten da. Espektroak eremu estu bat hartzen du, non zenbait trantsizio agertzen baitira, absortzio zaratatsu zabal batean eraikiak. 0-0 trantsizioa (37476 cm^{-1}) urdinera lerrokatuta dago trimeroaren jatorrizko bandarekin alderatuta, hidrogeno lotura sare ziklikoen sorrera aurreratuz. Jatorrizko bandaren gorrialderantz agertzen diren trantsizio ahulak tamaina handiagoko konplexuen zatiketaren ondorio dira.

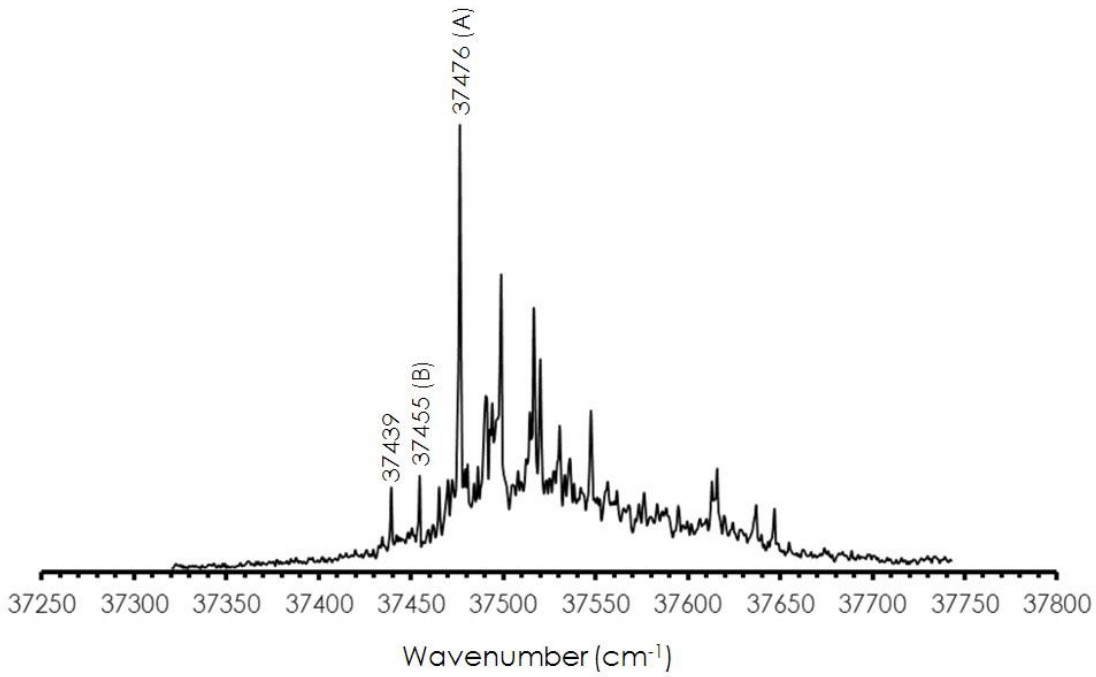

3.16 Irudia: Bentzil alkohol tetrameroaren bi koloreko REMPI espektroa. Ionizazio laserra 35714 cm^{-1}-tan finkatu zen neurketarako.

"Hole burning" teknikak ematen duen informaziorik gabe, espektroan konformero bat baino gehiago detektatzeko modu bakarra IDIRS teknikan trantsizio posible guztiak zundatzea da. 37476 cm^{-1}-ko banda zundatzean, 3.17 Irudiko IR espektroa lortu zen. Banda horretatik urdinera agertzen diren gainontzeko trantsizioak zundatzean, espektro bera lortu zen. 3313 cm^{-1}-tan agertzen den absortzio sendoa aurkezten du espektroak, zeinak OH luzaketa-bibrazio banda batzuen ekarpena duena. Banda horren albo banatan, 3353 cm^{-1}-tan sorbalda bat eta 3253 cm^{-1}-tan banda satelite bat agertzen dira. Gorrialdera haratago joanda, CH taldeen luzaketa-bibrazioen bandak agertzen dira. Argi eta garbi, espektro honek hidrogeno lotura sare zikliko baten eraketaren sinadura da; izan ere, OH talde guztiak multzokatuta daude, antzeko giroan daudela adieraziz.

Monomeroen konbinazio ugari eta lau bentzil alkohol molekulen moldaketa espazialak direla eta, tetrameroak panorama konformazional konplexua aurkezten du. Bilaketa konformazionalean aurkitutako egitura garrantzitsuenak optimizatu ondoren, egitura ziklikoak eta gutxienez hiru OH···O loturak aurkezten dituzten familiak aurkitu ziren. Bestalde, badirudi familia ziklikoa egonkorrena dela kasu honetan.

Energia-leiho zabal batean dauden egitura zikliko guztien artean, BnzA4_01 (ikusi 3.17 Irudia) da, alde handiz, konformaziorik egonkorrena. *Gauche* konformazioan dauden lau BnzA molekulen homo-agregatua da. Gainera, agregatuak C_2 simetria-ardatz bat du, hidrogeno lotura sareari eta ondo antolatutako CH···π elkarrekintzei esker. Gainerako egiturek gutxienez monomero bat dute *anti* konformazioan, beraz, ez dute simetria elementurik. Interesgarria da nola BnzA-ren homo-agregazioa egitura egonkorrenak sortarazten duen, dimeroaren eta trimeroaren kasuetan bezala.

IR espektro esperimentalaren esleipenari dagokionez, 3.17 Irudian, aukeratutako egituren simulazioen eta esperimenturaren arteko konparaketa aurkezten da. Ikusi daitekeenez, isomero guztien absortzioa posizio egokian aurresaten dute. Haien arteko alderik garrantzitsuena bandaren inguruko simetria da. Espektro esperimentala ez da simetrikoa, baina zenbait espezieren ekarpenagatik izan daiteke. Nolanahi ere, isomero batzuen simulazioak, hala nola 03 isomeroa, leialki erreproduzitzen du espektro esperimentala, azken honek zenbait espezieren ekarpena izan dezakeela adieraziz.

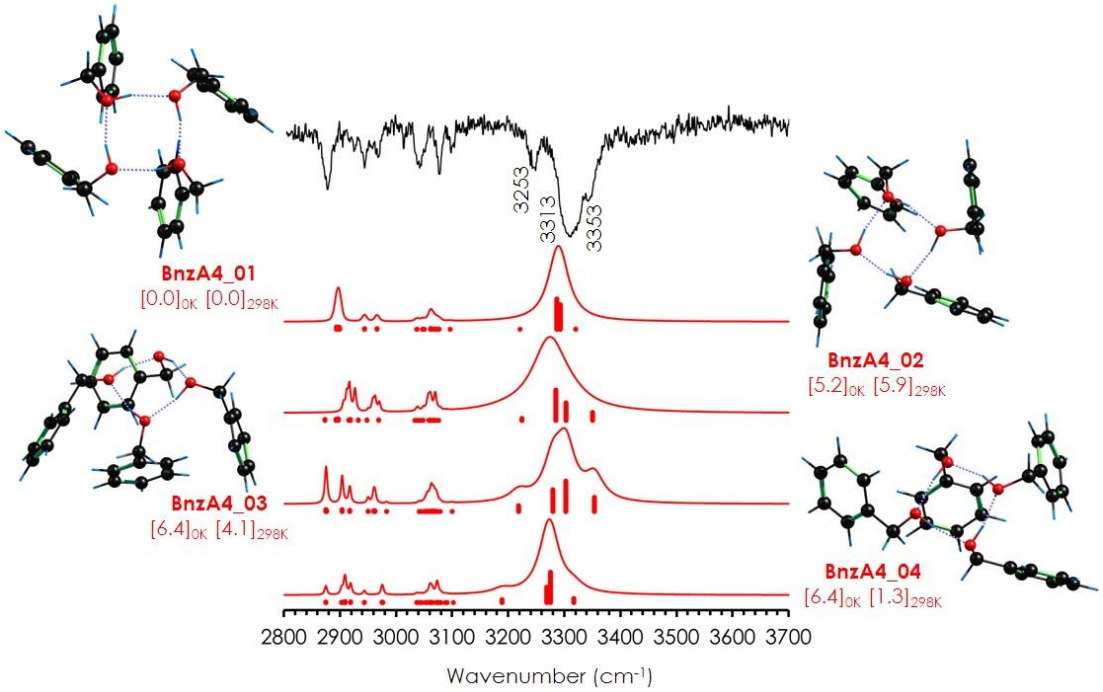

3.17 Irudia: $BnzA_4$-ren IDIR espektroaren eta egitura egonkorrenen simulazioen arteko konparaketa. Bibrazio-maiztasunen kalkulua B3LVP(ED=GD3BJ)/6-311++G(d,p) mailan burutu da, eta 0.954-ko eskala-faktorea erabili da OH eta CH taldeen anharmonizitatea zuzentzeko. Espektroa 37536 cm^{-1}-ko banda zundatuz lortu zen. Energia balioak kJ/mol-etan ematen dira.

3.16 Irudiko espektrora itzuliz, B notazioarekin markatutako banda aztertuz, IR espektro desberdin bat lortu zen (ikusi 3.18 Irudia). 3.17 Irudiko espektroaren antzeko absortzio asea du, baina gorrira lerrokatuta eta 3700 cm^{-1}-tan banda bat duena. Azken banda honek espektroa 4:1 ur-konplexu baten zatiketari dagokiola adierazten du.[20] Espektroaren izaera zabalak konplexua xehetasunez aztertzea eragozten du, baina hidrogeno lotura sare zikliko baten sorrera aurreratzeko aukera eman digu, non ur molekula bar parte hartzen duen, propofol/ur konplexuetan behatu den moduan.[21]

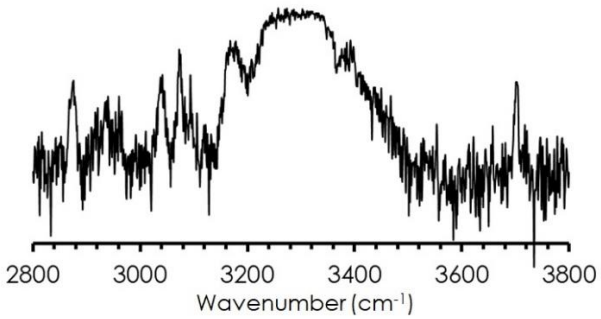

3.18 Irudia: $BnzA_4$-ren IDIR espektroa, 37455 cm^{-1}-ko banda (B) zundatuz lortua.

3.3. 2-Feniletanolaren espektroskopia

BnzA karakterizatzeko sistema esperimental berdina erabili zen 2-feniletanolaren (PEAL) espektroskopia aztertzeko. PEAL-ez bustitako paper xurgatzaile zati bat 80ºC-taraino berotu zen lagin konpartimentuaren barruan. Laginaren lurrina 1.5 bar He-rekin nahastu zen espantsioa sortzeko.

3.3.1. 2-Feniletanol monomeroa

BnzA-rekin alderatuta, PEAL-ren aparteko metilo taldeak askatasun gradu gehigarri bat ematen dio molekulari (ikusi 3.1 Irudia). Hortaz, hidroxilo taldearen orientazioaz gain, $C_{ortho}C_{ipso}C_{\alpha}C_{\beta}$ eta $C_{ipso}C_{\alpha}C_{\beta}O$ angelu diedroek har ditzaketen balioak ere aztertu behar ziren. Azken optimizazioak bost konformazio egonkor erakutsi zituen (ikusi 3.19 Irudia). *Gauche* eta *anti* konformazioak biak egonkorrak dira, Gg konformazioa minimo orokorra izanik. Konformazio honetan, OH taldeak eraztun aromatikorantz begiratzen du. NCI-ren analisien irudikapena erakusten duen moduan (3.19b Irudia), OH···π motako elkarrekintza ahul bat dago.

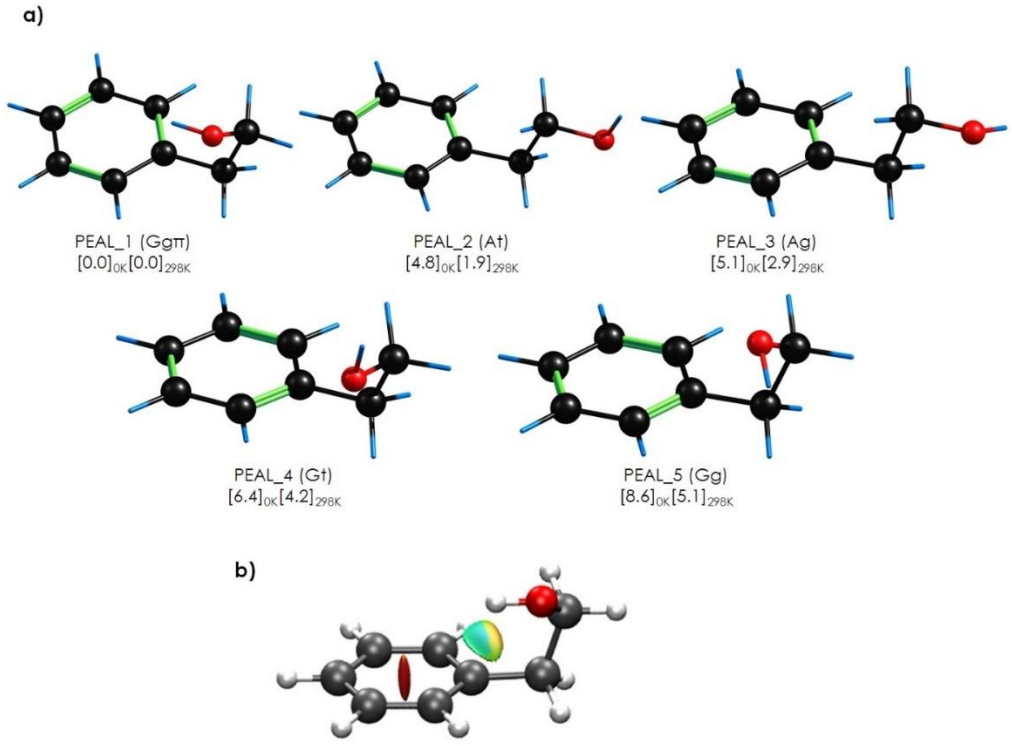

3.19 Irudia: a) PEAL-ren egitura egonkorrenak, B3LYP-ED=GD3BJ/6-311++G(d,p) mailan kalkulatuak. Energiak kJ/mol-etan daude. b) PEAL_1 egituraren 3D-ko NCI irudikapena.

PEAL-ren espektroskopia elektronikoaren azterketaren emaitzak hurrengo 3.20 Irudian bildu dira. Mons-en taldean[22] aldez aurretik aztertu zuten PEAL-ren MRES espektroskopia. Jatorrizko banda 37627 cm^{-1}-tan agertzen da (izartxo gorria), eta intentsitate ahulagoko trantsizio batzuek jarraitzen diote, jadanik argitaratutako emaitzekin ados. Orokorrean, espektroa nahiko garbia da eta aktibitate bibrazional eskasa aurkezten du. Aurreko ikerketen arabera, 37627 cm^{-1}-tan agertzen den banda Ggπ isomeroari dagokio, eta 37675 cm^{-1}-tan agertzen den trantsizio ahula, aldiz, At isomeroari dagokio. Izan ere, azken isomero horri dagokion bandaren intentsitatea bere egonkortasun ahulagoarekin bat datoz (4.8 kJ/mol B3LYP-ED=GD3BJ/6-311++G(d,p) mailan). Bi isomero horien presentzia "UV/UV hole burning" esperimentuekin egiaztatu zen (ikusi 3.21 Irudia). Izartxoekin markatutako trantsizioak IR/UV esperimentuetan erabili ziren kitzikatze uhin luzera gisa, non bi IR espektro desberdin lortu ziren (ikusi 3.22 Irudia).

Dimeroaren aktibitate bibrazionala kontraste handian dago monomeroaren espektroarekin. Gorrialdean agertzen den lehen banda 37460 cm^{-1}-tan agertzen da, zeinak 167 cm^{-1}-ko lerrakuntza duen monomeroaren jatorrizko bandarekin alderatura. Gainontzeko espektroak 3.20 Irudian trimeroari eta tetrameroari dagozkie. Bien jatorrizko bandak dimeroaren gorrirantz agertzen dira, eta hondo zaratatsu baten gainean zenbait trantsizio diskretuak azaltzen dituzte.

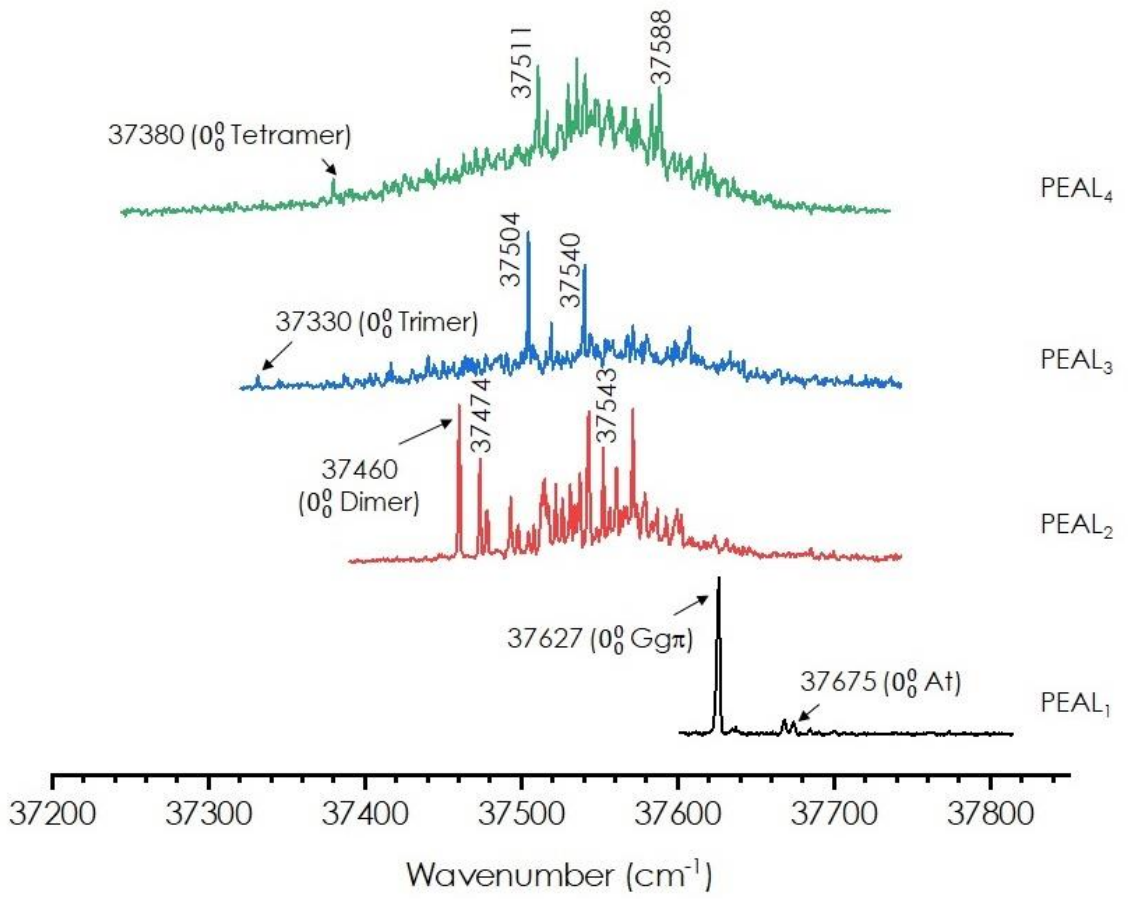

3.20 Irudia: PEAL eta bere tetramerorainoko agregatuen bi koloreko REMPI espektroak. Ionizazio laserra 35714 cm-1-tan finkatu zen.

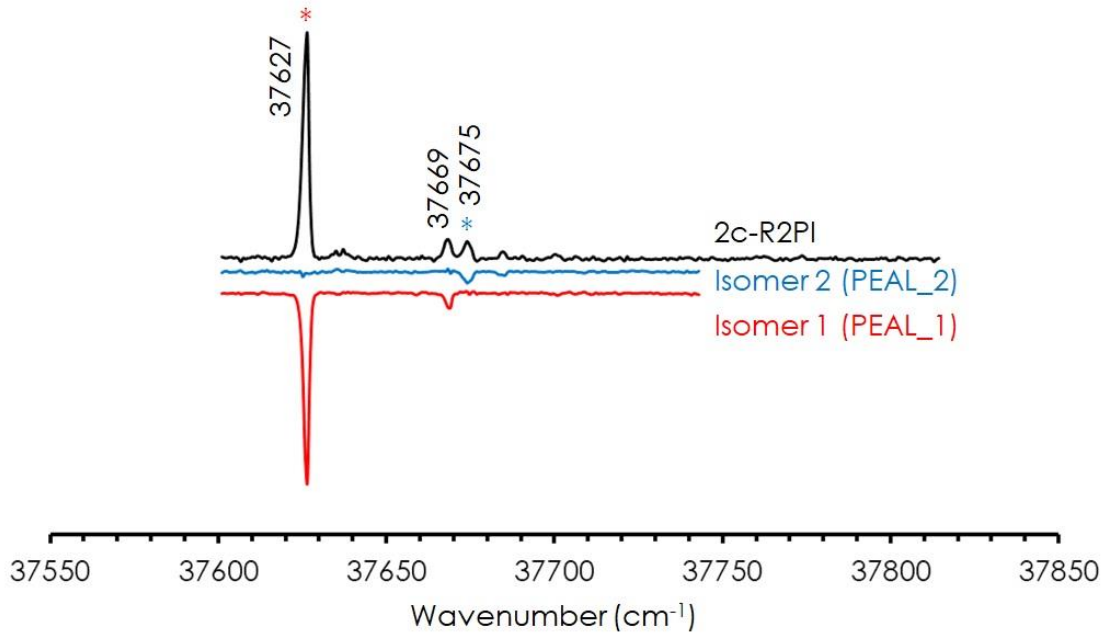

3.21 Irudia: PEAL-ren bi koloreko REMPI espektroa, "UV/UV hole burning" esperimentuetan lortutako REMPI espektroekin batera. Ionizazio laserra 35714 cm^{-1}-tan finkatu zen. Izartxoekin markatutako trantsizioak zundatu ziren "hole burning" esperimentuetan.

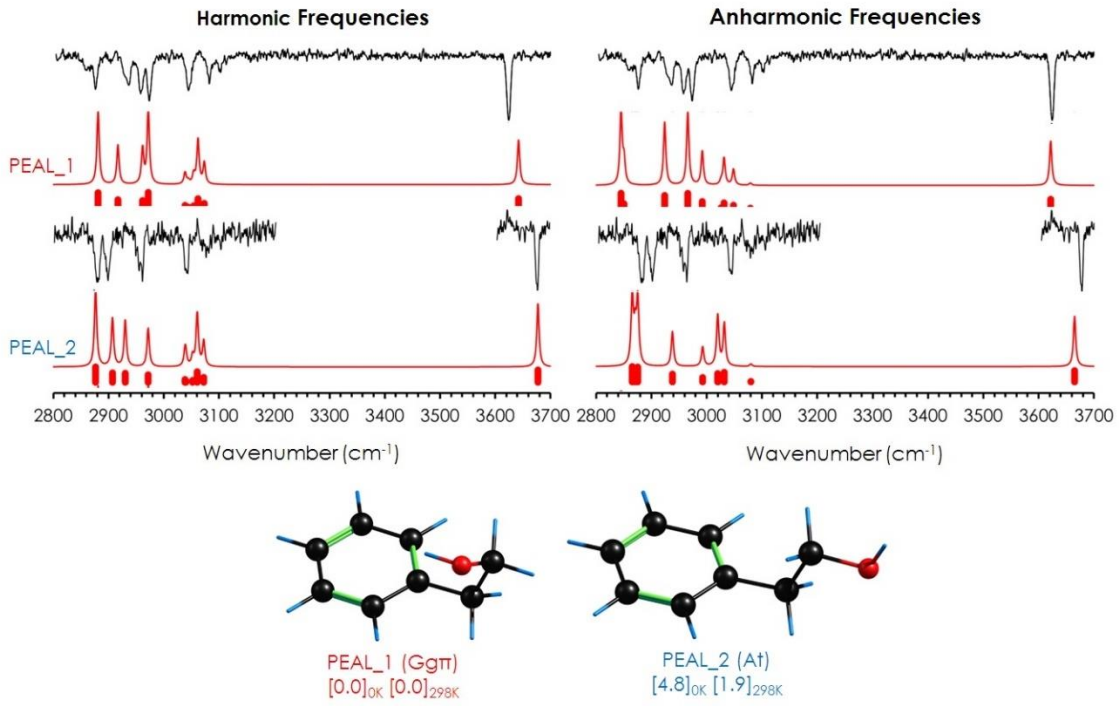

3.22 Irudia: PEAL-ren IDIR espektroa, egitura egonkorrenen bibrazio-maiztasun harmoniko eta anharmonikoen predikzioekin konparatuta. Espektroen simulazioak B3LYP(ED=GD3BJ)/6-311++G(d,p)

mailan kalkulatu ziren. Kalkulu harmonikoetarako, 0.9565-ko eskala faktorea erabili zen OH talderako, eta 0.962-koa CH taldeetarako. Maiztasun anharmonikoen kalkuluetan inolako eskala faktorerik ez ziren behar.

Monomeroaren karakterizazio espektroskopikoa detektatutako isomeroen IDIR espektroen neurketarekin jarraitzen du. 3.22 Irudiak bi espektro esperimentalen eta PEAL-ren egitura egonkorrenen predikzioen arteko konparazioa aurkezten du, B3LYP-ED=GD3BJ/6-311++G(d,p) mailan. Bi espektroek ondo ebatzitako CH eta OH bandak aurkezten dituzte. OH askearen posizioan aldaketa nabarmen bat antzeman daiteke, zeinak -CH_2CH_2OH taldearen antolakuntza desberdin bat adierazten duena. Aldaketa hau CH eremuan ere behagarria da. Aurresaten den moduan, OH bandaren lerrakuntza PEAL_1 egituran sortutako OH···π elkarrekintzaren ondorioz ematen da. BnzA-ren kasuan bezala, maiztasun anharmonikoen kalkuluak maila berdinean burutu ziren, zeinak xehetasunez erreproduzitzen duten OH luzaketa-bibrazio moduen posizioak. Hala ere, CH bibrazioak ez dira hain ondo aurresaten, ziur aski, Fermi erresonantzien edo bestelako efektuen agerpena dela eta, zeinak Hamiltondar konplexuago bat behar duten predikzio xeheagoak burutzeko.

3.3.2. 2-Feniletanol dimeroa

BnzA-ren kasuan bezala, dimeroaren formazioa asimetria bat sortzen du, zeinak eraztun aromatikoarekiko CH_2CH_2OH taldearen orientazio posible guztiak kontuan hartzera eskatzen duena. Aurreko atalean monomeroaren bi konformero identifikatu dira. Hori dela eta, ikerketaren konplexutasuna murrizteko, detektatutako konformeroak dituzten dimeroen egiturak soilik hartuko dira kontuan azterketa teorikorako. PEAL-ren konformaziorik egonkorrenaren bi unitatez osatutako dimeroen kasuan, Ggπ, lau diastereoisomero aurkitu daitezke. Hala bada, bi monomeroen eta bere estereoisomeriaren konbinazioak panorama konformazional izugarri zaila emango zuen, soilik dimeroan.

Panorama konformazional horren azterketa B3LYP=ED=GD3BJ/6-311++G(d,p) maila konputazionalean hurrengo 3.23 Irudian aurkezten da. Bitxia bada ere, familia egonkorrenaren (gorria) partaideen egiturak aurretik karakterizatutako BnzA dimeroaren antzekoak dirudi. Izan ere, lehen lau egiturak diastereoisomeroak dira, elkarrekintza berdina aurkezten dutelako CH_2CH_2OH taldearen orientazio desberdinekin. Izan ere, talde alifatiko gehigarriak molekula emaileari ematen dion flexibilitateak, bere eraztunarekin OH···π elkarrekintzak sortzeko ahalmena ematen dio, bere kidearekin sortu beharrean.

Harrigarria bada ere, gutxienez At konformazioan monomero bat duten dimeroak nahiko ezegonkorrak dira (ikusi PEAL2_08 eta PEAL2_17 egiturak), eta, beraz, isomero horien populazio oso txikia espero da izpi molekularrean.

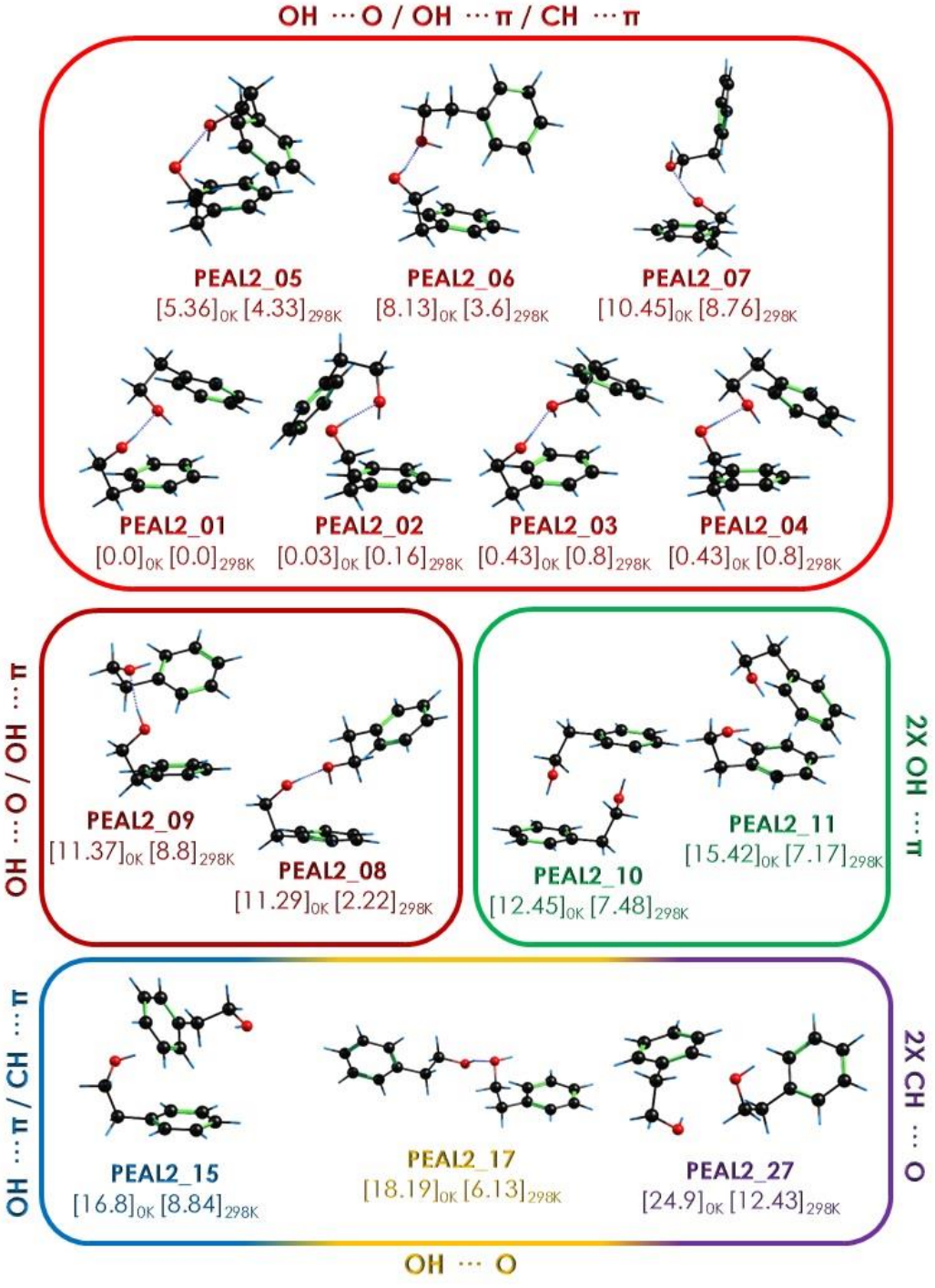

3.23 Irudia: PEAL dimeroaren konformero egonkorrenen laburpena, B3YLP(ED=GD3BJ)/6-311++G(d,p) maila konputazionalean optimizatuak. Energiak kJ/mol-etan ematen dira.

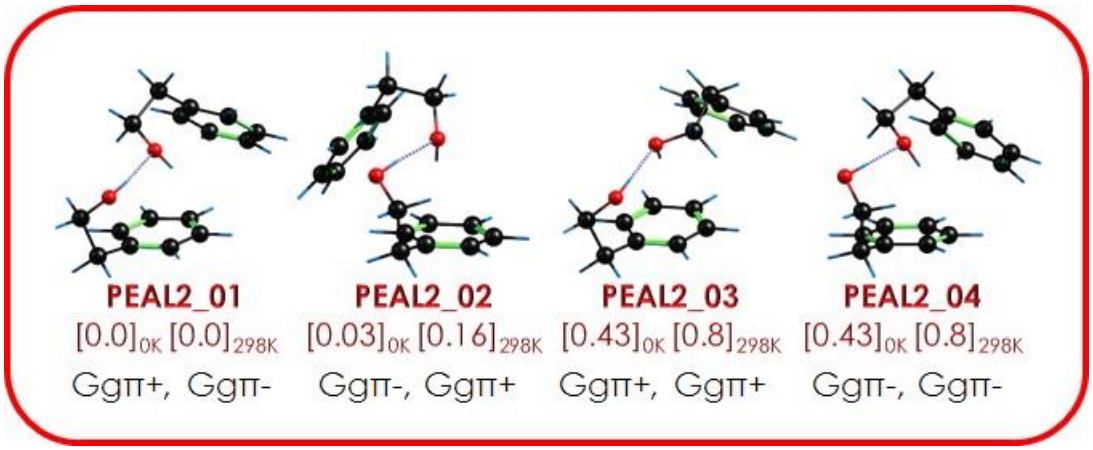

3.24 Irudia: $PEAL_2$-ren diastereoisomero egonkorrenak.

3.23 Irudiak egonkortasun desberdina duten bestelako isomeroen elkarrekintzak aurkezten ditu. Argi dago elkarrekintza nagusia OH···O eta OH···π hidrogeno loturak direla, non monomeroak beti *gauche* konformazioan dauden. +/- konformazioak modulazio fin bat sartzen du azken lotura-energiaren balioan, BnzA-ren kasuan baino txikiagoa, etilo taldearen malgutasuna askatasun-maila nahikoa duelako molekulek elkarrekintza nagusiak egokitu eta optimiza ditzaten. Izan ere, familiarik egonkorrena monomero egonkorren (Ggπ) konbinazio posible guztiak ditu. Elkarrekintza nagusi horiek eraztun aromatikoen arteko bestelako CH···π/π···π elkarrekintzekin batera agertzen dira. Edozein elkarrekintza galtzeak familia ezegonkorragoen sorpenean amaitzen du. Interesgarria bada ere, kalkuluek agregatu hetero-kiralak aurresaten dute egitura egonkorrenak bezala, BnzA-ren kasuaren kontrakoa.

Gibbs lotura energia aske erlatiboaren diagramak familia gorria egonkorrena bezala ere azaltzen dute tenperatura-leiho zabal batean (ikusi A3.8 Irudia). Bestalde, ez dago beste egituren egonkortze nabarmenik. Ondorioz, bestelako familien egitura egonkorren presentziak espantsioan baztertu egiten dira.

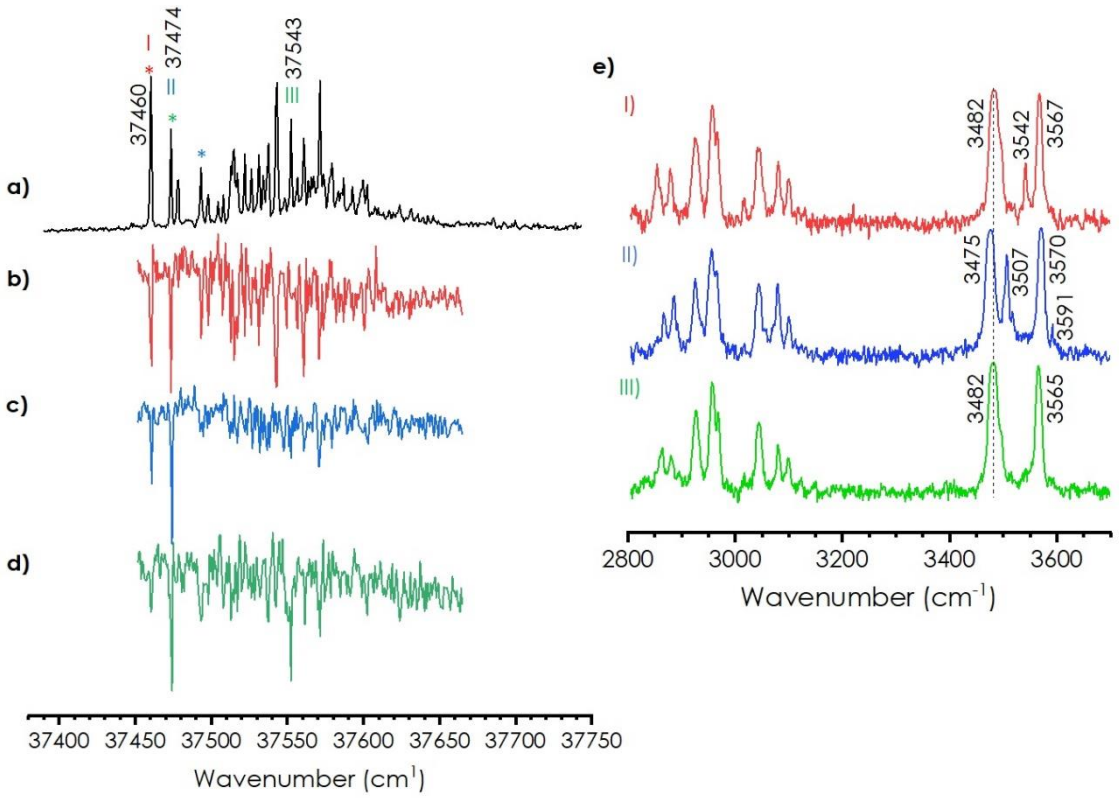

3.25 Irudia: a) $PEAL_2$-ren bi koloreko REMPI espektroa, b) 37460 cm^{-1} (izartxo gorria), c) 37493 cm^{-1} (izartxo urdina) eta d) 37474 cm^{-1} (izartxo berdea) trantsizioak zundatzean lortutako "UV/UV hole burning" espektroekin batera. Ionizazio laserra 35714 cm^{-1}-finkatu zen. e) $PEAL_2$-ren IDIR espektroak. Erromatar zenbakiak IR espektroak lortzeko zundatutako trantsizioak markatzen dituzte.

"UV/UV hole burning" teknikan, REMPI espektroaren trantsizio bibronikoen azterketak konplexutasun harrigarria erakutsi zuen: gutxienez hiru espezieen ekarpenak espektro elektronikoan identifikatu ziren, 3.25 Irudian adierazten diren bezala. Hala ere, "hole burning" esperimentuak ez ziren oso erabakigarriak; izan ere, BnzA-an gertatu zen bezala, espezie batzuek trantsizio bibroniko gainjarriak dituzte, eta beraz, haien ekarpen erlatiboa ezin da banandu ohiko "hole burning" tekniken bitartez. Alabaina, IDIR espektroen neurketak gutxienez $PEAL_2$-ren hiru isomero desberdin zeudela frogatu ahal izan zuen (3.25 Irudiaren eskuinaldeko atala).

Isomero bakoitzaren trantsizio elektronikoak zein diren argitzeko, "IR/UV hole burning" esperimentuak burutu ziren, IR laserra konpartitu gabeko OH bandetan finkatuz (ikusi 3.26 Irudia).

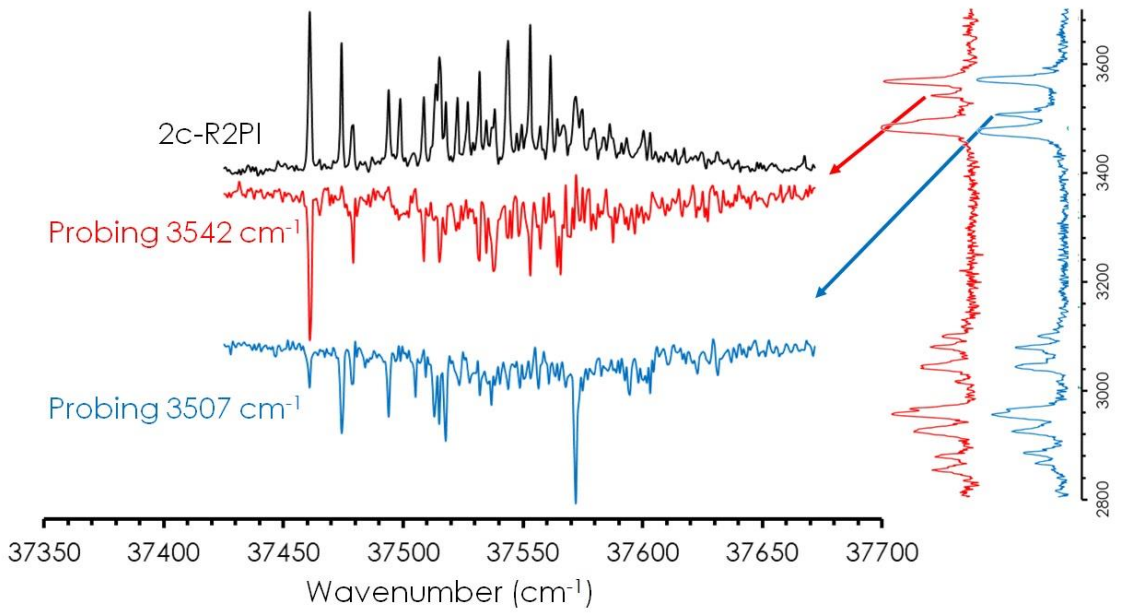

3.26 Irudia: $PEAL_2$-ren lortutako "IR/UV Hole Burning" espektroak.

OH eremuko erdiko banda zundatuz, bi espektro desberdin lortu ziren. Hauek trantsizio elektroniko gehienak aurkezten dute, espezieen arteko gainezarpenak konfirmatuz. Burututako esperimentu guztiak panorama konformazional oso zaila nabarmentzen du PEAL dimerorako. Isolatutako isomeroak identifikatzeko, aurresapen teorikoekin konparazio handiago bat egitea beharrezkoa da. Laburbilduz, hainbat teknika espektroskopikoekin lortutako datutatik ondorio hauek atera daitezke:

- Bi koloreko REMPI espektroak trantsizio eta progresio elektronikoen bilduma bat aurkezten du. Trantsizio eta progresio horiek gutxienez hiru isomero desberdinen ekarpenetik datoz, jatorrizko banda bera dutelarik, baina IR espektro desberdinak.
- Kolore urdin eta gorriko isomeroen IR espektroek bi egituren ekarpenak aurresaten dituzten OH bandak aurkezten dituzte (hiru OH banda daude biren ordez, dimero baterako). Kolore berdeko IR espektroa aztarna gorrien eta urdinen ekarpen komuna dela dirudi (3.25 Irudia).

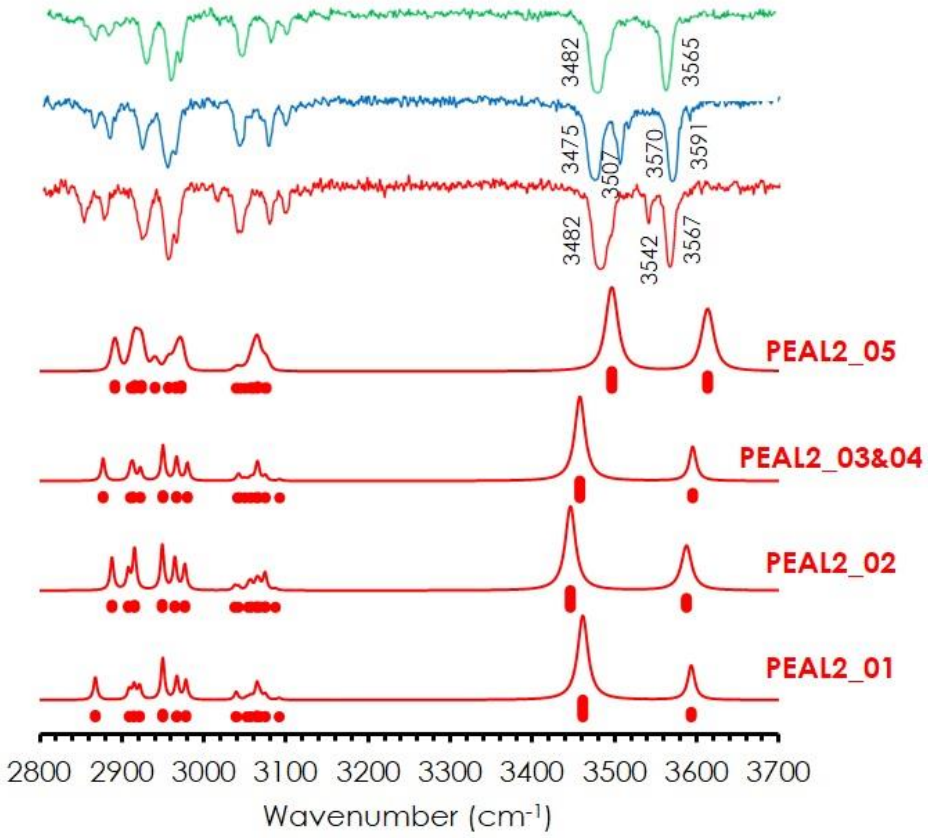

3.27 Irudia: $PEAL_2$-ren IDIR espektroaren eta egitura egonkorrenen simulazioen arteko konparaketa. Maiztasunen kalkulua B3LYP(ED=GD3BJ)/6-311++G(d,p) mailan egin zen, eta 0.9565-ko eskala faktorea erabili zen OH eta CH taldeen anharmonizitatea zuzentzeko.

3.27 Irudiak espektro esperimentalaren eta $PEAL_2$-ren isomero egonkorrenen predikzioen arteko konparaketa aurkezten du. Arreta berezia jarri zitzaien kalkulatutako diastereoisomeroei, energia erlatiboan oso hurbil baitaude. Dimero horien barruko elkarrekintza oso antzekoa den arren, badirudi kalkuluek OH bandaren posizioetan alde batzuk daudela. Desberdintasun horiek azal ditzakete esperimentalki isolatutako isomero bakoitzean behatutako OH banda ugariak. Familia horren energia altuagoko egiturak ere esperimentuarekin alderatu ziren (ikusi A3.9 Irudia), baina haien predikzioak ez ziren 3.27 Irudikoak bezain onak. Predikzio teorikoen banden posizioan dagoen alde txikia bat dator hiru isomeroen espektro esperimentalen artean ere atzemandako alde txikiekin. Gainera, kalkuluen ziurgabetasunak kontuan hartuta, zaila da esleipen argi bat proposatzea. Kalkuluen zehaztasuna frogatzeko, $PEAL_2$-ren egitura egonkorrenen IR espektroak ere M06-2x/6-311++G(d,p) eta B3LYP-ED=GD3BJ/def2TZVP maila konputazionaletan kalkulatu ziren (ikusi 3.28 Irudia).

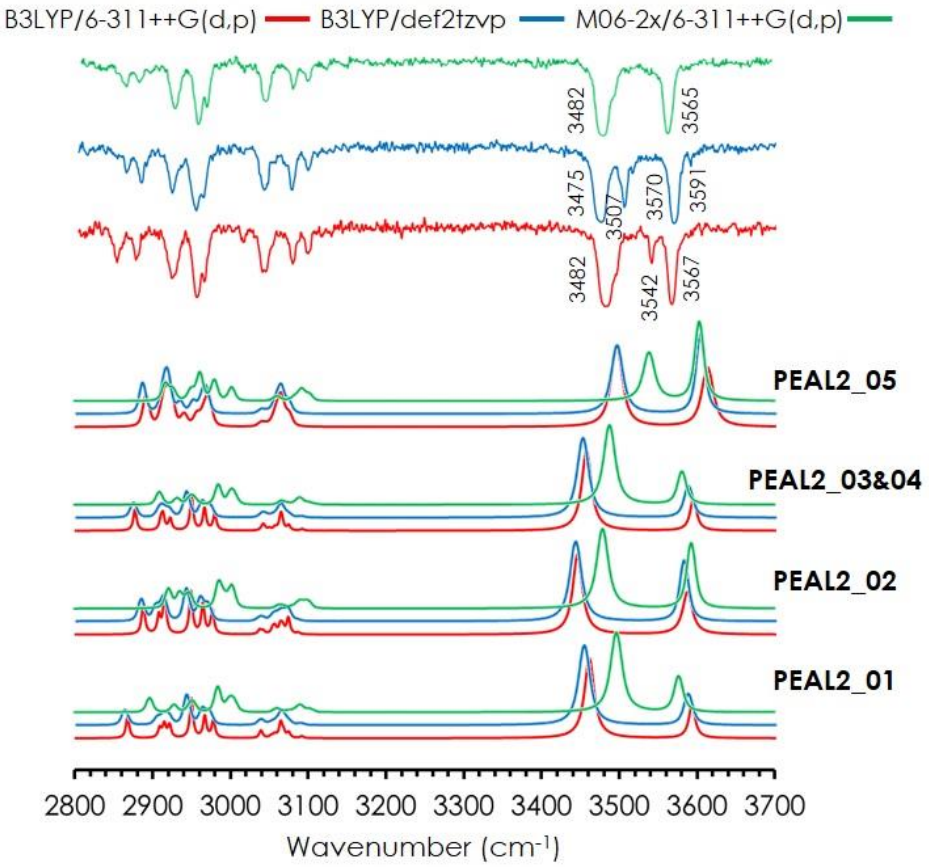

3.28 Irudia: $PEAL_2$-ren egitura egonkorrenen IR espektroen simulazioa maila konputazional desberdinetan. OH taldeen eskala faktorea 0.9565-an finkatu zen B3LYP/6-311++G(d,p) mailarako, 0.962-an B3LYP/def2TZVP mailarako eta 0.937-an M06-2X/6-311++G(d,p) mailarako. CH taldeen eskala faktorea 0.962-an mantendu zen maila konputazional guztietan.

Oro har, probatutako metodo konputazional guztiek desberdintasun berberak dituzte $PEAL_2$-ren egituren arteko bibrazio-maiztasunen predikzioetan. Dispertsioaren bidez zuzendutako B3LYP metodoan ezarritako def2TZVP basearen erabilerak ez du alderik Pople-ren ξ-hirukoitza base-multzoak kalkulatutako bibrazio-maiztasunekin. M06-2x/6-311++G(d,p) metodoak, berriz, hobeto aurresaten ditu OH talde lotzaileei dagozkien banden posizioa. Konparazio hauen arabera, ondoriozta daiteke kalkulatutako lau egitura egonkorrenetatik, hiru isomero daudela espantsio supersonikoan.

3.28 Irudiko espektroei begiratuta, ikus daiteke trantsizio ahul eta estu bat 3542 cm^{-1}-tan espektro gorrian, eta 3507 cm^{-1}-tan espektro urdinean. Banda horren jatorria ez da argia, baina ziurrenik, konbinazio-banda bat izan litzateke, hidroxilo taldeen luzaketa-bibrazio eta librazio-moduen arteko konbinazio batetik sortua. Antzeko konbinazio-bandak jadanik ikertu dira beste sistema batzuetan, hala nola karbonilo taldeak duten molekula organikoetan[23] edo amina protonatuetan.[24] Kasu horretan, identifikazio

zehatz batek asko lagun lezake PEAL dimeroan eta zerikusia duten beste sistema batzuk karakterizatzen. Izan ere, antzeko trantsizio ahulak jadanik behatu dira BnzA trimeroaren espektroetan (ikusi 3.14 Irudia).

3.3.3. 2-Feniletanol trimeroa

BnzA-ren eta aurreko dimeroaren emaitzak ikusita, panorama konformazional konplexua aurreikus dezakegu $PEAL_3$-rentzako. Jadanik aurkeztutako BnzA trimeroak fase isolatuan konformazio linealen sorpena erakutsi zituen, nahiz eta egitura ziklikoak ez ziren energian oso altuak aurreikusi.

PEAL trimeroaren energia potentzialaren gainazala familia-multzo zabal eta konplexu batez osatuta dago, CH_2CH_2OH taldeak hiru PEAL molekuletan har ditzakeen konbinazio posible guztiak direla eta. Sistema arrazoizko tamaina batean mantentzeko, energia-leihoa murriztu zen analisirako, eta konformazio egonkorrenak bakarrik hartu ziren kontuan. 3.29 Irudian $PEAL_3$-ren bi familia egonkorrenen egiturak biltzen dira. BnzA trimeroaren antzera, familia horiek hidrogeno lotura sare lineal edo zikliko batean kokatutako egiturek osatzen dituzte.

Familia linealaren konformazio egonkorrenetara hurbilago begiratuz gero, trimeroak aldez aurretik eratutako dimero egonkorrei hirugarren PEAL molekula bat gehituz sortzen direla behatu daiteke. Beraz, agregatu horiek bi OH···O hidrogeno loturek eta OH···π interakzio gehigarri batek osatzen dituzte. Azkenik, badirudi eraztun aromatikoak pilaketa elkarrekintzen bitartez antolatzen direla. Interesgarria bada ere, agregazio homo-kirala ez da antolamendu egonkorrena PEAL trimeroan. Hala eta guztiz ere, aurkeztutako egitura guztiak energian hurbil daude, eta, espantsioan dimero egonkor bat baino gehiago esleitu zenez, trimeroaren egitura desberdinak batera egon litezke. PEAL3_07 egitura adieraztekoa da, izan ere, bertan monomero bat protoi hartzaile bikoitz gisa jokatzen duelako. Egitura hori egonkortu egiten da tenperatura altuagotan. Hortaz, tenperatura jokoan sartzen denean, agregatuan hidrogeno lotura sarearen moldaketa berri bat egon daiteke.

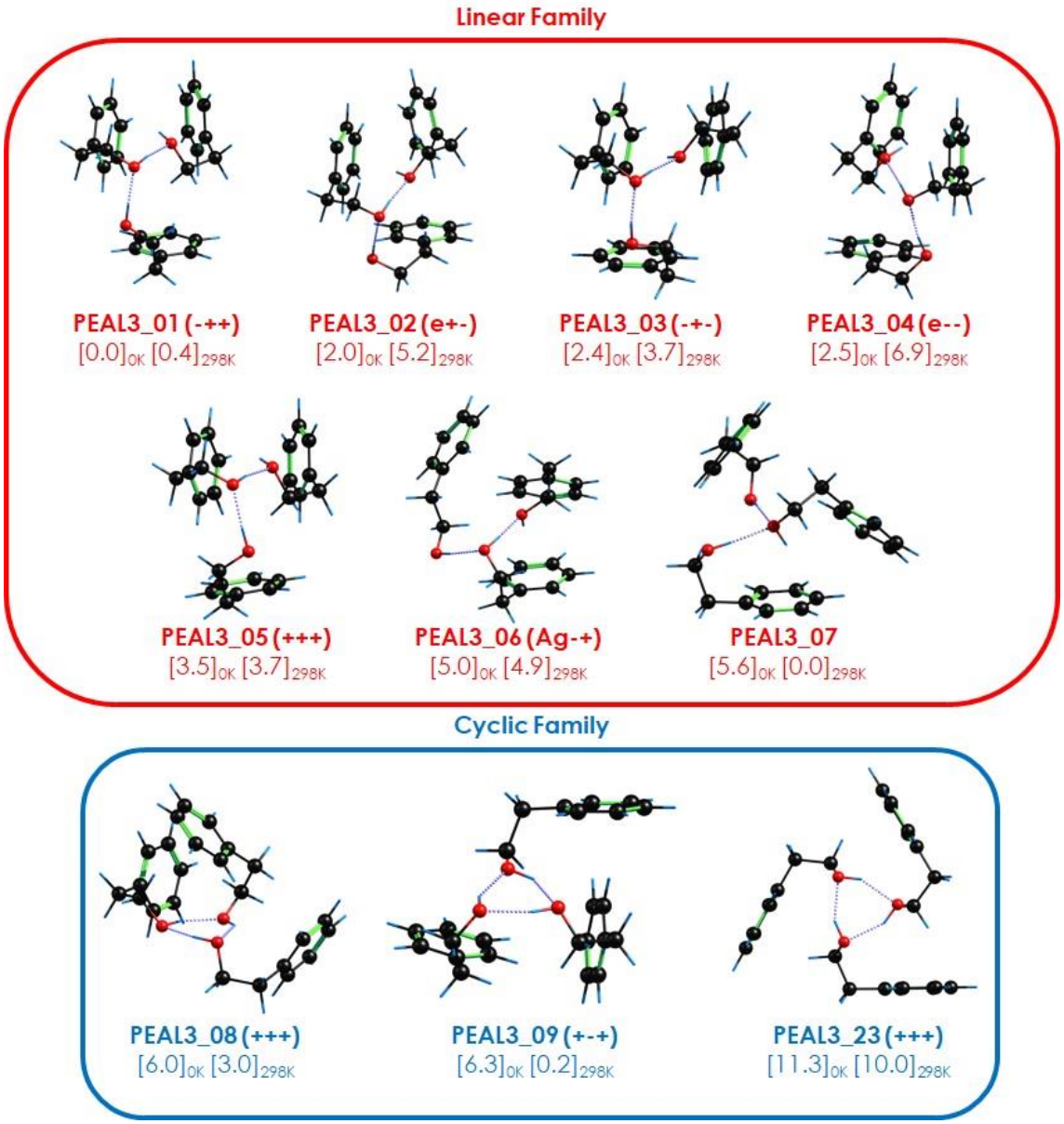

3.29 Irudia: $PEAL_3$-ren familia egonkorrenak, B3LYP(ED=GD3BJ)/6-311++G(d,p) mailan kalkulatuak. Energia erlatiboaren balioak egitura bakoitzaren azpian adierazten dira, kJ/mol-tan. Egitura bakoitzaren izena PEAL molekula bakoitzaren Ggπ konformazioaren angelu diedroen orientazioarekin adierazten da. Angelu diedroen analisia hidrogeno lotura sarearen ordena jarraituz egin zen, beraz, lehen seinua lehen protoi emaileari dagokio. PEAL3_02, 04 eta 06 egituren kasuan, lehen PEAL molekula konformazio desberdin batean aurkitzen da (e – eklipsatua, Ag – *anti gauche*).

Hidrogeno lotura sare ziklikoa ez da lineala bezain egonkorra. Hala ere, egitura horiek ez daude energia hain altuetan, eta beraz, espantsioan ere aurki daitezke, bereziki tenperatura altuagotan, entropiari esker egonkortzen baitira (ikusi A3.12 Irudia). Bitxia bada ere, C_3 homo-ziklo simetrikoa ez da egitura egonkorrena familia ziklikoaren barruan, BnzA-rentzat aurkitutakoaren kontra.

3.30 Irudia PEAL trimerorako neurtutako REMPI espektroa aurkezten du. Tamaina honetako agregatuetan ohikoa den bezala, seinalearen ahultasunak "UV/UV hole burning" esperimentuak aurrera eramatea eragozten du.

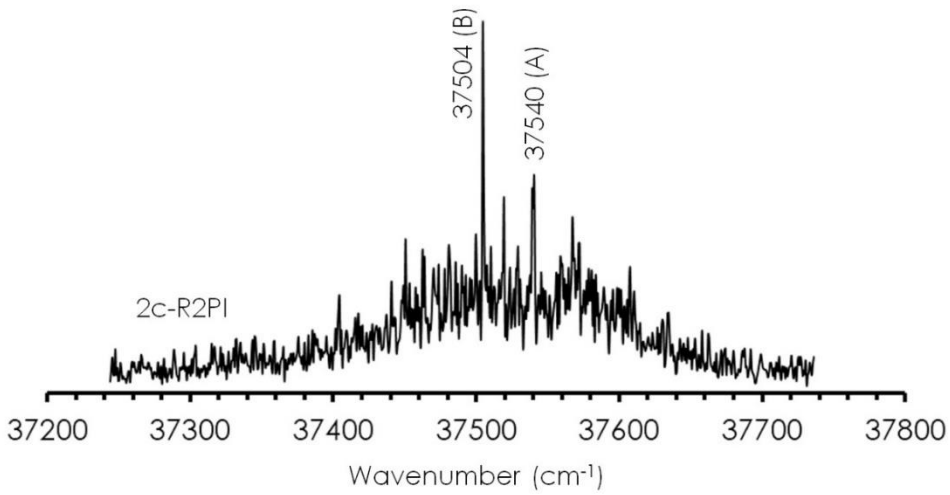

3.30 Irudia: $PEAL_3$-ren bi koloreko REMPI espektroa. Ionizazio laserra 35714 cm^{-1}-tan finkatu zen.

Absortzio espektroak hondo zaratatsutik nabarmentzen diren trantsizio elektroniko diskretu batzuk aurkezten ditu. Espektroko banda-kopuru txikiak konformazio gutxiago aurreikusten ditu, $BnzA_3$-rekin alderatuta. IDIRS esperimentuetarako hainbat uhin-luzera probatu ziren, eta bi IR espektro ezberdin lortu ziren REMPI espektroan (A) eta (B) gisa markatutako trantsizioak zundatzean. Gainerako trantsizioen azterketan ez ziren IR espektro gehigarririk lortu.

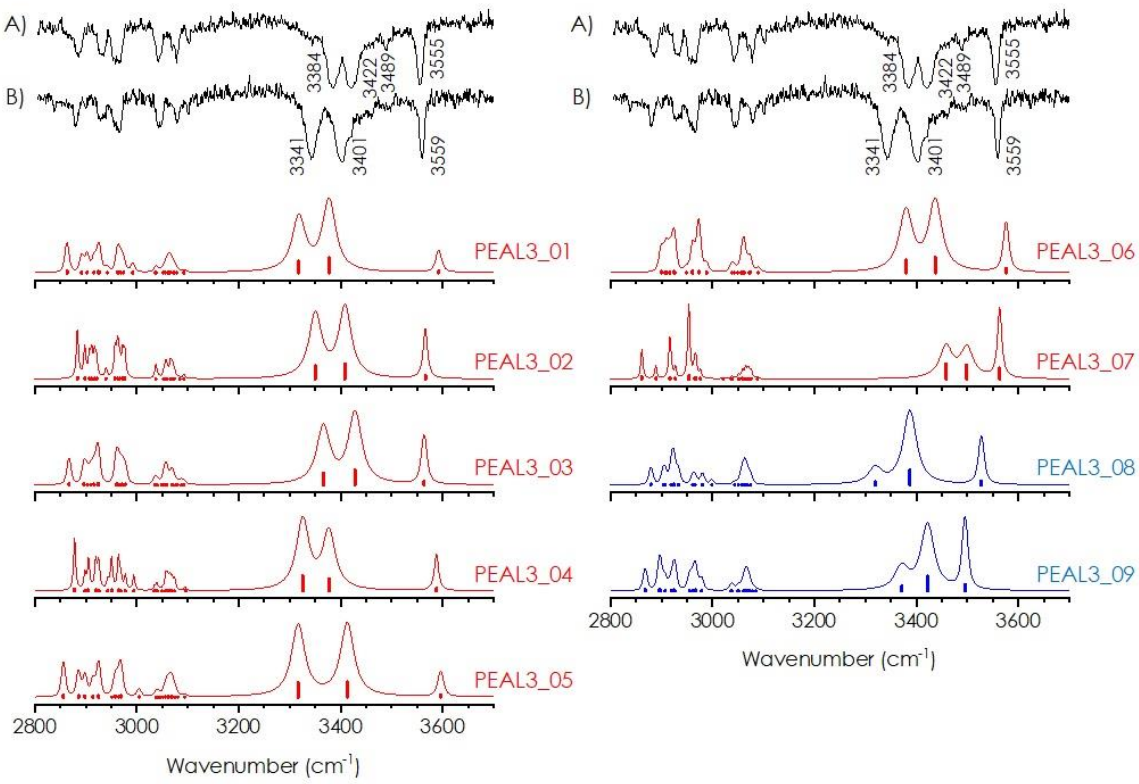

3.31 Irudia: $PEAL_3$-ren IDIR espektroen eta egitura egonkorrenen simulazioen arteko konparaketa. Maiztasunen kalkulua B3LYP(ED=GD3BJ)/6-311++G(d,p) mailan egin zen, eta 0.9565-ko eskala faktorea erabili zen OH eta CH taldeen anharmonizitatea zuzentzeko. (A) eta (B) espektroak UV laserra 37540 eta 37504 cm^{-1} uhin-luzeratan finkatuz lortu ziren, hurrenez hurren.

3.31 Irudian, $PEAL_3$-rako lortutako IR espektro esperimentalen eta konformazio egonkorrenetarako predikzio konputazionalen arteko konparazioa ageri da. Bi espektroek OH luzaketa-bibrazio banda pare bat eta elkarrekintza ahulago batean inplikatutako OH banda bat dituzte. Espektroen arteko antzekotasunak bi isomeroek antzeko egiturak dituztela iradokitzen du. Hala ere, OH banden artean ezaugarri ahulagoak (3489 cm^{-1}) aurki daitezke, zeinak agerian uzten duen konformazio gehigarrien edo banda konbinatuen presentzia, $BnzA_3$ kasuaren moduan.

3.31 Irudian egitura linealen predizkioak behatutako bandak ondo erreproduzitzen dituztela argi dago, baina predikzio hauek, berriro ere, oso antzekoak dira esleipen zehatz bat egiteko. Espantsioan zenbait dimero egiturak detektatu zirenez, eta kalkuluek trimero egonkor gehienek dimeroei hirugarren PEAL molekula bat gehitzean osatzen direla erakutsi zutenez, pentsa liteke gutxienez trimero egituren bi familia aurkitu ahal direla, horietako bakoitza aipatutako dimero batean oinarrituta. Simulatutako espektroetan antzekotasunak izan arren, OH···O elkarrekintza-indarraren aldaketa txikiak teoriak atzeman zituen. PEAL3_01 eta _04 egiturek ongi

erreproduzitzen dute B espektroa; eta PEAL3_02 eta PEAL3_03 egiturez, aldiz, hobeto erreproduzitzen dute A espektroko banden kokapena. PEAL3_07 egitura, protoi-hartzaile bikoitza duena, ziurtasunez baztertu daiteke, espektro esperimentalekin duen bat-etortze eskasa dela eta.

Emaitza esperimentalen eta PEAL3_08 eta _09 egitura ziklikoen predikzioen arteko alderaketa interesgarria da, izan ere, 3489 cm^{-1}-tan agertzen diren absortzio ahulak azaldu dezaketelako. Horrez gain, gainerako OH banda lotzaileak 3330-3430 cm^{-1} tartean aurresaten dira. Isomero hauen egonkortasun erlatibo txikiak isomero linealekin alderatuz gero espantsioan populazio txikia aurreratzen du, zeinak IR espektroetan behatutako intentsitate ahuleko absortzioekin bat datoz. Hala eta guztiz ere, nabaritasun ahul horiek ez dira nahikoak egitura horien presentzia jet-an baieztatzeko.

3.3.4. 2-Feniletanol tetrameroa

PEAL tetrameroaren agregatuaren hazierak BnzA-ren antzeko agregazio-bidea jarraitu zuen, nahiz eta bere panorama konformazionala gero eta konplexuagoa izan. Konputazioaren ikuspegitik, $PEAL_4$-ak egitura antolaketa kopuru ia infinitua du. Aurreko PEAL agregatuekin alderatuta, tetramero tamainan, azterketa konputazionalak egitura ziklikoak baino ez zituen azaldu energia-leiho zabal batean. 3.32 Irudian PEAL tetrameroarentzat aurkitutako antolamendurik egonkorrenak ageri dira. Ikusi daitekeenez, homo-kiralitatea eta simetria faltan daude konformazio egonkorrenetan. Egitura egonkorrena, PEAL4_01, monomeroen konformazio nahasketa batez osatuta dago. Antzeko konfigurazioa ikus daitezke gainerako egituretan. Gainera, konformazioen arteko energia-aldea txikia da, zeinak espezie bat baino gehiago batera egotea (edo elkar konektatuta egotea) ahalbidetzen duen baldintza esperimentaletan, PES-aren topologiak hozte-prozesuaren bitartean erlaxatzeko aukerak ematen ez badu behintzat.

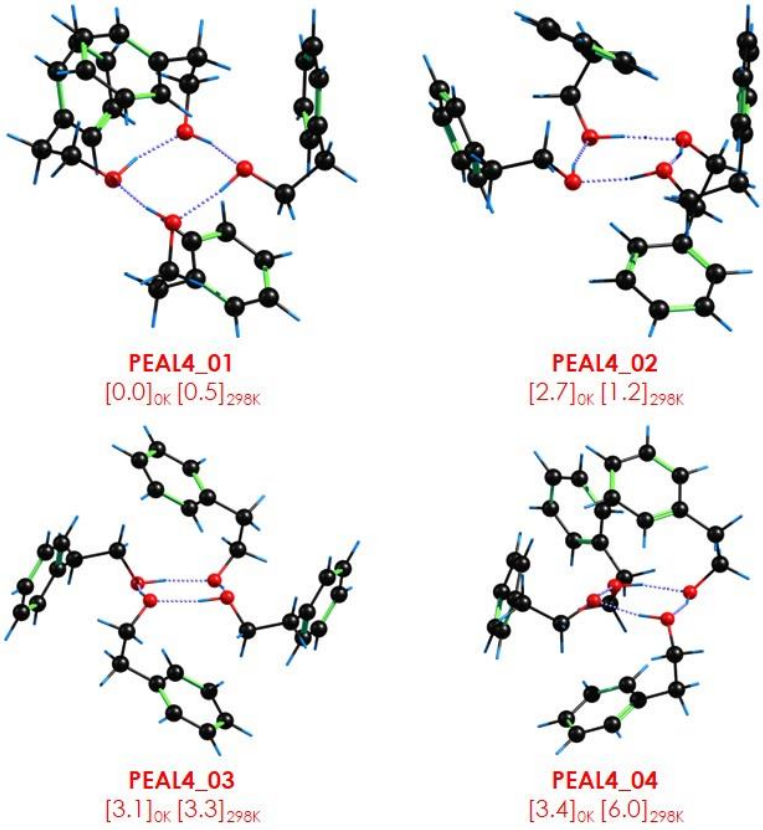

3.32 Irudia: PEAL tetrameroan aurkitutako egitura esanguratsuenak, B3LYP-ED=GD3BJ/6-311++G(d,p) mailan kalkulatuak. Energia balioak egitura bakoitzaren azpian kJ/mol-etan adierazten dira.

Agregatu honen seinale ahula izan arren, bi koloretako REMPI espektroa neurtzea posiblea izan zen (3.33 Irudia). Antzeman daitekeenez, espektro oso pilatua da, 37300-37700 cm^{-1} tartean zabaltzen dena. Lehenengo trantsizio bibroniko diskretua 37380 cm^{-1}-tan agertzen da, eta beraz, 0_0^0.moduan hartu da. Espektroak intentsitatea irabazten du urdinera joan ahala, non trantsizio indartsuagoak ikusten diren. 37510 eta 37588 cm^{-1}-ko trantsizioak zundatu ziren IDIR espektroak neurtzeko, 3.34 Irudian ageri direnak.

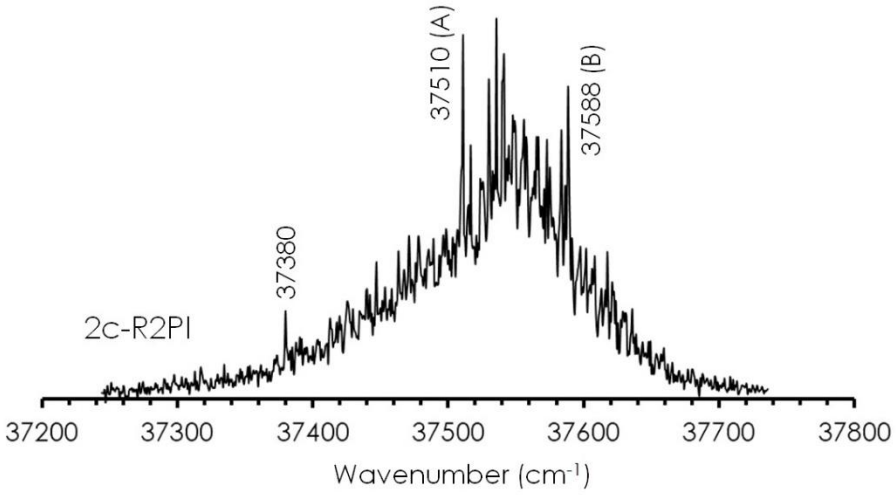

3.33 Irudia: $PEAL_4$-ren bi koloreko REMPI espektroa. Ionizazio laserra 35714 cm^{-1}-tan finkatu zen.

$BnzA_4$-an ikusi zen moduan, PEAL-eko OH taldeen luzaketa-bibrazio guztiak 3250-3300 cm^{-1} tartean multzokatuta agertzen dira bi espektro esperimentaletan. Horrek argi adierazten du hidrogeno lotura sare zikliko baten sorpena. Bestalde, OH···π elkarrekintzei dagozkien banden gabezia hidrogeno lotura sarearen konponketa linealak baztertzeko aukera ematen du.

Espektro esperimentalen arteko desberdintasunak konfigurazio zikliko desberdina duten konformazio bat baino gehiagoren presentziak adierazten du. A espektroak bi absortzio sendo eta zabal ditu 3235 eta 3287 cm^{-1}-tan, 3340 cm^{-1}-tan agertzen den sorbalda batekin batera. B espektroak, berriz, absortzio zabalago bat aurkezten du, zeinaren gainean hiru ezaugarri bereiz daitezke (3330, 3295 eta 3274 cm^{-1}). Horiez gain, laugarren banda bat ageri da 3151 cm^{-1}-tan.

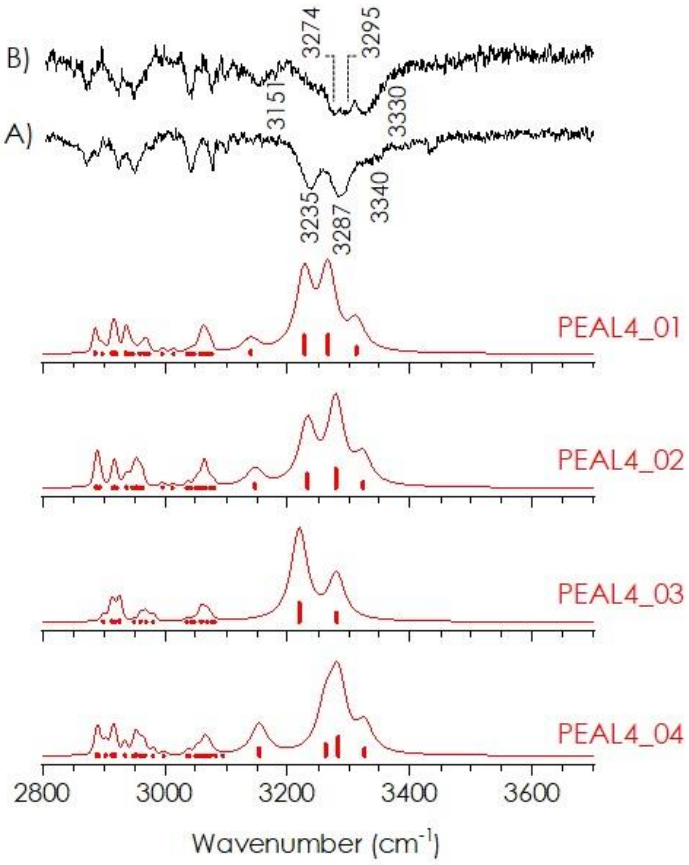

3.34 Irudia: $PEAL_4$-ren IDIR espektroen eta egitura egonkorrenen simulazioen arteko konparaketa. Maiztasunen kalkulua B3LYP(ED=GD3BJ)/6-311++G(d,p) mailan egin zen, eta 0.9565-ko eskala faktorea erabili zen OH eta CH taldeen anharmonizitatea zuzentzeko

3.34 Irudian PEAL tetramero egonkorrenen predikzio konputazionalen eta espektro esperimentalen arteko konparaketa aurkezten da. IR banda hain zabalen esleipen zehatza ez da erraza. Alabaina, konformazio egonkorrenek oso ongi erreproduzitzen dituzte behatutako ezaugarriak. Hain zuzen, PEAL4_01 eta _02 egiturek ederki aurresaten dute gorrirantz agertzen den OH banda, 3151 cm^{-1}-tan. Bestalde, PEAL4_03 egituraren simulatutako espektroa zehaztasunez erreproduzitzen ditu A espektroaren banden kokapena.

Sistema honetan konformazio bat baino gehiago zehazki esleitzea ez da prozesu erraza. Optimizatutako egitura guztiek antolamendu ziklikoak dituzte, eta, ondorioz, guztien antzeko predikzioak dituzte, espektro esperimentalarekin bat datozenak. Esperimentu gehiago, edo beste teknika espektroskopiko batzuekin konbinatu egin beharko lirateke esleipen zehatzagoa lortzeko. Hala ere, energia-irizpide bat ezarriz, espektro esperimentalak $PEAL_4$-ren hiru konformazio egonkorrenei behin-behinean esleitu daitezke.

3.4. Emaitzen eztabaida

Aurreko ataletan BnzA eta PEAL agregatuen azterketa espektroskopiko sakona aurkezten da. Oro har, alkohol aromatiko bakoitzaren agregazioa OH···O hidrogeno loturek zuzentzen dute. Elkarrekintza hau uraren eta alkohol txiki asetuen agregazioan nagusia da.[25] Beste talde funtzional batzuen presentziak elkarreragin molekularra aldatu egiten du, hidrogeno lotura hartzaile gehigarri edo alternatibo gisa jokatuz, alegia. Arestian aztertutako agregatuetan, elkarrekintza ez-kobalente gehigarriak, eraztun aromatikoak parte hartzen dutenak bereziki, konformazioaren azken formaren erantzule direla erakutsi dute.

Bai BnzA zein PEAL molekulak sistema interesgarriak dira alkohol aromatikoen agregazio-lehentasunak aztertzeko, haien OH taldeek eraztun aromatikoari zuzenean lotuta ez daudelako. Hortaz, hodei aromatikotik isolatzen dira, deslokalizazio-efektuak saihestuz. Baina, aldi berean, eraztun aromatikoa bigarren mailako elkarrekintzen iturri garrantzitsua da. Gainera, BnzA-tik PEAL-era dagoen malgutasun aldaketari esker, askatasun-gradu gehigarriek agregazio-prozesuan duten eragina kalkula dezakegu, batez ere, emaitza hauek fenol molekularen ereduekin alderatzen direnean. Fenolaren tortsioarekiko zurruntasuna dela eta, elkarrekintza-energia gehiena OH···O hidrogeno lotura arrunt bakarra eratzetik dator, baina fenolaren eraztun aromatikoen arteko dispertsioa dimeroaren geometria aldatzeko gaitasuna du.[17]

Alkilo katearen luzapen gehigarriak agregatuen azterketa zaildu zuen, zentro kiral bat sortu zelako. Dimeroen azterketa esteoisomero egituren arteko egonkortasun alde txikia baztergarria ez zela erakutsi zuen: dimeroen egitura egonkorrenak konformazio homo- eta hetero-kiraletan banandu egiten dira. Banaketa horrek garrantzi handiagoa hartzen du agregatu handiagotan, non egitura dibertsitatea zabaltzen den familia bakoitzean dauden enantiomero posibleen konbinaketak direla eta.

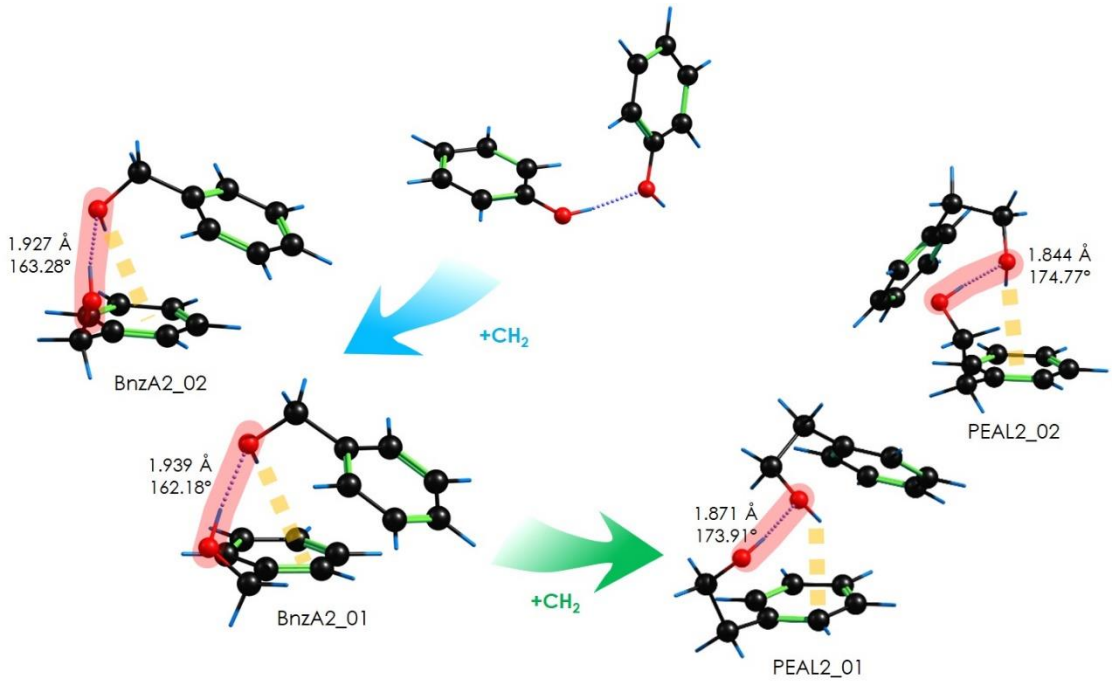

3.35 Irudia: BnzA eta PEAL dimeroen esleitutako egituren eta jadanik argitaratutako fenol dimeroaren arteko konparaketa.[17] Egiturak B3LYP(ED=GD3BJ)/6-311++G(d,p) mailan kalkulatu egin dira. OH···O elkarrekintzak gorriz adierazten dira, eta bigarren mailako OH···π elkarrekintzak, aldiz, lerro-eten hori batez adierazten dira.

3.35 Irudian BnzA eta PEAL dimeroei esleitutako egiturak ageri dira, fenol dimeroarekin alderatuta. Eraztun aromatikoaren eta hidroxilo taldearen arteko metileno taldeak emandako malgutasunak OH···π elkarrekintza gehigarriak eratzea ahalbidetzen du. Izan ere, bigarren metilo talde baten adizioa PEAL molekulan sistemaren malgutasuna handitzen du, aipatutako OH···π elkarrekintzaren eraketa monomeroan ahalbidetuz. Dimeroari dagokionez, PEAL-ren konformazio egonkorrenak $BnzA_2$-an baino OH···O hidrogeno lotura indartsuagoa aurkezten du, distantzia laburragoarekin eta angelu zabalagoarekin. Behaketa hori dimeroen IR espektro esperimentaletan ere behatu zen, non OH···O elkarrekintzei esleitutako bandak PEAL-an gorrirantzko lerrakuntza handiagoa aurkezten duten BnzA-an baino (~ 15-20 cm^{-1}). Konplexu bakoitzeko dimero egonkorrenen dentsitate elektronikoaren gainazalaren analisi topologikoak elkarrekintza-indar horren desberdintasunak baieztatu egin zuen (ikusi 3.36 Irudia). Izan ere, dentsitate gradiente murriztuaren zenbakizko irudikapenean, OH···O elkarrekintza balio negatiboetan agertzen da PEAL-an BnzA-an baino.

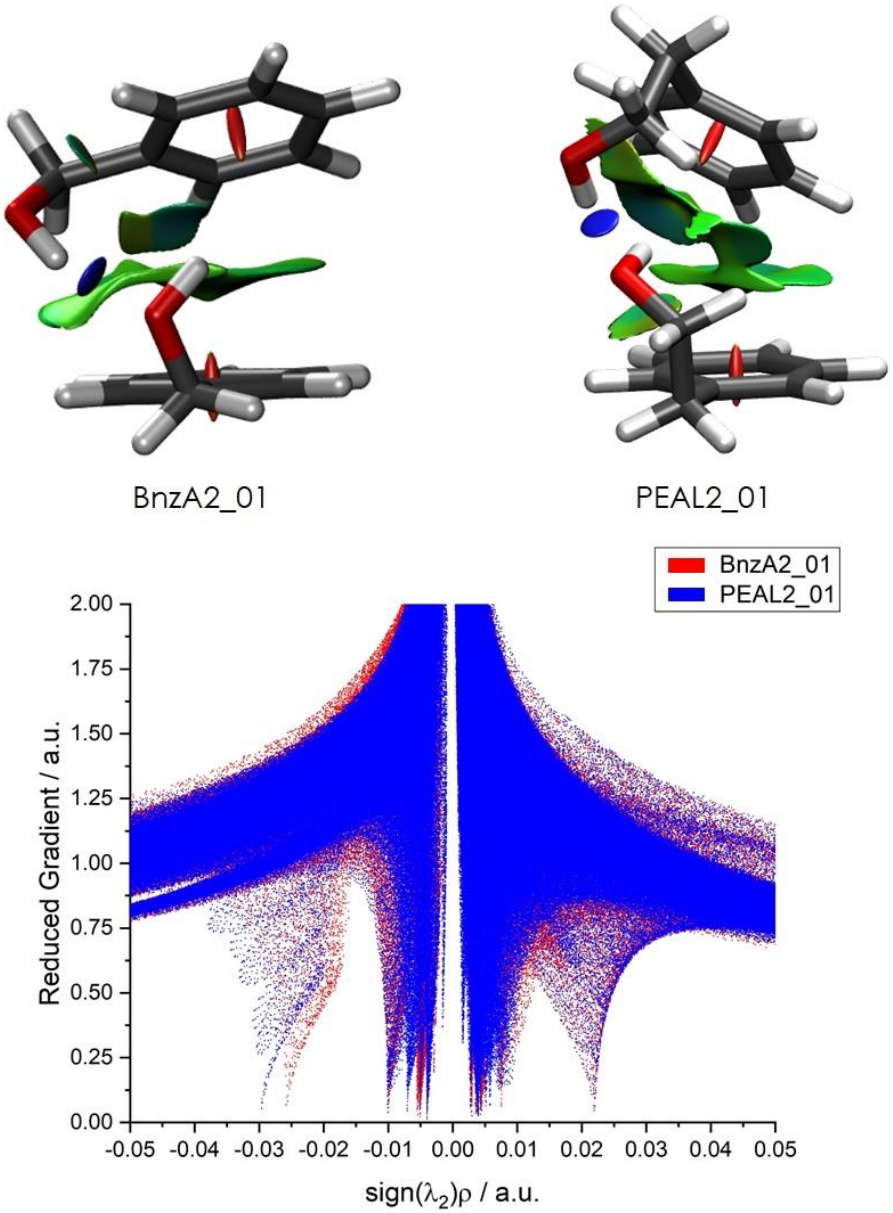

3.36 Irudia: 3D-ko NCI-en irudikapena BnzA2_01 eta PEAL2_01 egituretarako, bi dimeroen RDG vs sign(λ_2)ρ diagramen irudikapenekin batera.

BnzA eta PEAL dimeroek panorama konformazional aberatsa erakutsi dute, non familia konformazional bakoitza hainbat interakzio ez-kobalenteen bidez egonkortu egiten da. Espero zen bezala, esleitutako egiturek OH···O elkarrekintza indartsuak sortzen dituzte alkohol taldeen artean, baina OH···π motako elkarrekintza gehigarriek $BnzA_2$ eta $PEAL_2$ konplexuen azken forma moldatzen dute. Patroi kooperatibo hau bestelako alkohol dimeroetan aurkitu zen, hala nola, 1-feniletanolean,[14] 1-indanolean,[26] eta propargil alkoholan.[27,28]

Fenol dimeroa, OH talde protoi-hartzaileak bere bazkide molekulatik urrun seinalatzen du, BnzA-an eta PEAL-an, berriz, OH···π elkarrekintzak sortzen ditu, zeinen arrastoak IR espektroan bereizgarriak diren. Arrasto horiek OH banda askeen eta elkarrekintza indartsuetan parte hartzen duten OH banden artean azaltzen dira. Interakzio gehigarri horrek 3-6 kJ/mol-eko egonkortasun erlatiboa ematen du $BnzA_2$-an, eta 8-10 kJ/mol-ekoa $PEAL_2$-an, OH···O hidrogeno lotura bakarra duten egiturekin alderatuta. Beraz, badirudi hidroxilo taldearen eta eraztun aromatikoaren arteko kate alifatikoa luzatzeak agregazioaren elkarrekintza-lehentasunean zuzeneko eragina duela.

Horrez gain, katearen luzapenak ere askatasun-graduak handitu zituen, PES intermolekularraren konplexutasuna handituz, bereziki PEAL-ren kasuan. OH taldearen eta eraztun aromatikoaren artean etilenoaren ordezkapenak eragindako malgutasun gehigarriari esker, leiho zabalagoa sortu zen OH···O eta OH···π hidrogeno loturak duten dimero egonkorrentzat. 3.3.3 atalean ikusi dugunez, IR espektro esperimentalek zenbait konformazioen ekarpena zuten, ziur aski, $PEAL_2$-ren diastereoisomero posible guztienak. Haien predikzioak oso antzekoak direnez, beste esperimentu batzuk egin beharko lirateke diastereoisomeroen ekarpen zehatza identifikatzeko. Bestalde, erresonantzia edo konbinazio banden presentziak behatu dira, intentsitate ahuleko bandak gisa. Antzeko konbinazio bandak deskribatu egin dira karbonilo taldeak dituzten molekulen konplexu monohidratatuetan.[23] Egia bada, azken esleipen bat lagungarria izan litzateke, banda horiek agregatuen egiturarekiko oso sentikorrak baitira. Halaber, sistema hauen espektroskopia errotazionalak esleipen zehatzago bat eman lezake.

Hirugarren molekula baten adizioak panorama teoriko zein esperimentala zailtzen du. Ur-trimeroetan,[18] alkohol asetuetan[19] eta fenolan,[17] hidrogeno lotura sare zikliko bat sortzen da hidroxilo taldeen artean. BnzA3_06 egiturak C_3 simetria-ardatz bat aurkezten du, fenol trimeroan behatutakoaren modukoa. Hala ere, kalkuluen arabera $BnzA_3$-ren egitura ziklikoak ez dira linealak bezain egonkorrak. Alde hau are handiagoa da $PEAL_3$-an. Antolaketa ziklikoak egitura lineak egonkorrenaren 10 kJ/mol gainetik daude, eta hauen presentzia espantsioan ez da detektatu. Nahiz eta kate linealek kooperatibitatea galdu, OH···O hidrogeno lotura baten ordezkapena OH···π lotura batez faboratu egiten da, eraztun aromatikoak modu egokiagoan antolatzen direlarik egitura ziklikoekin alderatuz. Joera hau jadanik behatu zen 1-indanol[26] eta 2-fluoroetanoletan,[29] non hiru OH···O hidrogeno loturen bidez sortutako kooperatibitatea hidrogeno lotura ahulagoek osatutako kate lineal batez ordezkatzen zen.

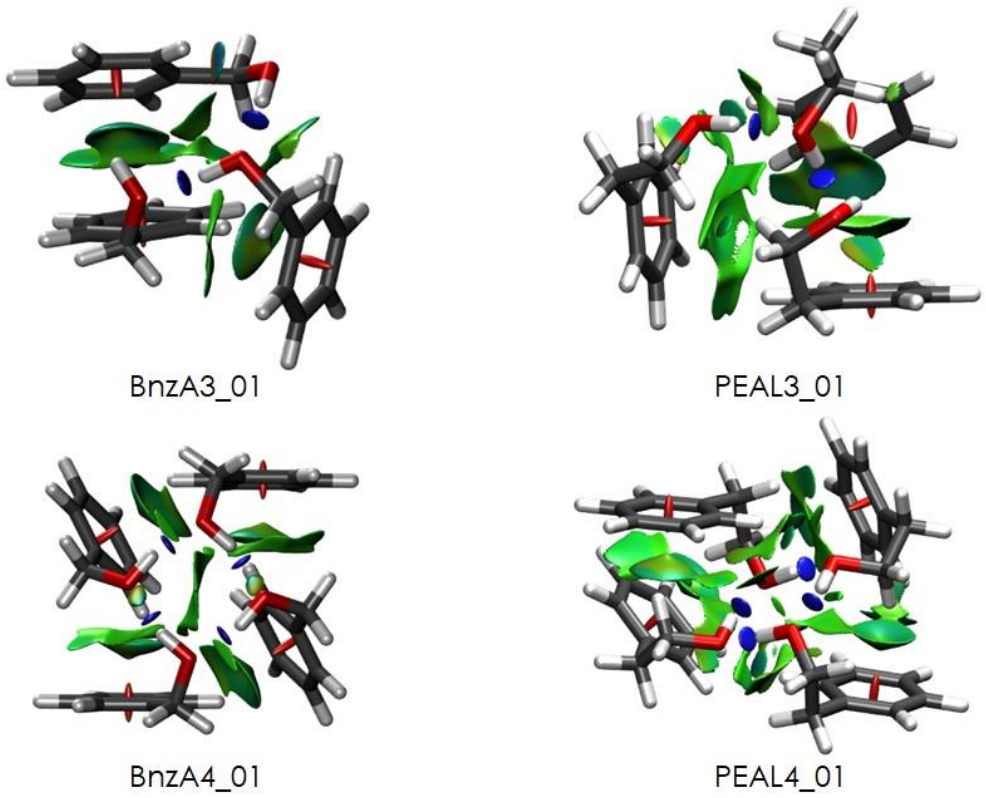

3.37 Irudia: Esleitutako BnzA eta PEAL trimero eta tetramero egonkorrenen 3D-ko NCI irudikapenak.

3.37 Irudiak NCI-ren irudikapenak aurkezten ditu BnzA eta PEAL trimero eta tetramero egonkorrenetarako. Oro har, bi sistemen trimero linealak oso antzekoak dira. Dimeroetan behatutako hidrogeno lotura sarea luzatu egiten da OH···O elkarrekintza gehigarri baten bidez, kateak OH···π lotura batean amaitzen delarik. BnzA-an ikusi zen moduan, eraztun aromatikoek modu desberdinetan antola daitezkete, geometria egonkor desberdinak sortuz. Joera hau ere behatu egin da PEAL egituretan. $BnzA_3$-ren egitura egonkorrena (BnzA3_01) monomeroen homo-agregazioaren ondorioz sortzen da. Aldiz, PEAL-ren kasuan lehentasun hori galdu egiten da, beharbada, metileno talde gehigarriak malgutasun handiagoa ematen duelako, eraztun aromatikoen arteko aldarapen txikiagoak dituzten egiturak ahalbidetuz hain egonkorrak ez diren monomeroen konformazioen kontura.

Sistema hauetan aztertutako agregatu handienak tetrameroak izan ziren. Bi kasuetan, neurtutako infragorri espektroek hidrogeno lotura sare ziklikoen eraketari dagozkie, predikzio konputazionalen arabera. Bitxia bada ere, hidrogeno lotura sare ziklikoen eta linealen arteko alde energetikoa handitu egiten da. BnzA-ren egitura egonkorrena, BnzA4_01, C_2 egitura simetrikoa da. Gainera, agregatu homo-kirala da, BnzA molekula guztiek G+ konformazioa aurkezten dutelako. Lehentasun-konformazional hau guztiz

galtzen da PEAL tetrameroan. Konformazio egonkorrenean PEAL monomeroek ez dute ezta konformazio berdina erakusten. Bestalde, malgutasun gehigarria dela eta, simetria baxuko egiturak eratzen dira, non eraztun aromatiko guztiak plano berean kokatzen diren. Aipatzekoa da uran,[29] alkohol asetuetan,[30,31] eta antzeko sistema aromatiko[7] eta ez-aromatikoetan[6] antolaketa ziklikoak egitura egonkorrenak direla.

3.5. Ondorioak

Kapitulu honetan, bi alkohol aromatikoen agregazio-lehentasunen lehen uneak aztertu dira. Espantsioen bidezko hozketa, masan bereizgarriak diren laser espektroskopia teknikekin konbinatuta, konplexu mota hauek karakterizatzeko tresna bikaina dela behin ere erakutsi du.

Lortutako emaitzen arabera, OH taldeek eta haien elkarrekintzek molekulen agregazioa zuzentzen dute. OH···O hidrogeno lotura sendoak nukleazioaren indar nagusiak diren arren, OH···π eta π···πelkarrekintza sekundarioek konformazioei azken forma ematen diete; bereziki ikertutako trimeroetan, non OH···OH···OH···π hidrogeno lotura sareak OH···O sare zikliko kooperatiboagoak baino egonkorragoak diren. Tetramero tamainan, egitura linealak ez dira hauteman. Horren arabera, puntu honetan joera aldaketa bat dago, non egitura ziklikoak egonkorrenak bilakatzen diren.

BnzA eta PEAL molekulen pausuz pausuko agregazioaren karakterizazio sakonak fase isolatuan alkoholen hasierako nukleazio-prozesuak gidatzen dituzten indarrak hobeto ulertzera lagundu digu. Alkilo katearen luzapenak guztiz aldatu du molekulen elkarrekintzen lehentasunak, izan ere, trimero tamainan hidrogeno sare zikliko arruntak egonkorragoak diren egitura linealen ordez aldatu direlako. Beraz, agregazioaren lehen uneetan, eraztun aromatikoen alde hidrofobikoetan aurkitzen diren indar dispertsiboen eta alde hidrofilikoetan ematen diren elkarrekintzekin arteko lehiaketa ematen da. Bestalde, elkarrekintzen arteko alde txikiak, eta kiralitate desberdineko agregatuen arteko energia alde txikiak, kapitulu honetan ikertutako sistemak teoria konputazional berriak probatzeko eta fintzeko banku-lana bilakatzen du.

3.6. Erreferentziak

[1] I. León, J. Millán, F. Castaño and J. A. Fernández, A Spectroscopic and Computational Study of Propofol Dimers and Their Hydrated Clusters, *ChemPhysChem*, 2012, **13**, 3819–3826.

[2] I. León, I. Usabiaga, J. Millán, E. J. Cocinero, A. Lesarri and J. A. Fernández, Mimicking anesthetic--receptor interactions in jets: the propofol--isopropanol cluster, *Phys. Chem. Chem. Phys.*, 2014, **16**, 16968–16975.

[3] I. León, J. Millán, E. J. Cocinero, A. Lesarri, F. Castaño and J. A. Fernández, Mimicking anaesthetic–receptor interaction: a combined spectroscopic and computational study of propofolphenol, *Phys. Chem. Chem. Phys.*, 2012, **14**, 8956–8963.

[4] I. León, R. Montero, A. Longarte and J. A. Fernández, IR mass-resolved spectroscopy of complexes without chromophore: Cyclohexanol·(H2O)n, n = 1–3 and cyclohexanol dimer, *J. Chem. Phys.*, 2013, **139**, 174312.

[5] M. Juanes, I. Usabiaga, I. León, L. Evangelisti, J. A. Fernández and A. Lesarri, The Six Isomers of the Cyclohexanol Dimer: A Delicate Test for Dispersion Models, *Angew. Chemie Int. Ed.*, 2020, **59**, 14081–14085.

[6] I. León, R. Montero, A. Longarte and J. A. Fernández, Influence of dispersive forces on the final shape of a reverse micelle, *Phys. Chem. Chem. Phys.*, 2015, **17**, 2241–2245.

[7] I. León, J. Millán, E. J. Cocinero, A. Lesarri and J. A. Fernández, Shaping Micelles: The Interplay Between Hydrogen Bonds and Dispersive Interactions, *Angew. Chemie Int. Ed.*, 2013, **52**, 7772–7775.

[8] H. S. Im, E. R. Bernstein, H. V. Secor and J. I. Seeman, Supersonic jet studies of benzyl alcohols: Minimum energy conformations and torsional motion, *J. Am. Chem. Soc.*, 1991, **113**, 4422–4431.

[9] C. E. H. Dessent, W. D. Geppert, S. Ullrich and K. Müller-Dethlefs, Ionization-induced conformational changes: REMPI and ZEKE spectroscopy of salicyl and benzyl alcohol, *Chem. Phys. Lett.*, 2000, **319**, 375–384.

[10] M. Mons, E. G. Robertson and J. P. Simons, Intra- and Intermolecular π-Type Hydrogen Bonding in Aryl Alcohols: UV and IR-UV Ion Dip Spectroscopy, *J. Phys. Chem. A*, 2000, **104**, 1430–1437.

[11] H. L. Fang and R. L. Swofford, Molecular conformers in gas-phase ethanol: A temperature study of vibrational overtones, *Chem. Phys. Lett.*, 1984, **105**, 5–11.

[12] V. Barone, Anharmonic vibrational properties by a fully automated second-order perturbative approach, *J. Chem. Phys.*, 2004, **122**, 14108.

[13] J. Bloino, A VPT2 Route to Near-Infrared Spectroscopy: The Role of Mechanical and Electrical Anharmonicity, *J. Phys. Chem. A*, 2015, **119**, 5269–5287.

[14] R. Medel and M. A. Suhm, Understanding benzyl alcohol aggregation by chiral modification: the pairing step, *Phys. Chem. Chem. Phys.*, 2020, **22**, 25538–25551.

[15] R. S. Ruoff, T. D. Klots, T. Emilsson and H. S. Gutowsky, Relaxation of conformers and isomers in seeded supersonic jets of inert gases, *J. Chem. Phys.*, 1990, **93**, 3142–3150.

[16] P. Felder and H. H. Günthard, Conformational interconversions in supersonic jets: Matrix IR spectroscopy and model calculations, *Chem. Phys.*, 1982, **71**, 9–25.

[17] N. A. Seifert, A. L. Steber, J. L. Neill, C. Pérez, D. P. Zaleski, B. H. Pate and A. Lesarri, The interplay of hydrogen bonding and dispersion in phenol dimer and trimer: structures from broadband rotational spectroscopy, *Phys. Chem. Chem. Phys.*, 2013, **15**, 11468–11477.

[18] F. N. Keutsch, J. D. Cruzan and R. J. Saykally, The Water Trimer, *Chem. Rev.*, 2003, **103**, 2533–2578.

[19] R. W. Larsen, P. Zielke and M. A. Suhm, Hydrogen-bonded OH stretching modes of methanol clusters: A combined IR and Raman isotopomer study, *J. Chem. Phys.*, 2007, **126**, 194307.

[20] N. Guchhait, T. Ebata and N. Mikami, Structures of hydrogen-bonded clusters of benzyl alcohol with water investigated by infrared-ultraviolet double resonance spectroscopy in supersonic jet, *J. Chem. Phys.*, 1999, **111**, 8438–8447.

[21] I. León, J. Millán, E. J. Cocinero, A. Lesarri and J. A. Fernández, Water Encapsulation by Nanomicelles, *Angew. Chemie Int. Ed.*, 2014, **53**, 12480–12483.

[22] M. Mons, E. G. Robertson, L. C. Snoek and J. P. Simons, Conformations of 2-phenylethanol and its singly hydrated complexes: UV–UV and IR–UV ion-dip spectroscopy, *Chem. Phys. Lett.*, 1999, **310**, 423–432.

[23] T. L. Fischer, T. Wagner, H. C. Gottschalk, A. Nejad and M. A. Suhm, A Rather Universal Vibrational Resonance in 1:1 Hydrates of Carbonyl Compounds, *J. Phys. Chem. Lett.*, 2021, **12**, 138–144.

[24] C.-K. Lin, R. Shishido, Q.-R. Huang, A. Fujii and J.-L. Kuo, Vibrational spectroscopy of protonated amine–water clusters: tuning Fermi resonance and lighting up dark states, *Phys. Chem. Chem. Phys.*, 2020, **22**, 22035–22046.

[25] M. A. Suhm, *Adv. Chem. Phys.*, 2009, 1–57.

[26] J. Altnöder, A. Bouchet, J. J. Lee, K. E. Otto, M. A. Suhm and A. Zehnacker-Rentien, Chirality-dependent balance between hydrogen bonding and London dispersion in isolated (±)-1-indanol clusters, *Phys. Chem. Chem. Phys.*, 2013, **15**, 10167–10180.

[27] J. Saini and K. S. Viswanathan, Discerning Near-Isoergic Isomers. A Matrix Isolation Infrared and ab Initio Study of the Propargyl Alcohol Dimers, *J. Phys. Chem. A*, 2017, **121**, 1448–1459.

[28] D. Mani and E. Arunan, Rotational spectra of propargyl alcohol dimer: A dimer bound with three different types of hydrogen bonds, *J. Chem. Phys.*, 2014, **141**, 164311.

[29] J. Thomas, X. Liu, W. Jäger and Y. Xu, Unusual H-Bond Topology and Bifurcated H-bonds in the 2-Fluoroethanol Trimer, *Angew. Chemie Int. Ed.*, 2015, **54**, 11711–11715.

[30] N. A. Seifert, J. Thomas, W. Jäger and Y. Xu, Rotational spectra and theoretical study of tetramers and trimers of 2-fluoroethanol: dramatic intermolecular compensation for intramolecular instability, *Phys. Chem. Chem. Phys.*, 2018, **20**, 27630–27637.

[31] T. B. Adler, N. Borho, M. Reiher and M. A. Suhm, Chirality-Induced Switch in Hydrogen-Bond Topology: Tetrameric Methyl Lactate Clusters in the Gas Phase, *Angew. Chemie Int. Ed.*, 2006, **45**, 3440–3445.

6. Kapitulua

Kafeina-Fenol elkarrekintzen azterketa

Hurrengo artikulutik moldatuta: I. Usabiaga, A. Camiruaga, C. Calabrese, A. Maris and J. A. Fernández, *Chem. – A Eur. J.*, 2019, **25**, 14230–14236.

6.1. Sarrera

Aurreko kapituluetan aztertutako sistemek agregatu molekularren azterketan teoria eta esperimentuen arteko lotura erakutsi zuten: datu esperimentalek predikzio konputazionalen arabera bakarrik interpreta daitezke. Baina, aldi berean, metodo konputazionalen garapena eta probak datu-multzo esperimental handia behar dute kimika kuantikoko kalkulu mailak doitzeko. Konputazioaren aldetik, bereziki zaila den sistema aurkezten dugu hemen: kafeina-fenol (Caf+Ph) dimeroa. Kafeina (6.1 Irudia), kafean dagoen metilxantina bat da, eta bere eragin estimulatzaileen erantzulea da.[1] Bere egiturak lau nitrogeno atomo, bi oxigeno atomo eta sistema aromatiko bat ditu. Hortaz, beste molekula batzuekin elkarrekintzak sortzeko gune ugari aurkezten ditu. Fenola, aldiz, hidroxilo ordezkatzaile bat duen bentzenozko eraztun batek eratutako molekula sinplea da. Jakina da tabakoaren osagaietako bat dela.[2] Beraz, kafea edaten duten erretzaileen odolean bi molekulak kontaktuan egon daitezke, eta horien agregazioak zeluletako errezeptoreekin sortzen duten elkarrekintzak alda dezake.[3-6] Hala ere, lan honen helburu nagusia ez da osasunarekin lotutako arazo horiek aztertzea, baizik eta agregatuetatik lortutako informazio espektroskopikoa erabiltzea, elkarrekintza ez-kobalenteek moldatzen dituzten metodo konputazional ezberdinen koherentzia/inkoherentzia ebaluatzeko.

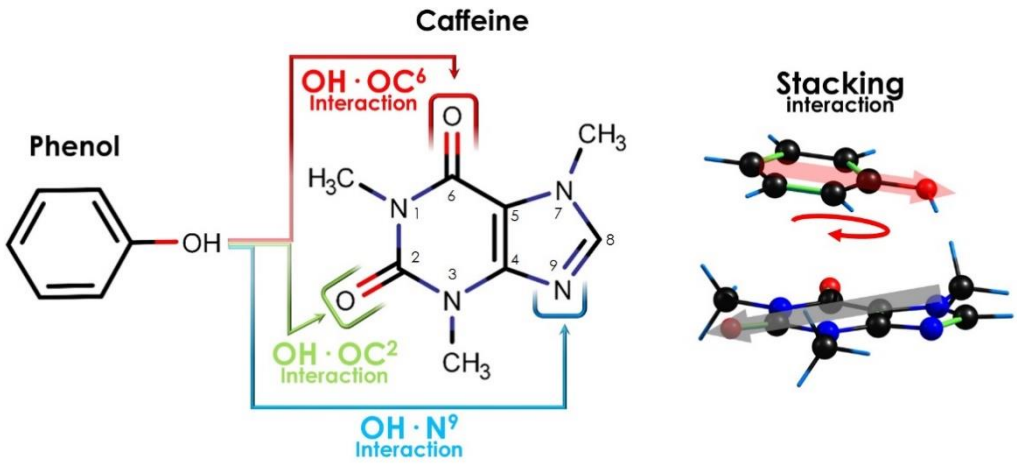

6.1 Irudia: Fenol eta kafeinaren egiturak (atomo zenbakikuntzarekin). Lau elkarrekintza gune nagusiak azpimarratu egin dira: OH·OC6, OH·OC2, OH·N9, eta pilaketa elkarrekintzak.

6.1 Irudiak fenolaren eta kafeinaren egiturak aurkezten ditu. Ikusi daitekeenez, kafeinak hidrogeno loturak sortzeko zenbait ainguratze-puntu ditu. Elkarrekintza horien egonkortasuna, eraztun aromatikoen arteko pilaketa elkarrekintzen, edo kafeinaren metilo taldearen eta fenolaren eraztun aromatikoaren arteko CH···π elkarrekintza gehigarrien bidez moldatuta egon daitezke. Elkarrekintza guzti horiek bi molekulak

modu askotara egonkortu ditzaketenez, egonkortasunean oso hurbil dauden isomero konformazional ugari egon ahal dira.

Lan honetan erabilitako metodologia tesian aurkeztutako gainerako azterlanen berdina izan zen, baina azterketa konputazionala metodo eta base ezberdinekin handiagotu egin zen. Lau metodo konputazional erabili ziren, DFT, metodo hibrido eta "ab initio" metodoak konbinatuz: M06-2X, MN15, B3LYP eta MP2. Aurreko kapituluetan ikusi dugunez, M06-2X metodoarekin hainbat egoeratan emaitza onak lortu ziren.[7,8] Hala eta guztiz ere, funtzional honen errendimenduari buruzko zalantzak agertu dira, bereziki zenbait elkarrekintza ahulen artean lehiaketa estua dagoenean.[9] Beraz, MN15 erabili zen, Thrular-en taldeak garatutako funtzional horren azken bertsioa lan hau egin zen unean.[10] Horrez gain, tesian aldez aurretik aipatutako dispertsio enpirikoarekin zuzendutako B3LYP funtzionala (ED=GD3BJ)[11] ere erabili zen. Funtzional horrek emaitza bikainak eman zituen elkarrekintza ez-kobalenteen bidez lotutako sistementzat.[12,13] Azkenik, MP2 "ab initio" metodoa sartu zen, dispertsio indarren predikzioak arestian aipatutako DFT metodoekin alderatzeko. Pople-ren eta Aldrich-en ξ-hirukoitza base-multzoak erabili ziren funtzional bakoitzerako, MP2-rako izan ezin. Kasu horretan, 6-311++G(d,p) basea erabili zen, kostu konputazional handia zela eta.

6.2. Kafeina-Fenol konplexuaren panorama konformazionala

Caf+Ph-ren elkarrekintza energia potentzialaren gainazala (iPES) bilaketa konformazionaletik optimizatutako egituren azterketa osoa eginez eraiki zen. Lau metodo konputazional erabili zirenez, optimizazio prozesuek bide desberdinak hartu zituzten. Hala ere, egitura egonkor gehienen optimizazioak geometria berdinean amaitu zuten. Maila desberdinetan optimizatutako egituren RMSD balioaren alderaketa minimo lokalen arteko konparazio erraza ahalbidetu zuen. Caf+Ph dimeroaren panorama konformazionalaren azterketa zenbait isomero posible zeudela erakutsi zuen, fenola eta kafeinaren elkarrekintza-gune desberdinen arteko loturen arabera. Haien arteko desberdintasunak elkarrekintza sekundarioen ondorio dira, zeinak kasu bakoitzean maximizatu egiten diren. Esate baterako, 6.2 Irudian erakusten den moduan, fenolak OC6 taldearekin elkarrekintza sortzen badu, eraztun aromatikoarekin (1 eta 6 isomeroak) edo metilo talde batekin (7 eta 17 isomeroak) ere elkarreragin dezake. Edo, besterik gabe, OH···O hidrogeno lotura maximizatu dezake, eraztun fenolikoa kafeinatik urrun jartzean (12 isomeroa, ikusi A6.1-6.4 Irudiak 6.Eranskinean). Probabilitate handiarekin, konputatutako egitura asko energia-potentzial baxuko hezien bitartez

konektatuta daude, eta horren ondorioz, sistema osoa sinplifikatzen da hozketa prozesuan, espantsioan egitura kopuru txikiago bat sortuz. Hori dela eta, kalkulatutako egituren egonkortasun erlatiboari buruzko informazioa espektro esperimentalak doitzeko erabilgarria izan daiteke.

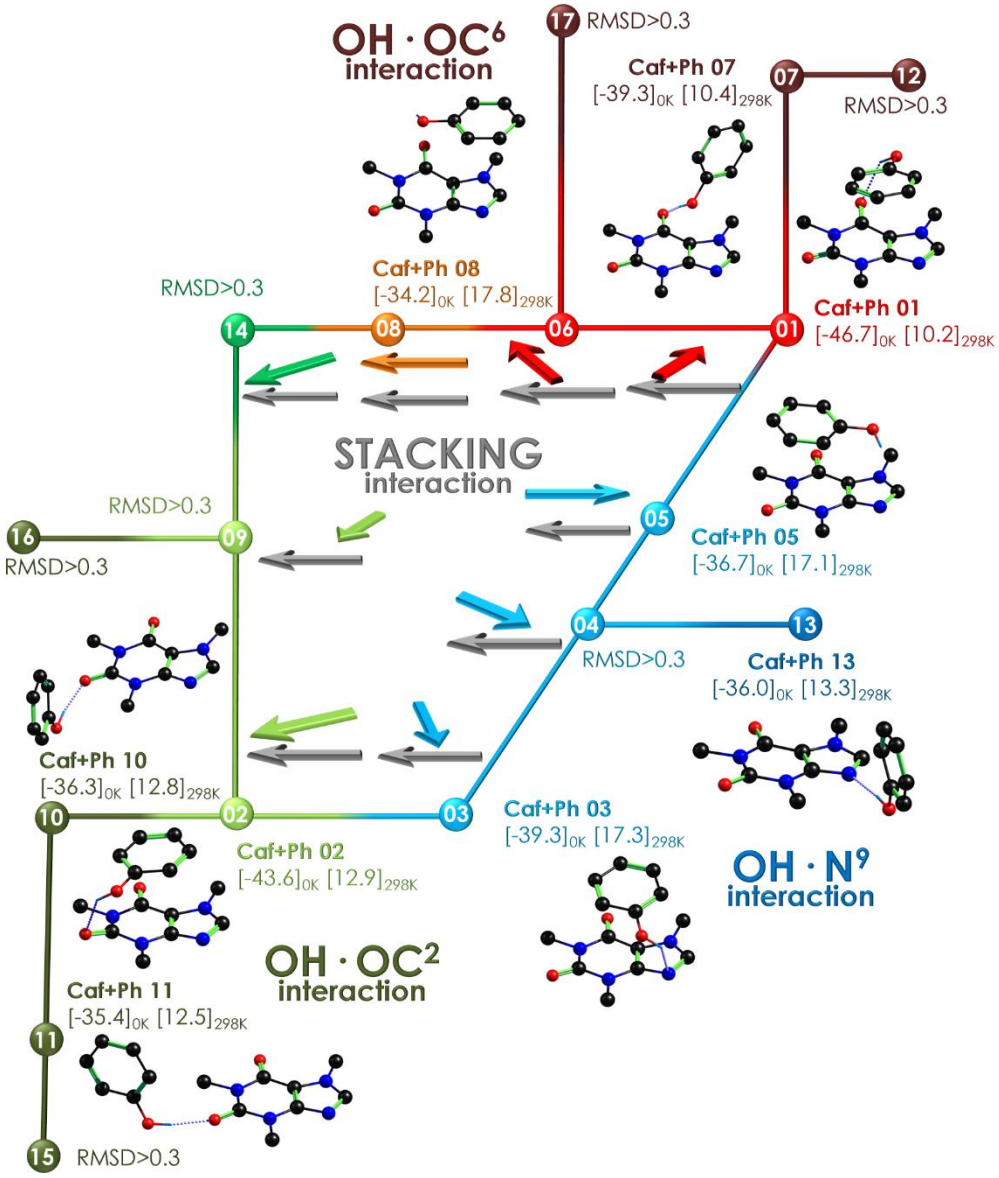

6.2 Irudia: Caf+Ph dimeroaren egiturak, antzekotasunen eta elkarrekintza-gunearen arabera sailkatuta. Gibbs lotura energia askeen balioak (kJ·mol^{-1}) 0 eta 298 K-tan ematen dira. Balio horiek sei metodo konputazionalen bataz besteko balioak dira. Horretarako, atomoen arteko RMSD<0.3-eko balioa duten egiturak soilik hartu ziren kontuan. MP2 metodoen energia balioak ez ziren erabili batez bestekoan, izan ere, metodo honekin optimizatutako egituretan aldaketa estruktural handiak zeudelako. Geziak pilatutako bi molekulen orientazio erlatiboa adierazten dute. 6 Eranskinean irudi honen bertsio landuagoak aurki daitezke, maila konputazional bakoitzean kalkulatutako egituren egonkortasun erlatiboarekin.

Konplexu honetan, lotura-energia zuzenki erlazionatuta dago egituraren egonkortasunarekin, monomeroek konformazio bakarra baitute. 6.3 Irudian ikerketa honetan erabilitako sei maila teorikoetan lortutako $\Delta\Delta G_B$-ren batez besteko balioak aurkezten dira, 0 eta 298 K-tan. RMSD‹0.3-eko balioa duten egiturak bakarrik hartu dira kontuan. Horren arabera, isomero baten optimizazioa bi maila konputazionaletan oso egitura desberdinetan amaitzen bada, gainerako analisietatik baztertu egiten da.

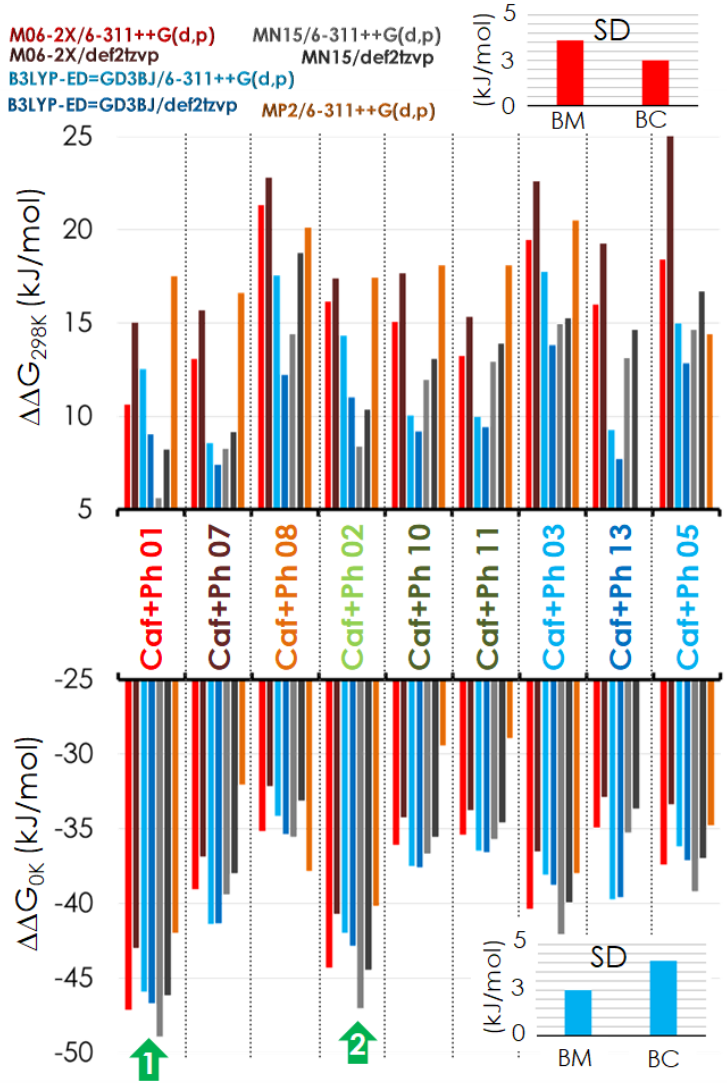

6.3 Irudia: RMSD‹0.3 duten Caf+Ph egituren Gibbs lotura energia aske erlatiboaren ($\Delta\Delta G_B$) diagramak 0 eta 298 K-tan. $\Delta\Delta G_B$ espezie bakoitzaren ΔG balioaren eta minimo orokorraren balioaren arteko kenketa da. SD = desbideratze estandarra, BM = metodoen artean, BC = konformeroen artean.

6.3 Irudiak 0 eta 298 K-tan kalkulatutako Caf+Ph konformeroen Gibbs lotura energia aske erlatiboen balioak biltzen ditu. Metodo teoriko guztien arabera, 1 isomeroa 0 K-tan egitura egonkorrena da, 2 isomeroaz jarraituta. Hala ere, desadostasun batzuk aurkitu ziren gainerako egituren energia-ordena erlatiboan: $\Delta\Delta G_B$-ren desbideratze estandarra

(SD) zazpi metodo konputazionalen artean (BM), konformeroen arteko (BC) $\Delta\Delta G_B$-ren desbideratze estandarra baino handiagoa da. Horrek esan nahi du konformazio gehienen arteko energia-aldea konputazioen errorearen barruan dagoela. Errore guzti horien estimazioa RMSD>0.4-eko balioa duten egiturak kontuan hartu gabe egin dira, konformero horietan, optimizazio prozedurak egitura oso desberdinetan amaitzen zirelako. Harrigarria bada ere, MP2 mailako kalkuluetan joera berak hauteman ziren, eta balioen desbiderapenari dagokionez, SD handienetako bat aurkeztu zuen. MP2-ren bidezko optimizazioak isomero-kopuru txiki bat ere ekarri zuen, MP2 metodoaren arabera beste kalkulu-mailetan aurkitutako konformazio batzuk egitura bakar batean bateratu baitziren (ikusi A6.1 Taula 6.Eranskinean).

Emaitza teorikoen desadostasunak tenperatura altuagotan maximizatzen dira. Adibidez, 298 K-tan BM eta BC desbideratze estandarren arteko erlazioa alderantzizkoa da. Horrek esan nahi du errore konputazionala konformazioen arteko energia-aldea baino handiagoa dela. Hortaz, komenigarria da familiak eta joera orokorrak kontuan hartzea konformazio bakarren ordez. Gertaera horien beste froga batzuk A6.5 Irudian aurki daitezke. Irudi horretan, zazpi maila teorikoen emaitzetatik eraikitutako Gibbs energia askearen diagramak aurkezten dira.

Arestian aipatutako joerak kontuan hartuz, konputazio metodo guztiek familia egonkorrenek OH···OC elkarrekintza sendoak beti dituztela adierazten dute. Elkarrekintza horiek dituzten isomeroak 10, 11, 15 eta 16 dira $OH{\cdot}OC^2$ familiarentzat; eta 07, 12 eta 17 $OH{\cdot}OC^6$ familiarentzat.

6.3. Kafeina-Fenol konplexuaren espektroskopia

Lehen pausua monomeroen REMPI espektroa neurtzea izan zen. 6.4 Irudian kafeinaren, fenolaren eta Caf+Ph dimeroaren UV absortzioak aurkezten dira. Antzeman daitekeenez, bai fenolak bai kafeinak ondo ebatziak eta diskretuak diren trantsizio bibronikoak aurkezten dute, aurreko ikerketetan lortutako emaitzekin bat datozenak.[14-17] Hala ere, bi kromoforoen presentziaren, egoera kitzikatuaren bizitza labur baten, edo maiztasun txikiko bibrazio-modu ugari dituzten dimero konformazio ugarien ondorioz, Caf+Ph-ren REMPI espektroa 35200 cm^{-1}-an hazten den egiturarik gabeko absortzio gisa agertzen da. Ikerketa aitzindari batean, de Vries eta lankideak 7-metilxantina eta teobromina homo-dimeroen REMPI espektroak aurkeztu zituzten. Bi kasuetan,

absortzio zabalak antzeman zitekeen, hemen aurkeztutako Caf+Ph dimeroaren antzekoak.[14]

Dimeroaren kasuan, trantsizio diskretuen gabeziak isomeroak bereizteko teknika espektroskopikoen erabilera eragotzi zuen, hala nola, "UV/UV hole burning" teknika. Hala eta guztiz ere, REMPI espektroan ekarpenak eragin dezaketen isomero kopurua zehaztu daiteke IR/UV espektroekin, UV laserra uhin-luzera desberdinetan zundatuz.

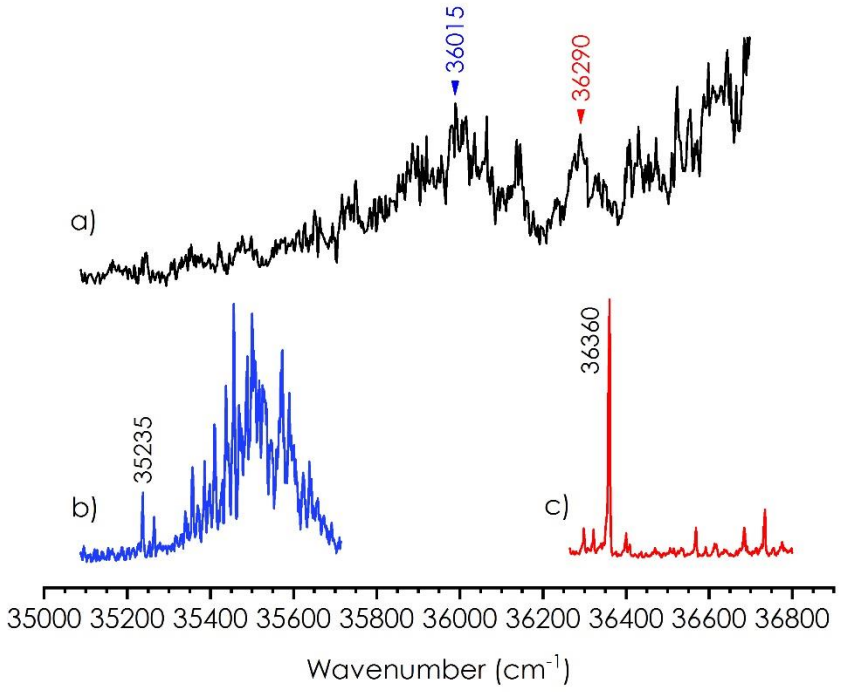

6.4 Irudia: a) Kafeina+Fenol dimeroaren, b) Kafeinaren eta c) Fenolaren kolore bakarreko REMPI espektroak.

6.5 Irudian fenolaren, kafeinaren eta Caf+Ph dimeroaren IDIR espektroak aurkezten dira. Hauek OH/CH luzaketa-bibrazio eremuan neurtu dira, zunda laserra 36015 eta 36290 cm^{-1}-ko trantsizioetan kokatuz. Fenolaren eta kafeinaren IR espektroa jadanik argitaratutako ikerketekin bat datoz:[14,18] kafeinak soilik CH luzaketa-bibrazioak aurkezten ditu, 2960 cm^{-1}-tan banda bakar gisa agertzen direnak; fenolan, aldiz, 3062 cm^{-1}-tan CH absortzio ahulak eta bere hidroxilo taldeari dagokion OH luzaketa-bibrazioaren banda 3662 cm^{-1}-tan aurkezten ditu. Caf+Ph dimeroan behatutako OH banda fenolaren bandatik 200 cm^{-1} lerrokatuta dago gorrirantz. Lerrakuntza hori fenol-ura eta fenol-amoniako dimeroek aurkezten dituzten banden lerrakuntzen bitartean dago.[19]

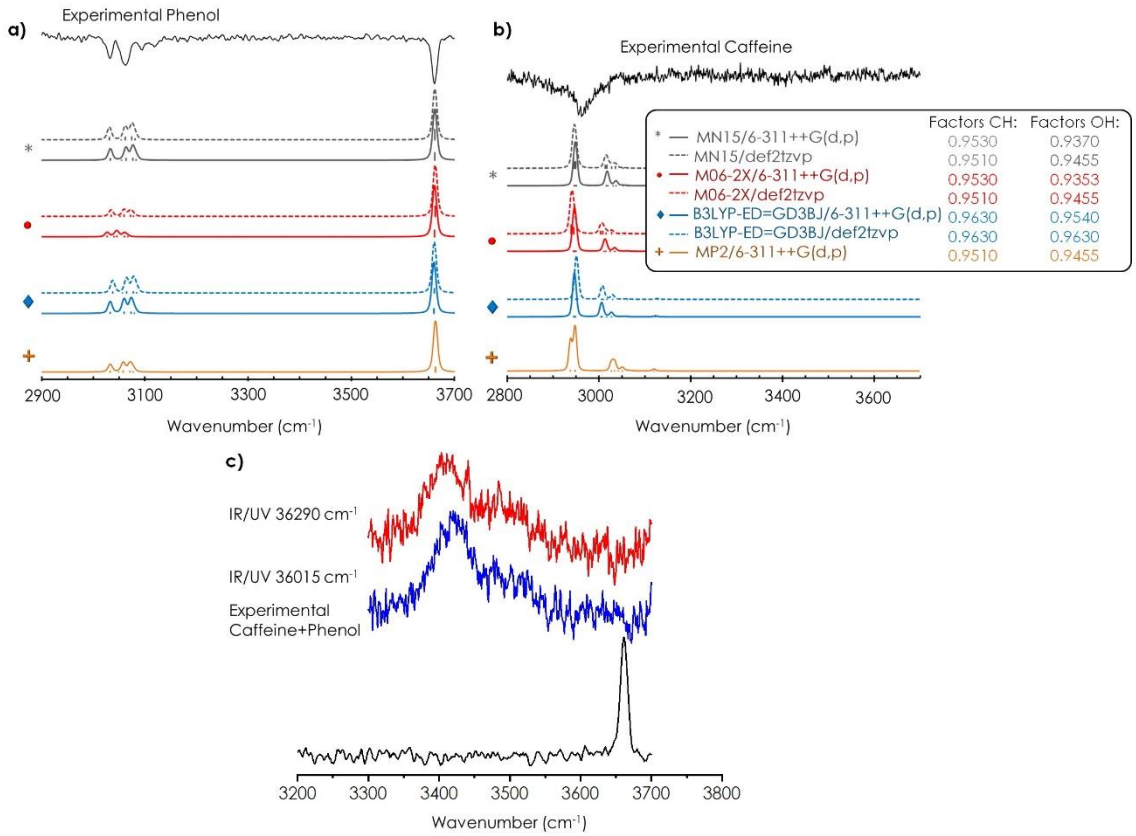

6.5 Irudia: a) Fenolaren, b) Kafeinaren, eta c) Caf+Ph dimeroaren IDIR espektro esperimentalak. Konparaketak monomeroen predikzio konputazionalekin metodo bakoitzean anharmonizitatea kontuan hartzeko eskala faktoreak determinatzera lagundu dute.

Monomeroen IR espektroak kalkulatutako bibrazio-maiztasunen anharmonizitatea kontuan hartzeko eskala faktoreak frogatu eta doitzeko erabili ziren. Ikusi daitekeenez, maila konputazional guztiek oso antzeko predikzioak burutzen dituzte, eta emaitza esperimentalak zehaztasunez erreproduzitzen dituzte. Hala ere, eskala faktore nabarmenki desberdinak behar dira maila konputazional bakoitzerako. Interesgarria bada ere, def2tzvp basea duten metodoetan antzeko eskala faktorea behar da CH eta OH bibrazioetarako, eta B3LYP-ED=GD3BJ/def2tzvp mailaren kasuan, eskala faktore bakarra bi taldeentzat.

6.5 Irudian antzeman daitekeenez, Caf+Ph-ren bi uhin-luzera desberdinen zundaketatik lortutako bi IR espektroak zaratatsuak dira, baina nabarmenak diren alde txikiak aurkezten dituzte. Horrek esan nahi du UV uhin-luzeraren arabera kitzikatutako populazioa aldatzen dela, espektroan isomero desberdinen ekarpenak daudela egiaztatuz. Gainera, espektroaren eskualde horretan OH banda bakarra espero da, eta aldiz, absortzio zabalak sorbalda bat aurkezten du. Azken hau isomero gehiago egoteagatik edo konplexu handiagoren zatiketatik ager daiteke. Hala eta guztiz ere,

dimeroaren seinale ahulak eta trimeroen seinalerik masa-espektroan ez izateak aukera horiek baztertzen dute. Beste zatiketa-iturri posiblea ur-konplexuak dira, baina sistema esperimental honetan ur-konplexuen eraketa hain zaila da horien formazioa espantsioan baztertu daitekeela.

IR espektroen esleipen zehatza burutzeko, predikzio konputazionalekiko konparaketak beharrezkoak dira. Alabaina, fenolaren OH bandaren lerrakuntzak molekulen arteko hidrogeno lotura sendo baten eraketa aurreratzen du.

6.6 Irudian Caf+Ph egitura guztien predikzioak zazpi metodo konputazionaletan biltzen dira, emaitza esperimentalekin alderatuta. Metodo konputazionalen arteko desadostasunak ez dira soilik egonkortasun erlatiboaren balioetara mugatzen, aurreko atalean ikusi dugun moduan, baizik eta bibrazio-moduen maiztasunen predikzioetara ere zabaltzen dira.

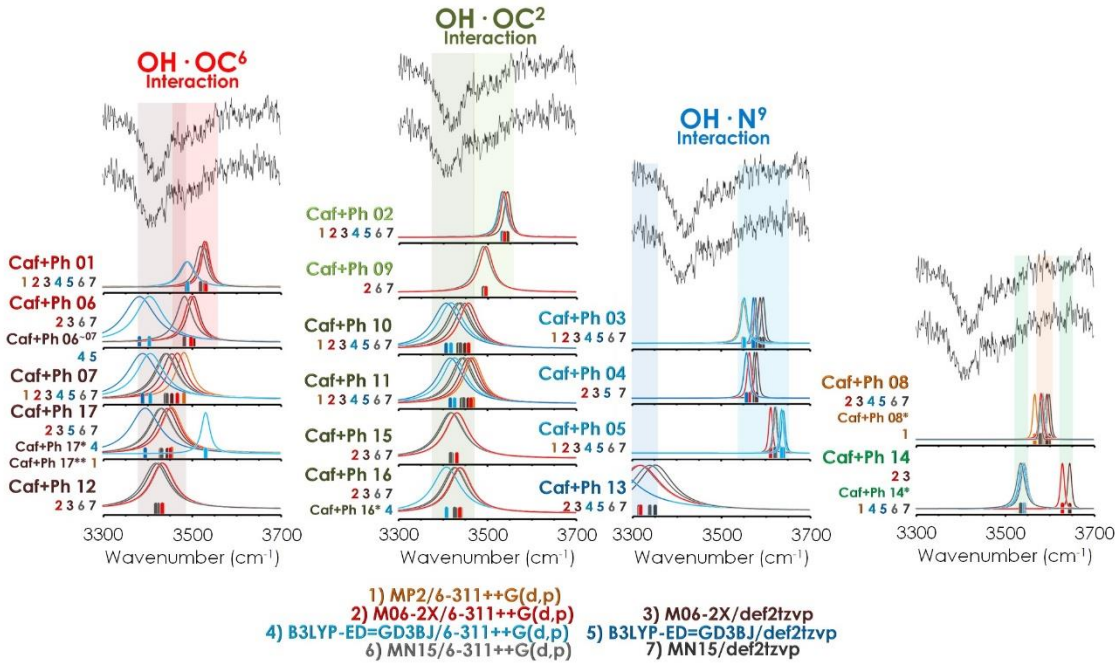

6.6 Irudia: Caf+Ph-ren IR espektroen eta horren egituren predikzio konputazionalen arteko konparaketa. Egiturak elkarrekintza motaren arabera sailkatzen dira. Banden simulazioak koloreztatu egin dira metodo konputazionalaren arabera.

Esperimentuaren eta predikzio teorikoen arteko konparaketa ez du esleipen zehatz bat eskaintzen, edozein isomero lortutako espektroa bakarrik azaldu ezin duelako. Argi dago fenola kafeinaren N^9-rekin lotzen den egiturak baztertu daitezkela, hauek esperimentalki behatutako bandatik urdinera (Caf+Ph 03, 04 eta 05) edo gorrira (Caf+Ph 13) absortzioak aurresaten dituztelako. Era berean, 8 isomeroaren predikzioak ez datoz

bat espektro esperimentalarekin. Ondorioz, aipatutako isomero edo isomero familiak baztertu egin daitezke.

Bestalde, 14 isomeroak sorbaldaren posizioa erreproduzi dezake maila konputazional guztietan, M06-2X metodoaren bi mailak aparte. Hori ere bat datoz RMSD balioen desbiderapen handiarekin, M06-2X mailan isomeroek egitura aldaketa nabarmenak jasaten dutelako. Egitura-aldaketa horiek beste isomero batzuetan ere gertatzen dira, hala nola, Caf+Ph 06, 08 16 eta 17 isomeroetan, zeinak IR espektro teoriko oso desberdinak ematen duten. Gainerako espezie eta familien simulazioak espektro esperimentalarekin bateragarriak diren trantsizioak dituzte. Esleipen zehatzago baterako, egituren egonkortasun erlatiboaz gain, energia potentzialaren gainazalaren forma ere hartu behar da. Hala ere, maila konputazional bakoitzak eskaintzen dituen balioen arteko desberdintasunek ez dute argitzen zein metodo den egokiena panorama konformazional zehatzena deskribatzeko, bereziki 298 K-tan. Nabarmenki, tenperatura altuetan egonkortzen diren familiak espektroen absortzio indartsuaren posizioa hoberen erreproduzitzen dutenak dira (3450 cm^{-1} inguru).

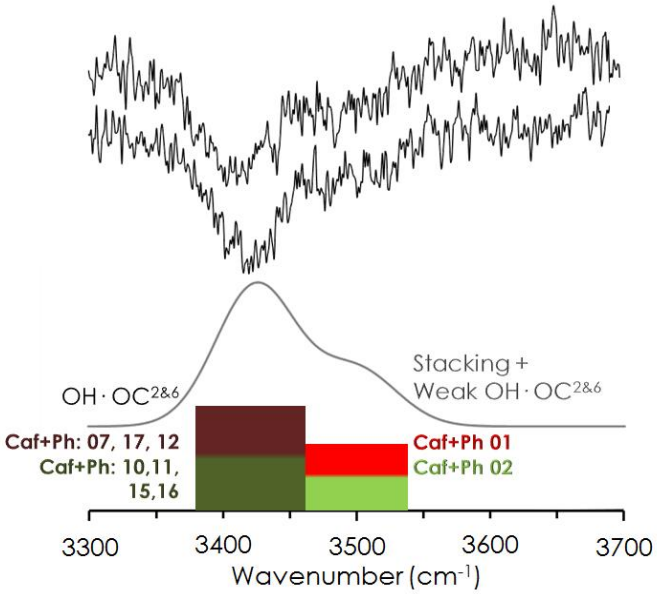

6.7 Irudia: Caf+Ph konplexuari esleitutako lau isomero-familien ekarpenak dituen IR espektroaren simulazioa. Barren zabalera bandaren kokapenaren predikzioaren ziurgabetasuna adierazten du.

6.7 Irudiak Caf+Ph konplexuaren azken esleipena laburtzen du. Simulatutako espektroa lau isomero-familia nagusien predikzioen konboluzioa da. Barren zabalerak trantsizioaren posizioaren ziurgabetasuna adierazten du. Argi dago familia horien trantsizioak espektro esperimental guztia azaltzen dutela: absortzioaren maximoak oso ondo korrelazionatzen da tenperatura altuetan egonkorrak diren familien OH luzaketa-

bibrazioekin, zeinak $OH\cdots OC^{2,6}$ hidrogeno lotura sendoak aurkezten duten. Era berean, absortzio honen sorbalda ondo erreproduzitzen da 0 K-tan egonkorrak diren egituren presentziarekin. Azken hauek pilaketa elkarrekintzak dituzte $OH\cdot OC^{2,6}$ hidrogeno loturaz gain.

$OH\cdots OC^{2}$ eta $OH\cdots OC^{6}$ hidrogeno loturen artean lehiaketa argi bat dago. Bien presentziak behaketa esperimentalak azaltzen ditu, eta haien energia aldea ez da hain handia horietako bat baztertzeko. Badirudi elkarrekintza horiek Caf+Ph-ren agregazioaren indar nagusiak direla. Karbonilo taldeak fenolaren hidroxilo taldearen ainguratze-puntu gisa jokatzen dute, bestelako hidrogeno loturen aukerak esperimentalki baztertu ziren eta ($OH\cdot N^{9}$, adibidez).

Caf+Ph-ren dentsitate elektroniko murriztuaren gradientearen analisi topologikoa elkarrekintza ez-kobalenteen adierazpen grafikoagoa ematen du. 6.8 Irudian isomero egonkorren (Caf+Ph 01 eta 02) NCI-ak irudikatzen dira, zeinak IR espektroaren sorbalda txikiaren erantzule diren. Absortzio indartsuaren erantzule den isomeroaren (Caf+Ph 07) NCI-en irudikapena ere aurkezten da. 01 eta 02 isomeroen arteko aldea protoi hartzaile gisa jokatzen duen kafeinaren C=O taldearen aldaketa da. Bietan, OH···O elkarrekintza gainazal urdin baten moduan irudikatzen da. Gainera, bi eraztun aromatikoen arteko $\pi\cdots\pi$ elkarrekintzak behatu daiteke gainazal berde gisa. RDG vs $\mathrm{sign}(\lambda_2)\rho$ grafikan antzeman daitekeen moduan, 01 eta 02 isomeroen indar dispertsiboek antzeko modulua aurkezten dute. Hala ere, aldea nabarmena da emaitza horiek 07 isomeroarenekin konparatzean. Honen gainazala guztiz desberdina da, eta indar dispertsiboen presentzia nabarmenki murrizten da. Behaketa hori dentsitate gradiente murriztuaren irudikapenean ere antzeman daiteke (grafiko urdina). Gainera, OH···O hidrogeno loturaren indarrean desberdintasunak daude, dentsitate elektronikoaren murrizketa balio negatiboagoetan agertzen delako 07 isomeroan 01 edo 02 isomeroekin alderatuz gero.

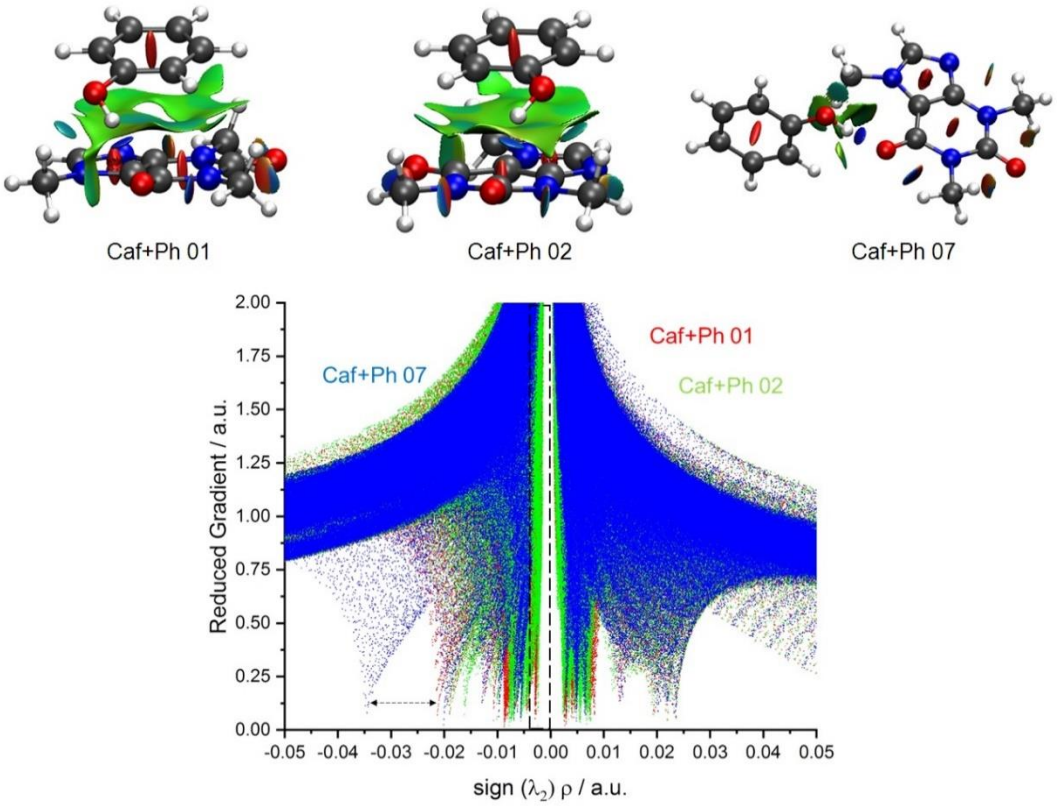

6.8 Irudia: Esleitutako Caf+Ph egituren elkarrekintza nagusien 3D-ko NCI irudikapena.

Emaitza horien arabera, argi dago Caf+Ph agregatuaren panorama konformazionala moldatzeko zaila izan dela. Badirudi fenola kafeinaren inguruan flotatzen ari dela, hidrogeno loturak eta pilaketa elkarrekintzak maximizatuz hartutako antolaketaren arabera. Horrez gain, elkarrekintza ahuletan deskribatzeko erabilitako funtzionalen arteko desberdintasunak, minimo lokalen predikzio zehaztugabeak sortu ditu, bereziki tenperatura igotzen denean. Horrek guztiak isomero egonkorrena ez ezik beste egitura egonkor batzuk ere kontuan hartzeko garrantzia nabarmentzen du, batez ere, erakarpen-indarrak zenbait elkarrekintza ahulen arteko oreka badira.

6.4. Ondorioak

Kapitulu honetan, Caf+Ph agregatuaren azterketa konputazional eta esperimental konbinatua aurkeztu dugu. Konplexuaren tamaina ez dago haren zailtasunarekin erlazionatuta, eta azkenean, modelatzeko oso zaila den sistema izan da. Kafeinak elkarrekintza gune ezberdinak zituen fenolarentzat, minimo lokal ugariekin, hidrogeno lotura, CH···π eta π···π elkarrekintzen oreka batean oinarrituta. Azterketa

konputazionalerako lau funtzional desberdin erabili ziren: M06-2X, MN15, B3LYP eta MP2. Horietako hiruk 6-311++G(d,p) eta def2TZVP baseekin konbinatu ziren, guztira zazpi maila konputazional osatuz. Denek adierazten dute 01 isomeroa egitura egonkorrena bezala, 02 isomeroaz jarraituta. Konformazio horietan, fenolak kafeinarekin elkarreragiten du π···π elkarrekintzen eta $OC^{2,6}$ taldeekiko hidrogeno loturen bidez. Esleipen hori bat datoz kafeina-ur konplexuetan behatutako joerarekin, non ura kafeinaren karbonilo taldeei lehentasunez lotzen den.[16,17,20] Hala ere, minimo lokalen egonkortasun erlatiborako ez zen adostasunik lortu. Horrek adierazten du erabilitako metodoak elkarrekintza indartsuenak zehaztasunez moldatzeko gai direla, baina elkarrekintza ahulagoak modu desberdinean orkatzen dutela. Predikzioen arteko desadostasunen aldea elkarrekintza sekundarioen indarrean dago, eta, ondorioz, maiztasun txikiko bibrazio-moduetan.

Lan honetatik sortutako egoera antzeko ikerketen emaitzen gain-interpretazioari buruz ohartarazten du. Izan ere, informazio esperimental mugatuak eta kalkuluen zehaztasun inplizitoak atera daitezkeen ondorioak mugatzen dituzte. Fenolak OC^{6} taldearen lehentasunez elkarreragiten duela esan dezakegu, OC^{2} bigarren elkarrekintza-gune probableena izanik. Elkarrekintza horiek 3450 cm^{-1} inguruko absortzio zabala eragiten dute. Beste isomero batzuek espektroan ekarpenak izan dezakete, elkarrekintzak oxigeno atomo berdinekin nagusiak izanda, baina elkarrekintza sekundarioen ekarpenen proportzio desberdinarekin (batez ere pilaketa eta CH···π elkarrekintzak). Caf+Ph moduko sistema txiki batean antzemandako desadostasunak anplifikatu daitezke sistema handiagoetan, hala nola, proteinen tolesturan edo proteina-ligando agregatuetan, non indar dispertsiboen bidezko elkarrekintzak funtsezko zeregina dute sistemaren azken forman.

6.5. Erreferentziak

[1] A. Nehlig, J.-L. Daval and G. Debry, Caffeine and the central nervous system: mechanisms of action, biochemical, metabolic and psychostimulant effects, *Brain Res. Rev.*, 1992, **17**, 139–170.

[2] A. Rodgman and T. Perfetti, *The Chemical Components of Tobacco and Tobacco Smoke*, CRC Press, Boca Raton, 2nd Editio., 2013.

[3] T. T. Lang, J. D. Young and C. E. Cass, Interactions of Nucleoside Analogs, Caffeine, and Nicotine with Human Concentrative Nucleoside Transporters 1 and 2 Stably Produced in a Transport-Defective Human Cell Line, *Mol. Pharmacol.*, 2004, **65**, 925 LP – 933.

[4] B. B. Fredholm, K. Bättig, J. Holmén, A. Nehlig and E. E. Zvartau, Actions of Caffeine in the Brain with Special Reference to Factors That Contribute to Its Widespread Use,

Pharmacol. Rev., 1999, **51**, 83 LP – 133.

[5] S. Zevin and N. L. Benowitz, Drug Interactions with Tobacco Smoking, *Clin. Pharmacokinet.*, 1999, **36**, 425–438.

[6] J. Istvan and J. D. Matarazzo, Tobacco, alcohol, and caffeine use: A review of their interrelationships., *Psychol. Bull.*, 1984, **95**, 301–326.

[7] I. Usabiaga, J. González, P. F. Arnáiz, I. León, E. J. Cocinero and J. A. Fernández, Modeling the tyrosine–sugar interactions in supersonic expansions: glucopyranose–phenol clusters, *Phys. Chem. Chem. Phys.*, 2016, **18**, 12457–12465.

[8] A. Camiruaga, I. Usabiaga, A. Insausti, I. León and J. A. Fernández, Sugar–peptidic bond interactions: spectroscopic characterization of a model system, *Phys. Chem. Chem. Phys.*, , DOI:10.1039/C7CP00615B.

[9] C. Pérez, I. León, A. Lesarri, B. H. Pate, R. Martínez, J. Millán and J. A. Fernández, Isomerism of the Aniline Trimer, *Angew. Chemie Int. Ed.*, 2018, **57**, 15112–15116.

[10] H. S. Yu, X. He and D. G. Truhlar, MN15-L: A New Local Exchange-Correlation Functional for Kohn–Sham Density Functional Theory with Broad Accuracy for Atoms, Molecules, and Solids, *J. Chem. Theory Comput.*, 2016, **12**, 1280–1293.

[11] S. Grimme, J. Antony, S. Ehrlich and H. Krieg, A consistent and accurate ab initio parametrization of density functional dispersion correction (DFT-D) for the 94 elements H-Pu, *J. Chem. Phys.*, 2010, **132**, 154104.

[12] I. Usabiaga, A. Camiruaga, C. Calabrese, A. Maris and J. A. Fernández, Exploring Caffeine–Phenol Interactions by the Inseparable Duet of Experimental and Theoretical Data, *Chem. – A Eur. J.*, 2019, **25**, 14230–14236.

[13] E. Caldeweyher, C. Bannwarth and S. Grimme, Extension of the D3 dispersion coefficient model, *J. Chem. Phys.*, 2017, **147**, 34112.

[14] M. P. Callahan, Z. Gengeliczki, N. Svadlenak, H. Valdes, P. Hobza and M. S. de Vries, Non-standard base pairing and stacked structures in methyl xanthine clusters, *Phys. Chem. Chem. Phys.*, 2008, **10**, 2819–2826.

[15] A. Oikawa, H. Abe, N. Mikami and M. Ito, Solvated phenol studied by supersonic jet spectroscopy, *J. Phys. Chem.*, 1983, **87**, 5083–5090.

[16] D. Kim, H. M. Kim, K. Y. Yang, S. K. Kim and N. J. Kim, Molecular beam resonant two-photon ionization study of caffeine and its hydrated clusters, *J. Chem. Phys.*, 2008, **128**, 134310.

[17] P. B. Balbuena, W. Blocker, R. M. Dudek, F. A. Cabrales-Navarro and P. Hirunsit, Vibrational Spectra of Anhydrous and Monohydrated Caffeine and Theophylline Molecules and Crystals, *J. Phys. Chem. A*, 2008, **112**, 10210–10219.

[18] E. Aguado, I. León, E. J. Cocinero, A. Lesarri, J. A. Fernández and F. Castaño, Molecular recognition in the gas phase: benzocaine–phenol as a model of anaesthetic–receptor interaction, *Phys. Chem. Chem. Phys.*, 2009, **11**, 11608–11616.

[19] A. Iwasaki, A. Fujii, T. Watanabe, T. Ebata and N. Mikami, Infrared Spectroscopy of Hydrogen-Bonded Phenol–Amine Clusters in Supersonic Jets, *J. Phys. Chem.*, 1996, **100**, 16053–16057.

[20] V. B. Singh, Spectroscopic signatures and structural motifs in isolated and hydrated caffeine: a computational study, *RSC Adv.*, 2014, **4**, 58116–58126.

7. Kapitulua

Xantina deribatuen espektroskopia: teobromina eta teofilina

Hurrengo artikulutik moldatuta: A. Camiruaga, I. Usabiaga, V. C. D'mello, G. A. García, S. Wategaonkar and J. A. Fernández, *Phys. Chem. Chem. Phys.*, 2019, 21, 26430-26437.

7.1. Sarrera

Molekula biologikoen propietate fotofisiko eta fotokimikoei buruzko ikerketek gero eta interes handiagoa dute, osasunean babestu gabeko larruazalaren esposizioak eragin dezakeen kaltea dela eta, hala nola, melanomen agerpena edo oxidazio handiko espezieek eragindako azalaren zahartzea. Jakina da DNA-ren eta UV fotoien arteko elkarreraginak mutazio kaltegarriak eragin ditzakeela. Izan ere, zelula eukariotikoek mutazio horiek zuzentzeko mekanismoak garatu dituzte. Teoria batzuen arabera, UV erradiazioak eragindako kalteak murrizteko mekanismo gisa, DNA baseek bizitza laburreko egoera kitzikatu elektronikoak aurkezteko eboluzionatu egin dute.[1-5]

Testuinguru horretan, UV erradiazioaren eta bestelako metabolitoen arteko elkarreraginak arreta askoz gutxiagoa erakarri du, nahiz eta metabolito batzuk DNA-rekiko erlazio estruktural handia izan. Hori da, hain zuzen, xantinaren eta haren deribatuen kasua. Horien aktibitate biologikoa DNA baseekin duten antzekotasunarekin zuzenki erlazionatuta dago, baita antzeko elkarrekintza ez-kobalenteak sortzeko gaitasuna ere.[6-8] Purinaren hezurdura aromatiko berarekin, xantinak N-H eta C=O taldeak timinaren antzeko antolamendu batean aurkezten ditu. Antolamendu horrek errezeptore berberei afinitate handiarekin lotzeko aukera ematen dio. Xantinaren bi deribatu, teobromina (TB) eta teofilina (TP), aktibitate biologikoa ere dute. TP-ren eta TB-ren arteko desberdintasuna metilo talde bakar baten posizioa da, N7-ra lehengoari lotuta dagoena eta N1-ra bigarrenari. Halaber, aldaketa sinple horrek nahikoa da molekularen propietate biologikoak nabarmenki aldatzeko.

TP-ren eta TB-ren espektroskopia aztertu da dagoeneko: Callahan eta kideak 7-metilxantinaren, TP-ren, TB-ren eta kafeinarena lehen REMPI espektroak argitaratu zuten;[9] eta ikerketa berri batean, Kim eta kideak deVries-en taldeak aurkeztutako antzeko REMPI espektroak argitaratu zuten,[10] baina absortzio zabalagoekin. Azken egileen emaitzetan, TP-ren eta TB-ren jatorrizko bandak 150 eta 120 cm^{-1}-ko zabalera aurkezten zuten, kafeinaren 7 cm^{-1}-ko zabalerarekin alderatuta. Emaitza horiek ulertzeko, Kim-en taldeak kitzikapen elektronikoan zehar egituraren aldaketak espektroan izan dezakeen eragina aztertu zuten.[10] Lan honetan, espantsio supersonikoetan TP-ren eta TB-ren metilo taldeen posizioak egoera elektronikoen dinamiketan eta ionizazio prozesuan duen eragina aztertu egin da. Horretarako, TIFR[11]-ekin (Tata Institute of Fundamental Research) eta DESIRS laborategiarekin (SOLEIL Synchrotron, St. Aubin, Frantzia) lankidetzan, zero elektroiko energia zinetikoa (*Zero Electron Kynetic Energy*, ZEKE) eta atalase espektro fotoelektronikoa (*Threshold*

PhotoElectron Spectra, TPES) neurtu ditugu, ionizazio energia zehatzak eta katioien egitura bibronikoak eskuratzeko. Emaitza esperimentalak osatzeko, oinarrizko egoeraren zein egoera kitzikatuaren kalkuluak burutu ziren, baita katioien oinarrizko egoera elektronikoarenak ere.

7.2. Panorama konformazionala

TB-ren eta TP-ren panorama konformazionala zenbait tautomeroz eta errotameroz osatuta dago. 7.1 Irudiak TB eta TP tautomeroen egonkortasun erlatiboa aurkezten du, tautomerizazio prozesuen energia-hesien estimazio batekin batera. TB-ren kasuan, tautomero egonkorrena di-zeto forma da, non hidrogeno atomoa N1-taldeari atxikituta dagoen. Hidrogeno atomo horren transposizioa alboko karbonilo taldeen O atomoetara bi enol tautomero posible sortzen ditu. Gainera, forma enoliko bakoitzak bi errotamero dauzka, OH taldearen orientazioaren arabera. Kalkuluen arabera, forma enoliko egonkorrenak zetona baino 80 $kJ \cdot mol^{-1}$ ezegonkorragoa da. Hortaz, espantsio supersonikoan teobromina enolikoen populazioa oso baxua izatea espero da. Kalkulu hauek guztiak jadanik argitaratutako ikerketekin bat datoz.

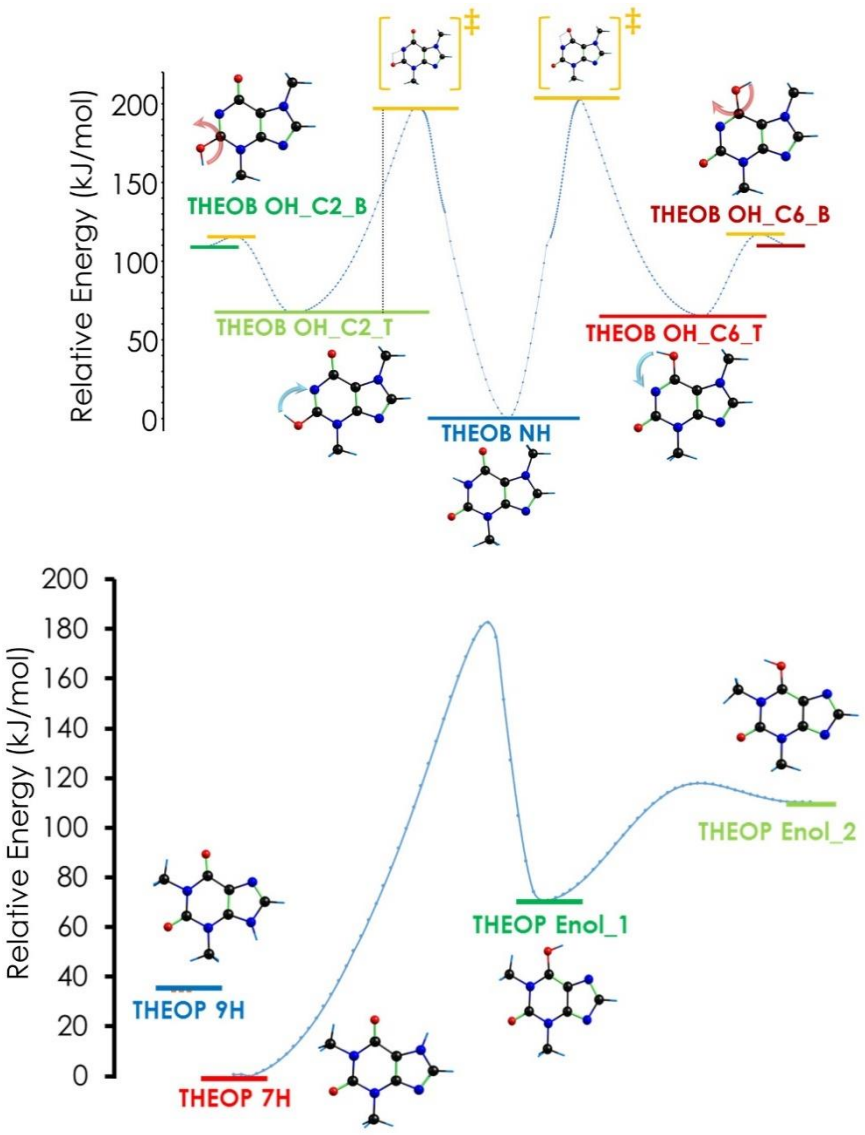

7.1 Irudia: Goiko taula: TB tautomeroen egonkortasun erlatiboa, dimentsio bakarreko energia-hesiekin batera; beheko taula: TP tautomeroen egonkortasun erlatiboa, dimentsio bakarreko energia-hesiekin batera. Energia-hesien predikzioak pausu bakoitzean egituraren optimizazioa M06-2X/6-311++G(d,p) mailan eginez lortu ziren.

TP-rentzat bi zeto forma posible daude, H atomoak N7-ri edo N9-ri lotuta dagoen arabera. Tautomerorik egonkorrena N7H izenekoa da, eta hurrengo tautomeroarekin (N9H) duen energia aldea 36 $kJ \cdot mol^{-1}$-koa da. Bestalde, hidrogeno atomoaren transposizioa tautomero enoliko bat sor dezake, baina prozesu horrek energia-hesi oso altua dauka. Hori dela eta, TP-ren populaziorik handiena espantsioan N7H forman egotea espero da.

Metilo taldeen errotazio zaildua zenbait errotamero sor ditzake. Izan ere, errotamero horien egonkortasuna antzekoa da, eta haien arteko isomerizazio-hesiak espantsioaren hozketa prozesuan zehar gaindi daitezke. Metilo taldeen errotaziorako energia

potentzialaren gainazala aztertzeko egindako kalkuluak 7.2 Irudian laburbiltzen dira. Ikusi daitekeenez, errotazio-hesiak 10 cm^{-1} inguruan daude TB-ren N3-ra atxikitutako metiloarentzat, eta 180 cm^{-1}-koak N7-ari lotutakoarentzat. Emaitza horiek arestian aipatutako Kim-en taldearen lanarekin bat datoz.[10] TP-ren kasuan, N1-ari eta N3-ri atxikitutako metilo taldeen errotazio-hesien arteko aldea txikiagoa da, N1 metil taldearen errotazio librea C=O taldeek murrizten baitute. Hala ere, balio horiek eraztun aromatiko bati lotutako metilo talde bat biratzeko espero litzatekeenaren antzekoak dira.[13,14] Ondorioz, espantsioan TB-ren eta TP-ren errotamero ezberdinak edukitzea espero da.

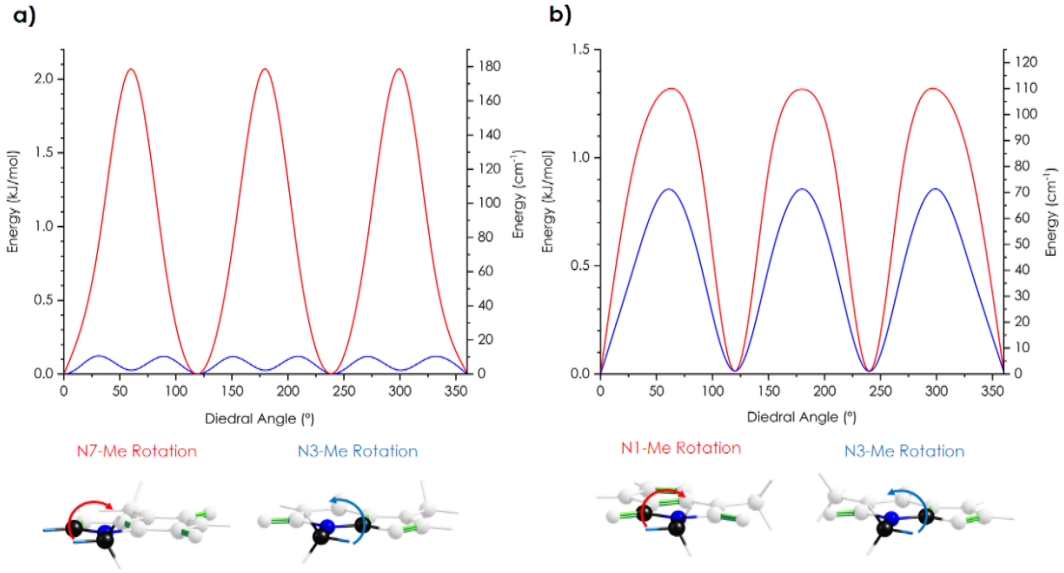

7.2 Irudia: a) TB-ren eta b)TP-ren metilo taldeen errotazioen energia-hesiak, M06-2X/6-311++G(d,p) mailan kalkulatuak.

7.3. Teobrominaren eta teofilinaren espektroskopia

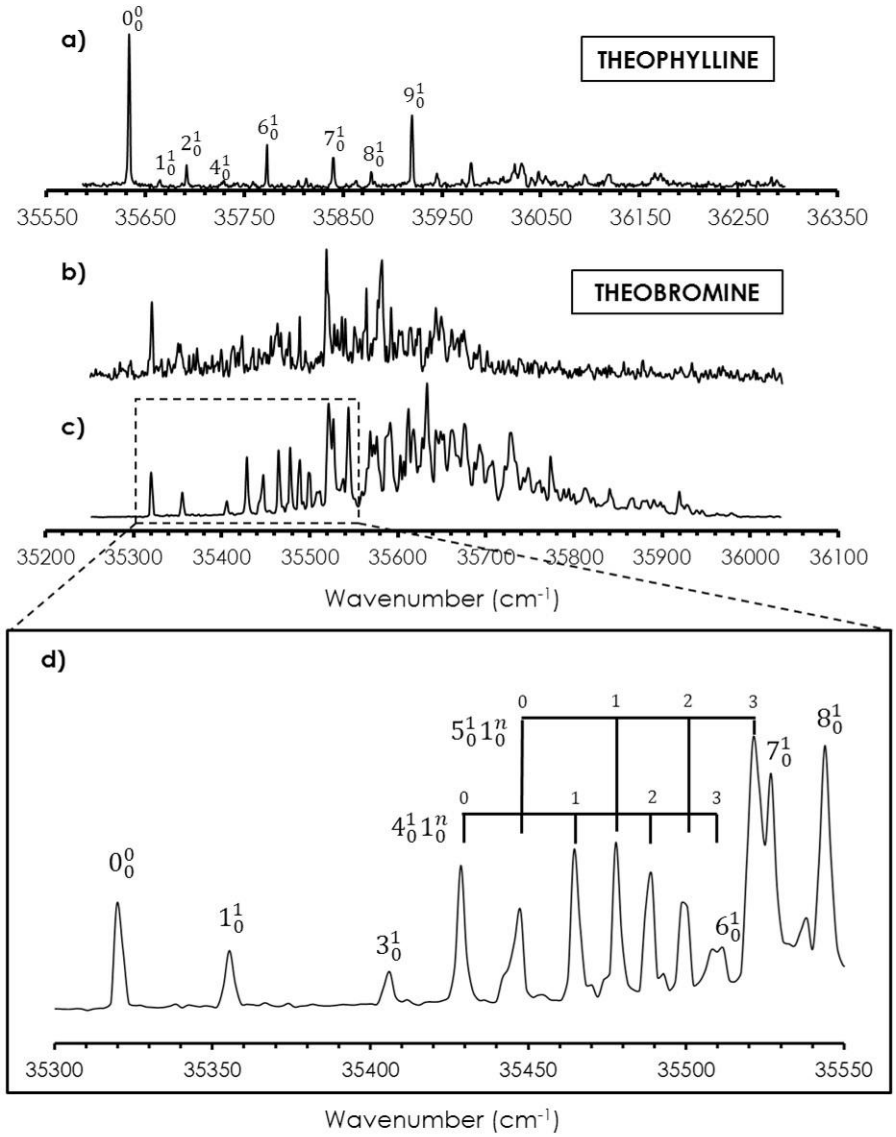

7.3 Irudia: a) TP-ren REMPI espektroa; b) TB-ren REMPI espektroa laser desortzioa erabiliz; c) TB-ren REMPI espektroa beroketa balbula erabiliz; d) (c) espektroaren lehen 250 cm^{-1}-en handipena, trantsizio nagusien behin behineko esleipenarekin. Balio espektroskopiko garrantzitsuak 7.1 Taulan aurkitu daitezke. Esleitutako trantsizioak 7.Eranskinaren A7.1 eta A7.2 Tauletan bildu dira.

TB eta TP antzeko egiturak izan arren, espektro elektronikoan desberdintasun nabarmenak dituzte (ikusi 7.3 Irudia). TP-ren espektroan, 0_0^0 trantsizioa indartsuena da. Horren ondoan, maiztasun-txikiko bibrazio-moduei dagozkien trantsizioak beha daitezke. Aitzitik, TB-ren espektroan 0_0^0 transtizioa intentsitate ahulagoa aurkezten du. Aldiz, gainontzeko trantsizioak intentsuagoak dira, eta hondo zaratatsu baten gainean agertzen dira. ν_1 (35.6 cm^{-1}) bibrazio-modu bereziki aktiboa da, ν_4 (109.1 cm^{-1}) eta ν_5 (127.9 cm^{-1}) bibrazio-moduetara akoplatzen dena.

Hemen aurkeztutako TB-ren espektroa de Vries-en taldeak[9] lortutakotik hurbilago dago Kim-en taldeak lortutakotik baino.[10] Bitxia bada ere, de Vries-en taldeak aurkeztutako espektroak 7.3 Irudikoarenak baino trantsizio gutxiago ditu. Horrez gain, lehenengo 200 cm^{-1}-etako banden posizioak ez datoz guztiz bat gure espektroekin. Azalpen bat espantsioaren tenperatura desberdin bat izan daiteke, errotameroen populazio desberdin bat emanez. Egoera kitzikatuaren erdi-bizitzaren ondoriozko banden zabaltzea bazter daiteke, Kim-en taldearen lanaren arabera.[10] TB-ren REMPI espektroa laser desortzio iturri bat erabiliz ere neurtu zen (7.3b Irudia). Nahiz eta orokorrean espektroan seinale/zarata erlazio murriztua izan, bi espektroen arteko bandak bat datoz.

Absortzio espektroetan beste espezie batzuek izan dezaketen ekarpenak aztertzeko, TB-ren eta TP-ren IDIR espektroak neurtu ziren, UV laserra trantsizio desberdinetan eta erresonantziaz-kanpo finkatuz. 7.4 Irudiak espektro esperimentalen eta kalkuluetatik lortutako espektro teorikoen arteko konparaketa aurkezten du. Argi dago espektro esperimentala espezie egonkorrenei dagokiela, hots, TP-ren N7H-zeto formari eta TB-ren di-zeto formari. Alabaina, badirudi TB-ren espektroak bi tautomero enolikoen ekarpenak izan dezakeela, zaratatik ia bereizezinak diren eta OH eremuan agertzen diren absortzio ahulak direla eta. Hala ere, esperimentu osagarriak beharko lirateke esleipen hori egiaztatzeko, eta oraingoz, zeto tautomeroa bakarrik hartuko dugu kontuan.

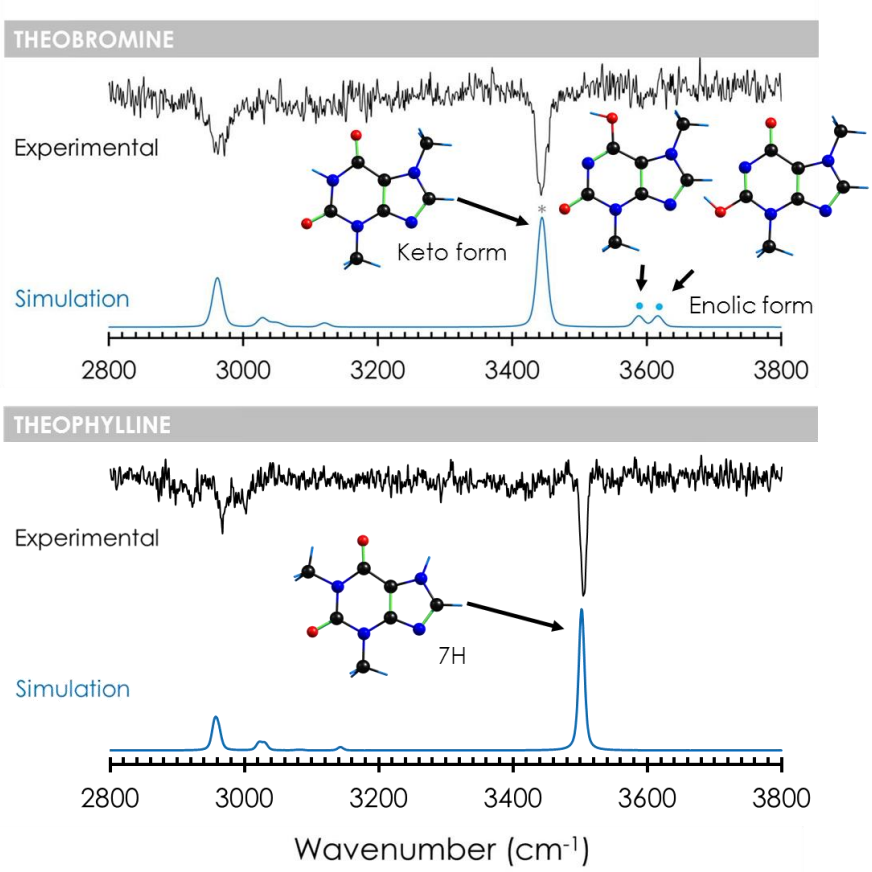

7.4 Irudia: TB-ren (goiko taula) eta TP-ren (beheko taula) IDIR espektroen eta M06-2x/6-311++G(d,p) mailan simulatutako espektroen arteko konparaketa. 0.962-ko (CH), 0.936-ko (OH) eta 0.953-ko (NH) eskala faktoreak erabili ziren anharmonizitatea zuzentzeko.

TB eta TP egituren arteko desberdintasun txikiek beren egitura elektronikoan duten eragina sakonago aztertzeko, ZEKE eta TPES espektroskopiak erabili ziren. 7.5 Irudiak bi molekulen ZEKE espektroak konparatzen du.

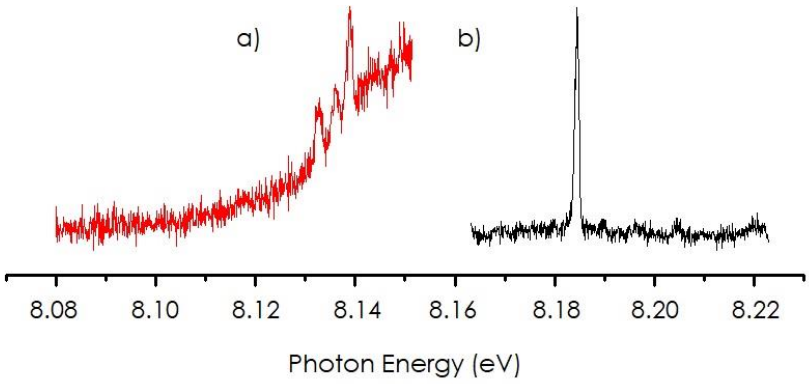

7.5 Irudia: a)TB-ren eta b)TP-ren ZEKE espektro esperimentalak.

Berriz ere, bi molekulen emaitza esperimentalen arteko alde nabarmenak lortu ziren. TP-ak ionizazio adiabatiko atalase estua aurkezten du 66011 cm^{-1}-tan (8.184 eV). TB-ren

kasuan, aldiz, espektroak absortzio jarraiatu baten gainean zenbait banda aurkezten du. Lehen banda estua 65601 cm^{-1}-tan (8.133 eV) agertzen da, eta ionizazio adiabatiko atalase gisa hartu da. TB-ren eta TP-ren UV jatorrizko bandei eta ionizazio adiabatikoen energia balioei buruzko datu espektroskopiko garrantzitsuak 7.1 Taulan bildu dira, maila konputazional desberdinetan lortutako ionizazio-energiekin batera. ZEKE-rekin lortutako ionizazio-energiak zehatzagoak dira REMPI-rekin edota espektroskopia foto-elektronikoarekin lortutakoekin alderatuz gero. Izan ere, ZEKE espektroetan ionizazio-atalasea ondo zehaztutako trantsizio gisa ikus daiteke.

7.1 Taula: Teobromina eta teofilina molekulen egonkortasun erlatiboa eta datu espektroskopikoak.

	Teobromina			**Teofilina**	
	Zeto	*C2-Enol*	*C6-Enol*	*7H*	*9H*
Egonkortasun erlatiboa (kJ/mol)	0	69.3	65.4	0	36.3
0-0 trantsizioa (cm^{-1})	35319.8	-	-	35633.3	-
Ionizazio-energia adiabatikoak (eV)					
Esperimentala					
IP	8.120	-	-	8.170	-
ZEKE	8.133	-	-	8.184	-
TPEPICO	8.137	-	-	8.187	-
Teorikoa					
M06-2X/6-311++G(d,p)	8.217	8.169	8.078	8.266	8.235
M06-2X/aug-cc-pVDZ	8.120	8.074	7.975	8.165	8.147
PBE0/aug-cc-pVDZ	8.088	8.010	7.921	8.113	8.065
CCSD(T)/cc-pVTZ	7.961	7.928	7.832	8.009	7.989

Hemen aurkeztutako balioak, nahiz eta baldintza elektrostatiko esperimentalengatik handiagoak izan, Kim-en taldeak argitaratutakoekin bat datoz (8.10 eV TP-rentzako eta 8.06 eV TB-rentzako).[10] Ikuspuntu teorikotik, balio esperimentalekin bat etortzea ez da perfektua. Emaitza esperimentalak hoberen erreproduzitzen dituen metodoa M06-2X/aug-cc-pVDZ da. Interesgarria bada ere, nahiz eta M06-2X/6-311++G(d,p) metodoaren balioak 0.1 eV goitik egon, TP-ren ionizazio energia TB-rena baino 49 meV gehiago dela aurresaten du. Balio horiek bat datoz esperimentalki behatutako 50 meV-ko aldearekin bi molekulen ionizazio energien artean. Predizkzio hobeagoak lor litezke metodo konputazional garestiagoekin,[15] baina hori lan honen irismenetik kanpo dago. Hala ere, metodo teoriko guztiek teofilinaren ionizazio energia teobrominarena baino apur bat handiagoa dela iragartzen dute, esperimentalki antzeman daitekeen bezala.

Katioiaren espektrokopiaren ikuspegi zabalago bat lortzeko, sintoniza daitekeen VUV sinkrotron erradiazioa TP-ren eta TB-ren TPES espektroak neurtzeko erabili zen, hurrengo 7.6 Irudian aurkezten direnak. Nahiz eta bereizmena ZEKE teknikarena baino

txikiagoa izan, bi molekulen espektroak kalkuluei esker eslei daitekeen egitura bibroniko aberatsa aurkezten dute.

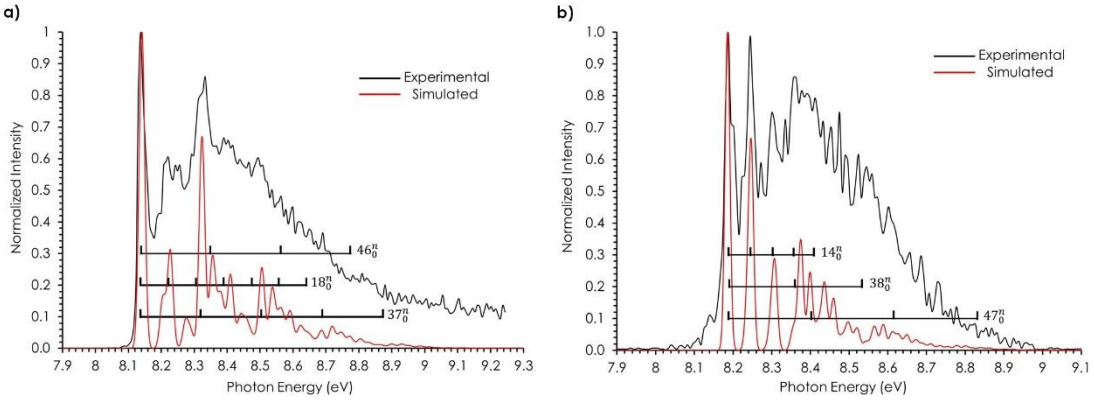

7.6 Irudia: a) TB-ren eta b) TP-ren atalase espektro fotoelektronikoa (TPES), Franck-Condon kalkulu multidimentsionalei esker eskuratutako simulazioekin konparatuta. Hiru progresio nagusiak nabarmentzen dira. Simulatutako espektroak 0.083 eta 0.085 eV lerrokatu dira, hurrenez hurren, espektro esperimentalekin bat egiteko. Ikusi A7.3 eta A7.4 taulak eranskinetan trantsizio bibrazionalen esleipenerako.

Espektro fotoelektronikoen simulaziorako, optimizatutako egituren datu konputazionalak erabili ziren PGOPHER programan.[16,17] Franck-Condon faktoreen kalkulu multidimentsionala burutu zen TB-ren eta TP-ren egoera neutroan eta ionikoan PBE0/aug-cc-pVDZ mailan optimizatutako egiturak erabiliz. 7.6 Irudian ikusi daitekeenez, simulatutako espektroek ondo erreproduzitzen dituzte esperimentalki behatutako absortzio banda nagusiak. Bestalde, banda horien agerpenaren atzean dauden bibrazio-moduak eraztunaren planokoak dira. Modu horiek bat datoz sistema aromatiko baten ionizazio prozesuarekin, non elektroi baten erauzketa eraztuna ahuldu eta zabaldu egiten duen. Ondorioz, Franck-Condon faktoreek eraztunaren zabalkuntzarekin erlazionatutako progresioak sustatzea espero da.

7.4. Emaitzen eztabaida

Lortutako datu espektroskopikoei esker, biologikoki garrantzitsuak diren bi molekuletan (TP eta TB) metilo talde bakar baten posizioak duen eragina azter daiteke. REMPI espektroek metilo taldeen posizioa kitzikapen elektronikoan eragin handia dutela adierazten dute. TP-ren espektroak oso banda kopuru mugatua aurkezten du, haien artean progresiorik sortzen ez dituztenak. Aldiz, TB-ren espektroa metatuagoa da, zenbait bibrazio-modu akoplatuekin. Metaketa horren erantzule ν_1 modua (35.6 cm^{-1}) da, beste bibrazio-moduekin erraz akoplatzen delako.

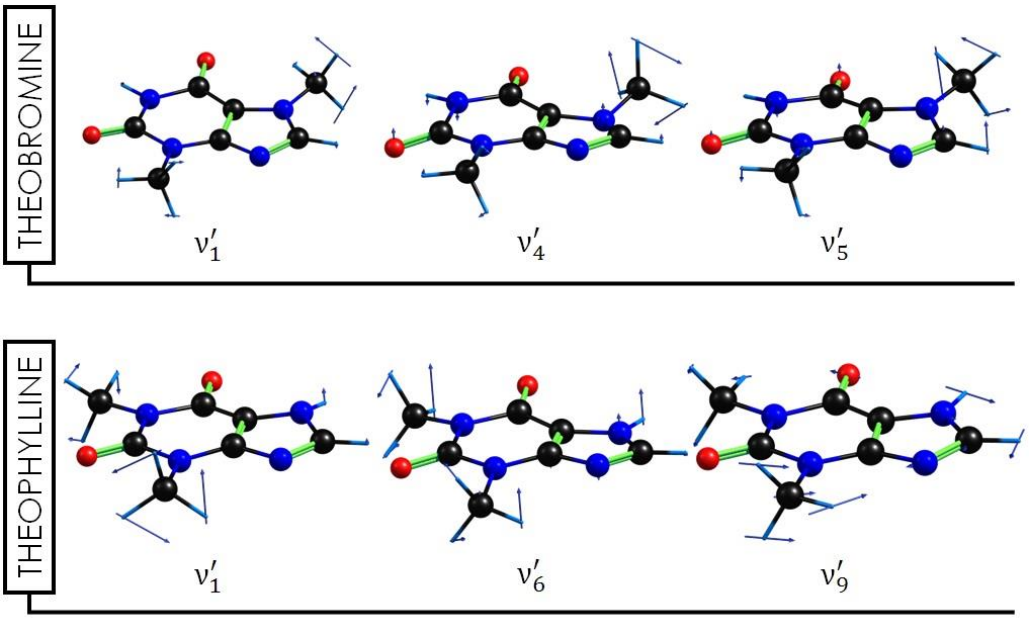

7.7 Irudia: TB-ren eta TP-ren REMPI espektroetan aktibitate handien aurkezten duten bibrazio-moduen arteko konparaketa. Kalkuluak S_1 egoeran egin ziren CAM-B3LYP/aug-cc-pVDZ mailarekin.

7.7 Irudian TB-ren espektroan esleitutako bi progresio nagusien atzean dauden hiru bibrazio-moduak aurkezten dira, baita horien antzekoak TP-ren kasurako. ν_1 modua erantzule nagusia dirudi, eta bi metilo taldeen tortsioei dagokio. Modu horrek ν_4 eta ν_5 moduekin akoplatzen da, metilo taldeen tortsioei eta eraztun aromatikoen deformazioari dagozkienak. Eraztun aromatikoaren planoan ematen diren aldaketa horiek bat datoz kitzikapen elektronikoan zehar ematen den eraztunaren geometriaren aldaketekin. Izan ere, jadanik ikertutako N7 taldearen piramidalizazio prozesua egoera kitzikatuan TB-ren REMPI espektroaren aktibitate bibroniko aberatsa azal dezake.[10,18] TP-ren kasuan, antzeko metilo taldeen tortsioak ν_6 eta ν_9 moduekin akoplatzen dira. Hala ere, TB-rekin alderatuta, modu horiek ez dute aktibitate hain handia aurkezten, ziur aski, lehen aipatutako eraztunaren deformazioaren gabezia dela eta. Azalpen honen egiaztapena ZEKE espektroetan aurki daiteke 7.5 Irudian, non TP-ren absortzio diskretua TB-ak aurkeztutako absortzio jarraituaren kontra dago. Izan ere, TB-ren jatorrizko bandaren zabalkuntza ZEKE espektroan bigarren mailako aldaketa estruktural bati dagokio, hala nola, S_1-an ikusitako piramidalizazioa.[19]

Espektro foto-elektronikoak S_1 egoera horren eraginari buruzko informazio gehigarria ematen du. Bertan, ionizazioa jatorrizko maila elektronikotik (S_0) lortzen da. 7.6 Irudian trantsizio bibronikoak oso antzekoak dira bi espektroetan. Horrek esan nahi du ZEKE eta REMPI espektroetan behatutako TB-ren eta TP-ren arteko desberdintasunak S_1 egoerei dagozkiela. Orokorrean, simulazioek ondo erreproduzitzen dute TPES espektroak, eta

kalkulu hauen arabera, bibrazio-modu aktiboenak bi molekuletan eraztunaren planoan ematen dira (ikusi 7.8 Irudia). Izan ere, sistema aromatikotik elektroi baten erauzketak dentsitate elektronikoaren eta C-C eta C-N loturen murrizketa eragiten du. Horrek modu horien aktibazioa sustatzen du, espektroan progresioak sortuz.

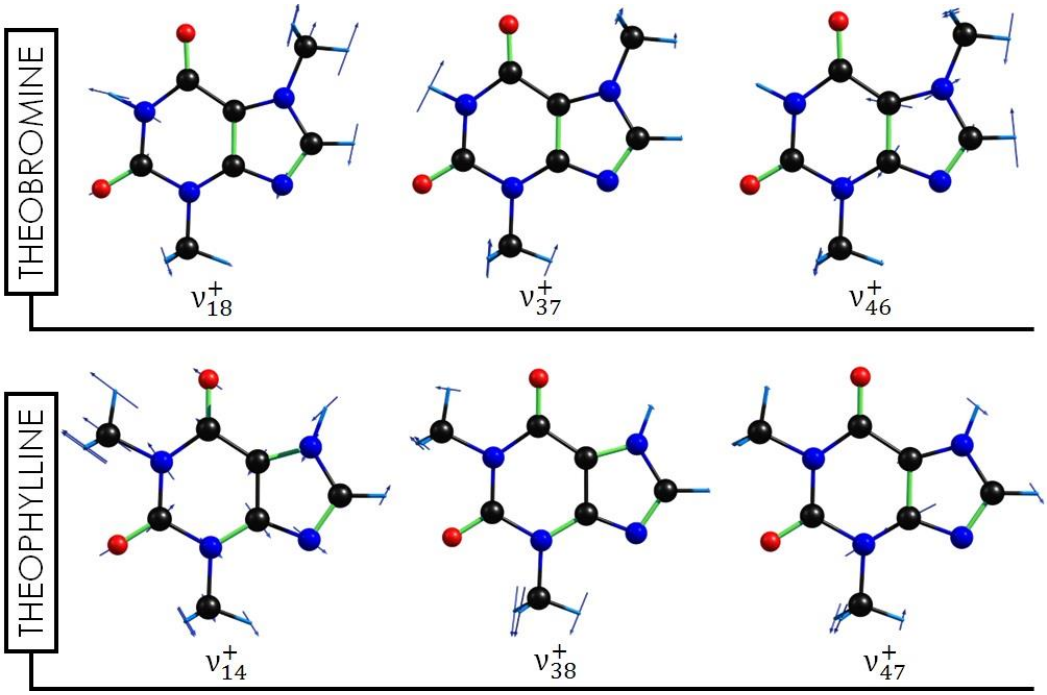

7.8 Irudia: TB-ren eta TP-ren PEPICO espektroetan aktibitate handien aurkezten duten bibrazio-moduen arteko konparaketa. Kalkuluak I_0^+ egoeran egin ziren CAM-B3LYP/aug-cc-pVDZ mailarekin.

Aurreko behaketek nukleobaseen egoera kitzikatuaren dinamikekin aurka daude.[5] Ikerketa esperimental zein konputazionalak purina eta pirimidina nukleobaseetan kitzikapen elektronikoak eraztunaren deformazioa eragiten duela ondorioztatzen zuten. Hala ere, deformazioa koordenatu desberdinetan gertatzen da, zeinak ordezkatzailearen menpe dauden. Adibidez, deformazio-koordenatua C5=C6 da pirimidina baseen kasuan; eta amino talde baten ordezkapena C4 posizioan, bigarren deformazio bat eragiten du C2-an.[20-29] Amino taldea C2-an ordezkatzen bada, aldiz, deformazioa ezeztu egiten da. Bestalde, guaninaren C1-ren metilazioak ns-ko erdibizitzak sortzen du, $n\pi^*$-$\pi\pi^*$ ebakidura-konikoaren desagerpenaren ondorioz.[30]

Lan honen emaitzen arabera, metilo taldeen kokapena egoera kitzikatuaren dinamika nabarmenki aldatzen du. Horrez gain, ordezkapena N7-an ematen denean, metilo taldearen tortsioaren eta eraztunaren deformazioaren artean akoplamendu bat dagoela frogatu da. Hala ere, hori $n\pi^*$ egoeraren egonkortasun desberdinaren ondorioa ere izan daiteke, zeina N atomoen elektroi-pare bakartien kitzikapenaren bitartez eraikitzen den.[31] Horren arabera, elektroi-ezparekatu desberdinak kitzikatzen dira TB-an

TP-rekin alderatuta, energia maila kitzikatuen arteko aldea aldatuz. Hortaz, metilazioak egoera kitzikatuaren dinamika bi modutan alda ditzake: metil taldeen tortsioen eta eraztunaren deformazioaren arteko akoplamendua hobetuz, edota maila elektroniko kitzikatuen arteko ordena aldatuz. Metilo taldeen tortsioen eta bibrazio molekularren arteko akoplamendua molekularen fotofisikan ere eragina dauka, bibrazio-energia intramolekularraren sakabanaketan lagunduz. [13,14,32-36]

Nukleobaseen portaeran ikusitako desberdintasunak xantinekin alderatuz gero $n\pi^*$ egoeren kokapen ezberdinei izan daiteke, jadanik lehen egoera kitzikatuarekin gainezarrita dagoena nahiz eta metilaziorik ez egon. Gainera, egoera horrek badirudi N-H lotutaren disoziazioarekin erlazionatuta dagoela, ezinezkoa dena xantina molekuletan.[37] Dena den, hemen aurkeztutako emaitzak nukleobaseetan egindako aldaketak kontuan hartzea garrantzitsua dela adierazten dute beraien fotofisikaren azterketarako.

7.5. Ondorioak

Kapitulu honetan teofilinaren eta teobrominaren ikerketa espektroskopiko sakona aurkezten da. Bi molekulen arteko desberdintasun bakarra metilo taldeen kokapena da. Hala ere, alde txiki horrek nahikoa da kitzikapen espektroan aldaketa nabarmenak sortarazteko. N7-an kokatutako metilo taldearen tortsioen eta eraztun aromatikoaren bibrazio-moduen arteko akoplamendua dela eta, teobrominaren REMPI espektroak teofilinarena baino espektroskopia aberatsagoa aurkezten du. Nahiz eta ionizazio energia adiabatiko antzekoak izan, ZEKE eta TPE espektroak adierazten duten moduan, berriro ere egitura aberatsago bat aurkitzen da TB-ren ZEKE espektroan, S_1 egoeran ematen den geometriaren aldaketa bati esleitutakoa. Bi molekulek nolabaiteko aktibitate bibrazionala aurkezten dute PEPICO espektroetan, katioian ematen diren geometria aldaketak direla eta. Aldaketa horiek eraztun aromatikoaren bibrazioei dagozkiela ondorioztatu da.

Nukleobaseekin alderatuta, metilo ordezkatzaileen joera desberdina behatu da. Xantinen kasuan, metiloen ordezkapenak $n\pi^*$ egoeraren sorpenean ekarpenak ditu, zeinak $\pi\pi^*$ egoera kitzikatuarekin gainezar daitekeena. Gainera, emaitza hauek ordezkatutako nukleobaseei buruzko ikerketa fotofisikoen garrantzia azpimarratzen dute.

7.6. Erreferentziak

[1] A. C. Rios and Y. Tor, On the Origin of the Canonical Nucleobases: An Assessment of Selection Pressures across Chemical and Early Biological Evolution, *Isr. J. Chem.*, 2013, **53**, 469–483.

[2] S. Mondal and M. Puranik, Ultrafast structural dynamics of photoexcited adenine, *Phys. Chem. Chem. Phys.*, 2017, **19**, 20224–20240.

[3] A. A. Beckstead, Y. Zhang, M. S. de Vries and B. Kohler, Life in the light: nucleic acid photoproperties as a legacy of chemical evolution, *Phys. Chem. Chem. Phys.*, 2016, **18**, 24228–24238.

[4] M. M. Brister, M. Pollum and C. E. Crespo-Hernández, Photochemical etiology of promising ancestors of the RNA nucleobases, *Phys. Chem. Chem. Phys.*, 2016, **18**, 20097–20103.

[5] C. E. Crespo-Hernández, B. Cohen, P. M. Hare and B. Kohler, Ultrafast Excited-State Dynamics in Nucleic Acids, *Chem. Rev.*, 2004, **104**, 1977–2020.

[6] K. Nemeková, J. Labuda, V. Milata, J. Blakoviová and J. Sochr, Interaction of DNA and mononucleotides with theophylline investigated using electrochemical biosensors and biosensing, *Bioelectrochemistry*, 2018, **123**, 182–189.

[7] G. R. Zimmermann, R. D. Jenison, C. L. Wick, J.-P. Simorre and A. Pardi, Interlocking structural motifs mediate molecular discrimination by a theophylline-binding RNA, *Nat. Struct. Biol.*, 1997, **4**, 644–649.

[8] G. M. HILL, D. M. MORIARITY and W. N. SETZER, *Sci. Pharm.*, 2011, 79.

[9] M. P. Callahan, Z. Gengeliczki, N. Svadlenak, H. Valdes, P. Hobza and M. S. de Vries, Non-standard base pairing and stacked structures in methyl xanthine clusters, *Phys. Chem. Chem. Phys.*, 2008, **10**, 2819–2826.

[10] D. Kim, K. Y. Yang, H. M. Kim, T.-R. Kim, N. J. Kim, S. Shin and S. K. Kim, Site-dependent effects of methylation on the electronic spectra of jet-cooled methylated xanthine compounds, *Phys. Chem. Chem. Phys.*, 2017, **19**, 22375–22384.

[11] A. Bhattacherjee and S. Wategaonkar, Conformational preferences of monohydrated clusters of imidazole derivatives revisited, *Phys. Chem. Chem. Phys.*, 2015, **17**, 20080–20092.

[12] L. Nahon, N. de Oliveira, G. A. Garcia, J.-F. Gil, B. Pilette, O. Marcouillé, B. Lagarde and F. Polack, DESIRS: a state-of-the-art VUV beamline featuring high resolution and variable polarization for spectroscopy and dichroism at SOLEIL, *J. Synchrotron Radiat.*, 2012, **19**, 508–520.

[13] A. M. Gardner, W. D. Tuttle, L. Whalley, A. Claydon, J. H. Carter and T. G. Wright, Torsion and vibration-torsion levels of the S1 and ground cation electronic states of para-fluorotoluene, *J. Chem. Phys.*, 2016, **145**, 124307.

[14] L. D. Stewart, J. R. Gascooke and W. D. Lawrance, A strong interaction between torsion and vibration in S0 and S1 m-fluorotoluene, *J. Chem. Phys.*, 2019, **150**, 174303.

[15] H. Y. Zhao, K.-C. Lau, G. A. Garcia, L. Nahon, S. Carniato, L. Poisson, M. Schwell, M. M. Al-Mogren and M. Hochlaf, Unveiling the complex vibronic structure of the canonical adenine cation, *Phys. Chem. Chem. Phys.*, 2018, **20**, 20756–20765.

[16] C. M. Western, PGOPHER: A program for simulating rotational, vibrational and electronic spectra, *J. Quant. Spectrosc. Radiat. Transf.*, 2017, **186**, 221–242.

[17] C. M. Western and B. E. Billinghurst, Automatic and semi-automatic assignment and fitting of spectra with PGOPHER, *Phys. Chem. Chem. Phys.*, 2019, **21**, 13986–13999.

[18] D. Kim, H. M. Kim, K. Y. Yang, S. K. Kim and N. J. Kim, Molecular beam resonant two-photon ionization study of caffeine and its hydrated clusters, *J. Chem. Phys.*, 2008, **128**, 134310.

[19] H. Ottosson, Exciting excited-state aromaticity, *Nat. Chem.*, 2012, **4**, 969–971.

[20] C. Plützer and K. Kleinermanns, Tautomers and electronic states of jet-cooled adenine investigated by double resonance spectroscopy, *Phys. Chem. Chem. Phys.*, 2002, **4**, 4877–4882.

[21] C. Plützer, E. Nir, M. S. de Vries and K. Kleinermanns, IR–UV double-resonance spectroscopy of the nucleobase adenine, *Phys. Chem. Chem. Phys.*, 2001, **3**, 5466–5469.

[22] J. Andréasson, A. Holmén and B. Albinsson, The Photophysical Properties of the Adenine Chromophore, *J. Phys. Chem. B*, 1999, **103**, 9782–9789.

[23] S. K. Mishra, M. K. Shukla and P. C. Mishra, Electronic spectra of adenine and 2-aminopurine: an ab initio study of energy level diagrams of different tautomers in gas phase and aqueous solution, *Spectrochim. Acta Part A Mol. Biomol. Spectrosc.*, 2000, **56**, 1355–1384.

[24] D. C. Lührs, J. Viallon and I. Fischer, Excited state spectroscopy and dynamics of isolated adenine and 9-methyladenine, *Phys. Chem. Chem. Phys.*, 2001, **3**, 1827–1831.

[25] H. Kang, B. Jung and S. K. Kim, Mechanism for ultrafast internal conversion of adenine, *J. Chem. Phys.*, 2003, **118**, 6717–6719.

[26] A. L. Sobolewski and W. Domcke, On the mechanism of nonradiative decay of DNA bases: ab initio and TDDFT results for the excited states of 9H-adenine, *Eur. Phys. J. D - At. Mol. Opt. Plasma Phys.*, 2002, **20**, 369–374.

[27] M. Barbatti and H. Lischka, Can the Nonadiabatic Photodynamics of Aminopyrimidine Be a Model for the Ultrafast Deactivation of Adenine?, *J. Phys. Chem. A*, 2007, **111**, 2852–2858.

[28] I. Hünig, C. Plützer, K. A. Seefeld, D. Löwenich, M. Nispel and K. Kleinermanns, Photostability of Isolated and Paired Nucleobases: NH Dissociation of Adenine and Hydrogen Transfer in its Base Pairs Examined by Laser Spectroscopy, *ChemPhysChem*, 2004, **5**, 1427–1431.

[29] C. M. Marian, A new pathway for the rapid decay of electronically excited adenine, *J. Chem. Phys.*, 2005, **122**, 104314.

[30] C. M. Marian, The Guanine Tautomer Puzzle: Quantum Chemical Investigation of Ground and Excited States, *J. Phys. Chem. A*, 2007, **111**, 1545–1553.

[31] M. S. de Vries, eds. A. M. Rijs and J. Oomens, Springer International Publishing, Cham, 2015, pp. 271–297.

[32] W. D. Tuttle, A. M. Gardner, L. E. Whalley and T. G. Wright, Vibration and vibration-torsion levels of the S1 state of para-fluorotoluene in the 580–830 cm−1 range: Interactions and coincidences, *J. Chem. Phys.*, 2017, **146**, 244310.

[33] D. J. Kemp, E. F. Fryer, A. R. Davies and T. G. Wright, Vibration-modified torsional potentials and vibration-torsion ("vibtor") levels in the m-fluorotoluene cation, *J. Chem. Phys.*, 2019, **151**, 84311.

[34] D. J. Kemp, L. E. Whalley, A. M. Gardner, W. D. Tuttle, L. G. Warner and T. G. Wright, Complexity surrounding an apparently simple Fermi resonance in p-fluorotoluene revealed using two-dimensional laser-induced fluorescence (2D-LIF) spectroscopy, *J. Chem. Phys.*, 2019, **150**, 64306.

[35] J. R. Gascooke, L. D. Stewart, P. G. Sibley and W. D. Lawrance, Pervasive interactions between methyl torsion and low frequency vibrations in S0 and S1 p-fluorotoluene, *J. Chem. Phys.*, 2018, **149**, 74301.

[36] J. R. Gascooke, E. A. Virgo and W. D. Lawrance, Torsion-vibration coupling in S1 toluene: Implications for IVR, the torsional barrier height, and rotational constants, *J. Chem. Phys.*, 2015, **143**, 44313.

[37] M. Zierhut, W. Roth and I. Fischer, Dynamics of H-atom loss in adenine, *Phys. Chem. Chem. Phys.*, 2004, **6**, 5178–5183.

9. Kapitulua

Ondorioak

9.1. Ondorioak

Agregazioen mekanismoak, prozesu horiek gidatzen dituzten elkarrekintza ez-kobalenteak, eta talde funtzional biologikoki esanguratsuak dituzten sistema-ereduen egituren karakterizazioa aztertu egin dira, metodologia esperimental eta teorikoen konbinaketa erabiliz. Lortutako emaitzek erabilitako metodologia horren eraginkortasuna frogatzen dute. Metodo konputazionalen etengabeko garapena eta horien aurreikuspenen zehaztasunaren hobekuntzak gero eta konplexutasun handiagoa duten molekula agregatuen esplorazioa bultzatzen du.

Bentzil alkohol eta 2-feniletanol alkohol aromatikoei buruzko ikerketek OH···O hidrogeno loturek agregazio prozesuaren elkarrekintza nagusia direla ezagutarazi dute; aldiz, OH···π eta π-π elkarrekintza gehigarriek konplexuen azken egitura moldatzen dute. Konplexuen molekula kopurua handitzeak, egitura linealen eta ziklikoen arteko trantsizio-puntua aurkitzea ahalbidetu du. Trimeroek, oraindik, OH···OH···OH···π elkarrekintza linealak aurkezten dute, OH···π loturaren sendotasun erlatibori esker, eta kontuan izanda molekula emailearen eraso-angeluan hain zorrotza ez dela. Hori dela eta, gainerako molekulek molda daitezke gainontzeko elkarrekintzen indarrak maximizatzeko. Laugarren molekularen adizioarekin, monomeroek hidrogeno lotura sare ziklikoak eratzen dituzte, lotura-angeluen tentsio txikiago bati esker. Mota honetako egiturek egonkorragoak dira efektu kooperatiboei esker, zeinak, orokorrean, agregatuen egonkortasuna nabarmenki handitzen duen.

Azukre deribatuen agregazio lehentasunen karakterizazioa oso interesgarria da, hidroxilo taldeek dituzten malgutasun altua dela eta. Gainera, azukreek aurkezten duten malgutasun altuak immunitate sisteman jokatzen duten eginkizunarekin zuzenki erlazionatuta dago. 4.Kapituluan, fenil-β,D-glukopiranosa molekula desberdinekin konbinatu egin da, molekula edo talde desberdinekin sortzen dituen elkarrekintzak ulertzeko asmoz.

N-metilazetamidarekin, parazetamolarekin edo fenolarekin eratutako konplexuetan, fenil-β,D-glukopiranosak O2H eta O6H hidroxilo taldeekin hidrogeno loturak sortzeko lehentasuna aurkeztu egin ditu. Gainera, ordezkatzaile aromatikoa elkarrekintza horiek sendotzeko joera duela behatu da. β-PhGlc+Par eta β-MeGlc+Par dimeroen lotura-energien arteko aldarapenak eraztun aromatikoak ~20 kJ/mol-eko handipena sortarazten duela erakutsi du, 51 kJ/mol-tik 70.5 kJ/mol-tara. Beraz, eraztun aromatikoaren presentziak mespretxagarria ez den modulazioa bat ezartzen du Glc-ren

agregazioan. Horrek esan nahi du, O1 posizioaren ordezkapena tamaina handiko talde batekin azukrearen elkarrekintzen lehentasuna alda dezakeela. Antzeko lehentasunen aldaketa bat behatu egin da β-PhGlc eta β-PhGal homo-dimeroekin, non C_4 posizioaren egituraren aldaketa txikiak, OH taldea axialetik ekuatorialera, nabarmenki aldatzen duela dimeroen egitura.

Azkenik, azukre unitateen pilaketa elkarrekintzak sortzeko joera aztertu ditugu Caf+PhGlc dimeroan. Zalantzarik gabe, pilaketa elkarrekintzak espezifikotasun baxua aurkezten dute, eta gainontzeko hidrogeno loturak behar ditu orientazio jakin bat faboratzeko.

Azukre agregatuen ikerketek oinarri gisa balio izan zuten konplexu handiagotara mugitzeko. GL1 eta GLOMe molekula nahiko konplexuak dira, zeinak glukolipidoen lehentasun konformazionalak aztertzeko eredu gisa hartu diren. Sistema hauetan, O3H taldeak gantz-azido baten ordez ordezkatu egin da. Lortutako emaitzak karbonilo taldearen influentzia azpimarratzen du, zeinak ordezkatu gabeko monosakaridoetan aurkezten den hidrogeno lotura sarearen kooperatibitatea apurtzen du. Aldiz, alkil katearen presentziak ez du hidroxilo taldeen lotzeko lehentasuna aldatzen. Glukolipidoen konplexu mono-hidratatuan, espero ez ziren elkarrekintzak isolatu dira. Karbonilo taldearen presentziak nabarmenki aldatzen du urak lotzeko lehentasuna, ordezkatu gabeko ur-azukre konplexuetan behatzen den "gune aktibo" edo lotura-gune oso desberdin bat sortaraziz.

Tesi honen azken ataletan, xantina agregatuen espektroskopia aztertu da. Caf+Ph zailtasun handiko dimeroa izan da, non metodologia konputazional hedatuago baten erabilera behar izan duena elkarrekintza ez-kobalenteen karakterizazio zuzena lortzeko. Fenol eta kafeinaren artean π-π pilaketa elkarrekintzak eta nahiko sendoak diren hidrogeno loturak sortzen direla ondorioztatu da. Datu esperimentalekiko konparaketak, metodo konputazionalek elkarrekintza ez-kobalente desberdinen oreka batez eratutako konplexuen deskribapenak egiteko arazoak azpimarratu ditu.

Xantinen eta bestelako molekulen arteko elkarrekintzen azterketak elkarrekintza ez-kobalenteen garrantziarekin espekulatzea ahalbidetu du kimika prebiotikoaren lehen alditan. Xantina deribatuen eta nukleobaseen arteko agregazio lehentasunetan ez dira behatu aldaketa nabarmenik. Izan ere, lan honetan aurkeztutako emaitzak, adenina eta teobrominaren arteko trimeroetan pilaketa motako egiturak sortzen direla erakusten dute. Joera hori, DNA-ren helize bikoitzetan ere antzematen dena, anplifikatuta egon ahal da disoluzioan, molekula hauen hidrofobizitate altua kontuan hartuz gero. Emaitza

horiek panorama prebiotiko konplexu bat adierazten dute, non konposatu organiko kopuru zenbatezina agregatu egonkorrak eratzeko lehiatzen duten, nolabait, molekula berriak auto-katalizatzeko.